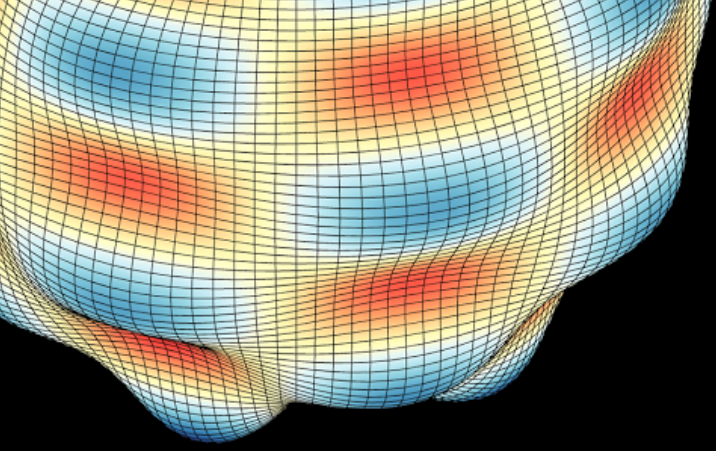

DEVELOPMENT OF INVERSION TECHNIQUES IN ASTEROSEISMOLOGY

Gaël Buldgen

Université de Liège
Faculté des sciences
Département d'Astrophysique, de Géophysique et d'Océanographie

Université de Liège
Faculté des sciences
Département d'Astrophysique, de Géophysique et d'Océanographie

DEVELOPMENT OF INVERSION TECHNIQUES IN ASTEROSISMOLOGY

Gaël Buldgen

Astrophysique **S**tellaire **T**héorique et **A**stérosismologie

Sart-Tilman
Liège, Belgique
Année Académique 2016 – 2017

Supervisors :
Prof. Marc-Antoine Dupret
Dr. Daniel Reese

Dissertation submitted in partial fulfilment
of the requirements for the degree of
Doctor of Philosophy in Science.

Jury Members:
Prof. Marc-Antoine Dupret (Co-Supervisor, Université de Liège)
Dr. Daniel R. Reese (Co-Supervisor, Observatoire de Paris-Meudon)
Prof. Arlette Noels-Grötsch (Université de Liège)
Prof. Georges Meynet (Observatoire de Genève)
Dr. Andrea Miglio (University of Birmingham)
Prof. Ian Roxburgh (Queen Mary University of London)
Prof. Jørgen Christensen-Dalsgaard (Stellar Astrophysics Centre, Aarhus)
Dr. Valérie Van Grootel (Secretary, Université de Liège)
Prof. Pierre Magain (President of the Jury, Université de Liège)

ABSTRACT

Stars are born, evolve and die. A small sentence, a simple statement implying great consequences for our vision of the Universe. Throughout the history of mankind, we have attempted to grasp the nature of the objects in the night, basing our reasoning on religious or philosophical considerations, or scientific arguments. We have come a long way since the days of unalterable perfect spheres, understanding that stars generate their energy through nuclear fusion and are the chemical engines at the origin of the most of the heavy elements of the Universe, even those composing our bodies. As a result, we can state, thanks to stellar evolution theory, that we are all stardust.

Stellar evolution has encountered many successes during the 20^{th} century and is now considered one of the most well constrained theory in astrophysics. These successes are due to improvements of theoretical modelling and continuous confrontations to observations. It is of course impossible to witness the evolution of a star directly, since the timescales involved are far greater than any human life. It is also impossible to analyse directly the internal structure of stars since their opacity makes it impossible for any photon to escape directly from the inner regions of the star.

The problem of the timescales of stellar evolution is solved by looking at many different stars. Indeed, the night sky offers a snapshot of the lifetime of different objects of different masses, ages and chemical compositions. Studying clusters allowed for the first tests of the theory of stellar evolution and improved greatly the way we compute stellar models. In opposition, studying the internal structure of individual stars was for long very complicated. Fortunately, the stars are not only subject to changes on large timescales. In fact, a vast number of them present pulsations, a dynamical phenomenon similar to earthquakes. As seismologists on earth use seisms to constrain the internal structure of the earth, so do asteroseismologists constrain the internal structure of stars by listening to their pulsations.

In this work, we will focus on developing and applying specific techniques to extract relevant structural information out of stellar oscillation spectra. We will base our approach on so-called linear inversion techniques using the variational analysis of stellar pulsation equations. First, we will show how these methods can be adapted to extract specific indicators focusing the information of the oscillation spectra on individual quantities related to specific physical aspects of stellar structure. We will show how these quantities can provide additional constraints in the modelling of solar-like stars and help us build more accurate models of stellar structure by testing their physical ingredients. After having presented the theoretical developments, we will present a few applications to solar-like stars, like the 16Cygni binary system and a few targets of the Kepler LEGACY sample. We will show the crucial role of inversion techniques in further reducing the uncertainties on fundamental parameters of stars such as mass, radius and age, which play a crucial role in multiple domains of astrophysics.

Besides those specific cases, we will take a long look at our star, the Sun, and present new developments in the field of global helioseismology. The results presented in this chapter indicate that the solar modelling problem seem to stem from inaccuracies in various physical ingredients other than the chemical abundances of heavy elements. With these results, we demonstrate the need for a full re-investigation of the solar problem. Consequently, a collaborative effort of the community is required if asteroseismology is, as argued by many authors, to play a key role in astrophysics by determining precise and accurate stellar masses, radii and ages.

RESUME

Les étoiles naissent, évoluent et meurent. Cette phrase, en apparence innocente, a de fortes implications sur notre vision de l'Univers. Au cours de l'histoire de l'humanité, nous avons tenté de saisir la nature des objets célestes, à l'aide d'arguments religieux, philosophiques ou de raisonnements scientifiques. Beaucoup de chemin a été parcouru depuis les jours où les étoiles étaient vues comme des sphères parfaites et immuables. Aujourd'hui, nous savons que les étoiles produisent leur énergie par fusion thermonucléaire en leur coeur et sont ainsi les moteurs chimiques à l'origine de presque tous les éléments lourds de l'Univers, y compris ceux constituant le corps humain. Ainsi, nous pouvons affirmer grâce à la théorie de l'évolution stellaire que nous sommes tous des poussières d'étoiles.

Durant le $20^{ième}$ siècle, l'évolution stellaire a rencontré de nombreux succès et est désormais considérée comme une des théories les mieux établie en astrophysique. Ces succès sont dus aux améliorations constantes des modèles théoriques et à leur confrontation aux observations. Il est bien entendu impossible de suivre directement l'évolution d'une étoile, car les échelles temporelles associées dépassent largement la durée de vie humaine. De même, il est impossible d'analyser directement la structure interne d'une étoile, car leur opacité empêche les photons de s'échapper directement des couches internes et d'ainsi nous transmettre leurs informations.

Le problème des échelles de temps peut être résolu par l'observation d'une multitude d'étoiles. En effet, le ciel nocturne offre la possibilité d'analyser simultanément un instant de la vie de milliers d'étoiles de masses, d'âges et de compositions chimique différents. Ainsi, l'étude d'amas d'étoiles a déjà permis de fortes améliorations des modèles stellaires. Au contraire, l'étude de la structure interne d'étoiles individuelles s'est longtemps révélée bien plus ardue. Fort heureusement, un grand nombre d'étoiles présentent des variations sur des échelles de temps très courtes, associées à leur pulsations, similaires aux séismes que nous connaissons. Ainsi, comme les sismologues usent des séismes pour étudier la structure interne de notre planète, les astérosismologues sondent la structure interne des étoiles en écoutant leurs pulsations.

Dans ce travail, nous nous concentrerons sur le développement et l'application de techniques spécifiques visant à extraire un maximum d'informations utiles des spectres d'oscillations stellaires. Notre approche fera usage de techniques d'inversions linéaires se basant sur l'analyse variationnelle des équations de pulsations stellaires. Dans un premier temps, nous montrerons comment ces méthodes peuvent être adaptées afin de concentrer toute l'information du spectre d'oscillation dans des indicateurs spécifiques reliés à des aspects précis de la structure stellaire. Nous montrerons que ces quantités servent alors de contraintes additionnelles aux modèles stellaires et permettent d'améliorer grandement l'exactitude de ces modèles et de tester leurs ingrédients physiques. Après avoir présenté les développements théoriques, nous décrirons l'application de ces méthodes au système binaire 16Cygni ainsi que quelques cibles de l'échantillon du Kepler LEGACY. Nous montrerons le rôle crucial des inversions dans la réduction des incertitudes sur les paramètres fondamentaux des étoiles tels que la masse, l'âge et le rayon, qui jouent un rôle central dans d'autres domaines de l'astrophysique.

A coté de ces quelques études spécifiques, nous reviendrons longuement sur notre étoile, le Soleil, et présenterons de nouveaux développements dans le domaine de l'héliosismologie globale. Les résultats présentés dans le présent manuscrit semblent indiquer que le problème des modèles solaires résulte d'erreurs dans un ensemble d'ingrédients physiques autres que les abondances des éléments lourds. Grâce à ces résultats, nous démontrons la nécessité d'une ré-étude complète du problème solaire. En conséquence, un effort collaboratif de la communauté est requis afin de permettre, comme le prétendent divers auteurs, à l'astérosismologie de jouer son rôle de référence pour d'autres champs de l'astrophysique dans la détermination des masses, âges et rayons stellaires.

REMERCIEMENTS

Au moment d'achever ce manuscrit résumant 4 années de travail, il convient de prendre un instant pour remercier, certainement insuffisamment, les personnes qui y ont contribué.

Tout d'abord, il me faut remercier mes promoteurs, Marc-Antoine et Daniel. C'est grâce à leurs enseignements, à leur rigueur et à leur soutien permament que ce travail a pu être réalisé. Merci à Daniel pour ses conseils pour dénouer le code "spaghetti" qu'est InversionKit (bien que je craigne qu'il ne soit pas devenu plus lisible avec mes apports), pour ses qualités d'enseignant, sa patience et sa rigueur qui m'ont permis d'apprendre tant de choses durant cette thèse. Merci à Marc-Antoine pour son soutien quotidien et les heures de discussion passées dans son bureau, pour son enthousiasme et son ouverture d'esprit devant chaque problème rencontré, quelle que soit sa complexité.

Il me faut ensuite remercier Arlette, pour son aide précieuse durant ces 4 années de thèse, pour son énergie, sa bienveillance et les connaissances et l'expérience qu'elle partage sans compter avec les membres du groupe.

Merci également à Richard, pour son travail acharné sur CLES et LOSC, sa réactivité face à chaque bug, problème ou requête d'un utilisateur malhabile, qui ont été indispensables à chaque étape de cette thèse. Merci aussi à Mélanie, pour sa participation aux modifications soutenues de CLES.

Un tout grand merci à Sébastien, pour ses heures de discussions et d'échanges, pour ses relectures acharnées des articles et de ce manuscrit, mais aussi pour avoir partagé avec moi ses grandes connaissances en physique stellaire et en astérosismologie.

I also wish to thank all members of the jury, for taking the time to read this manuscript. Especially, I wish to thank the external members for their trip to Liège to take part in the defence. Thank you Andrea for allowing me to come to Birmingham and for the fruitful discussions about my project. Thank you Prof. Christensen-Dalsgaard for inviting me twice in Aarhus and for the interest you have shown for my work. Thank you Prof. Roxburgh for your questions and discussions in conferences. Merci à vous, Prof. Meynet pour les discussions intéressantes lors de mon séjour à Genève et pour votre accueil chaleureux. Merci également au Prof. Pierre Magain et au Dr. Valérie Van Grootel d'avoir accepté de prendre part à mon jury de thèse en qualité de président et secrétaire.

Ensuite, merci aux autres membres du groupe ASTA et aux résidents du B5c +1. Merci à Nicolas Grevesse, pour son enthousiasme, ses connaissances et ses encouragements permanents. Merci à Judith, Clémentine, Artem, Fran, Audrey, Alice, Manu, Michaël et Monika pour la formidable ambiance qu'ils insufflent (ou ont insufflé) à l'étage. Merci à Catarina et Mathieu pour m'avoir supporté (respectivement deux ans chacun) dans leur bureau. Merci à Sandrine et Angela pour leur aide face aux nombreux problèmes techniques/administratifs que j'ai pu rencontrer durant ma thèse. Parmi les résidents de l'étage, je me dois également de remercier tout particulièrement Laetitia et Cyrielle, pour m'avoir accueilli lors des "pauses café" durant 3 ans avant de me laisser la machine et le sofa lors de leur départ. Leur responsabilité dans le travail abattu durant cette thèse est loin d'être négligeable.

Merci également aux membres de la communauté rencontrés en conférence, tout particulièrement à Charly, Rhita, Mathieu, Kevin et Patrick, pour les discussions intéressantes, les soirées passées ensemble et leur compagnie durant les semaines de conférences. Merci à Olivier et Morgan pour leur accueil à Montpellier lors de ce séjour fructueux.

Il me faut également remercier ma famille, mes parents, mon frère et ma soeur pour leur soutien durant cette thèse. Je tiens à remercier tout particulièrement mon parrain, Xavier, pour sa soif de savoir contagieuse et ses qualités humaines. Merci aussi aux amis, anciens du master astro, du bachelier physique, pour leur présence durant mon passage à l'Ulg et pour les soirées mémorables passées ensemble. Vielen Dank an die Mitglieder von Dojang Belgien (ja Johannes... du auch...), für ihre Unterstützung und für den Training der geholfen hat, Blut von meinem Kopf wegzunehmen während der Zeit dieser Arbeit.

Enfin, et bien évidemment, merci à Fatima, pour son amour, sa présence et son soutien infaillibles à mes cotés durant ces années parfois difficiles. Il n'est pas un mystère pour ceux qui la pratiquent que la recherche peut être source de joie comme de frustrations, et qu'un résultat est souvent précédé par une multitude d'échecs. Qu'il me soit permis ici de dire que je ne te remercierai jamais assez pour avoir supporté mes échecs, mes doutes et mes peurs continuellement durant toutes ces années et qu'il n'est pour moi de plus grand bonheur que de te savoir auprès de moi.

CONTENTS

1. INTRODUCTION, CONTEXT AND OVERVIEW

1.1 A brief history of stellar seismology

Stellar variability was observed for the first time 400 years ago, when Fabricius noticed the recurring luminosity variations of Mira Ceti. Yet, it is only in 1927 that Eddington discussed the potential of stellar pulsations to test the physical conditions of stellar structure. Two decades later, the theory of stellar pulsations, the forefather of modern asteroseismology, was established in Liège by Paul Ledoux (Ledoux and Walraven (1958), Ledoux and Smeyers (1966)).

During the next 50 years, the field evolved at a steady pace. Solar oscillations were observed for the first time in 1960 and 1962 (Leighton (1960), Leighton, Noyes, and Simon (1962)). However, their nature was only confirmed in 1975 (Deubner (1975)) and their origin discussed by Stein and Leibacher (1974). The large frequency separation (see section 3.2), defining the regular properties appearing in the power spectra of stellar acoustic oscillations, theorised by Vandakurov (1967), was observed by Claverie et al. (1979). Meanwhile, the ability to classify individual solar pulsation modes (Scuflaire (1974b)) paved the way for more developed seismic investigations. In the meantime, the effects of rotation on solar pulsations were observed and discussed (Rhodes, Ulrich, and Deubner (1979), Ulrich, Rhodes, and Deubner (1979), Deubner, Ulrich, and Rhodes (1979)).

The late 80s saw the beginning of the development of inversion techniques in helioseismology, first to determine the rotational profile of the Sun (Kosovichev (1988)), then its acoustic structure (Kosovichev and Fedorova (1991), Christensen-Dalsgaard, D. Gough, and Toomre (1985), Antia and Basu (1994b)). These investigations helped to refine our views of solar structure and the issues they unveiled are still at stake today. For example, Spiegel and Zahn (1992) provided a theoretical description of the transition region between the convective and radiative zone of the Sun, called the tachocline. In this region, it is believed that turbulence, rotation and potentially the magnetic field come into play and a full physical description of this region still lacks today. The importance of microscopic diffusion was demonstrated with helioseismic inversions (Basu, Christensen-Dalsgaard, Schou, et al. (1996)) and solar models showed that the solution of the famous solar neutrino

problem was to be found in theoretical physics (Bahcall and Peña-Garay (2004)). All these successes led to the definition of the framework of the standard solar model (Bahcall, Huebner, et al. (1982)), now widely applied to study stars other than the Sun.

However, while helioseismology was providing striking examples of the potential of stellar pulsations, asteroseismology of solar-like stars was having more difficult beginnings. The very low amplitude of solar-like oscillations hindered their detection and confirmation from ground-based observations. The first confirmed observations of solar-like oscillations were made on Procyon in 1999, nearly ten years after their first observations (T. M. Brown, Gilliland, et al. (1991)). Other pulsations were detected on η *Boo* (Kjeldsen, Bedding, Baldry, et al. (2003)), β *Hyi* (Bedding, Butler, et al. (2001)) and α *Cen* (Bouchy and Carrier (2001)). Detailed seismic modelling was only possible for α *Cen* (see Miglio and Montalbán (2005)) since other stars did not show enough individual modes to derive strong seismic constraints from the observations.

In 1999, the WIRE mission was recycled into observing stellar pulsations after its initial technical difficulties. This spacecraft was followed in 2003 by the Canadian MOST satellite, the first mission specially dedicated to asteroseismic observations. However, the real breakthrough was achieved by the CoRoT mission (Baglin et al. (2009)) launched in 2006, followed soon after by the Kepler mission (Borucki et al. (2010)) launched in 2009. These satellites, dedicated to both exoplanetology and asteroseismology, provided a tremendous amount of data for giants, subgiants and main-sequence stars. The combination of high quality photometry to long duration follow-ups allowed the detection of non-radial solar-like oscillations in thousands of stars (see figure 1.1 for an illustration). The major successes

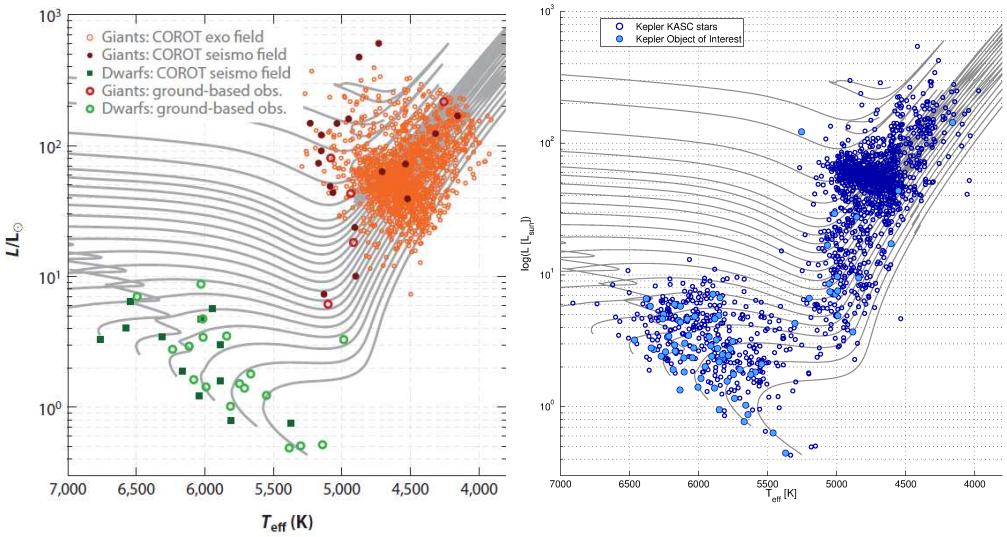

Figure 1.1: Confirmed targets of solar-like oscillations from the CoRoT (left) and Kepler (right) missions, reprinted from Chaplin and Miglio (2013).

of these missions include amongst others, the detection of the so-called mixed modes in solar-like pulsators (see section 3.1.2) which can be used to probe the core of evolved stars. The detection of non-radial oscillations in giants (De Ridder et al. (2009)) and their theoretical analysis by M.-A. Dupret, Belkacem, et al. (2009) paved the way for ensemble asteroseismology, Galactic archeology, as well as detailed studies of the transport of angular momentum during stellar evolution.

The quality of the data allowed us to test the accuracy of detailed seismic modelling and established asteroseismology as the golden path to provide fundamental parameters

of stars to other fields of astrophysics such as exoplanetology and Galactic archeology.

The CoRoT and Kepler missions are often said to have paved the way for the "space photometry revolution" and this breakthrough will soon be followed by the forthcoming TESS and Plato2.0 missions. However, as we will see later in this manuscript, seismic stellar modelling is not limited by the precision of the data anymore, but rather by the accuracy of the physical description of stellar structure. While it is of primordial importance to determine fundamental parameters through seismic studies, the primary goal of the space photometry revolution is above all to raise questions on our depictions of stellar structure and evolution using asteroseismology.

1.1.1 Seismic modelling of solar-like stars

The advent of the space photometry missions caused a significant change of scenery in asteroseismology. Where before the targets were few and the observations imprecise, stellar modellers now have high quality data for thousands of stars. For example, the very best dwarfs exhibiting solar-like oscillations have been compiled in the so-called Kepler LEGACY sample, which counts 66 stars for which precise individual frequencies can be identified. The number of individual frequencies for these stars vary from around 20 to 60 detected frequencies. The mean error vary from star to star and are found in between 0.05 and 0.003 μHz. The amount of data and its precision triggered the development of various approaches to exploit the information it contained. Fortunately, thanks to the experience acquired in helioseismology, the development of asteroseismic modelling techniques did not start from scratch. In fact, a lot of the properties of solar-like oscillations had been theoretically studied before the advent of the space photometry missions.

The use of seismic data to constrain stellar models is of course much less straightforward than in the solar case since, for most stars, fundamental parameters such as mass, radius and age are completely unknown to the modeller. Relating these parameters to seismic constraints was, and still is, a struggle (see for example Pijpers (2006) for a review of methods used in helio- and asteroseismology). Indeed, seismic data only probes the acoustic structure of stars, which implies that relating seismic data to structural constraints will always be dependent on various assumptions on the physical processes acting on stellar structure and evolution, such as, for example, the equation of state or the opacity tables used to build the stellar model, but also the hydrodynamical processes thought to act during the evolution of the observed star. Ultimately, this means that while seismic constraints are essential to ensure an accurate and precise reproduction of stellar structure (see for example the papers by Yveline Lebreton on "à la carte stellar modelling" for a clear review of the importance of seismic constraints (Lebreton, Goupil, and Montalbán (2014a), Lebreton, Goupil, and Montalbán (2014b)), the outcome of seismic modelling will be dependent on the physical ingredients used in the numerical models and on the hypotheses made on the evolution of the star.

Moreover, the use of solar-like oscillations to constrain structural models is also hindered by the presence of the so-called surface effect problem (see section 3.9). Directly using the frequencies in a minimization approach will lead to biased results that do not reproduce the inner structure of the star. Therefore, stellar seismologists use the results of theoretical analyses to determine which seismic constraints should be used to accurately reproduce the inner stellar structure. As we will see in section 3.2, the regularity of solar-like oscillation spectra allows us to define specific seismic indices, which can be used as constraints in a minimization technique. Currently, seismic fitting can be very simple, for example through the use of scaling laws based on the assumption of homology of all stars (Mosser, Belkacem, et al. (2010), Kallinger et al. (2010)), or very elaborate, for

example through the use of individual specific frequency combinations in highly efficient minimization techniques. Various modellers will have their recipe to derive their seismic model of a given star, some preferring the small frequency separations or the ratios of the small frequency separation over the large frequency separation to ensure a minimal dependency in the surface layers. Some alternative approaches have been developped, like the phase matching technique (I. W. Roxburgh (2015a)) or the ε fitting technique (I. W. Roxburgh (2016a,b)). The minimization techniques may also vary, some relying on local Levenberg-Marquardt approaches (see Miglio and Montalbán (2005), Miglio, Montalbán, and Maceroni (2007)), others preferring global MCMC techniques (Silva Aguirre, Basu, et al. (2013)), genetic algorithms (Metcalfe, Monteiro, et al. (2010)) or more recently neural networks (Verma, Hanasoge, et al. (2016)).

While the methods do vary a lot in their specific treatment of seismic information, the outcome of each approach and their roots are still very similar. In fact, each of these techniques fall into the category of the so-called "forward modelling approach", which was defined by Douglas Gough as "the execution of the forward problem using models with a few adjustable parameters and the calibration of those parameters by fitting theory to observations (D. Gough (1985))". The main problem with this approach is that it is limited to the parameter space defined beforehand. For example, one usually uses up to 5 parameters to describe the entire complexity of the structure and evolution of a given observed star. Although forward modelling is essential and allows asteroseismology to deliver constraints to other fields of astrophysics, it has its intrinsic flaws and has to be complemented by other methods to ensure the most efficient use of seismic information.

Besides the classical forward modelling technique, other approaches have been derived to determine specific characteristics of stars. For example, the so-called glitch fitting techniques rely on the fact that very sharp changes in stellar structure such as ionisation zones of abundant elements, such as helium, or the transition region from convective to radiative transport of energy will leave specific oscillating features in the frequency spectrum of the star (Houdek and D. O. Gough (2007), Monteiro, Christensen-Dalsgaard, and Thompson (1994, 2000), and Verma, Antia, et al. (2014)). By identifying those features, one can link the period of the oscillatory pattern to the acoustic depth at which the sharp transition is located. By using stellar models to reproduce the intensity of the oscillating feature associated with helium ionisation, one can also get an estimate of its abundance in the convective envelope. This is of primary importance since helium is a key element of stellar structure and cannot be constrained in solar-like stars by spectroscopy. However, since stellar models are used to calibrate the amplitude of the glitch, it should be noted that the derived abundance will be to some extent model-dependent.

1.1.2 Seismic inversions

In the previous sections, we have introduced seismic modelling and defined the "forward modelling approach". However, in the strict mathematical sense of the problem, this can already be considered as an inversion. The inversion problem is that of the inference of a given parametric model including given physical assumptions based on experimental results. Therefore, the interested reader who uses sources outside the field of solar and stellar seismology (such as Tarantola (2005) or Vogel (2002)) might be confused to find analyses techniques that would be called "forward approaches" to be qualified as "inversion techniques".

In most cases, seismic inversion techniques will refer to the determination of the profile of a given thermodynamical quantity based on asymptotic or variational integral relations between relative frequency differences and structural corrections, or between

rotational splittings and the rotational profile of the star. Non-variational inversions have also been developed (I. W. Roxburgh (2010), I. W. Roxburgh (2015b)) and can be applied to asteroseismic targets. Unfortunately, their use has been up to now rather limited and convergence difficulties have been mentionned by their developers.

Consequently, the most common inversion techniques are linked to the variational formulation used along with linear (see this work and the multiple references within) or non-linear (see Marchenkov, I. Roxburgh, and S. Vorontsov (2000), Antia (1996) or Corbard et al. (1999)) regularization techniques. As we stated in Sect. 1.1, inversion techniques were first developed in order to determine the solar rotation profile (see Thompson et al. (1996)) using the kernel formulation of Ledoux (1949).

In addition, asymptotic inversions based on the Duvall asymptotic integral relations were performed by Kosovichev and Fedorova (1991), and Christensen-Dalsgaard, Duvall, et al. (1985). In 1988, Gough & Kosovichev already foresaw that the variables in the variational relations could be changed, implying that additional quantities besides the adiabatic sound speed and the density could be probed with inversions. Later, Dziembowski, Pamyatnykh, and Sienkiewicz (1990) published the full integral expression between frequency differences and structural thermodynamical quantities based on the variational principle of stellar oscillations (Lynden-Bell and Ostriker (1967)). From there on, the scene was set for inversions to play their crucial role in the development of helioseismology and in achieving its successes (see Basu (2016), Christensen-Dalsgaard (2002), Kosovichev (2011) and references therein for thorough reviews on helioseismology). Today, inversion techniques are also used in local helioseismology (Gizon and Birch (2005)), to study the upper layers of the solar convective envelope.

The main advantage of inversions is that they do not rely on a given set of parameters[1] and thus offer additional tests of solar and stellar structure that can help refine the physical ingredients of numerical models. However, the ill-posed nature of the problem and the various hypotheses of the variational formalism still mean that inversion techniques are far from straightforward. The main question, after the successes of variational helioseismic inversions, was whether these techniques could be adapted to improve our use of asteroseismic data and provide additional tests beyond the stringent limitations of the classical forward modelling approaches. Such attempts were made by D. O. Gough and Kosovichev (1993b), D. O. Gough and Kosovichev (1993a), Basu (2003), Takata and Montgomery (2002), but were not pursued. Until very recently, the only inversion techniques successfully applied to observed asteroseismic targets are the fully non-linear techniques of Roxburgh and Voronstov (I. W. Roxburgh (2015b) and I. Roxburgh and S. Vorontsov (2003)).

1.2 Framework and objectives

Due to the current observational context and stalemates in stellar modelling, further investigating the possibilities of implementing inversions in asteroseismology became relevant. The goal of this thesis was to develop new approaches to probe various structural characteristics of stars using variational seismic inversion techniques applicable to the limited amount of data in asteroseismology. Indeed, linear structural inversions were defined for the Sun, which counts hundreds of thousands of observed oscillation modes. In the best cases of Kepler observations, having 50 individual frequencies is already considered outstanding. Moreover, not knowing the fundamental parameters of the observed star such as the mass or the radius leads to additional difficulties that are

[1] Although they do rely on various hypotheses that we will describe in detail in this manuscript.

not present in helioseismology.

Ultimately, this work tries to improve the modelling capabilities of the asteroseismic community and provide additional constraints on the models of solar-like stars. Many questions are raised and a lot still remain unanswered. With the results presented here, we hint at the limitations of linear inversion techniques, at the problem of the independency of seismic constraints, at the biases of seismic forward modelling and at the capabilities of asteroseismology to provide very accurate fundamental parameters.

However, determining accurate fundamental parameters can only be achieved by improving stellar models. In this work, we try to show that structural inversions can be used to such an end. We will show how the methods are validated in hare-and-hounds exercises and can be applied to current observed asteroseismic targets. We also re-investigate the solar metallicity problem and demonstrate the importance of the modelling of the base of the convective envelope, besides breaking the ten-year-old stalemate on the choice of the abundance tables for stellar and solar modelling. Our results point at the limitations of the standard solar model and advocate for significant investigations to improve numerical stellar models to avoid hiding physical inaccuracies behind compensatory effects.

I

THEORETICAL BACKGROUND

2. STELLAR MODELS AND THEIR PHYSICAL INPUTS

In this chapter we present a brief introduction to stellar modelling. Thanks to the increase of computational power during the 20^{th} century, stellar astrophysicists are now able to compute evolutionary sequences of numerical models without much effort. This revolution has allowed us to test stellar physics on a large scale by comparing the models to stellar clusters. In the last decade, the observation of stellar oscillations on a large number of stars paved the way for the study of individual targets using asteroseismology. In this manuscript, we will only recall the basic elements of stellar models and focus more on physical aspects rather than numerical techniques (We refer to textbooks such as those of Kippenhahn, Weigert, and A. Weiss (2012) or Maeder (2009) for more in-depth presentations).

The structure of this chapter is divided in three main subjects. First, we present the timescales associated with stellar physics and how they are used in the computation of stellar evolutionary models. We then present the equations used to describe stellar structure and evolution. We conclude with a brief discussion related to the physical ingredients of stellar models and their associated uncertainties.

2.1 Timescales of stellar evolution

The question of timescales is central both for stellar evolution and the theory of stellar pulsations. In this section, we briefly present the timescales associated with the physical phenomena occuring in stellar interiors. As we will see, their orders of magnitude are relevant to both the successes and recurring problems in our description of stellar structure.

The dynamical timescale: The dynamical time is the timescale associated with dynamical phenomena occuring in stellar interiors. It is of the order of magnitude of the free fall

time of the star. Mathematically, it is calculated with the following formula:

$$t_{dyn} = \sqrt{\frac{R^3}{GM}}, \tag{2.1}$$

with R the radius of the star, M its mass and G the gravitational constant.

A good example of a dynamical phenomenon are stellar oscillations and one can easily show that the timescale of acoustic waves is the dynamical timescale. When looking at the typical values of t_{dyn} for the Sun, one finds the typical order of magnitude observed for periods of solar oscillations (i. e. around 20 minutes.). Other, perhaps more spectacular, examples of dynamical phenomena include Supernovae explosions and initial collapse of interstellar clouds.

The Kelvin-Helmholtz timescale: This timescale is related to the cooling of the star if all sources of nuclear energy were cut off. It is considered to be a thermal timescale and is defined as:

$$t_{K-H} = \frac{GM^2}{LR}, \tag{2.2}$$

with L the luminosity of the star.

This timescale is much larger than the dynamical timescale presented before, typically for the Sun, one has an order of magnitude of 3×10^7 years. This timescale is also associated with the initial stellar contraction phases, where the gravitional energy is used to increase the temperature in the central regions. It can thus also be linked to the Virial theorem describing proto-stellar contractions.

The thermal relaxation timescale: This timescale is locally defined for each layer of the star and is related to the cooling of each of these layers. It is defined as:

$$t_{th,i} = \int_{\Delta m_i} \frac{c_V T dm}{L}, \tag{2.3}$$

with c_V the specific heat at constant volume of the layer, and T its temperature.

The relaxation timescale varies extensively with depth and can be, in upper regions, of the order of the dynamical timescale. In these regions, dynamical phenomena such as pulsations cannot be separated from thermal phenomena. This has strong implications for stellar pulsations since one often uses the adiabatic approximation, completely neglecting the thermal effects.

The nuclear timescale: The nuclear timescale is associated with the burning of chemical elements through nuclear fusion reactions and thus to changes in the chemical composition. As the longest phase of the life of stars is the so-called main sequence, where they burn hydrogen into helium in their core, the nuclear timescale is associated with hydrogen burning and is defined as:

$$t_{nuc} = \frac{E_{nuc}}{L}, \tag{2.4}$$

with E_{nuc} the energy generated by the nuclear fusion of hydrogen into helium. This timescale is much larger then all other timescales presented before.

Typically, one finds for the Sun an order of magnitude of 10^{10} years. This means that

chemical composition variations can be neglected when studying stars using dynamical phenomena such as pulsations.

The fact that the nuclear timescale is completely different from the others is extremely important for stellar evolutionary models, since it allows us to consider that we move from one equilibrium configuration to the other, applying restricted changes in the chemical composition along the evolutionary sequence. It is no surprise that the evolutionary phases that are associated with similar values of the thermal and nuclear timescales, such as the helium flash at the end of the main sequence of low mass stars, are associated with numerical problems and to this day only a few evolutionary codes are able to evolve models through these phases using specific numerical techniques.

2.2 Equations of stellar structure

Before introducing the equations of stellar pulsations and the theoretical background of seismic inference and its application to observations, a small introduction to the equations of stellar structure is necessary. As such, stellar structure is described by the classical set of partial differential equations of fluid mechanics, supplemented by the equations of energy transfer and energy generation through nuclear reactions. A stellar model is ultimately the solution of all these equations and although stars can be structurally completely different, they are still described by the same general system of equations that we will derive in the next section. However, the diversity of physical phenomena occurring in stellar interiors means that although we know the basic equations, we cannot, to this day, build completely consistent and perfectly trustworthy models of stellar structure. The problems associated with extra-mixing of chemical elements and angular momentum transfer are striking examples of the limitations and weaknesses of our understanding of stellar modelling.

2.2.1 The general case

To fully understand the hypotheses hiding behind stellar models, it is useful to start from the general equations of hydrodynamics and see what simplifications are made to reach an essentially simple system of differential equations describing stellar structure. Thus, we will start with a more general description.

The first equation used is the conservation of mass:

$$\frac{\partial \rho}{\partial t} + \vec{\nabla} \cdot (\rho \vec{v}) = 0, \tag{2.5}$$

where ρ is the local density of the fluid and $\vec{v}$ the local velocity vector. This means that we do not consider any form of mass loss in the stellar structure. However, in the upper layers of the star, the radiation pressure does induce a mass loss which is at the origin of the solar wind for example, and can cause significant changes in the evolution of massive stars and of course change the surface abundances observed in such objects. This phenomenon has to be included in the boundary conditions of equation 2.5 when relevant. For example, if we look at the Sun, we find that the solar wind accounts approximately for $10^{-14} M_\odot/year$, thus around $10^{-4} M_\odot$ for its entire stay on the main sequence. It seems negligible when considering that a $10^{-2} M_\odot$ precision on mass determinations for a solar-like star other than the Sun is currently the very best we can expect for binary systems, let alone isolated stars (see for example Pourbaix and Boffin (2016) for the αCen binary system, where a precision of $5 \times 10^{-3} M_\odot$ is achieved.).

The second equation which intervenes is the conservation of momentum for an ideal fluid

$$\frac{\partial \vec{v}}{\partial t} + \vec{v} \cdot \vec{\nabla} \vec{v} = -\vec{\nabla} \psi - \frac{\vec{\nabla} P}{\rho}, \tag{2.6}$$

where ψ is the gravitational potential and P the local pressure of the fluid. We note that we neglect here the magnetic field. The effects of rotation can be included in the definition of the velocity vector, $\vec{v}$. It is indeed well known that rotation plays a role in the way chemical elements and angular momentum are mixed during stellar evolution. However, the current failures to reproduce observations (Deheuvels, Doğan, et al. (2014) and Mosser, Goupil, et al. (2012)) illustrates the large uncertainties on how angular momentum is transported within stars and thus how rotational profiles change during the evolution. Neglecting the microscopic viscosity is justified due to the very high Reynolds number found at the temperatures of stellar interiors. However, this does not mean that turbulence does not play a role in stellar structure, as we will see later.

The third equation is Poisson's equation for the gravitational potential:

$$\triangle \psi = 4\pi G \rho. \tag{2.7}$$

Equations 2.5, 2.6 and 2.7 only take into account dynamical effects. Consequently, we have to include thermal effects, which are characterised by the energy conservation equation, the fourth equation of stellar structure:

$$T \frac{\partial S}{\partial t} + T \vec{v} \cdot \vec{\nabla} S = \varepsilon - \frac{\vec{\nabla} \cdot \vec{F}}{\rho}, \tag{2.8}$$

where T is the local temperature, S the entropy, ε the energy generation rate and $\vec{F}$ the energy flux. ε is a combination of gravitational and nuclear generation of energy, where for the second source, one has to take into account the energy loss by neutrinos when computing the energy of each nuclear reaction. The energy flux is related to the physical phenomena transporting energy through layers of stellar material. The most common phenomena are radiation and convection, although conduction plays a significant role in the degenerate core of more evolved stars. In this brief introduction, we will only present radiation and convection since they are the dominant mechanisms found in the models of main-sequence solar-like stars. We thus have the following decomposition for the energy flux

$$\vec{F} = \vec{F}_{rad} + \vec{F}_{conv}, \tag{2.9}$$

with $\vec{F}_{rad}$ being the radiative energy flux and $\vec{F}_{conv}$ the convective energy flux.

The case of radiation can be quickly treated. Due to the small mean free path of photons in most layers of stellar material, the flux can be approximated by that of a diffusive transport and written:

$$\vec{F}_{rad} = -\frac{4ac}{3} \frac{T^3}{\kappa \rho} \vec{\nabla} T, \tag{2.10}$$

where a is the radiation density constant, c the speed of light, and κ is the "mean" opacity, which is usually the Rosseland mean of spectral opacities defined as follows

$$\frac{1}{\kappa} = \frac{\int_0^\infty \frac{1}{\kappa_\nu} \frac{\partial B_\nu(T)}{\partial T} d\nu}{\int_0^\infty \frac{\partial B_\nu(T)}{\partial T} d\nu}, \tag{2.11}$$

with κ_ν the spectral opacity at a given frequency in the radiation spectrum and B_ν the Planck function for a given temperature and frequency. As can be seen, the Rosseland mean opacity is a harmonic mean which attributes more weight to the regions of low opacity in its calculation.

While the diffusion approximation holds very well for the internal structure of stars, it is absolutely not valid for stellar atmospheres, where the mean free path of the photon becomes much larger. In those regions, a full treatment of the radiation transfer is necessary. In low-mass stars, such as those we will study in this thesis, the effects of radiation pressure are quite limited in the interior. Consequently, most of the uncertainties on the thermal stratification of the radiative regions of these stars are linked to the opacity calculations. For more massive stars, these uncertainties are magnified through the important role of radiation pressure which can cause heavy elements to "levitate" inducing local accumulations. These accumulations can be strong enough to change radiative layers into fully mixed convective layers, thus affecting the chemical abundances and strongly influencing the evolution of those stars.

This parenthesis leads us to the second component of the energy flux, the convective flux. Convective transport of energy is basically linked to macroscopic motions of the fluid itself. The main issue is the timescale and vigorousness characterizing this phenomenon in stellar interiors. Typically, the Reynolds number, describing the degree of turbulence of these motions, are of the order of 10^{10}, far beyond what is achievable by numerical simulations to this day. Due to the small timescales and high non-linearity of these motions, it is impossible to properly treat convection in stellar interiors and an analytical, phenomenological approach dating back to Ludwig Prandtl (1925) is often used. This approximation is called the mixing-length theory (MLT) and links an average of the convective flux to local thermodynamical quantities in the case where radiative losses are negligible as follows:

$$< F_{conv} > \approx \rho c_P T \sqrt{\frac{P}{\rho}} \alpha_{MLT}^2 (\nabla - \nabla_{ad})^{3/2}, \tag{2.12}$$

where c_P is the specific heat at constant pressure, ∇ the temperature gradient of the layer and ∇_{ad} the adiabatic gradient of the layer. The quantity α_{MLT} is the so-called mixing length parameter which determines the extent of the mixing by convection through the relation

$$l = \alpha_{MLT} H_P(r), \tag{2.13}$$

hence defining l as the **radial** distance travelled by the fluid element before its disintegration and $H_P = \frac{dr}{d\ln P}$ the pressure scale height and r the radial position. We emphasise the word "radial" because turbulence is of course a three-dimensional phenomenon and this aspect is totally neglected in the MLT formalism. Moreover, as we will recall in the next section, turbulence is generated by a number of eddies of different wavelength, transporting the energy from the macroscopic to the microscopic scales. Again, this aspect is absent from MLT theory, which reduces the whole spectrum to one single characteristic scale, l. The effects of convection on the mean flow are treated up to the first order in the turbulent closure problem, while non-linear coupling has been shown to be of utmost importance when describing a turbulent medium. The Boussinesq approximation is used to describe the radial displacement of the fluid element. In other words, it assumes among others pressure equilibrium in the derivation of the buyoancy force, which is in disagreement with values of α_{MLT} for standard solar models, found to be around 1.8, thus of the order

of the pressure scale height. This is particularly problematic in the region near the surface, where the velocity of convective elements is of the order of the local sound speed (in other words, where the Mach number is large). During their travel through the media, the radiative losses of the elements are approximated but no continuous exchange of matter and energy is considered during the displacement. Although extremely simple and full of intrinsic flaws, the MLT approach is found to perform rather well for very turbulent deep layers of stars.

Other approaches, like the Full Spectrum of Turbulence method, have also been implemented in stellar evolution codes (like the CESTAM code in Paris (Marques, Goupil, et al. (2013)) or the latest version of the Cles evolution code (Scuflaire, Théado, et al. (2008))). This approach is described in Canuto, Goldman, and Mazzitelli (1996). It attempts to take into account the fact that convective motions will be characterised by a spectrum of eddies of various characteristic lengths, whereas the MLT reduces this spectrum to one single eddy. In practice, the formalism can be reduced to an expression very similar to that of the classical MLT. It is well known that both theories are not accurate for upper layers of stars were convection becomes clearly non-adiabatic. Moreover, both theories treat convection as a local phenomenon although turbulent convection is intrisically a non-local process. Consequently, a more accurate (although still imperfect) description of convection can only be obtained by hydrodynamical simulations, typically large eddy simulations (LES), where the turbulence is fully treated until a certain grid resolution under which a turbulence closure model is used. Some of these simulations are now averaged and "patched" onto stellar models. These models are then used to analyse the effects of upper layers on pulsation frequencies, but also to calibrate the mixing length parameter, which hides all the complexity of turbulence in the MLT formulation. 3D simulations are very useful to analyse the effect of turbulent pressure, which leads to an expansion of the superficial layers and thus an increase in radius which is far from negligible for helio- and asteroseismic studies.

Besides the inherent problems linked to the physical phenomenon itself, we must stress that determining properly boundaries of convective regions is also far from obvious. Typically, stellar models consider sharp transitions between fully mixed convective regions and partially mixed radiative regions. This can lead to strong uncertainties due to processes like overshooting, undershooting and semi-convection and sometimes to some confusion in the way to properly characterise convective regions in stellar evolution codes (see Gabriel, Noels, et al. (2014)). Usually, the classic criterion used to derive the onset of convection is the Schwarzschild criterion (Schwarzschild (1906)),

$$\nabla_{rad} > \nabla_{ad}, \tag{2.14}$$

stating that the so-called radiative gradient is superior to the local adiabatic gradient, defined as $\left(\frac{d\ln T}{d\ln P}\right)_S$, with S the entropy. This implies that the border of a convective region will be set by the Schwarzschild criterion at a point where $\nabla_{rad} = \nabla_{ad}$ on the convective side of the border and $\nabla_{rad} < \nabla_{ad}$ on the radiative side of the border. The radiative gradient is defined in equation 2.10 as the temperature gradient required in the medium to transport all the energy through radiation. If the Schwarzschild criterion is fulfilled, macroscopic motions will occur and transport the energy outwards. Such situations occur in massive stars, where the the CNO cycle of nuclear reactions occurs in a very narrow region in the centre which in turn leads to the apparition of a convective core, and in outer envelopes of cool stars where the increase in opacity blocks the transport by radiation.

The last equation we need to introduce to properly treat stellar structure is the equation of state. This equation relates the behaviour of the matter to thermodynamical

variables and chemical composition. This equation is written:

$$P = P(T, \rho, \chi), \tag{2.15}$$
$$U = U(T, \rho, \chi), \tag{2.16}$$
$$\kappa = \kappa(T, \rho, \chi), \tag{2.17}$$

if we choose T and ρ as independent variables and use χ to characterise the chemical composition and U is the internal energy of the stellar plasma. In practice, the equation of state can be computed using two different approaches: the physical or the chemical approach. The first one is based on the treatment of individual particles (nucleons and electrons) through their Coulomb potential and thus includes a systematic treatment of non-ideal effects. This approach does not make any hypothesis on the ions in the gaz. The chemical approach is based on the consideration of atoms and ions and includes non-ideal effects in a simple heuristic manner. This is what is found in the CEFF (Christensen-Dalsgaard and Daeppen (1992)), FreeEOS (Irwin (2012)), MHD (Hummer and Mihalas (1988), Mihalas, Dappen, and Hummer (1988), Daeppen et al. (1988), Mihalas, Hummer, et al. (1990)) and SAHA (Baturin et al. (2013)) equations of state. The physical approach is used to compute the OPAL equation of state (Rogers and Nayfonov (2002) and Rogers, Swenson, and Iglesias (1996)).

Although the physical approach can be thought to be more realistic, the chemical approach offers the advantage to be a very versatile tool for which the chemical composition can be quickly changed and for which supplementary thermodynamic quantities can be easily and consistently computed due to analytical formulas. For example, when the OPAL equation of state was released (Rogers, Swenson, and Iglesias (1996)), it was found that it did not satisfy some basic thermodynamic relations. This led to a recalculation of the OPAL tables in 2002 (Rogers and Nayfonov (2002)).

2.2.2 Equilibrium structure and evolution equations

The equations defined in section 2.2.1 do not constitute the equations actually solved when computing stellar models. It is of course unrealistic to think that we could solve every equation, taking into account every time dependence and physical effect within a general geometry to describe stellar structure. We know from section 2.1 that various timescales are found in stellar structure and evolution and that we can, to some extent, separate dynamical, thermal and chemical effects.

In practice, the structure is described by an average equilibrium structure. Due to the hypothesis of hydrostatic equilibrium, if one neglects the effects of rotation and of a magnetic field, the geometry of an isolated star can be considered spherical. Assuming hydrostatic equilibrium[1] means that dynamical effects can be separated and the time derivatives eliminated from dynamical equations. During its main sequence, the star is also in thermal or secular equilibrium, meaning that all energy produced within the core by nuclear reaction is transported outwards such that the energy gains and losses in the core compensate each other. This means that we end up with the following system of

[1]Which is a completely relevant hypothesis for most evolutionary phases with the exception of the initial collapse of the molecular cloud and the supernovae phases.

equations:

$$\frac{\partial r}{\partial m} = \frac{1}{4\pi r^2 \rho}, \tag{2.18}$$

$$\frac{\partial P}{\partial m} = \frac{-Gm}{4\pi r^4}, \tag{2.19}$$

$$\frac{\partial l}{\partial m} = \varepsilon, \tag{2.20}$$

$$\frac{\partial T}{\partial m} = \frac{-GmT}{4\pi r^4 P}\nabla, \tag{2.21}$$

where equation 2.20 is only equation 2.8 written in another form, with l the local value of the luminosity at a radius r and ∇ being the temperature gradient defined as $\frac{d\ln T}{d\ln P}$, determined according to the transport of energy, in other words equation according to 2.10 in a purely radiative zone and for example according to the equations of the MLT for convective regions. These equations describe stellar structure and the remaining time derivatives are related to changes of chemical composition, which of course induce changes in the temperature and pressure throughout the star. Hence, the last equations needed to compute evolutionary models are related to changes in chemical composition:

$$\frac{\partial X_i}{\partial t} = \frac{m_i}{\rho}\left(\sum_j r_{i,j} - \sum_k r_{i,k}\right), \quad i = 1,...,I, \tag{2.22}$$

with X_i being the mass fraction of each nuclei i of mass m_i undergoing nuclear reactions defined by the production and destruction rates of the chemical species, respectively $r_{i,j}$ and $r_{i,k}$. Computing an evolutionary sequence with most stellar evolution codes means that the model is evolved from one state of thermal and hydrostatic equilibrium to another one. As stated before, only a few stellar evolution codes are able to compute the evolution of a model through the helium flash or other phases of evolution where instabilities develop.

2.3 Ingredients of stellar models

In this section, we will briefly discuss some more tedious aspects of stellar structure. Our goal is not to provide a full description of these problems, which are still a matter of debate in the community, but rather to present a short overview of some physical aspects of stellar structure not always included in the recipe of stellar models we described earlier. We will separate our discussion between macroscopic aspects, linked to the description of the hydrodynamics of the stellar interior, and the microscopic aspects, linked to processes occurring at small scales that have a significant impact on stellar models.

2.3.1 Uncertainties on macroscopic processes

Describing stellar structure requires numerous approximations on the large scale effects acting on the fluid flows. Indeed, analysing in details all macroscopic processes acting on small timescales like turbulence, magnetic fields, rotation or instabilities during an entire stellar evolution and describing their interactions with each other is almost impossible. Therefore, one relies on a number of assumptions on these processes. In this section, we will briefly describe some of these processes and their importance and refer to additional references for the interested reader.

The first obvious ingredient of the macrophysic aspects of stellar models is convection. As described before, the most commonly used description for the motions of the fluid

in convective layers is the local mixing length theory (MLT, Böhm-Vitense (1958)). This description uses a single free parameter to determine the distance over which an element will be moved before dispersing its characteristics within its surroundings. While the mixing-length theory holds well in lower regions, it completely fails in upper regions of the stellar structure. In those layers, the hypothesis of adiabaticity is not valid since the thermal timescale describing the heat exchange between the fluid element and its surroundings is of the same order as the dynamical timescale describing its motions. This means that the temperature gradient in upper regions of the convective envelope described by the MLT formulation is undoubtedly wrong. A first amendment to these errors can be done when taking into account the full spectrum of turbulence, as done in Canuto, Goldman, and Mazzitelli (1996). This method described as the FST approach, offers theoretically a better modelling of the non-adiabatic convective zones by taking into account various eddies as contributing to the convective flux rather than a single eddy characterised by the mixing length. This formalism allows us to derive the root mean squared turbulent pressure, the root mean squared turbulent velocity as well as the turbulent viscosity. In a first paper in 1991, Canuto & Mazzitelli presented a model for convection where the turbulent mixing length scale was the depth in the convective region. This model did not require a free adustable parameter, like the MLT model and provided acceptable results for a solar calibration. In 1996, the model was further improved by taking into account a self-consistent rate for the energy input (here buyoancy) into the turbulent cascade. However, this self-consistent model of convection required a free adjustable parameter, in a similar fashion to the MLT approach, and is often refereed to as the FST (full spectrum of turbulence) or CM (Canuto-Mazziteli) model of convection in the litterature, including the present manuscript.

The problem of overshooting is another central problem of astrophysics, intrinsically linked to the borders of convective regions. This problem results from the Schwarzschild criterion used to derive the boundary of the convective zone. In fact, this criterion provides a dynamical boundary, in other words, the region where the acceleration of the fluid element is 0. However, due to its inertia, an element will not necessarily stop there since its velocity is not 0 at the point where the criterion is satisfied. The real border of a convective layer is actually found where the velocity of convective elements is 0 and thus there is no convective flux. In practice, it is very difficult to derive such a limit, although upper boundaries for the overshooting regions have been derived (see I. W. Roxburgh (1989)). Consequently, in the absence of a proper theory characterizing this convective penetration, often called over- or undershooting depending on the situation, one relies on parametric formulations.

In figure 2.1, we compare temperature gradients in the superadiabatic zone for solar models between the MLT, FST and a 3D LES simulation[2]. As stated before, the LES simulations provide the most reliable description of these regions but the computation time and the limited range of physical parameters does not make them suitable for "à la carte" stellar modelling yet. We can see that the FST provides a much higher temperature gradient in the upper region and that the MLT formalism performs better with respect to the LES simulation for this model. Other formulations, separating convection into a combination of a mean flow to which perturbations are added can be found in Yang and Li (2007). This method, based on Reynolds-stresses models, has been tested using helioseismic data and found to improve the agreement with observed solar frequencies by 30%. However, the major weakness of this approach is the number of free parameters introduced (6 in Yang and Li (2007)) to take into account the various correlations between

[2]We mention that the model for the LES is not perfectly solar but has a slightly higher mass of $1.02 M_{\odot}$.

turbulent stresses necessary to close the analytical model.

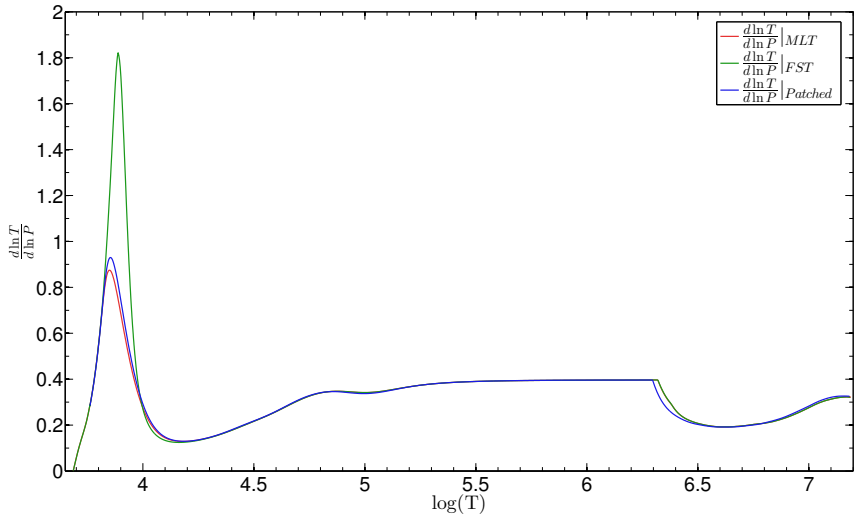

Figure 2.1: Illustration of the difference in temperature gradients for FST (green) and MLT (red) formalisms for standard solar models, compared to a patched 3*D* simulation (courtesy of T. Sonoi) in blue.

Another macroscopic element of stellar models is rotation. Although it is often not implemented in stellar evolutionary codes, it is known to have a strong impact on physical properties of stellar models (see the serie of papers Meynet and Maeder (1997), Maeder (1997), Maeder and Zahn (1998), Maeder (1999), Meynet and Maeder (2000), Maeder and Meynet (2000), Maeder and Meynet (2001), Meynet and Maeder (2002), Maeder (2002), Meynet and Maeder (2003), Meynet and Maeder (2005), Hirschi, Meynet, and Maeder (2004), Hirschi, Meynet, and Maeder (2005) for an extensive description of the impact of rotation on stellar structure and evolution). For instance, strong differential rotation would cause the apparition of shear instabilities, thus inducing additional mixing in stellar interiors. Many of the remaining uncertainties focus on the evolution of angular momentum in stellar interiors. For a better understanding, let us recall the first consequence of rotation which is a modification of the mechanical equilibrium, which leads to a change in the geometry of the star and to the fact that equipotentials are now closer to each other at the poles than at the equator due to the breaking of spherical symmetry.

In a simplified description, this mechanical change leads to a thermal imbalance between polar and equatorial regions (due to Von Zeipel's theorem), which in turn triggers the development of a meridional circulation. In a more complete picture, the effects of winds, accretion and tides have to be taken into account since they will change the total angular momentum of the star and thus shape the structure of the meridional circulation. Moreover, the circulation has to be coupled to horizontal turbulence and magnetic fields. The study of this flow is one of the most long lasting problem in astrophysics since it appeared at the beginning of the 20^{th} and a first self-consistent explanation was first provided in Zahn (1992) but the specific properties of the coupling with additional processes is still under study. We also mention that some models without a large scale meridional circulation have also been proposed in the past (see for example I. W. Roxburgh (1964a), I. W. Roxburgh (1964b), Sharp, Smith, and Moss (1977) or Busse (1981)). We refer to the paper by Zahn (1992) or to the book by André Maeder (Maeder (2009)) for a full description of the phenomenon and only list the consequences of the existence of such a circulation.

The first consequence is that the circulation advects angular momentum and chemical species, changing the stratification of the star and its rotation profile significantly during the evolution. Indeed, it can be shown that meridional circulation will induce differential rotation by its advection of angular momentum. However, it will also indirectly trigger shear induced turbulence, which will lead to a reduction of the flow. This turbulence will mostly act on the horizontal stratification of the fluid, as is observed in geophysics. It has been shown by Zahn (1992) that in this case, the effects of shear induced turbulence could be treated as a diffusive process in the radial direction (other approaches have also been presented, see e.g. Pinsonneault et al. (1989)). The problem is actually even more complicated since the apparition of the instabilities will also be influenced by the interaction of the circulation with the magnetic field and the angular momentum loss through the stellar winds, particularly in the case of massive stars. We illustrate the interplay between all these processes in figure 2.2, from Mathis and Zahn (2005), which emphasises better than any long sentences the physical complexity of the problem faced by stellar modellers.

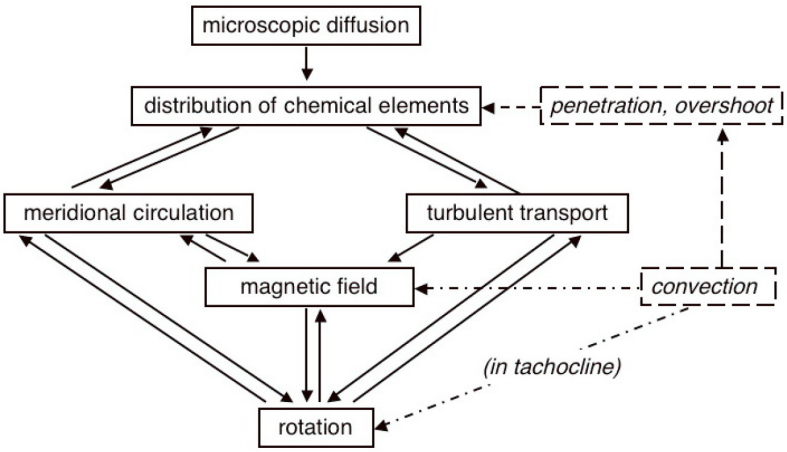

Figure 2.2: Illustration of the interaction between various macroscopic processes in stellar interiors (reprinted from Mathis and Zahn (2005))

In the helioseismic case, additional processes are also needed to reproduce the rotation profile of the Sun, illustrated in figure 2.3 for various latitudes. It was found that basic angular momentum conservation and meridional circulation are insufficient. One usually quotes the impact of gravity waves, presented in Kumar, Talon, and Zahn (1999) and Charbonnel and Talon (2005) or the influence of the magnetic field (Eggenberger, Maeder, and Meynet (2005)). However, all three processes can be invoked and combined to reproduce the rotation profile of the Sun and so far, helioseismology has not been able to discriminate between them. Recently, the unveiling of the rotation of the core of subgiants and red giants (Deheuvels, García, et al. (2012), Deheuvels, Doğan, et al. (2014), Mosser, Goupil, et al. (2012)) has further confirmed that our current state of stellar modelling did not reproduce at all the observed properties in terms of mixing. The problem had already been mentionned for specific cases where chemical peculiarities are also observed (see Richard, Michaud, Richer, et al. (2002)). Moreover, the question of rotation is actually closely related to lithium depletion (Zahn (2005), Richard, Michaud, and Richer (2005), Vick et al. (2010), Vick et al. (2011), Vick et al. (2013)), which is still not reproduced even by the standard models of the Sun.

Because of their impact on stratification, these interactions between rotation, turbulence and magnetic fields will not only affect the transport of angular momentum, but also

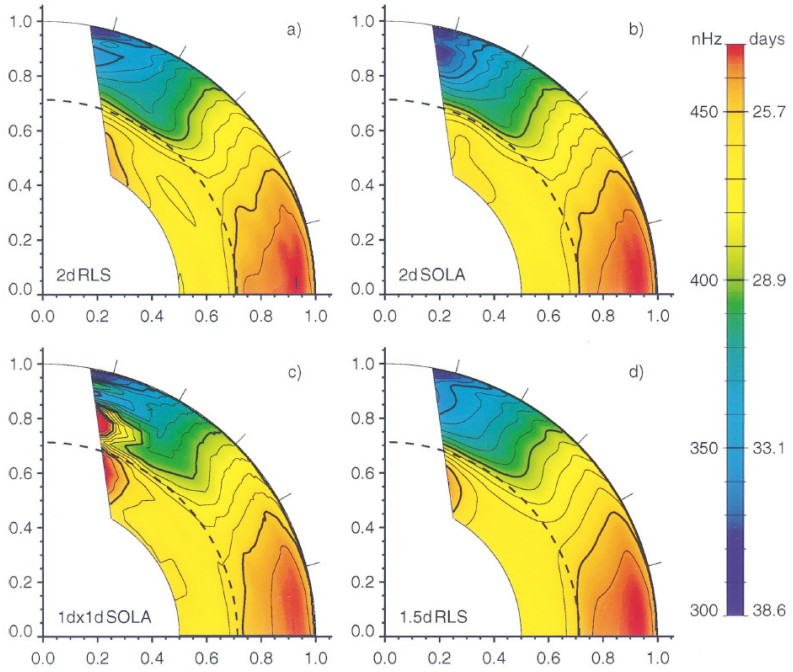

Figure 2.3: Illustration of the 2D rotation profile as obtained with various inversion techniques (reprinted from Schou, Antia, et al. (1998))

the transport of chemical species. This will of course impact the evolutionary track of stellar models of all masses, ages and chemical compositions. Currently, this "extra-mixing" problem is central to stellar modellers, first of all to understand the physical structure of stars but also to allow stellar models to fulfill their key role as references for the determination of fundamental parameters, such as ages, in other fields of astrophysics such as exoplanetology or Galactic archeology.

2.3.2 Uncertainties on microscopic ingredients

As can be seen from section 2.2.1, stellar evolution is not only a hydrodynamical problem, but also a matter of atomic or subatomic physics. It should also be noted that mixing processes are important for stellar evolution because they will change the course of the microscopic processes driving stellar structure and evolution. Since stellar evolution is due to nuclear reactions occuring in the central regions, it means that the evolution will be strongly dependent on the nuclear reaction rates. Fortunately, these ingredients have been quite reliably calculated in the past years and are not expected to change significantly in the near future. The last important change was linked to the $^{14}N(p,\gamma)^{15}O$ reaction which is a key component of the so-called CNO cycle and influences the evolution of massive stars (see for example Stancliffe et al. (2016) for a recent study) but also later evolutionary stages (Pietrinferni, Cassisi, and Salaris (2010)).

Another fundamental ingredient of stellar models is the equation of state. Currently, three main equations of state are used for solar-like stars, the OPAL equation of state (Rogers and Nayfonov (2002)), the Ceff equation of state (Christensen-Dalsgaard and Daeppen (1992)) and the FreeEOS equation of state (Irwin (2012)). Other possibilites are available, like the MHD equation of state (Hummer and Mihalas (1988), Mihalas, Dappen, and Hummer (1988), Daeppen et al. (1988), Mihalas, Hummer, et al. (1990)) or the series of SAHA equations of state (Baturin et al. (2013)). All of these have been calibrated for the Sun and tested

using helioseismology. While it can be argued that there is always room for improvement, the equation of state still remains quite robust for solar conditions and is not considered the main contributor to uncertainties in numerical models of solar-like stars. However, the situation is very different for cold stars, where additional corrections have to been taken into account, or for more peculiar objects, like white dwarfs, where cristallization may play an important role and these phase transitions have to be treated correctly in very peculiar conditions. In the more extreme case of neutron stars, relativistic effects have to be taken into account and reconciling general relativity and thermodynamics is not a straightforward task. In the present work, where we focus on solar-like stars, the equation of state will not be seen as a major problem, but it should still be kept in mind that changes in this fundamental ingredient can have an impact, although limited, on the stellar models presented here. As an illustration, we compare in figure 2.4 relative differences of the adiabatic exponent, $\Gamma_1 = \frac{\partial \ln P}{\partial \ln \rho}|_S$, for the OPAL, Ceff and FreeEOS equations of state in a standard solar model. As can be seen, the differences remain limited although larger discrepancies can occur for non-solar conditions.

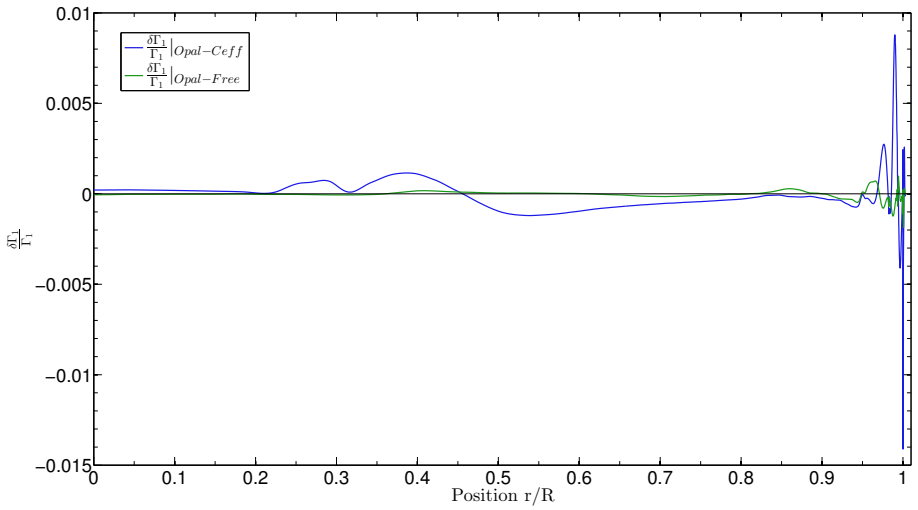

Figure 2.4: Relative differences in Γ_1 for a standard solar model built with the Ceff, FreeEOS and OPAL equations of state.

The most problematic microscopic ingredient is the opacity. In practice, various opacity tables are available, including the OPAL (Iglesias and Rogers (1996)), OP (Seaton (2005)), OPAS (Mondet et al. (2015)) or OPLIB (Colgan et al. (2016)) tables. The particularity of the OPAS tables is that they are only computed for a very limited range of physical conditions, corresponding to the radiative zone of the Sun. Thus, three possibilities are offered to stellar modellers. The main difficulty associated with opacities is the complexity of their determination. Correctly accounting for all the levels of transitions of all atoms in all ranges of density and temperature and properly accounting for the coupling beetween electronic levels constitutes a very tedious problem requiring years of calculations (as can be seen from the timelapse between the publication of two different opacity tables). The dominant aspect of this problem for stellar modelling is that the opacities have a strong impact on stellar structure. They condition the behaviour of the temperature gradient in the interior , thus strongly impact the sound speed gradient in radiative regions and the extension of convective regions. Consequently, they strongly impact the structural diagnostics derived from seismic modelling. As we will see in chapter 7, they play a

central role in the "solar metallicity problem", and the remaining differences between theoretical calculations and the experimental results seem to indicate that the problem is not closed despite the recent publication of updated opacity tables. Historically, new opacities have been linked to small revolutions in stellar physics, like the explanation of the pulsations of β Cephei stars (A. N. Cox et al. (1992) and Dziembowski and Pamiatnykh (1993)). Additional changes in the nickel opacity are also predicted to explain the behaviour of B type stars (see S. Salmon et al. (2012)). Therefore, opacity tables still remain the microphysics ingredient of stellar models that is the most likely to change in the future. We further discuss this ingredient in chapter 7, due to its key role in the current solar modelling problem.

Besides the opacity problem, some uncertainties on microscopic diffusion are also present in stellar models. While gravitational settling and thermal diffusion are well known, differences remain between various "recipes" of microscopic diffusion (see Turcotte et al. (1998)). Treating microscopic diffusion properly is quite complicated, since ideally, it should be done by following each individual element and see to which depth it sinks in the star during its evolution. The movement of each element depends, of course, on its ionisation state since its interaction with the medium will not be the same depending on whether it is fully ionised or not. Another crucial aspect of microscopic diffusion is the potential impact of radiative acceleration. This problem is closely linked to opacities since in this case one has to be able to properly take into account the transfer of momentum from photons to given ions which will counterbalance their settling during the evolution. Besides the obvious difficulty of this modelling and its intrinsic uncertainties, this aspect is also particularly difficult to model because of the unavailability of the data to stellar modellers (with the notable exception of the OP opacities). In fact, most opacity tables are given as the so-called Rosseland mean opacity, but not as spectral opacities which are required to properly treat this effect. However, an approximate formula to take their effects into account has been derived by LeBlanc and Alecian (2004). In figure 2.5, we illustrate the differences found in Turcotte et al. (1998) when comparing various treatments of microscopic diffusions for standard solar models. For more massive stars, including the effects of radiative acceleration is even more complicated. During the evolution of the model, they will induce strong local accumulations of certain chemical elements on very short timescales that are very difficult to treat with the current stellar evolution codes.

For massive stars, the increase in radiation pressure significantly magnifies the impact of the radiative accelerations compared to solar-like stars. This can lead to the apparition of local convective zones as well as to inversions of the mean molecular weight gradient which in turn will lead to thermoaline convection, thus connecting partially mixed zones and leading to an additional mixing between intermediate convective zones. Therefore the impact of these microphysical ingredients on stellar structure and evolution is manifold, since they can lead to the apparition of macroscopic phenomena (see Denissenkov (2010), Richard, Michaud, and Richer (2001), J. M. Brown, P. Garaud, and Stellmach (2013), Deal, Richard, and Vauclair (2016)).

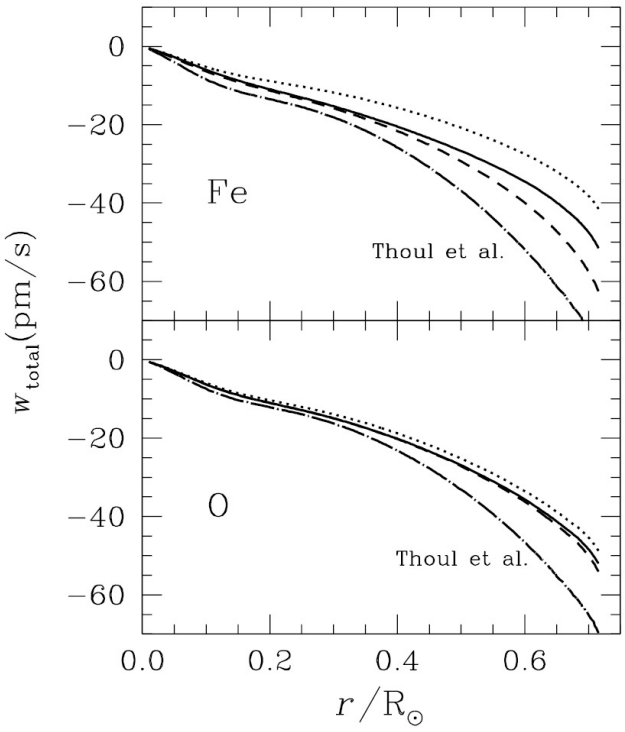

Figure 2.5: Differences in iron and oxygen diffusion velocities depending on the various assumptions used. The dot-dashed line is based on the Thoul, Bahcall, and Loeb (1994) diffusion routine, the dotted line assumes complete ionisation and no radiative force acting on the elements, the dashed line assumes partial ionisation of the elements where required by the thermodynamical conditions but does not include radiative accelerations. The solid line includes radiative accelerations and does not assume complete ionisation throughout the structure (reprinted from Turcotte et al. (1998)).

3. INTRODUCTION TO STELLAR OSCILLATIONS

3.1 Pulsation equations

In the previous chapter, we introduced the equilibrium structure of a star, which is dynamically defined by the hypothesis of hydrostatic equilibrium. However, this does not mean that no dynamical phenomena will occur inside stars, even on the main sequence. Although they are ignored in evolutionary codes because of the timescale differences, dynamical perturbations can be seen in the form of pulsations for many stars in the HR diagram.

In this chapter, we will describe the equations associated with non-radial stellar oscillations using the linear adiabatic approximation. While these approximations will be commented and references for other works will be mentioned, we will mostly focus on a description oriented towards inversion equations and not dig in all the subtleties hiding behind the derivation of each equation presented here.

3.1.1 Small perturbation method

As shown in Section 2.2.2, the structure of a star is approximated by static models, considered to represent what we call the equilibrium, "unperturbed" structure. Stellar oscillations are then treated as small perturbations that are superimposed to this equilibrium configuration of the star. The perturbations are considered to be very small, such that one only needs to take the linear terms into account in the mathematical development and can neglect higher orders. When calculating perturbations of fluid equations, one has the choice to use either the Eulerian description or the Lagrangian one. Namely, Eulerian perturbations describe the changes in the fluid at a fixed spatial position and are usually denoted by a $'$, while the Lagrangian perturbations are "attached" to the perturbed fluid particle and usually denoted by the symbol δ. The equilibrium variables are denoted with the subscript 0 to avoid further confusion in the equations. Both descriptions are equivalent to describe stellar pulsations and are in fact mathematically linked. If we

consider the physical quantity $f(\vec{r})$ and its Eulerian perturbations, one writes:

$$f(\vec{r}_0,t) = f_0(\vec{r}_0) + f'(\vec{r}_0,t), \tag{3.1}$$

for Lagrangian perturbations, one has:

$$f(\vec{r},t) = f_0(\vec{r}_0) + \delta f(\vec{r}_0,t), \tag{3.2}$$

and these definitions are linked as follows:

$$\delta f(\vec{r}_0,t) = f'(\vec{r}_0,t) + \vec{\xi}\cdot\vec{\nabla} f_0(\vec{r}_0), \tag{3.3}$$

with $\vec{\xi} = \vec{r} - \vec{r}_0$, defined as the displacement vector, $\vec{r}$ the perturbed position and $\vec{r}_0$ the equilibrium position. One then develops the structural equations in terms of these perturbations to obtain a system which describes linear stellar pulsations. It should be noted that considering first order perturbations implies intrinsically that the oscillations have small amplitudes. This is of course justified for the solar-like oscillations we will study in practice, but is not justified for oscillations of very high amplitudes.

3.1.2 Equations of linear adiabatic non-radial oscillations

In this section, we will apply the formalism of linear perturbations to the dynamical equations describing stellar structure. We will present the main steps to obtaining the system of equations associated with the eigenvalue problem of stellar oscillations. Since the derivation of this system implies additional hypotheses, we provide a few additional comments on each of these supplementary approximations.

Basic equations

The first equation we need is the continuity equation:

$$\rho' + \vec{\nabla}\cdot(\rho_0\vec{\xi}) = 0, \tag{3.4}$$

we also develop the conservation of momentum equation:

$$\rho_0\frac{\partial^2\vec{\xi}}{\partial t^2} = -\vec{\nabla}P' - \rho_0\vec{\nabla}\psi' - \rho'\vec{\nabla}\phi_0, \tag{3.5}$$

and Poisson's equation for gravitation:

$$\triangle\psi' = 4\pi G\rho'. \tag{3.6}$$

As in section 2.2.2, in addition to the above equations which are the perturbations of dynamical equations, we also have to add the perturbed equation of conservation of energy. In other words, this could mean that we would fully consider heat transfer between the oscillations and the fluid. However, in practice, the heat transfer is often neglected and the oscillations are considered adiabatic. This is justified by the fact that the oscillations occur on a timescale much shorter than the thermal relaxation timescale. In other words, the Lagrangian perturbation of entropy is neglected and the following relation between pressure and density is used to close the system of equations of stellar oscillations:

$$P' + \vec{\xi}\cdot\vec{\nabla}P_0 = c^2(\rho' + \vec{\xi}\cdot\vec{\nabla}\rho_0). \tag{3.7}$$

with $c^2 = \frac{\Gamma_{1,0} P_0}{\rho_0}$, the squared adiabatic sound speed abd $\Gamma_{1,0} = \left(\frac{\partial \ln P}{\partial \ln \rho}\right)_S$ the first adiabatic exponent. While this is valid for the deeper regions of stars where the specific heat is extremely high, it is not valid in the upper regions of stars where the thermal timescale can be of the same order of the dynamical timescale. This is of uttermost importance for solar-like oscillators, as it leads to what is often called "surface effects" in the litterature. It is a central problem of asteroseismology which also partially originates from the fact that we do not properly describe the coupling between oscillations and convection in the atmosphere[1]. Non-adiabatic effects are also necessary if one wishes to derive instability strips in the HR diagram since they have to be taken into account to know whether the oscillations will be damped or not. For solar-like oscillations, taking into account non-adiabatic effects also allows to derive the damping rates of the oscillations, which can then be compared to the linewidths of the modes in the power spectrum. We will come back to this when describing various pulsators and the various excitation mechanisms for stellar pulsations.

Equations 3.4, 3.5, 3.6 and 3.7 constitute the system of partial differential equations that are solved to compute linear adiabatic stellar oscillations in a non-rotating star. Including rotation increases the complexity of the problem since spherical symmetry is then broken. To some extent, perturbative analyses of a certain order can be used for slow to intermediate rotators but for very fast rotators such as δ Scuti, a fully two-dimensional resolution of the problem is required. In this section, we only focus on slow rotators for which the spherical symmetry is not broken; an introduction to the effects of rotation will be presented in section 3.3.

The displacement vector $\vec{\xi}$ can be separated into a radial and a horizontal component

$$\vec{\xi} = \xi_r \vec{e}_r + \vec{\xi}_h. \tag{3.8}$$

Introducing this decomposition in the equations 3.4, 3.5, 3.6 and 3.7 and separating the gradients into radial gradients and horizontal gradients leads to some simplifications due to the fact that equilibrium variables are only dependent of the radial distance r, as a consequence of spherical symmetry. The system is then the following:

$$\rho' + \frac{1}{r^2}\frac{\partial}{\partial r}(\rho_0 r^2 \xi_r) + \rho_0 \vec{\nabla}_h \cdot \vec{\xi}_h = 0, \tag{3.9}$$

$$\rho_0 \frac{\partial^2 \xi_r}{\partial t^2} = -\frac{\partial P'}{\partial r} - \rho' \frac{d\psi_0}{dr} - \rho_0 \frac{\partial \psi'}{\partial r}, \tag{3.10}$$

$$\rho_0 \frac{\partial^2 \vec{\xi}_h}{\partial t^2} = -\vec{\nabla}_h P' - \rho_0 \vec{\nabla}_h \psi', \tag{3.11}$$

$$\frac{1}{r^2}\frac{\partial}{\partial r}(r^2 \frac{\partial \psi'}{\partial r}) + \frac{\Delta_h \psi'}{r^2} = 4\pi G \rho', \tag{3.12}$$

$$P' + \xi_r \frac{dP_0}{dr} = \frac{\Gamma_{1,0} P_0}{\rho_0}(\rho' + \xi_r \frac{d\rho_0}{dr}). \tag{3.13}$$

We can now see that the angular derivatives only appear in the $\vec{\nabla}_h$ operator. It can be demonstrated that the solutions of this separable system will be of the form:

$$F(r,\theta,\phi,t) = \sqrt{4\pi} f(r) Y_\ell^m(\theta,\phi) e^{-i\omega t}, \tag{3.14}$$

[1]The other source of the problem is the crude modelling of the upper regions by the MLT theory, causing an erroneous description of the propagation of the oscillations even if these were fully adiabatic. The neglect of the turbulent pressure also causes an inaccuracy in the radius and thus is a major contributor to the surface effects.

with $Y_\ell^m(\theta,\phi)$ the spherical harmonic of degree ℓ and azimuthal order m. These functions are the eigenfunctions of the Legendrian operator, Δ_h, since they verify the following property:

$$\nabla_h^2 Y_\ell^m(\theta,\phi) = -\ell(\ell+1)Y_\ell^m(\theta,\phi). \tag{3.15}$$

The temporal dependency is of course a periodic function since we are looking for periodic oscillations. After a few algebra, the system can be simplified and is written

$$\omega^2\left[\rho' + \frac{1}{r^2}\frac{d}{dr}\left(r^2\rho_0\xi_r\right)\right] = \frac{\ell(\ell+1)}{r^2}\left(P' + \psi'\right), \tag{3.16}$$

$$\omega^2\rho_0\xi_r = \frac{dP'}{dr} + \rho'\frac{d\psi_0}{dr} + \rho_0\frac{d\psi'}{dr}, \tag{3.17}$$

$$\frac{1}{r^2}\frac{d}{dr}\left(r^2\frac{d\psi'}{dr}\right) - \frac{\ell(\ell+1)}{r^2}\psi' = 4\pi G\rho'. \tag{3.18}$$

It is important to notice that this separation of variables and the form of the obtained system is a consequence of the hypotheses we have made. If the effects of rotation or magnetism are taken into account or if the star is not isolated, the separation of variables is not applicable anymore [2]. It is often useful to rewrite this system using the definitions of two characteristic frequencies, namely S_ℓ^2, the squared Lamb frequency and N^2, the squared Brunt-Vaisälä frequency.

$$S_\ell^2 = \frac{\ell(\ell+1)c^2}{r^2}, \tag{3.19}$$

$$N^2 = g_0\left(\frac{1}{\Gamma_{1,0}}\frac{d\ln P_0}{dr} - \frac{d\ln\rho_0}{dr}\right), \tag{3.20}$$

The system is now written

$$\frac{dP'}{dr} + \rho_0\frac{d\psi'}{dr} + g_0\frac{P'}{c^2} = (\omega^2 - N^2)\rho_0\xi_r, \tag{3.21}$$

$$\frac{P'}{\rho_0 c^2}(1 - \frac{S_\ell^2}{\omega^2}) - \frac{\ell(\ell+1)}{\omega^2 r^2}\psi' - \frac{g_0\xi_r}{c^2} + \frac{1}{r^2}\frac{d\left(r^2\xi_r\right)}{dr} = 0, \tag{3.22}$$

$$\frac{1}{r^2}\frac{d}{dr}\left(r^2\frac{d\psi'}{dr}\right) - \frac{\ell(\ell+1)}{r^2}\psi' = 4\pi G\left(\frac{P'}{c^2} + \frac{\rho_0 N^2}{g_0}\xi_r\right), \tag{3.23}$$

A quick analysis of the system informs us that there is no explicit dependence on m, the azimuthal order. Consequently, there is a $2\ell+1$ degeneracy in the solutions of this eigenvalue problem given that $-\ell < m < \ell$. Again, this stems from the spherical symmetry of the problem and any effect breaking this hypothesis will introduce an m dependency in the solutions.

Boundary conditions

From the end of section 3.1, we can see that we have a system of equations of the fourth order, with the following unknowns ξ_r, P', ψ' and $\frac{d\psi'}{dr}$. Consequently, we have to provide four boundary conditions. Detailed derivation of these boundary conditions can be found in Unno et al. (1989). We will first deal with the central boundary conditions. These can

[2] Before the breaking of the spherical symmetry that can be induced by each of these phenomena.

be obtained by expanding the solution near $r = 0$. We obtain that $\xi_r \propto r^{\ell-1}$, ψ' and $P' \propto r^{\ell}$. If $\ell = 0$, then $\xi_r \propto r$. From these relations, one can show that

$$\frac{d\psi'}{dr} \approx \frac{\ell}{r}\psi', \tag{3.24}$$

$$\xi_r = \ell \xi_h. \tag{3.25}$$

These two equations provide the first two boundary conditions. Two other conditions are then applied at the surface. They can take various forms, depending on the authors and the options of the oscillation codes. Typically, these are free surface conditions for the equation of motion (e.g. $\delta P = 0$) and a continuous connection to the analytical solution of Poisson's equation in the absence of matter. The main issue with these boundary conditions is that they are certainly limited, due to the breakdown of the adiabatic approximation in the surface layers.

Physical nature of the modes

The solutions of the stellar oscillation equations can be obtained through numerical techniques, using various sets of pulsations variables and discretization techniques. However, to gain some physical insight on the nature of the modes, it is interesting to look into some more approximate developments.

First, we start by noticing that the perturbation of the gravitional potential will have a small effect on the pulsations, especially for high ℓ and n modes, *i.e.* with many nodes. Thus, the perturbation of the gravitational potential can be considered negligible. This approach is called the Cowling approximation and can be mathematically justified by the fact that the perturbation of the gravitational potential is an integral of the density perturbation which is directly linked to the eigenfunctions. By eliminating it from the equations, the system is reduced to the second order

$$\frac{d\xi_r}{dr} = -\left(\frac{2}{r} + \frac{1}{\Gamma_1 H_P}\right)\xi_r + \frac{1}{\rho c^2}\left(\frac{S_\ell^2}{N^2} - 1\right)P', \tag{3.26}$$

$$\frac{dP'}{dr} = \rho\left(\omega^2 - N^2\right)\xi_r + \frac{P'}{\Gamma_1 H_P}, \tag{3.27}$$

This first approximation is justified up to a good accuracy. Following Gabriel and Scuflaire (1979), the problem can be even more simplified with the following change of variables

$$v = f_1 r^2 \xi_r, \tag{3.28}$$

$$w = f_2 \frac{P'}{\rho}, \tag{3.29}$$

with f_1 and f_2 defined as follows

$$f_1 = \exp\left(\int_0^r \frac{1}{\Gamma_1}\frac{d\ln P}{dr}dr\right), \tag{3.30}$$

$$f_2 = \exp\left(-\int_0^r \frac{N^2}{g}dr\right). \tag{3.31}$$

The system 3.26-3.27 can then be rewritten

$$\frac{dw}{dr} = \left(\omega^2 - N^2\right)\frac{f_2}{r^2 f_1}v, \tag{3.32}$$

$$\frac{dv}{dr} = \left(\frac{S_\ell^2}{\omega^2} - 1\right)\frac{r^2 f_1}{c^2 f_2}w. \tag{3.33}$$

This system can then be reduced to a second order differential equation by eliminating either v or w. Each case leads to

$$\frac{d}{dr}\left(\frac{1}{1-\frac{S_\ell}{\omega^2}}\frac{c^2 f_2}{r^2 f_1}\frac{dv}{dr}\right)+\left(\omega^2-N^2\right)\frac{f_2}{r^2 f_1}v=0, \tag{3.34}$$

or

$$\frac{d}{dr}\left(\frac{1}{N^2-\omega^2}\frac{r^2 f_1}{f_2}\frac{dw}{dr}\right)+\left(\frac{S_\ell^2}{\omega^2}-1\right)\frac{r^2 f_1}{c^2 f_2}w=0. \tag{3.35}$$

From these equations, we can see that the function will be oscillatory only if $\omega < S_\ell$ and $\omega < N$ simultaneously or if $\omega > S_\ell$ and $\omega > N$ at the same time (see Scuflaire (1974a) for a more thorough description of the spatial properties of various oscillation modes). The modes will behave exponentially between the regions where these conditions are met. They are said to be trapped in the cavities defined by the conditions for which the solution is an oscillating function. The modes of low frequency are called g modes while the modes of high frequency are called p modes. This analysis can be used to plot so-called propagation diagrams, which are useful for understanding the behaviour of the modes and the regions they are probing most efficiently.

Pressure modes

Pressure modes are defined by the condition

$$\omega^2 > S_\ell^2, \tag{3.36}$$

and

$$\omega^2 > N^2, \tag{3.37}$$

meaning that they are the high frequency modes propagating in the upper regions of the star. Their reflexion point is characterised by the point where the oscillation frequency is equal to the Lamb frequency. Moreover, since the Brunt-Väisälä frequency is rather small in upper regions, and that S_ℓ^2/ω^2 can be neglected in equation 3.34 or 3.35, this basically means that the behaviour of the pressure modes is determined through the local adiabatic sound speed, c^2. Pressure modes are actually acoustic waves for which the restoring force is generated by pressure gradients.

Gravity modes

Gravity modes are low frequency modes defined by

$$\omega^2 < S_\ell^2, \tag{3.38}$$

and

$$\omega^2 < N^2. \tag{3.39}$$

These non-radial oscillation modes propagate in deep regions of stars and can be useful for probing their internal structure. Similarly to what is done for the pressure modes, one can then consider in equation 3.34 or 3.35 that $N^2-\omega^2 \approx N^2$. Their restoring force is buoyancy, which only acts on non-radial density perturbations thereby generating non-radial oscillations. Gravity modes do not propagate in convective regions, which makes them difficult to observe for low mass stars having an extended convective envelope. However, these modes have been used in γ Doradus stars to constrain the overshooting parameter (Bouabid (2011)).

Mixed modes

In some particular cases, equations 3.36 and 3.37 are satisfied in the upper regions and equations 3.38 and 3.39 are satisfied in the deep regions. Such oscillation modes are called mixed modes. Their physical behaviour is linked to the width of the evanescent region between the envelope and the core: some pressure modes, coming from the upper regions, can tunnel into the core and propagate as gravity waves. These modes have been observed in intermediate-mass stars and in subgiants and red giants. Their discovery by CoRoT and Kepler led to the ability to distinguish stars in the RGB from those in the so-called red clump, which are burning helium in their core (Beck, Bedding, et al. (2011), Bedding, Mosser, et al. (2011), Montalbán et al. (2013)). They have also been used to gain information on the rotational profile of the core and upper layers of subgiants and red giants (Deheuvels, Doğan, et al. (2014), Mosser, Goupil, et al. (2012)), thus demonstrating the failure of stellar models to reproduce adequatly the transport of angular momentum during stellar evolution. Recently, some attempts have been made to explain these results (Belkacem, Marques, Goupil, Sonoi, et al. (2015), Belkacem, Marques, Goupil, Mosser, et al. (2015), Pinçon, Belkacem, and Goupil (2016)). Further progress has been made in understanding their characteristics thanks to the development of an asymptotic expansion of these modes (Takata (2016)).

3.2 Asymptotic properties of pressure and gravity modes

Although the crude approximation we have made in the preceding section can provide some physical insight in the behaviour of the modes, less approximate developments can be used to derive interesting properties of oscillations in a specific range of ℓ and n. In this section we will present analytical results for what is called the asymptotic approximation of stellar oscillations. A full description of the mathematical developments can be found in Tassoul (1980).

The basic equations of this analysis is the second order system given by equations 3.26 and 3.27 which is obtained by applying the Cowling approximation to the full fourth-order system of stellar pulsations. The system is then rewritten as a function of a modified displacement function

$$X = c^2 \sqrt{\rho} \vec{\nabla} \cdot \vec{\xi}. \tag{3.40}$$

By neglecting the variation of the gravity, g and density, ρ when compared to the perturbed thermodynamical quantities, one can obtain a second order differential equation for X

$$\frac{d^2X}{dr^2} = -K(r)X, \tag{3.41}$$

with

$$K(r) = \frac{1}{c^2}\left[S_\ell^2\left(\frac{N^2}{\omega^2} - 1\right) + \omega^2 - \omega_c^2\right], \tag{3.42}$$

where we defined the acoustic cut-off frequency, ω_c as

$$\omega_c^2 = \frac{c^2}{4H_P}\left(1 - \frac{dH_P}{dr}\right), \tag{3.43}$$

If $K(r)$ is positive, the solution will be an oscillating function. However, if $K(r)$ is negative, the solution will show an exponential behaviour. In the surface layers, the dominant term

of $K(r)$ will be $(\omega^2 - \omega_c^2)$ because S_ℓ^2 becomes negligible. Consequently, the behaviour of the mode will be dictated by the difference $(\omega^2 - \omega_c^2)$. If $\omega < \omega_c$ the mode will show an exponential decay in the upper regions and thus be trapped in the star. If, in contrast, ω is larger than ω_c, it will show an oscillating behaviour in the atmosphere and thus will lose its energy very quickly.

The analytical solution to equation 3.41 is found by using the JWKB approximation (standing for Jeffreys, Wentzel, Kramers, and Brillouin) which was used in quantum mechanics and applied by Unno et al. (1989) in the context of stellar pulsations. The fundamental hypothesis is that the solution will vary faster than the equilibrium quantities. In other words, $X(r)$ varies more rapidly than $K(r)$ and can be described by a function of the form

$$X(r) = a(r)e^{i\phi(r)}, \tag{3.44}$$

where $\phi(r)$ varies much faster than $a(r)$ and one can derive a local wavelength of the form

$$n = \frac{d\phi}{dr}. \tag{3.45}$$

This solution can be inserted in equation 3.41 and one can find that the behaviour of the solution will again be sinusoidal or exponential depending on the sign of $K(r)$. After some additional mathematical developments and the proper treatment of the boundary conditions at the reflexion points, one can derive the asymptotic form of the eigenfunctions and show that the frequencies of modes trapped between two turning points r_1 and r_2 must satisfy the following relation

$$\int_{r_1}^{r_2} K^{1/2}(r)dr = \left(n - \frac{1}{2}\right)\pi. \tag{3.46}$$

3.2.1 Asymptotic expression of pressure modes

For pressure modes which have $\omega^2 \gg |N|^2$, it can be shown that equation 3.46 reduces to the so-called Duvall law (Duvall (1982))

$$\int_{r_t}^{R} \left(1 - \frac{(\ell(\ell+1))^2 c^2}{\omega^2 r^2}\right) \frac{dr}{c} = \frac{(n + \alpha(\omega))\pi}{\omega}, \tag{3.47}$$

with $\alpha(\omega)$ depending on the surface regions, r_t being the lower turning point where $S_\ell(r_t) = \omega$ and R the upper turning point where $\omega_c(R) = \omega$, which is valid for moderate values of ℓ.

This relation can be further simplified by noticing that for low ℓ modes, $r_t \approx 0$ and the argument of the integral in equation 3.47 is approximately $\frac{dr}{c}$. This implies a simple behaviour of the frequencies of pressure modes to the leading order

$$\frac{\omega_{n,\ell}}{2\pi} \approx \left(n + \frac{\ell}{2} + \frac{1}{4} + \alpha\right)\Delta\nu, \tag{3.48}$$

which introduces the definition of the large frequency separation

$$\Delta\nu = \int_0^R \left(\frac{dr}{c}\right)^{-1} \approx \nu_{\ell,n} - \nu_{\ell,n-1}. \tag{3.49}$$

From this first order analysis, one would expect a uniform spacing in n defined by the large frequency separation. However, this is only a very crude analysis and Tassoul (1980)

and D. O. Gough (1986) have shown that the asymptotic developments have to be pushed up to second order in $1/\omega$ to retrieve the deviations from the degeneracy expected from equation 3.48. The asymptotic expression of the oscillation frequency is then given by

$$\nu_{n,\ell} = \left(n + \frac{\ell}{2} + \frac{1}{4} + \alpha\right)\Delta\nu - \left(A\ell\left(\ell+1\right) - \delta\right)\frac{\Delta\nu}{\nu_{n,\ell}^2}, \tag{3.50}$$

with

$$A = \frac{1}{4\pi^2\Delta\nu}\left(\frac{c(R)}{R} - \int_0^R \frac{dc}{dr}\frac{dr}{r}\right). \tag{3.51}$$

In figure 3.1, we show that the frequencies are indeed, to a first degree of approximation regularly spaced.

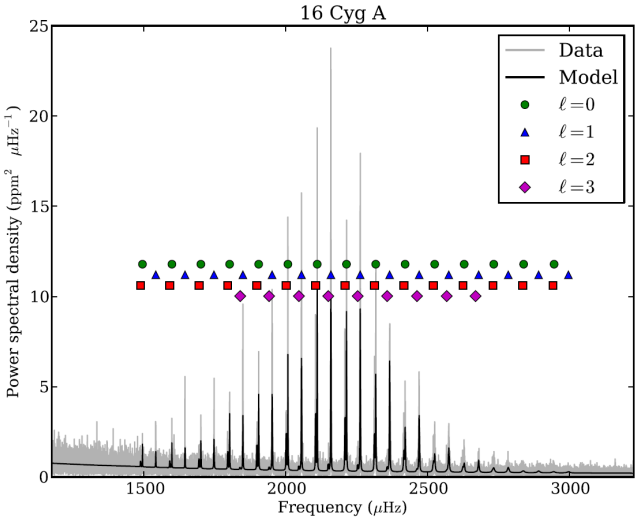

Figure 3.1: Power spectrum of 16CygA using the entire Kepler data set, illustrating the regularity in frequency of solar like oscillations. The symbols are used to identify the modes of various ℓ (reprinted from Davies et al. (2015)).

From equation 3.50 we define so-called small frequency separation

$$\delta\nu = \nu_{n,\ell} - \nu_{n-1,\ell+2} \approx -\left(4\ell+6\right)\frac{\Delta\nu}{4\pi^2\nu_{n,\ell}}\left(\frac{c(R)}{R} - \int_0^R \frac{dc}{dr}\frac{dr}{r}\right). \tag{3.52}$$

In this expression, the term $c(R)$ is often neglected and the small frequency separation is considered to probe the internal layers of the star. The large and small frequency separations are often combined to build the asteroseismic HR diagram (or JCD diagram) used to estimate the average properties of an observed target. Such a diagram is illustrated for theoretical models in figure 3.2. The large frequency separation is indeed related to the mean density of the star while the small frequency separation is a probe of the evolutionary stage (Christensen-Dalsgaard (1993a)). In practice however, both of these quantities are affected by surface effects, and I. W. Roxburgh and S. V. Vorontsov (2003) have demonstrated that using frequency ratios was more efficient to suppress the effects of the upper layers that would bias analyses based on pressure modes. Moreover it can be shown that the accuracy of equation 3.52 is not always satisfied. Asymptotic developments up to the fourth order can be found in I. W. Roxburgh and S. V. Vorontsov (1994b) and developments for intermediate and high ℓ acoustic oscillations can be found in Brodsky and S. V. Vorontsov (1993) and I. W. Roxburgh and S. V. Vorontsov (1996).

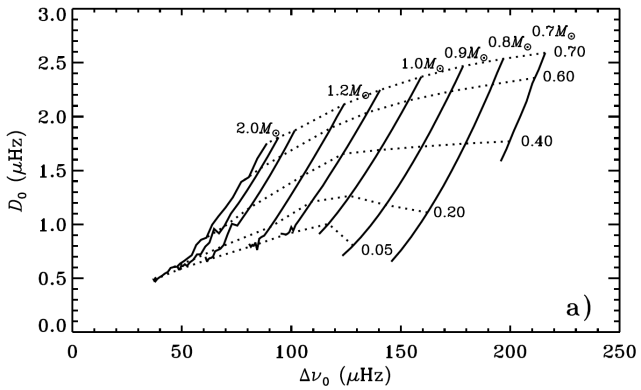

Figure 3.2: Asteroseismic HR diagram for models of various masses. Each line corresponds to one evolutionary track associated with a given mass and set of physics (reprinted from Christensen-Dalsgaard (1993b)). The small and large frequency separations are noted D_0 and $\Delta\nu_0$ instead of $\delta\nu$ and $\Delta\nu$.

3.2.2 Asymptotic expression of gravity modes

Since gravity modes do not propagate in convective regions, their asymptotic behaviour is mostly described by the nulls in the Brunt-Väisälä frequency. Thus, various cases have to be considered and we refer to Tassoul (1980) for a description of each of them. In this section, we will briefly describe the characteristics of a model with a radiative core surrounded by a convective envelope. In this particular case, it can be shown that the asymptotic expression of the period of low degree, high order gravity modes is

$$P_k = \frac{\pi^2}{\sqrt{\ell(\ell+1)}\int_0^{r_C}\frac{N}{r}dr}(2n+\ell+\alpha), \tag{3.53}$$

where in the example we have chosen the situation of a radiative core, hence the value 0 for the lower border and r_C would be the position of the convective envelope of the star. Asymptotically, the g modes are equally spaced in period, which means that one can derive a period spacing, denoted ΔP

$$\Delta P = P_{k+1} - P_k. \tag{3.54}$$

In practice of course, the period spacing of observed gravity modes will not be constant. It has been shown that the structure of the period spacing can be used to constrain the chemical composition gradient of deep regions in intermediate-mass stars (Miglio, Montalbán, Noels, et al. (2008), Bouabid (2011)).

3.3 Effects of rotation

We have seen in section 3.1 that for a non-rotating star, the solutions are degenerate and all the frequencies can be characterised by two quantum numbers only, their degree, ℓ and their radial order, n. However, if the rotation of the star is taken into account, we will see that rotation will break the symmetry of the system and the solutions have to be characterised by three quantum numbers, ℓ, n and the azimuthal order, m. The effects of slow rotation can be treated as a perturbation of spherically symmetric solutions and to the first order for a rigid rotation, the frequencies are given by

$$\nu_{n,\ell}^m = \nu_{n,\ell}^0 + m\beta_{n,\ell}\Omega, \tag{3.55}$$

with Ω the rotation rate of the star, $\nu^m_{n,\ell}$ the frequency including the effect of rotation,$\nu^0_{n,\ell}$ the frequency of the non-rotating star, and $\beta_{n,\ell}$ the Ledoux constant related to rotation. If one considers a differential rotation in radius, the rotational splitting will be symmetrical and one can apply a variational analysis leading to an integral relation between the splitting and the rotational profile. If the horizontal variations of the rotational profile are taken into account, the rotational splitting is not constant anymore. This integral relation was used in the solar case to carry out inversions of the solar rotation profile. To this day, various mechanisms have to be invoked to reproduce the inverted solar rotation profile (Kosovichev (1988), Kosovichev, Schou, et al. (1997), Schou, Christensen-Dalsgaard, and Thompson (1994)). The two-dimensional integral relation is

$$\delta\omega_{n,\ell,m} = \frac{m\mathscr{R}^m_{n,\ell}}{\int_0^R \rho_0 \left[\xi^2_{r,0} + \ell(\ell+1)\xi^2_{h,0}\right] r^2 dr}, \tag{3.56}$$

with $\mathscr{R}^m_{n,\ell}$ defined as follows

$$\begin{aligned}\mathscr{R}^m_{n,\ell} = \int_0^\pi \sin\theta d\theta \int_0^R \Bigg(&|\xi_r|^2 P^m_\ell(\cos\theta)^2 + |\xi_h|^2 \left[(\frac{dP^m_\ell}{d\theta})^2 + \frac{m^2}{\sin^2\theta} P^m_\ell(\cos\theta)^2 \right] \\ &- P^m_\ell(\cos\theta)^2 \left[\xi^*_r \xi_h + \xi_r \xi^*_h\right] - 2P^m_\ell(\cos\theta) \frac{dP^m_\ell}{d\theta} \frac{\cos\theta}{\sin\theta} |\xi_h|^2 \Bigg) \Omega(r,\theta)\rho_0(r) r^2 dr,\end{aligned} \tag{3.57}$$

which is often written in the so-called *kernel* form

$$\delta\omega_{n,\ell,m} = m \int_0^R \int_0^\pi K_{n,\ell,m}(r,\theta)\Omega(r,\theta) r dr d\theta, \tag{3.58}$$

with $K_{n,\ell,m}$ the rotational kernel associated with the splitting. A review on the various methods used for rotational inversions can be found in Schou, Christensen-Dalsgaard, and Thompson (1994).

As stated before, some rotation inversions have been carried out for subgiants and red giants, showing trends in their surface and core rotation that also points towards unknown mechanisms of angular momentum redistribution.

The first order approximation is well suited for the Sun, or other typical slow rotators, but if one wishes to study stars rotating faster, it is of course insufficient. It is possible to push further the perturbative developments, leading to higher order expressions. However, it is also possible to develop fully two-dimensional pulsation codes taking into account the complex geometry of the pulsation modes in fast rotators (D. R. Reese, Prat, Barban, van't Veer-Menneret, et al. (2012), D. R. Reese, Prat, Barban, van 't Veer-Menneret, et al. (2013), Ouazzani, M.-A. Dupret, and D. R. Reese (2012)). Recently, even a non-adiabatic version of these codes has been developed, but the problem of fast rotators is the absence of regularity in the oscillation spectra. This means that mode identification is almost impossible and while trends and local regularities can be found, there is to this day no clear solution to this problem.

3.4 Pulsation mechanisms

In this section, we will briefly list the various physical mechanisms that can lead to the excitation of stellar pulsations. This section limits itself to the minimal amount of information needed and thus consistutes more an informative summary rather than an extended description of each mechanism.

Efficient driving means that some energy of the medium can be injected in the oscillations. It can be demonstrated that driving will occur in a given shell of stellar material if in the work integral

$$\eta = \frac{\frac{-\pi}{\omega}\int_0^M \mathscr{R}\left(\frac{1}{\sigma}\left(\frac{d\delta L}{dm} - \delta\varepsilon\right)\frac{\delta T}{T}\right)dm}{\int_0^M |\vec{\xi}|^2 dm}, \tag{3.59}$$

both $\left(\frac{d\delta L}{dm} - \delta\varepsilon\right) > 0$ and $\frac{\delta T}{T} > 0$. Meaning that heat is increased at the hot phase of the cycle. Formally, it implies that the occurence of oscillations will result from the balance between driving and damping effects in the star. However, pulsations will only be vibrationally unstable if the eigenmodes also have large amplitudes in the driving region. In addition, if the thermal timescale is much shorter than the pulsation period, heat will not be directly transferred through stellar material and cannot be used to drive pulsations.

3.4.1 The κ mechanism

The κ mechanism is probably the most well-known pulsation mechanism, being responsible for the variability of classical pulsators. To understand how the energy is transferred to the oscillations, one has to write, in this case, the Lagrangian variation of the radiative luminosity

$$\frac{\delta L_r}{L_r} = \frac{dr}{d\ln T}\frac{d}{dr}\left(\frac{\delta T}{T}\right) - \frac{\delta\kappa}{\kappa} + 4\frac{\delta T}{T} + 4\frac{\delta R}{R}. \tag{3.60}$$

Usually, the opacity decreases under compression and the pressure perturbation increases outwards. Moreover, the variation of opacity with pressure is rather small, such that most of the time, the effects of opacity are rather small and linked to damping rather than mode excitation (see eq. 3.59). However, in partial ionisation zones, the opacity will behave "abnormaly". There, an opacity peak is present and can trigger the driving of pulsations. Driving only occurs if the opacity peak coincides with the transition region, where the thermal timescale and the oscillation period (related to the dynamical timescale) are of the same order of magnitude. This mechanism can occur in the ionisations of any chemical species, being helium, hydrogen or more massive elements. Most of the self-excited pulsators are actually driven by the κ mechanism (see Pamyatnykh (1999) for a description of the instability domains of these pulsators in the H-R diagram.).

3.4.2 Convective blocking

In this case, the Lagrangian perturbation of luminosity must be written as both the perturbation of the radiative and convective contributions, denoted L_r and L_c respectively, to the total luminosity. In other words, one has

$$\frac{\delta L}{L} = \frac{\delta L_r}{L} + \frac{\delta L_c}{L}. \tag{3.61}$$

The analysis of the excitation of pulsation is much more complicated when coupled with convective motions, since the interaction between convection and oscillation is very poorly modelled. At the base of the upper convective zone, the contribution of radiation to the energy transport will quickly decrease as convection takes over. The gradient of the perturbation of the radiative flux can be written as

$$\frac{d\delta L_r}{dm} \approx 4\pi r^2\left(\frac{dF_r}{dr}\right)\frac{\delta L_r}{L_r}. \tag{3.62}$$

It can be shown that, at the base of a convective envelope, δL_r is positive under a compression. Since the radiative flux is decreasing in this region, $\frac{d\delta L_r}{dm}$ is negative and the flux variation can efficiently drive pulsations modes if the base of the convective envelope is located at the transition region. The driving is however controlled by convection, which quickly takes over as the dominating transport mechanism. It has been shown that while the timescale of the convective transport is indeed longer than the pulsation period at the base of the convective zone, it is only so on a very limited region and one needs to use a time dependent convection treatment rather than the more crude frozen convection formalism. This pulsation mechanism could be responsible for the pulsation of γ Doradus stars (see M.-A. Dupret, Grigahcène, et al. (2005) and Guzik, Kaye, et al. (2000)).

3.4.3 The ε mechanism

It can be shown that the rate of production of thermonuclear energy, ε, is extremely sensitive to temperature (see Kippenhahn, Weigert, and A. Weiss (2012)). Looking back at equation 2.8, we can see that it will indeed increase rapidly under compression. However, the main problems with this driving mechanism are linked to the nuclear timescales, which are extremely long compared to the dynamical ones and the fact that eigenfunctions have generally very low amplitude in the core. As a consequence, the driving of gravity or acoustic modes is only expected for a few intermediate reactions or in very specific cases, for example where the nuclear reactions occur in thin shells. Another problem with this driving mechanism comes from radiative damping. In fact, for this mechanism to operate, the driving due to compression must dominate the radiative damping which is very high in the stars identified as possible pulsators driven by the ε mechanism. Some examples of possible pulsations have been proposed in the litterature (Chené et al. (2011), Cody (2012)).

3.4.4 Stochastic excitation

The driving mechanisms we described in the previous sections are linked to so-called self-excited pulsations. However, the type of oscillations we will further discuss in this thesis are externally driven and damped, and constitute what is called *solar-like oscillations*. These pulsations show very small amplitudes but have been observed for an extensive number of targets and have provided a lot of information on stellar structure and evolution.

Stochastic oscillations are generated in the super-adiabatic region of the star by the effects of turbulent convection. A simple image would be to say that the convective plumes act on the surface of the star like small fingers on a drum. Given the right resonant frequency, they can excite normal modes that will propagate inside the stellar structure. In a Fourier power spectrum, stochastic oscillations will appear as a speckle-like lorentzian profile, which can be demonstrated to result from both convective driving and damping. The main difficulty in the non-adiabatic modelling of solar-like oscillations is the fact that they are intrisically coupled to the modelling of turbulence and the way it interacts with pulsations. Indeed, it is the interaction between time dependent convection and pulsations that will provide the effective damping rates and driving of the oscillations. The difficulties encountered in this modelling are closely related to what is called the surface effect problem that will be further discussed in section 3.9. We refer to the review of Chaplin and Miglio (2013) or classical textbooks for a more thorough description of these processes. The interested reader can also see Belkacem, Goupil, et al. (2011) for further insights on the non-adiabatic properties of solar-like oscillations.

3.5 Observed pulsators in the HR diagram

In this section, we will briefly present some of the most well-known pulsating stars in the HR diagram. Each family is represented in figure 3.3. The main purpose of this section is to show the variety of pulsating stars that can be found. We redirect the interested reader to review papers related to each type of pulsator in each subsection. In this thesis, we will only deal with main-sequence, solar-like oscillators, for they are the ones for which classical linear inversion techniques are the most well suited. A more thorough description of each type of pulsator can be found in Unno et al. (1989), Christensen-Dalsgaard (2003), Aerts, Christensen-Dalsgaard, and Kurtz (2010), J. P. Cox (1980) or in dedicated reviews.

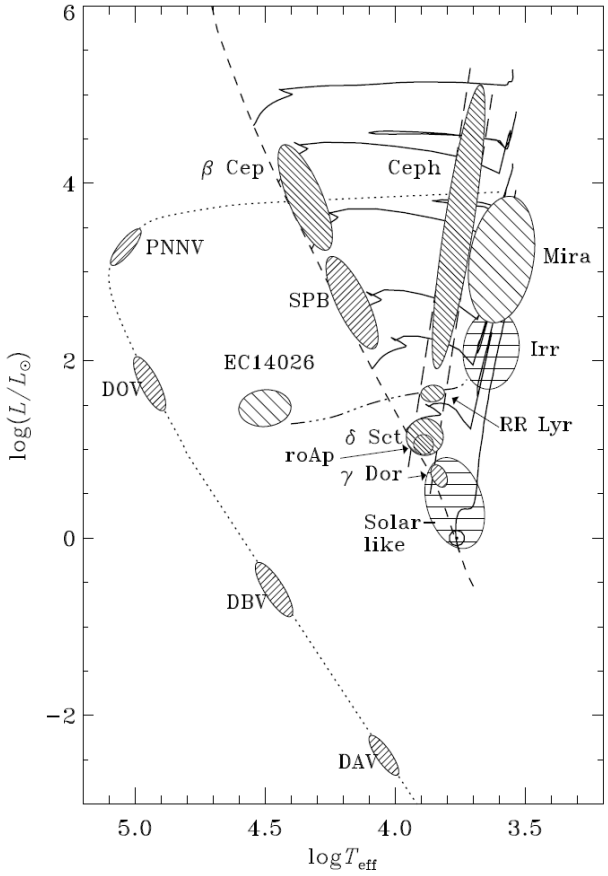

Figure 3.3: Hetzsprung-Russel diagram showing the various classes of pulsating stars observed in the universe (reprinted from Christensen-Dalsgaard (2003))

3.5.1 Solar-like stars

The Sun is the most well-known pulsating star, with hundreds of thousands of observed pulsating modes. As such it defines a whole class of pulsating stars using the same excitation mechanism. The quality of the observed data has made the Sun an excellent laboratory for theoretical physics and stellar evolution. The observed oscillation modes are pressure modes, excited by turbulence in the upper layers of the convective zone, working like thousands of small fingers hitting the surface of a drum. The typical oscillation period is of the order of a few minutes.

A particular characteristic of solar-like oscillations is their relatively low amplitudes making them relatively hard to observe on stars other than the Sun. Their amplitudes

scale with L/M. They have also been observed by the satellite CoRoT in a β Cephei (Belkacem, Samadi, et al. (2009)) and B and O type stars (Degroote et al. (2010) and Neiner et al. (2009)). An example of solar like oscillations is given in Fig 3.1, where one can see a typical example of the regularity present in the spectrum of such pulsators. The power of the spectrum is maximal around a given frequency, denoted ν_{max}, the frequency of maximum power, which follows an empirical relation (Kjeldsen and Bedding (1995))

$$\nu_{max} \approx \frac{M/M_{\odot}}{(\sqrt{T_{eff}/5777})(R/R_{\odot})^2} 3.05(mHz). \tag{3.63}$$

Another important frequency for solar-like pulsations is the acoustic cutoff frequency, denoted ν_c, which marks the upper limit of the resonant cavity for pressure modes. Beyond this frequency, one does not speak about eigenmodes but rather travelling waves. Attempts to provide a physical basis for the empirical relation 3.63 have been presented in Belkacem, Goupil, et al. (2011).

Before the advent of space missions dedicated to asteroseismology, the very low amplitude of solar-like oscillations meant that only a few of these pulsators had been observed. Since the era of CoRoT and Kepler, the sample has now increased and the quality of the seismic data is unparalleled, paving the way for accurate seismic modelling of a large number of solar-like oscillators (Chaplin and Miglio (2013) and Christensen-Dalsgaard (2012)). The sample should increase even more in the coming years thanks to K2, Tess and Plato.

3.5.2 Subgiants and red giants

With the advent of the CoRoT mission, one of the first big results of the mission was the detection of solar-like oscillations in stars beyond the main sequence. Observations of oscillation modes had been made by ground-based facilities, but CoRoT paved the way for the detection of an unprecedented wealth of seismic data, showing precise individual modes that could be used for detailed seismic modelling for thousands of giants.

After the main sequence, the core contraction leads to an increase of the frequency of gravity modes. Simultaneously, the expansion of the envelope leads to a decrease of the frequency range of pressure modes. In the case of subgiants and red giants, the frequency range of both g and p modes become similar and a p mode can "tunnel" into the core in the form of a g mode. This mechanism of so-called avoided crossing leads to the formation of mixed modes, probing efficiently both the envelope and the core. These modes have been successfully used to analyse the rotation of the core of subgiants and red giants (e.g. Deheuvels, Doğan, et al. (2014), Mosser, Goupil, et al. (2012), Beck, Montalban, et al. (2012)) and to distinguish between helium burning giants and those who had not reached that evolutionary stage yet (Bedding, Mosser, et al. (2011), Montalbán et al. (2013)).

In addition to these discoveries, the advent of space photometry led to the birth of ensemble asteroseismolgy as well as Galactic archeology, thus showing the enormous potential of seismology of evolved stars. To this day, the field is still rapidly evolving with new theoretical developments resulting from the comparison of models with observations.

3.5.3 Other well-known pulsators

γ Doradus stars

γ Doradus stars are main-sequence stars with masses around $1.5M_{\odot}$, of spectral type $A0$ to $F5$. They show oscillations due to high radial order gravity modes of low degree with periods ranging from 0.3 to 3 days.

δ Scuti stars

The δ Scuti stars are stars of spectral type A or F. They show mostly low order p modes as well as gravity modes. They are known to show hundreds of "modes" with frequencies between 20 minutes and 8 hours. The main problem of these stars is their high rotation velocities and the non-linear behaviour of the modes, thus preventing their identification.

Rapidly oscillating Ap stars

Rapidly oscillating Ap stars are main-sequence stars of around $2M_{\odot}$, located in the δ Scuti instability strip. These stars show high order low degree pressure modes with periods of 5 to 20 minutes.

Slowly pulsating B dwarfs

Slowly pulsating B dwarfs are stars of spectral type B2 to B9, having masses from $3M_{\odot}$ up to $8M_{\odot}$. They show high order gravity modes with periods ranging from 1 to 3 days.

β Cephei stars

β Cephei stars are massive stars, from $7M_{\odot}$ to $20M_{\odot}$, of spectral type B0 to B3. Their oscillation periods are of about 2 to 8 hours, due to both low order gravity and pressure modes.

The classical instability strip: Cepheids, RR Lyrae

Cepheids and RR Lyraes are pulsating stars showing periods of about 1 to 50 days and 8 to 12 hours respectively. The pulsations are radial modes of low order excited by the κ mechanism. While these stars are presented as typical pulsators, especially the Cepheids due to the use of their period luminosity relation in distance calculations, they don't show much potential for asteroseismology due to the limited number of observed modes (one or two).

SdB stars

Type B subdwarfs are evolved stars on the so-called horizontal branch. These stars are burning helium in their core and have the peculiarity of having lost most of their hydrogen envelope. They can exhibit gravity modes with periods ranging from 0.5 to 3 hours and low order p modes of the order of a few minutes. They have sufficiently rich oscillation spectra to be used in detailed asteroseismic studies. Their evolutionary path is unknown. One hypothesis advances that the loss of their envelope could be explained by their belonging to a binary system. Accordingly, their seismic study is quite important to constrain both stellar evolution theory and our picture of binary systems.

White dwarfs

Pulsating white dwarfs have been known since the 1970*s*. They exhibit high order gravity modes which probe the upper regions of the star. Their periods depend on the star type and go from 5 to 80 minutes for DOV stars, 2 to 15 minutes for DBV stars and 0.5 to 25 minutes for DAV stars. In the case of these evolved targets, asteroseismology is an efficient tool to probe the chemical composition of each layer of material and put constraints on the equation of state of these stars. It should be noted that they have also been the amongst the first stars other than the Sun for which asteroseismic inversions have been considered Takata and Montgomery (2002).

3.6 The variational principle

The derivation of the variational principle of adiabatic stellar oscillations is a consequence of fundamental developments in the larger context of fluid dynamics. It should be noted

that in the pionneering work of Chandrasekhar (1964) or Lynden-Bell and Ostriker (1967), these authors speak of gaseous spheres and the derivation of the variational principle is done under very general conditions.

Historically, the variational principle stems from stability analyses and the interest in such properties can be found in the Adam's prize essay "A Treatise on the Stability of a Given State of Motion" by Edward John Routh in 1877. In this section, we will start with the functional analysis of the Navier-Stokes equations and gradually move on to the specific case of adiabatic stellar oscillations. The results we present are similar to those of Lynden-Bell and Ostriker (1967).

3.6.1 Functional analysis of fluid flows

In section 3.1, we described the particular case of adiabatic stellar oscillations. However, to illustrate the very general nature of the variational principle, it is interesting to use the general Navier-Stokes equations for a perturbed perfect fluid. We will thus use the system of equations 3.4, 3.5, 3.6 and 3.7 , for which we introduce small perturbations and consider Fourier modes to describe the oscillations. In other words, the perturbations are written: $\delta f = f^{'} \exp^{i\omega t}$, with ω the frequency of the Fourier mode. Simple algebra leads to the following system of equations:

$$\rho^{'} = -\nabla \cdot (\rho_0 \vec{\xi}), \tag{3.64}$$

$$-\omega^2 \vec{\xi} + 2i\omega(\vec{v}_0 \cdot \vec{\nabla} + \vec{\Omega}\times)\vec{\xi} + (\vec{v}_0 \cdot \vec{\nabla})^2 \vec{\xi} + \vec{\Omega} \times (\vec{\Omega} \times \vec{\xi}) = -\vec{\nabla}\phi^{'} + \frac{\rho^{'}}{\rho_0^2}\vec{\nabla}P_0 - \frac{\vec{\nabla}P^{'}}{\rho_0}, \tag{3.65}$$

$$\Delta\phi^{'} = 4\pi G \rho^{'}, \tag{3.66}$$

for which we have introduced the perturbations of density, pressure, gravitational potential and the displacement vector, $\rho^{'}$, $P^{'}$, $\phi^{'}$ and $\vec{\xi}$. These functions only depend on the position inside the fluid, $\vec{r}$, because of the separation of variables induced by the Fourier development. Now besides these perturbations, we have considered one of the most general case of a fluid flow with an advective current, $\vec{v}_0$ in the corotating frame, the rotation of the fluid being at a constant velocity $\vec{\Omega}$. The rest of the quantities, P_0 and ρ_0 are the equilibrium pressure and density. One could also introduce a magnetic field in these equations and see its effect on the frequencies. This has been done in Clement (1964) and leads to similar equations. The only hypothesis of physical importance that has never been removed is that of adiabatic oscillations. In every variational study, the energy equation has been decoupled from the dynamical ones by considering an adiabatic relation in the form of equation 3.7 between pressure and density. We will further comment on this in the next section.

To derive the variational principle, one needs, as stated in the title, to perform a functional analysis of the equations of fluid flows. Therefore, we start by considering a Hilbert space, $\mathscr{H}$, of the vector functions of displacement fields inside the fluid. We add that the functions of this space must satisfy the boundary conditions of the eigenvalue problem under study and that their first derivatives must be piecewise continuous. We start by defining the scalar product on the Hilbert space as

$$< \vec{\xi}, \vec{\psi} >= \int_V \vec{\xi}^* \cdot \vec{\psi} \rho_0 dV, \tag{3.67}$$

for each $\vec{\xi}$ and $\vec{\psi} \in \mathscr{H}$. We can now rewrite the pulsation equation in a symbolic form where we isolate three operators

$$-\omega^2 \mathscr{A}(\vec{\xi}) + \omega \mathscr{B}(\vec{\xi}) + \mathscr{C}(\xi) = 0. \tag{3.68}$$

These operators are defined as follows

$$\mathscr{A}(\vec{\xi}) = -\vec{\xi}, \tag{3.69}$$

$$\mathscr{B}(\vec{\xi}) = -(2i\vec{v}_0 \cdot \vec{\nabla})\vec{\xi} - 2i\Omega \times \vec{\xi}, \tag{3.70}$$

$$\begin{aligned}\mathscr{C}(\vec{\xi}) &= \mathscr{C}_1(\vec{\xi}) + \mathscr{C}_2(\vec{\xi}) + \mathscr{C}_3(\vec{\xi}) + \mathscr{C}_4(\vec{\xi}) + \mathscr{C}_5(\vec{\xi}) \\ &= -\vec{\nabla}\phi' + \frac{\rho'}{\rho_0^2}\vec{\nabla}P_0 - \frac{\vec{\nabla}P'}{\rho_0} - (\vec{v}_0 \cdot \vec{\nabla})^2 - \vec{\Omega} \times \vec{\Omega} \times \vec{\xi}.\end{aligned} \tag{3.71}$$

3.6.2 Symmetry of linear adiabatic non-radial oscillations

The symmetry of pulsation operators is a crucial mathematical property to derive the variational principle and consequently, to be able to perform inversions. In this section, we will present a demonstration of this property for the general case presented in Lynden-Bell and Ostriker (1967). We will also comment on some simplifications applied during the analysis of symmetry and their implications for inversion techniques. To demonstrate the symmetry of the operators presented in Eq. 3.69-3.71, one has to prove that

$$\int \vec{\xi}^* \cdot \mathscr{F}(\vec{\psi})\rho_0 dV = \left[\int \vec{\psi}^* \cdot \mathscr{F}(\vec{\xi})\rho_0 dV\right]^*, \tag{3.72}$$

with $\mathscr{F}$ being each of the operators associated with pulsations and $\vec{\psi}$ and $\vec{\xi}$ being any vector functions defined on the hilbert space associated with linear adiabatic oscillations. For $\mathscr{A}$, the demonstration is trivial and stems from the symmetry of the classical scalar product between vectors. Indeed, one has

$$\int \rho_0 \vec{\xi}^* \cdot \vec{\psi} dV = \left[\int \rho_0 \vec{\xi} \cdot \vec{\psi}^* dV\right]^*. \tag{3.73}$$

The demonstration of the symmetry of the $\mathscr{B}$ operator is somewhat longer and requires a few more developments. The starting expression is the following

$$\int \vec{\xi}^* \cdot \mathscr{B}_1(\vec{\psi}) dV = -\int \vec{\xi}^* \cdot (2i\vec{v}_0 \cdot \vec{\nabla})\vec{\psi}\rho_0 dV, \tag{3.74}$$

we then use an integration by parts using the following formula

$$\rho_0 \vec{\xi}^* \cdot (\vec{v}_0 \cdot \vec{\nabla})\vec{\psi} = \nabla \cdot \left((\vec{\xi}^* \cdot \vec{\psi})\rho_0 \vec{v}_0\right) - \rho_0 \vec{\psi} \cdot (\vec{v}_0 \cdot \vec{\nabla})\vec{\xi}^* - \vec{\psi} \cdot \vec{\xi}^* \vec{\nabla} \cdot (\rho_0 \vec{v}_0), \tag{3.75}$$

which is easily demonstrated by expanding the equation into components as follows

$$\rho_0 \xi_i^* v_{0,j} \frac{\partial \psi_i}{\partial x_j} = \frac{\partial(\rho_0 v_{0,j} \xi_i^* \psi_i)}{\partial x_j} - \psi_i \frac{\partial(\rho_0 v_{0,j} \xi_i^*)}{\partial x_j}. \tag{3.76}$$

The first term can be written $\nabla \cdot ((\rho_0 \vec{\xi}^* \cdot \vec{\psi})\vec{v}_0)$ which will give a surface integral due to Gauss's Theorem. However, the velocity of the steady flow, $\vec{v}_0$, is always parallel to the normal of the unperturbed surface. Therefore, this surface integral is exactly 0. Similarly, the second term can be separated in two contributions, the first one including the term $\nabla \cdot (\rho_0 \vec{v}_0)$, being 0 for the reasons we invoked before, the second one being $-\rho_0 \vec{\psi} \cdot ((\vec{v}_0 \cdot \vec{\nabla})\vec{\xi}^*)$, the one we seek.

We then have the symmetry property satisfied since

$$
\begin{aligned}
&-\int \vec{\xi}^* \cdot (2i\vec{v}_0 \cdot \vec{\nabla})\vec{\psi}\rho_0 dV = 2i\int \rho_0 \vec{\psi} \cdot ((\vec{v}_0 \cdot \vec{\nabla})\vec{\xi}^*)dV \\
&= \left[-2i\int \rho_0 \vec{\psi}^* \cdot ((\vec{v}_0 \cdot \vec{\nabla})\vec{\xi})dV\right]^*.
\end{aligned} \tag{3.77}
$$

The same developments can be used to deal with the $\mathscr{C}_4$ term

$$
\begin{aligned}
&-\int \rho_0 \vec{\xi}^* \cdot (\vec{v}_0 \cdot \vec{\nabla})(\vec{v}_0 \cdot \vec{\nabla})\vec{\psi}dV = -\int \nabla \cdot ((\vec{\xi}^* \cdot (\vec{v}_0 \cdot \vec{\nabla})\vec{\psi})\rho_0 \vec{v}_0)dV \\
&+\int \rho_0 (\vec{v}_0 \cdot \vec{\nabla})\vec{\xi}^* \cdot (\vec{v}_0 \cdot \vec{\nabla})\vec{\psi}dV,
\end{aligned} \tag{3.78}
$$

where the first integral is actually an integral over the unperturbed surface of the star. Again, since the velocity of the steady flow is perpendicular to this surface, this contribution is exactly 0. Consequently, $\mathscr{C}_4$ is symmetric. The demonstration is similar to that of $\mathscr{B}_1$ where one would write $(\vec{v}_0 \cdot \vec{\nabla})\vec{\psi}$ intead of $\vec{\psi}$ in the developments.

For $\mathscr{B}_2$, the demonstration is trivial

$$
-\int_V 2i\rho_0 \vec{\psi} \cdot (\vec{\Omega} \times \vec{\xi})dV = -\int_V 2i\rho_0 \left[\vec{\psi}, \vec{\Omega}, \vec{\xi}\right] dV = 2i\int_V \rho_0 \left[\vec{\xi}, \vec{\Omega}, \vec{\psi}\right] dV, \tag{3.79}
$$

since using the definition of the mixed product leads to

$$
\left[\vec{\psi}, \vec{\Omega}, \vec{\xi}\right]_{i,j,k} = \xi_i(\Omega_j \psi_k - \Omega_k \psi_j) = -\left[\vec{\xi}, \vec{\Omega}, \vec{\psi}\right]_{i,j,k}. \tag{3.80}
$$

Demonstrating the symmetry of the other terms of $\mathscr{C}$ requires a little bit more developments. First, we start with $\mathscr{C}_1$ by expressing the perturbation of the gravitational potential undergone by a mass element due to the displacement induced by oscillations. One finds

$$
\begin{aligned}
d\phi' &= -\left(\frac{Gdm}{|\vec{r} - \vec{r}' - \vec{\xi}|}\right) + \left(\frac{Gdm}{|\vec{r} - \vec{r}'|}\right) \\
&= -\vec{\xi} \cdot \vec{\nabla}\left(\frac{Gdm}{|\vec{r} - \vec{r}'|}\right),
\end{aligned} \tag{3.81}
$$

which can then be integrated over the unperturbed volume to yield

$$
\begin{aligned}
\phi' &= -\int_V \vec{\xi} \cdot \nabla\left(\frac{G\rho_0}{|\vec{r} - \vec{r}'|}\right)dV \\
&= -\int_S \left(\frac{G\rho_0 \vec{\xi}}{|\vec{r} - \vec{r}'|}\right)dS + \int_V \left(\frac{G\nabla \cdot (\rho_0 \vec{\xi})}{|\vec{r} - \vec{r}'|}\right)dV,
\end{aligned} \tag{3.82}
$$

we then use the definition of the scalar product to quickly demonstrate the symmetry of

$\mathscr{C}_1$

$$\begin{aligned}\int \rho_0(\vec{r})\vec{\psi}(\vec{r})\cdot\vec{\nabla}\phi'(\vec{r}')dV' &= \int_V \rho_0(\vec{r})\vec{\psi}(\vec{r})\cdot\vec{\nabla}\left(\int_S \frac{G\rho_0(\vec{r}')\vec{\xi}(\vec{r}')}{|\vec{r}-\vec{r}'|}dS' - \int_V \frac{G\nabla\cdot(\rho_0(\vec{r}')\vec{\xi}(\vec{r}'))}{|\vec{r}-\vec{r}'|}dV'\right)dV \\ &= \int_S \rho_0(\vec{r})\vec{\psi}(\vec{r})\left(\int_S \frac{G\rho_0(\vec{r}')\vec{\xi}(\vec{r}')}{|\vec{r}-\vec{r}'|}dS'\right)dS \\ &\quad - \int_S \rho_0(\vec{r})\vec{\psi}(\vec{r})\left(\int_V \frac{G\nabla\cdot(\rho_0(\vec{r}')\vec{\xi}(\vec{r}'))}{|\vec{r}-\vec{r}'|}dV'\right)dS \\ &\quad + \int_V \nabla\cdot(\rho_0(\vec{r})\vec{\psi}(\vec{r}))\left(\int_V \frac{G\nabla\cdot(\rho_0(\vec{r}')\vec{\xi}(\vec{r}'))}{|\vec{r}-\vec{r}'|}dV'\right)dV \\ &\quad - \int_V \nabla\cdot(\rho_0(\vec{r})\vec{\psi}(\vec{r}))\left(\int_S \frac{G\rho_0(\vec{r}')\vec{\xi}(\vec{r}')}{|\vec{r}-\vec{r}'|}dS'\right)dV. \end{aligned} \tag{3.83}$$

For $\mathscr{C}_2$ and $\mathscr{C}_3$ one has to introduce the definition of the eulerian perturbation of pressure under the hypothesis of adiabaticity to obtain

$$\begin{aligned} &-\int \frac{\vec{\xi}^*\cdot(\nabla\cdot(\rho_0\vec{\psi}))\vec{\nabla}P_0}{\rho_0}dV - \int \vec{\xi}^*\cdot\vec{\nabla}P'dV \approx \int_V \nabla\cdot\vec{\xi}^*P'dV - \int \frac{\vec{\xi}^*\cdot(\nabla\cdot(\rho_0\vec{\psi}))\vec{\nabla}P_0}{\rho_0}dV \\ &= -\int_V \frac{P'(\tilde{P}')^*}{\Gamma_1 P_0}dV + \int_V \vec{\xi}^*\cdot\vec{\nabla}P_0\frac{P'}{\Gamma_1 P_0}dV - \int \frac{\vec{\xi}^*\cdot(\nabla\cdot(\rho_0\vec{\psi}))\vec{\nabla}P_0}{\rho_0}dV \\ &= \int_V \vec{\xi}^*\cdot\vec{\nabla}P_0\left(\frac{P'}{\Gamma_1 P_0} - \frac{\nabla\cdot(\rho_0\vec{\psi})}{\rho_0}\right)dV - \int_V \frac{P'(\tilde{P}')^*}{\Gamma_1 P_0}dV \\ &= -\int_V \frac{P'(\tilde{P}')^*}{\Gamma_1 P_0}dV + \int_V (\vec{\xi}^*\cdot\vec{\nabla}P_0)\left(\vec{\psi}\cdot\left(\frac{\vec{\nabla}P_0}{\Gamma_1 P_0} - \frac{\vec{\nabla}\rho_0}{\rho_0}\right)\right)dV \\ &= -\int_V \frac{P'(\tilde{P}')^*}{\Gamma_1 P_0}dV - \int_V \frac{N^2}{\rho_0|\vec{\nabla}\phi_0|^2}(\vec{\xi}^*\cdot\vec{\nabla}\phi_0)(\vec{\psi}\cdot\vec{\nabla\phi_0})dV. \end{aligned} \tag{3.84}$$

In this development, the first equality is not perfectly true since we neglected one surface term stemming from the use of Gauss's theorem in the integral of $\vec{\xi}^*\cdot\vec{\nabla}P'$. However, this surface term can be symmetrical depending on the boundary conditions used for the oscillation equations. For the last term, $\mathscr{C}_5$, one has to write

$$-\int_V \rho_0\vec{\psi}\cdot(\vec{\Omega}\times(\vec{\Omega}\times\vec{\xi}))dV = -\int_V \rho_0|\vec{\Omega}|^2(\vec{\psi}\cdot\vec{\xi})dV + \int_V \rho_0(\vec{\Omega}\cdot\vec{\psi})(\vec{\Omega}\cdot\vec{\xi})dV, \tag{3.85}$$

and the symmetry is quickly demonstrated. We have now shown that each term is symmetric, using the definition of the Brunt-Väisälä frequency and the following identity:

$$\vec{x} = \frac{<\vec{x},\vec{y}>}{|y|^2}\vec{y}, \tag{3.86}$$

if $\vec{x}$ and $\vec{y}$ are aligned. In other words, we assume here that the gradients of density, pressure and gravitational potential are aligned. This property is however to be used with caution for density and pressure gradients in fast rotating stars with non-cylindrical rotation law.

If we now consider that $\vec{\psi} = \vec{\xi}$, we can write

$$\omega^2 <\vec{\xi},\mathscr{A}(\vec{\xi})> = \omega <\vec{\xi},\mathscr{B}(\vec{\xi})> + <\vec{\xi},\mathscr{C}(\vec{\xi})>, \tag{3.87}$$

using our notation of scalar product, where each term is symmetric.

This expression will then be used to derive the variational principle, the fundamental property of pulsation equations necessary to inversion equations. However, the fact that we neglected a surface term in these developments means that the surface regions will not perfectly be represented and that the property of symmetry is valid within a given accuracy, even for stellar models. However, since the neglected term is often very small, the accuracy is still excellent. Another hypothesis in these developments is that of adiabaticity of stellar pulsations, which is made from the start on and implies that surface regions will never be properly treated. Indeed, the upper regions will never be sought for using inversions since the hypotheses are well known to break down in these layers.

The main difficulty with non-adiabatic equations is that they are intrinsically asymmetrical. As we will in the next section, the symmetry of the equations is the mathematical property that leads to the variational principle. Consequently, there is no variational principle for non-adiabatic stellar oscillations although integral relations can still be derived.

3.6.3 The variational principle

We start from equation 3.87 and consider a pair $(\omega, \vec{\xi})$ of solutions which is close to another pair of solutions $(\omega_0, \vec{\xi}_0)$, such that it can be written in a variational form with:

$$\vec{\xi} = \vec{\xi}_0 + \delta\vec{\xi}, \tag{3.88}$$

$$\omega = \omega_0 + \delta\omega, \tag{3.89}$$

with δ denoting the variational perturbation of ω and $\vec{\xi}$, not to be mistaken with the Lagrangian perturbations used for stellar pulsation equations. We search a condition such that $\delta\omega = 0$, namely that the pair $(\omega_0, \vec{\xi}_0)$ is a stationary solution of of Eq 3.87.

Therefore, we start by writing equation 3.87 for the pair $(\omega, \vec{\xi})$ and use the expressions 3.88-3.89 to simplify some terms thanks to the symmetry of the operators we demonstrated in section 3.6.2. We then have the following expression

$$\begin{aligned} 2\omega_0\delta\omega < \vec{\xi}_0, \mathscr{A}(\vec{\xi}_0) > = & -2\omega_0^2 < \delta\vec{\xi}, \mathscr{A}(\vec{\xi}_0) > + 2\omega_0 < \delta\vec{\xi}, \mathscr{B}(\vec{\xi}_0) > \\ & + 2 < \delta\vec{\xi}, \mathscr{C}(\vec{\xi}_0) > + \delta\omega < \vec{\xi}_0, \mathscr{B}(\vec{\xi}_0) > . \end{aligned} \tag{3.90}$$

We then re-arrange the expression to isolate $\delta\omega$

$$\delta\omega = \frac{-2\omega_0^2 < \delta\vec{\xi}, \mathscr{A}(\vec{\xi}_0) > + 2\omega_0 < \delta\vec{\xi}, \mathscr{B}(\vec{\xi}_0) > + 2 < \delta\vec{\xi}, \mathscr{C}(\vec{\xi}_0) >}{2\omega_0 < \vec{\xi}0, \mathscr{A}(\vec{\xi}_0) > - < \vec{\xi}_0, \mathscr{B}(\vec{\xi}_0) >}. \tag{3.91}$$

This expression shows that the only way for $\delta\omega$ to be 0 regardless of the perturbation $\delta\vec{\xi}$ is to impose the condition

$$-\omega_0^2 \mathscr{A}(\vec{\xi}_0) + \omega_0 \mathscr{B}(\vec{\xi}_0) + \mathscr{C}(\vec{\xi}_0) = 0. \tag{3.92}$$

This means that $\vec{\xi}_0$ must be an eigenfunction and that eigenfunctions are a stationary solution of Eq 3.87. In other words, this implies that a modification of the eigenfunction, $\vec{\xi}_0$, does not imply a modification of the eigenvalue, ω_0 to the first order. This stationarity property consistutes *the variational principle of stellar adiabatic oscillations*. It implies that the calculation of the eigenvalue will always be superior to that of the eigenfunctions of the oscillations. Moreover, equation 3.91 can always be used to check the quality of the

calculation of computed oscillations. It is important to link this result to that of symmetry, since symmetry is the fundamental mathematical property allowing the derivation of the stationarity of the operator for eigenfunctions. In the following section, we will also see how the variational principle is fundamental for linear stellar inversions, both structural and rotational.

3.6.4 Integral relations between frequencies and structure

In the previous sections, we have dealt with proving the symmetry of the fluid operators and the variational principle of linear adiabatic oscillations in the fluid equations. We derived these properties for a very general case of the flow. However, while in some applications these general expressions should be applied, we have seen in chapter 3.1.2 that stellar oscillations could be computed using simplified equations not including rotation, magnetic fields or even a velocity in the equilibrium flow. In this section, we will show how these simplified equations can lead to a quite simple integral relation.

First, we re-write the fluid equations using the various simplifications applied when calculating stellar oscillations. We obtain

$$-\rho_0\omega^2\vec{\xi} = -\frac{\nabla\cdot(\rho_0\vec{\xi})}{\rho_0}\vec{\nabla}P_0 - \rho_0\vec{\nabla}\phi' - \vec{\nabla}P', \tag{3.93}$$

where we already considered that the displacement vector is a Fourier mode written in the form $\delta\vec{r} = \vec{\xi}e^{-i\omega t}$. Again, we will only consider adiabatic oscillations. The eigenvalue problem can again be written in a simplified symbolic form for the fluid operator, denoted here $\mathscr{D}$

$$\omega^2\vec{\xi} = \mathscr{D}(\vec{\xi}). \tag{3.94}$$

Given the results of the previous section, this operator is obviously symmetric and satisfies the variational principle. One then writes the scalar product of equation 3.94 with $\vec{\xi}$ to get

$$\omega^2 = \frac{<\vec{\xi},\mathscr{D}\vec{\xi}>}{<\vec{\xi},\vec{\xi}>}. \tag{3.95}$$

We then perturb all quantities in equation 3.95, namely the operator, the frequencies and the displacement vector, as follows

$$\omega^2 = \omega_0^2 + \delta\omega^2, \tag{3.96}$$

$$\mathscr{D} = \mathscr{D}_0 + \delta\mathscr{D}, \tag{3.97}$$

$$\vec{\xi} = \vec{\xi}_0 + \delta\vec{\xi}, \tag{3.98}$$

We can then introduce these expressions in equation 3.95 and linearise the equation

$$<\vec{\xi}_0,\delta\omega^2\vec{\xi}_0> + <\vec{\xi}_0,\omega_0^2\delta\vec{\xi}> = <\vec{\xi}_0,\delta\mathscr{D}(\vec{\xi}_0)> + <\vec{\xi}_0,\mathscr{D}_0(\delta\vec{\xi})>, \tag{3.99}$$

where we have used the fact that ξ_0 is an eigenfunction of $\mathscr{D}_0$. We can also use the symmetry of $\mathscr{D}_0$ and equation 3.94, which leads to the variational principle of adiabatic stellar oscillations, which in turn allows us to eliminate the terms with $\delta\vec{\xi}$ and simplify the starting expression. Finally, we obtain a simple relation between frequency and structural perturbations

$$\delta\omega^2 = \frac{<\vec{\xi}_0,\delta\mathscr{D}(\vec{\xi}_0)>}{<\vec{\xi}_0,\vec{\xi}_0>}. \tag{3.100}$$

This symbolic expression is actually the only expression needed to compute structural inversions and is a consequence of a series of mathematical properties of adiabatic stellar oscillations. The first property is the symmetry of the operator, which leads to the existence of the variational principle for stellar oscillations which in turn allows for a formally simple relations between pulsation frequencies and acoustic structure. Equation 3.100 expresses the impact of perturbations on the fluid operator, in other words, how the acoustic structure of the pulsating star affects the eigenfrequencies. If we now take the example of an observed star and the numerical model used to represent its structure, this mathematical relation means that as long as the numerical model is sufficiently good, any frequency difference can be considered to only be caused by the inaccurate reproduction of the acoustic structure of the star by the numerical model. Of course, the very definition of "sufficiently good" is somewhat problematic and we will further investigate onto what "sufficiently good" means in Part II. This topic is linked to the validity domain of equation 3.100, which is only a first order approximation.

Moreover, it is also clear that this expression is not valid for: rapidly rotating stars, strongly magnetic stars or stars in close binary systems. Indeed, we neglected all these effects in the derivation of this relation. Of course the intrinsic non-adiabaticity of stellar oscillations will in practice cause equation 3.100 to be wrong, but the problem of surface effects, as we call them, is in reality far worse. Firstly, the very crude modelling of the surface regions will inevitably cause the perturbations of the fluid operators in these regions to be of high amplitude, thus non-linear, but to make it worse, the hypothesis of adiabaticity, a prerequisite for structural inversions, will make it impossible to probe the upper layers since neither the frequencies, nor the eigenfunctions of the numerical model will be realistic. In practice, this implies that we use empirical frequency corrections to minimise these so-called surface effects.

A last comment can be made on the mathematical nature of equation 3.100. Behind the notation of the scalar product is actually hiding an integral, meaning that equation 3.100 is an integral relation. This means that the problem of inferring corrections on the acoustic structure of the stellar model will be an ill-posed problem and will require specific techniques to be solved.

3.7 Inversion equations

In the previous sections, we have demonstrated that the symmetry of the operator associated with linear adiabatic stellar oscillations could be used to derive a variational principle for the pulsation equations. From this mathematical property, we have shown that a relatively simple integral relation could be derived relating differences in the eigenvalues of the problem, thus the oscillation frequencies, to corrections on the fluid operator, in other words on the acoustic structure of the numerical model of the star. This means that given the structural corrections, one can start to change the physical ingredients of stellar models and see which can be used to reproduce the changes necessary to fit the inverted acoustic properties. In this section, we will derive the analytical expressions used in practice for structural inversions, introduce terms such as structural kernels, structural pairs, but also present some additional insights on the complicated problem of surface effects.

3.7.1 Derivation of the structural kernels of the (ρ, c^2) structural pair

We start this section by rewriting equation 3.100

$$\delta\omega^2 = \frac{< \vec{\xi}_0, \delta\mathscr{D}(\vec{\xi}_0) >}{< \vec{\xi}_0, \vec{\xi}_0 >}. \tag{3.101}$$

While this equation directly shows the link between the differences in eigenvalues and the differences in the fluid operator, it does not give a practical relation to infer the corrections on the acoustic structure of the model. While the variational principle has been known since Chandrasekhar (1964), it is only in Dziembowski, Pamyatnykh, and Sienkiewicz (1990) that one finds a rewriting of the equations of the linear perturbations of frequencies allowing for a direct inversion. In this section, we will show how to derive the integral relations allowing us to determine density, ρ, and squared adiabatic sound speed, c^2, corrections. We start by analysing the denominator of the right hand side of equation 3.101, which is written

$$< \vec{\xi}, \vec{\xi} >= \int \rho_0 \vec{\xi}^* \cdot \vec{\xi} dV. \tag{3.102}$$

We then have to separate radial and horizontal components using

$$\vec{\xi} = \xi_r \vec{e}_r + \vec{\xi}_h. \tag{3.103}$$

Each of these components depend on the radial and the angular coordinates. For a non-magnetic, isolated, slow-rotating star, we have seen that the model is, to a very good approximation, spherically symmetric. We then use the decomposition onto spherical coordinates, where $\tilde{f}$, considered as a Fourier mode, represents any perturbed thermodynamical quantity of the acoustic structure

$$\tilde{f} = \sqrt{4\pi} f(r) Y_\ell^m(\theta, \phi) e^{i\omega t}, \tag{3.104}$$

$$\vec{\xi}_h = \sqrt{4\pi}\xi_h(r) \left(\frac{\partial Y_\ell^m}{\partial \theta} \vec{e}_\theta + \frac{1}{\sin\theta} \frac{\partial Y_\ell^m}{\partial \phi} \vec{e}_\phi \right) e^{i\omega t}. \tag{3.105}$$

In this expression, $\vec{e}_\phi$ et $\vec{e}_\theta$ are the direction vectors associated with the θ and ϕ axes of the spherical coordinates. We then have the same properties of the Lagrangian operator as in the pulsation equations and the scalar product of two eigenfunctions can be expressed as very simple expressions. For the radial component, one has

$$\delta r^2 = \int_0^R \oint |\sqrt{4\pi}\xi_r(r) Y_\ell^m|^2 r^2 \rho_0 d\Omega dr, \tag{3.106}$$

$$= 4\pi \int_0^R |\xi_r(r)|^2 r^2 \rho_0 dr, \tag{3.107}$$

with $d\Omega$ a solid angle element. A similar expression is derived for the horizontal component, thanks to the properties of spherical harmonics

$$\delta h^2 = 4\pi \int_0^R \ell(\ell+1) |\xi_h(r)|^2 r^2 \rho_0 dr.$$

One then ends up with the well-known expression for the inertia of the mode in the denominator of the right hand side of the integral relation between frequencies and structure:

$$< \vec{\xi}_{n,\ell}, \vec{\xi}_{n,\ell} >= 4\pi \int_0^R \left[|\xi_r(r)|^2 + \ell(\ell+1) |\xi_h(r)|^2 \right] \rho_0 r^2 dr. \tag{3.108}$$

The numerator of the expression must now be dealt with, remembering that it stems from the original eigenvalue problem equation, $\omega_0^2\vec{\xi}_0 = \mathscr{D}_0(\vec{\xi}_0)$, which is written in the form 3.101 for small perturbations. Our goal is now to find $\delta\mathscr{D}_0$. Thus, we start from the equation of momentum for adiabatic pulsations

$$\omega^2\vec{\xi} = \frac{\nabla\cdot(\rho_0\vec{\xi})}{\rho_0^2}\vec{\nabla}P_0 + \vec{\nabla}\phi' + \frac{\vec{\nabla}P'}{\rho_0}. \tag{3.109}$$

We now apply the scalar product over the functional space and apply a perturbation to the model. This perturbation is considered at fixed radius, thereby preserving the total volume of the star[3]. We will denote by δ this perturbation, which is not to be mistaken for the Lagrangian perturbations used in the pulsation equations previously presented. We can use the variational principle to proceed to a first elimination of some eigenfunction perturbations

$$\int_V \rho_0\delta\omega^2|\vec{\xi}_0|^2dV = -\int_V \omega^2\delta\rho_0|\vec{\xi}_0|^2dV + \overbrace{\int_V \bar{\delta}\left[\left(\frac{\nabla\cdot(\rho_0\vec{\xi}_0)}{\rho_0}\right)^*\vec{\xi}_0\cdot\vec{\nabla}P_0\right]dV}^{I} + \int_V \rho_0\vec{\xi}_0^*\cdot\vec{\nabla}\bar{\delta}\phi' dV$$
$$+\int_V \delta\rho_0\vec{\xi}_0^*\cdot\vec{\nabla}(\phi')dV + \overbrace{\int_V \vec{\xi}_0^*\cdot\vec{\nabla}(\bar{\delta}P')dV}^{II}. \tag{3.110}$$

In these developments, we introduce the notation $\bar{\delta}$ which implies a perturbation of the thermodynamical quantity for which every occurence of $\delta\vec{\xi}$ has been eliminated. We now can use the hydrostatic equilibrium to write that

$$\vec{\nabla}P_0 = \frac{dP_0}{dr}\vec{e}_r = -\frac{Gm(r)\rho_0}{r^2}\vec{e}_r, \tag{3.111}$$
$$m(r) = \int_0^r 4\pi\rho_0 r^2 dr, \tag{3.112}$$
$$\Rightarrow \delta\frac{dP_0}{dr} = -\frac{Gm(r)\delta\rho_0}{r^2} - \frac{G\rho_0}{r,2}\left[\int_0^r 4\pi\delta\rho_0 r^2 dr\right]. \tag{3.113}$$

Now if we consider terms *I* and *II*, use the definition of the adiabatic eulerian pressure perturbation,

$$P' = -\Gamma_1 P_0\vec{\nabla}\cdot\vec{\xi} - \vec{\xi}\cdot\vec{\nabla}P_0, \tag{3.114}$$

and carry out an integration by parts, we can explicitely write every component as follows

[3]It should be noted that such perturbations can be defined at fixed mass as in Christensen-Dalsgaard and Thompson (1997)

$$
\begin{aligned}
I+II &= \int_V \left(-\frac{\delta\rho_0}{\rho_0^2}\frac{d\rho_0}{dr}\frac{dP_0}{dr}\xi_{r,0}^2 - \frac{\delta\rho_0}{\rho_0}\Lambda_\ell\xi_{r,0}\frac{dP_0}{dr} + \left[\frac{1}{\rho_0}\frac{d\delta\rho_0}{dr}\xi_{r,0} + \frac{\delta\rho_0}{\rho_0}\Lambda_\ell\right]\xi_{r,0}\frac{dP_0}{dr} \right. \\
&\left. + \frac{1}{\rho_0}\left[\frac{d\rho_0}{dr}\xi_{r,0} + \Lambda_\ell\rho_0\right]\xi_{r,0}\frac{d\delta P_0}{dr}\right)|Y_\ell^m|^2 dV - \int_V \xi_{r,0}\frac{d}{dr}(\xi_{r,0}\frac{d\delta P_0}{dr})|Y_\ell^m|^2 dV \\
&- \int_V \frac{\xi_{h,0}\xi_{r,0}}{r}\frac{d\delta P_0}{dr}|r^2\vec{\nabla}_h Y_\ell^m|^2 dV + \int_V (\vec{\xi}_0)^2\cdot\delta\vec{\nabla}(P_0\Gamma_{1,0})dV, \\
&= \int_V \left(-\frac{\delta\rho_0}{\rho_0^2}\frac{d\rho_0}{dr}\frac{dP_0}{dr}\xi_{r,0}^2 + \frac{1}{\rho_0}\frac{d\delta\rho_0}{dr}\frac{dP_0}{dr}\xi_{r,0}^2 + \frac{1}{\rho_0}\left[\frac{d\rho_0}{dr}\xi_{r,0} + \Lambda_\ell\rho_0\right]\xi_{r,0}\frac{d\delta P_0}{dr}\right)|Y_\ell^m|^2 dV \\
&- \int_V \xi_{r,0}\frac{d\xi_{r,0}}{dr}\frac{d\delta P_0}{dr}|Y_\ell^m|^2 dV - \int_V \ell(\ell+1)\frac{\xi_{h,0}\xi_{r,0}}{r}\frac{d\delta P_0}{dr}|Y_\ell^m|^2 dV - \overbrace{\int_V \xi_{r,0}^2\frac{d^2\delta P_0}{dr^2}|Y_\ell^m|^2 dV}^{III} \\
&+ \int_V (\nabla\cdot\vec{\xi}_0)^2(\delta c^2\rho_0 + \delta\rho_0 c^2)|Y_\ell^m|^2 dV, \qquad (3.115)
\end{aligned}
$$

where we also introduced the following definitions

$$
\begin{aligned}
\nabla\cdot\vec{\xi} &= \frac{1}{r^2}\frac{d(r^2\xi_r(r))}{dr}Y_\ell^m(\theta,\phi) + \xi_h(r)\nabla_h\cdot(\vec{r\nabla}_h Y_\ell^m(\theta,\phi)), \\
&= \frac{1}{r^2}\frac{d(r^2\xi_r(r))}{dr}Y_\ell^m(\theta,\phi) - \frac{\ell(\ell+1)}{r}\xi_h(r)Y_\ell^m(\theta,\phi) = \Lambda_\ell(r)Y_\ell^m(\theta,\phi) \qquad (3.116) \\
\nabla\cdot(\rho_0\vec{\xi}) &= \frac{d\rho_0}{dr}\xi_r Y_\ell^m(\theta,\phi) + \rho_0\Lambda_\ell(r)Y_\ell^m(\theta,\phi), \qquad (3.117) \\
\vec{\xi}^*\cdot\vec{\nabla}(f(r)Y_\ell^m(\theta,\phi)) &= \xi_r|Y_\ell^m|^2(\theta,\phi)\frac{df(r)}{dr} + r\xi_h f(r)|\nabla_h Y_\ell^m(\theta,\phi)|^2, \qquad (3.118)
\end{aligned}
$$

Now we consider the term *III*:

$$
\begin{aligned}
III &= -\int_V \frac{2}{r}\frac{d\delta P_0}{dr}\xi_{r,0}^2|Y_\ell^m|^2 dV - \int_V 8\pi G\rho_0\delta\rho_0\xi_{r,0}^2|Y_\ell^m|^2 dV - \int_V \frac{G\delta m(r)}{r^2}\frac{d\rho_0}{dr}\xi_{r,0}^2|Y_\ell^m|^2 dV \\
&- \int_V \frac{Gm(r)}{r^2}\frac{d\delta\rho_0}{dr}\xi_{r,0}^2|Y_\ell^m|^2 dV. \qquad (3.119)
\end{aligned}
$$

By recombining this expression and using the definition of the equilibrium pressure we obtain after a few simplifications[4]

$$
\begin{aligned}
III &= 2\int_V \Lambda_\ell\frac{d\delta P_0}{dr}|Y_\ell^m|^2 dV - \int_V \frac{d\rho_0}{dr}\xi_{r,0}^2\frac{G\delta m(r)}{r^2}|Y_\ell^m|^2 dV + \int_V 8\pi G\rho_0\delta\rho_0\xi_{r,0}^2|Y_\ell^m|^2 dV \\
&+ 2\int_V \xi_{r,0}\frac{d\xi_{r,0}}{dr}\frac{G\rho_0\delta m(r)}{r^2}|Y_\ell^m|^2 dV + 2\int_V \xi_{r,0}\frac{d\xi_{r,0}}{dr}\frac{G\delta\rho_0 m(r)}{r^2}|Y_\ell^m|^2 dV. \qquad (3.120)
\end{aligned}
$$

Finally, one has to separate the integral over the angular coordinates and permute the integrals in the mass perturbation using the following property

$$
\int_0^R f(r)\left(\int_0^r g(r')dr'\right)dr = \int_0^R g(r')\left(\int_{r'}^R f(r)dr\right)dr', \qquad (3.121)
$$

[4]The perturbation of the gravitational potential can be easily transformed using Gauss's theorem and Poisson's equation, considering continuity conditions which induce the elimination of the surface terms.

so that one can move up the $\delta\rho$ term to the first integral. By further recombining the third an fourth term of the equation by integrating by parts, one obtains

$$\delta\omega^2 \int_0^R \rho_0 \left[\xi_{r,0}(r)^2 + \ell(\ell+1)\xi_{h,0}(r)^2\right] r^2 dr = -\int_0^R \omega^2 \delta\rho_0 \left[\xi_{r,0}(r)^2 + \ell(\ell+1)\xi_{h,0}(r)^2\right] r^2 dr$$
$$+2\int_0^R \delta\rho_0 (\xi_{r,0}\frac{d\phi'}{dr} + \frac{\ell(\ell+1)}{r}\xi_{h,0}\phi')r^2 dr - 2\int_0^R \xi_{r,0}\Lambda_\ell \delta\rho_0 G m(r) dr + \int_0^R 4\pi G\rho_0 \delta\rho_0 \xi_{r,0}^2 r^2 dr$$
$$+2\int_0^R \xi_{r,0}\frac{d\xi_{r,0}}{dr} G\delta\rho_0 m(r) dr - \int_0^R 4\pi\delta\rho_0 G(\int_r^R \xi_{r,0}^2 \frac{d\rho_0}{dr} + 2\Lambda_\ell \rho_0 \xi_{r,0} d\tilde{r}) r^2 dr$$
$$+\int_0^R \Lambda_\ell^2 (\delta c^2 \rho_0 + \delta\rho_0 c^2) r^2 dr. \tag{3.122}$$

This expression can be written in a shorter way by isolating the perturbations of the squared adiabatic sound speed and density:

$$\frac{\delta\omega_{n,\ell}}{\omega_{n,\ell}} = \int_0^R \left[K^{n,\ell}_{c^2,\rho_0}\frac{\delta c^2}{c^2} + K^{n,\ell}_{\rho_0,c^2}\frac{\delta\rho_0}{\rho_0}\right] dr, \tag{3.123}$$

where we have defined the $K^{n,\ell}_{c^2,\rho_0}$, $K^{n,\ell}_{\rho_0,c^2}$, the structural kernels of the (ρ, c^2) structural pair. It should be noted that these functions are only depending on unperturbed variables, thus only on the theoretical model that is built to carry out the inversion. The mathematical expression of the structural kernels is the following

$$K^{n,\ell}_{c^2,\rho_0} = \frac{c^2\rho_0\Lambda_\ell^2(r)r^2}{2E_{n,\ell}\omega_{n,\ell}^2}, \tag{3.124}$$

$$K^{n,\ell}_{\rho_0,c^2} = \frac{1}{2E_{n,\ell}\omega_{n,\ell}^2}\left(-\omega^2\rho_0\left[\xi_{r,0}(r)^2 + \ell(\ell+1)\xi_{h,0}(r)^2\right]r^2 + 2\rho_0(\xi_{r,0}\frac{d\phi'}{dr} + \frac{\ell(\ell+1)}{r}\xi_{h,0}\phi')r^2\right.$$
$$-2\xi_{r,0}\Lambda_\ell\rho_0 G m(r) + 4\pi G\rho_0^2\xi_{r,0}^2 r^2 + 2\xi_{r,0}\frac{d\xi_{r,0}}{dr}G\rho_0 m(r)$$
$$\left.-4\pi\rho_0 G(\int_r^R \xi_{r,0}^2\frac{d\rho_0}{dr} + 2\Lambda_\ell\rho_0\xi_{r,0}d\tilde{r})r^2 + \Lambda_\ell^2 c^2\rho_0 r^2\right), \tag{3.125}$$

where $E_{n,\ell}$ is the mode inertia, defined as

$$E_{n,\ell} = 4\pi\int_0^R \left[|\tilde{\xi}_r^{n,\ell}(r)|^2 + \ell(\ell+1)|\tilde{\xi}_h^{n,\ell}(r)|^2\right]\rho_0 r^2 dr. \tag{3.126}$$

These kernels are illustrated in figure 3.4. They were the first structural kernels to be derived and are still used today in helioseismology to carry out inversions of the radial sound speed profile of the Sun (see chapter 7). However, from the (ρ, c^2) structural pair, one can derive additional kernels, for various other pairs, allowing much more efficient diagnostics than just inverting the sound speed profile. We will see in chapter 4 that some general approaches can indeed be designed to change the structural variables in the integral relation between structural corrections and frequency differences. In the following sections, we will only present the more classical, well known structural kernels.

3.7.2 Derivation of the structural kernels of the (ρ, Γ_1) structural pair

From the previous developments, it is very straightforward to derive the structural kernels for the (ρ, Γ_1) structural pair. One simply has to introduce the definition of the squared

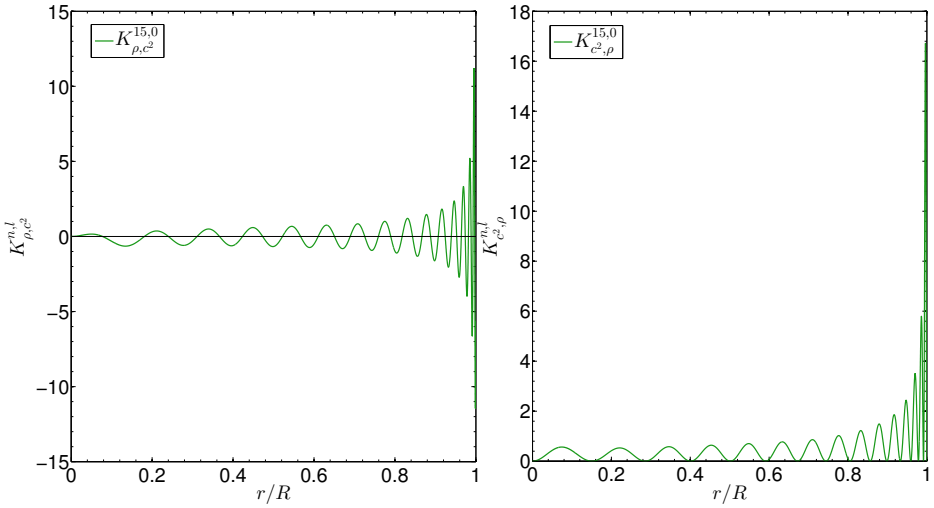

Figure 3.4: Kernels of the (ρ, c^2) structural pair for the $\ell = 0$, $n = 15$ mode of a solar model.

adiabatic sound speed and its linear perturbation

$$c^2 = \frac{\Gamma_1 P_0}{\rho_0}, \tag{3.127}$$

$$\frac{\delta c^2}{c^2} = \frac{\delta \Gamma_1}{\Gamma_1} + \frac{\delta P_0}{P_0} - \frac{\delta \rho_0}{\rho_0}, \tag{3.128}$$

$$\frac{d\delta P_0}{dr} = -\frac{G\rho_0 \delta m(r)}{r^2} - \frac{Gm(r)\delta\rho_0}{r^2}, \tag{3.129}$$

$$\delta P_0 = \int_r^R \left(\frac{G\rho_0 \delta m(\bar{r})}{\bar{r}^2} + \frac{G\delta\rho_0 m(\bar{r})}{\bar{r}^2}\right) d\bar{r}. \tag{3.130}$$

We can now use the expression in equation 3.125 to obtain

$$\frac{\delta\omega_{n,\ell}}{\omega_{n,\ell}} = \int_0^R K^{n,\ell}_{c^2,\rho} \frac{\delta\Gamma_1}{\Gamma_1} dr + \int_0^R (K^{n,\ell}_{\rho,c^2} - K^{n,\ell}_{c^2,\rho}) \frac{\delta\rho_0}{\rho_0} dr + \overbrace{\int_0^R \frac{K^{n,\ell}_{c^2,\rho}}{P_0} \left[\int_r^R \frac{G}{\bar{r}^2}(\delta m(\bar{r})\rho_0 + m(\bar{r})\delta\rho_0) d\bar{r}\right] dr}^{I}. \tag{3.131}$$

In this equation, the term I must be slightly modified to isolate density perturbations, one simply uses the same techniques as in the derivation of the (ρ, c^2) kernels,

$$I = \int_0^R \frac{Gm(r)\rho_0}{r^2} \frac{\delta\rho_0}{\rho_0} \left[\int_0^r \frac{K^{n,\ell}_{c^2,\rho}}{P_0} d\bar{r}\right] dr + \int_0^R 4\pi\rho_0 r^2 \frac{\delta\rho_0}{\rho_0} \left[\int_r^R \frac{G\rho_0}{\bar{r}^2} \left(\int_0^{\bar{r}} \frac{K^{n,\ell}_{c^2,\rho}}{P_0} d\tilde{r}\right) d\bar{r}\right] dr. \tag{3.132}$$

The expression of the (ρ, Γ_1) kernels are then simply obtained by introducing these developments in the definitions of the (ρ, c^2) kernels. One then has the following definitions

$$K^{n,\ell}_{\Gamma_1,\rho_0} = K^{n,\ell}_{c^2,\rho_0}, \tag{3.133}$$

$$K^{n,\ell}_{\rho_0,\Gamma_1} = K^{n,\ell}_{\rho_0,c^2} - K^{n,\ell}_{c^2,\rho_0} + \frac{Gm\rho_0}{r^2} \int_0^r \frac{\Gamma_1 \Lambda_\ell^2 \bar{r}^2}{2E^{n,\ell}\omega^2} d\bar{r} + \rho_0 r^2 \int_r^R \frac{4\pi G\rho_0}{\bar{r}^2} \left[\int_0^{\bar{r}} \frac{\Gamma_1 \Lambda_\ell^2 \tilde{r}^2}{2E^{n,\ell}\omega^2} d\tilde{r}\right] d\bar{r}. \tag{3.134}$$

We illustrate these kernels in figure 3.5. Currently, they are used in helioseismology to carry out inversions of the radial density profile of the Sun. They can also be used to compute inversions of the acoustic radius and mean density of a star in the context of asteroseismology, as oresented in section 5.2. Their main advantage is that the value of Γ_1 is nearly 5/3 throughout the whole stellar structure, allowing the relative differences in Γ_1 to be very small in comparison to density or squared adiabatic sound speed differences.

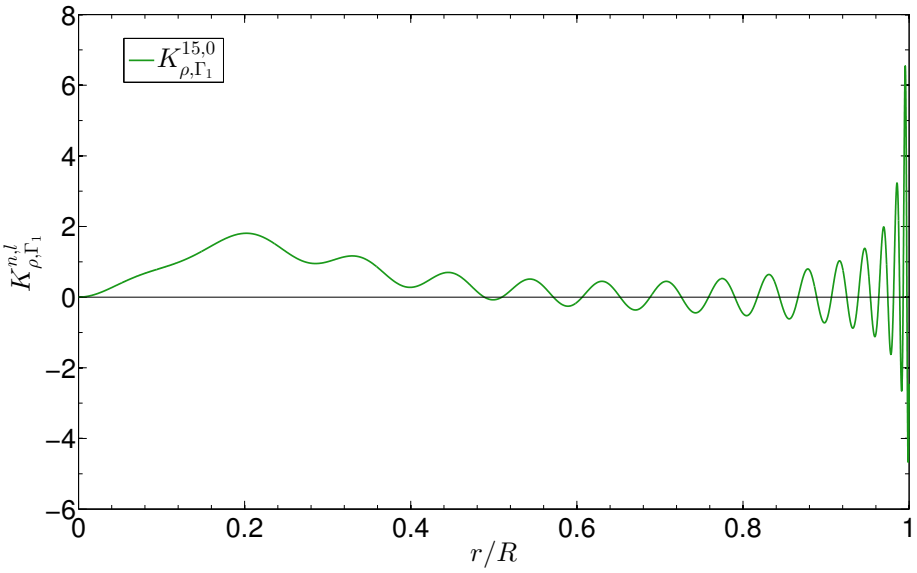

Figure 3.5: Kernels of the (ρ,Γ_1) structural pair for the $\ell = 0$, $n = 15$ mode of a solar model.

3.7.3 Derivation of the structural kernels of the (ρ,Y) structural pair

From the (ρ,Γ_1) structural pair, it is easy to derive additional kernels linked to the helium mass fraction, denoted Y, by expanding the relative perturbations of Γ_1 using the equation of state. One has

$$\frac{\delta\Gamma_1}{\Gamma_1} = \frac{\partial \ln\Gamma_1}{\partial \ln P}|_{\rho,Y,Z}\frac{\delta P}{P} + \frac{\partial \ln\Gamma_1}{\partial \ln \rho}|_{P,Y,Z}\frac{\delta\rho}{\rho} + \frac{\partial \ln\Gamma_1}{\partial Y}|_{P,\rho,Z}\delta Y + \frac{\partial \ln\Gamma_1}{\partial Z}|_{P,\rho,Y}\delta Z. \tag{3.135}$$

In many textbooks and papers, one often finds that the metallicity term is to be neglected. It is true that in most cases, the δZ term will be much smaller than the δY term and since the state derivative of Γ_1 is nearly zero in most of the stellar structure, this term can be neglected. We illustrate all these state derivatives of Γ_1 in figure 3.6. However, we will see in section 7.3 that this is not always the case in the framework of helioseismology and that one can indeed, using the appropriate structural kernels, estimate the metallicity of the solar convective envelope.

Another problem of equation 3.135 is that it introduces uncertainties due to the equation of state. One can find an example in section 4.2 of problems induced by a non-linear behaviour of these derivatives. In fact, implying that equation 3.135 is satisfied implies another degree of linearisation for non-acoustic variables. If one compare these derivatives for various equations of state, one can see that the differences can be quite large depending on the structural differences between the models (see the test cases of chapter 4.2). For example, standard solar models will show resonably small differences in their equation of

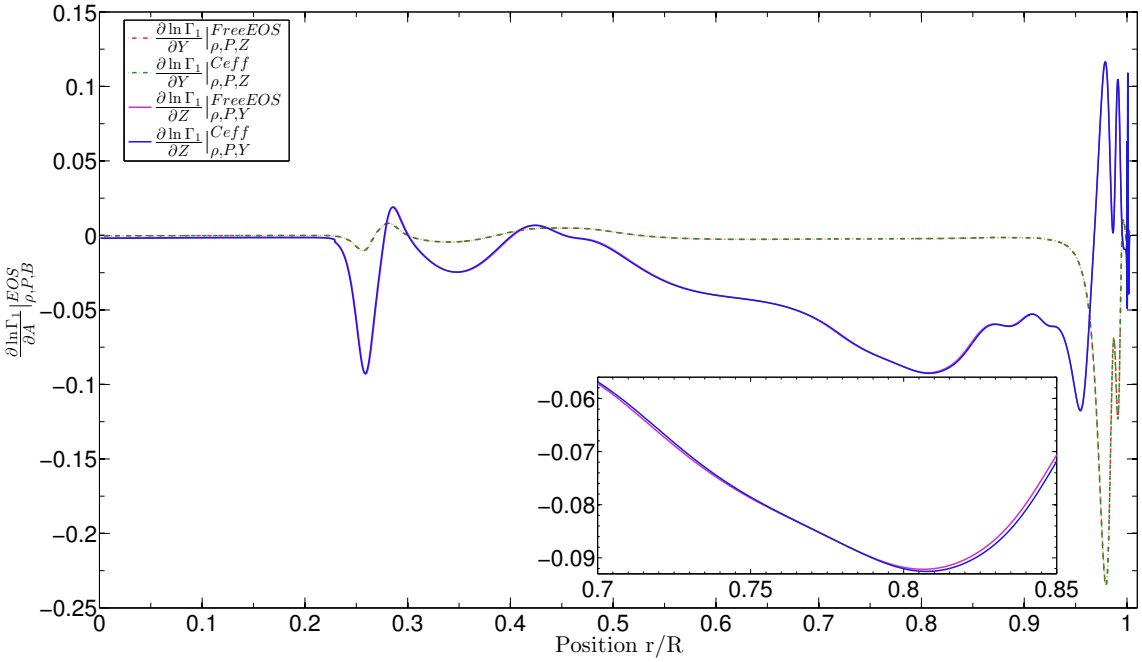

Figure 3.6: State derivatives of Γ_1 with respect to various thermodynamic quantities such as ρ, P, as well as with respect to Y and Z, used in the derivation of structural kernels.

state, as shown in figure 2.4, but this is due to the fitting technique that allows the models to be very close and to the fact the equations of state are optimised for the solar case. In asteroseismology, larger differences between the model and the observed star can be expected, for example, but not only, due to differences in fundamental parameters such as mass, radius or age. These differences can lead to large variations, for example by shifting the position of the ionisation zones, strongly altering the Γ_1 derivatives. Consequently, These this supplementary linearisation might be rendered invalid. However, we will see that this does not necessarily mean that inversions cannot be performed using the (ρ, Y) kernels, but rather that helium abundance determinations using direct asteroseismic inversions will be very difficult.

Historically, the (ρ, Y) kernels have been used to determine the density profile of the Sun. However, it was shown by Basu and Christensen-Dalsgaard (1997a) that at the level of accuracy expected in helioseismology, the biases induced by the introduction of the linearisation of the equation of state were to be avoided, and the (ρ, Γ_1) kernels were used instead. Introducing equation 3.135 in the definition of the (ρ, Γ_1) kernels, one gets

$$K^{n,\ell}_{Y,Z,\rho_0} = K^{n,\ell}_{Y,\rho_0} \frac{\partial \ln \Gamma_1}{\partial Y}|_{P,\rho,Z}, \tag{3.136}$$

$$K^{n,\ell}_{Z,Y,\rho_0} = K^{n,\ell}_{Y,\rho_0} \frac{\partial \ln \Gamma_1}{\partial Z}|_{P,\rho,Y}, \tag{3.137}$$

$$\begin{aligned} K^{n,\ell}_{\rho_0,Y,Z} = & K^{n,\ell}_{\rho_0,\Gamma_1} + K^{n,\ell}_{\Gamma_1,\rho_0} \frac{\partial \ln \Gamma_1}{\partial \ln \rho}|_{P,Y,Z} + \frac{Gm\rho_0}{r^2} \int_0^r \frac{K^{n,\ell}_{\Gamma_1,\rho_0}}{P} \frac{\partial \ln \Gamma_1}{\partial \ln P}|_{\rho,Y,Z} d\bar{r} \\ & + \rho_0 r^2 \int_r^R \frac{4\pi G \rho_0}{\bar{r}^2} \left[\int_0^{\bar{r}} \frac{K^{n,\ell}_{\Gamma_1,\rho_0}}{P} \frac{\partial \ln \Gamma_1}{\partial \ln P}|_{\rho,Y,Z} d\tilde{r} \right] d\bar{r}. \end{aligned} \tag{3.138}$$

These kernels are presented in figure 3.7. One can notice the naturally small amplitude of the Y kernels compared to the density kernels. This small amplitude was the main

motivation for their use in helioseismic inversions. This choice has since been criticised in helioseismology because the small differences in density observed in helioseismology can be significantly influenced by the effects of the equation of state introduced by the decomposition of Γ_1 (Basu and Christensen-Dalsgaard (1997a)). However, the problem is not so important in the field of asteroseismology and the use of kernels associated with the helium mass fraction is actually the most efficient way to ensure accurate asteroseismic inversions. In figure 3.8, we illustrate the kernels associated with the metallicity contribution, often neglected in the integral relation. As can be seen, the amplitude of these kernels is similar to that of the Y kernels. Consequently, the neglect of the δZ term relies on the fact that, usually, $\delta Z \ll \delta Y$. This is of primary importance for the solar case, where Y is constrained by helioseismology.

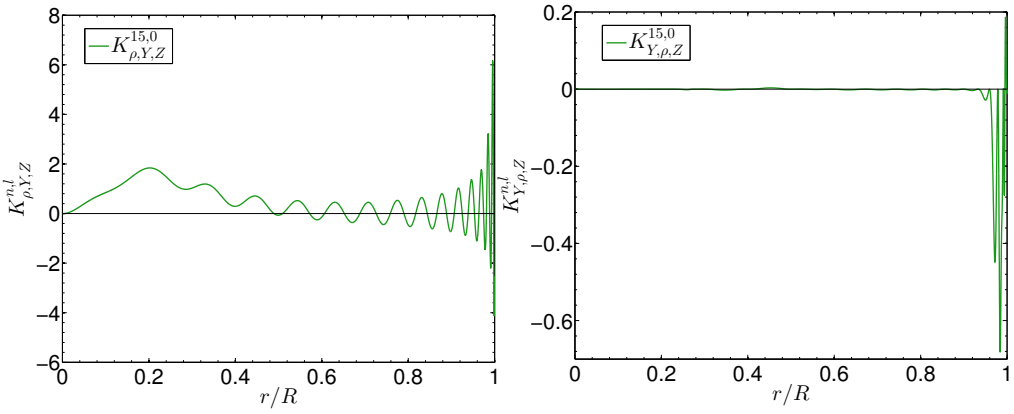

Figure 3.7: Kernels of the (ρ, Y) structural pair for the $\ell = 0$, $n = 15$ mode.

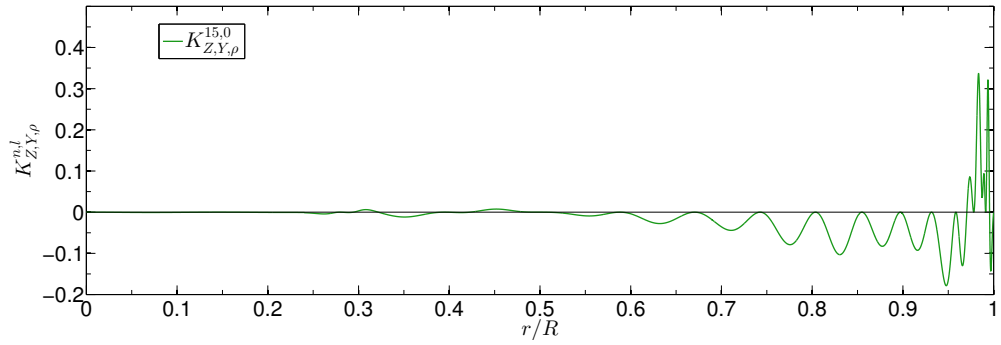

Figure 3.8: Kernel associated with Z in the (ρ, Y) pair for the $\ell = 0$, $n = 15$ mode.

3.8 Numerical inversion techniques

From the previous sections, we have seen that carrying out a structural inversion is actually related to solving an integral relation of the form

$$\frac{\delta \nu^{n,\ell}}{\nu^{n,\ell}} = \int_0^1 K^{n,\ell}_{s_1,s_2} \frac{\delta s_1}{s_1} dx + \int_0^1 K^{n,\ell}_{s_2,s_1} \frac{\delta s_2}{s_2} dx, \tag{3.139}$$

with s_1 and s_2 being thermodynamical quantities such as the density, the squared adiabatic sound speed, or any other quantities for which structural kernels can be derived.

While equation 3.139 is fairly short, it is the perfect example of a very complicated class of mathematical problems, the so-called ill-posed problems. These are recurrently found in fundamental or applied science, from the geophysical, helioseismic or asteroseismic inversions, to the reconstruction of velocity maps in doppler tomography, medical imaging or the determination of an instrumental response. Some very general considerations on the mathematical nature of inverse problems can be found in the following textbooks (Tarantola (2005), Vogel (2002)). In this section, we will only briefly cover the topic of inverse problems and present the method used in this work to solve them.

3.8.1 Ill-posed and well-posed problem

An ill-posed problem is generally defined in opposition to a well-posed problem. Following Hadamard's definition, a well-posed problem respects three conditions:

1. a solution exists,
2. this solution is unique,
3. this solution depends continuously on the data.

In the case of helio- and asteroseimic applications, the first condition is obviously fulfilled, since the solution is actually *observed*. The second condition is however not met. Indeed, an infinite number of solutions can reproduce the observations, since these only provide a finite number of constraints on an unknown function. The third condition is not met either since a small change in the observed frequencies can lead to significant changes in the inversion results, especially in asteroseismic applications were the problem is even more complicated.

Consequently, the mathematical nature of inverse problems requires a regularisation. This is done by using a priori assumptions on the behaviour of the solution to ensure uniqueness. The type of assumptions can vary depending on the problem considered and some inversion techniques are only applicable to a given physical phenomenon since most of them rely on specific conditioning to find a solution. Even for the same physical phenomenon, each inversion will be a unique problem for which the quality of the solution might vary. For example, in asteroseismology, the number of frequencies, the precision of their determination, the nature of the modes, the quality of the reference model will significantly affect the capability to carry out a structural inversion. As an example, trying to gain information on a low mass solar-like star in the middle of the main sequence using pressure modes will not be as difficult as computing an inversion for a more massive subgiant star with mixed modes. The complexity of the problem leads us to consider inversions only for the best targets and to treat them individually and with great care. In what follows, we will describe the linear inversion technique used in this work and provide references for other methods for the interested reader.

3.8.2 The SOLA inversion technnique

The most famous inversion technique in the field of helio- and asteroseismology is probably the SOLA method. SOLA stands for Substractive Optimally Localised Averages. This method was developed by Pijpers and Thompson (1994) as a variation of the MOLA method (Multiplicative Optimally Localised Averages). The MOLA inversion technique was first presented in a paper by Backus and Gilbert (1967) and described for geophysical applications. However, the philosophy of this method makes it very general and well-suited for helioseismic and asteroseismic applications[5]. The general idea of the OLA methods is to try obtain local averages of the structural profile.

[5]Even if the SOLA method is now favoured for the reasons we will see in this section.

The problem with the helio and asteroseismic inversion is the following, if we look at the relation between frequencies and structure

$$\frac{\delta\nu^{n,\ell}}{\nu^{n,\ell}} = \int_0^1 K^{n,\ell}_{s_1,s_2}\frac{\delta s_1}{s_1}dx + \int_0^1 K^{n,\ell}_{s_2,s_1}\frac{\delta s_2}{s_2}dx, \tag{3.140}$$

we can see that we will have one equation per observed frequency. In this expression, one seeks to determine the structural variable δs_1 and δs_2, given the knowledge of the frequency differences, $\delta\nu$ and the kernel functions, $K^{n,\ell}_{s_i,s_j}$, which only depend on the reference model. However, with each of these equations, we wish to determine two continuous structural functions, s_1 and s_2. In other words, we only have a finite number of constraints to determine an infinite number of unknown values. This means of course that to some extent we will be limited in what we can obtain as corrections. If we could solve perfectly the problem, we would try to change the arguments of one of the integrals into a Dirac distribution while simultaneously eliminating the other argument. For example, if one wishes to determine $\delta s_1/s_1$ in x_0, one needs to find the inversion coefficients, denoted here c_i, such that

$$\sum_i c_i K^i_{s_1,s_2} = \delta(x-x_0), \tag{3.141}$$

$$\sum_i c_i K^i_{s_2,s_1} = 0. \tag{3.142}$$

This is of course impossible with a finite number of observed frequencies and even in helioseismology, one has to find a compromise. This is done by accepting that one will not get the exact local value of the correction, but a local average. The localisation is done by building a cost function that will be minimised. The first difference between MOLA and SOLA comes from the fact that in the MOLA technique, one minimises the multiplication of the structural kernels by the penalty function while in the SOLA method, one minimises the difference between the kernels and a target function. Moreover, the MOLA method uses a parabola as its penalty function while the SOLA method uses a Gaussian target function. If we come back to the previous example, where one wishes to determine a local correction on s_1, we can introduce the proper terms found in the litterature on the MOLA and SOLA methods. The terms used to refer to these combination of kernels are the averaging and cross-term kernels, which are defined as follows

$$K_{avg} = \sum_i c_i K^i_{s_1,s_2}, \tag{3.143}$$

$$K_{cross} = \sum_i c_i K^i_{s_2,s_1}, \tag{3.144}$$

where the term averaging stands for the fact that it is this linear combination that is used to match a certain target, measuring the local average of the structural quantity $\frac{\delta s_j}{s_j}$. The cross-term kernel is related to the fact that there will always be at least two integrals in the relation between frequencies and structure (unlike in rotation inversions). This means that the correction will always be, to a limited degree, influenced by the second variable in the integral relations since it will be impossible to fully cancel its contribution.

While the MOLA method was the first one to be invented and applied, it is now supplanted by the SOLA method for two main reasons. First, the SOLA method is much less costly in terms of numerical operations. Indeed, it is only necessary to initialise the matrix with structural kernels once, while this matrix must be re-initialised at each point for the MOLA method. Moreover, the use of kernels with a predefined finite width in the

SOLA function avoids an extreme localisation of the structural kernels which could result in bad fits. The structural kernels, being related to the eigenfunctions of the oscillations, are indeed oscillating functions, and trying to obtain an average on a very small interval can lead to an increase in the oscillatory behaviour in the averaging kernel. We illustrate this in figure 3.9 where one can see the progressive apparition of oscillations if one searches for an excessively local correction.

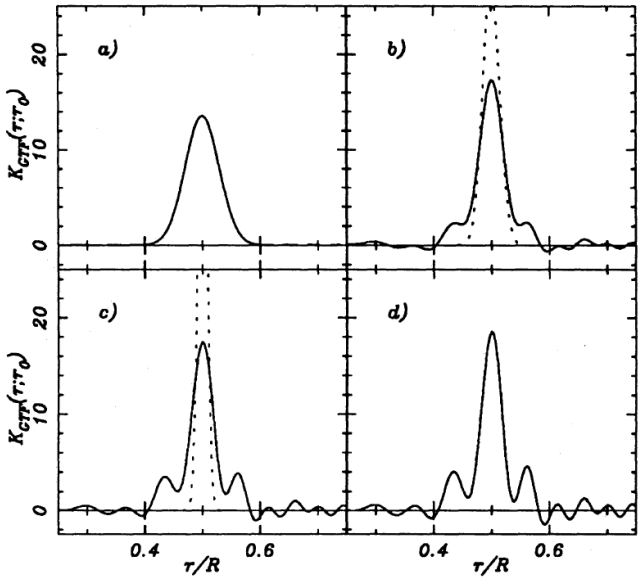

Figure 3.9: Comparison of averaging kernels for the SOLA and MOLA method. The width of the Gaussian target, illustrated with a dotted line, is 0.042 in subpanel a) and is then decreased to 0.021 in subpanel b) and 0.01 in c). Subpanel d) shows the kernel one would obtain with the MOLA method for similar magnifications of the observational errors. (Reprinted from Pijpers and Thompson (1994)).

In helioseismology, the very large number of observed frequencies allows for an inversion of full structural profiles, using the following definition of the target function

$$\mathscr{T}(x,x_0) = Ax\exp-\left(\frac{x-x_0}{\Delta(x_0)}+\frac{\Delta(x_0)}{2x_0}\right)^2, \tag{3.145}$$

with A being a normalisation constant and $\Delta(x_0) = \Delta_A c(x_0)/c(r_A)$, where $r_A = 0.2R_\odot$ and reflects the fact that the modes won't be able to probe with the same efficiency all radii of the solar structure (Thompson (1993)). Hence, in this definition, Δ_A is the parameter used to change the resolution of the kernels. In practice, it is known that pressure modes are not very efficient at probing the very deep layers of the Sun, below $0.1R_\odot$. The advantage of the function defined in equation 3.145 is that it is exactly zero in the center, and thus behaves similarly to the structural kernels in this region.

In conclusion, in helioseismology, the cost function to be minimised by the SOLA method will be the following

$$\begin{aligned}\mathscr{S}(c_i(x_0)) = &\int_0^1 [K_{avg}(x,x_0)-\mathscr{T}(x,x_0)]^2\,dx+\beta\int_0^1 K^2_{cross}(x,x_0)dx+\frac{\mu}{<\sigma_2>}\sum_i c_i^2(x_0)\sigma_i^2\\ &+\lambda\left[\int_0^1 K_{avg}(x,x_0)dx-1\right]+\sum_{n=0}^{N-1}a_n\sum_i\frac{c_i(x_0)\psi_n(\nu_i)}{E_i}.\end{aligned} \tag{3.146}$$

In this expression, the first two integrals are easily recognised to be related to the averaging and cross-term kernels. In other words, they are the terms containing the structural kernels and control the quality of the fit. The third term is related to the propagation of the observational errors. Indeed, the inversion assigns a coefficient to each individual frequency difference, meaning that the observational errors of each mode will also be amplified. Hence, one should properly take into account their contribution to the uncertainties of the final result. The fourth term is related to the unimodularity constraint on the averaging kernel, implying that its integral must be equal to 1. This constraint is use to further stabilise the inversion process. The variable λ, associated with this term, is not a free parameter of the inversion, unlike μ and β, but a Lagrangian multiplier.The fifth and last term is related to the surface effects correction further described in section 3.9.

We mention here that the notation μ for the trade-off parameter associated with the amplification of the error bars is not universal and chosen here to be consistent with figure 3.10. In the rest of the manuscript, we will follow the convention adopted in Backus and Gilbert (1967) were μ is replaced by $\tan(\theta)$, where θ is now a free parameter. This convention is based on the mathematical analysis of the trade-off curves and the definition of the optimal value of the trade-off parameter for MOLA inversions.

A quick look at equation 3.146 shows that some terms may have antagonising effects. Indeed, fitting the target function may require the use of large inversion coefficients. However, one wishes to reduce their amplitude since this also induces a decrease in precision. Similarly, damping the cross-term contribution can only be done by using small coefficients but will not always ensure an accurate fit to the target function. The fact that we have to deal with these antagonising contributions means that inversions with the SOLA method will always be a trade-off problem between precision, cross-term contribution and accuracy. To deal with this problem, one draws trade-off curves that show how the fit of the target function behaves with different values of the parameter. Some of these curves are illustrated in figure 3.10. They are part of the classical analysis of inversion techniques to allow the user to define the smallest width of the target function without inducing an inacceptable contribution from the cross-term or amplification of the errors.

In asteroseismology, carrying out inversions is much more complicated for two reasons. First, the number of modes and the precision of their detection is strongly reduced since for the best asteroseismic targets, one can have up to 55 individual frequencies usually with larger error bars (see Davies et al. (2015), Lund et al. (2017), and I. W. Roxburgh (2017) for an illustration for Kepler targets). This means that the trade-off problem will be much more difficult than in the helioseismic case since one has much less seismic information to work with.

Another problem of asteroseismic inversions is the importance of non-linearity. Indeed, the SOLA method is a linear inversion technique and the equations which are used are based on the linear approximation between frequency differences and structural corrections. In asteroseismic cases, the ability to carry out a structural inversion is thus also linked to the ability to carry out an accurate forward modelling of the observed target, using all the available information in the litterature.

Even if the target is properly modelled and a structural inversion can be performed, the small number of frequencies does not allow us to carry out inversions of a full structural profile, although a few corrections at some radii can be determined. However, SOLA inversions can still be used to compute inversions of integrated quantities, allowing us to focus all the seismic information in the modes into the determination of custom-made seismic indicators based on structural considerations.

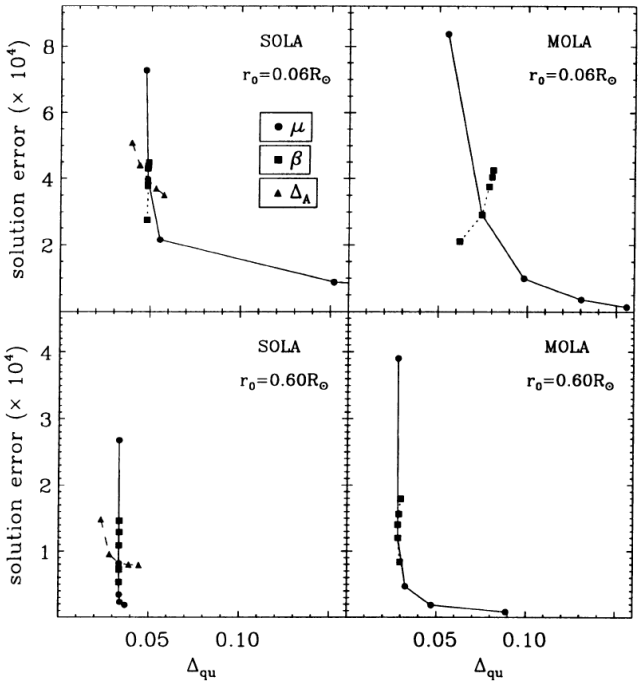

Figure 3.10: Trade-off curves for the SOLA inversion technique for solar structural inversions, the parameter μ is associated with the observational errors, β with the cross-term and Δ_A with the width of the target function. The trade-off curves are plotted for both the SOLA and MOLA techniques. The ordinate is the 1σ error value of the inverted result and the abscissa, Δ_{qu}, is the interquartile interval of the averaging kernels associated with the inversion. (Reprinted from Rabello-Soares, Basu, and Christensen-Dalsgaard (1999)).

The first main change in this inversion process is that the target is not a localised function anymore, but rather a "well-defined" function that can be fitted by the structural kernels. Indeed, the small number of frequencies implies that not all target functions can be fitted by the structural kernels. Ultimately asteroseismic inversions are built based on the same principle as helioseismic inversions and the definition of the cost function is nearly the same. For a given integrated quantity, $\mathscr{A}$, one would have

$$\mathscr{S}_{\mathscr{A}} = \int_0^1 [K_{avg}(x) - \mathscr{T}_{\mathscr{A}}]^2 dx + \beta \int_0^1 K_{cross}^2 dx + \frac{\mu}{<\sigma_2>} \sum_i c_i^2(x_0)\sigma_i^2 + \lambda \left[\sum_i c_i - k\right]. \tag{3.147}$$

In this expression, we simply introduced $\mathscr{T}_{\mathscr{A}}$ which is the target function of the inversion associated with the integrated quantity. It is simply defined as follows

$$\frac{\delta \mathscr{A}}{\mathscr{A}} = \int_0^1 \mathscr{T}_{\mathscr{A}} \frac{\delta s_{\mathscr{A}}}{s_{\mathscr{A}}} dx, \tag{3.148}$$

where $s_{\mathscr{A}}$ is the structural variable that is used in the integral definition of $\mathscr{A}$. For example, in the case of the mean density inversions illustrated in D. R. Reese, Marques, et al. (2012), one has

$$\frac{\delta \bar{\rho}}{\bar{\rho}} = \int_0^1 4\pi x^2 \frac{\rho}{\bar{\rho}} \frac{\delta \rho}{\rho} dx. \tag{3.149}$$

Further examples of these targets functions will be found in part II of this thesis.

Another difference in equation 3.147 is the absence of surface corrections. As stated in section 3.9.2, adding a surface correction in the cost function reduces significantly the quality of the fit, meaning that no proprer seismic diagnostic can be derived from the inversion. A workaround is to apply empirical corrections on the frequencies and to use this corrected dataset as input for the structural inversions. Of course, this means that the correction will suffer from the inaccuracies in the empirical corrections of surface effects.

Similarly, the cross-term contribution will play a significant role in asteroseismic inversions. Eliminating the cross-term is even more complicated in this framework than in helioseismology. Therefore, the asteroseismic inversions in this work had to be made using either Γ_1, the adiabatic exponent, or Y, the helium mass fraction, as the structural variable related to the cross-term contribution. Using these variables allows to reduce the cross-term significantly, as will be shown in part II. This is a consequence of the thermodynamic properties of stellar materials which make $\Gamma_1 \approx 5/3$ nearly everywhere in the stellar structure. Consequently, the contribution of Γ_1 to the cross-term integral is naturally much smaller than if one used ρ or c^2 as a secondary variable. This is illustrated in figure 2.4 for standard solar models, but similar conclusions can be found in the asteroseismic context, as we will see in Part II. For the helium mass fraction, Y, the justification is found in equation 3.136 and illustrated in figure 3.7, where one sees that the structural kernels linked to helium actually have very small amplitudes nearly everywhere except in the helium ionisation zones. This means that their contribution to the cross-term will be rather small and even more so if one has insights on the helium abundance in the convective zone thanks to other methods.

The last term in the cost function of asteroseismic inversions is an additional constraint based on dimensional arguments and linked to homologous relations. It can be shown that if the integrated quantity $\mathscr{A}$ depends on stellar mass as $M^{k/2}$, with k an integer factor described through dimensional analysis, then a non-linear generalisation of the SOLA method can be developped and used in asteroseicmic inversions. The term in the cost function of the asteroseismic SOLA inversion is there to ensure a certain unimodularity based on dimensional arguments. To avoid repetition, we refer to section 5.3.3 for the description of this non-linear process and all the details linked to the scaling process involved in seismic inversions.

3.9 Correcting surface effects

In the previous sections, we showed that to derive the integral relations between frequency differences and structural corrections, one had to neglect some surface terms. In addition to these approximations, the hypothesis of adiabaticity is obviously wrong in the upper regions, where the thermal and dynamical timescales are of the same order of magnitude. Another inaccuracy comes from the fact that upper regions are poorly modelled. This means that the cavity in which the waves propagate is not properly modelled and the stratification of the regions where the modes are generated, in solar-like oscillations, is wrong. These effects are completely disregarded when deriving the kernels and thus the frequencies have to be corrected so that they can be used to probe the acoustic structure of a given star. In this section we will present the usual correction that is adopted in most helioseismic inversions and discuss some applications in asteroseismology.

3.9.1 Helioseismic inversions

Dealing with surface corrections means that we are looking at modifications occuring only in the upper regions of the star. We will first analyse the behaviour of these so-called

surface effects. We thus impose that we are looking at a given perturbation, $\delta\mathscr{D}_{surf}$, of high amplitude in the surface layers, but negligible in the lower regions, where all the hypotheses of adiabatic computations are well met.

At a given frequency, one can see that the behaviour of the eigenfunctions does not depend on ℓ in the surface regions, especially for low degree modes (which are those observed in asteroseismology). The behaviour of the frequencies of such modes is illustrated in Fig. 3.11.

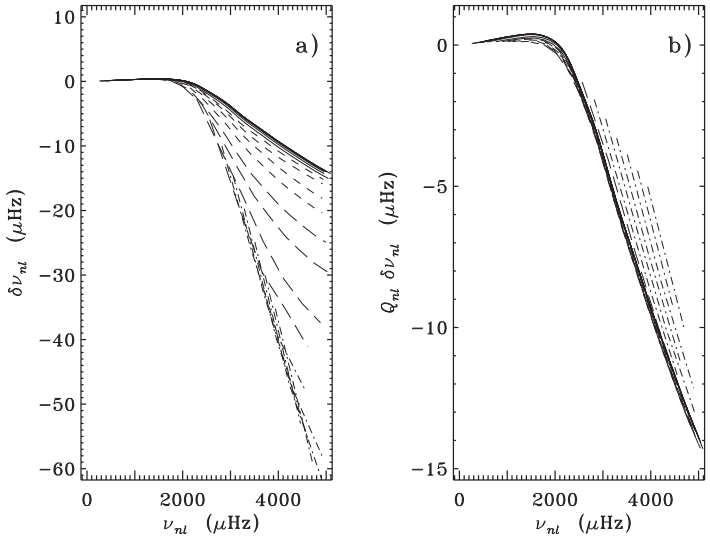

Figure 3.11: Behaviour of individual frequencies with and without scaling, each curve representing modes of various ℓ. Once the scaling has been applied, very little dependance in ℓ is seen (Reprinted from Christensen-Dalsgaard (2003)).

As a first approximation, we thus assume that the eigenfunctions do not depend on ℓ and define an equation similar to equation 3.100 for the surface effect

$$\frac{<\vec{\xi}_{n,\ell}, \delta\mathscr{D}_{surf}(\vec{\xi}_{n,\ell})>}{2\omega_{n,\ell}^2} = E_{n,\ell}\frac{\delta\omega_{n,\ell}}{\omega_{n,\ell}}. \tag{3.150}$$

This equation is very similar to equation 3.100, since we are trying to determine the impact of a perturbation of the model on the frequencies. In this particular case, the perturbation is located in the surface regions and equation 3.150 will thus behave like the eigenfunctions in these regions. In other words, it will not be strongly dependent on ℓ, especially if the modes are of low degree. We follow here the developments of Christensen-Dalsgaard (2003), introducing a $Q_{n,\ell}$ function defined as

$$Q_{n,\ell} = \frac{E_{n,\ell}}{\bar{E}_0(\omega_{n,\ell})}, \tag{3.151}$$

with $\bar{E}_0$ being the inertia of the radial mode at a fixed ω, interpolated in $\omega_{n,\ell}$. One obtains the following relations

$$Q_{n,\ell}\delta\omega_{n,\ell} = \frac{<\vec{\xi}_{n,\ell}, \delta\mathscr{D}_{surf}(\vec{\xi}_{n,\ell})>}{2\omega_{n,\ell}\bar{E}_0(\omega_{n,\ell})}. \tag{3.152}$$

Figure 3.11 illustrates the effects of this scaling for a comparison between a reference model and a model with a modified opacity in the upper regions. Consequently, this implies

that the quantity $Q_{n,\ell}\delta\omega_{n,\ell}$ is largely independent of ℓ and, in turn, the surface corrections will also only depend on ω for a given ℓ. A first correction is thus to apply this scaling method to eliminate the ℓ dependency of the surface effects. However, this scaling is of course not sufficient to correct the observed biases.

From the analysis of the variational equation 3.123, we know that no particular care is taken to account for the surface effects. Indeed, the hypotheses of equation 3.123 are not even satisfied in the surface regions and these inaccuracies mean that there is no theoretical expression for $\mathscr{D}_{surf}$. Thus, we have to add another function to the integral relations, attempting to take into account surface effects. This function is usually denoted $\mathscr{G}(\omega)$. Using the $Q_{n,\ell}$ factor to normalise the expression, one gets a surface term independent of ℓ. In fact, $\mathscr{G}(\omega)$ is simply an empirical modelling of the effects of the operator $\delta\mathscr{D}_{surf}$, which form is unknown. For the (ρ_0, c_2) structural pair, one gets the following relation

$$\frac{\delta\omega_{n,\ell}}{\omega_{n,\ell}} = \int_0^R \left[K^{n,\ell}_{c^2,\rho_0} \frac{\delta c^2}{c^2} + K^{n,\ell}_{\rho_0,c^2} \frac{\delta\rho_0}{\rho_0} \right] dr + \frac{\mathscr{G}(\omega)}{Q_{n,\ell}}. \tag{3.153}$$

The inversion technique now includes an additional function, taking into account the surface effects that need to be either modelled or eliminated. In practice, it can also be shown that $\mathscr{G}$ must be a slowly varying function of frequency because any variation in a model leads to an oscillating signature in the frequencies whose frequency is proportional to the acoustic depth of the perturbation. In the case of surface effects, this signature is going to be very slowly varying.

The most usual way to model the function $\mathscr{G}$ is to use Legendre polynomials to model the surface effects and impose in the inversion technique an additional condition imposing

$$\sum_i c_i(r_0)\mathscr{G}(\omega_i) = 0. \tag{3.154}$$

This additional condition thus imposes that the model of the surface effect should be simultaneously cancelled by the inversion, when it derives the inversion coefficients used to recombine the frequencies. In practical cases, the series of Legendre polynomial goes up to order 6 or 7. One should note that there is no physical justification behind the choice of the Legendre polynomials and that one rather speaks of "well chosen functions[6]" without further arguments

Another method to model surface effects is to use a low-pass filter on the oscillation data (Basu et al. (1996a)). One then uses an asymptotic form of the relation between frequency and structure, in the form

$$S_i \frac{\delta\omega_i}{\omega_i} \simeq \mathscr{H}_1(\frac{\omega_i}{L}) + \mathscr{H}_2(\omega_i), \tag{3.155}$$

where $L = \ell + 1/2$. This expression is derived from the perturbative analysis of the asymptotic relations of pressure modes given in equation 3.47. The exact analytical expression of the functions $\mathscr{H}_1$ and $\mathscr{H}_2$ can be found in Christensen-Dalsgaard, D. O. Gough, and Perez Hernandez (1988). The filtering is done in three steps, with the hopes of delivering a correction for the surface effects in the form

$$\sum_i a_i S_i \frac{\delta\omega_i}{\omega_i} = \mathscr{G}(\omega_i). \tag{3.156}$$

First, one fits a spline combination on equation 3.155. This allows to obtain an equation linking frequency corrections to $\mathscr{H}_2(\omega)$.

[6] See Christensen-Dalsgaard (2003)

The second step is then to apply a low pass filter to this relation to isolate any slowly varying function of ω. One then obtains a filtered function, $\mathscr{H}_2(\omega)$, that is supposed to be linked to $\mathscr{G}(\omega)$.

Thirdly, one fits this filtered $\mathscr{H}_2(\omega)$ to obtain a relation similar to equation 3.156. This fit then allows to define coefficients to correct the individual frequencies such that one eliminates the surface effects based on the asymptotic fit. One should note that due to this correction, the structural kernels are modified and have much lower amplitudes in the surface regions. This method also has the disadvantage of introducing correlations between frequency differences, meaning that the treatment of the propagation of errors is slightly more expensive numerically.

3.9.2 Asteroseismic methods

In asteroseismology, the context is completely different. First, one only has a few observed modes. Typically, the low ℓ solar spectra used in global helioseismology to probe the lower internal structure of the Sun contains a few thousands of modes (see for example Basu, Chaplin, et al. (2009)), while the best Kepler dwarf targets have from around 20 to 55 observed frequencies (see for example Appourchaux et al. (2014) and Lund et al. (2017)). This of course means, as stated before, that linear inversion techniques used in helioseismology are not sufficiently efficient to carry full structural profiles determinations. Besides the limitations on the diagnostic provided by inversions, the small number of frequencies has an impact on the way one could treat surface effects in asteroseimic inversions.

In helioseismology, fitting a 6^{th} order polynomial function alongside a custom-made target to infer corrections is not a problem, since one has thousands of structural kernels that can be recombined. In asteroseismology, adding the constraint of fitting a 6^{th} order polynomial is unrealistic. Indeed, the inversion would be only trying to eliminate the surface term without giving any weight to the inversion target. As we will see, an inversion is always a trade-off problem and in asteroseismology, one has to use all available means to avoid an unfavourable trade-off situation. Therefore other methods of corrections should be employed that do not affect the trade-off problem of the inversion.

One way to deal with these effects is to apply a correction on the frequencies before using them in the inversion. Up to now, three main approaches can be found in the litterature. Historically, the first one is a power-law correction proposed in Kjeldsen, Bedding, and Christensen-Dalsgaard (2008), based on considerations on the solar oscillation spectrum. While of course this correction works for the Sun, it does not perform well for other stars. The second one is a correction proposed by Ball and Gizon (2014). This approach is still purely empirical, but takes into account the fact that the frequency correction should be proportional to the inverse of the mode inertia, as shown in the variational expression. Moreover, the Ball and Gizon correction was tested using stellar models patched to averaged 3D atmospheres and thus certainly takes into account some part of the surface effects (Ball, Beeck, et al. (2016)). More recently, another correction law has been proposed by Sonoi et al. (2015) using a more extended sample of patched models.

However, it should be noted that none of these corrections takes into account non-adiabatic effects (although studies have been performed by Houdek, Trampedach, et al. (2017) for radial modes in the solar case), which are the second contributor to the so-called "surface effects". These empirical corrections thus still need to be improved and connected to more solid theoretical background since ultimately, the surface effect problem is a consequence of our current incapacity to understand and model the physics of the upper

layers of stars and the way the oscillation modes propagate through them. In what follows, we will show theoretical developments for which these effects are not important since we only work with models. However, the results related to observed targets neglect these effects and thus should not be regarded definitive, even if they do give a feel for what inversions are capable of achieving.

II

THEORETICAL DEVELOPMENTS

4. OBTAINING NEW STRUCTURAL KERNELS

4.1 General Introduction

The use of additional structural kernels besides those of the classical adiabatic squared sound speed and density pair is not new. Indeed, in D. O. Gough and Kosovichev (1988), such changes were advocated for using primary acoustic variables but also additional thermodynamical variables like the temperature or the hydrogen abundance, assuming a given equation of state and thermal balance hypothesis. Inversions with the squared isothermal sound speed, defined by $u = \frac{P}{\rho}$ or the Ledoux convective parameter, $A = \frac{d\ln\rho}{d\ln r} - \frac{1}{\Gamma_1}\frac{d\ln P}{d\ln r}$[1], were already performed in the early 1990's (see D. O. Gough and Kosovichev (1993a), D. O. Gough and Kosovichev (1993b), D. O. Gough and Kosovichev (1988)). While these inversions were indeed successfull in helioseismology, their application to asteroseismic targets was not straightforward. However, it was already clear that being able to change the thermodynamical variables of the integrals in the variational expression could lead to potentially more suitable variables, therefore making it easier to probe stellar structure with seismic data. In these studies, the method of conjugated function was used, but its development had been undertaken in the framework of helioseismology. Therefore, it could not be implemented as such for asteroseismic inversions.

In this chapter, we present two methods suitable for changing the thermodynamical variables of the variational integral relations. We test the new kernels thanks to variational expressions and demonstrate the possibility for non-linearities to appear in certain structural pairs. These results have been published in Astronomy and Astrophysics under the reference Buldgen, D. R. Reese, and M. A. Dupret (2017) and the following section is a reproduction of this publication.

[1]This quantity is also called the Ledoux discriminant in some publications. Moreover, the definition we have adopted here, which is based on the manual of the Liège Oscillation Code (LOSC) written by R. Scuflaire, appears to be unfortunately the exact opposite of what can be found in the publications referenced in this manuscript.

4.2 Analysis of the linear approximation of seismic inversions for various structural pairs

4.2.1 Introduction

Asteroseismology is now considered the golden path to the study of stellar structure. This young research field benefits from high quality data for a large sample of stars stemming from the successes of the CoRoT, Kepler, and K2 missions (Baglin et al. (2009), Borucki et al. (2010), Chaplin, Lund, et al. (2015)). More specifically, the detection of solar-like oscillations in a large sample of stars now allows a more accurate study of stellar structure. In the future, the Tess and Plato missions (Rauer et al. (2014)) will carry on what is now called the space-photometry revolution.

Historically, the successes of asteroseismology were preceded by the successes of helioseismology, the study of solar pulsations. Indeed, the quality of seismic data of the Sun is still far beyond what is achievable for other stars, even in the era of the space missions. In the particular field of helioseismology, numerous methods were developed to obtain constraints on the solar structure. Amongst them, inversion techniques led to the successful determination of the position of the base of the convective envelope, the helium abundance in this region, and the rotational profile of the Sun (Schou, Antia, et al. (1998)). The determination of the sound speed and density profiles also demonstrated the importance of microscopic diffusion for solar models (e.g. Basu and Antia (2008)).

In the context of asteroseismology, the use of these inversion techniques can now be considered for a limited number of targets under the conditions of validity of all the hypotheses hiding behind the basic equations defining their applicability domain. The most constraining of these hypotheses is to assume a linear relation between frequency differences and structural differences. In this section, we propose to analyse in depth the issues surrounding the linearity of these relations for various structural pairs and more specifically for kernels of the convective parameter. To that extent, we derive new structural kernels for the convective parameter and helium abundance and compare their linear behaviour to other, pre-existing kernels. Differences in the verification of the linearity of the frequency-structure relation mean that care should be taken when combining seismic diagnostics of various kernels, even in the solar case. Differences can stem from the intrinsic non-linear behaviour of the structural variables considered, but can also be the results of inaccuracies in terms of numerical quality of the models and/or kernels.

4.2.2 The variational principle and linear frequency-structure equations

The variational principle is a well-known property of adiabatic stellar oscillation equations. In fact, it can be extended to more general objects than stars and generalised beyond the classical case presented in helio- and asteroseismology. The history of the variational principle can be traced back to stability analysis in structural mechanics, but its application in seismology stems from the pioneering work of Chandrasekhar (1964) and the generalisation of his study by other authors the following years (Clement (1964), Lynden-Bell and Ostriker (1967)).

Far beyond the historical interest of the discovery of this mathematical property, the hypotheses that lay behind this principle are still important since they are at the heart of intrinsic limitations of the frequency-structure relation. From the mathematical point of view, the variational principle is a consequence of the symmetry of the operator associated with adiabatic stellar pulsations. Mathematically, this means that given two functions $\vec{\xi}$

and $\vec{\psi}$ and $\mathscr{D}$ the operator associated with adiabatic oscillations, we have the property

$$< \xi, \mathscr{D}(\psi) >=< \psi, \mathscr{D}(\xi) >, \tag{4.1}$$

where $<,>$ denotes the scalar product associated with the functional space defined as

$$< \vec{\xi}, \vec{\psi} >= \int_V \rho \vec{\xi}.\vec{\psi}^* dV, \tag{4.2}$$

with the symbol * denoting the complex conjugate. The absence of symmetry in the non-adiabatic case is the reason why all inversions are carried out using the hypothesis of adiabaticity of stellar oscillations.

Moreover, the hypothesis of linearity of the frequency-structure relations is a strong restriction to the validity of seismic inversions and in this section we briefly discuss how this hypothesis influences structural diagnostics from inversion techniques. The relation between perturbations of the frequencies and small perturbations of the stellar structure can be obtained by perturbing the variational expression of the pulsation frequencies. The symmetry of the stellar pulsation operator is then used to eliminate perturbations of the eigenfunctions in the resultant expression. Other effects such as perturbations of the eigenfunctions associated with each pulsation frequency can be neglected to first order. This implies that a direct relation can be obtained between structural differences and pulsation frequencies only. This relation is formally written:

$$\delta\nu = \frac{< \vec{\xi}, \delta\mathscr{D}(\vec{\xi}) >}{< \vec{\xi}, \vec{\xi} >}, \tag{4.3}$$

with $\delta\nu$ the perturbation of an oscillation frequency, $\delta\mathscr{D}$ the associated perturbation to the operator of adiabatic oscillations. The eigenfunctions $\vec{\xi}$ and the unperturbed operator $\mathscr{D}$ are known and defined from the reference model.

In practice, Eq. (4.3) implies that small differences in frequencies can be used to analyse the associated differences in the operator of adiabatic pulsations. The main problem is the scalar product which implies integral relations and thus an ill-posed problem. However, it should be noted that the validity of the variational expression is limited, since we are speaking of small perturbations, the term "small" being misleading because it is often retroactively defined. In other words, perturbations are small because the variational expression is satisfied, but the quantification of how small a perturbation can be and if all variables can be similarly perturbed remains uncertain.

The classical equation for inversion techniques is the result of further developments introduced in the variational expression, assuming spherical symmetry of the star, and carrying out integration by parts and permutation of integrals. This ends leading to the following formally simple equation (see D. O. Gough and Thompson (1991) for a full demonstration of this expression and its hypotheses.):

$$\frac{\delta\nu^{n,\ell}}{\nu^{n,\ell}} = \int_0^R K^{n,\ell}_{\rho,c^2} \frac{\delta\rho}{\rho} dr + \int_0^R K^{n,\ell}_{c^2,\rho} \frac{\delta c^2}{c^2} dr + \mathscr{O}(\delta^2), \tag{4.4}$$

with the following definition:

$$\frac{\delta x}{x} = \frac{x_{obs} - x_{ref}}{x_{ref}}. \tag{4.5}$$

The quantity x can be the oscillation frequency of a particular mode, $\nu^{n,\ell}$, the density, ρ, the squared adiabatic sound speed, c^2, or other quantities for which kernels can be derived.

First of all, we note that to this expression is usually added the surface effects term, which is an empirical correction that is added to Eq. (4.4) to take into account the improper modelling of surface layers in the computation of oscillation frequencies of stellar models. In this study, we do not consider this surface term since we will only compare theoretical models and the validity of the linear approximation for various test cases between these models.

In terms of seismic diagnostic, the linear hypothesis puts strong restrictions on the applicability of inversion techniques. In fact, in some regions of the Hertzsprung-Russell diagram, it seems obvious that differences in frequencies may not be linearly related to structural changes. For example, in evolved stars, changes in the mixed modes frequencies will have strong impact on the coupling of the p and g mode cavities. Thus a small change in frequency will imply a strong change in the eigenfunctions. In this particular case, the second order terms neglected in the variational analysis may well become dominant and have to be modelled to efficiently use kernel based inversions as a seismic diagnostic.

For the case of p modes observed in solar-like stars, one could say that provided the model is good enough, the linear approximation may be used. However, the linear approximation as presented is usually for a slow-rotating, non-magnetic, isolated star[2]. The problem is not to carry out the inversion, since that can be done provided a sufficient number of frequencies is available, but to decide whether the inverted results can be trusted. The errors due to linearity are intrinsically not seen by the inversion technique. However, it is still possible to witness their effects on inversion results and indirectly assess the quality of the reference model. To do so, one simply has to start from various reference models and analyse the variation of the results with the model. This simple and straightforward method is well-adapted to global optimisation techniques which generate a large sample of models. However, this does not mean that using a large number of models, one can go beyond the linear approximation of the variational principle, it only implies that one can analyse the errors coming from the non-linear effects and decide whether the results should be trusted or not.

An other important aspect of asteroseismic inversions which has been reported by Basu (2003) and described in Buldgen, D. R. Reese, and M. A. Dupret (2015) is that the inversion scales its results implicitly. This scaling stems from the assumption that integral relations are defined on the same domain for the reference model as for the observed target. In other words, if we define R_{Ref}, the radius of the reference model and R_{Tar}, the radius of the observed target, the inversion will wrongly consider that both radii are equal. However, since the inversion uses seismic information, the mean density of the observed target is known. Consequently, the mass of the scaled target, denoted here $\tilde{M}_{Tar}$, which is studied by the inversion is $\tilde{M}_{Tar} = R_{Ref}^3 \bar{\rho}_{Tar}$, with $\bar{\rho}_{Tar}$ the mean density of the observed target. This means that structural quantities such as the squared sound speed, or indicators defined by integrated quantities, are not determined for the observed target itself, but for the scaled one and are related to the observed quantities through an homology. While this does not reduce the diagnostic potential of inversion techniques, it should of course be taken into account when comparing results inverted from various reference models.

4.2.3 Changing the structural pair

The calculation of new kernels is particularly interesting in the context of asteroseismology, where the change of structural variables can significantly improve the ability to fit a

[2]By isolated, we mean that it is not in a close binary system where the gravitational influence of the neighbouring companion would change the geometry of the star and its oscillation modes

certain target while reducing the contribution from the so-called "cross-term". Additional kernels have also been used in helioseismology to test the equation of state used in solar models and to try to determine the helium abundance in the convective envelope. In this section, we present two methods to derive additional structural kernels from Eq. 4.4 and discuss in more details their implementation and respective strengths and weaknesses.

Direct method

We call this approach direct because it consists in a direct change of variables within Eq. 4.4 (or any similar relation), from which a linear differential equation is derived (This equation can be of the first, second or third order depending on the variables involved). The resolution of this equation allows us to determine new kernels, provided the proper boundary conditions are applied.

In practice, this method gives access to any function of ρ, c^2, Γ_1 or their integrals (e.g. hydrostatic pressure, P or the gravitational acceleration, g), or combinations of these variables (e.g. the squared isothermal sound speed, $u = \frac{P}{\rho}$)[3]. However, it should be noted that this method does not give access to any function of the derivative of the density without further integration by parts when deriving the differential equation. The kernels that can be obtained through the direct method are listed in Table 4.1. We mention that this list contains only kernels for which the equations have been derived, but one could be interested to define new thermodynamical variables and to obtain kernels for these new variables.

Table 4.1: Summary of the properties of the differential equations for various structural pairs with the direct method.

Pair	Order of o.d.e.	Integration by parts
ρ, Γ_1 (or Y)	0-algebraic	No
g, Γ_1 (or Y)	1	No
P, Γ_1 (or Y)	2	No
c^2, Γ_1 (or Y)	2	No
u, Γ_1 (or Y)	2	No
A, Γ_1 (or Y)	3	Yes
N^2, c^2	3	Yes

This method has been partially presented in a previous paper Buldgen, D. R. Reese, and M. A. Dupret (2015) and referred to as Masters' method, because it was developed as an extension of an approach presented in Masters (1979) for geophysical applications that was mentioned in D. O. Gough and Thompson (1991) as a potential method for obtaining kernels for the Brunt-Väisälä frequency[4]. Originally, Masters' approach proposed to solve directly the integral relations between structural kernels used in geophysics. In asteroseismology, the method could have been similar. First, we start with Eq. 4.4 and consider for example the change from the (ρ, c^2) structural pair to the (g, c^2) structural pair, where g is the gravitational acceleration and is written:

$$g = \frac{Gm(r)}{r^2}, \tag{4.6}$$

[3]More generally, this function could be written $f(\rho, P, g, \Gamma_1)$ or $f(\rho, P, g, Y)$ with any f that can be written in terms of linear perturbations of these quantities.

[4]We describe how this can be done in appendix 4.2.6

with $m(r)$ the mass of stellar material contained in a sphere of radius r and being defined:

$$m(r) = \int_0^r 4\pi\tilde{r}^2\rho d\tilde{r}. \tag{4.7}$$

If we consider the linear relative perturbation of the gravity acceleration, we obtain:

$$\frac{\delta g}{g} = \frac{\frac{G\delta m}{r^2}}{\frac{Gm}{r^2}} = \frac{\delta m}{m} = \frac{1}{m}\int_0^r 4\pi\tilde{r}^2\delta\rho d\tilde{r}. \tag{4.8}$$

This expression can be used directly in the integral relations for the structural kernels. Indeed, if kernels of the pair (g, c^2) can be found, they must satisfy the following relation:

$$\begin{aligned}\frac{\delta\nu^{n,\ell}}{\nu^{n,\ell}} &= \int_0^R K^{n,\ell}_{g,c^2}\frac{\delta g}{g}dr + \int_0^R K^{n,\ell}_{c^2,g}\frac{\delta c^2}{c^2}dr \\ &= \int_0^R K^{n,\ell}_{\rho,c^2}\frac{\delta\rho}{\rho}dr + \int_0^R K^{n,\ell}_{c^2,\rho}\frac{\delta c^2}{c^2}dr.\end{aligned} \tag{4.9}$$

From the second equality, we have the integral relation that we searched. One has only to introduce the perturbation of the gravitational acceleration and permute the integrals such that the perturbation of density is in the outermost integral. From there it is easy to obtain a simple relation between kernels. Indeed, Eq. 4.9 must be satisfied for any perturbation within the linear regime, since the kernels must be dependent on the reference model only. We then obtain simple relations for each kernel:

$$K^{n,\ell}_{c^2,g} = K^{n,\ell}_{c^2,\rho} \tag{4.10}$$

$$4\pi r^2\rho\int_r^R \frac{K^{n,\ell}_{g,c^2}}{m} = K^{n,\ell}_{\rho,c^2}. \tag{4.11}$$

The proposition of Masters (1979) was to solve directly this integral relation, which can be done using, for example, an iterative relaxation method to solve the integral equation. In practice, we favour a more efficient approach by deriving a differential equation for these kernels, simply by taking the derivative of Eq. 4.11 after having divided it by $r^2\rho$. We then obtain the following very simple differential equation:

$$-m\frac{d}{dr}\left(\frac{K^{n,\ell}_{\rho,c^2}}{\rho r^2}\right) = K^{n,\ell}_{g,c^2}, \tag{4.12}$$

Since this equation is extremely simple, the kernels are straightforward to obtain. However, this development was just for the sake of illustration and a good example of the difficulties associated with this method is illustrated in appendix 4.2.6.

A more elaborated case, which has already been involved in practical applications is that of the (u,Γ_1) and (u,Y) kernels. These kernels are obtained by solving a second order differential equation which is recalled here:

$$\begin{aligned}-y\frac{d^2\mathscr{K}'}{(dy)^2} + \left[\frac{2\pi y^{3/2}\tilde{\rho}}{\tilde{m}} - 3\right]\frac{d\mathscr{K}'}{dy} =& y\frac{d^2\mathscr{K}}{(dy)^2} - \left[\frac{2\pi y^{3/2}\tilde{\rho}}{\tilde{m}} - 3 + \frac{\tilde{m}\tilde{\rho}}{2y^{1/2}\tilde{P}}\right]\frac{d\mathscr{K}}{dy} \\ &+ \left[\frac{\tilde{m}\tilde{\rho}}{4y\tilde{P}^2}\frac{d\tilde{P}}{dx} - \frac{\tilde{m}}{4y\tilde{P}}\frac{d\tilde{\rho}}{dx} - \frac{3}{4y^{1/2}\tilde{P}}\frac{d\tilde{P}}{dx} - \frac{\tilde{m}\tilde{\rho}}{2y^{3/2}\tilde{P}}\right]\mathscr{K},\end{aligned} \tag{4.13}$$

with $\mathscr{K} = \frac{K^{n,\ell}_{u,\Gamma_1}}{r^2\rho}$ and $\mathscr{K}' = \frac{K^{n,\ell}_{\rho,\Gamma_1}}{r^2\rho}$ in the case of the differential equation of the (u,Γ_1) kernels or with with $\mathscr{K} = \frac{K^{n,\ell}_{u,Y}}{r^2\rho}$ and $\mathscr{K}' = \frac{K^{n,\ell}_{\rho,Y}}{r^2\rho}$ for the equation of the (u,Y) kernels. Furthermore, in Eq. 4.13, one has the following definitions: $x = \frac{r}{R}$, $y = x^2$, $\tilde{m} = \frac{m}{M}$, $\tilde{\rho} = \frac{R^3\rho}{M}$, $\tilde{P} = \frac{R^4 P}{GM}$. We also recall here that using kernels such as the (ρ,Y) or the (u,Y) kernels requires to introduce the equation of state by using the following definition:

$$\frac{\delta\Gamma_1}{\Gamma_1} = \left(\frac{\partial \ln\Gamma_1}{\partial \ln P}\right)_{Z,Y,\rho} \frac{\delta P}{P} + \left(\frac{\partial \ln\Gamma_1}{\partial \ln \rho}\right)_{Z,Y,P} \frac{\delta\rho}{\rho} + \left(\frac{\partial \ln\Gamma_1}{\partial Y}\right)_{Z,P,\rho} \delta Y + \left(\frac{\partial \ln\Gamma_1}{\partial Z}\right)_{Y,P,\rho} \delta Z. \tag{4.14}$$

Two hypotheses are made when using helium kernels. First, one assumes that the equation of state of the reference model and that of the target model are the same. Secondly, one usually drops the last term in δZ of Eq. (4.14). This is often considered to be a benign hypothesis and we will review its impact for various kernels in section 4.2.4.

The problem of this method is that, when deriving the differential equation for the kernels, one may be faced with discontinuous terms within the equation coefficients. These discontinuities are due to the effects of the transition from radiative regions to convectives regions and have to be treated correctly if one does not wish to introduce numerical errors in the resolution. Typically, these discontinuities appear when taking first or second derivatives of the density (or any quantity related to the density through an algebraic relation). For example, the second derivative of the adiabatic squared sound speed, c^2 shows a discontinuity at the base of the convective envelope. This also means that the differential equation must be solved on separated domains and that continuity conditions have to be applied for each sub-domain. These conditions typically serve as constraints to solve the differential equations of structural kernels. For example, for the (u,Γ_1) and (u,Y) kernels, the resolution of the second order differential equation uses one central boundary condition that is derived from the differential equation itself and one "boundary" condition that stems from the integral equation. Namely, one assumes that the kernels have to satisfy their integral equation at some point of the sub-domain. For the next sub-domain, a continuity relation on the kernels is derived, since they have to be continuous for continuous variables, and the integral relation is again used to obtain an additional condition for the sub-domain.

In practice, the use of the integral relation for the additional condition is not trivial, since sometimes one can be confronted with integrals of the layers above the layer on which one wishes to solve the differential equation[5]. The problem is even more complicated when facing separated domains. Thus, one has to find a workaround based on the linearity of the problem and ends up solving a system of two differential equations on each sub-domain, where the equations are simultaneously connected through continuity relations and integral equations. With a little algebra, this can be done using a simple direct solver and finite difference discretisation (In our case, we used the prescriptions of D. R. Reese (2013) for the grid on which the equation is solved). This leads in practice to a good accuracy in the results when care is taken in the computation of the derivatives of the coefficients and of the already known kernels. Indeed, these derivatives can be a source of significant numerical noise when calculated on a reference model of poor quality or when the eigenfunctions have been computed with a poor accuracy.

[5]Thus the arguments of the integral are unknown.

Method of conjugated functions - Application to the A-Y kernels

The method of conjugated functions is quite different from what is done in the direct method, although the starting point is still the equality of two variational expressions for different structural variables. This method was presented for the first time in a paper by Elliott (1996) in the context of helioseismology and a more thorough presentation of the method can be found in Kosovichev (1999). In this section, we recall the basis of the method and apply it to the derivation of new kernels associated with the (A,Y) structural pair.

The quantity A is called the convective parameter and is closely related to the Brunt-Väisälä frequency. It is defined as follows:

$$A = \frac{d\ln\rho}{d\ln r} - \frac{1}{\Gamma_1}\frac{d\ln P}{d\ln r} \tag{4.15}$$

This quantity has the convenient property to be zero in adiabatically stratified convective regions. It is also very sensitive to changes in depth of the base of the convective zone and changes in upper regions of convective envelopes. The problem we will define is thus related to determining the change of structural variables from (ρ,Y) kernels to the (A,Y) kernels. The (ρ,Y) pair is a convenient starting point but one could choose other starting variables. Thus, our goal is to find the functions $K^{n,\ell}_{A,Y}$ and $K^{n,\ell}_{Y,A}$ for a given stellar model such that for two models that are sufficiently close to each other, we have:

$$\begin{aligned}\frac{\delta\nu^{n,\ell}}{\nu^{n,\ell}} &= \int_0^R K^{n,\ell}_{\rho,Y}\frac{\delta\rho}{\rho}dr + \int_0^R K^{n,\ell}_{Y,\rho}\delta Y dr \\ &= \int_0^R K^{n,\ell}_{A,Y}\delta A dr + \int_0^R K^{n,\ell}_{Y,A}\delta Y dr.\end{aligned} \tag{4.16}$$

First, we have to relate the linear perturbation of A to the other structural variables. In the approach of conjugated functions, one starts by defining a system of differential equations between the model perturbations, where one wishes to relate the different perturbed structural quantities found in the starting and final integral relations. In this particular case, one has a system of 3 differential equations that relates all the quantities together. This system is written:

$$\begin{aligned}r\frac{d}{dr}\left(\frac{\delta\rho}{\rho}\right) &= \delta A + \frac{Gm}{rc^2}\frac{\partial\ln\Gamma_1}{\partial Y}|_{P,\rho}\delta Y + \frac{Gm}{c^2 r}\left[\frac{\partial\ln\Gamma_1}{\partial\ln P}|_{\rho,Y}+1\right]\frac{\delta P}{P}, \\ &\quad + \frac{Gm}{c^2 r}\left[\frac{\partial\ln\Gamma_1}{\partial\ln\rho}|_{P,Y}-1\right]\frac{\delta\rho}{\rho} - \frac{Gm}{rc^2}\frac{\delta m}{m},\end{aligned} \tag{4.17}$$

$$r\frac{d}{dr}\left(\frac{\delta m}{m}\right) = \frac{4\pi r^3\rho}{m}\left(\frac{\delta\rho}{\rho}-\frac{\delta m}{m}\right), \tag{4.18}$$

$$r\frac{d}{dr}\left(\frac{\delta P}{P}\right) = \frac{Gm\rho}{rP}\left[\frac{\delta P}{P}-\frac{\delta\rho}{\rho}-\frac{\delta m}{m}\right]. \tag{4.19}$$

As we will show in this section, the method of conjugated functions uses equations closely related to the system presented above. A major advantage is that this approach leads to a system with simple coefficients, for which the problem of numerical derivatives will not be as important as for the direct method. However, this method uses more hypotheses than the direct method and is consequently less well-suited for asteroseismology. Typically, the problem stems from the boundary conditions that are used to close the system and select a unique solution. For the surface boundary conditions, we have to assume that the mass of the observed target is the same as the mass of the reference model. At first,

we thought that only the mean density was required to be fitted to ensure a verification of the variational expression but we will see how we were mistaken in the next section. Indeed, it can be argued that kernels for structural pairs such as the (A,Γ_1) pair or the (A,Y) pair will never offer a good accuracy in the asteroseismic case as will be illustrated in section 4.2.4.

The goal of the method of conjugated functions is to determine the unknown tridimensional vector $\vec{v}=(v_1,v_2,v_3)$, which is a conjugated function linked to the structural kernels (see Eq. 4.33), solution of the following system (related to the system of equations 4.17 to 4.19):

$$-r\frac{d\vec{v}}{dr}-\vec{v}=\mathscr{A}^T\vec{v}+\mathscr{C}^T\vec{K}_1, \tag{4.20}$$

where we have used the following definitions:

$$\mathscr{A}=\begin{pmatrix} \frac{Gm}{rc^2}\left[\frac{\partial \ln\Gamma_1}{\partial \ln\rho}|_{P,Y}-1\right] & -\frac{Gm}{rc^2} & \frac{Gm}{rc^2}\left[\frac{\partial \ln\Gamma_1}{\partial \ln P}|_{\rho,Y}+1\right] \\ \frac{4\pi r^3\rho}{m} & -\frac{4\pi r^3\rho}{m} & 0 \\ \frac{-Gm\rho}{rP} & \frac{-Gm\rho}{rP} & \frac{Gm\rho}{rP} \end{pmatrix}, \tag{4.21}$$

$$\vec{K}_1=(K^{n,\ell}_{\rho,Y},K^{n,\ell}_{Y,\rho}), \tag{4.22}$$

$$\mathscr{C}=\begin{pmatrix} 1 & 0 & 0 \\ 0 & 0 & 0 \end{pmatrix}. \tag{4.23}$$

We also introduce the following definitions:

$$\vec{x}=\begin{pmatrix} \frac{\delta\rho}{\rho} \\ \frac{\delta m}{m} \\ \frac{\delta P}{P} \end{pmatrix},\quad \vec{s}_1=\begin{pmatrix} \frac{\delta\rho}{\rho} \\ \delta Y \end{pmatrix},\quad \vec{s}_2=\begin{pmatrix} \delta A \\ \delta Y \end{pmatrix}, \tag{4.24}$$

$$\mathscr{B}=\begin{pmatrix} 1 & \frac{Gm}{rc^2}\frac{\partial \ln\Gamma_1}{\partial Y}|_{P,\rho} \\ 0 & 0 \\ 0 & 0 \end{pmatrix}, \tag{4.25}$$

$$\vec{K}_2=(K^{n,\ell}_{A,Y},K^{n,\ell}_{Y,A}), \tag{4.26}$$

$$\mathscr{D}=\begin{pmatrix} 0 & 0 \\ 0 & 1 \end{pmatrix}. \tag{4.27}$$

We use the following boundary conditions for $r=0$:

$$3\tilde{v}_1(0)+3\tilde{v}_2(0)=-\frac{K^{n,\ell}_{\rho,Y}}{r^2\rho}(0), \tag{4.28}$$

$$\tilde{v}_3(0)=0, \tag{4.29}$$

with $\tilde{v}_i=\frac{v_i}{r^2\rho}$. Using $\tilde{v}_i$ as variables for the system is motivated by the central limit of the structural kernels, such as $K^{n,\ell}_{\rho,Y}$, which goes as $\mathscr{O}(r^2)$ in central regions. These boundary conditions can be obtained from the limit as r goes to 0 of Eq. 4.20 itself similarly to what is presented in Unno et al. (1989) for the pulsation equations. The last boundary condition of equation 4.20, at $r=R$ is defined as follows:

$$\frac{\delta\rho}{\rho}(R)v_1(R)+\frac{\delta m}{m}(R)v_2(R)+\frac{\delta P}{P}(R)v_3(R)=0, \tag{4.30}$$

and results from the elimination of surface term in the integration by parts in Eq. 4.39 which can be changed using l'Hospital's theorem to avoid having to define $\frac{\delta P}{P}(R)$ with the equation of hydrostatic pressure, thus considering both $P(R)$ and $\delta P(R)$ to be 0:

$$\frac{\delta\rho}{\rho}(R)v_1(R)+\frac{\delta m}{m}(R)v_2(R)+\left(\frac{\delta\rho}{\rho}(R)+\frac{\delta m}{m}(R)\right)v_3(R)=0. \tag{4.31}$$

The main problem with this equation is that both the δm and $\delta\rho$ terms are unknown, it is thus impossible to derive a simple boundary conditions and the components of $\vec{v}$ without an additional hypothesis. In helioseismology, one states that the mass of the observed target is known and one ends up with a simple equation only with $\delta\rho$. One then simplifies the $\delta\rho$ term and ends up with the following simple relation:

$$v_1(R)+v_3(R)=0. \tag{4.32}$$

This problem is intrinsic to the method of conjugated functions since one defines the boundary conditions of the system using an expression containing structural perturbations.

Using these definitions, it can be proven that if $\vec{v}$ is the solution to this problem, then the structural kernels $K^{n,\ell}_{A,Y}$ and $K^{n,\ell}_{Y,A}$, for each perturbation of the model defined by $\vec{x}$ and $\vec{s}_2$, can be determined using the following relations:

$$K^{n,\ell}_{A,Y}=v_1, \tag{4.33}$$

$$K^{n,\ell}_{Y,A}=K^{n,\ell}_{Y,\rho}+K^{n,\ell}_{A,Y}\frac{Gm}{rc^2}\frac{\partial\ln\Gamma_1}{\partial Y}|_{\rho,P}, \tag{4.34}$$

To demonstrate this property, let us first rewrite the system of equations 4.17 to 4.19 in its vector form using the definitions we have just introduced:

$$r\frac{d\vec{x}}{dr}=\mathscr{A}\vec{x}+\mathscr{B}\vec{s}_2, \tag{4.35}$$

One can also write a trivial matrix relation between vectors $\vec{s}_1$ and $\vec{s}_2$:

$$\vec{s}_1=\mathscr{C}\vec{x}+\mathscr{D}\vec{s}_2, \tag{4.36}$$

We now apply the scalar product of Eq. 4.35 and Eq. 4.36 with $\vec{v}$, defining the scalar product on the functional space as:

$$<a,b>=\int_0^R a(r)b(r)dr, \tag{4.37}$$

which is done in this case for each component of $\vec{v}$ and $\vec{x}$. We then obtain:

$$<\vec{v},r\frac{d\vec{x}}{dr}>=<\vec{v},\mathscr{A}\vec{x}>+<\vec{v},\mathscr{B}\vec{s}_2>, \tag{4.38}$$

$$-<r\frac{d\vec{v}}{dr}+\vec{v},\vec{x}>+[r\vec{v}.\vec{x}]_0^R=<\vec{v},\mathscr{A}\vec{x}>+<\vec{v},\mathscr{B}\vec{s}_2>, \tag{4.39}$$

where we have applied an integration by parts and thus obtained a differential equation for $\vec{v}$. If one considers both equations 4.39 and 4.20, we obtain:

$$<\vec{K}_1,\mathscr{C}\vec{x}>=<\vec{v},\mathscr{B}\vec{s}_2>, \tag{4.40}$$

The new kernels can then be determined using:

$$< \vec{K}_2, \vec{s}_2 > = < \vec{K}_1, \mathscr{C}\vec{x} > + < \vec{K}_1, \mathscr{D}\vec{s}_2 > \tag{4.41}$$

$$= < \vec{v}, \mathscr{B}\vec{s}_2 > + < \vec{K}_1, \mathscr{D}\vec{s}_2 >, \tag{4.42}$$

where we have used Eq. 4.40. If we develop the scalar products, we obtain the following integral relations:

$$\int_0^R K^{n,\ell}_{A,Y}\delta A dr + \int_0^R K^{n,\ell}_{Y,A}\delta Y dr = \int_0^R v_1(\delta A + \frac{Gm}{rc^2}\frac{\partial \ln \Gamma_1}{\partial Y}|_{P,\rho}\delta Y)dr + \int_0^R K^{n,\ell}_{Y,\rho}\delta Y dr. \tag{4.43}$$

From these relations, we directly obtain the relations 4.33 and 4.34 and have thus demonstrated that determining the vector $\vec{v}$ satisfying Eq. 4.20 allowed us to determine the kernels of the (A,Y) structural pair.

However, a few comments must be made on Eq. 4.31 since it leads to a strong limitation in the use of the method of conjugated functions. As previously stated, the boundary conditions applied are that the mass of the observed target and the reference model are the same. In asteroseismology, this is not necessarily the case. When using this method for other kernels, we could avoid this limitation by using the relation $\frac{\delta m}{m} = \frac{\delta \bar{\rho}}{\bar{\rho}}$ if the radius is fixed. Ultimately, one ends up with the same implicit scaling presented before for the direct method. It is a considerable advantage of the direct method that it does not explicitly uses any hypothesis on the mass of the observed target.

In this particular case, scaling the perturbations is impossible since the quantities δA and δY are adimensional and not expressed as relative perturbations, obviously because $\frac{\delta A}{A}$ would be undetermined when A goes to zero for the reference model. Consequently, the trick of the implicit scaling cannot be used and we are limited by the accuracy of radii determinations for asteroseismic targets.

However, even with scaled models, the problem can still be present for the helium integrals. Indeed, for the density or the sound speed, the link is quickly done since these variables are explicitly part of what is called the acoustic structure of the stellar model and are directly linked to the oscillation frequencies. The question is more difficult when one thinks about the helium mass fraction. The problem is to link the helium mass fraction profile of the scaled target model to the helium profile of the real target. As such, there is no clear link between both profiles and helium cannot be directly related to the dynamical time since it is not an explicit variable of the acoustic structure. Therefore, caution as to be taken when determining helium abundances from inversion techniques when there is no strong constraints on the radius[6].

We illustrate the (A,Y) kernels in Fig. 4.1 for various degrees and radial orders. It should be noted that the kernels associated with the convective parameter A of the (A,Γ_1) structural pair are quite similar to the kernels associated with A for the (A,Y) structural pair and could thus be used to carry out inversions of similar indicators without the need to introduce the equation of state in the problem. The main problem is then to cope with the high amplitude of the cross-term kernels but ultimately, the presence of pairs of kernels with similar behaviours can be used to check the robustness of the inversion for observed data since it should lead to similar results if the cross-term is properly damped for both structural pairs. One additional striking feature of the (A,Y)

[6]As such the mass of the model would not be a problem if one considers that the mean density can be very accurately determined using seismology. Thus, if one knows the radius accurately, an accurate estimate of the mass can be determined provided good seismic data.

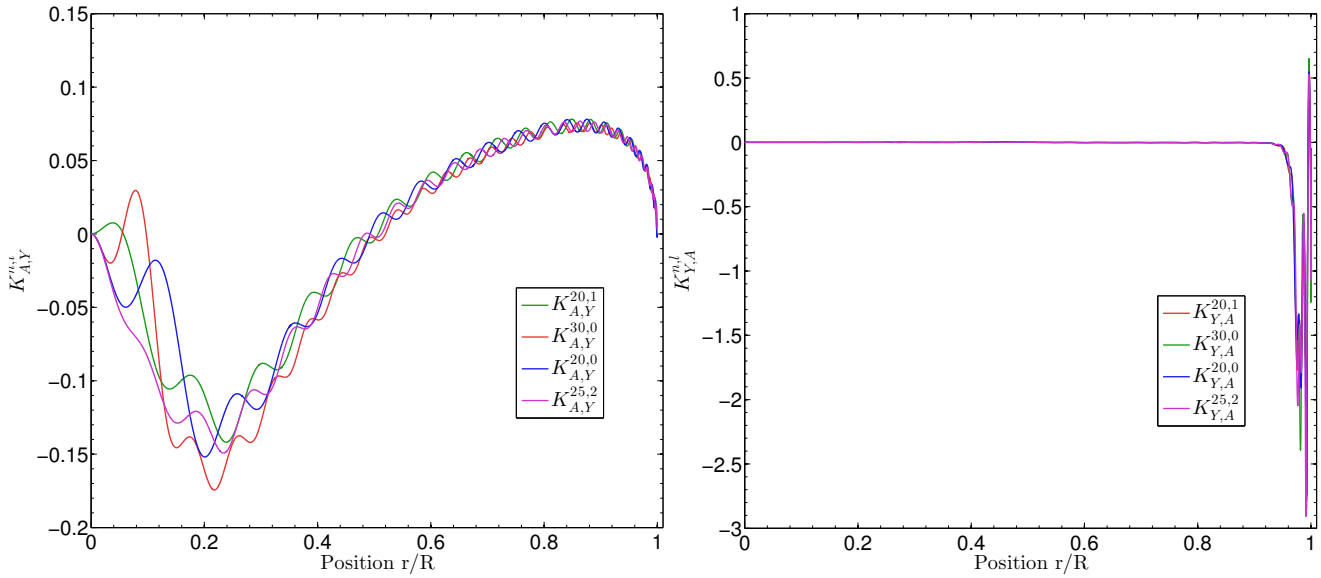

Figure 4.1: Illustration of various kernels for the (A,Y) structural pairs for various degrees and radial orders.

structural pair is the high amplitude of the helium kernels when compared to those of the convective parameter. It is pretty unusual since as was already noticed for the (ρ,Y) structural pairs and confirmed for other structural kernels we derived, the helium kernels tend to have very low amplitudes and are thus very well adapted as cross-terms of inversions[7]. This makes these kernels very interesting for inversions of helium abundance using appropriated indicators in the solar case, where the data is abundant and the radius of the observed target is very well constrained and used to build the standard solar model used as a reference for the inversion. In terms of numerical quality, the verification of the initial system of differential equations is done up to relative differences of the order of 10^{-14} on the average. Typically the resolution is more accurate (10^{-16} or less) in central regions and less accurate at the surface (10^{-13}). It should be noted that the numerical quality of the results is naturally still subject to the number of points of the models and the variables and unknowns considered in the system of equations.

4.2.4 Numerical experiments

In this section, we describe a few numerical experiments carried out to analyse the importance of various hypotheses used to compute structural kernels. All models were computed using the Clés stellar evolution code (Scuflaire, Théado, et al. (2008)) with the following ingredients: the CEFF equation of state (Christensen-Dalsgaard and Daeppen (1992)), the OPAL opacities from Iglesias and Rogers (1996), supplemented at low temperature by the opacities of Ferguson et al. (2005) and the effects of conductivity from Potekhin et al. (1999) and Cassisi et al. (2007). The nuclear reaction rates are those from the NACRE project (Angulo et al. (1999)), supplemented by the updated reaction rate from Formicola et al. (2004) and convection was implemented using the classical, local mixing-length theory (Böhm-Vitense (1958)). We also used the implementation of microscopic diffusion from Thoul, Bahcall, and Loeb (1994), for which three groups of elements are considered and treated separately: hydrogen, helium and the metals (all considered to have diffusion speeds

[7] Although errors on the equation of state can be non-negligible at the levels of accuracy of helioseismology.

of ^{56}Fe). The oscillation frequencies and eigenfunctions were computed using the Liège adiabatic oscillation code (Scuflaire, Montalbán, et al. (2008)). We took much care to analyse the numerical quality of the eigenfunctions and the models before computing structural kernels. Irregularities and poor quality of the computed eigenfunctions can bias the results and lead to wrong structural kernels and thus wrong inferences from inverted results. From our experience in hare-and-hounds exercises and inversions, we have determined that adding seismic constraints to the model is very efficient at bringing the reference model into the linear regime thus validating the inversion process. In other words, fitting the average large and small frequency separations is already a big improvement in terms of linearity, although individual seismic constraints, such as individual frequency ratios and individual small frequency separations are the best way to maximise the chances of being in the linear regime. Individual large frequency separations can also be used, but due to their sensitivity to surface effects, they should not be used in observed cases. As such, since in this study we did not use very elaborate seismic fitting techniques, our tests serve the only purpose of isolating various contributions to the errors and to test various hypotheses usually done when carrying out structural inversions in the context of helio- and asteroseismology.

We started by computing 4 target models with different physical ingredients summarised in Table 4.2. Among these effects, we tested opacity changes, changes in the equation of state, the impact of the metallicity, the impact of individual abundance tables along with changes of typical parameters used for seismic fits such as the mixing-length parameter, α_{MLT} and the hydrogen abundance. For each target, we computed reference models with the same mass and similar physical ingredients. To ensure that both target models and reference models had the same radius, we used a minimisation algorithm to fit the mean density of the target model varying the age of the reference model. In other words, since on the main sequence the radius is changed due to slight core contraction and envelope expansion, we could ensure with this simple method a straightforward fit of all targets. Of course, this approach is limited. For instance, a model which includes efficient microscopic diffusion or a completely different chemical composition will not be strongly constrained by the fit of the mean density and thus will surely not be lying in the linear regime. This should be kept in mind throughout this section since it is not what is done in typical seismic studies where all the available information is used. The verification of the linear

Table 4.2: Physical ingredients of the target models used for the hare-and-hounds exercises.

	Target Model 1	**Target Model 2**	**Target Model 3**	**Target Model 4**
Mass ($M_\odot$)	1.0	1.0	1.0	1.0
Radius ($R_\odot$)	1.0712	1.0822	1.0394	1.0770
Age (Gyr)	5.0	5.0	5.0	4.5
EOS	CEFF	OPAL	CEFF	OPAL
Abundances	GN93	GN93	AGSS09	AGSS09
X_0	0.7	0.7	0.7	0.67
X_0	0.015	0.015	0.015	0.02
$\alpha_{\rm MLT}$	1.7	1.7	1.7	1.7
Mixing	–	–	–	Settling+turbulent diffusion

relations between frequencies and structural profiles is demonstrated by plotting the relative differences between the right-hand side and left-hand side of the linear integral

relations, denoted $\mathscr{E}^{n,\ell}_{s_1,s_2}$ defined as follows:

$$\mathscr{E}^{n,\ell}_{s_1,s_2} = \frac{\frac{\delta\nu^{n,\ell}}{\nu^{n,\ell}} - \left(\int_0^R K^{n,\ell}_{s_1,s_2}\frac{\delta s_1}{s_1}dr + \int_0^R K^{n,\ell}_{s_2,s_1}\frac{\delta s_2}{s_2}dr\right)}{\frac{\delta\nu^{n,\ell}}{\nu^{n,\ell}}} \tag{4.44}$$

with s_1 and s_2 being any of the structural variables for which structural kernels can be obtained. Using this approach offers a straightforward method to compare the validity of the linear relations for each kernel and each mode, pointing out possible weaknesses and inaccuracies. For each comparison, we used the modes with $\ell = 0$, 1, 2 and 3 and n between 6 and 41.

Limits of the linear regime

First of all, we illustrate in Figure 4.2 the verification of the linear relations between frequency differences and structural differences for various structural pairs for target 1 and two reference models, with slightly different α_{MLT} and X_0 values. The model associated with the left panel has $\alpha_{MLT} = 1.5$ and $X_0 = 0.69$, whereas the model used as a reference for the right panel has $\alpha_{MLT} = 1.9$ and $X_0 = 0.715$. We can also see that all structural pairs do not satisfy the linear relations to within the same accuracy. Typically, kernels for the convective parameter A can be problematic, especially kernels of the (A,Y) structural pair. This can mean that all perturbations of the quantities may not be in the linear regime, and that for some kernels, second order terms should be considered. Ultimately this can be the case for variables other than the convective parameter and the (A,Y) kernels can sometimes satisfy the linear relations whilst the (ρ,c^2) kernels do not. Two other problems of hare-and-hounds exercises using various kernels have to be mentioned: first, the insufficient numerical quality of the model and of the eigenfunction themselves; second, the changes of the parameters of the models can sometimes be inappropriate to test these relations and thus, inversion techniques. This means that we are intrinsically limited in our tests for robustness of inversions and that to some extent, other approaches could be sought to fully constrain the limitations of inversions in the context of asteroseismology. The first point is quite straightforward and linked to various problems that can be found in stellar evolution codes. For example, the quality of numerical derivatives, which is a function of both the derivation scheme that is used and the quality of the grid on which the model or the eigenfunction is computed. Another highly underestimated error is the finite accuracy with which a stellar evolutionary model satisfies hydrostatic equilibrium. In other words, the intrinsic consistency of thermodynamical quantities used to describe the acoustic structure of the model must be checked. To these two sources of errors, we must add the possible differences stemming from intrinsic methods used to compute the models in various stellar evolutionary codes.

Intrinsic non-linearity is a recurring problem when using the frequency structure relations. In figure 4.3, we illustrate the arguments of the structural integrals from the (ρ,c^2) pair and (A,Y) pair. The ρ and c^2 arguments have very regular patterns naturally more concentrated towards the surface regions due to the higher amplitude of the kernels. Similarly, the amplitude of the Y contribution in the lower right panel is only important in the surface regions. Although smaller than the other contributions, this helium integral is a factor 2 larger than the helium integral from the (ρ,Y) structural pair. As we will see later, this has important implications for the limitations of the linear regime with the (A,Y) kernels. In the lower-left panel of Fig. 4.3, we can see that the A term is much more important in the surface regions, with a small contribution coming from the base of the convective envelope. This means that in practice, this structural pair might well be very sensitive to surface effects. From the numerical point of view, this means

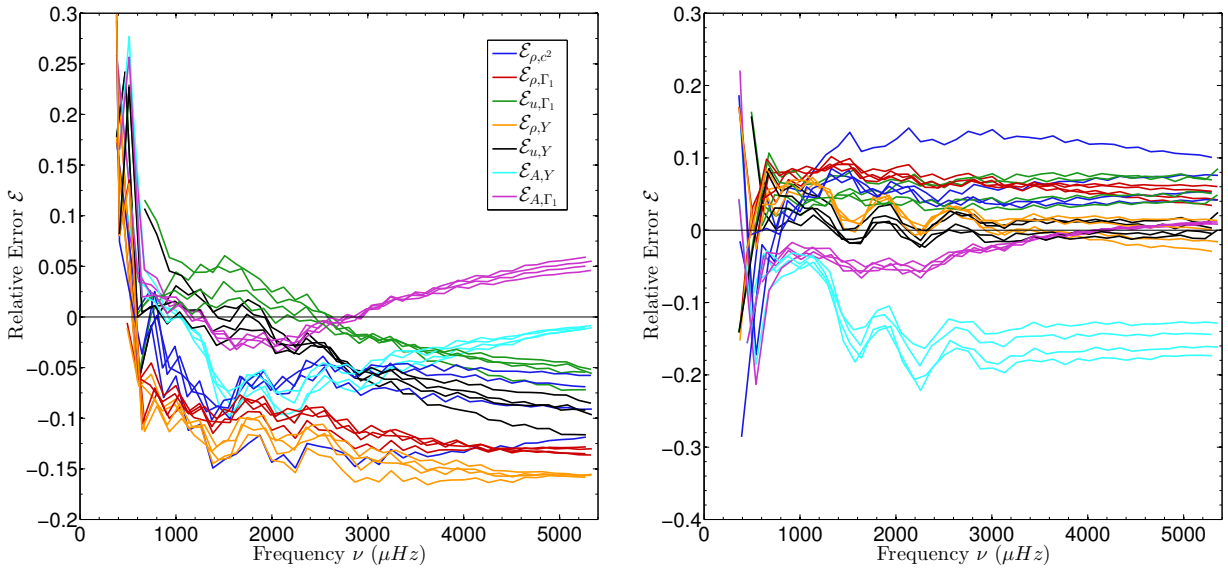

Figure 4.2: Left panel: verification of the linear integral relations between structure and frequencies for target 1 and a model with $\alpha_{MLT} = 1.5$ and $X_0 = 0.69$. Right panel: same as left panel but for a model with $\alpha_{MLT} = 1.9$ and $X_0 = 0.715$. We clearly see that different structural pairs do not satisfy the linear relations to within the same accuracy. Each curve corresponds to a given ℓ of the modes.

that to use the (A,Y) or (A,Γ_1) pair, a very good quality of the grid as well as of the structure equations in the uppermost regions of the model is necessary to avoid important numerical uncertainties. We emphasise here that being able to build the (ρ,c^2) pair to within a good accuracy does not mean that numerical errors remain small when building new kernels from the existing ones. This is particularly true for the (A,Y) and (A,Γ_1) kernels but can also be seen for other pairs.

Another extreme is the case where the perturbation of certain thermodynamic quantities can be considered small and thus within the linear regime while other cannot. In this case, certain linear relations might be valid while others are not. The case can be illustrated with kernels related to helium. Let us take two models, with the same mass, radius, chemical composition and mixing-length parameter. In one of the models, we include microscopic diffusion but not with its full intensity by multiplying the diffusion speeds by a factor D smaller than one (here for example, we chose 0.5). The surface helium abundance has significantly changed. We see a difference in mass fraction of the order of 0.025, in other words, nearly 10%. It is obvious that the changes cannot be considered small and it is then no surprise to see that these models are within the linear regime for the (A,Γ_1) kernels but not the (A,Y) kernels. Again this means that caution is required when changing the structural pair in an inversion process and that usually, the validity of the linear regime can be assessed by using different reference models to carry out the inversion with one structural pair. Ultimately, if the inversion result, let us say, changes significantly with the structural pair that is used, then there is a problem with the inversion process. In the case of the Y kernels, the problem can also arise due to the assumption that the equation of state is known, since it is used to derive the kernels. In these test cases, we always used the same equation of state for both target and reference model, except when it is specifically mentioned as in the other test cases below.

However, even when the equation of state is the same, we noticed that Eq. 4.17 is not always perfectly satisfied. If the same equation is written for the (A,Γ_1) kernels, then the agreement is improved, meaning that some of the errors seen for the (A,Y) kernels can be attributed to the verification of Eq. 4.14. This hypothesis has been tested and we clearly saw a disagreement between the left-hand side and the right-hand side of equation 4.14. This disagreement did not seem to arise from numerical uncertainties but rather from the intrinsic non-linearity of the equation, due for example to shifts in the ionisation zones that were not reproduced by the linear expansion with derivatives of Γ_1. Knowing this, it thus seems perfectly normal to see a stronger non-linear behaviour for the (A,Y) kernels since they have a much higher helium contribution than other kernels. This of course implies limitations on direct helium determinations from kernel inversions and requires further investigation.

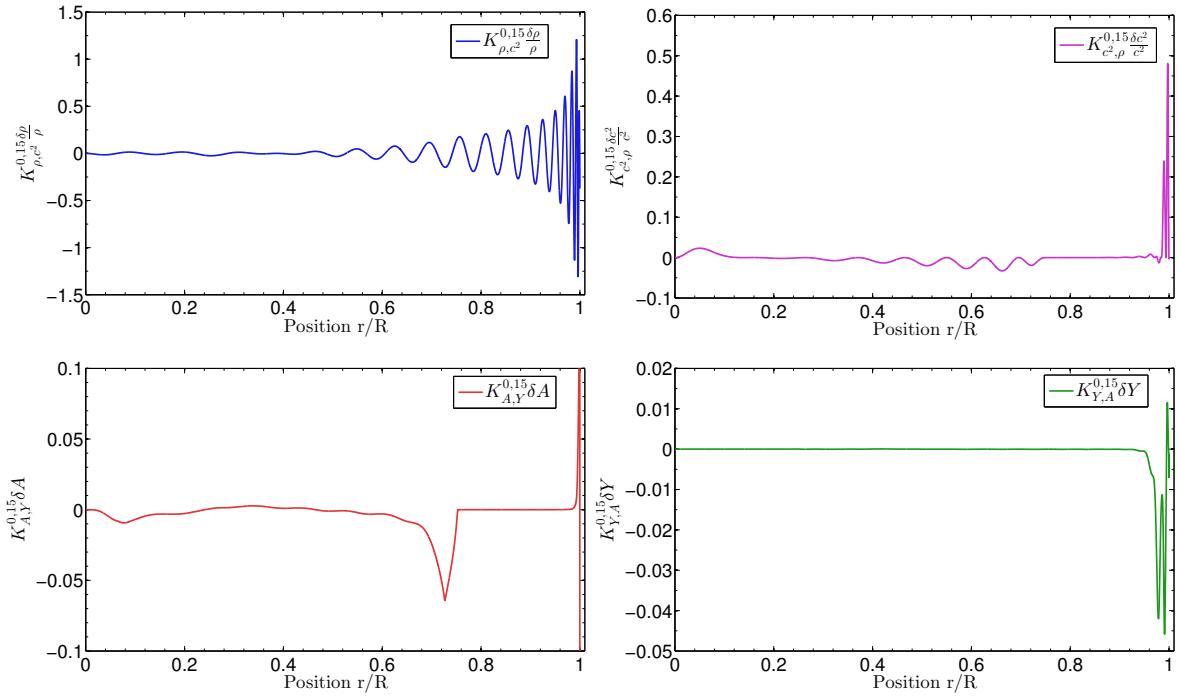

Figure 4.3: Arguments of the integrals of the linear relations between frequency and structure. ρ argument (upper left) and c^2 argument (upper right) from the (ρ,c^2) pair. A argument (lower left) and Y argument (lower right) from the (A,Y) pair. Each curve corresponds to a given ℓ of the modes.

Effects of metallicity

The effect of metallicity are extremely important to quantify since they are often neglected when trying to assess the helium abundance. Using a few models, we review the impact of small changes of metallicity on the verification of the linear relations. This impact is illustrated in figure 4.4. An important point to mention is that in asteroseismic observed cases, the metallicity is calculated through the spectroscopic observations of $[Fe/H]$. One then uses the Sun as a reference but it should be emphasised that there is no agreement to this day on the solar metallicity and that this uncertainty as such has an impact on linear relations, especially when using Y related kernels.

In figure 4.4, we can disentangle the impact of metallicity, since on the left-hand plot, both the target and reference models have the same Z, whereas on the right-hand plot,

we changed the metallicity by 0.002. Of course, since the models do not have the same age, some changes can be seen due to intrinsic differences in the models, but it is still striking to see that the difference in Z can have an impact in some contexts, which is in contradiction with what was previously believed. The case of the high frequency range of the (A,Y) kernel is a very good illustration of how this can be a problem. However, we note that other kernels, such as the (A,Γ_1) pair were affected by the changes in metallicity, but not as much, so the intrinsic differences coming from Z is at least a few per cent. From inspection of the behaviour of the (ρ,Γ_1) pair, we can say that the differences for the (ρ,Y) pair also stem from intrinsic differences and not only from the term in δZ neglected in Eq. 4.14. This means that metallicity can be extremely important for some fitting processes in terms of the validity of the linear structural relations due to the intrinsic differences that can be generated between the target and reference models.

We also plotted in purple the verification of the linear relations for a model with a metallicity change of 0.001. We can see that the errors are divided by approximatively a factor 2. This means that the effect of the metallicity is rather global and goes beyond the neglect of the additional term in Eq. 4.14. This is further confirmed by the impact of the metallicity on the (A,Γ_1) structural pair, where the δZ contribution is not explicitely involved. Figure 4.4 also shows that the (ρ,c^2) kernels are not affected by metallicity changes, as expected, thus leaving their diagnostic potential unaltered.

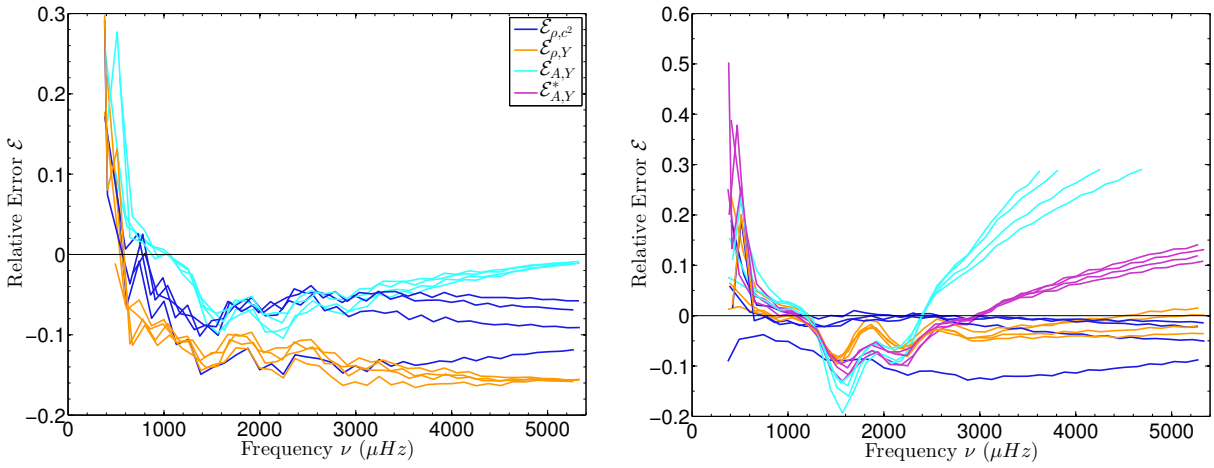

Figure 4.4: Left panel: Verification of the linear integral relation for a reference model which has the same metallicity as target 1. Right panel: effects of a 0.002 shift to the metallicity on the verification of the linear integral relations. The effects of a 0.001 shift to the metallicity for the (A,Y) kernels only is shown in purple and referenced with a $*$. Each curve corresponds to a given ℓ of the modes.

Effects of the equation of state

In figure 4.5, we illustrate the same plot as figure 4.4, but changing the equation of state of the target model to the OPAL equation of state (Rogers and Nayfonov (2002)). The reference models are built with the CEFF equation of state which is used to compute the derivatives of Γ_1 and derive consistent variational expressions. Figure 4.5 thus illustrates the impact that not knowing the equation of state of the target has on the verification of the linear structural relations. While there is some impact, it is not as large as expected.

Of course this does not mean in any case that the equation of state is not important for the linear integral relations used in inversions, but when compared to the impact of

metallicity, it seems that in this case Z has a larger impact. This is not to be generalised but means that we have to be careful with the approximations made and perhaps, in the case of the solar metallicity problem, both the uncertainties on metallicity and the equation of state have to be taken into account. One point worth mentionning about this test case is that both the CEFF and the OPAL equations of state are very similar for solar conditions, so the small impact is a result of similarities between theoretical equations of state and might not be representative of the differences between the true equation of state in the Sun and one of the theoretical ones.

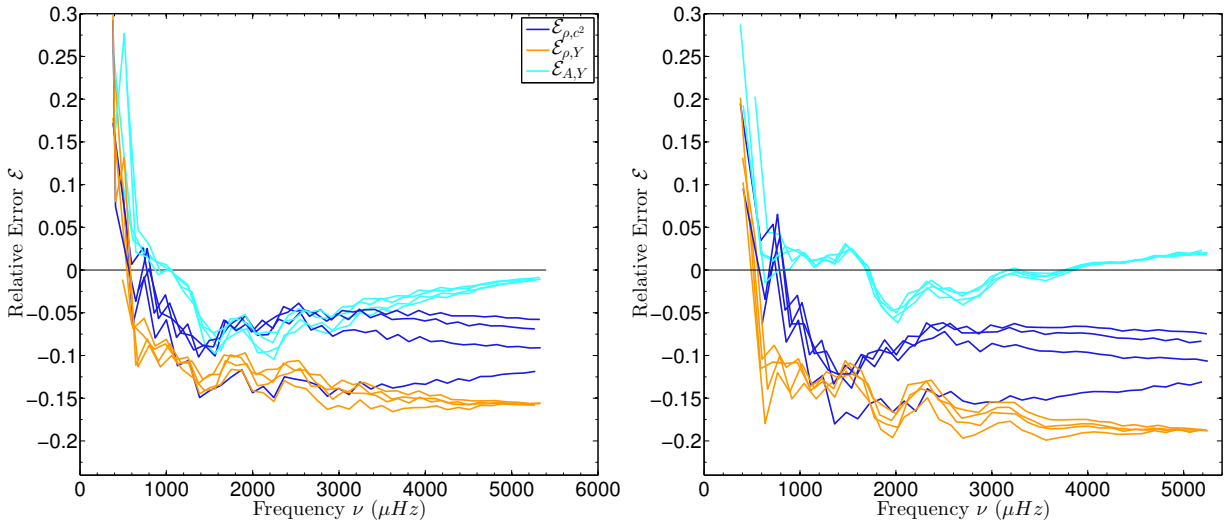

Figure 4.5: Left panel: Verification of the linear integral relation for a reference model which has the same equation of state as target 1. Right panel: effects of a change from the CEFF equation of state on the OPAL equation of state to the verification of the linear integral relations. Each curve corresponds to a given ℓ of the modes.

Effects of abundances and radii inaccuracies

To test the impact of microphysics, we computed the target model with the AGSS09 (Asplund, Grevesse, Sauval, and Scott (2009)) heavy elements mixture and the same metallicity as the reference model, computed with the GN93 abundances (Grevesse and Noels (1993)). Indeed, this changes significantly the thermodynamic quantities inside the star and affects significantly the opacity. As such, this test can be seen as one way to demonstrate that microphysics also has a large impact on the verification of the linear integral relation used to carry out inversions. From the right hand side panel of Fig. 4.6, we can see that all the kernels are affected by the microphysics. The effects are mostly seen for the (ρ, c^2), (ρ, Γ_1) and (ρ, Y) pairs, but the good results of the other pairs are likely due to chance since all profiles have been significantly affected by the modified microphysics. The problem of the radius fit that was discussed in section 4.2.3 is illustrated on the left side panel of figure 4.6. The tendency is clearly seen since introducing progressively an error on the mean density produces an important error on the verification of the linear relations. The problem would be similar if one would consider the mean density to be known within an excellent accuracy but the mass to be unknown. In such case, a small error on the mass introduces an error of the order of R^3 thus an even larger departure from the linear integral relation. The problem is intrinsically due to the adimensional nature of A, meaning that it cannot be scaled to take into account our ignorance of the

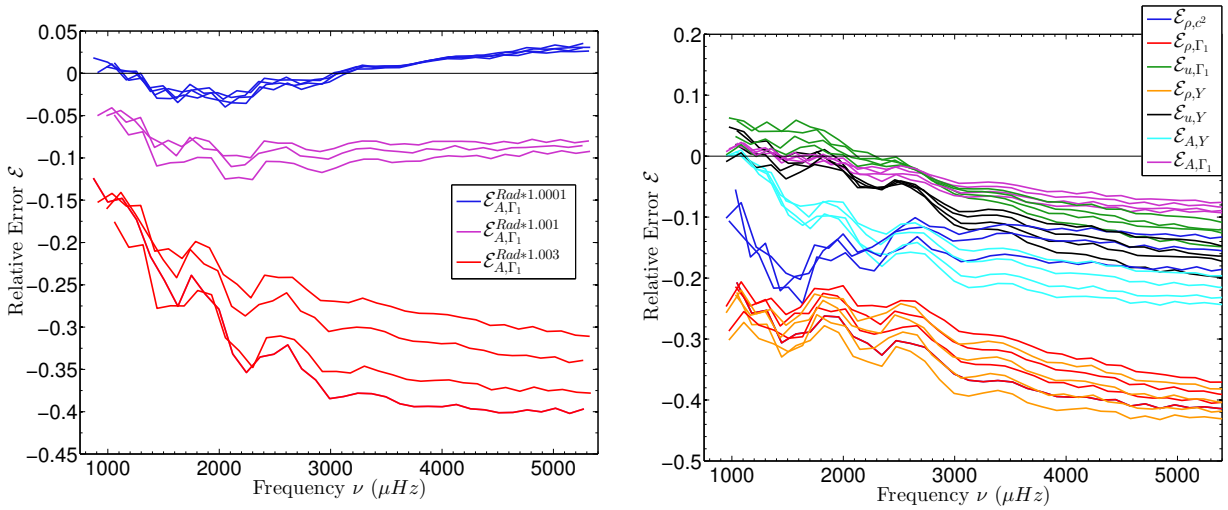

Figure 4.6: Left panel: effect of mismatches in radii between the reference and target models. The relative values of the mismatches are respectively 10^{-4} for the blue dots, 10^3 for the magenta dots and 3×10^{-3} for the red dots. Right panel: effects of changes in the abundances of heavy elements for different structural pairs. Each curve corresponds to a given ℓ of the modes.

mass or radius of the target. Indeed, this effect is not seen for any kernel computed with the direct method if the proper scaling is applied to the structural variables. This leads to intrinsic limitations of the application of the (A,Γ_1) and (A,Y) kernels in asteroseismology. The problem may not be solved in this case by changing the fitting method since fitting seismic constraints may not always ensure a good fit of the radius of the observed target. Ultimately, these kernels are only limited to the very best asteroseismic targets for which excellent interferometric measures of the radii are available.

Effects of extra-mixing

The extra-mixing term is very common in stellar physics. It is used to introduce additional hydrodynamical processes not taken into account in standard stellar models. The problem of lithium abundances is a good illustration that some extra-mixing is actually taking place in real stars. Thus, it seems perfectly normal to ask the question whether the non-inclusion of additional mixing processes could affect the verification of linear integral relation between frequencies and structural quantities. The answer to this question is illustrated in Fig. 4.7. To carry out this test case, we used target model 4 which includes turbulent diffusion in addition to microscopic diffusion. To test the robustness of the linear relations, we used reference models for which turbulent diffusion had been inhibited. For example, in the left panel of Fig. 4.7, the reference model had a slightly higher helium of 0.005 abundance and a less efficient turbulent diffusion. The verification of the linear relations is still good, but it seems that the (A,Γ_1) and the (ρ,Γ_1) structural pairs are strongly affected by the neglect of extra-mixing. This statement is confirmed when looking at the right panel of Fig. 4.7 for which the reference model has a nearly constant extra-mixing throughout all layers of the model. The (ρ,c^2) and (u,Γ_1) kernels seem not to be too much affected by extra-mixing. In general, the impact of extra-mixing is much reduced for the models we tested here. This statement, of course, only applies for physical conditions similar to solar and for the fitting process we use in these numerical tests. This does not mean that the problem could not reappear for models with convective cores,

for which extra mixing could change significantly the evolutionary path and the acoustic structure.

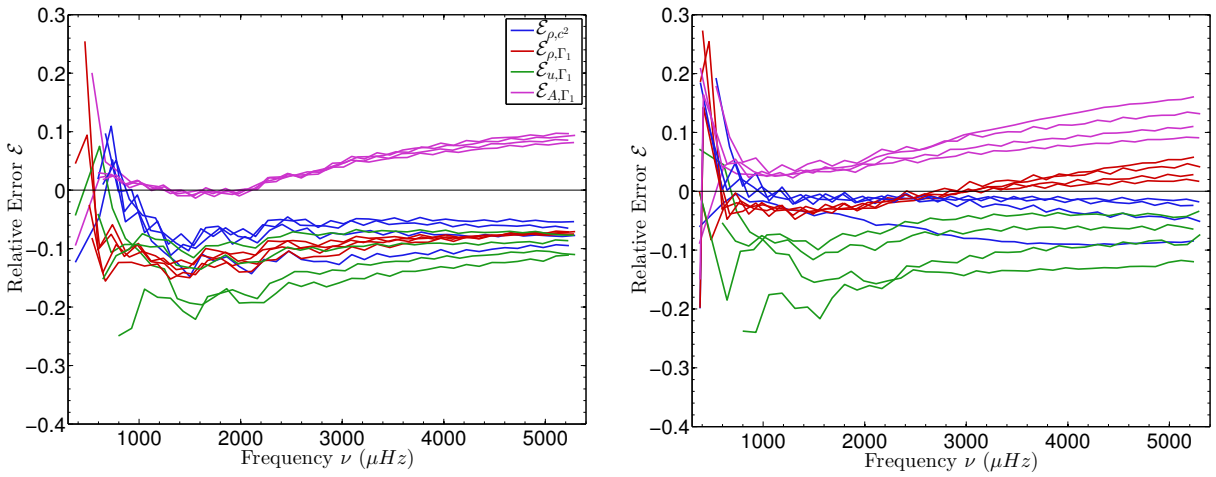

Figure 4.7: Effect of extra mixing on the verification of linear structural relations for both models. The left panel is associated with a model with a slightly inhibited extra-mixing intensity, whereas the right panel has a nearly constant extra-mixing throughout the model layers, but with an even smaller intensity. Each curve corresponds to a given ℓ of the modes.

4.2.5 Conclusion

In this section, we analysed the verification of the linear integral relations between frequency and structural quantities frequently used in helioseismology for various structural pairs. In Sect. 4.2.3 and Sect. 4.2.3, we presented the two methods to change the structural variables in the linear integral relations. The direct method we present in this section has the advantage of being more general than the method of conjugated functions, which explicitly uses the same radius for the observed target and the reference model. Although this is implied in the direct method, it is not used as a pre-requisite in the derivation of the equations leading to the kernels. Moreover, it has been shown that it is possible circumvent the problem by re-scaling the information provided by the inversion (see Buldgen, D. R. Reese, and M. A. Dupret (2015) or Basu (2003) for a discussion of this problem). In that sense, the method we propose offers a good alternative that is applicable in the asteroseismic case. However, we have also shown that the method we propose leads to somewhat complicated coefficients which can be difficult to derive if the numerical quality of the model is not ensured.

Furthermore, in Sect. 4.2.3, we showed how the conjugated functions approach could be used to derive (A,Y) kernels. These kernels have the particularity of showing a very high sensitivity to the chemical composition since they are the only structural kernels for which the helium kernels have a higher amplitude than those associated with the secondary variable of the structural pair. This property is extremely important in the context of structural inversions since the amplitude of helium kernels was the main motivation behind their use as a cross-term in helioseismology but also their main handicap for direct kernel-based inferences of the helium profile using classical inversion techniques such as the SOLA or the RLS method. However, by no means would these inversions be independent of the equation of state since it is introduced in the very equations leading

to the (A,Y) kernels.

In Sect. 4.2.4, we presented various experiments showing the intrinsic limitations in the linear regime of structural pairs. These limitations can be due to numerical inaccuracies or to the intrinsic non-linear behaviour of different variables. The most striking example is that of helium, for which extra-mixing can change significantly the local abundance while hardly changing the sound speed or density profile. In that sense, the numerical experiments we presented, although intrinsically limited, show that changing the structural pair in the integral relations is not often innocent, especially at the verge of non-linearity[8].

In addition, we analysed the importance of various structural changes, such as the impact of metallicity changes. We showed that small changes of metallicity could affect significantly the linear structural relations, especially for the (A,Y) structural pair. However, we stress here that the linear behaviour of the integral relations is strongly dependent on the fitting process. This emphasises again that in the asteroseismic case, all information available should be used to ensure the verification of the linear structural relations.

In addition to the effect of metallicity, we also analysed the impact of the equation of state on the integral relations. Surprisingly, we find them to be less important than previously stated and even less important in some cases than the metallicity effects on the verification of the linear relations. This could have an impact on the potential of inversion techniques in the solar case. Changing the equation of state has little impact, and may be the result of a bias from the fitting process we used or it may be due to the similarity under solar conditions of most equations of state.

We also analysed the importance of radius constraints and constraints on the microphysics by changing the heavy elements mixture. The test case on the radius inaccuracies shows the importance of this additional constraint for kernels derived with the method of conjugated functions, whereas the kernels derived with the direct method are found to be more robust if the proper scaling is applied when analysing the inversion results. However, we also emphasise that adimensional variables, like A or Y, cannot be rescaled. The test case on the heavy elements mixture showed the important sensitivity to microphysics in stellar models. As such, the reference and target models were quite different and it is not surprising that linear structural relations are strongly affected. However, from our experience in seismic modelling, we know that these differences can be reduced by introducing additional constraints. Ultimately, models with different abundances can be very similar in terms of thermodynamical quantities due to compensations.

Finally, we also analysed the importance of additional mixing acting during the evolution of the target model. We found that for solar conditions, additional extra-mixing processes could change slightly the verification of the linear relations, but that these changes were not as significant as those obtained from inaccuracies in metallicity, for example. We stress that this analysis should be extended to other parts of the HR diagram, where extra-mixing can have a more significant impact on the acoustic structure of stellar models, and thus on the verification of the linear relations between frequencies and structure.

To conclude, the advent of the space photometry era and the quality of data provided by past and upcoming space missions will allow us to use new seismic approaches to extract efficiently seismic information. However, it is still important to provide a theoretical framework for these methods, to test their limitations and to determine what additional information (spectroscopic, interferometric, ...) or methodological improvement are necessary to enable the use of seismic inversions in asteroseismology. As such, this study only gives answers to limited theoretical questions and is only one step towards the improvement of our use of seismic information.

[8]Which may well be the case in the context of asteroseismic inversions.

4.2.6 Appendix: Convective parameter kernels from the direct method

As stated in the core of this section, kernels for the structural pair (A,Y) or (A,Γ_1) can be also obtained from the direct method. We give a few steps in the derivation of the third order differential equation that leads to these kernels and discuss a few problems regarding its numerical resolution. The first step is to introduce the helium and A perturbations in the linear integral equation.

$$\begin{aligned}\int_0^R K^{n,\ell}_{\rho,Y}\frac{\delta\rho}{\rho}dr+\int_0^R K^{n,\ell}_{Y,\rho}\delta Y dr &= \int_0^R K^{n,\ell}_{A,Y}\delta A dr+\int_0^R K^{n,\ell}_{Y,A}\delta Y dr\\ &=\int_0^R K^{n,\ell}_{A,Y}\left[r\frac{d}{dr}\left(\frac{\delta\rho}{\rho}\right)+\frac{Gm}{rc^2}\frac{\delta m}{m}\right.\\ &\quad -\frac{Gm}{rc^2}\left(\frac{\partial\ln\Gamma_1}{\partial\ln\rho}|_{P,Y}-1\right)\frac{\delta\rho}{\rho}\\ &\quad \left.-\frac{Gm}{rc^2}\left(\frac{\partial\ln\Gamma_1}{\partial\ln P}|_{\rho,Y}+1\right)\frac{\delta P}{P}\right]dr\\ &\quad +\int_0^R\left[K^{n,\ell}_{Y,A}-K^{n,\ell}_{A,Y}\frac{Gm}{rc^2}\frac{\partial\ln\Gamma_1}{\partial Y}|_{\rho,P}\right]\delta Y dr. \end{aligned} \tag{4.45}$$

Then, we have to use the definition of hydrostatic pressure and mass and permute the integrals. We can already notice that the term with the derivative of density will be problematic and will require an integration by parts.

$$\begin{aligned}&\left[K^{n,\ell}_{A,Y}r\frac{\delta\rho}{\rho}\right]_0^R-\int_0^R\frac{d(rK^{n,\ell}_{A,Y})}{dr}\frac{\delta\rho}{\rho}dr\\ &+\int_0^R 4\pi r^2\rho\left[\int_r^R\frac{GK^{n,\ell}_{A,Y}}{\bar{r}c^2}d\bar{r}\right]\frac{\delta\rho}{\rho}dr\\ &-\int_0^R\frac{Gm\rho}{r^2}\left[\int_0^r K^{n,\ell}_{A,Y}\frac{Gm}{\bar{r}c^2}\left[\frac{\partial\ln\Gamma_1}{\partial\ln P}|_{\rho,Y}+1\right]d\bar{r}\right]\frac{\delta\rho}{\rho}dr\\ &-\int_0^R 4\pi r^2\rho\left[\int_r^R\frac{G\rho}{\bar{r}^2}\left(\int_0^{\bar{r}}\frac{GK^{n,\ell}_{A,Y}}{\tilde{r}c^2P}\left(\frac{\partial\ln\Gamma_1}{\partial\ln P}|_{\rho,Y}+1\right)d\tilde{r}\right)d\bar{r}\right]\frac{\delta\rho}{\rho}dr\\ &-\int_0^R K^{n,\ell}_{A,Y}\frac{Gm}{rc^2}\left[\frac{\ln\Gamma_1}{\ln\rho}|_{P,Y}-1\right]\frac{\delta\rho}{\rho}dr=\int_0^R K^{n,\ell}_{\rho,Y}\frac{\delta\rho}{\rho}dr.\end{aligned} \tag{4.46}$$

The first term of this equation is exactly zero for $r=0$. However, it is not for $r=R$ and it is a strong hypothesis to consider that the surface relative density differences are exactly zero. Nevertheless, it is the only way to obtain an equation for the (A,Y) kernels with the direct method. The problem is exactly the same for the (N^2,c^2) kernels which can be easily derived but will also face the same problem due to the density derivative. Moreover, one could argue that the contribution of the surface term is negligible when compared to the integrals and that this term has no impact on the final result of the kernels[9]. This simplification could also be seen as a boundary condition, stating that the kernels we are searching for have to be exactly 0 at the surface boundary. Ultimately, after a few additional algebraic operations, we obtain a third order differential equation that we write

[9]This could be done by analysing how accurate Eq. 4.46 is without the additional term.

here as a function of $\mathscr{K} = \frac{K^{n,\ell}_{A,Y}}{r^2\rho}$ and $\mathscr{K}' = \frac{K^{n,\ell}_{\rho,Y}}{r^2\rho}$.

$$
\begin{aligned}
&-\frac{r^6}{m}\frac{d^3\mathscr{K}}{dr^3}+\left[\frac{4\pi r^8\rho}{m^2}-\frac{10r^5}{m}-\frac{r^6}{m}\frac{d\ln\rho}{dr}-\frac{r^5A_1}{m}\right]\frac{d^2\mathscr{K}}{dr^2}\\
&-\left[\frac{20r^4}{m}-\frac{16\pi r^7\rho}{m^2}+\frac{2r^6}{m}\frac{d^2\ln\rho}{dr^2}+2\frac{r^5}{m}\frac{dA_1}{dr}+\frac{7r^5}{m}\frac{d\ln\rho}{dr}\right.\\
&\left.-\frac{4\pi r^8\rho}{m^2}+\frac{5r^4A_1}{m}-\frac{4\pi r^7\rho A_1}{m^2}-\frac{4\pi r^6\rho}{c^2m}\right]\frac{d\mathscr{K}}{dr}\\
&-\left[\left[\frac{5r^4}{m}-\frac{4\pi r^7\rho}{m^2}\right]\left[\frac{d\ln\rho}{dr}+\frac{dA_1}{dr}\right]+4GA_2\right.\\
&+\frac{r^5}{m}\frac{d^2A_1}{dr^2}+\frac{r^6}{m}\frac{d^3\ln\rho}{dr^3}+\frac{16\pi^2r^8\rho^2}{c^2m^2}+\frac{8\pi r^6\rho}{c^3m}\frac{dc}{dr}\\
&\left.-\frac{4\pi r^6}{c^2m}\frac{d\rho}{dr}+\frac{24\pi r^5\rho}{c^2m}+\left[\frac{7r^5}{m}-\frac{4\pi r^8\rho}{m^2}\right]\frac{d^2\ln\rho}{dr^2}\right]\mathscr{K}\\
&=\frac{r^5}{m}\frac{d^2\mathscr{K}'}{dr^2}+\left[\frac{5r^4}{m}-\frac{4\pi r^7\rho}{m}\right]\frac{d\mathscr{K}'}{dr},
\end{aligned}
\tag{4.47}
$$

with the following additional definitions:

$$A_1 = \frac{Gm}{rc^2}\left[\frac{\partial\ln\Gamma_1}{\partial\ln\rho}|_{P,Y}-1\right] \tag{4.48}$$

$$A_2 = \frac{Gm\rho r}{c^2P}\left[\frac{\partial\ln\Gamma_1}{\partial\ln P}|_{\rho,Y}+1\right] \tag{4.49}$$

Now the central boundary conditions are found using additional transformations. Typically, we solve the equation using r^2 as the independent variable for radial position. Taking the limit of the differential equation when r^2 goes to 0 and simplifying leads to simple central boundary conditions. Surface conditions are found by stating that Eq. 4.46 has to be satisfied and that the kernels must be 0 at the surface. One must also take care of the discontinuous coefficients, meaning that, again, the system must be solved in the radiative and convective regions independently and reconnected using proper continuity conditions. We face the same problem as for the (u,Y) or (u,Γ_1) kernels but can use the same algebraic manipulation to solve the system. Ultimately, we have to solve three discretised equations on two different domains (six systems in total) and reconnect those solutions. Now in addition to the numerical cost of such manipulations, we can see in Eq. 4.47 third derivatives of the density and second derivatives of the A_1 function. From numerical experiments not presented here, we have seen that these coefficients contain numerical noise due to the quality of the reference model. The noise can be reduced by increasing the quality of the model and of the finite difference scheme, but smoothing is still necessary to a certain extent. The concern with the smoothing process is that it could in some pathological cases change significantly the form of the kernels. In conclusion, despite the applicability of the method to the (A,Y) kernels and the fact that it uses different hypotheses to obtain structural kernels, we state that for the (A,Y) kernels, the direct method is not well suited in large scale automated studies. Moreover, due to the intrinsic problems of inversions with the adimensional variables mentioned before and the difficulties in determining accurate radii, the (A,Y) pair might well be restricted to solar inversions for which the conjugated functions method is perfectly valid and should be preferred since it leads to simpler equations.

4.3 General Conclusion

The developments presented in this chapter are crucial for both helio- and asteroseismology. As we will see in the next chapter, as well as in Part III of this thesis, they are necessary to fully exploit the capabilities of in depth astero- and helioseismic investigations. This chapter only gave a hint of the technical aspects of the methods and of the difficulties linked to its implementation. The development of inversion techniques for more evolved targets will likely require further improvements of the numerical techniques used in InversionKit for the kernel calculations. Also, investigations into more efficient kernel formulations for g-modes should be carried out to extend the applicability domain of asteroseismic inversions.

In practice, gravity modes have already been used in Takata and Montgomery (2002) for a white dwarf, implying that such inversions are achievable. However, it should be noted that a localised inversion will likely be difficult since it required 116 individual frequencies to achieve a full profile inversion in the hare-and-hounds exercises in Takata and Montgomery (2002). Moreover, they did not consider uncertainties in the fundamental parameters of the target, which would have dominated the inversion of the convective parameter.

In conclusion, while the methods presented here are very general, a full assessment of the linearity domain of g-modes should be done. This is crucial to determine whether the variational formulation can be used in its linear form with the current observational constraints or whether non-linear approaches should be favoured. In that sense, it appears that the method of Roxburgh and Vorontsov (I. W. Roxburgh (2010)) would intrinsically be more robust, although it could be up against convergence problems and lead to multiple solutions (I. W. Roxburgh (2015b)).

5. INVERSIONS OF INTEGRATED QUANTITIES

5.1 General introduction

The following sections encompass the papers related to the development of inversion techniques of integrated quantities in the context of asteroseismology. The motivation behind the derivation of such indicators was to attempt to improve the use of the seismic information contained in Kepler and CoRoT data. Indeed, despite the quality of the data, it appeared that the number of individual frequencies and the absence of high degree modes made full structural profile inversions impossible with the classical, linear methods applied in helioseismology, with the exception of a few corrections in u for the very best asteroseismic targets.

Initially, the goal of these developments was to determine the mass of a star using seismic inversion techniques. It quickly became clear that the mass could not be determined by inversions but that the mean density could be obtained by such methods. These initial developments led to the paper of D. R. Reese, Marques, et al. (2012) and laid the foundations of the studies presented here. The first objective of the inversion of integrated quantities is to provide an additional selection process to models built using a forward modelling approach, thus improving the constraints on their internal structure. A very important aspect of this selection process is that the inversion of indicators focusses very efficiently all the information on one particular aspect of the profile of a given quantity, while corrections obtained using Gaussian targets might sometimes simply show that the target and the model agree, simply because the target function of the inversion is suboptimal.

Besides providing these additional constraints to stellar models, inversions of integrated quantities also raise the question of the independent amount of information provided by seismic observations. Indeed, the first physical quantity determining the frequency values is the mean density. In addition to this trend, glitches can be used to analyse potential sharp transitions in the stellar structure and some independent information is also present in the frequency ratios, such as the r_{02} or the r_{01}, which are often used as constraints in forward modelling techniques.

However, there is no current way to properly assess the exact amount of independent information that can be derived using asteroseismology. In a way, indicator inversions can give us some basis to start studying this problem since redundancy between indicators and degeneracies in the way each quantity behaves when changes are applied to the models can point towards the limitations of the seismic data provided by the space photometry missions. Knowing these limitations is crucial, first of of all, to overcome them, but also to avoid overestimating the capabilities of stellar seismology which in a long term perspective, would be harmful for the field.

In section 5.2, we present the results of inversions of the first indicators developed during this thesis, namely the acoustic radius, denoted τ, an evolutionary stage indicator, denoted t and further tests of mean density inversions. These results were published in Astronomy and Astrophysics under the reference Buldgen, D. R. Reese, M. A. Dupret, and Samadi (2015). Tests were carried out to determine the robustness of the inversions towards modelling mismatches and surface effects such as non-adiabatic effects in the frequency values of the target or the impact of turbulent pressure in the upper convective envelope. While these inversions are successful and seem to indicate some robustness of the method, it does not mean that further investigations should not be carried out. Indeed, additional studies using patched models with three-dimensional atmospheres have shown that surface effects can, as expected, strongly affect the inversion results.

Section 5.3 presents the development and hare-and-hounds exercises associated with an indicator of internal mixing processes, chemical composition and consequently evolutionary stage, denoted t_u, which have been published in Astronomy and Astrophysics under the reference Buldgen, D. R. Reese, and M. A. Dupret (2015). This indicator was the first fully custom-made seismic indicator for which the derivation of the kernels and the building of the target function were motivated by structural considerations. The main goal was to provide an alternative to the t indicator, which could be determined only for low-mass young main-sequence stars without a convective core. The t_u indicator was proven to be very efficient at determining mismatches in chemical composition and mixing that would lead to changes in the deep regions. Hare-and-hounds exercises have shown that fitting the frequency ratios defined in I. W. Roxburgh and S. V. Vorontsov (2003) allowed for a better agreement with t_u but that the inverted indicator would be slightly more sensitive to structural differences between target and model in some cases.

In section 5.4, we present the results associated with indicators specialised in analysing convective regions of stellar structure. Both indicators showed promising results in hare-and-hounds exercises and could potentially be applied to all Kepler LEGACY targets. The main limitations of this method are the validity of the linear approximation for more massive models and the impact of surface effects on the determination of these indicators. These developments are described in an article currently submitted to Astronomy and Astrophysics.

5.2 Stellar acoustic radii, mean densities, and ages from seismic inversion techniques

5.2.1 Introduction

Determining stellar global characteristics such as mass, radius, or age as accurately as possible is crucial for understanding stellar evolution, determining properties of exoplanetary systems, or characterising stellar populations in the galaxy. Although these quantities can be estimated using classical observations, such as photometry and spectroscopy, or in special cases such as binary systems, significant progress has only been made in recent

years with the advent of high-precision asteroseismology missions, namely CoRoT and Kepler. Indeed, these missions are providing a wealth of data of unprecedented quality for large numbers of stars. Hence, it is crucial to develop techniques that are able to determine global stellar parameters from pulsation data as accurately as possible and with the least computational effort (see Chaplin and Miglio (2013) for a review on this topic).

Estimating stellar ages is the most problematic case since there is no direct observational method to measure this quantity. Therefore, it has to be estimated by relating the evolutionary stage empirically to some phenomena like rotation, activity, lithium depletion, or by using model-dependent methods like isochrone placements (see Soderblom (2010) for an extensive review of age determination methods). Currently, the most promising method to determine stellar ages is carrying out asteroseismic modelling of stars. These ages are estimated to be $\sim 10\%$ accurate in the best cases (Soderblom (2010)).

Many of the techniques used for exploiting stellar pulsation data are variants of grid or parameter search methods. On one end of the spectrum, there are simple methods that estimate global stellar parameters, such as the mass and radius, through empirical scaling relations based on seismic indicators such as the large frequency separation and frequency at maximum power. Search methods using a dense grid of models, calculated once and for all, can also be used to find optimal models for a whole set of observed stars. However, it is clear that this method can only handle a limited number of free parameters when describing the models. On the other end of the spectrum, there are sophisticated search methods such as genetic algorithms (Charpinet et al. (2008), Metcalfe, Monteiro, et al. (2010)) or MCMC methods (Bazot, Bourguignon, and Christensen-Dalsgaard (2012)) that are able to deal with much larger multi-dimensional parameter spaces thanks to an optimised search strategy. These methods will typically calculate stellar models as needed, which make them considerably slower than scaling relations or simple grid search methods, thereby limiting the number of observed stars that can be treated this way. A common point in these search methods is their reliance on stellar models, which unfortunately do not fully represent the physical complexity of the phenomena taking place in stars. Hence, these inaccuracies can lead to biases in the results and to persistent differences between the model and observed frequencies. Therefore, there is currently a need for less model-dependent methods that are applicable to a large number of stars, and are able to characterise, as accurately as possible, the global parameters and evolutionary stage of a star.

In this context, seismic inversion techniques become particularly interesting since they are able to invert the differences between observed and theoretical frequencies and translate them into appropriate structural corrections on the models. In that sense, these techniques overcome the limitations imposed by the set of physical ingredients used for the construction of the models. Therefore, they allow us to obtain more detailed information on the stellar structure as well as insights into new physical phenomena that need to be included in the models. For instance, helioseismic inversions have provided detailed solar rotation profiles, which were different from theoretical predictions, and have shown that the solution to the lacking solar neutrino problem should come from improving neutrino physics rather than revising the solar structure. In contrast to the solar case, asteroseismic space missions cannot resolve the objects they observe and hence are limited to low-degree modes. As a result, it is difficult to obtain reliable inversions of full structural profiles for stars other than the Sun. A useful alternative is to invert for global

stellar properties. Recently, D. R. Reese, Marques, et al. (2012) showed how this could be done for the mean density of a star. This approach represents an important step of progress compared to using typical seismic indices for two reasons. Firstly, it can provide custom-made global quantities that are directly related to the stellar structure rather than to the pulsation spectra of the stars. Secondly, the associated averaging kernels that are obtained as a by-product give useful indications on the accuracy of the result.

In the current section, we wish to extend this approach to other stellar quantities, namely the acoustic radius and an age indicator based on the integral of the sound speed derivative. These characteristics are not chosen fortuitously. Indeed, they allow us to compare our inversion results with those obtained by current asteroseismic proxies, the large frequency separation, and the small frequency separation (Vandakurov (1967), Tassoul (1980)). The outline of the section will be as follows. We will define our general approach to the specific inverse problem of global characteristics in Sect. 5.2.2. Section 5.2.3 will show how this methodology applies to the acoustic radius and age indicator. Sections 5.2.4 and 5.2.5 will present inversion results for different tests cases. In Sect. 5.2.4, we use the model grid of D. R. Reese, Marques, et al. (2012), chosen without any optimisation process[1], to carry out a first series of tests and conclude that an optimization process is necessary to choose the appropriate reference model for each inversion. We present this type of method in Sect. 5.2.5 and test it in different cases that include: changes to the metallicity, modifications to the mixing length parameter, non-adiabatic effects in the frequencies, and the effects of turbulent pressure. These test cases are chosen to illustrate current limitations and uncertainties in stellar modelling i.e. the uncertainties in the convection treatment, here mimicked by a mixing-length coefficient mismatch; the uncertainties in chemical composition, mimicked by a metallicity changes; the intrinsic non-adiabaticity of stellar oscillations and the unknown surface effects such as turbulent pressure. Each test case is carried out separately to isolate any effects that the inversion could not correct. We show that using inversion techniques on a appropriate reference model can improve the accuracy with which global stellar characteristics are determined in that it provides accurate results in all these cases. Section 5.2.6 summarises our results and discusses the strengths and weaknesses of the method.

5.2.2 General approach

Inverse problems and ways of solving them

As stated in the introduction, we seek to establish a new framework for linear inversion techniques that allows us to determine stellar global characteristics. As for any inversion carried out, our method needs a reference model, an observed star and their respective oscillation frequencies. The reference model has to be close enough to the observational target so that the relation between their relative frequency differences and their structure differences can be deduced from the variational principle. This leads to the following typical linear form:

$$\frac{\delta\nu_{n,\ell}}{\nu_{n,\ell}} = \int_0^1 K^{n,\ell}_{s_1,s_2}\frac{\delta s_1}{s_1}dx + \int_0^1 K^{n,\ell}_{s_2,s_1}\frac{\delta s_2}{s_2}dx + \frac{\mathcal{G}(\nu)}{Q_{n,\ell}}, \tag{5.1}$$

where s_1 and s_2 are structural variables like ρ_0, Γ_1, c^2, $u_0 = P_0/\rho_0$, etc. As we will see in the next section, choosing the right couple of variables for the right inversion is not always straightforward. The function $\mathcal{G}(\nu)$ is an ad-hoc correction for the surface term

[1]See D. R. Reese, Marques, et al. (2012) Section 6 for further details on this particular point

assumed to be a slowly varying function depending only on the frequency. It is usually expressed as a sum of Legendre polynomials and normalised by the factor $Q_{n,\ell}$, which is the mode inertia normalised by the inertia of a radial mode interpolated to the same frequency (Christensen-Dalsgaard (1986)). The functions $K^{n,\ell}_{s_i,s_j}$ are the inversion kernels, derived from the reference model and its eigenmodes (D. O. Gough and Thompson (1991)). The behaviour of the kernels is critical to ensure a successful linear inversion, especially when working with asteroseismic targets where the number of frequencies is rather small compared to helioseismic inversions.

The symbol $\delta s/s$ denotes the relative difference between the value of s for the reference model and the target at a given $x = \frac{r}{R}$. We use the classical definition of the relative differences between target and model:

$$\frac{\delta s}{s} = \frac{s_{\rm obs} - s_{\rm ref}}{s_{\rm ref}}. \tag{5.2}$$

Other definitions were sometimes used in the past for helioseismic inversions (see Antia and Basu (1994b)), but these definitions were not used in this study.

It is well known that the inversion problem is ill-posed and that the quality of the inversion (in terms of accuracy but also of reliability) depends critically on the quantity and the accuracy of available data. Therefore, in the asteroseismic context, inversions of structural profiles such as the density, the sound speed, or even the helium abundances are out of reach for linear inversion techniques. However, we can still compromise and search for global quantities.

The Substractive Optimally Localised Averages (SOLA) inversion method (Pijpers and Thompson (1994)) naturally lends itself to obtaining global quantities. When using SOLA, we build a linear combination of the inversion kernels that matches a pre-defined target. In other words, we wish to determine the values of the coefficients of the linear combination of frequency differences that will give us information about one global characteristic of the observed target. Using Eq. (5.1), we can define a target $\mathscr{T}$, which can be any function of $x = \frac{r}{R}$. For example, let us assume we wish to determine the value of a global characteristic A_{obs} the relative perturbation of which is defined by

$$\frac{\delta A_{\rm obs}}{A} = \int_0^1 \mathscr{T}(x)\frac{\delta s_1}{s_1}dx + \int_0^1 \mathscr{T}_{\rm cross}(x)\frac{\delta s_2}{s_2}dx. \tag{5.3}$$

Assuming that Eq. (5.1) is satisfied for our model and our target, we wish to build the linear combination of frequency differences such that

$$\begin{aligned}\sum_i c_i \frac{\delta \nu_i}{\nu_i} &= \int_0^1 \mathscr{T}(x)\frac{\delta s_1}{s_1}dx + \int_0^1 \mathscr{T}_{\rm cross}(x)\frac{\delta s_2}{s_2}dx \\ &= \frac{\delta A_{\rm obs}}{A}.\end{aligned} \tag{5.4}$$

This is of course an ideal scenario. For real inversions, the result is more likely to be an estimate $\delta A_{\rm inv}/A$, which is expressed as follows:

$$\frac{\delta A_{\rm inv}}{A} = \int_0^1 K_{avg}(x)\frac{\delta s_1}{s_1}dx + \int_0^1 K_{\rm cross}(x)\frac{\delta s_2}{s_2}dx + \sum_i c_i \frac{\mathscr{G}(\nu_i)}{Q_i}. \tag{5.5}$$

The functions $K_{\mathrm{avg}}(x)$ and $K_{\mathrm{cross}}(x)$ are the so-called averaging and cross-term kernels and the third term accounts for surface effects. The averaging and cross-term kernels are directly related to the structural kernels of Eq. (5.1) by the inversion coefficients

$$K_{\mathrm{avg}}(x) = \sum_i c_i K^i_{s_1,s_2}(x), \tag{5.6}$$

$$K_{\mathrm{cross}}(x) = \sum_i c_i K^i_{s_2,s_1}(x). \tag{5.7}$$

Thus, in order for the inversion to be accurate, these kernels need to be as close as possible to their respective target functions. One should note that the cross-term kernel will always be present in an inversion result, as a direct consequence of Eq. (5.1). If A is only related to s_1, the function $\mathscr{T}_{\mathrm{cross}}$ is simply 0. In this particular case, the contribution of the integral of s_2 in Eq. (5.1) has to be eliminated. When using the SOLA method, we build a cost function (see Backus and Gilbert (1967) for the original definition of the OLA cost function and its analysis in the context of geophysics)

$$\begin{aligned}\mathscr{J}_{\mathrm{A}} = &\int_0^1 \left[K_{\mathrm{avg}}(x) - \mathscr{T}(x)\right]^2 dx + \beta \int_0^1 \left[K_{\mathrm{cross}}(x) - \mathscr{T}_{\mathrm{cross}}(x)\right]^2 dx + \tan(\theta) \sum_i (c_i \sigma_i)^2 \\ &+ \lambda \left[\sum_i c_i - f\right] + \sum_{m=1}^{M_{\mathrm{surf}}} a_m \sum_i c_i \frac{\psi_m(\nu_i)}{Q_i}.\end{aligned} \tag{5.8}$$

There can be three to five terms in the cost function, depending on whether or not a supplementary constraint and/or surface corrections are included. The first two terms are responsible for making the averaging and the cross-term kernels match their respective targets $\mathscr{T}$ and $\mathscr{T}_{\mathrm{cross}}$. The third term of the cost function defines the trade-off between reducing the measurement error bars on the result and improving the match to the target functions. One usually talks of the magnification of the measurement errors. The fourth term is a supplementary constraint on the inversion, usually a unimodularity constraint in the classical SOLA approach. In the following section, we will follow the prescriptions of D. R. Reese, Marques, et al. (2012) and use a constraint on the sum of the inversion coefficients. The parameters β and θ are trade-off parameters that regulate the balance between different terms in the inversion, and λ is a Lagrange multiplier. Since the parameters β and θ are free, one can adjust them to modify the results of the inversion, but great care has to be taken since they can lead to non-physical results. Finally, the fifth term corrects surface effects in the inversion.

Because of the form of Eq. (5.5), one has to be careful of the sources of errors on the inverted solution. When the real value of A_{obs} is known (for example in theoretical analysis), one can nearly always find a set of free parameters so that A_{inv} will be equal to A_{obs}. However, one cannot use the same set of parameters for another inversion and expect the same result. It is therefore necessary to introduce a criterion for which the inversion can be considered as successful and reliable. In this study, we set the parameters by testing several values and choosing the best compromise between reducing the errors and matching the kernels to the target functions. However, the problem is far more complicated since one should analyse how these parameters depend not only on the modes used to carry out the inversion but also on the reference model for every integral quantity. This problem will be discussed in further studies on larger samples to provide relevant results.

The error bars on the inversion result are deduced from the errors bars on the frequency differences, where the errors on individual frequencies are considered to be independent:

$$\sigma_{\delta A/A} = \sqrt{\sum_i c_i^2 \sigma_i^2}, \tag{5.9}$$

with $\sigma_i = \sigma_{\frac{\delta \nu_i}{\nu_i}}$. However, it is clear that Eq. (5.9) does not take other sources of errors in the inversion into account, such as non-linear effects in the frequency differences, the mismatch between the averaging or cross-term kernels and their respective target functions, or the errors arising from neglected surface terms in the derivation of the kernels themselves. In other words, the inversion is dependent on the mathematical hypotheses leading to the variational principle (Lynden-Bell and Ostriker (1967)) and on other additional simplifications leading to expression (5.1) (see D. O. Gough and Thompson (1991)). In fact, Eq. (5.9) only takes into account the amplification of the observational errors, the so-called error magnification, but this is not representative of the accuracy of the method since it does not include all sources of error.

In the test cases of Sect. 5.2.4 and 5.2.5, the error analysis was performed using the difference between Eq. (5.4) and Eq. (5.5), following the method of D. R. Reese, Marques, et al. (2012). This leads to the following equation:

$$\begin{aligned}\frac{\delta A - \delta A_{inv}}{A} = &\int_0^1 \left(\mathscr{T}(x) - K_{\text{avg}}(x)\right) \frac{\delta s_1}{s_1} dx + \int_0^1 \left(\mathscr{T}_{\text{cross}}(x) - K_{\text{cross}}(x)\right) \frac{\delta s_2}{s_2} dx \\ &- \sum_i c_i \frac{\mathscr{G}(\nu_i)}{Q_i}.\end{aligned} \tag{5.10}$$

The first integral is the error contribution originating from the error on the fit of the target to the averaging kernel. We will write it σ_{Avg}. The second integral is the error contribution originating from the error on the fit of the target to the cross-term kernel. We will write it σ_{Cross}. The third term originates from the surface effects. The above equation does not take other sources of error into account, such as the non-linear effects not taken into account in Eq. (5.1), numerical errors, or the neglected non-adiabatic effects. In what follows, we will lump these errors together with the surface effects and call this σ_{Res} i. e. the residual errors that are left after having substracted σ_{Avg} and σ_{Cross} from the total error. Of course, σ_{Res} can only be obtained in theoretical test cases, where the differences in structural profiles are known beforehand and this specific contribution can be isolated from the kernel contributions.

Accuracy and reliability of the solution

As discussed in the previous section, inversion techniques have to be used with care, especially when modifying the values of the free parameters. First of all, it is necessary to recall that linear inversion techniques are limited to targets, models, and oscillation modes for which Eq. (5.1) is satisfied to a sufficient accuracy. This means that the reference model already has to be close to the target before the inversion can be computed. Therefore, we propose making use of the forward modelling method before calculating global characteristics with the inversion technique. For the present study, we used the Optimal Stellar Model (OSM) software developed by R. Samadi (Observatoire de Paris-Meudon) to compute our reference models. We discuss the fitting process in Sect. 5.2.5 and present further discussions in Sect. 5.2.6.

Once the reference model is obtained to sufficient accuracy, one may carry out the inversion. The free parameters β and θ of the SOLA method can be modified to improve the result. During this optimisation, the contributions from the matching of the averaging kernel, the cross-term kernel, and the error magnification must be considered. In fact, one has to compromise on the error contributions. One often talks about trade-off between precision and accuracy (see Pijpers and Thompson (1994) for a discussion on this problematic in the context of the SOLA method). In some of our test cases, we see that the error magnification can be quite important but on the other hand, having extremely small error bars on an inaccurate result is also unacceptable.

5.2.3 Inversion procedure for acoustic radius and age indicator

Definition of targets and motivations

As mentioned in the previous section, the first step is to define the global characteristic and its associated target. For this study, we work with the acoustic radius of the star, denoted τ, and an age indicator, t, based on the integral of the derivative of the sound speed appearing in the asymptotic limit of the small frequency separation. Therefore, the global characteristics we wish to determine are:

$$\tau = \int_0^1 \frac{dx}{c}, \tag{5.11}$$

$$t = \int_0^1 \frac{1}{x}\frac{dc}{dx}dx. \tag{5.12}$$

The acoustic radius is sensitive to surface effects because of the $1/c$ factor, whereas the age indicator is mostly sensitive to the central regions of the star. During the evolution of the star, the mean molecular weight grows because of nuclear reactions, leading to a local minimum in the sound speed profile. Therefore its derivative is very sensitive to the intensity of this minimum and can be related to the age of the star. These targets are also asymptotically related to the large and small frequency separation as follows (Vandakurov (1967), Tassoul (1980)):

$$\tau \simeq \frac{1}{2\Delta\nu}, \tag{5.13}$$

$$t \simeq \frac{-4\pi^2\nu\tilde{\delta}\nu}{(4\ell+6)\Delta\nu}, \tag{5.14}$$

where we use the symbol $\tilde{\delta}\nu$ to represent the small frequency separation to avoid confusion with the frequency perturbation, $\delta\nu$. It is well known that Eq. (5.14) is not very accurate for typical solar-like pulsators and that its agreement for models of the Sun in its current evolutionary stage is in fact fortuitous (Christensen-Dalsgaard (1991)).

The average large frequency separation is currently the only way to estimate the acoustic radius of a star. This quantity is expected to be sensitive to surface effects like convection and can also be used to characterise structural changes that mimic the evolution of the stellar radius, for example, its increase due to the contraction of the core during the evolution of the star. Moreover, the average large separation is also combined with the small frequency separation or other frequency combinations (see Christensen-Dalsgaard (1993a), White, Bedding, et al. (2011)) to build asteroseismic H-R diagrams. The motivation behind this approach is to estimate the mass and age of the star using seismic indicators that provide nearly independent information. However, asteroseismic diagrams are intrisically limited by two aspects: firstly, the exact relation between frequency separations and the

stellar structure is not trivial; secondly, there is only a limited number of different frequency combinations that can be used. In constrast, inversion techniques allow us to target the structural characteristics of our choise based on their relation with stellar properties. Thus, they offer more specific constraints and potentially allow us to distinguish between the different contributions from micro- and macro-physics.

Target for the acoustic radius inversion

To define the target function of the inversions, we have to calculate the first order relative perturbation of these quantities. For the acoustic radius it is straightforward :

$$\frac{\delta\tau}{\tau} = \frac{1}{\tau}\int_0^1 \frac{-1}{c}\frac{\delta c}{c}dx = \int_0^1 \frac{-1}{2\tau c}\frac{\delta c^2}{c^2}dx. \tag{5.15}$$

This result means that the target function is

$$\mathscr{T}_\tau = \frac{-1}{2c\tau}. \tag{5.16}$$

Since in this case the perturbation of the acoustic radius is only related to the structural variable c^2, the contribution of the cross-term kernel has to be suppressed. However, when using the perturbation of c^2, and the couple ρ, c^2 in Eq. (5.1), the cross-term will involve the relative difference in density between the model and the target, potentially leading to high pollution of the solution by the cross-term. It is possible to circumvent this problem by using the structural couple ρ, Γ_1. Indeed, the relative differences on Γ_1 are expected to be small, thereby leading to a smaller cross-term. This can be done by using the following equations:

$$\frac{\delta c^2}{c^2} = \frac{\delta\Gamma_1}{\Gamma_1} + \frac{\delta P}{P} - \frac{\delta\rho}{\rho}, \tag{5.17}$$

$$P(x) = \int_x^1 \frac{m(y)\rho}{y^2}dy, \tag{5.18}$$

$$m(x) = \int_0^x 4\pi x^2\rho dx. \tag{5.19}$$

Using these equations leads to new target functions defined on the ρ, Γ_1 couple, where we neglected the contribution of the turbulent pressure that is considered a surface effect:

$$\mathscr{T}_{\tau,\text{avg}} = \frac{1}{2c\tau} - \frac{m(x)}{x^2}\rho\left[\int_0^x \frac{1}{2c\tau P}dy\right] - 4\pi x^2\rho\left[\int_x^1 (\frac{\rho}{y^2}\int_0^y \frac{1}{2c\tau P}dt)\right]dy. \tag{5.20}$$

$$\mathscr{T}_{\tau,\text{cross}} = \frac{-1}{2c\tau}. \tag{5.21}$$

These definitions can be used directly in Eq. (5.8). Furthermore, we optimise the inversion by defining a supplementary constraint based on homologous relations and extending the method to the non-linear regime, following the approach of D. R. Reese, Marques, et al. (2012).

Supplementary constraint and non-linear extension for the acoustic radius

The idea behind the supplementary constraint is that the result of the inversion should be exact for models that are homologous. In what follows, a procedure satisfying this condition will be described as unbiased (not to be confused with the statistical meaning of

the word.). To reach this goal, we make use of the knowledge that when using homology, if the density of the model is scaled by a factor h^2, the frequencies will scale as h. With simple analysis of the definition of the acoustic radius, Eq. (5.11), we can see that it scales as the inverse of the frequencies, $1/h$. Therefore, to the first order, the relative variation of the acoustic radius should be the opposite of the relative variation of the frequencies. This means that if $\delta\nu/\nu = \varepsilon$, then $\delta\tau/\tau = -\varepsilon$. Furthermore, we know that for linear inversion techniques, the inverted correction is obtained from a linear combination of relative frequency differences. Therefore, if the sum of the coefficient is equal to -1, the inverted correction will be exact for models in a homologous relation.

The non-linear extension is based on an iterative process involving successive scalings of the model to reach an optimal point for which there is no further correction with the inversion technique. We see after some development that this process can be by-passed and that the solution can be obtained directly. However, to grasp the philosophy of this extension, it is easier to see it first as an iterative process. First, we carry out an inversion of the acoustic radius for a first reference model with a given τ_{ref} and obtain a new estimate of the acoustic radius $\tau_{inv,0}$. We now define a scale factor $q_0 = \frac{\tau_{inv_0}}{\tau_{ref}}$, used to scale the reference model, bringing it closer to the observed target. We can use this scaled model as a reference model for which another inversion can be carried out. Indeed, the frequencies have been scaled by the factor $h_0 = \frac{1}{q_0}$, and the relative differences between the frequencies of the scaled reference model and those of the target are now given by:

$$\frac{\nu_{\text{obs}} - h_0\nu_{\text{ref}}}{h_0\nu_{\text{ref}}} = \frac{1}{h_0}\left(\frac{\delta\nu}{\nu} + 1\right) - 1, \tag{5.22}$$

where ν_{obs} is the observed frequency and ν_{ref} the frequency of the unscaled reference model. Now for the j^{th} iteration, the inverted acoustic radius can be expressed as follows:

$$\begin{aligned}
\tau_{\text{inv,j+1}} &= \frac{\tau_{ref}}{h_j}\left[1 + \sum_i c_i\left[\frac{\nu_{\text{obs},i} - h_j\nu_{\text{ref},i}}{h_j\nu_{\text{ref},i}}\right]\right] \\
&= \frac{\tau_{\text{ref}}}{h_j}\left[1 + \sum_i c_i\left[\frac{1}{h_j}(\frac{\delta\nu_i}{\nu_i} + 1) - 1\right]\right] \\
&= \tau_{\text{ref}}\left[\frac{2}{h_j} + \left[\frac{1}{h_j^2}\left(\sum_i c_i\frac{\delta\nu_i}{\nu_i} - 1\right)\right]\right],
\end{aligned} \tag{5.23}$$

where we have also used the fact that the sum of the inversion coefficient is -1 for an unbiased acoustic radius inversion. Now we also obtained that $\tau_{inv,j+1} = \frac{\tau_{ref}}{h_{j+1}}$, by definition of our iterative process. Using this definition and rewriting Eq. (5.23) in function of q_j and q_{j+1}, we obtain the following expression:

$$q_{j+1} = 2q_j + q_j^2\left[\sum_i c_i\frac{\delta\nu_i}{\nu_i} - 1\right] = f(q_j). \tag{5.24}$$

where we have introduced the function, f. If the above iterations converge, then the limit, q_{opt}, will be a fixed point of f, i.e. $f(q_{\text{opt}}) = q_{\text{opt}}$. Convergence is guaranteed over a neighbourhood around q_{opt} provided $|f'(q_{\text{opt}})| < 1$. Given the simplicity of f, we choose to bypass the iterative method by solving directly $f(q) = q$. There are two solutions. The first is $q = 0$. However, it leads to an unphysical result, and would tend not to be the

result of an iterative process since $f^{'}(0) = 2$. The second solution is

$$q_{\text{opt}} = \frac{-1}{\sum_i c_i \frac{\nu_{\text{obs},i}}{\nu_{\text{ref},i}}}. \tag{5.25}$$

Furthermore, it turns out that $f^{'}(q_{\text{opt}}) = 0$. Hence, had we applied an iterative method, the convergence would have been quadratic. The associated acoustic radius is $\tau_{\text{inv}} = q_{\text{opt}}\tau_{\text{ref}}$. However, one must be aware that the error bars given by Eq. (5.9) on the final result are modified as follows if we assume that $\sigma_i \ll 1$ and that the errors on the individual frequencies are independent (see Appendix 5.2.7 for the demonstration of this formula):

$$\sigma_{\tau_{\text{min}}} = q_{\text{opt}}^2 \tau_{\text{ref}} \sqrt{\sum_i c_i^2 \sigma_i^2}. \tag{5.26}$$

Target for the age indicator inversion

By considering the perturbation of Eq. (5.12), we obtain the following target:

$$\frac{\delta t}{t} = \frac{1}{t}\int_0^1 \frac{1}{x}\frac{d\delta c}{dx} dx = \frac{1}{t}\int_0^1 \frac{1}{x}\frac{dc}{dx}\frac{\frac{d\delta c}{dx}}{\frac{dc}{dx}} dx. \tag{5.27}$$

The fact that we divide and multiply by the sound speed derivative is simply because of the fact that the kernels are unable to match the function $1/x$ in the centre. Therefore, we use this operation to define an easier target for the inversion and express the problem in terms of the relative perturbation of the sound speed derivative. The target is then given by

$$\mathscr{T}_t(x) = \frac{\frac{1}{x}\frac{dc}{dx}}{\int_0^1 \frac{1}{x}\frac{dc}{dx} dx}. \tag{5.28}$$

If we now consider Eq. (5.1), we can use an integration by parts to obtain inversion kernels in terms of the sound speed derivative

$$\int_0^1 K^{n,\ell}_{c^2,\rho}\frac{\delta c^2}{c^2} dx = -\int_0^1 \left(\int_0^x \frac{2K^{n,\ell}_{c^2,\rho}}{c} dy\right)\frac{dc}{dx}\frac{\frac{d\delta c}{dx}}{\frac{dc}{dx}} dx + \left[\left(\int_0^x 2\frac{K^{n,\ell}_{c^2,\rho}}{c} ds\right)\delta c\right]_0^1. \tag{5.29}$$

In the second term of this expression, the central evaluation is exactly 0 because the kernels are proportional to x^2 and the surface evaluation has been neglected because numerical tests have shown that its amplitude was 60 to 150 times smaller than the first term for modes with higher degree and radial order, and even smaller for lower degree and radial order modes. We then define the structural kernels for the sound speed derivative as follows:

$$K^{n,\ell}_{dc/dx,\rho} = -\frac{dc}{dx}\int_0^x \frac{2K^{n,\ell}_{c^2,\rho}}{c} dy. \tag{5.30}$$

By identification, we also obtain that $K^{n,\ell}_{\rho,dc/dx} = K^{n,\ell}_{\rho,c^2}$, which will be associated with the cross-term kernel. When deriving the targets for the acoustic radius, it was rather straightforward to obtain the cost function for the inversion. In the case of the age indicator, we show in Sect. 5.2.4 that the cost function defined in Eq. (5.8) is not adequate. Therefore, we defined a new way to carry out a SOLA inversion: trying to match the

anti-derivative of the averaging kernel with the anti-derivative of the target function. This modification is motivated by the oscillatory behaviour of the structural kernels, which is unsuitable for the age indicator inversion. Using this method, the cost function is defined as follows:

$$J_t = \int_0^1 \left[\int_0^x \mathscr{T}(y)dy - \int_0^x K_{\text{avg}}(y)dy \right]^2 dx + \beta \int_0^1 K^2_{\text{cross}}(x)dx + \tan(\theta) \sum_i (c_i \sigma_i)^2 + \lambda \left[\sum_i c_i - f \right]. \tag{5.31}$$

The fourth term contains the supplementary constraint we will define in the next section, and once again we do not consider the ad-hoc surface correction term. As for the acoustic radius, we can determine the value of the number f using homologous relations and add a non-linear extension to the method.

Supplementary constraint and non-linear extension for the age indicator

The supplementary constraint is obtained in the same way as for the acoustic radius inversion. We know that the frequencies scale with $\sqrt{\upsilon/\varepsilon^3}$ for a scale factor of υ in mass and ε in radius, or in other terms a scaling factor υ/ε^3 in density. It is easy to show that the adiabatic sound speed will scale as $\sqrt{\upsilon/\varepsilon}$ and therefore its derivative will scale as $\sqrt{\upsilon/\varepsilon^3}$. This means that the first order relative correction of the age indicator has to be the same as the frequency correction for models in a homologous relation. Again, we can find a constraint on inversion coefficients so that the inverted correction will be exact for models in a homologous relation. In this case, it means that the sum of the inversion coefficients needs to be equal to 1 to ensure that the correction will be the same for both frequencies and t.

It is also possible to try to extend this inversion to the non-linear regime using the iterative method of Eq. (5.22). Using this definition and the constraint on the sum of the inversion coefficients, we obtain:

$$\begin{aligned} t_{\text{inv}} &= h t_{\text{ref}} \left[1 + \sum_i c_i \left[\frac{1}{h} \left(\frac{\delta \nu_i}{\nu_i} + 1 \right) - 1 \right] \right] \\ &= t_{\text{ref}} \left(1 + \sum_i c_i \frac{\delta \nu_i}{\nu_i} \right). \end{aligned} \tag{5.32}$$

We now see that the inverted result is independent of the scaling factor h meaning that the effect of the iterative process described for the acoustic radius is already included in the linear method. However, this does not mean that the SOLA method is non-linear, nor that a non-linear inversion could not be defined by some other approach.

Comparison with asymptotic laws based on frequency separations

In the following sections, we will compare the results of SOLA inversions to other techniques based on frequency separations. We stress that these methods are not inversion techniques; we simply express asymptotic laws in a differential formulation to relate them to a linear combination of frequency differences.

It was shown by Vandakurov (1967) that the average large frequency separation is asymptotically related to the acoustic radius in the following way:

$$\tau \approx \frac{1}{2 \langle \Delta \nu \rangle}. \tag{5.33}$$

When we linearise this relation we obtain

$$\frac{\delta\tau}{\tau} \approx -\frac{\delta\langle\Delta\nu\rangle}{\langle\Delta\nu\rangle} = \sum_i c_i \frac{\delta\nu_i}{\nu_i}, \tag{5.34}$$

where we used the fact that the average large separation is simply a linear combination of frequencies to derive coefficients c_i. In much the same way as was done for inversion coefficients, these coefficients can be inserted into Eqs. (5.6) and (5.7) to obtain averaging and cross-term kernels for this method. These kernels can then be directly compared with those coming from the SOLA inversion technique, thereby allowing a quantitative comparison of the two methods. In our study, the average large separation was determined by a χ^2 fit (Kjeldsen, Bedding, and Christensen-Dalsgaard (2008)). If we apply the non-linear extension to the above relation, we obtain the following result:

$$\tau_{\rm inv} = -\frac{\tau_{\rm ref}}{\sum_i c_i \frac{\delta\nu_i}{\nu_i} - 1} = \frac{\tau_{\rm ref}}{\left(\frac{\langle\Delta\nu\rangle_{\rm obs}}{\langle\Delta\nu\rangle_{\rm ref}}\right)} = \frac{\gamma_\tau}{\langle\Delta\nu\rangle_{\rm obs}}. \tag{5.35}$$

where $\gamma_\tau = \tau_{\rm ref}\langle\Delta\nu\rangle_{\rm ref}$. Although Eq. (5.35) is very similar to Eq. (5.33), there are some subtle, yet important, differences. Indeed, the proportionality constant γ_τ is not, in general equal to 1/2 (as given by the original asymptotic formula), but has been specifically adapted to the reference model for that particular range of modes. Likewise, SOLA inversions are calibrated on the reference model, but they also go a step further by optimising the frequency combination so as to be as sensitive as possible to the acoustic radius.

We now turn our attention to the age indicator and the small frequency separation. We know from Tassoul (1980) that the small frequency separation is asymptotically and approximately related to the derivative of the sound speed by the following relation:

$$\tilde{\delta}\nu \approx \frac{-(4\ell+6)\Delta\nu}{4\pi^2\nu_{n,\ell}} \int_0^R \frac{dc}{dr}\frac{dr}{r}, \tag{5.36}$$

which can be reformulated in the form of Eq. (5.14). The relative perturbation of this equation will be a frequency combination, thereby allowing us to write

$$\frac{\delta\frac{\nu\tilde{\delta}\nu}{\Delta\nu}}{\frac{\nu\tilde{\delta}\nu}{\Delta\nu}} = \sum_i c_i \frac{\delta\nu_i}{\nu_i} \approx \frac{\delta t}{t}. \tag{5.37}$$

In other words, by using the relative perturbation of Eq. (5.14), we can define inversion coefficients leading to the following estimate of the indicator t :

$$t_{\rm inv} = t_{\rm ref}\left(1 + \sum_i c_i \frac{\delta\nu_i}{\nu_i}\right) = \frac{t_{\rm ref}\left(\frac{\nu\tilde{\delta}\nu}{\Delta\nu}\right)_{\rm obs}}{\left(\frac{\nu\tilde{\delta}\nu}{\Delta\nu}\right)_{\rm ref}} = \gamma_t \left(\frac{\nu\tilde{\delta}\nu}{\Delta\nu}\right)_{\rm obs}. \tag{5.38}$$

Again we find a proportionality constant γ_t adapted to the reference model and the observed modes. Using Eq. 5.36, one would find $\gamma_t = \left\langle -4\pi^2/(4\ell+6)\right\rangle$. We will see in the next sections that the indicators determined by directly applying the asymptotic relations are inaccurate compared to the SOLA method and the estimates defined in this section. In D. R. Reese, Marques, et al. (2012), the same technique is also applied to the scaling relationship between the mean density and the large frequency separation, and to another technique, which includes the empirical surface corrections of Kjeldsen, Bedding, and

Christensen-Dalsgaard (2008) . In Sect. 5.2.5, we will compare the three above procedures for estimating the mean density. Following the notations of D. R. Reese, Marques, et al. (2012) , we will refer to Kjeldsen et al.'s approach as the KBCD method[2]. The methods presented in this section are summarised in Table 5.1.

Table 5.1: Methods used for the determination of t, τ and $\bar{\rho}$.

$\bar{\rho}$ determination	t determination	τ determination
SOLA with $\theta = 10^{-2}$, $\beta = 10^{-6}$	SOLA with $\theta = 10^{-8}$, $\beta = 10^{-2}$	SOLA with $\theta = 10^{-2}$, $\beta = 10^{-6}$
$\langle \Delta\nu \rangle$ estimate	$\left\langle \tilde{\delta}\nu \right\rangle$ estimate	$\langle \Delta\nu \rangle$ estimate
KBCD estimate with $b = 4.9$	–	–

5.2.4 Test case with a grid of models

Targets and grid properties

The first test carried out used the model grid and the targets of D. R. Reese, Marques, et al. (2012). The goal of this test was to determine the reliability of the inversion when no forward modelling[3] was performed. The model grid consists of 93 main-sequence and pre-main sequence models with masses ranging from $0.8 M_\odot$ to $0.92\ M_\odot$ and ages ranging from 28 Myr to 17.6 Gyr. These models were downloaded from the CoRoT-HELAS website and additional information on their physical characteristics can be found in Marques, Monteiro, and Fernandes (2008) and D. R. Reese, Marques, et al. (2012).

We present the results for two targets, models A' and B, following the naming convention of D. R. Reese, Marques, et al. (2012). The characteristics of these targets are summarised in Table 5.2. The results for the first target were similar to those for B so we do not present them here. Model A' is in fact the first target of D. R. Reese, Marques, et al. (2012), denoted model A in their study, to which has been added an ad-hoc 50% increase of the density in the surface regions in the form of a hyperbolic tangent. Model B is radically different from the models of the grid since it includes rotational mixing, diffusion and follows the solar mixture of Asplund, Grevesse, and Sauval (2005) rather than that of Grevesse and Noels (1993), as used in the grid. We used a set of 33 oscillation modes ranging from $\ell = 0$ to $\ell = 2$ and from $n = 15$ to $n = 25$. The error bars on the observed frequencies were set to 0.3 μHz.

Results for the acoustic radius

The results for the acoustic radius for models A' and B are represented in Fig. 5.1. The values of the parameters θ and β are chosen so as to improve the match between the averaging and cross-term kernels, and their respective targets. The optimal values are $\theta = 10^{-2}$ and $\beta = 10^{-6}$. The small value of β is due to the fact that the second target ($\mathscr{T}_{\text{cross}}$ defined by Eq. 5.21) will be multiplied by the corrective term $\delta\Gamma_1/\Gamma_1$, which is rather small. Likewise, θ could be reduced because the error bars were not dramatically affected by changes in the value of this parameter. Because the structure of the target is known, it is possible to plot all error contributions to the inversion results as in Eq.

[2] Eq. (26) in D. R. Reese, Marques, et al. (2012).

[3] Strictly speaking, the term "forward modelling" refers to solving the direct problem (see e.g. Tarantola (2005) , Sect. 1.3), i.e. predicting the results (or in our case the pulsation frequencies) for a given model. However, in the asteroseismic literature (see e. g. Charpinet et al. (2008), the term "forward modelling" has also come to mean "execution of the forward problem using [stellar] models with a few adjustable parameters, and the calibration of those parameters by fitting theory to observations" D. Gough (1985)). In what follows, we use this latter definition.

Table 5.2: Characteristics of targets A' and B.

	Model A'	**Model** B
τ (s)	2822.07	2823.53
t (s^{-1})	-2.640×10^{-3}	-2.534×10^{-3}
Mass ($M_\odot$)	0.9	0.92
Radius ($R_\odot$)	0.821	0.825
Age (Gyr)	1.492	2.231
$T_{\rm eff}$ (K)	5291	5291
$\log(g)$ (dex)	4.563	4.569

(5.10) and the error analysis described at the end of Sect. 5.2.2. These contributions are represented for targets A' and B in Fig.5.1 and the kernels for model A' are represented in Fig. 5.2. We see that the cross-term is not responsible for the errors of the SOLA inversions and that the matching of the averaging kernel is the leading error term. Also, we sometimes observe a compensation of the residual error and the averaging kernel error for the SOLA method and that the correction based on the large frequency separation can have smaller errors than SOLA, despite its oscillatory behaviour. The value of the least-square fits of the kernels for model $A^{'}$ for the τ and t inversions are illustrated in figure 5.7, where we compute the squared difference between the kernel and its target for each reference model of the grid. However, it should be noted that these errors tend to compensate and that this compensation is the reason for the slightly more accurate results for model B, as can be seen on the right-hand side of the figure. These compensations have also been observed for mean density inversions, but in the case of model $A^{'}$ and other test cases, they did not occur, as can be seen in the error plots in Fig. 5.1. Thus, this technique is unable to account for surface effects and its reliability for observed stars is questionable. If we directly use the asymptotic relation for the acoustic radius, i.e. if we apply Eq. (5.33), we obtain $\tau = 2691$ s for model A' and $\tau = 2890$ s for Model B, which is even less accurate than both SOLA inversions and the improved $\Delta\nu$ approach.

Results for the age indicator

The results of the age indicator inversions for models A' and B are the same, thus we only present them for model A'. They show the limit of our inversion techniques when there is no criterion to choose the reference model. From Fig. 5.3, it is clear that the SOLA inversion technique failed to reproduce the results for a subgrid of models. This is simply due to the large range of ages of the reference models. One has to recall that the SOLA approach is based on the integral Eq. (5.1), which itself is based on the variational principle, only valid for small perturbations. The error plot also shows that SOLA inversions benefit from error compensations, which is problematic for observed stars. The second problem is that when plotting the averaging and cross-term kernels, we see that the results are rather poor (see Fig. 5.3). The parameters for these inversions were $\theta = 10^{-6}$ and $\beta = 10^{-4}$. When carrying out an inversion on an observed star, one can only assess the quality of the inversion based on how well the averaging and the cross-term kernels fit their respective target functions. Therefore being able to obtain accurate results is not sufficient: the accuracy must be related to the quality of the fit of the targets, otherwise one would never be able to determine if the inversion was successful or not. Figure 5.4 illustrates the exact opposite for both our techniques. Therefore, we modified the age indicator inversion by using the anti-derivative of the target function rather than the target itself, as described in Sect. 5.2.3. We then see that the inversion failed on a larger subgrid

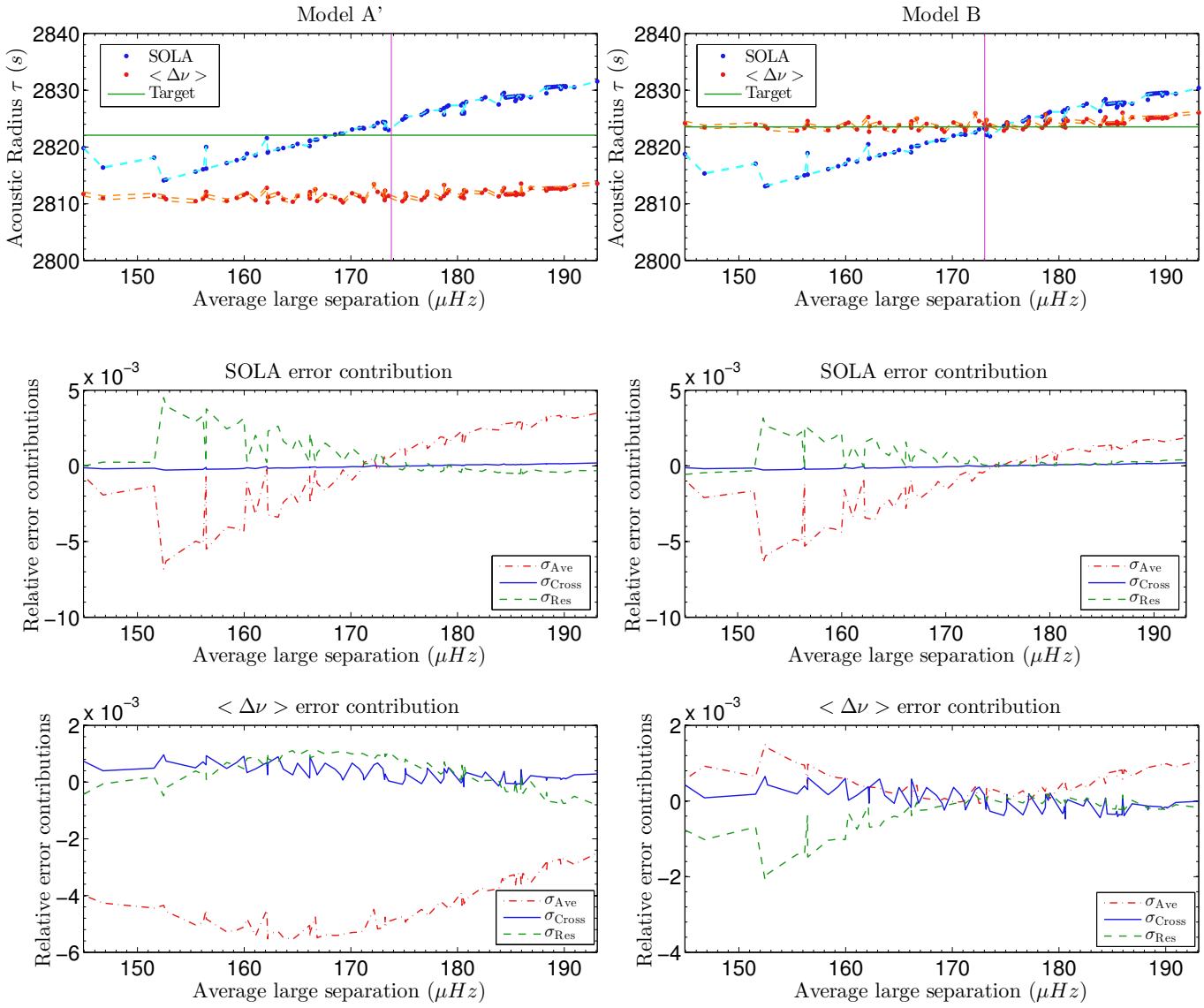

Figure 5.1: The left-hand panels show inversion results for model A', whereas the right-hand side is for model B. The top panels show SOLA inversion results (blue) and estimates based on the large frequency separation (red), the vertical line (magenta) indicates the value of the large frequency separation of each target. The figures below show the different error from Eq. (5.10) terms, which appear in the SOLA inversions (middle panels) and the large separation (lower panels). The results and error contributions are given for every model of the grid such that the abscissa of these figures is the average large separation of each reference model.

than before, but this failure is inevitable because of the properties of the reference grid. The set of parameters for these inversions was $\theta = 10^{-8}$ and $\beta = 10^{-2}$. The parameter β was increased to annihilate the effect of the cross-term and θ was reduced thanks to its small impact on the error bars. However, we need to define a criterion to select a model for which the result is reliable. We simply take the model with the closest average small

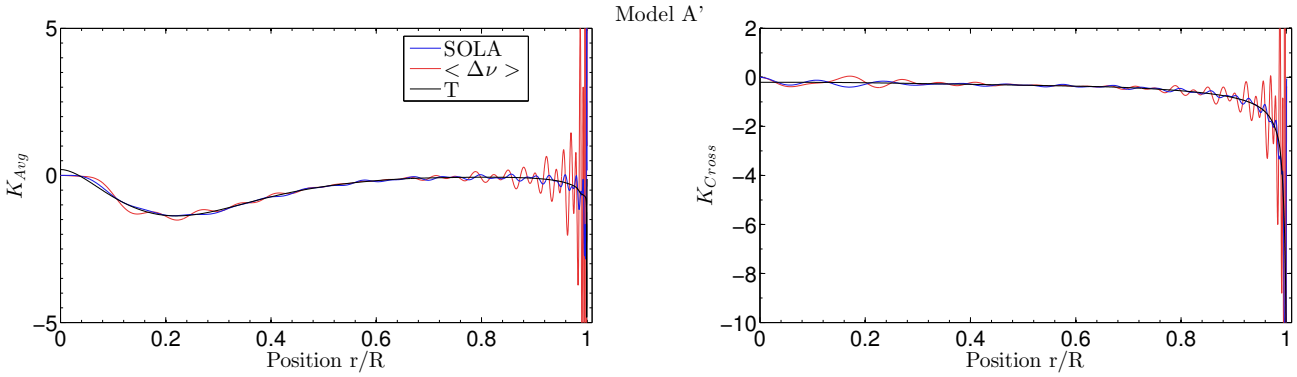

Figure 5.2: Averaging and cross-term kernels for the inversion of the acoustic radius for model A'. The target function is represented in black, the results for the $\Delta\nu$ relation in red, and those from SOLA inversions in blue.

frequency separation to the target. The results for this choice are illustrated in Fig. 5.5. In this case, it is clear that the SOLA inversion is superior to the estimate based on the small frequency separation and this leads to the definition of a new framework in which to carry out inversions for this indicator more accurately.

5.2.5 Test case for targets using forward modelling

Definition of the framework

In the previous section, we saw that by simply choosing the best model of the grid in terms of the arithmetic average of the small frequency separation, we could achieve very accurate results. However, the validity of Eq. (5.1) for the best model of the grid and the target is still questionable, and one could wish to achieve an even greater accuracy. Using forward modelling of the target is the best way to obtain a model that is sufficiently close to enable the use of the variational principle, thereby leading to successful linear inversions. We chose the software Optimal Stellar Model (OSM)[4], developed by Réza Samadi, to carry out the forward modelling using the arithmetic average of the large separation and small frequency separations of the observed frequency set as seismic constraints and the mass and age of the reference model as free parameters. This optimization strategy is purely arbitrary and further studies will be needed to determine how other approaches can be used. However, regardless of what quantities (e.g. individual small separations or other seismic indicators) and analysis methods (e.g. MCMC algorithms or genetic algorithms) are used to select the reference model, the inversion will be carried out afterwards, since it is able to depart from the physical assumptions used by the stellar evolution code when constructing the reference model. To ensure that differences still remain between our reference model and our targets, we deliberately use different values for the metallicity or mixing-length parameter, add turbulent pressure to the target, or use non-adiabatic computations for the observed frequencies. Therefore the forward modelling process will always intentionally be unable to reproduce the target within an accuracy that would make the inversion step useless. The tests were carried out using the CESTAM evolutionary code (Code d'Evolution Stellaire, avec Transport, Adaptatif et Modulaire) Marques, Goupil, et al. (2013), and the Adipls cite adipls , the LOSC (Liège OScillation Code) Scuflaire, Montalbán,

[4]The OSM software can be downloaded from `https://pypi.python.org/pypi/osm/`

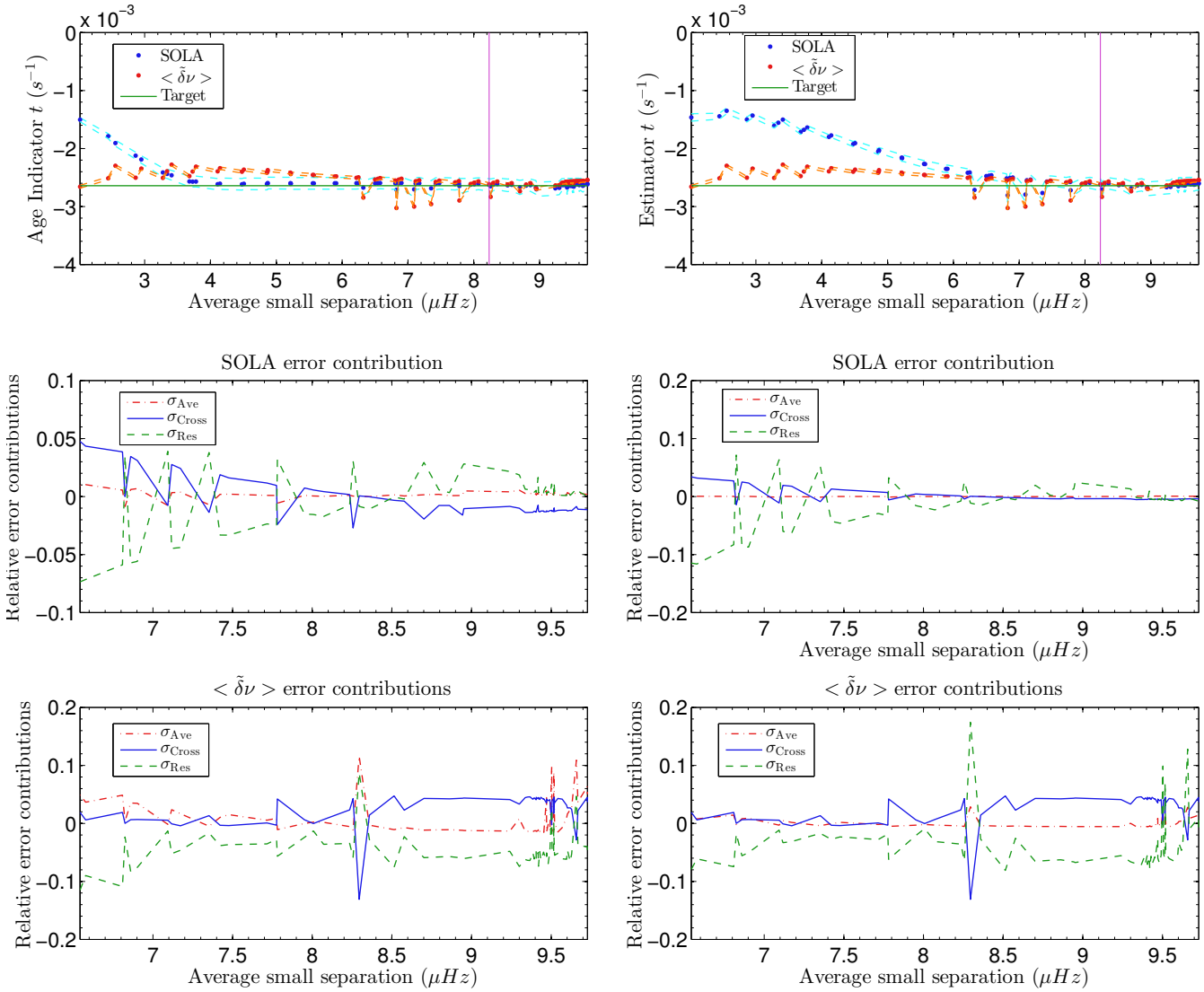

Figure 5.3: Inversion results for the age indicator and estimates based on the small frequency separation, using the grid of models. The left column shows the results in which the averaging kernels are optimised, whereas in the right column, the anti-derivative of the averaging kernels are optimised. The top two panels show the inversion results where the vertical line (magenta) indicates the value of the small frequency separation of the target, the middle two panels show the errors from Eq. (5.10) in the SOLA inversions, and the bottom two panels are the errors from Eq. (5.10) from the improved small frequency separation technique. The results and error contributions are given for every model of the grid such that the abscissa of these figures is the average large separation of each reference model.

et al. (2008) and MAD pulsation (M. A. Dupret (2001) M.-A. Dupret, Samadi, et al. (2006)) codes. We used the same modes as for the model grid tests, namely with ℓ ranging from 0 to 2 and n ranging from 15 to 25. The error bars on the frequencies were set to 0.33 μHz. We will compare the results from the SOLA method with those from improved estimates based on the average large separation as in the previous section. One could ask why we

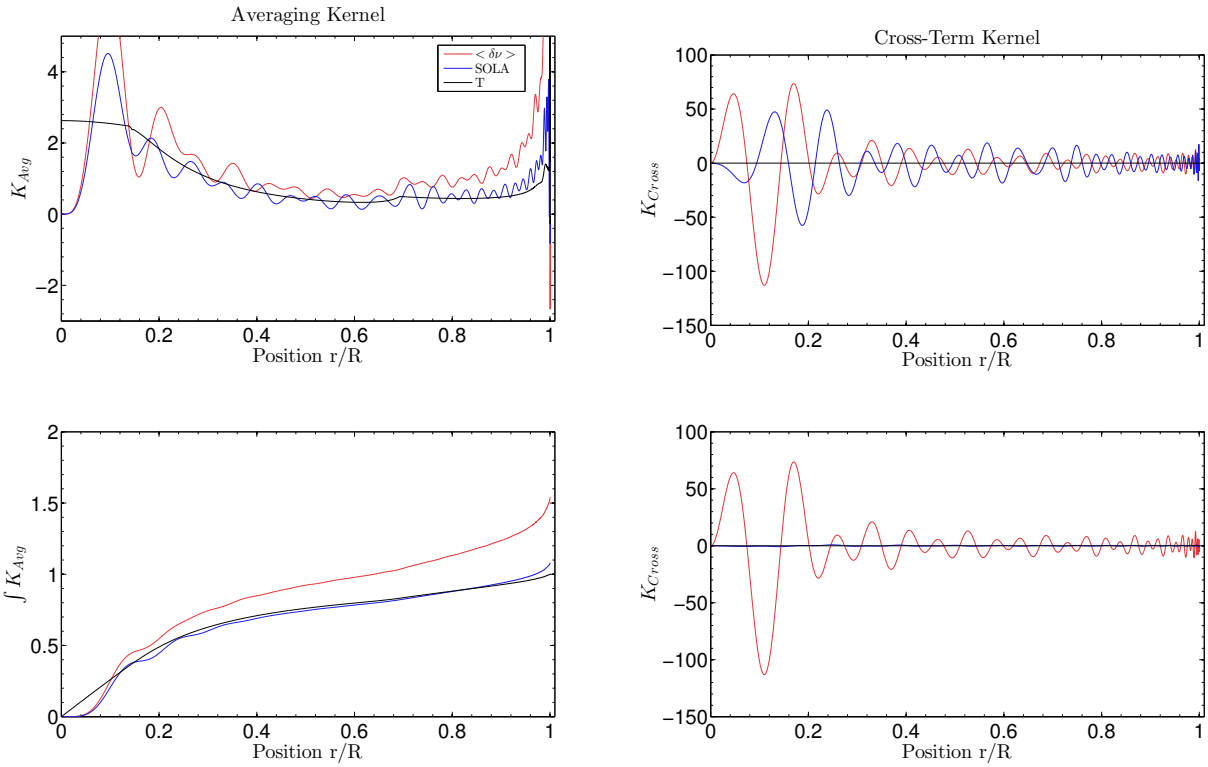

Figure 5.4: The upper panels illustrate the averaging and cross-term kernels for the model with the best small frequency separation by optimising on the averaging kernel itself. The lower panels illustrate the same results by optimising the anti-derivative of the averaging kernel. The target function is in black, the results for the small frequency separation estimate in red and those for SOLA inversions in blue.

are not using the arithmetic average of the large separation to carry out the correction. In fact this quantity is already fitted to within 0.2 μHz of its target value with the forward modelling process, and cannot therefore be improved upon. Concerning the values of the θ and β parameters, we keep the same values as in the previous section, i.e. $\theta = 10^{-2}$ and $\beta = 10^{-6}$ for the acoustic radius and the mean density, $\theta = 10^{-8}$ and $\beta = 10^{-2}$ for the age indicator.

Test case with different metallicity and $\alpha_{\rm MLT}$

The first test made use of a 0.95 $M_\odot$ and a 1.05 $M_\odot$ model, denoted targets 1 and 2, respectively. The characteristics of the targets are summarised in the Table 5.3. The first step was to carry out the forward modelling of these targets with the OSM software using the fixed parameters $Z = 0.0135$ and $\alpha_{\rm MLT} = 1.522$ for the reference models. In tables 5.4 and 5.5, we summarise the inversion results with their error bars for both models. We can see from this table that the error bars are underestimated for the acoustic radius and mean density inversions. This results from the definition (5.9), which only accounts for the propagation of observational errors but neglects the contributions related to the inversion process itself or to the validity of Eq. (5.1). However, the error bars from the age indicator are more important. We stress that quantifying errors of inversion techniques is still problematic and require further theoretical studies. We also analysed the different

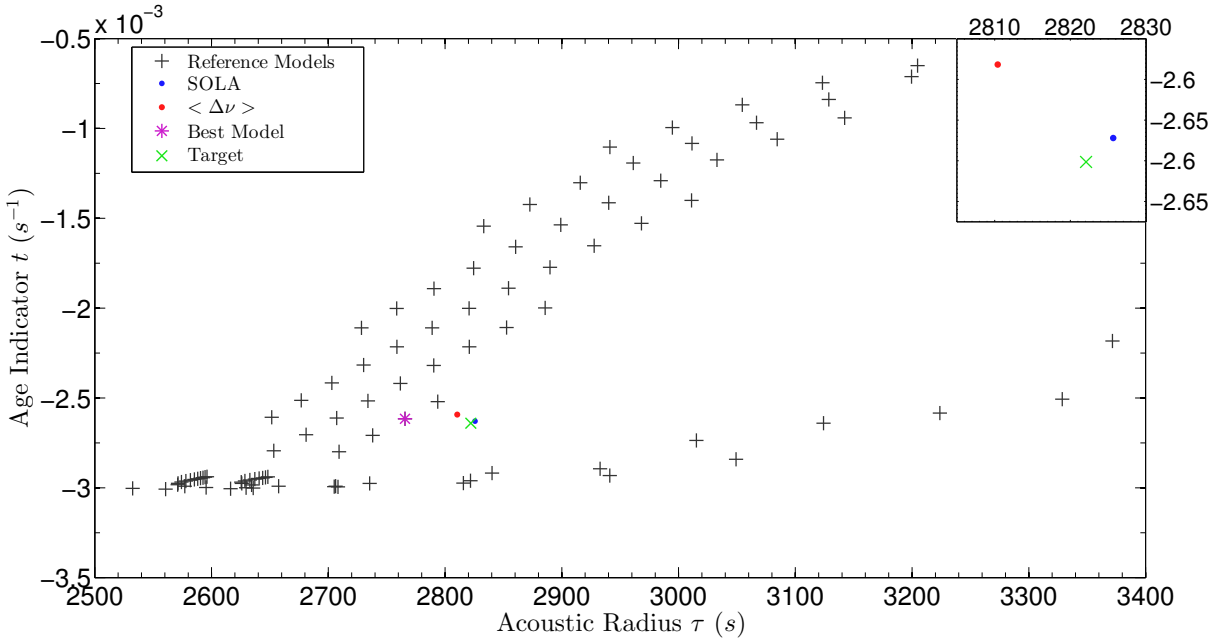

Figure 5.5: Inversion results for the model with the best small frequency separation. In the main part of the figure, the grid models are represented by the black +, the best model is the purple $*$, model A' the green X, the SOLA result is in blue, and the large frequency separation result in red. The inset shows an enlarged view of the region around model A'.

contributions σ_i and found that compensation was present to a lesser extent in SOLA inversions than in the other correction techniques. This is a direct consequence of the quality of the kernel fits with SOLA.

We also observed that the cross-term kernel contribution could sometimes be rather important in the mean density and acoustic radius inversions. First of all, we can tell

Table 5.3: Characteristics of targets 1 and 2.

	Model 1	**Model** 2
Mass ($M_\odot$)	0.95	1.05
Radius ($R_\odot$)	0.868	0.988
Age (Gyr)	1.8	1.5
$T_{\rm eff}$ (K)	5284	5912
$\log(g)$ (dex)	4.538	4.469
Z	0.015	0.0135
$\alpha_{\rm MLT}$	1.522	1.7

that the inversion of the age indicator is far more accurate when there are no metallicity effects. Indeed, modifying the metallicity affects the entire star, whereas changing the mixing length only influences the convective envelope, thereby having a negligible impact on the age indicator inversions. Furthermore, test cases carried out for this model with up to 50 or 70 frequencies showed an improvement in the accuracy of the method. The inversion step, as well as the estimate based on the large frequency separation should

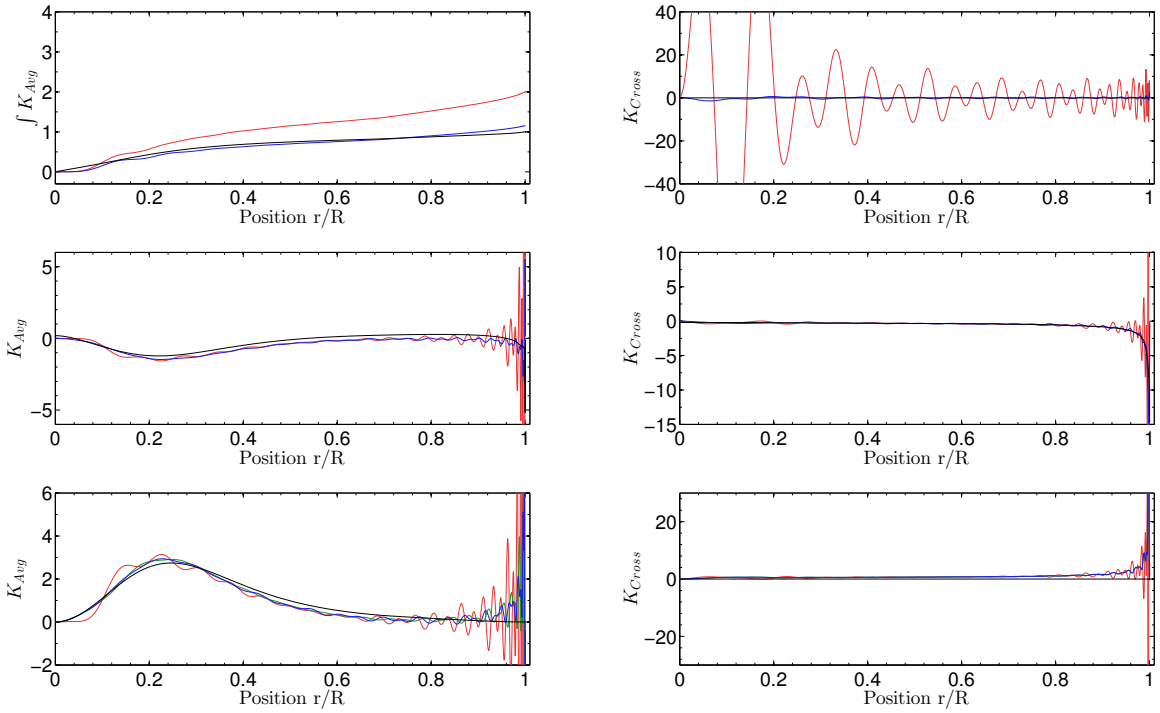

Figure 5.6: Kernels for the test case with different metallicity. Averaging kernels (left) and cross-term kernels (right) for the age indicator inversion (top panels), the acoustic radius inversion (middle panels), and the mean density (lower panels). The SOLA method is in blue, the $\langle \Delta\nu \rangle$ estimate in red and when implemented, the KBCD approach is in green. The target function in all panels is plotted in black.

only be considered if there is a sufficient number frequencies with small error bars. If this is not the case, then one should avoid carrying out an inversion. We will discuss more extensively the observed weaknesses of the method and possible problems in Sect. 5.2.6. Two supplementary results can be observed for this first test case: the SOLA method is again more accurate when dealing with surface effects, here the variations of $\alpha_{\rm MLT}$, confirming what had been guessed from the results of the previous section. The second comment is related to the estimates based on the frequency separations. We see that the results improve even if we already fitted the arithmetic average of the large separation during the forward modelling process. This means that the χ^2 large separation is more efficient at obtaining the acoustic radius and the mean density of a star and should be preferred over the average large separation. The case of the age indicator is also different since the estimate is determined through the combination given in Eq. (5.14) and not the small separation alone.

Test case with non-adiabatic frequencies

In this section we present the results for a 0.9 $M_\odot$ model, denoted target $1_{\rm nad}$, for which non-adiabatic effects have been taken into account. The frequencies have been calculated with the MAD oscillation code, using a non-local, time-dependent treatment of convection

Table 5.4: Inversion results for the test case with a different metallicity, Model_1.

Method	$\bar{\rho}$ (g/cm^3)	τ (s)	t (s^{-1})
Reference Value	2.036	3007.77	-0.002523
SOLA	$2.055 \pm 1.17 \times 10^{-4}$	2993.91 ± 0.08	$-0.002548 \pm 1.27 \times 10^{-4}$
$\langle \Delta\nu \rangle$ or $\tilde{\delta}\nu$ estimates	$2.054 \pm 1.33 \times 10^{-3}$	2995.10 ± 0.334	$-0.002560 \pm 2.71 \times 10^{-5}$
KBCD	$2.055 \pm 4.2 \times 10^{-4}$	–	–
Target Value	2.047	2995.01	-0.002539

Table 5.5: Inversion results for the test case with a different α_{MLT}, Model_2.

Method	$\bar{\rho}$ (g/cm^3)	τ (s)	t (s^{-1})
Reference Value	1.523	3471.91	-0.002452
SOLA	$1.533 \pm 9.89 \times 10^{-5}$	3460.29 ± 0.1	$-0.002460 \pm 1.38 \times 10^{-4}$
$\langle \Delta\nu \rangle$ or $\tilde{\delta}\nu$ estimates	$1.530 \pm 9.95 \times 10^{-4}$	3464.43 ± 0.45	$-0.002464 \pm 2.835 \times 10^{-5}$
KBCD	$1.534 \pm 3.14 \times 10^{-4}$	–	–
Target Value	1.533	3461.49	-0.002458

taking the variations of the convective flux and of the turbulent pressure due to the oscillations into account (see Grigahcène et al. (2005), M. A. Dupret (2001), M.-A. Dupret, Samadi, et al. (2006) for the description of this treatment). A second test case was carried out using a 1 $M_\odot$ model, denoted target 2_{nad}, and a reference model with a slightly less accurate fit. The characteristics of both targets are summarised in Table 5.6. In both test cases, the difference between the frequencies from the target and reference models lay in the fact that only the former includes non-adiabatic effects. The results are summarised in Tables 5.7 and 5.8 for both targets. The kernels from the various inversions and estimates are illustrated in Fig. 5.8. The accuracy of the results is clearly related to how well the kernels match their target functions, thereby accounting for the reliability of the inversion technique. We observe that the SOLA inversion technique leads to accurate results for all characteristics in the first test case. For the second test case, we first carried out inversions and estimates based on a set of 33 frequencies. The results were accurate for the mean density and the acoustic radius. However, the age indicator estimate was as accurate as the value obtained through the forward modelling because the inversion over-corrected this value. Therefore, we carried out a second set of inversions, using 40 frequencies ranging from $n = 15-28$ for $\ell = 0$ and from $n = 15-27$ for $\ell = 1,2$ to see if the result for the age indicator could be improved. This second test is presented in Table 5.8 where we can see that the SOLA inversion leads to more accurate results than all of the other techniques. This illustrates two effects: firstly, when the model and the target are less well fitted, the inversion requires more frequencies to reach a good accuracy; secondly, a few more frequencies can greatly improve the accuracy of the inversion. This second effect is typical of ill-posed problems. One has to be aware that the accurate result for the second frequency set does not mean that using 40 frequencies is sufficient in all cases. Analysing the different contributions to the error showed that in this case, the estimates based on frequency combinations could not accurately reproduce non-adiabatic effects in the frequencies. We can thus conclude that the SOLA method is optimal to correct the errors introduced in the forward modelling and particulary surface effects.

Test case with turbulent pressure

In the last test case, we included the effects of turbulent pressure when calculating, thanks to the LOSC code, the adiabatic pulsation frequencies of a 1 $M_\odot$ target. The turbulent

Table 5.6: Characteristics of targets $1_{\rm nad}$ and $2_{\rm nad}$.

	Model $1_{\rm nad}$	**Model** $2_{\rm nad}$
Mass ($M_\odot$)	0.9	1.0
Radius ($R_\odot$)	0.858	0.942
Age (Gyr)	6.0	3.0
$T_{\rm eff}$ (K)	5335	5649
$\log(g)$ (dex)	4.5248	4.4895
Z	0.0135	0.0135
$\alpha_{\rm MLT}$	1.62	1.62

Table 5.7: Inversion results for test case 1, $\text{Model}_{\rm 1nad}$, using 33 non-adiabatic frequencies.

Method	$\bar{\rho}$ (g/cm^3)	τ (s)	t (s^{-1})
Reference Value	1.986	3042.76	-0.001873
SOLA	$2.01 \pm 1.15 \times 10^{-4}$	3024.60 ± 0.08	$-0.001893 \pm 7.8 \times 10^{-5}$
$\langle \Delta\nu \rangle$ or $\tilde{\delta}\nu$ estimates	$1.986 \pm 1.3 \times 10^{-3}$	3042.80 ± 0.34	$-0.001903 \pm 2.56 \times 10^{-5}$
KBCD	$2.015 \pm 4.1 \times 10^{-4}$	–	–
Target Value	2.006	3023.88	-0.001894

pressure was included in the computation of the evolution of the model by adding a supplementary term $P_{\rm turb}$ using the following phenomenological approach:

$$P_{\rm turb} = \langle \rho v_R^2 \rangle = C_{p_{\rm turb}} \rho v_R^2, \tag{5.39}$$

with v_R the radial speed of the convective elements given by the mixing length theory. The value of the turbulent pressure coefficient $C_{p_{\rm turb}}$ was chosen to be 1.58 to match effects of 3D simulations for the Sun. The characteristics of the target are summarised in Table 5.9 and the results are summarised in Table 5.10. We see that the SOLA method can account for the effects of turbulent pressure and improve the accuracy with which global stellar characteristics are determined in this case. The kernels for this inversion are illustrated in Fig. 5.9. As was the case previously, the SOLA kernels seem to be more regular and closer to their target functions than those of the other techniques.

5.2.6 Conclusion

In this section, we have analysed four different methods for obtaining various stellar parameters. These include asymptotic relations based on two different implementations of large and small frequency separations, a scaling law for the mean density, which includes the Kjeldsen, Bedding, and Christensen-Dalsgaard (2008) surface corrections, and inversions based on the SOLA method. A comparison of these different methods reveals the following strengths and weaknesses:

- **Arithmetic average of the large and small frequency separations:** This method is the simplest to implement and is useful in forward modelling. The method is, however, less accurate than the other methods.
- **Large frequency separation from a χ^2 adjustment and arithmetic average of the age indicator (based on Eq. 5.14):** This remains simple but is more accurate than the previous approach, as demonstrated by the improvement in the results when this method is applied after the forward modelling (which uses the previous approach). This version of the large frequency separation is more accurate because it uses the information from all of the modes, rather than simply those with the

Table 5.8: Inversion results for test case 2,$\text{Model}_{2\text{nad}}$, using 40 non-adiabatic frequencies.

Method	$\bar{\rho}$ (g/cm^3)	τ (s)	t (s^{-1})
Reference Value	1.588	3399.79	-0.002285
SOLA	$1.691 \pm 9.4 \times 10^{-5}$	3294.84 ± 0.09	$-0.002150 \pm 8.5 \times 10^{-5}$
$\langle \Delta\nu \rangle$ or $\tilde{\delta}\nu$ estimates	$1.659 \pm 7.9 \times 10^{-4}$	3326.93 ± 0.3	$-0.002248 \pm 2.54 \times 10^{-5}$
KBCD	$1.696 \pm 2.65 \times 10^{-4}$	–	–
Target Value	1.684	3295.87	-0.002190

Table 5.9: Characteristics of target 1_{turb}.

	Model 1_{turb}
Mass ($M_\odot$)	1.0
Radius ($R_\odot$)	0.868
Age (Gyr)	4.0
T_{eff} (K)	5683
$\log(g)$ (dex)	4.469
Z	0.0135
α_{MLT}	1.62

lowest and highest n values. The reason why using the average age indicator works better than the average small frequency separation is less obvious, but is likely to be related to the fact that in the former case one isolates an integral that only depends on the stellar structure and does not contain a mode-dependent coefficient in front, before carrying out the average. In spite of these improvements, this approach remains sensitive to surface effects as shown, for instance, in Fig. 5.1 (left column).

- **The mean density from the Kjeldsen et al. (2008) surface-correcting approach**: This approach produces superior results compared to the two previous methods because it is able to correct for surface effects. However, changes in metallicity affect both this method and SOLA inversions more than the previous methods, since such changes modify the entire star rather than just the near-surface layers.
- **SOLA inversions**: Although this approach is the most complicated, it also turns out to be the most accurate. Indeed, apart from the case where the metallicity was modified, it is able to deal with incorrect assumptions in the reference models since it focusses on optimising the averaging and cross-term kernels. Furthermore, a key feature of SOLA inversions is that the quality of these kernels is closely related to the quality of the results, unlike what sometimes happens for scaling laws where fortuitous compensations lead to good results. This is important because it provides a way to estimate the quality of the inversion results. However, one must be careful to choose a reference model that is sufficiently close to the target, particularly for the age indicator inversions. This naturally leads to the use of forward modelling before application of this method. A quick inspection of the values in Tables 5.5,5.4,5.8,5.7,5.10 shows that SOLA inversions have improved the accuracy by a factor ranging from 10 to several hundred for τ and $\bar{\rho}$ and from 1.125 to more than 20 for t, when compared to results from the forward modelling.

A couple of further comments need to be made concerning SOLA inversions of the age indicator. Firstly, great care should be taken when calculating the quantity $\frac{1}{x}(\frac{dc}{dx})$, which intervenes in the target function. Indeed, this quantity is prone to

Table 5.10: Inversion results for test case using turbulence pressure, $\text{Model}_{1\text{turb}}$.

Method	$\bar{\rho}$ (g/cm^3)	τ (s)	t (s^{-1})
Reference Value	1.557	3429.59	-0.001877
SOLA	$1.575 \pm 9.6 \times 10^{-5}$	3409.72 ± 0.1	$-0.001894 \pm 6.7 \times 10^{-5}$
$\langle \Delta\nu \rangle$ or $\tilde{\delta}\nu$ estimates	$1.570 \pm 1.02 \times 10^{-3}$	3415.93 ± 0.4	$-0.001902 \pm 2.6 \times 10^{-5}$
KBCD	$1.576\ 3.3 \times 10^{-4}$	–	–
Target Value	1.573	3409.76	-0.001888

numerical noise as x approaches 0. In our calculations, we reduced this noise by numerically calculating the derivative with respect to x^2, but note that it was still necessary to inspect this function before carrying out the inversion. Secondly, as can be seen from the top left panel of Fig. 5.4, the target function does not go to 0 in the centre, as opposed to the structural kernels, which behave as $\mathcal{O}(r^2)$ in the centre. Therefore this target will be difficult to fit, even with more frequencies, and we need to find a workaround to be able to retrieve the effects of stellar evolution with an inversion technique. In fact, the lower left panel of Fig. 5.4 shows that optimising the anti-derivative is not always sufficient to solve this problem.

In future studies, we plan to analyse in more detail under what conditions SOLA inversions yield good results. In particular, we will investigate, in a systematic way, how close the reference model needs to be to the observed star for the inversion to be reliable. It will also be important to test the quality of the averaging and cross-term kernels as a function of the number and type of modes available. We also plan to extend SOLA inversions to other structural quantities, including age indicators that do not suffer from the difficulties mentioned above. This highlights the great potential of the SOLA method, since it allows us to choose the global structural characteristic that we wish to determine, offering a promising new diagnostic method into stellar structural properties.

5.2.7 Appendix: Demonstration of the error propagation formula for the non-linear extension of the acoustic radius inversion

Equation (5.26) is obtained with a little algebra. First, we treat the observed frequencies, $\nu_{obs,i}$, and the inverted acoustic radius, τ_{inv}, as independent stochastic variables

$$\nu_{\text{obs},i} = \bar{\nu}_{\text{obs},i}(1+\varepsilon_i), \tag{5.40}$$

$$\tau_{\text{inv}} = \bar{\tau}_{\text{inv}}(1+\varepsilon_\tau), \tag{5.41}$$

with ε_i being the individual noise realisations for each frequency, ε_τ the resultant deviation on τ_{inv}, and $\bar{\nu}_{\text{obs}}$ and $\bar{\tau}_{\text{inv}}$ the average of the stochastic variables $\nu_{\text{obs},i}$ and τ_{inv}, respectively.. Furthermore, we assume that:

$$\varepsilon_i \ll 1. \tag{5.42}$$

Using the fact that $\tau_{\rm inv} = q_{\rm opt}\tau_{\rm ref}$, with the definition of q_{opt} given in Eq. (5.25), and the separation into stochastic and average contributions defined previously, we obtain:

$$\begin{aligned}\bar{\tau}_{\rm inv}(1+\varepsilon_\tau) &\simeq \frac{-\tau_{\rm ref}}{\sum_i c_i \dfrac{\bar{\nu}_{{\rm obs},i}}{\nu_{{\rm ref},i}} \left[1 + \dfrac{\sum_i c_i \dfrac{\bar{\nu}_{{\rm obs},i}}{\nu_{{\rm ref},i}} \varepsilon_i}{\sum_i c_i \dfrac{\bar{\nu}_{{\rm obs},i}}{\nu_{{\rm ref},i}}} \right]} \\ &= \frac{-\tau_{\rm ref}}{\sum_i c_i \dfrac{\bar{\nu}_{{\rm obs},i}}{\nu_{{\rm ref},i}}} \left[1 - \frac{\sum_i c_i \dfrac{\bar{\nu}_{{\rm obs},i}}{\nu_{{\rm ref},i}} \varepsilon_i}{\sum_i c_i \dfrac{\bar{\nu}_{{\rm obs},i}}{\nu_{{\rm ref},i}}} \right], \end{aligned} \tag{5.43}$$

where we assumed that ε_i is much smaller than 1, thereby allowing us to linearise the above equation. We now apply the formula for the variance of a linear combination of independent stochastic variables and obtain

$$\bar{\tau}_{\rm inv}^2 \sigma_\tau^2 = \frac{\tau_{\rm ref}^2}{\left(\sum_i c_i \dfrac{\bar{\nu}_{{\rm obs},i}}{\nu_{{\rm ref},i}} \right)^4} \sum_i c_i^2 \sigma_i^2, \tag{5.44}$$

where we used the following equivalences:

$$\sigma_i^2 = \sigma^2_{\frac{\delta\nu_i}{\nu_i}} = \sigma^2_{\frac{\nu_{{\rm obs},i}}{\nu_{{\rm ref},i}}} = \left(\frac{\bar{\nu}_{{\rm obs},i}}{\nu_{{\rm ref},i}} \right)^2 \sigma^2_{\varepsilon_i}. \tag{5.45}$$

Equation 5.44 then leads directly to Eq. (5.26) when using the definition of $q_{\rm opt}$ given in Eq. (5.25).

5.2.8 Appendix: Supplementary figures

Figures 5.7, 5.8 and 5.9 illustrate the quality of the kernel fits for some of the test cases we presented in the core of this section. Although these plots are redundant from the visual point of view, we wish here again to stress that they are crucial to the understanding of the quality of a SOLA inversion and justify the accuracy of the results presented in the previous sections.

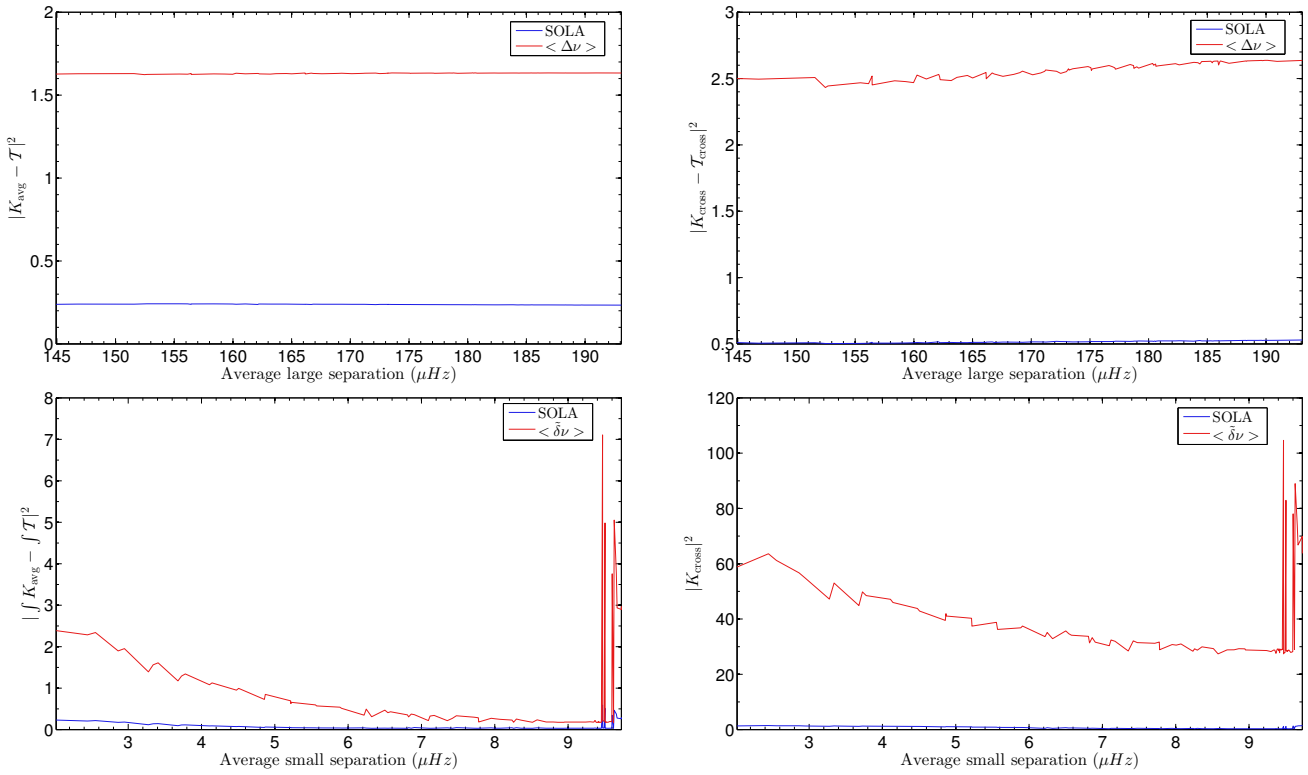

Figure 5.7: Least square fits of the kernels for model A'.

Kernels for τ, $\bar{\rho}$ and t for Model 1_{nad}

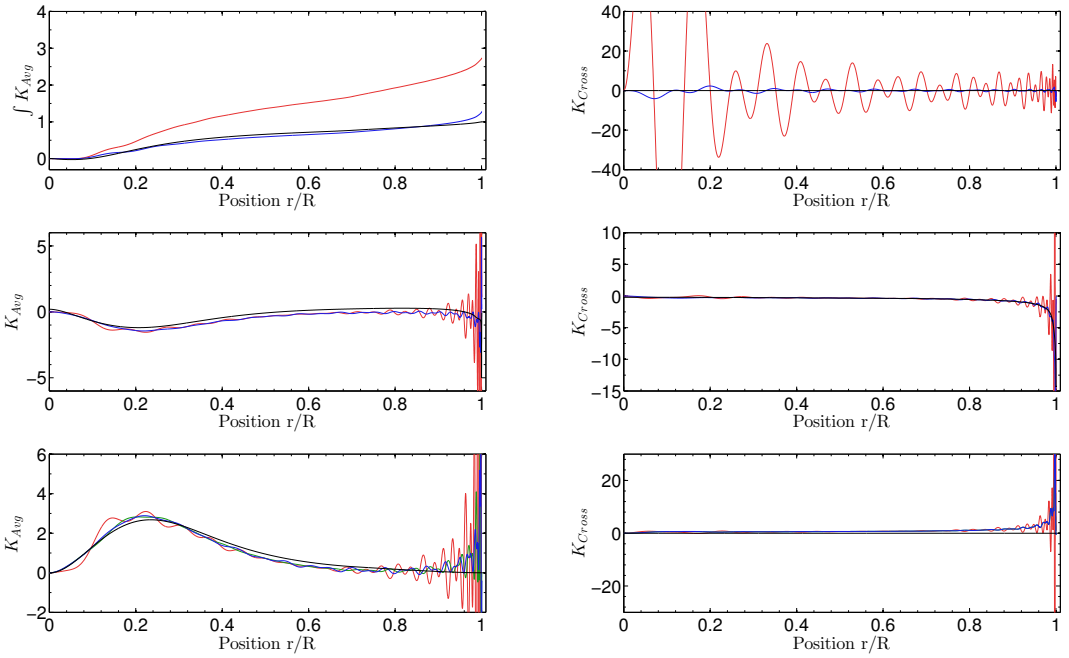

Figure 5.8: same as Fig. 5.6 for the first test case with non-adiabatic frequencies.

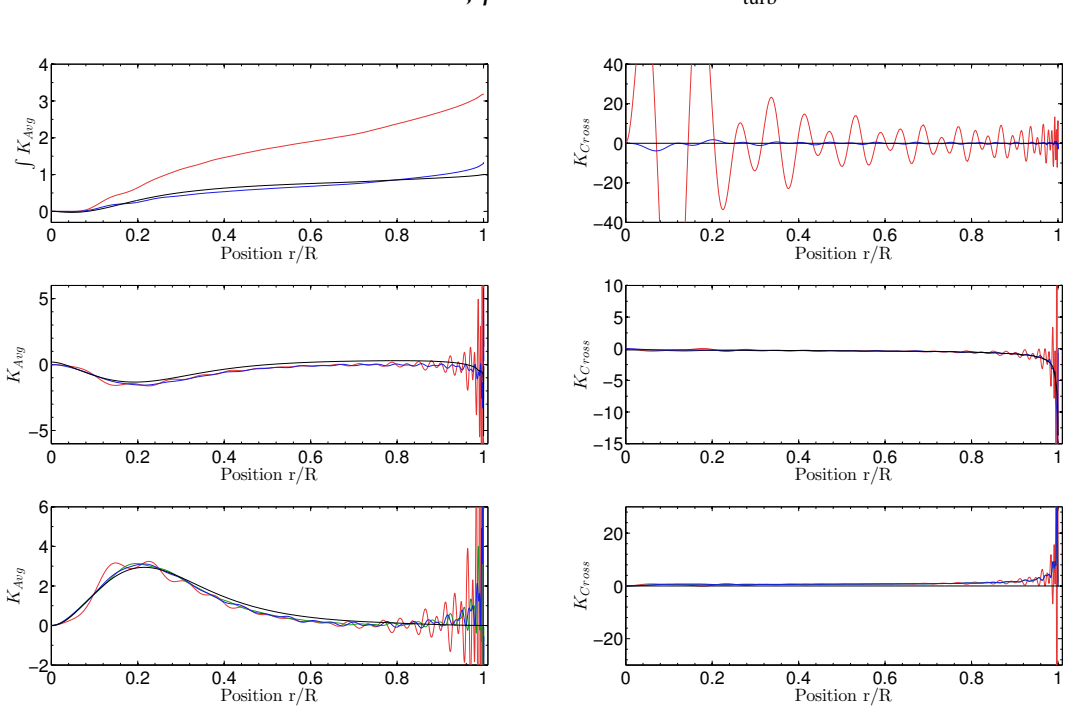

Figure 5.9: Same as Fig. 5.6 for the test case with turbulent pressure.

5.3 Using seismic inversions to obtain an indicator of internal mixing processes in main-sequence solar-like stars

5.3.1 Introduction

Determining accurate and precise stellar ages is a major problem in astrophysics. These determinations are either obtained through empirical relations or model-dependent approaches. Moreover, accurate stellar ages are crucial when studying stellar evolution, when determining properties of exoplanetary systems or when characterising stellar populations in the galaxy. However, the absence of a direct observational method for measuring this quantity makes such determinations rather complicated. Age is usually related empirically to the evolutionary stage or determined through model dependent techniques like the forward asteroseismic modelling of stars. However, this model-dependence is problematic because, if a physical process is not taken into account during the modelling, it will introduce a bias when determining the age, as well as in the determination of other fundamental characteristics like the mass or the radius (see, for example, Eggenberger, Meynet, et al. (2010) for the impact of rotation on asteroseismic properties, and Miglio, Girardi, et al. (2015), for a discussion in the context of ensemble asteroseismology, and T. M. Brown, Christensen-Dalsgaard, Weibel-Mihalas, et al. (1994), for a comprehensive study of the relation between seismic constraints and stellar model parameters). It is also clear that asteroseismology probes the evolutionary stage of stars and not the age directly. In other words, we are able to analyse the stellar physical conditions but relating these properties to an age will, ultimately, always depend on assumptions made during the building of the evolutionary sequence of the model. A general review of the impact of the hypotheses of stellar modelling and of asteroseismic constraints on the determination of stellar ages is presented in Lebreton, Goupil, and Montalbán (2014a) and Lebreton, Goupil,

and Montalbán (2014b).

In the sense of this age determination issue, the question of additional mixing processes is central (M.-A. Dupret (2008)) and can only be solved by using less model dependent seismic analysis techniques and new generations of stellar models. These new seismic methods should be able to provide relevant constraints on the physical conditions in the central regions and help with the inclusion of additional mixing in the models. In this context, seismic inversion techniques are an interesting way to relate structural differences to frequency differences and therefore offer a new insight into the physical conditions inside observed stars. From the observational point of view, the high quality of the Kepler and CoRoT data as well as the selection of the Plato mission (Rauer et al. (2014)) allows us to expect enough observational data to carry out inversions of global characteristics. In the context of helioseismology, structural inversion techniques have already led to noteworthy successes. They have provided strong constraints on solar atomic diffusion (see Basu, Christensen-Dalsgaard, Schou, et al. (1996)), thus confirming the work of Elsworth et al. (1990). However, application of structural inversion techniques in asteroseismology is still limited. Inversions for rotation profiles have been carried out (see Deheuvels, Doğan, et al. (2014) for example for an application to Kepler subgiants), but as far as structural inversions are concerned, one can use either non-linear cite see for an example of the differential response technique (I. W. Roxburgh (2010), I. W. Roxburgh (2015b)), or linear inversion techniques applied to integrated quantities as in D. R. Reese, Marques, et al. (2012) and Buldgen, D. R. Reese, M. A. Dupret, and Samadi (2015).

In our previous paper (see Buldgen, D. R. Reese, M. A. Dupret, and Samadi (2015)), we extended mean density inversions based on the SOLA technique (D. R. Reese, Marques, et al. (2012)) to inversions of the acoustic radius of the star and an indicator of core conditions, denoted t. We also developed a general approach to determining custom-made global characteristics for an observed star. We showed that applying the SOLA inversion technique (Pijpers and Thompson (1994)) to a carefully selected reference model, obtained via the forward-modelling technique, could lead to very accurate results. However, it was then clear that the first age indicator was limited to rather young stars and that other indicators should be developed. Moreover, the model dependence of these techniques should be carefully studied and there is a need to define a more extended theoretical background for these methods. The influence of the number but also the type of modes used for a specific inversion should be investigated. In the end, one should be able to define whether the inversion should be carried out or not, knowing the number of observed frequencies and the quality of the reference model according to its selection criteria.

In this study, we offer an answer to these questions and provide a new indicator for the mixing processes and the evolutionary stage of an observed star. We structure our study as follows: Section 5.3.2 introduces a technique to obtain equations for new structural kernels in the context of asteroseismology and applies it to the (u,Γ_1) and the (u,Y) kernels, where u is the squared isothermal sound speed, Γ_1 the adiabatic gradient and Y the current helium abundance profile. Section 5.3.3 introduces a new indicator of mixing processes and evolutionary stages, which is not restricted to young stars, as was the case for the indicator presented in Buldgen, D. R. Reese, M. A. Dupret, and Samadi (2015). Having introduced this new indicator, we test its accuracy using different physical effects such as including atomic diffusion processes with high velocities (up to 2.0 times the solar microscopic diffusion velocities) in the target, changing the helium abundance, changing the

metallicity and changing the solar mixture of heavy elements. Section 5.3.4 analyses the impact of the type and number of modes on the inversion results whereas Section 5.3.5 studies how the accuracy depends on the reference model. We also tested our method on targets similar to the binary system 16CygA and 16CygB using the same modes as those observed in Verma, Faria, et al. (2014) to show that our method is indeed applicable to current observational data. Section 5.3.6 summarises our results and presents some prospects on future research for global quantities that could be obtained with the SOLA inversion technique.

5.3.2 (u,Γ_1) and (u,Y) structural kernels

Integral equations for structural couples in the asteroseismic context

In D. O. Gough and Thompson (1991), it is demonstrated that one could deduce a linear integral relation between the perturbations of frequencies and the perturbation of structural variables from the variational principle. This equation is obtained by assuming the adiabatic approximation and spherical symmetry, and by neglecting surface integral terms. It is only valid if the stellar models are close to each other. If one is working with the structural pair (c^2,ρ), where c^2 is the adiabatic squared sound velocity and ρ the density, this relation takes on the form:

$$\frac{\delta\nu_i}{\nu_i} = \int_0^1 K^i_{\rho,c^2}\frac{\delta\rho}{\rho}dx + \int_0^1 K^i_{c^2,\rho}\frac{\delta c^2}{c^2}dx + \frac{\mathscr{G}(\nu)}{Q_i} + \mathscr{O}(2), \tag{5.46}$$

where $x = \frac{r}{R}$ with R the stellar radius, and where the classical definition of the relative differences between the target and model for any structural quantity s has been used:

$$\frac{\delta s(x)}{s} = \frac{s_{\text{obs}}(x) - s_{\text{ref}}(x)}{s_{\text{ref}}}. \tag{5.47}$$

In what follows, we always use the subscript or superscript "obs" when referring to the observed star, "ref" for the reference model variables in perturbation definitions, and inv for inverted results. Other variables, like the kernel functions, which are denoted without subscripts or superscripts, are of course related to the reference model and are known in practice. Finally, one should also note that the suffix i is only meant to be an index to classify the modes. Moreover, since it is clear that some hypotheses are not suitable for surface regions, a supplementary function, $\mathscr{G}(\nu)$ was added to model these so-called surface effects. It is defined as a linear combination of Legendre polynomials, normalised by the factor Q_i, which is the mode inertia normalised by the inertia of a radial mode interpolated to the same frequency. We emphasise here that neither this normalisation coefficient nor the treatment of surface effects are uniquely defined and that other techniques have also been used (see Dziembowski, Pamyatnykh, and Sienkiewicz (1990), Däppen et al. (1991), Basu et al. (1996b) for example).

The kernels of the couple (ρ,Γ_1) have already been presented in D. O. Gough and Thompson (1991) who also mentionned the use of another method, defined in Masters (1979) to modify Eq. 5.46 and obtain such relations for the (c^2,Γ_1) couple and also the (N^2,c^2) couple. Other approaches to obtaining new structural kernels were presented (see Elliott (1996), Kosovichev (1999) for example for the application of the adjoint equations method to this problem). The latter approach has been used in helioseismology where it was assumed that the mass of the observed star is known to a sufficient level of accuracy to impose surface boundary conditions. In the context of asteroseismology, we cannot make this assumption. Nevertheless, the approach defined in Masters (1979) allows us to find

ordinary differential equations for a large number of supplementary structural kernels, without assuming a fixed mass[5].

Another question arises in the context of asteroseismology: what about the radius? We implicitly define our integral equation in non-dimensional variables but how do we relate the structural functions, for example $c^2_{\rm obs}(r)$ defined for the observed star and $c^2_{\rm ref}(r)$ defined for the reference model? What are the implications of defining all functions in the same domain in $x = \frac{r}{R_{ref}}$ varying from 0 to 1? It was shown by Basu (2003) that an implicit scaling was applied by the inversion in the asteroseismic context. The observed target is homologously rescaled to the radius of the reference model, while its mean density is preserved. This means that the oscillation frequencies are the same, but other quantities such as the adiabatic sound speed c, and the squared isothermal sound speed $u = \frac{P}{\rho}$, will be rescaled. Therefore, when inverted, they are not related to the real target but to a scaled one.

This can be demonstrated with the following simple test. We can take two models a few time steps from one another on the same evolutionary sequence knowing that they should not be that different. (Here, we consider $1M_\odot$, main-sequence models.) We then test the verification of Eq. 5.46 by plotting the following relative difference

$$\mathscr{E}^i_{\rho,c^2} = \frac{\frac{\delta\nu_i}{\nu_i} - \mathscr{S}^i}{\frac{\delta\nu_i}{\nu_i}}, \tag{5.48}$$

with $\mathscr{S}^i$ defined as

$$\mathscr{S}^i = \int_0^1 \left(K^i_{\rho,c^2} \frac{\delta\rho}{\rho} + K^i_{c^2,\rho} \frac{\delta c^2}{c^2} \right) dx. \tag{5.49}$$

The results are plotted in blue in the left panel of Fig. 5.10, where we can see that this equation is not satisfied. However, one might think that this inaccuracy is related to the neglected surface terms or to non-linear effects. Therefore we carry out the same test using the (ρ,Γ_1) kernels, plotted in red in the right-hand panel of Fig. 5.10. We see that for these kernels, the equation is satisfied. Moreover, when separating the contributions of each structural term, we see that the errors arise from the term related to c^2 in the first case. Using the scaled adiabatic sound speed, however, leads to the blue symbols in the right-hand panel of Fig. 5.10 and we directly see that in this case, the integral equation is satisfied. This leads to the conclusion that inversion results based on integral equations are always related to the scaled target and not the target itself, as concluded by Basu (2003). We see in Sect. 5.3.3 that this has strong implications for the structural information given by inversion techniques.

Differential equation for the (u,Γ_1) and the (u,Y) kernels

As mentioned in the previous section, the method described in Masters (1979) allows us to derive differential equations for structural kernels. In what follows, we will apply this method to the (u,Γ_1) and the (u,Y) kernels. However, this approach can be applied to many other structural pairs such as: (c^2,Γ_1), (c^2,Y), (g,Γ_1), (g,Y), ..., with $c^2 = \frac{\Gamma_1 P}{\rho}$ the squared adiabatic sound speed , $g = \frac{Gm}{r^2}$ the local gravity, $\Gamma_1 = \left(\frac{\partial \ln T}{\partial \ln P}\right)_S$ the adiabatic

[5]The method of adjoint equations previously described could also be used but would require an additional hypothesis to replace the missing boundary condition.

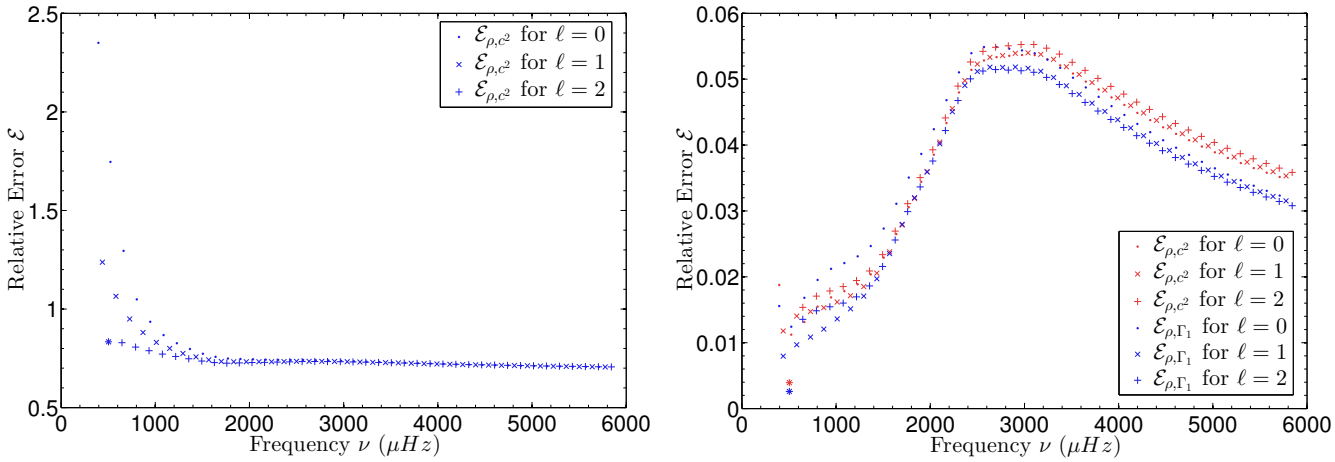

Figure 5.10: Verification of Eq. 5.46 for a set of 120 modes with the $\cdot$ being the 40 radial modes, the $\times$ being the 40 dipolar modes and the $+$ being the 40 quadrupolar modes. The left plot illustrates this verification for the (ρ, c^2) couple when no scaling is applied to c^2 whereas the right plot illustrates the same verification for the (ρ, c^2) couple when scaling is applied to c^2, as well as the (ρ, Γ_1) couple where no scaling is needed.

gradient and Y the local helium abundance. We do not describe these kernels since they are straightforward to obtain using the same technique as that which will be used here for the (u, Γ_1) kernels. One should also note that a differential equation cannot be obtained for the couple (N^2, c^2), with N^2 the Brunt-Väisälä frequency, defined as: $N^2 = g\left(\frac{1}{\Gamma_1}\frac{d\ln P}{dr} - \frac{d\ln\rho}{dr}\right)$, without neglecting a supplementary surface term.

The first step is to assume that if these kernels exist, they should satisfy an integral equation of the type given in Eq. 5.46, thereby leading to:

$$\begin{aligned}\frac{\delta\nu_i}{\nu_i} &= \int_0^1 K^i_{\rho,\Gamma_1}\frac{\delta\rho}{\rho}dx + \int_0^1 K^i_{\Gamma_1,\rho}\frac{\delta\Gamma_1}{\Gamma_1}dx,\\ &= \int_0^1 K^i_{u,\Gamma_1}\frac{\delta u}{u}dx + \int_0^1 K^i_{\Gamma_1,u}\frac{\delta\Gamma_1}{\Gamma_1}dx. \end{aligned} \tag{5.50}$$

From that point, we use the definition of u to express the first integral in terms of a density perturbation. This is done using the definition of the pressure, P, and the cumulative mass up to a radial position, r:

$$P = \int_r^R \frac{G\tilde{m}\tilde{\rho}}{\tilde{r}^2}d\tilde{r} + P_{surf}, \tag{5.51}$$

$$m = \int_0^r 4\pi\tilde{r}^2\tilde{\rho}d\tilde{r}, \tag{5.52}$$

where we neglect the pressure perturbation at the surface. In what follows, we use the non-dimensional forms $\hat{P} = \frac{PR^4}{GM^2}$, where M is the stellar mass, R the stellar radius and G the gravitational constant, $\hat{m} = \frac{m}{M}$ and $\hat{\rho} = \frac{R^3\rho}{M}$. To avoid any confusion in already rather intricate equations, we drop the hat notation in what follows and denote these non-dimensional variables P, m and ρ. Using Eqs. 5.51 and 5.52, one can relate u perturbations

to P and ρ perturbations as

$$\frac{\delta u}{u} = \frac{\delta P}{P} - \frac{\delta \rho}{\rho}. \tag{5.53}$$

However, using Eq. 5.51, one can also relate P perturbations to ρ perturbations. Doing this, one should note that the surface pressure perturbation is usually neglected and considered as a so-called surface effect. Using non-dimensional variables and combining Eqs. 5.51 and 5.52 in Eq. 5.53, one obtains an expression relating u perturbations solely to ρ perturbations. (Of course, this is an integral relation due to the definition of the hydrostatic pressure, P). One can use this relation to replace $\frac{\delta u}{u}$ in Eq. 5.50 and after the permutation of the integrals stemming from the definition of the hydrostatic pressure perturbation, one obtains the following integral equation relating K^i_{ρ,Γ_1} to K^i_{u,Γ_1}:

$$\begin{aligned}\int_0^1 K^i_{\rho,\Gamma_1}\frac{\delta\rho}{\rho}dx + \int_0^1 K^i_{\Gamma_1,\rho}\frac{\delta\Gamma_1}{\Gamma_1}dx = \int_0^1 \Bigg(&\frac{m(x)\rho}{x^2}\left[\int_0^x \frac{K^i_{u,\Gamma_1}}{\bar{P}}d\bar{x}\right] \\ &+4\pi x^2\rho\left[\int_x^1 \frac{\tilde{\rho}}{\tilde{x}^2}\left[\int_0^{\tilde{x}} \frac{K^i_{u,\Gamma_1}}{\bar{P}}d\bar{x}\right]d\tilde{x}\right] - K^i_{u,\Gamma_1}\Bigg)\frac{\delta\rho}{\rho}dx \\ &+\int_0^1 K^i_{\Gamma_1,u}\frac{\delta\Gamma_1}{\Gamma_1}dx.\end{aligned} \tag{5.54}$$

One should be careful when solving this equation since one is faced with multiple integrals, with certain equilibrium variables associated with $\tilde{x}$ or $\bar{x}$. Therefore care should be taken when integrating to check the quality of the result. To obtain a differential equation, we note that it is clear that the equation is satisfied if the integrands are equal, meaning that the kernels are related as follows:

$$K^i_{\rho,\Gamma_1} = \frac{m(x)\rho}{x^2}\left[\int_0^x \frac{K^i_{u,\Gamma_1}}{\bar{P}}d\bar{x}\right] + 4\pi x^2\rho\left[\int_x^1 \frac{\tilde{\rho}}{\tilde{x}^2}\left[\int_0^{\tilde{x}} \frac{K^i_{u,\Gamma_1}}{\bar{P}}d\bar{x}\right]d\tilde{x}\right] - K^i_{u,\Gamma_1}, \tag{5.55}$$

$$K^i_{\Gamma_1,\rho} = K^i_{\Gamma_1,u}. \tag{5.56}$$

Given this integral expression, one can simply derive and simplify the expression to obtain a second-order ordinary differential equation in x as follows:

$$\begin{aligned}-y\frac{d^2\kappa'}{(dy)^2} + \left[\frac{2\pi y^{3/2}\tilde{\rho}}{\tilde{m}} - 3\right]\frac{d\kappa'}{dy} =& y\frac{d^2\kappa}{(dy)^2} - \left[\frac{2\pi y^{3/2}\tilde{\rho}}{\tilde{m}} - 3 + \frac{\tilde{m}\tilde{\rho}}{2y^{1/2}\tilde{P}}\right]\frac{d\kappa}{dy} \\ &+\left[\frac{\tilde{m}\tilde{\rho}}{4y\tilde{P}^2}\frac{d\tilde{P}}{dx} - \frac{\tilde{m}}{4y\tilde{P}}\frac{d\tilde{\rho}}{dx} - \frac{3}{4y^{1/2}\tilde{P}}\frac{d\tilde{P}}{dx} - \frac{\tilde{m}\tilde{\rho}}{2y^{3/2}\tilde{P}}\right]\kappa,\end{aligned} \tag{5.57}$$

where $\kappa = \frac{K^i_{u,\Gamma_1}}{x^2\rho}$, $\kappa' = \frac{K^i_{\rho,\Gamma_1}}{x^2\rho}$ and $y = x^2$. The central boundary condition in terms of κ and κ' is obtained by taking the limit of Eq. 5.57 as y goes to 0. The additional boundary conditions are obtained from Eq. 5.55. Namely, we impose that the solution satisfies Eq. 5.55 at some point of the domain. This system is then discretised using a finite difference scheme based on D. R. Reese (2013), and solved using a direct band-matrix solver.

Two quality checks can be made to validate our solution, the first being that every kernel satisfies Eq. 5.55, the second being that they satisfy a frequency-structure relation

(as in Eq. 5.50) within the same accuracy as the classical structural kernels (ρ,Γ_1) or (ρ,c^2). We can carry out the same analysis as in section 5.3.2, keeping in mind that the squared isothermal sound speed will also be implicitly rescaled by the inversion since it is proportional to $\frac{M}{R}$, as is the squared adiabatic sound speed, c^2. The results of this test are plotted in Fig. 5.11 along with an example of the verification of the integral equation for the kernel associated with the $\ell=0$, $n=15$ mode.

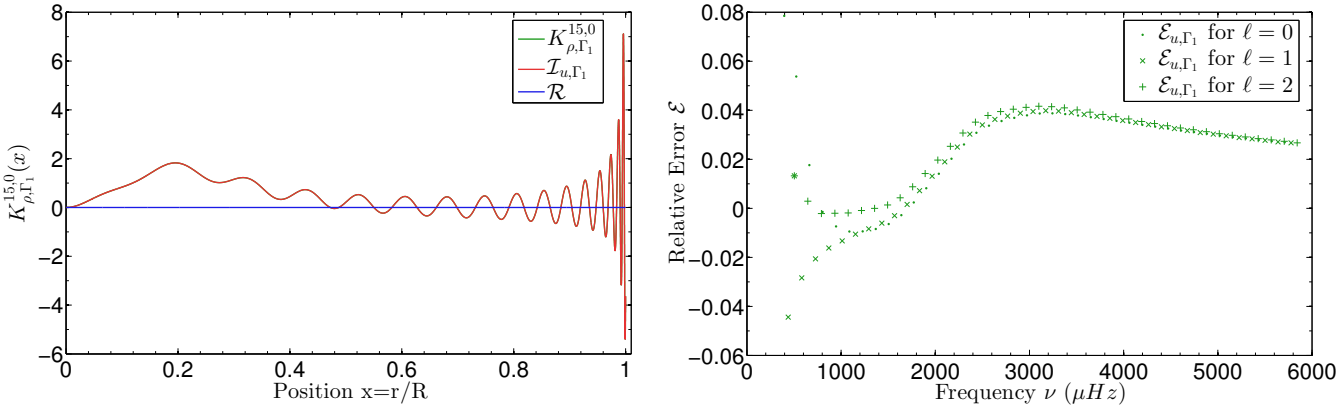

Figure 5.11: (left) Plot illustrating the verification of Eq. 5.55 for $n=15$, $\ell=0$ kernel $K^{15,0}$, where $\mathscr{I}_{u,\Gamma_1}$ is the right-hand side of this equation and $\mathscr{R}$ is the residual. (right) Same test as in Fig. 5.10 for the (u,Γ_1) kernels.

The equation for the (u,Y) kernels is identical when using the following relation:

$$\begin{aligned}\frac{\delta\nu_i}{\nu_i} &= \int_0^1 K^i_{\rho,Y}\frac{\delta\rho}{\rho}dx+\int_0^1 K^i_{Y,\rho}\delta Y dx,\\ &= \int_0^1 K^i_{u,Y}\frac{\delta u}{u}dx+\int_0^1 K^i_{Y,u}\delta Y dx.\end{aligned} \tag{5.58}$$

meaning that Eq. 5.57 can simply be transposed using the definitions: $\kappa=\frac{K^i_{u,Y}}{x^2\rho}$ and $\kappa'=\frac{K^i_{\rho,Y}}{x^2\rho}$. One could also start from Eq. 5.50, use the definition:

$$\begin{aligned}\frac{\delta\Gamma_1}{\Gamma_1} &= \left(\frac{\partial ln(\Gamma_1)}{\partial ln(P)}\right)_{Z,Y,\rho}\frac{\delta P}{P}+\left(\frac{\partial ln(\Gamma_1)}{\partial ln(\rho)}\right)_{Z,Y,P}\frac{\delta\rho}{\rho}+\left(\frac{\partial ln(\Gamma_1)}{\partial Y}\right)_{Z,P,\rho}\delta Y\\ &+\left(\frac{\partial ln(\Gamma_1)}{\partial Z}\right)_{Y,P,\rho}\delta Z,\end{aligned} \tag{5.59}$$

and neglect the δZ contribution. This assumption is particularly justified if one places spectroscopic constraints on the metallicity. Nevertheless, the term associated with δZ is smaller than the three other terms and if one is probing the core regions, the $\frac{\delta\Gamma_1}{\Gamma_1}$ contribution is already very small. Consequently, all of the terms of Eq. 5.59 are small compared to the integral contribution. Still, this assumption is not completely sound if one wishes to probe surface regions. When comparing the $\left(\frac{\partial ln(\Gamma_1)}{\partial Z}\right)_{Y,P,\rho}$ to the $\left(\frac{\partial ln(\Gamma_1)}{\partial Y}\right)_{Z,P,\rho}\delta Y$, we notice that their amplitude is comparable and that $\left(\frac{\partial ln(\Gamma_1)}{\partial Z}\right)_{Y,P,\rho}$ is even often larger. However, we have to consider that it will be multiplied by δZ, which is much smaller than δY. Moreover, the functions are somewhat alike in central regions and, as a consequence,

there will be an implicit partial damping of the δZ term when damping the δY contribution if it is in the cross-term of the inversion. We can control the importance of this assumption by switching from the (u,Y) kernels to the (u,Γ_1) kernels. Indeed, if the error is large, the inversion result will be changed by the contribution from the neglected term. In conclusion, in the case of the inversion of t_u, we present and use in the next sections, this assumption is justified, but this is not certain for inversions of helium mass fraction in upper layers, for which only numerical tests for the chosen indicator will provide a definitive answer.

Knowing these facts, we can search for the (u,Y) kernels using the previous developments. It is in fact straightforward when using the (ρ,Y) kernels, which are directly obtained from (ρ,Γ_1) or (ρ,c^2). However, one should also note that by using Eq. 5.59, we assume that the equation of state is known for the target which might introduce small errors[6]. Again, Fig. 5.12 illustrates the tests of our solutions by plotting the errors on the integral equation (Eq. 5.58), and by seeing how well our solution for the $\ell=0$, $n=15$ mode verifies Eq. 5.55. The (u,Γ_1) and (u,Y) kernels of this particular mode are illustrated in figure 5.13. The kernels associated with u are very similar, except for the surface regions where some differences can be seen.

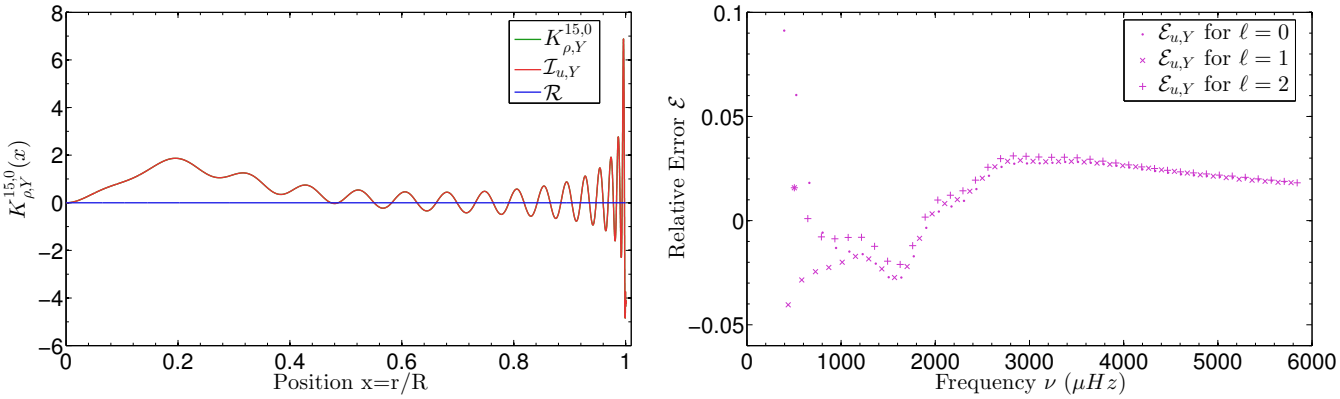

Figure 5.12: Same as Fig. 5.11 for the (u,Y) kernels.

5.3.3 Indicator for internal mixing processes and evolutionary stage based on the variations of u

Definition of the target function and link to the evolutionary effect

Knowing that it is possible to obtain the helium abundance in the integral Eq.5.58, we could be tempted to use it to obtain corrections on the helium abundance in the core and thereby gain insights into the chemical evolution directly. However, Fig. 5.13 reminds us of the hard reality associated with these helium kernels. Their intensity is only non-negligible in surface regions, making it impossible to obtain information on the core helium abundance using them.

Another approach would be to use the squared isothermal sound speed, u, to reach our goal. Indeed, we know that $u=\frac{P}{\rho}\propto\frac{T}{\mu}$, and that during the evolution along the main sequence, the mean molecular weight will change. Moreover the core contraction can also lead to changes in the variation of the u profile. Using the same philosophy as for the

[6]However, these can be neglected when compared to other uncertainties on the structural properties of observed stars.

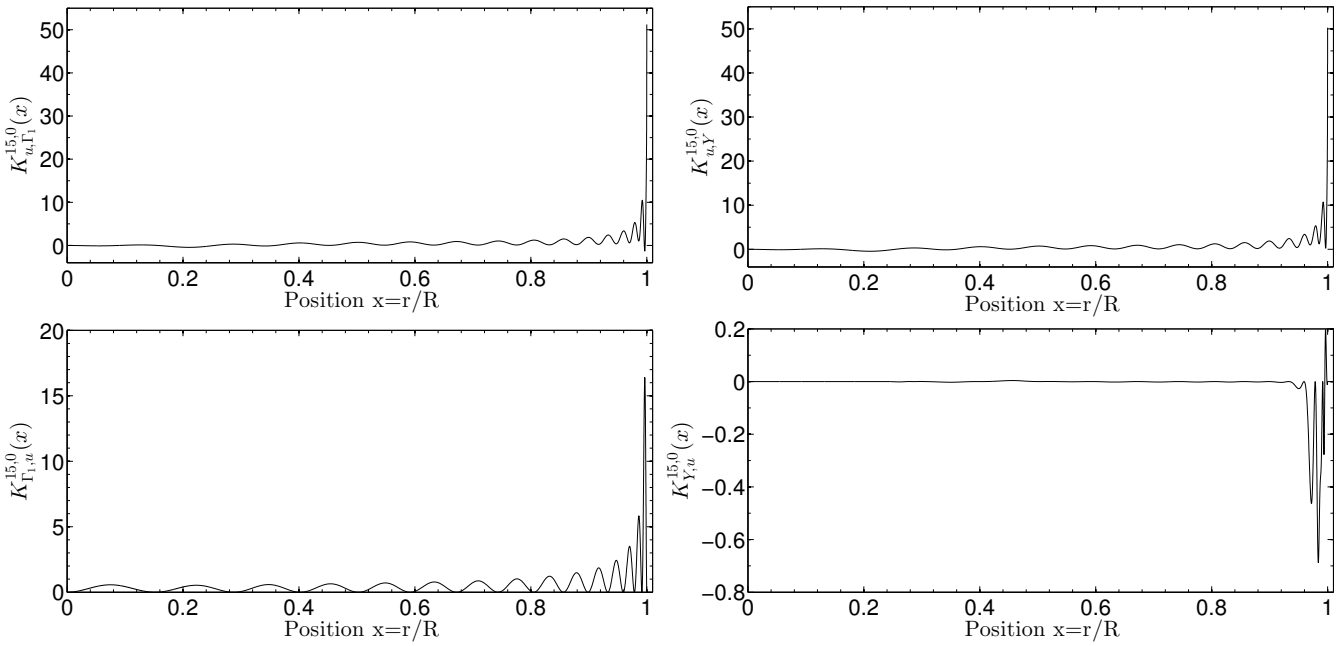

Figure 5.13: Structural kernels for the $n = 15$, $\ell = 0$ mode associated with the (u,Γ_1) couple on the left hand side and with the (u,Y) couple on the right hand side.

definition of the first age indicator (see Buldgen, D. R. Reese, M. A. Dupret, and Samadi (2015)) and ultimately for the use of the small separation as an indicator of the core conditions (see Tassoul (1980)), we build our indicator using the first radial derivative of u. Using u instead of c^2 allows us to avoid the dependence in Γ_1 which is responsible for the surface dependence of $\frac{dc}{dr}$. To build our indicator, we analyse the effect of the evolution on the profile of $\frac{du}{dr}$. This effect is illustrated in Fig. 5.14. As can be seen, two lobes tend to develop as the star ages. The first problem is that these variations have opposite signs, meaning that if we integrate through both lobes, the sensitivity will be greatly reduced. Therefore, we choose to base our indicator on the squared first radial derivative:

$$\bar{t}_u = \int_0^R f(r) \left(\frac{du}{dr}\right)^2 dr, \tag{5.60}$$

where $f(r)$ is an appropriate weight function. First, we consider that the observed star and the reference model have the same radius. The target function for this indicator can easily be obtained. We perturb the equation for t_u and use an integration by parts to relate the perturbations of the indicator to structural perturbations of u:

$$\begin{aligned}\frac{\delta\bar{t}_u}{\bar{t}_u} &= \frac{2}{\bar{t}_u}\int_0^R f(r)\frac{du}{dr}\frac{d\delta u}{dr}dr, \\ &= \frac{-2}{\bar{t}_u}\int_0^R u\frac{d}{dr}\left(f(r)\frac{du}{dr}\right)\frac{\delta u}{u}dr + \left[f(r)\frac{du}{dr}\delta u\right]_0^R.\end{aligned} \tag{5.61}$$

The last term on the second line is not suitable for SOLA inversions, given the neglect of surface terms in the kernels. We thus define the function f so that $f(0) = f(R) = 0$, thereby cancelling this term. This leads to the following expression:

$$\frac{\delta\bar{t}_u}{\bar{t}_u} = \int_0^R \mathscr{T}_{t_u}\frac{\delta u}{u}dr, \tag{5.62}$$

where

$$\mathscr{T}_{t_u} = \frac{-2u}{\bar{t}_u}\frac{d}{dr}\left(f(r)\frac{du}{dr}\right). \tag{5.63}$$

The weight function $f(r)$ must be chosen according to a number of criteria: it has to be sensitive to the core regions where the profile changes; it has to have a low amplitude at the boundaries of the domain, allowing us to do the integration by parts necessary for obtaining δu in the expression; and it should be possible to fit the target function associated with this $f(r)$ using structural kernels from a restricted number of frequencies. Moreover, Eq. (5.63) being related to linear perturbations, it is clear that non-linear effects should not dominate the changes of this indicator[7]. We also know that the amplitude of the structural kernels is 0 in the centre, so $f(r)$ should also satisfy this condition.

We define the weight function as:

$$f(r) = r^{\alpha}\,(r-R)^{\lambda}\exp\left(-\gamma\left(\frac{r-r_{opt}}{R}\right)^2\right), \tag{5.64}$$

which means that we have four parameters to adjust. The case of r_{opt} is quickly treated. Since we know that the changes will be localised in the lobes developing in the core regions, we chose to put $r_{opt} = 0$, and α and λ should be at least 1, so that the integration by part is exact and the central limit for the target function and the structural kernels is the same. Gamma depends on the effects of the non-linearities. However, since we have to perform a second derivative of u a more practical concern appears: we do not want to be influenced by the effects of the discontinuity at the boundary of the convective envelope. Ultimately, we use the following set of parameters: $\alpha = 1$, $\lambda = 2$, $\gamma = 7$, and $r_{opt} = 0$. One could argue that the optimal choice for r_{opt} would be either at the maximum of the second lobe or between both lobes to obtain the maximal sensitivity in the structural variations. These values were also tested, but the results were a little less accurate than using $r_{opt} = 0$ and they involved higher inversion coefficients and, hence, higher error magnification. We illustrate the weighted profile obtained for this optimal set of parameters in the right-hand side panel of Fig. 5.14. Furthermore, Eq. 5.62 is satisfied up to 5%, so we can try to carry out inversions for this indicator. It is also important to note that for the sake of simplicity, we do not choose to change the values of these parameters with the model, which would only bring additional complexity to the problem.

Because of the target function $\mathscr{T}_{t_u}$, we can now carry out inversions for the integrated quantity t_u using the linear SOLA inversion technique (Pijpers and Thompson (1994)). But first, we should recall the purpose of inversions and our adaptation of the SOLA technique to integrated quantities. Historically, inversions have been used to obtain seismically constrained structural profiles (Basu, Christensen-Dalsgaard, Schou, et al. (1996)) as well as rotational profiles (Schou, Christensen-Dalsgaard, and Thompson (1994)) in helioseismology. However, none of these methods are suited for the inversions we wish to carry here. As discussed in Buldgen, D. R. Reese, M. A. Dupret, and Samadi (2015), the SOLA inversion technique, which uses a so-called kernel-matching approach is well suited to our purpose. Indeed, this approach allows us to define custom-made target functions that will be used

[7] Otherwise, using the SOLA technique, which is linear, would be impossible.

to build a cost function, here denoted $\mathscr{J}$. In the case of the t_u quantity, one has the definition

$$\mathscr{J}_{t_u} = \int_0^1 \left[K_{\text{Avg}} - \mathscr{T}_{t_u}\right]^2 dx + \beta \int_0^1 K_{\text{Cross}}^2 dx + \tan(\theta) \sum_i^N (c_i \sigma_i)^2 + \eta \left[\sum_i^N c_i - k\right], \tag{5.65}$$

where K_{Avg} is the so-called averaging kernel and K_{Cross} is the so-called cross-term kernel defined as follows for the (u,Γ_1) structural pair (for (u,Y), replace K^i_{u,Γ_1} by $K^i_{u,Y}$ and $K^i_{\Gamma_1,u}$ by $K^i_{Y,u}$):

$$K_{\text{Avg}} = \sum_i^N c_i K^i_{u,\Gamma_1}, \tag{5.66}$$

$$K_{\text{Cross}} = \sum_i^N c_i K^i_{\Gamma_1,u}. \tag{5.67}$$

The symbols θ and β are free parameters of the inversion. Here, θ is related to the compromise between the amplification of the observational error bars (σ_i) and the fit of the kernels, whereas β is allowed to vary to give more weight to the elimination of the cross-term kernel. In this expression, N is the number of observed frequencies, the c_i are the inversion coefficients, used to determine the correction that will be applied on the t_u value. Eta is a Lagrange multiplier and the last term appearing in the expression of the cost-function is a supplementary constraint applied to the inversion that is presented in Sect. 5.3.3.

If the observed target and the reference model have the same radius, the inversion will measure the value of t_u for the observed target. However, if this condition is not met, the inversion will produce a scaled value of this indicator. By defining integral equations such as Eq. 5.60, or even Eq. 5.46, we have seen in Sect. 5.3.2 that we made the hypothesis that both the target and the reference model had the same radius. However, because the frequencies scale with $\left(\frac{M}{R^3}\right)^{1/2}$, the inversion will preserve the mean density of the observed target. Therefore, we are implicitly carrying out the inversion for a scaled target homologous to the observed target, which has the radius of the reference model but the mean density of the observed target. Simple reasoning demonstrates that the mass of this scaled target is: $\bar{M}_{tar} = M_{tar}\frac{R^3_{ref}}{R^3_{tar}}$. Thus, because t_u scales as M^2, there is a difference between the target value t_u^{obs} and the measured value, t_u^{inv}. Consequently, we can write the following equations:

$$\frac{t_u^{inv}}{\bar{M}^2_{tar}} = \frac{t_u^{obs}}{M^2_{tar}}, \tag{5.68}$$

$$\frac{t_u^{inv}}{R^6_{ref}} = \frac{t_u^{obs}}{R^6_{tar}}, \tag{5.69}$$

where we have used the definition of $\bar{M}_{tar}$ to express the mass dependencies as radius dependencies. Therefore, we use Eq. 5.69 as a criterion to determine whether the inversion was successful or not.

Non-linear generalisation

This section presents a general approach to the non-linear generalisation presented in D. R. Reese, Marques, et al. (2012) and Buldgen, D. R. Reese, M. A. Dupret, and Samadi

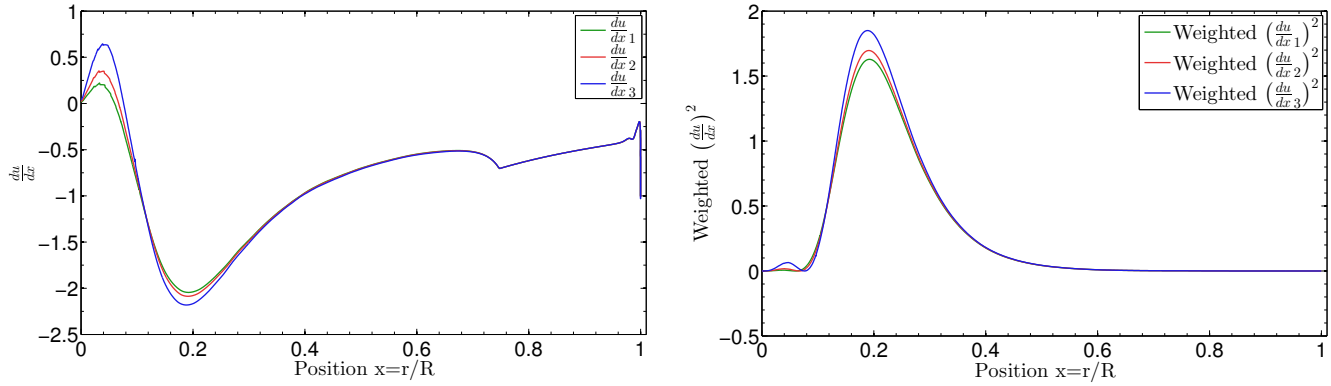

Figure 5.14: Left panel: structural changes in the scaled $\frac{du}{dx}$ profile with the evolution. The models are main sequence $1.0M_\odot$ models. Right panel: the same effects as seen when $\left(\frac{du}{dx}\right)^2$ is weighted according to Eq. 5.64.

(2015) for any type of global characteristic that can scale with the mass of the star. It is obvious that we can say that the frequencies scale as $M^{1/2}$. Of course, they scale as the mean density, namely $\sqrt{\frac{M}{R^3}}$. However, since the inversion works with a fixed radius and implicitly scales the target to the same radius as the reference model, the iterative process associated with this non-linear generalisation will never change the model radius. Therefore, we do not take this dependence into account and simply work on the mass dependence. We let A be a global characteristic, related to the mass of the star. It is always possible to define a factor k so that:

$$A \propto \nu^k. \tag{5.70}$$

And we directly obtain:

$$\frac{\delta A}{A} = k\frac{\delta \nu}{\nu}. \tag{5.71}$$

However, using the definition of the inverted correction of A, one has:

$$\frac{\delta A}{A} = \sum_i c_i \frac{\delta \nu_i}{\nu_i}, \tag{5.72}$$

where c_i are the inversion coefficients. Using the same reasoning as in Buldgen, D. R. Reese, M. A. Dupret, and Samadi (2015) and D. R. Reese, Marques, et al. (2012), we define the inversion as "unbiased" (a term that should not be taken in the statistical sense.) if it satisfies the condition

$$\sum_i c_i = k. \tag{5.73}$$

Now we can define an iterative process using the scale factor $s_0^k = \frac{A_{\mathrm{inv},0}}{A_{\mathrm{ref}}}$. We scale the reference model (in other words, multiply its mass and density by s^2, its pressure by s^4, leaving Γ_1 unchanged), carry out a second inversion, then define a new scale factor and so on until no further correction is made by the inversion process. In other words, we

search for the fixed point of the equation of the scale factor. At the j^{th} iteration, we obtain the following equation for the inversion value of A:

$$A_{\rm inv} = A_{\rm ref} s_j^{k-1} \left[s_j + \sum_i c_i \frac{\delta \nu_i}{\nu_i} + k(1-s_j) \right]. \tag{5.74}$$

This can be written in terms of the scale factor alone, noting that at the j^{th} iteration, $\frac{A_{inv}}{A_{ref}} = s_{j+1}^k$:

$$s_{j+1}^k = s_j^{k-1} \left[s_j + \sum_i c_i \frac{\delta \nu_i}{\nu_i} + k(1-s_j) \right]. \tag{5.75}$$

The fixed point is then obtained,

$$s_{\rm opt} = \frac{\sum_i c_i \frac{\delta \nu_i}{\nu_i}}{k} + 1, \tag{5.76}$$

and can be used directly to obtain the optimal value of the indicator A. We can also carry out a general analysis of the error bars treating the observed frequencies and $A_{\rm inv}$ as stochastic variables:

$$\nu_{{\rm obs},i} = \bar{\nu}_{{\rm obs},i}(1+\varepsilon_i), \tag{5.77}$$

$$A_{\rm inv} = \bar{A}_{\rm inv}(1+\varepsilon_A), \tag{5.78}$$

with ε_i and ε_A being the stochastic contributions to the variables. Using the hypothesis that $\varepsilon_i \ll 1$ we obtain the following equation for the error bars:

$$\sigma_A = A_{ref} \left[\frac{1}{k} \sum_i c_i \frac{\nu_i^{\rm obs}}{\nu_i^{\rm ref}} \right]^{k-1} \sqrt{(\sum_i c_i \sigma_i)^2}. \tag{5.79}$$

We note that in the particular case of the indicator t_u, $k = 4$. Indeed, $t_u \propto M^2$ whereas $\nu \propto M^{1/2}$.

Tests using various physical effects

To test the accuracy of the SOLA technique applied to the t_u indicator, we carried out the same test as in Buldgen, D. R. Reese, M. A. Dupret, and Samadi (2015) using stellar models that would play the role of observed targets. These models included physical phenomena not taken into account in the reference models. A total of 13 targets were constructed, with masses of 0.9 $M_\odot$, 1.0 $M_\odot$ and 1.1 $M_\odot$ but to avoid redundancy, we only present six that are representative of the mass and age ranges and of the physical effects considered in our study. We tested various effects for each mass. These effects fell into the following categories: those that come from microscopic diffusion using the approach presented in Thoul, Bahcall, and Loeb (1994) (multiplying the atomic diffusion coefficients by a factor given in the last line of Table 5.11[8]), those caused by a helium abundance mismatch, those that result from a metallicity mismatch, and those that stem from using a different solar heavy-element mixture. For the last case, the target was built using the GN93 abundances (Grevesse and Noels (1993)) and the reference model was built

[8]These values might seem excessive regarding the reliability of the implementation of diffusion. We stress here that our goal was to witness the impact of significant changes on the results. However, other processes or mismatches could alter the $\frac{du}{dr}$ gradient and thus be detected by the inversion.

using the AGSS09 abundances (Asplund, Grevesse, Sauval, and Scott (2009)).

All targets and reference models were built using version 18.15 of the Code Liégeois d'Evolution Stellaire (CLES) stellar evolution code (Scuflaire, Théado, et al. (2008)) and their oscillations frequencies were calculated using the Liège oscillation code (LOSC, Scuflaire, Montalbán, et al. (2008)). Table 5.11 summarises the properties of the six targets presented in this section. The selection of the reference model was based on the fit

Table 5.11: Characteristics of the 6 targets.

	Target$_1$	**Target**$_2$	**Target** $_3$	**Target**$_4$	**Target**$_5$	**Target**$_6$
Mass ($M_\odot$)	1.0	1.0	1.0	0.9	1.0	1.1
Radius ($R_\odot$)	1.076	1.159	1.14	0.89	1.193	1.297
Age (Gyr)	8.05	7.55	7.06	6.0	5.121	5.135
$T_{\rm eff}$ (K)	5597	5884	5712	5329	6081	5967
Z_0	**0.015**	0.0122	0.0122	0.0122	0.0122	0.0122
Y_0	0.2457	0.2485	0.2485	0.2485	**0.3078**	0.2485
Abundances	AGSS09	**GN**93	AGSS09	AGSS09	AGSS09	AGSS09
$\alpha_{\rm MLT}$	1.522	1.522	1.522	1.522	1.522	1.522
Diffusion factor	0	0	**2**	**1.6**	0	**1.6**

Note: Differences between target and reference model in bold.

of the large and small separation for 60 modes with $n = 7-26$ and $\ell = 0-2$ using a Levenberg-Marquardt minimisation code. The use of supplementary constraints will be discussed in Sect. 5.3.5 whereas the effects of the selection of the modes will be discussed in Sect. 5.3.4. The choice of 60 frequencies is motivated by the number of observed frequencies for the system 16Cyg *A* - 16Cyg *B* by Kepler, which is between 50 and 60 (Verma, Faria, et al. (2014)). The inversions were carried out using the (u, Y) and the (u, Γ_1) structural kernels.

If the inversion of t_u shows that there are differences between the target and the reference model, then we know that the core regions are not properly represented. Whether these differences arise from atomic diffusion or a helium abundance mismatch, the t_u indicator alone could not answer this question[9]. Therefore, the philosophy we adopt in this section is the following: Is the inversion able to correct mistakes in the reference models? If so, within what range of accuracy?. The capacity of disentangling different effects is partially illustrated in Sect. 5.3.5, but additional indicators are still required to provide the best diagnostic possible given a set of frequencies.

The results are given in Table 5.12 for the (u, Γ_1) kernels and Table 5.13 for the (u, Y) kernels along with the respective error contributions given according to the developments of D. R. Reese, Marques, et al. (2012) and Buldgen, D. R. Reese, M. A. Dupret, and Samadi (2015). We denote these error contributions: $\varepsilon_{\rm Avg}$, $\varepsilon_{\rm Cross}$, $\varepsilon_{\rm Res}$. These errors contributions

[9] To completely constrain the changes that are a consequence of multiple additional mixing processes with only one structural indicator is of course impossible.

are defined as

$$\varepsilon_{\text{Avg}} = \int_0^1 \left[K_{\text{Avg}} - \mathscr{T}_{t_u}\right] \frac{\delta u}{u} dx, \tag{5.80}$$

$$\varepsilon_{\text{Cross}} = \int_0^1 K_{\text{Cross}} \frac{\delta \Gamma_1}{\Gamma_1} dx, \tag{5.81}$$

if the (u,Γ_1) couple is used. If one prefers the (u,Y), $\varepsilon_{\text{Cross}}$ becomes

$$\varepsilon_{\text{Cross}} = \int_0^1 K_{\text{Cross}} \delta Y dx. \tag{5.82}$$

Finally, ε_{Res} is associated with the residual contribution, in the sense that it is what remains after one has taken into account both $\varepsilon_{\text{Cross}}$ and ε_{Avg}. The target function and their fits are illustrated in Fig. 5.15 for Target_4. As we can see from Tables 5.12 and 5.13, we obtain

Table 5.12: Inversion results for the 6 targets using the (u,Γ_1) kernels.

	$\frac{t_u^{\text{ref}}}{G^2R_{ref}^6}$ (g^2/cm^6)	$\frac{t_u^{\text{inv}}}{G^2R_{ref}^6}$ (g^2/cm^6) (u,Γ_1)	$\frac{t_u^{\text{obs}}}{G^2R_{tar}^6}$ (g^2/cm^6)	$\varepsilon_{\text{Avg}}^{u,\Gamma_1}$	$\varepsilon_{\text{Cross}}^{u,\Gamma_1}$	$\varepsilon_{\text{Res}}^{u,\Gamma_1}$
Target_1	4.032	3.568 ± 0.063	3.532	4.415×10^{-4}	-1.684×10^{-4}	9.767×10^{-3}
Target_2	3.434	3.24 ± 0.075	3.428	-1.301×10^{-3}	-4.419×10^{-4}	5.951×10^{-4}
Target_3	3.562	3.275 ± 0.067	3.252	5.789×10^{-3}	-1.178×10^{-3}	2.277×10^{-3}
Target_4	5.879	5.621 ± 0.147	5.536	1.388×10^{-2}	3.088×10^{-4}	8.062×10^{-4}
Target_5	2.845	2.669 ± 0.088	2.630	-6.498×10^{-4}	-4.493×10^{-3}	2.366×10^{-4}
Target_6	3.205	3.480 ± 0.091	3.498	1.496×10^{-2}	-1.11×10^{-3}	7.824×10^{-4}

Table 5.13: Inversion results for the 6 targets using the (u,Y) kernels.

	$\frac{t_u^{\text{ref}}}{G^2R_{ref}^6}$ (g^2/cm^6)	$\frac{t_u^{\text{inv}}}{G^2R_{ref}^6}$ (g^2/cm^6) (u,Y)	$\frac{t_u^{\text{obs}}}{G^2R_{tar}^6}$ (g^2/cm^6)	$\varepsilon_{\text{Avg}}^{u,Y}$	$\varepsilon_{\text{Cross}}^{u,Y}$	$\varepsilon_{\text{Res}}^{u,Y}$
Target_1	4.032	3.575 ± 0.063	3.532	8.34×10^{-4}	1.601×10^{-4}	1.1×10^{-2}
Target_2	3.434	3.423 ± 0.075	3.428	-1.301×10^{-3}	1.338×10^{-7}	2.127×10^{-5}
Target_3	3.562	3.283 ± 0.067	3.252	5.748×10^{-3}	8.296×10^{-3}	-4.794×10^{-3}
Target_4	5.879	5.624 ± 0.148	5.536	1.386×10^{-2}	1.337×10^{-3}	5.448×10^{-4}
Target_5	2.845	2.675 ± 0.089	2.630	-5.421×10^{-4}	-8.184×10^{-3}	3.168×10^{-4}
Target_6	3.205	3.480 ± 0.091	3.498	1.458×10^{-2}	1.214×10^{-2}	-9.721×10^{-3}

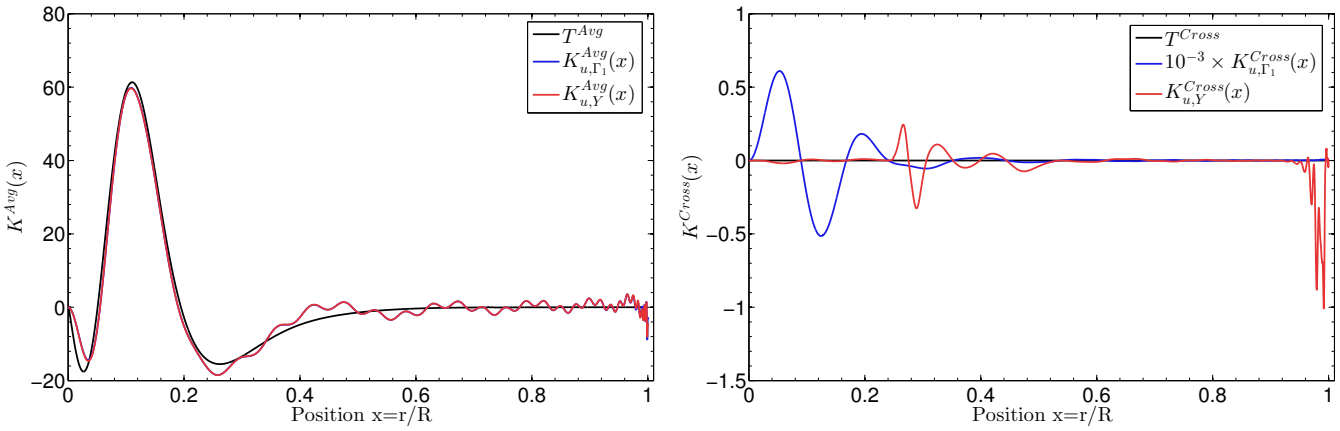

Figure 5.15: (left) Averaging kernels for both structural pairs and their respective targets. The red and blue curves are nearly identical, so that only the red curve is visible. (right) Cross-term kernels for both structural pairs, the target being 0.

accurate results for all cases. This means that the inversion is successful and that the regularisation process is sufficient for the values $\beta = 10^{-6}$ and $\theta = 10^{-5}$.

We see in the fifth column of Tables 5.12 and 5.13 that the averaging kernel fit is usually the dominant error contribution. In the next sections, we see how this result changes with the modes used or with the quality of the reference model. If we analyse the cross-term error contribution, we see that it is generally much less important than the averaging kernel mismatch error. We also see that despite the high amplitude of the cross-term kernels associated with Γ_1 shown in Fig. 5.15, the real error is quite small and often smaller than the error associated with the helium cross-term kernel. This is due not only to the small variations in Γ_1 between target and reference model but also to the oscillatory behaviour of the Γ_1 cross-term kernel. In contrast, the cross-term kernel of the (u,Y) kernel has a smaller amplitude, but nearly no oscillatory behaviour and is larger in the surface regions, where the inversion is naturally less robust. Nonetheless, the results of the (u,Y) kernels also show some compensation. We also note that they tend to have larger residual errors. However, there is no clear difference in accuracy between the (u,Γ_1) and the (u,Y) kernels. In the case of Target_2, we see that although the results are slightly improved, the reference value is within the error bars of the inversion results. In an observed case, this would mean that the reference model is already very close to the target as far as the indicator t_u is concerned. However, we wish to point out that it seems rather improbable that the only difference between a static model and a real observed star would be in its heavy-element mixture.

Analysing the residual contribution is slightly more difficult, since it includes each and every supplementary effect: surface terms, non-linear contributions, errors in the equation of state (when using kernels related to Y), etc. In this study, we can see that the residual error is well constricted. This is not the case, for example, if the parameter θ is chosen to be very small, or if the scaling effect is not taken into account[10]. In fact, the θ parameter is a regularizing parameter, in the sense that it does not allow the inversion coefficients to take on extremely high values. In that case, the inversion would be completely unstable because a slight error in the fit would be amplified and would lead to incorrect results. This is quickly understood knowing that the inversion coefficients are used to recombine the frequencies as

$$\frac{\delta t_u^{inv}}{t_u} = \sum_i^N c_i \frac{\delta \nu_i}{\nu_i}, \tag{5.83}$$

with N the total number of observed frequencies. Where this equation is subject to the uncertainties in Eqs. 5.62 and 5.50 (or, respectively Eq. 5.58), any error will be dramatically amplified by the inversion process. Therefore there is no gain in reducing θ since at some point, the uncertainties behind the basic equation of the inversion process will dominate and lead the method to failure. In this case, the inversion problem is not sufficiently regularised. Such an example is presented and analysed in the next section.

5.3.4 Impact of the type and number of modes on the inversion results

When carrying out inversions on observed data, we are limited to the observed modes. Therefore the question of how the inversion results depend on the type of modes is of utmost importance. The reason behind this dependence is that different frequencies

[10] In which case one would be searching for a result that is impossible to obtain.

are associated with different eigenfunctions, in other words different structural kernels, sensitive to different regions of the star. Therefore, the inverse problem will vary for each set of modes because the physical information contained in the observational data changes. Hence, we studied four targets using seven sets of modes. As in Sect. 5.3.3, we wish to avoid redundancy and so present our results for one target, namely Target_3, and five different frequency sets. As a supplementary test case, we defined two target models with the properties of 16CygA and 16CygB found in the litterature (Metcalfe, Chaplin, et al. (2012), White, Huber, et al. (2013), Verma, Faria, et al. (2014)). Using these properties, we added strong atomic diffusion to the 16CygA model and used $Z = 0.023$ as well as the GN93 mixture for 16CygB. In constrast, the reference models used $Z = 0.0122$ and the AGSS09 mixture. The characteristics of these models are also summarised in Table 5.14, where we used the set of observed modes given by Verma, Faria, et al. (2014) and ignored the isolated $\ell = 3$ modes for which there was no possibility to define a large separation.

All the sets for the test cases of this section are summarised in Table 5.15. The reference model was chosen as in Sect. 5.3.3, using the arithmetic average of the large and small frequency separations as constraints for its mass and age. With these test cases, we first analyse whether the inversion results depend on the values of the radial order n of the modes, with the help of the frequency Sets 1, 2 and 3 (see Table 5.15). Then we analyse the importance of the $\ell = 3$ modes for the inversion using Sets 4 and 5.

The inversion results for all these targets and sets of mode are presented in Tables 5.16 and 5.17 for the (u, Γ_1) kernels. A first conclusion can be drawn from the results using Sets 1, 2 and 3: low n are important for ensuring an accurate results. In fact, Set 2 provides much better results than Set 1,. Even using Set 3 (which is only Set 1 extended up to $n = 34$ for each ℓ) does not improve the results any further. This means that modes with $n > 27$ are barely used to fit the target.

This first result can be interpreted in a variety of ways. Firstly, using mathematical reasoning, we can say that the kernels associated with higher n have high amplitudes in the surface regions and are therefore not well suited to probing central regions. Another way to interpret this problem follows: When we use modes with high n, we come closer to the asymptotic regime, and the eigenfunctions are described by the JWKB approximation, all of which have a similar form and do not therefore provide useful additional information. Based on this, we see a clear difference between inverted structural quantities and the information deduced from asymptotic relations, which requires high n values to be valid, thereby highlighting the usefulness of inversions. The question of the importance of the modes $\ell = 3$ is also quickly answered from the results obtained with Set 4 and 5. For these test cases, we reach very good accuracy even without $n \leq 9$ unlike the previous test case using Set 2. Moreover, we use even fewer frequencies than for the first three sets. In fact, this is crucial to determine whether one can apply an inversion in an observed case, since a few $\ell = 3$ modes can change the results and make the inversion successful.

To further illustrate the importance of the octupole modes, we use the 16CygA and 16CygB clones to carry out inversions for their respective observed frequency sets. In a first test case, we use all frequencies and reach a reasonable accuracy for both targets. In the second test case, we do not use the octupole modes and we can observe a drastic change in accuracy. These results are illustrated in Table 5.17, where the notation "Small" (for small frequency set) has been added to the lines associated with the results obtained

Table 5.14: Characteristics of 16CygA and 16CygB clones.

	16CygA-clone	**16CygB-clone**
Mass ($M_\odot$)	1.11	1.06
Radius ($R_\odot$)	1.13	1.04
Age (Gyr)	6.9	6.7
$T_{\rm eff}$ (K)	5696	5772.9
Z_0	0.024	0.023
Y_0	0.241	0.242
Abundances	AGSS09	GN93
$\alpha_{\rm MLT}$	2.0	2.0
Diffusion coefficient	2	0

without using the $\ell = 3$ modes.

Looking again at the results for 16CygA, we see that although the inversion improves the value of t_u, the reference value lies within the observational error bars of the inverted result. The case of the truncated set of frequencies is even worse, since the inverted result is less accurate than the reference value. We therefore analysed the problem for the full frequency set. To do so we carried out a variety of inversions using higher values of θ. The results for $\theta = 10^{-4}$ are illustrated in Table 5.17. In this case we have lower error bars, but what is reassuring is that the result did not change drastically when we changed θ. This means that the problem is properly regularised around $\theta = 10^{-5}$ and $\theta = 10^{-4}$ and that we can trust the inversion results. Our advice is therefore to always look at the behaviour of the solution with the inversion parameters to see if there is any sign of compensation or other undesirable behaviour. In fact there is no law to select the value of θ and applying fixed values blindly for all asteroseismic observations is probably the best way to obtain unreliable results.

The case of the small frequency set is even more intriguing since the result improves greatly with $\theta = 10^{-4}$. The question that arises is whether the problem is not properly regularised with $\theta = 10^{-5}$ or whether we are faced with some fortuitous compensation effect that leads to very accurate results. If we are faced with fortuitous compensation, taking θ slightly larger than 10^{-4} or increasing β will drastically reduce the accuracy since any change in the linear combination will affect the compensation. However, if we are faced with a regularisation problem, the accuracy should decrease regularly with the change of parameters (since we are slightly reducing the quality of the fit with those changes). We emphasise again that one should not choose values of the inversion parameters where any small augmentation of the regularisation would drastically change the result. In this particular case, we were confronted with insufficient regularisation and choosing $\theta = 10^{-4}$ corrected the problem.

Table 5.15: Sets of modes used to analyse the impact of the number and type of frequencies on the inversion results

	$\rm Set_1$	$\rm Set_2$	$\rm Set_3$	$\rm Set_4$	$\rm Set_5$	16CygA	16CygB
$\ell = 0$	$n = 9-28$	$n = 5-27$	$n = 9-34$	$n = 11-24$	$n = 11-26$	$n = 12-27$	$n = 13-26$
$\ell = 1$	$n = 9-28$	$n = 5-27$	$n = 9-34$	$n = 11-24$	$n = 11-26$	$n = 11-27$	$n = 13-26$
$\ell = 2$	$n = 9-28$	$n = 5-27$	$n = 9-34$	$n = 11-24$	$n = 11-26$	$n = 11-24$	$n = 12-25$
$\ell = 3$	–	–	–	$n = 9-20$	$n = 12-22$	$n = 15-21$	$n = 17-24$

Table 5.16: Inversion results for Target_3 using the (u,Γ_1) kernels and Sets $1-5$ of Table 5.15.

	$\frac{t_u^{\text{ref}}}{G^2R_{ref}^6}$ (g^2/cm^6)	$\frac{t_u^{\text{inv}}}{G^2R_{ref}^6}$ (g^2/cm^6) (u,Γ_1)	$\frac{t_u^{\text{obs}}}{G^2R_{tar}^6}$ (g^2/cm^6)	$\varepsilon_{\text{Avg}}^{u,\Gamma_1}$	$\varepsilon_{\text{Cross}}^{u,\Gamma_1}$	$\varepsilon_{\text{Res}}^{u,\Gamma_1}$
Set_1	5.855	5.700 ± 0.161	5.538	2.805×10^{-2}	-4.246×10^{-5}	4.881×10^{-4}
Set_2	5.888	5.566 ± 0.088	5.538	4.062×10^{-3}	1.869×10^{-4}	3.505×10^{-4}
Set_3	5.895	5.690 ± 0.146	5.538	2.79×10^{-2}	9.25×10^{-6}	6.8×10^{-4}
Set_4	5.886	5.570 ± 0.110	5.538	6.074×10^{-3}	2.859×10^{-4}	-1.893×10^{-3}
Set_5	5.968	5.630 ± 0.105	5.538	1.644×10^{-2}	-4.072×10^{-4}	4.714×10^{-4}

Table 5.17: Inversion results for the 16CygA and 16CygB clones using the (u,Γ_1) kernels.

	$\frac{t_u^{\text{ref}}}{G^2R_{ref}^6}$ (g^2/cm^6)	$\frac{t_u^{\text{inv}}}{G^2R_{ref}^6}$ (g^2/cm^6) (u,Γ_1)	$\frac{t_u^{\text{obs}}}{G^2R_{tar}^6}$ (g^2/cm^6)	$\varepsilon_{\text{Avg}}^{u,\Gamma_1}$	$\varepsilon_{\text{Cross}}^{u,\Gamma_1}$	$\varepsilon_{\text{Res}}^{u,\Gamma_1}$
16CygA (Full, $\theta=10^{-5}$)	2.965	2.891 ± 0.083	2.885	2.641×10^{-3}	-1.780×10^{-3}	1.442×10^{-3}
16CygA (Full, $\theta=10^{-4}$)	2.965	2.872 ± 0.036	2.885	-4.033×10^{-3}	-9.487×10^{-4}	7.149×10^{-4}
16CygA (Small, $\theta=10^{-5}$)	2.965	2.971 ± 0.083	2.885	3.117×10^{-2}	-2.577×10^{-3}	5.000×10^{-4}
16CygA (Small, $\theta=10^{-4}$)	2.965	2.906 ± 0.031	2.885	8.240×10^{-3}	-1.778×10^{-3}	7.000×10^{-4}
16CygB (Full)	4.540	4.007 ± 0.095	3.783	4.547×10^{-2}	-2.407×10^{-4}	2.277×10^{-2}
16CygB (Small)	4.540	4.295 ± 0.113	3.783	1.093×10^{-1}	-1.715×10^{-3}	1.138×10^{-2}

5.3.5 Impact of the quality of the forward modelling process on the inversion results

In this section we present various inversion results using different criteria to select the reference model for the inversion. The previous results, only using the average large and small frequency separations as constraints for the mass and age of the model, are indeed a crude representation of the real capabilities of seismic modelling. It is well known that other individual frequency combinations can be used to obtain independent information on the core mixing processes and that we should adjust more than two parameters to describe the physical processes in stellar interiors.

Table 5.18: Characteristics of Target_7, Target_8, and of the models obtained with the Levenberg-Marquardt algorithm.

	Target_7	**$\text{Model}_{7.1}$**	**$\text{Model}_{7.2}$**	**$\text{Model}_{7.3}$**	**Target_8**	**$\text{Model}_{8.1}$**	**$\text{Model}_{8.2}$**
Mass ($M_\odot$)	0.9	0.933	0.908	0.957	1.0	1.009	1.029
Radius ($R_\odot$)	0.908	0.919	0.912	0.926	1.17	1.18	1.19
Age (Gyr)	3.075	3.34	3.69	3.45	4.168	4.322	4.489
T_{eff} (K)	5659	5701	5488	5713	6003	5985	5966
Z	0.0122	0.0122	0.0122	0.0105	0.0122	0.0185	0.0181
Y_0	0.308	0.274	0.269	0.243	0.3078	0.323	0.305
Abundances	AGSS09	AGSS09	AGSS09	AGSS09	AGSS09	AGSS09	AGSS09
α_{MLT}	1.522	1.522	1.297	1.522	1.522	1.522	1.522
Diffusion coefficient	1.6	0	0	0	1.6	0	0

To carry out these test cases, we built two target models including microscopic diffusion. As before, we did not include this process in the reference models obtained by fitting the so-called 56 observed frequencies. We used the modes $l=0, n=12-25$; $l=1, n=11-25$; $l=2, n=11-26$; $l=3, n=14-24$. The characteristics of the targets are summarised in Table 5.18 along with those of the best models obtained through seismic modelling. Table 5.19 contains information on the various constraints and free parameters used for the fit. We used various seismic constraints such as the individual large and small

Table 5.19: Constraints and free parameters used for the Levenberg-Marquardt fit.

	Constraints	***Parameters***
$\text{Model}_{7.0}$	$<\Delta\nu_{n,\ell}(\nu)>+<\tilde{\delta}\nu_{n,\ell}(\nu)>$	Mass + Age
$\text{Model}_{7.1}$	$\Delta\nu_{n,\ell}(\nu)+\tilde{\delta}\nu_{n,\ell}(\nu)+r_{01}(\nu)$	Mass + Age + Y_0
$\text{Model}_{7.2}$	$\Delta\nu_{n,\ell}(\nu)+\tilde{\delta}\nu_{n,\ell}(\nu)$	Mass + Age + Y_0+ α_{MLT}
$\text{Model}_{7.3}$	$\Delta\nu_{n,\ell}(\nu)+\tilde{\delta}\nu_{n,\ell}(\nu)$	Mass + Age + Y_0 + Z_0
$\text{Model}_{8.1}$	$<\Delta\nu>+r_{02}(\nu)$	Mass + Age + Y_0 + Z_0
$\text{Model}_{8.2}$	$<\Delta\nu>+r_{02}(\nu)+r_{01}(\nu)$	Mass + Age + Y_0 + Z_0

frequency separations, the individual r_{01} and r_{02}, defined as

$$r_{02}=\frac{\nu_{n-1,2}-\nu_{n,0}}{\nu_{n,1}-\nu_{n-1,1}}, \tag{5.84}$$

$$r_{01}=\frac{\nu_{n,0}-2\nu_{n,1}+\nu_{n+1,0}}{2(\nu_{n+1,0}-\nu_{n,0})}. \tag{5.85}$$

The free parameters were chosen to match what is done when trying to fit observations, although the final quality of the fit is much higher than one expects from an observed case, as illutrasted in Fig. 5.16 for Target_7[ll] and Fig. 5.17 for Target_8. Here one should note that the arithmetic average of the large frequency separations were fitted to within 1% in addition to the individual quantities plotted in Fig. 5.17. In all these cases the inversion improved the value of t_u. In some cases, the acoustic radius was not well fitted by the forward modelling process but the inversion could improve its determination. Table 5.21 illustrates the results of combined inversions, whereas Table 5.20 gives the results for all test cases. In fact, one could argue that the error contributions are not that different from what was obtained using only the average large and small frequency separations as constraints. However, our previous analysis of the dependence on the degree and radial order of the modes has shown us that having low n and $l=3$ modes was the best way to ensure accuracy.

Based on the above, the frequency set used for these test cases is of lower quality and this has been compensated for by the forward modelling process. To further illustrate the importance of the model selection, in Table 5.20 we repeat the results obtained by simply ajusting $<\Delta\nu>$ and $<\tilde{\delta}\nu>$ that we denote as $\text{Model}_{7.0}$. For Target_7 we see that the dominant source of error contribution, ε_{Avg} is ± 6 to 10 times smaller than what is for $\text{Model}_{7.0}$. As a result it is clear that using the information given by individual frequencies is crucial to ensure accurate results in observed cases.

The necessity of an acoustic radius inversion results from two aspects in the selection of the reference models. The first one is present in $\text{Model}_{7.2}$; the change of α induced during the fit had an important impact on the upper regions and therefore a change in the acoustic radius was observable. The second one is present in $\text{Model}_{8.1}$ and $\text{Model}_{8.2}$, where the observational constraints were sensitive to core regions, except for the arithmetic average of the large frequency separations. In this case, the upper regions are less constrained and the inversion is still necessary. However, we note that in most cases the acoustic radius of the reference model was very accurate. This is due to the lack of

[ll] We did not present the fit of the individual large frequency separations for $\text{Model}_{7.1}$ to avoid redundancy with $\text{Model}_{7.2}$ and $\text{Model}_{7.3}$.

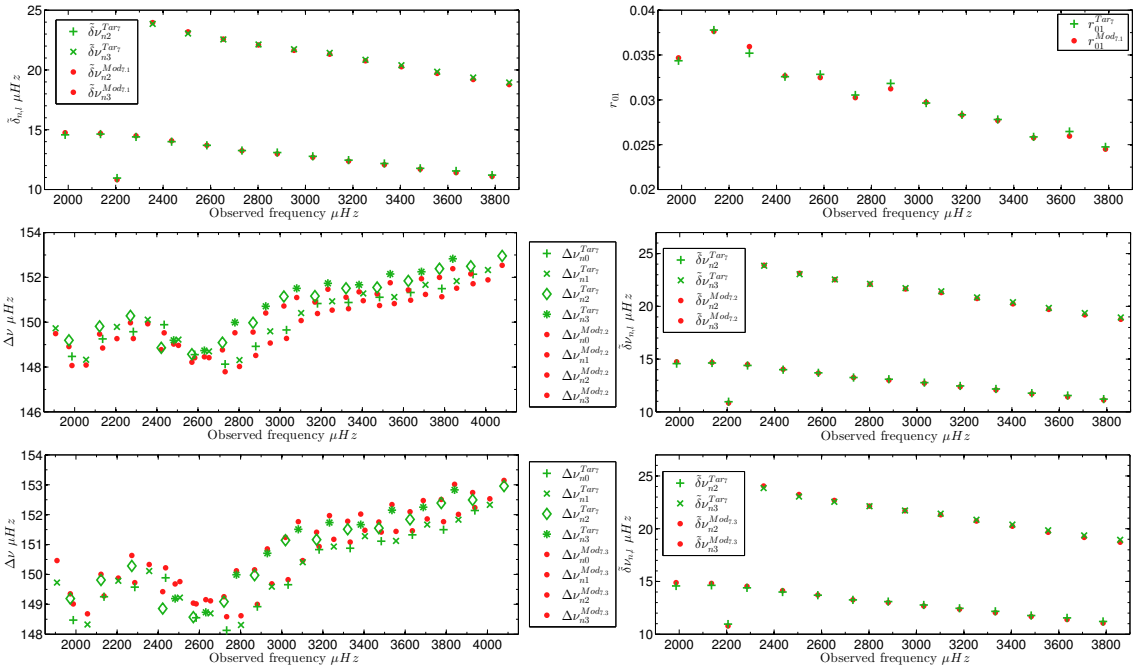

Figure 5.16: Results of the fit using the Levenberg-Marquardt algorithm for the first target as a function of the observed frequency: the upper panel is associated with $\text{Model}_{7.1}$ which used the average large frequency separation and the individual r_{01} and $\tilde{\delta}\nu_{n,\ell}$ as constraints; the central panel is associated with $\text{Model}_{7.2}$ which used individual $\Delta\nu_{n,\ell}$ and $\tilde{\delta}\nu_{n,\ell}$ as constraints; the lower panel is associated with $\text{Model}_{7.3}$ which also used individual $\Delta\nu_{n,\ell}$ and $\tilde{\delta}\nu_{n,\ell}$ as constraints.

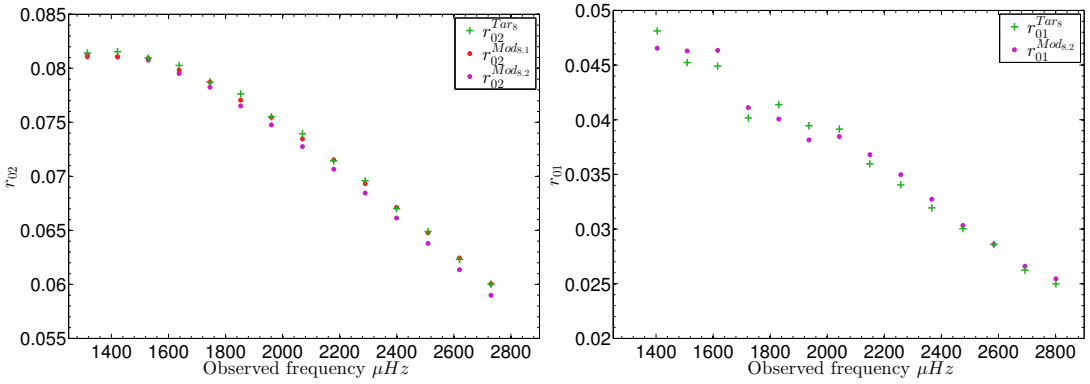

Figure 5.17: Results of the fit using the Levenberg-Marquardt algorithm for the second target as a function of the observed frequency: the red dots are associated with $\text{Model}_{8.1}$ which used individual r_{02} as constraints and the purple dots are associated with $\text{Model}_{8.2}$ which used individual r_{02} and r_{01} as constraints.

surface effects in the target models. If we were to include non-adiabatic computations or differences in the convection treatment, differences would be seen in the acoustic radii of the targets and reference models, but it is clear from these test cases that the acoustic radius combined with t_u alone is not sufficient to distinguish between effects of differences

in helium abundance and effects of microscopic diffusion. We also note that when using the individual r_{02} along with the $<\Delta\nu>$ (the test case of $\text{Model}_{8.1}$), we obtain a very good fit of t_u with the reference model. This is a consequence of the fact that r_{02} is very sensitive to core regions, and so the core characteristics are reproduced well. However, with the acoustic radius inversion, we note that the surface regions are not well fitted, and if we include r_{01}, as done in the test case of $\text{Model}_{8.2}$, we obtain a better fit of the acoustic radius, but t_u is then less accurate. The inversion of the indicator t_u informs us that the core regions are not reproduced well in this reference model. We can see that $\text{Model}_{8.1}$ or $\text{Model}_{7.2}$ and $\text{Model}_{7.3}$ reproduce the indicator t_u better. However, in all these cases the acoustic radius was not properly reproduced. Therefore the combined inversions indicate that something is wrong with the set of free parameters used because we cannot fit properly surface and core regions simultaneously, although the fit of the seismic constraints with the Levenberg-Marquardt algorithm is excellent in all cases.

We also mention that in all test cases carried out here, we did not consider the first age indicator t from Buldgen, D. R. Reese, M. A. Dupret, and Samadi (2015). In fact, the indicator t could also provide accurate results for Target_7. However, its inaccuracy for older models has been observed during this entire study, and we recommend limiting its use to young stars[12], where it can provide valuable information providing that the kernels are well optimised.

Table 5.20: Inversion results for various fits with the Levenberg-Marquardt algorithm.

	$\frac{t_u^{\text{ref}}}{G^2R_{ref}^6}$ (g^2/cm^6)	$\frac{t_u^{\text{inv}}}{G^2R_{ref}^6}$ (g^2/cm^6) (u,Γ_1)	$\frac{t_u^{\text{obs}}}{G^2R_{tar}^6}$ (g^2/cm^6)	$\varepsilon^{u,\Gamma_1}_{\text{Avg}}$	$\varepsilon^{u,\Gamma_1}_{\text{Cross}}$	$\varepsilon^{u,\Gamma_1}_{\text{Res}}$
$\text{Model}_{7.0}$	7.626	7.000 ± 0.24	6.703	4.952×10^{-2}	2.94×10^{-4}	-3.389×10^{-3}
$\text{Model}_{7.1}$	6.562	6.657 ± 0.122	6.703	-1.4×10^{-3}	-2.407×10^{-4}	-2.777×10^{-4}
$\text{Model}_{7.2}$	6.393	6.669 ± 0.123	6.703	-6.597×10^{-3}	-1.292×10^{-4}	-2.478×10^{-5}
$\text{Model}_{7.3}$	6.467	6.667 ± 0.121	6.703	-2.571×10^{-3}	-3.322×10^{-4}	-5.661×10^{-4}
$\text{Model}_{8.1}$	3.450	3.651 ± 0.092	3.568	2.458×10^{-2}	-2.302×10^{-4}	-1.745×10^{-3}
$\text{Model}_{8.2}$	3.337	3.637 ± 0.096	3.568	2.089×10^{-2}	-6.553×10^{-4}	-1.568×10^{-3}

Table 5.21: Combined (τ, t_u) inversion results for various fits with the Levenberg-Marquardt algorithm.

	$\frac{t_u^{\text{ref}}}{G^2R_{ref}^6}$ (g^2/cm^6)	$\frac{t_u^{\text{inv}}}{G^2R_{ref}^6}$ (g^2/cm^6) (u,Γ_1)	$\frac{t_u^{\text{obs}}}{G^2R_{tar}^6}$ (g^2/cm^6)	$\tau_{\text{ref}}(s)$	$\tau_{\text{inv}}(s)$	$\tau_{\text{obs}}(s)$
$\text{Model}_{7.2}$	6.393	6.657 ± 0.092	6.703	3230	3223 ± 0.028	3222
$\text{Model}_{8.1}$	3.450	3.651 ± 0.096	3.568	4509	4450 ± 0.028	4442
$\text{Model}_{8.2}$	3.337	3.637 ± 0.120	3.568	4517	4448 ± 0.017	4442

5.3.6 Conclusion

In this section, we have presented a new approach to constraining mixing processes in stellar cores using the SOLA inversion technique. We used the framework presented in Buldgen, D. R. Reese, M. A. Dupret, and Samadi (2015) to develop an integrated quantity, denoted t_u, that is sensitive to the effects of stellar evolution and to the impact of additional mixing processes or mismatches in the chemical composition of the core. We based our choice solely on structural effects and considerations about the variational principle and the ability of the kernels to fit their targets.

[12] We chose not to present these results and to focus our study on the t_u indicator.

The derivation of this new quantity was made possible using the approach of Masters (1979) to derive new structural kernels in the context of asteroseismology by solving an ordinary differential equation. We discussed the problem of the intrinsic scaling effect presented in Basu (2003) and discussed how it could affect the indicator t_u. We tested its sensitivity to various physical changes between the target and the reference model and demonstrated that SOLA inversions are able to significantly improve the accuracy with which t_u is determined, thereby indicating whether there is a problem in the core regions of the reference model.

We then analysed the importance of the number and type of modes in the observational data and concluded that the accuracy of an inversion of the indicator t_u increased with multiple values of the degree, ℓ, and low values of the radial order, n. Following from this, we emphasise that the observation of $\ell = 3$ modes is important for the inversion of the indicator t_u since it can improve the accuracy without the need of low n modes. Such modes are difficult to observe. Indeed, only a few octupole modes have been detected for around 15% of solar-like stars with Kepler. The use of other observational facilities, such as the SONG network (Grundahl et al. (2007)), might help us obtain richer oscillation spectra as far as octupole modes are concerned. The test cases for the 16CygA and 16CygB clones demonstrated that our method was applicable to current observational data and one could still carry out an inversion of t_u without these modes. However, it is clear that this method will only be applicable to the best observational cases with Kepler, Plato or SONG.

We also analysed the impact of the selection of the reference model on the inversion results and concluded that using individual frequency combinations is far more efficient in terms of accuracy and stability for the inversion results. However, we noticed in supplementary tests that there was what could be called a resolution limit for the t_u inversion which depends on the magnitude of the differences in the physics between the reference model and its targets but also on the weight given to the core in the selection of the reference model (see for example the case of $\text{Model}_{8.1}$ and the associated discussion). This leads to the conclusion that supplementary independent integrated quantities should be derived to help us distinguish between various physical effects and improve our sensitivity to the physics of stellar interiors. Nevertheless, the test cases of Sect. 5.3.5 showed that the SOLA method is much more sensitive than the forward modelling process used to select the reference model (here a Levenberg-Marquardt algorithm) and could indicate whether the set of free parameters used to describe the model is adequate.

5.4 Constraining convective regions with asteroseismic linear structural inversions

5.4.1 Introduction

Inversion techniques have been used for several decades in helioseismology to analyze the structure of the Sun. Amongst the greatest successes of this field, one finds the determination of the base of the solar convective envelope (Kosovichev and Fedorova (1991)) and the helium abundance in this region (Antia and Basu (1994a) and Kosovichev (1993)), as well as the inversion of the sound speed profile (Antia and Basu (1994b)). While for the Sun it is possible to determine a whole structural profile with linear techniques, the case of asteroseismic inversions is far more difficult. This is due to the small number of modes and the absence of oscillations of high harmonic degree, which can help to scan

through the whole structure of the star. Initial studies have been performed to carry out inversions based on the variational principle for stars other than the Sun (see Basu (2003), D. O. Gough and Kosovichev (1993a,b), and Takata and Montgomery (2002) for a few examples of such studies).

Since the advent of space photometry missions such as CoRoT Baglin et al. (2009) and Kepler (Borucki et al. (2010)), we now have seismic data with sufficiently small uncertainties to attempt structural inversions to constrain models of solar-like stars. In the future, the TESS and Plato 2.0 missions (Rauer et al. (2014)) will bring further data, carrying on what is now named the space photometry revolution.

While for some of the best Kepler targets, full profiles inversions could be attempted, they would require very specific conditions. For example, a convective parameter inversion as shown in Kosovichev (1993) would need a very accurate knowledge of the mass and radius of the target as shown in Buldgen, D. R. Reese, and M. A. Dupret (2017) from the analysis of the linear relations for various structural kernels. Secondly, an efficient way to deal with surface corrections without degrading the capabilities of the inversion technique would need to be found. As a workaround to these difficulties and to allow more versatile applications of these techniques, (D. R. Reese, Marques, et al. (2012)) adapted the classical inversion techniques so that they would focus on extracting global information such as the mean density from the oscillation spectra. This global information is defined by integrated quantities which are chosen for their particular ability to probe certain aspects of stellar structure (see for example Buldgen, D. R. Reese, and M. A. Dupret (2015) and Buldgen, D. R. Reese, M. A. Dupret, and Samadi (2015)).

The strength of this approach is that it focuses the entire information of the seismic spectra into to the determination of one piece of information at a time. Moreover, this information, which is a linear combination of frequency differences is related through the variational integral relations (Dziembowski, Pamyatnykh, and Sienkiewicz (1990)) to structural characteristics. Our goal is to further correct seismic models which have been built using the classical forward modelling method used in asteroseismology. Once the integrated quantity is defined, one can use the SOLA inversion technique (Pijpers and Thompson (1994)) to check whether it is possible to obtain corrections of the chosen structural indicator. The success of the operation depends on whether the integrated quantity will behave linearly and whether the target function can easily be fitted with the amount of seismic information available. Ultimately, one still faces the classical trade-off problem of inversion techniques and the fine-tuning of the parameters has to be done carefully if one wishes to extract efficiently the structural information from the seismic observations.

In this section, we will present results from hare-and-hounds exercises for new indicators based on an entropy proxy. We will start by presenting the kernels associated with the structural quantity we use in the inversions. We will show how this variable naturally reproduces the entropy plateaus in adiabatic convective regions and how its behaviour can be used to probe both convective cores and envelopes with custom-built indicators. Probing convective regions and their surrounding layers is crucial as they are likely subject to extra-mixing.

These questions are illustrated by the current uncertainties on the solar tachocline (see Zahn (2007) and references therein) and emphasize the physical complexity linked to convective envelopes. In the Sun, indications of mixing can be seen in the relative sound speed differences or from rotation inversions, where the change from differential to solid body rotation is associated with this particular region of solar structure. In asteroseismology, convective penetration has also been observed in the CoRoT target

HD52265 (Lebreton and Goupil (2012)). From a seismic point of view, glitch fitting techniques may help to position the acoustic depth of the convective envelope (see Monteiro, Christensen-Dalsgaard, and Thompson (1994, 2000) and Verma, Raodeo, et al. (2017)). However, these techniques also require very high data quality and currently, the signal related to the base of the convective zone is considered by some authors to be too weak to be fully exploited (Verma, Raodeo, et al. (2017)). In that sense, our approach takes a different path, by focusing on global information rather than localized signatures to provide additional constraints.

Besides additional mixing processes, inaccuracies in the physical ingredients and numerical techniques used in stellar models can leave their mark on the boundaries of convective regions and therefore on the whole stratification of the model (Gabriel, Noels, et al. (2014)). This, in turn, will adversely affect age determinations, and to a lesser degree, the accuracy with which other stellar parameters are obtained. For example, the inaccuracy with which is determined the extent of a convective core induces uncertainties on the age of an observed target that far exceed 10%, thus emphasizing the importance of constraining convective regions in the current context of the Plato 2.0 mission.

In Sect. 5.4.4, we will test the accuracy of both indicators for various targets and analyse their error contributions to see whether the inversion can be computed for the best solar-like targets at hand. Finally, we will conclude by summarising our results and comment on further analyses which have to be carried out to fully assess the potential of structural inversions in asteroseismology.

5.4.2 Kernels for the entropy proxy

Obtaining a new indicator with asteroseismic inversions means finding a new way to efficiently extract information from the frequencies. Due to the small number of observed modes, the target functions associated with the indicators must be constructed so that they can easily be fitted by structural kernels. Moreover, the choice of the structural variable must be physically motivated. For example, the use of the squared isothermal sound speed u in Buldgen, D. R. Reese, and M. A. Dupret (2015) to analyse deep regions is motivated by the approximate relation $u \approx \frac{T}{\mu}$ in the core. In Dziembowski, Pamyatnykh, and Sienkiewicz (1990), its use was motivated by the problem of measuring the helium abundance in the solar convective envelope.

In this study, we focus on convective regions. Specifically, we wish to be able to analyse the uncertainties linked to the detection of convective cores and extra-mixing at the boundaries of convective regions. However, we have to keep in mind the intrinsic limitations of inversions in asteroseismology. From our previous studies (Buldgen, D. R. Reese, and M. A. Dupret (2017)), we know that kernels like the (A,Γ_1) or (A,Y) kernels, where $A = \frac{d\ln\rho}{d\ln r} - \frac{1}{\Gamma_1}\frac{d\ln P}{d\ln r}$, cannot be used without a very accurate and precise determination of the radius, which far exceed observational uncertainties which are of the order of a percent in the case of interferometry. This means that we have to find a new structural pair which efficiently probes convective regions. In this section, we will derive new kernels associated with the variable $S_{5/3} = \frac{P}{\rho^{5/3}}$, with P the pressure and ρ the density, and justify its choice as an efficient probe of convective regions.

The choice of $S_{5/3}$ as a structural variable stems from its relation with the entropy of an ideal gas. If one considers the Sackur-Tetrode equation in this particular case, one finds

$$S = \frac{3k_B}{2}\left(\mu m_u \ln\left(\frac{P}{\rho^{5/3}}\right) + f(\mu)\right), \tag{5.86}$$

with k_B the Boltzmann constant, μ the mean molecular weight and m_u the atomic mass

unit. In this equation, f only depends on the mean molecular weight and various physical constants.

This quantity has the interesting property of forming a plateau in the adiabatic convection zones. The height of this plateau is related to the temperature and mean molecular weight gradients in the vicinity of the convective zone's boundary and thus to the stratification of these poorely modelled regions. We will illustrate this property in Sect. 5.4.3, when we will derive the seismic indicators.

Due to the limited number of frequencies in asteroseismology, the second variable of the structural pair must be chosen so that the cross-term will naturally be small. Two variables satisfy this condition: Γ_1, the adiabatic exponent defined as $\Gamma_1 = \left(\frac{\partial \ln P}{\partial \ln \rho}\right)_S$ and Y, the helium abundance. This means that the structural pairs we are aiming for are the $(S_{5/3},\Gamma_1)$ and $(S_{5/3},Y)$ pairs, which can be derived from the (ρ,Γ_1) and (ρ,Y) pairs. One could also use the (u,Γ_1) and (u,Y) pairs without any further difficulties to derive the differential equations. However, since in practice the (u,Y) and (u,Γ_1) kernels are already obtained from the numerical resolution of a second order differential equation, it is wiser to use the (ρ,Γ_1) and (ρ,Y) kernels as a starting point to avoid multiplying the sources of numerical errors.

Using the direct method presented in Buldgen, D. R. Reese, and M. A. Dupret (2017), the equation obtained for the $(S_{5/3},\Gamma_1)$ kernels is a second order differential equation written as follows

$$-y\frac{d^2\mathscr{K}'}{dy^2} - \left[3 - \frac{2\pi y^{3/2}\rho}{m}\right]\frac{d\mathscr{K}'}{dy} = \frac{5y}{3}\frac{d^2\mathscr{K}}{dy^2} - \left[5 - \frac{\rho m}{2Py^{1/2}} - \frac{10\pi y^{3/2}\rho}{3m}\right]\frac{d\mathscr{K}}{dy} - \left[\frac{m}{4y^{1/2}\rho}\frac{d\rho}{dy} + \frac{\rho^2 m^2}{4y^2P^2} - \frac{m\rho}{4Py^{3/2}}\right]\mathscr{K}, \tag{5.87}$$

with $y = (\frac{r}{R})^2$ where r is the radial position and R the total radius of the star, m the mass contained within the sphere of radius r, $\mathscr{K} = K^{n,\ell}_{S_{5/3},\Gamma_1}$, $\mathscr{K}' = K^{n,\ell}_{\rho,\Gamma_1}$. As was the case for the (u,Y) kernels, one can use exactly the same equation to obtain the $(S_{5/3},Y)$ kernels from the (ρ,Y) kernels by simply taking $\mathscr{K}' = K^{n,\ell}_{\rho,Y}$ and $\mathscr{K} = K^{n,\ell}_{S_{5/3},Y}$.

The $K^{n,\ell}_{\Gamma_1,S_{5/3}}$ and $K^{n,\ell}_{Y,S_{5/3}}$ are directly obtained from the following algebraic relations:

$$K^{n,\ell}_{\Gamma_1,S_{5/3}} = K^{n,\ell}_{\Gamma_1,\rho}, \tag{5.88}$$

$$K^{n,\ell}_{Y,S_{5/3}} = K^{n,\ell}_{Y,\rho} \tag{5.89}$$

Examples of such kernels are illustrated in Fig. 5.18.

The integral equations used as a starting point for the problem is used to derive the additional boundary condition required to solve the second order equation. This equation is written

$$K^{n,\ell}_{\rho,\Gamma_1} = \frac{Gm\rho}{r^2}\int_0^r \frac{K^{n,\ell}_{S_{5/3},\Gamma_1}}{P}dr + 4\pi r^2\rho\int_r^R \frac{G\rho}{\tilde{r}^2}\left[\int_0^{\tilde{r}} \frac{K^{n,\ell}_{S_{5/3},\Gamma_1}}{P}d\bar{r}\right]d\tilde{r} - \frac{5}{3}K^{n,\ell}_{S_{5/3},\Gamma_1}, \tag{5.90}$$

and the additional boundary condition imposed on the new structural kernels is that they satisfy this equation at one point. This can be done either iteratively or by decomposing

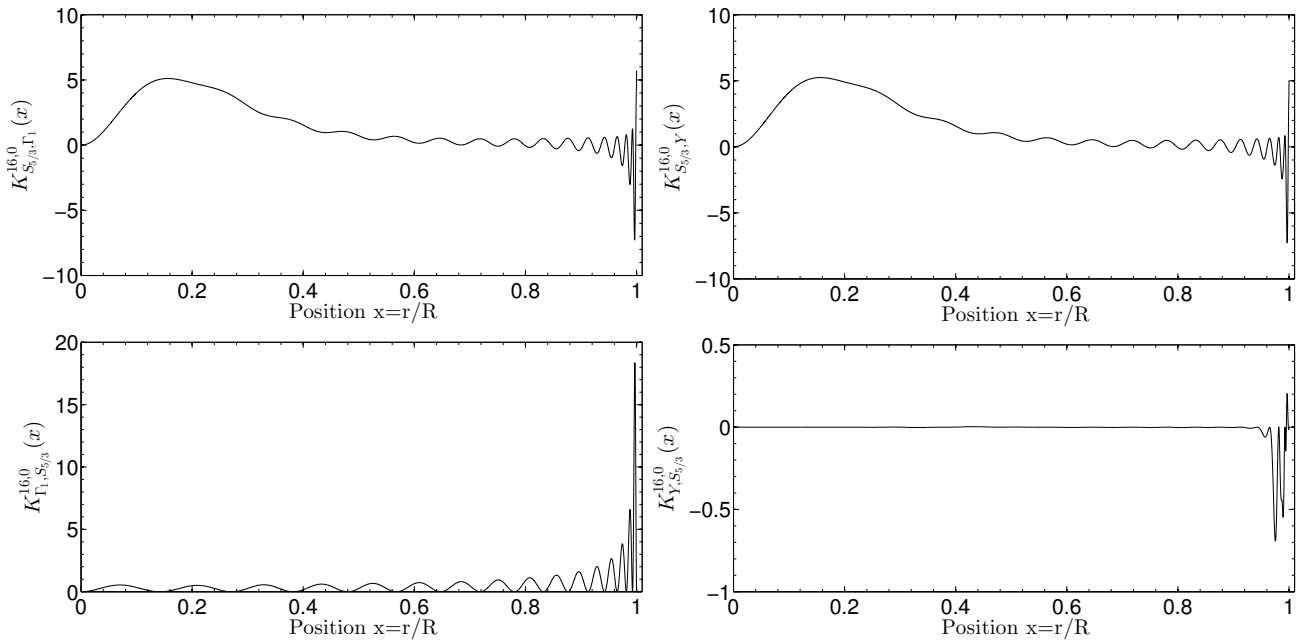

Figure 5.18: Structural kernels for the $n = 15, \ell = 0$ mode associated with the $(S_{5/3}, \Gamma_1)$ structural pair on the left hand side and with the $(S_{5/3}, Y)$ pair on the right hand side for Target 1 of table 5.22. The kernels are presented in their non-dimensional form.

the problem into an homogeneous and non-homogeneous component (see Buldgen, D. R. Reese, and M. A. Dupret (2017) for further details).

Once the kernels are derived, equation 5.90 also provides a first verification step to ensure that the kernels are in agreement with the initial steps of their derivation. The second verification is to ensure that the variational integral expressions are satisfied by the new kernels. In other words, ensure that we have:

$$\begin{aligned}\frac{\delta \nu^{n,\ell}}{\nu^{n,\ell}} &= \int_0^R K^{n,\ell}_{\rho,\Gamma_1} \frac{\delta \rho}{\rho} dr + \int_0^R K^{n,\ell}_{\Gamma_1,\rho} \frac{\delta \Gamma_1}{\Gamma_1} dr \\ &= \int_0^R K^{n,\ell}_{S_{5/3},\Gamma_1} \frac{\delta S_{5/3}}{S_{5/3}} dr + \int_0^R K^{n,\ell}_{\Gamma_1,S_{5/3}} \frac{\delta \Gamma_1}{\Gamma_1} dr \end{aligned} \tag{5.91}$$

Both verifications are illustrated in Figs. 5.19 for the $(S_{5/3}, \Gamma_1)$ pair and 5.20 for the $(S_{5/3}, Y)$ pair. The order of magnitude of the agreement is very similar to what is found for classical kernels such as the (ρ, c^2) and the (ρ, Γ_1) structural pairs. However, small differences can always be seen when changing the structural pair, as presented in Buldgen, D. R. Reese, and M. A. Dupret (2017). We recall that to ensure the verification of the variational equations, the scaling method mentioned in Buldgen, D. R. Reese, and M. A. Dupret (2017) is of course necessary since the observed target and the reference model may not have the same radius.

5.4.3 Using the entropy proxy to obtain indicators of convective regions

In this section, we illustrate the sensitivity of the entropy proxy, $S_{5/3}$, to convective regions and we show how to build seismic indicators useful for asteroseismic targets using the newly derived kernels.

Inverting an integrated quantity using the SOLA inversion technique actually consists in finding the linear combination of frequency differences which best reproduces the

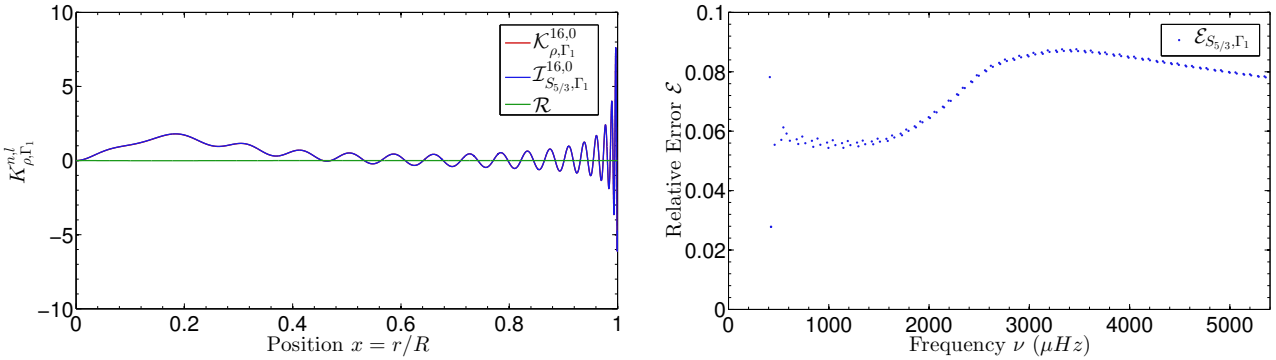

Figure 5.19: (Left panel) Verification of equation 5.90 for Target 1 of table 5.22 for the $n = 16, \ell = 0$ mode kernel $K^{16,0}_{S_{5/3},\Gamma_1}$, where $I^{16,0}_{S_{5/3},\Gamma_1}$ is the right hand side of this equation and $\mathscr{R}$ is the residual. All quantities are presented in their non-dimensional form. (Right panel) Verification of Eq. 5.91 for modes of degree $\ell = 0, 1, 2, 3$ and various radial orders between Target 1 of table 5.22 and a model of the same evolutionary sequence, 500 *My* younger.

correction to be applied to this integrated quantity. As noted before, the indicator is optimized to probe certain parts of the stellar structure. We first present the generic case of a quantity A, the linear perturbations of which are given by

$$\frac{\delta A}{A} = \frac{A_{Obs} - A_{Ref}}{A_{Ref}} = \int_0^1 \mathscr{T}_A \frac{\delta s_1}{s_1} dx, \tag{5.92}$$

with $\mathscr{T}_A$ the target function used for the inversion and s_1 a variable such as ρ, c^2 or $S_{5/3}$. We recall that a generic expression of the linear integral relations can be written.

$$\frac{\delta \nu^{n,\ell}}{\nu^{n,\ell}} = \int_0^R K^{n,\ell}_{s_2,s_1} \frac{\delta s_2}{s_2} dr + \int_0^R K^{n,\ell}_{s_1,s_2} \frac{\delta s_1}{s_1} dr \tag{5.93}$$

with s_2 the second variable of the integral relations and the $K^{n,\ell}_{s_i,s_j}$ the kernel functions related to each structural variable.

The inversion process estimates the differences between the observed integrated quantity, $A_{\rm Obs}$ and that of the reference model, $A_{\rm Ref}$ using the following relation

$$\left(\frac{\delta A}{A}\right)_{\rm Inv} = \sum_i c_i \frac{\delta \nu_i}{\nu_i}, \tag{5.94}$$

with $\delta\nu = \nu_{Obs} - \nu_{Ref}$ and the c_i being the inversion coeficients determined from the minimization of the SOLA cost function (see Pijpers and Thompson (1994) and Eq. 5.95). The inverted difference in Eq. 5.94 is not exactly the real difference in Eq. 5.92, due to the intrinsic limitations of the inversion.

The inversion process as a whole is a trade-off between various antagonistic terms. This is understood from the cost function used to carry out the SOLA inversion

$$\begin{aligned}\mathscr{J}_A = &\int_0^1 \left[K_{\rm Avg} - \mathscr{T}_A\right]^2 dx + \beta \int_0^1 K^2_{\rm Cross} dx + \tan(\theta) \sum_i^N (c_i \sigma_i)^2 \\ &+ \eta \left[\sum_i^N c_i - k\right],\end{aligned} \tag{5.95}$$

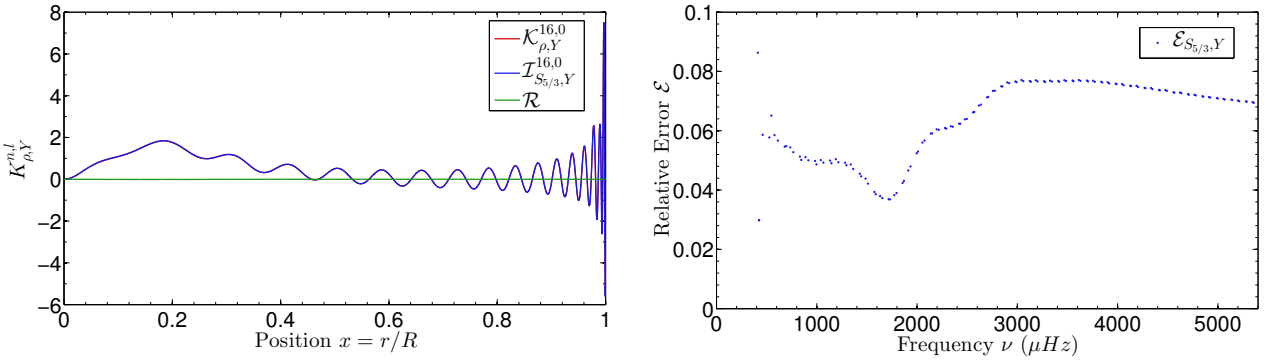

Figure 5.20: (Left panel) Verification of equation 5.90 for the $(S_{5/3,Y})$ structural pair for $n = 16, \ell = 0$ mode kernel $K^{16,0}_{S_{5/3},Y}$, where $I^{16,0}_{S_{5/3},Y}$ is the right hand side of this equation and $\mathscr{R}$ is the residual. All quantities are presented in their non-dimensional form. (Right panel) Verification of Eq. 5.91 for the $(S_{5/3,Y})$ structural pair for modes of degree $\ell = 0, 1, 2, 3$ and various radial orders. The models used are the same as in Fig. 5.19.

which contains four terms. The first term is associated with fitting the target function: it ensures the accuracy of the inversion and includes the averaging kernel, defined as

$$K_{\text{Avg}} = \sum_i^N c_i K^i_{s_1,s_2}, \tag{5.96}$$

with N the total number of individual observed frequencies. The second integral deals with the cross-term kernel, defined as

$$K_{\text{Cross}} = \sum_i^N c_i K^i_{s_2,s_1}, \tag{5.97}$$

which is a pollution term by the variable s_2 whose contribution has to be damped. The third term is linked with the propagation of observational error bars of the individual frequencies, denoted here σ_i. The last term is linked to the additional normalisation constraint on parameter k derived using homologous relations (see Sect. 5.4.3 and (D. R. Reese, Marques, et al. (2012)) for a description of this approach) and unlike β and θ, η is not a free parameter of the inversion but a Lagrange multiplier. The free parameters of the inversion, β and θ, are used to give more or less importance to each of the antagonistic terms and are thus called the trade-off parameters.

The optimal set of parameters is defined by analysing the amplitude of the first three individual terms of Eq. 5.95 and visually verifying that the fit is reliable. In practice, this implies that the inversion will be a compromise between precision, accuracy and cross-term. As stated in Sect. 5.4.2, the cross-term is damped by a suitable choice of variables which has been validated in previous studies (Basu (2003) and D. R. Reese, Marques, et al. (2012)). Consequently, the main part of the trade-off problem is to find a suitable compromise between precision and accuracy. This is done by comparing the terms responsible for these characteristics in so-called trade-off curves (see Backus and Gilbert (1967), Pijpers and Thompson (1994), Rabello-Soares, Basu, and Christensen-Dalsgaard (1999), and D. R. Reese, Marques, et al. (2012) for the full definition of this concept and various applications), where one plots the following quantities

$$||K_{\mathrm{Avg}}||^2 = \int_0^1 \left[K_{\mathrm{Avg}} - \mathscr{T}_A\right]^2 dx, \tag{5.98}$$

$$\sigma_{Inv} = \sqrt{\sum_i^N (c_i \sigma_i)^2}, \tag{5.99}$$

for various values of θ. In practice, a visual inspection of the agreement of the averaging kernels with their target is also informative on the quality and reliability of the inverted results. In practice, the set of inversion parameters will depend on the target function of the inversion and the observed seismic data.

In addition to these reliability assessments, further analyses can be performed, by separating the contribution to the linear correction derived from the frequencies using Eq. 5.94. Indeed, inversion techniques are subject to multiple error sources which can sometimes damp each other. To analyse this potential compensation, the linear correction of a given integrated quantity A can be decomposed into various contributions

$$\begin{aligned} A_{Obs} =& A_{Ref} + \left(\frac{\delta A}{A}\right)_{\mathrm{Inv}} + \int_0^1 (\mathscr{T}_A - K_{\mathrm{Avg}}) \frac{\delta s_1}{s_1} dx + \int_0^1 K_{Cross} \frac{\delta s_2}{s_2} dx \\ &+ \varepsilon_{\mathrm{Res}}, \\ =& A_{Ref} + \left(\frac{\delta A}{A}\right)_{\mathrm{Inv}} + \varepsilon_{\mathrm{Avg}} + \varepsilon_{\mathrm{Cross}} + \varepsilon_{\mathrm{Res}}, \end{aligned} \tag{5.100}$$

where we define three main error contributions: $\varepsilon_{\mathrm{Avg}}$, the error stemming from the mismatch between the averaging kernel and its target, which depends on the quality of the dataset and the value of the θ parameter, $\varepsilon_{\mathrm{Cross}}$, the error stemming from the non-zero cross-term contribution which depends on the choice of the variable s_2 and the parameter β, and $\varepsilon_{\mathrm{Res}}$, the residual error, which is defined as

$$\varepsilon_{\mathrm{Res}} = \frac{A_{\mathrm{Obs}} - A_{\mathrm{Ref}}}{A_{\mathrm{Ref}}} - \varepsilon_{\mathrm{Avg}} - \varepsilon_{\mathrm{Cross}}. \tag{5.101}$$

This contribution is the most difficult to assess, since it can originate from surface effects, the linearization of the equation of state and non-linear effects. In inversions of observed targets, the residual errors would also be influenced by physical processes not included in the derivation of the variational relations and on systematics in the frequency determinations. However, since its calculation requires the knowledge of the structural differences between the target and the reference model, the value of this residual error is not accessible in practical cases. As we will see in Sect. 5.4.4, we will use these error contributions in combination with the classical trade-off analysis to determine the degree of reliability of the inversion and its accuracy.

Convective cores and deep regions

Convective cores are one of the major difficulties when studying the evolution of stars with masses higher than approximately $1.2 M_\odot$. Indeed, their presence can lead to large uncertainties in age determinations and completely change the evolutionary track of a given model. Various studies focus on to the uncertainties linked to convective cores, for example the recent studies by Deheuvels, Brandão, et al. (2016) and Claret and Torres (2016) to calibrate overshooting, or the derivation of dedicated seismic indices to the detection of a convective core in a given star (see Miglio and Montalbán (2005)).

Looking at structural profiles of a model, the presence of a convective core can easily be seen in derivatives, where it introduces a discontinuity. This means that indicators

based on derivatives, such as the t_u indicator presented in Buldgen, D. R. Reese, and M. A. Dupret (2015), defined as

$$t_u = \int_0^R r(r-R)^2 \exp^{-7\left(\frac{r}{R}\right)^2} \left(\frac{du}{dr}\right)^2 dr \tag{5.102}$$

or t presented in Buldgen, D. R. Reese, M. A. Dupret, and Samadi (2015), defined as

$$t = \int_0^R \frac{1}{r}\frac{dc}{dr} dr \tag{5.103}$$

will be extremely sensitive to convective cores. However, the target function associated with these indicators is impossible to fit with the structural kernels if a convective core is present in the model. Indeed, both of the target functions for t and t_u are strongly discontinuous whereas the structural kernels are not. Using $S_{5/3}$ as the structural variable for the kernels, we recover the sensitivity to convective cores without the need for a derivative. Moreover, as can be seen in Fig. 5.18, the structural kernels associated with $S_{5/3}$ have an increased intensity in the deep regions, around $0.2r/R$, due to the mass dependency of the entropy proxy.

We define a new indicator for convective cores as follows:

$$S_{core} = \int_0^R \frac{f(r)}{S_{5/3}} dr \tag{5.104}$$

with $f(r)$ the weight function associated with the indicator:

$$\begin{aligned} f(r) =& r\left(10\exp\left(-26\left(\frac{r}{R}-0.17\right)^2\right)+3\exp\left(-5\left(\frac{r}{R}-0.23\right)^2\right)\right) \\ & \tanh\left(50\left(1-\frac{r}{R}\right)\right) \end{aligned} \tag{5.105}$$

The target function is built to fit the lobe around $0.2r/R$ present in every kernel of either the (S,Γ_1) or the (S,Y) structural pair.

The linear perturbation of this indicator leads to the following target function for the inversion:

$$\frac{\delta S_{core}}{S_{core}} = \frac{1}{S_{core}} \int_0^R -\frac{f(r)}{S_{5/3}} \frac{\delta S_{5/3}}{S_{5/3}} dr \tag{5.106}$$

This means that the target function of this inversion is defined as follows

$$\mathscr{T}_{S_{Core}} = \frac{-f(r)}{S_{Core} S_{5/3}(r)} \tag{5.107}$$

This function is illustrated in blue in Fig 5.21 along with the profile of $1/S_{5/3}$ in red. The product of both curves gives the argument of the integral defining the indicator. From visual inspection, it is clear that this argument probes the inner layers of the acoustic structure of the star. One should also note that this indicator is not restricted to stars with convective cores but can also be a complement to or a replacement for the t_u indicator.

If the convective core is well established and has quite a high plateau with a steep entropy variation, a peak tends to appear in the target function, as illustrated in Fig. 5.22. This peak is in fact due to the boundary of the convective core. Due to the $\mathscr{O}(r^2)$ behaviour of the structural kernels in the center, the entropy plateau of the convective

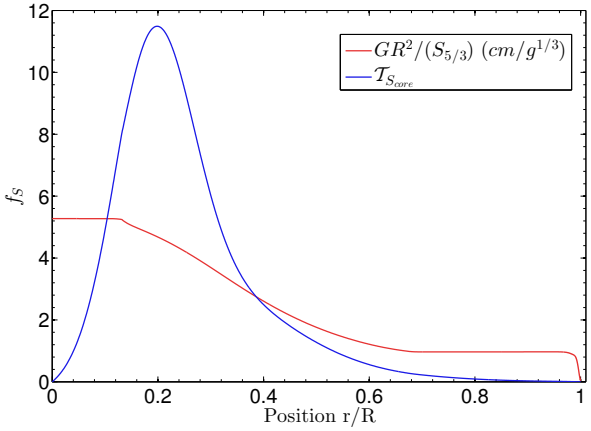

Figure 5.21: Target function of the core indicator S_{Core} plotted alongside the structural function $S_{5/3}^{-1}$. The model used is Target 3 of table 5.22. The target function is plotted in its non-dimensional form.

core is erased, but if its height and radial extent are sufficient, some traces remain in the kernels. Consequently the target function defined in Eq. 5.104 can still be fitted and is well adapted to extract information about convective cores. From numerical tests, the linear relations between frequencies and structure (Eq. 5.87) are still satisfied even in these particular cases. We will see in Sect. 5.4.4 how efficient the inversion actually is when confronted with these effects. The weight functions can also be adapted to be more easily fitted if required. Ultimately, the diagnostic power is limited by the detected modes and their error bars.

Convective envelopes

In this section, we will show that it is possible to probe the upper radiative zone and the convective envelope of certain Kepler targets. However, fully isolating the convective envelope is done thanks to high ℓ modes, as in helioseismology. Since these modes are not accessible to asteroseismology a complete scan of the structure is not achievable. However, a few $\ell = 3$ modes can still help with extracting information from the observations. The efficiency of this technique is mitigated by the difficulty to detect octupole modes, even for Kepler targets, and the low precision of their frequency determinations.

Our objective here is to probe the plateau in the convective envelope of $S_{5/3}$, shown in Fig. 5.23, and layers just below it. However, a compromise has to be found to exclude the uppermost region of the star, subject to surface uncertainties and a breakdown of the assumptions behind inversion techniques. Provided that the data quality is sufficient, the following indicator can be fitted

$$S_{env} = \int_0^R g(r) S_{5/3} dr, \tag{5.108}$$

which means that the target function for this inversion will be

$$\mathcal{T}_{S_{env}} = \frac{g(r) S_{5/3}(r)}{S_{env}}, \tag{5.109}$$

stemming from the relative linear perturbation of Eq. (5.108) and not forgetting the constant factor S_{env} in the denominator. The weight function $g(r)$ is somewhat complicated and has

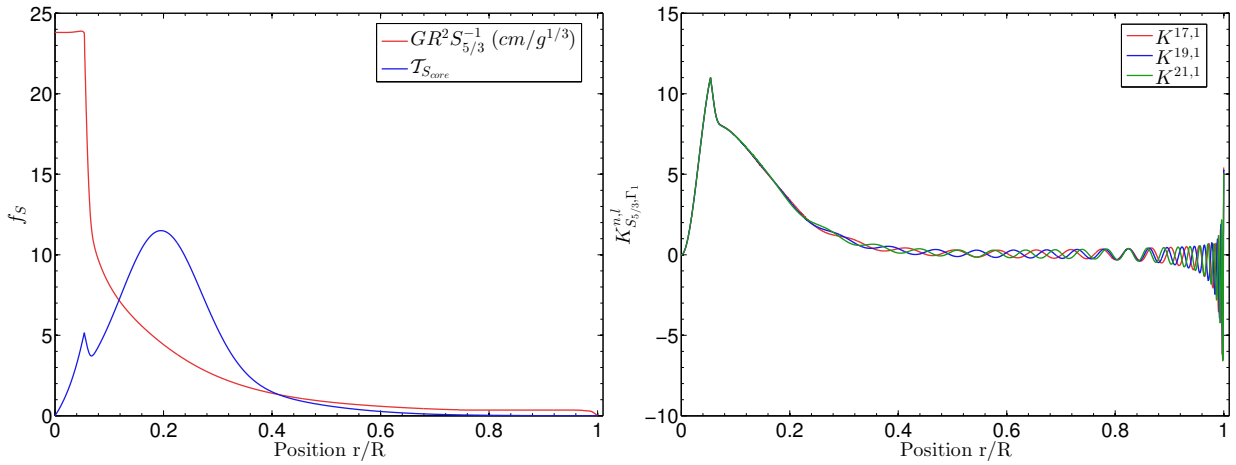

Figure 5.22: (Left panel) Structural profile of $S_{5/3}^{-1}$ in red, showing the plateau in the convective core. In blue, an example of the adaptation of a target function to include the trace of the convective core and its border. The target function is plotted in its non-dimensional form. (Right panel) Structural kernels associated with $S_{5/3}$ in the $(S_{5/3},\Gamma_1)$ structural pair, showing the trace of the entropy plateau in the convective core in the central regions. The model used is Target 6 of table 5.22. The kernels are plotted in their non-dimensional form.

been built to match the behaviour of kernels while trying to extract information in the upper regions. To explain the choice of $g(r)$, we separate it in three components:

$$g(r) = (g_1(r) + g_2(r))\, g_3(r), \tag{5.110}$$

with the following definitions:

$$g_1(r) = r^{1.5}\left(30\exp\left(-120\left(\frac{r}{R}-0.3\right)\right)^2 + 7\exp\left(-45\left(\frac{r}{R}-0.37\right)^2\right)\right), \tag{5.111}$$

$$g_2(r) = \frac{0.4r^{1.5}}{\exp\left(\left(\frac{R}{r}-1.7\right)/1.2\right)+1}, \tag{5.112}$$

$$g_3(r) = \tanh\left(50\left(1.0-\frac{r}{R}\right)\right). \tag{5.113}$$

The function g_1 is used to probe deeper regions where the entropy is influenced by the way it is reconnected to the plateau of the convective envelope. Looking at Fig. 5.23, we see that this corresponds to the regions where a slope starts in the entropy profile. The g_2 component is a Fermi-Dirac distribution that reproduces the entropy plateau in the convective envelope. The g_3 function eliminates the surface regions as efficiently as possible through the hyperbolic tangent. This component is steep in order to avoid affecting the lower part of the profile. The target function combining all three components is represented in Fig. 5.23. These components can be further adjusted depending on the reference model and the observed modes.

For example, we will see in Sec. 5.4.4, that octupole modes are required to carry out inversions of the S_{Env} indicator. The number of these modes and their error bars

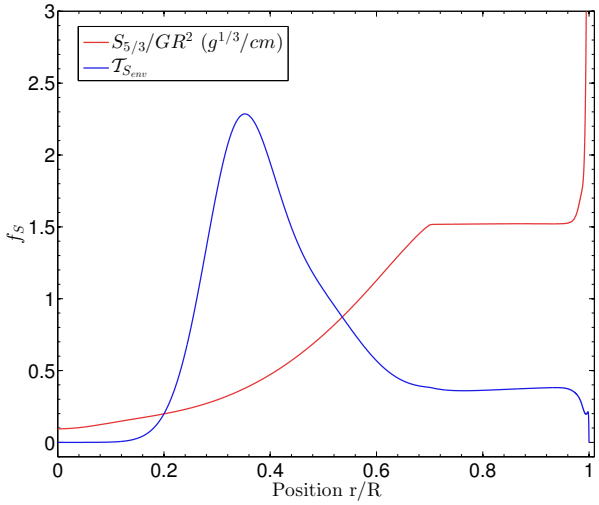

Figure 5.23: Target function of the envelope indicator S_{Env} plotted alongside the structural function $S_{5/3}$ for Target 1 of table 5.22. The target function is plotted in its non-dimensional form.

also influence the paramaters of the g_1 function. A larger number of precisely determined octupole modes allows for a higher position of the peak in the g_1 function and a more slowly decreasing slope towards the convective envelope, implying a better analysis of these regions. Besides the observed modes, the reference model also affects the building of the target function of the S_{Env} indicator. For example, a more massive star, having a shallower convective envelope, will require an adaptation of the g_2 and g_1 functions to avoid building a target that cannot be easily fitted with only low ℓ modes.

Non-linear generalisation

As in Buldgen, D. R. Reese, and M. A. Dupret (2015) and D. R. Reese, Marques, et al. (2012), one can improve the inversion by using a simple non-linear generalisation of the inversion procedure. To do this, we follow the procedure in section 3.2 of Buldgen, D. R. Reese, and M. A. Dupret (2015). From dimensional analysis, we can show that

$$S_{5/3} = \frac{P}{\rho^{5/3}} \propto \frac{GM^2R^5}{M^{5/3}R^4} \propto GRM^{1/3}. \tag{5.114}$$

This dimensional analysis is also crucial to know how the indicator value should be rescaled to be comparable for various reference models. We have seen in Buldgen, D. R. Reese, and M. A. Dupret (2015) that the inversion implicitly rescales the target model to the radius of the reference model without changing its mean density. This means that the quantity $S_{5/3}$ is then also rescaled. Consequently, when comparing inversions from various reference models, one should always be aware of this scaling and present them in a form proportional to the mean density. For example, using equations 5.104 and 5.105, one can carry out a dimensional analysis of the core conditions indicator, leading to

$$S_{Core} \propto \frac{R^2}{S_{5/3}} \propto \frac{R}{GM^{1/3}}, \tag{5.115}$$

meaning that the quantity GS_{Core} scales as $\rho^{-1/3}$. For S_{Env}, dimensional analysis from equations 5.108 and 5.113 leads to

$$S_{Env} \propto R^{3.5}M^{1/3}G. \tag{5.116}$$

Meaning that this quantity needs to be rescaled if it is to be compared for various reference models. In other words, one has $S_{Env}/GR^{4.5} \propto \rho^{1/3}$. To provide the coefficients for the non-linear generalisation, we focus on the mass dependency of the quantities, since the radius is implicitely kept constant by the inversion. Looking at Eq. 5.114, this means that $S_{5/3} \propto \nu^{2/3}$ in terms of the M dependency, thus leading to

$$\frac{\delta S_{5/3}}{S_{5/3}} = \frac{2}{3}\frac{\delta \nu}{\nu}, \tag{5.117}$$

for a homologous transformation which keeps the radius between models constant but changes their mean density through their mass. As stated Sect. 3.2 of Buldgen, D. R. Reese, and M. A. Dupret (2015), the coefficient in this linear relation between perturbations of the frequencies and that of a structural quantity, denoted k in our previous paper, is crucial to derive the non-linear generalisation. In this study, one has $k = 2/3$ in the relation between $S_{5/3}$ and the frequencies. Looking at Eq. 5.108, which defines S_{env}, we can see that since this indicator is proportional to $S_{5/3}$. Hence, one will have

$$\frac{\delta S_{Env}}{S_{Env}} = \frac{2}{3}\frac{\delta \nu}{\nu}, \tag{5.118}$$

and the value of 2/3 can be applied to Eq. 31 and 34 of Buldgen, D. R. Reese, and M. A. Dupret (2015) defining the optimal value of S_{Env} and its associated errors bars in the framework of this non-linear generalisation. Similary, the value k will also be fixed to 2/3 in the additional condition on the inversion coefficients (fourth term of Eq. 5.95) used to improve the regularisation of the inversion process.

Using the same analysis, it is easy to show that the S_{Core} indicator will satisfy a relation of the opposite sign, due to its opposite mass dependency,

$$\frac{\delta S_{Core}}{S_{Core}} = \frac{-2}{3}\frac{\delta \nu}{\nu}, \tag{5.119}$$

since it is proportional to $S_{5/3}^{-1}$. Consequently, the value $-2/3$ can also be used in Eq. 31, 34 and 28 of Buldgen, D. R. Reese, and M. A. Dupret (2015) to derive the non-linear generalisation of this indicator.

Relation between S_{core}, S_{env} and stellar structure

In the preceeding sections, we have shown how the entropy proxy could be used to obtain indicators of both convective cores and envelopes. In this section we will briefly show how they change with some specific aspects of stellar structure. We mention that these changes of course depend on the parameters used to build the target functions of the indicators. For example, placing the maximum of the gaussian functions deeper in the S_{Core} target function will increase the changes due to convective cores.

We illustrate the relation between convective cores and the S_{core} indicator in Fig. 5.24 by plotting the rescaled $S_{5/3}^{-1}$ profiles of two $1.3M_{\odot}$, $1.6Gy$ models with a solar chemical composition. The model plotted in blue in Fig. 5.24, included a 0.15 pressure scale-height adiabatic overshoot, causing its convective core to be larger at a given age and inducing changes in its entropy plateau. Similarly, the peak in the S_{core} target function is much more pronounced in the blue profile than in the red, indicating a more extended convective core. The changes seen in the indicator thanks to this small variation are of around one percent of the total value of the indicator. This is of course quite small but results from the fact that both models have the same age and chemical composition, and only differ in one

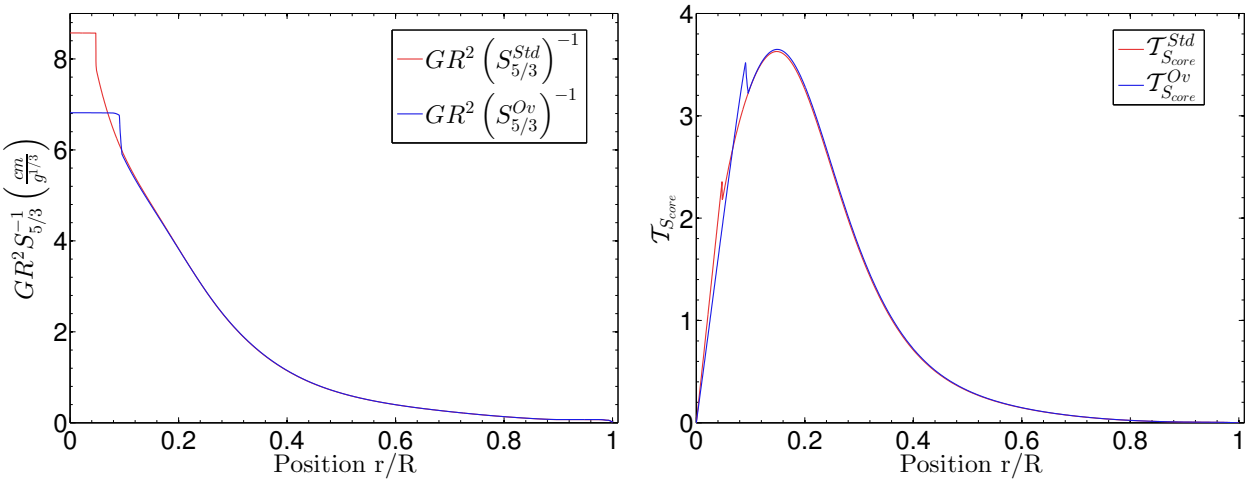

Figure 5.24: (Left panel) Scaled $S_{5/3}^{-1}$ profile used in inversions for two 1.3$M_\odot$ models. The blue curve is associated with a model built using a 0.15 pressure scale height adiabatic overshoot. (Right panel) Target function of the S_{core} indicator for both models.

physical ingredient. In a more realistic case, where the models are selected using seismic constraints, the differences between reference model and target can be much larger.

Similarly, we illustrate in Fig. 5.25 the effects of opacity changes on solar models. We compare solar models using the AGSS09 and the GN93 abundances and different opacity tables. To further increase the differences, we do not include microscopic diffusion in the AGSS09 solar model. This leads to variations in the position of the entropy plateau of the convective envelope of the models, as can be seen in the left panel of Fig. 5.25. This emphasizes the direct link between the entropy plateau and the temperature gradient in stellar models. The right panel of this figure illustrates the small changes in the target function of S_{Env}. The changes in the target function induce a change in the value of the indicator of less than one percent. Again this is quite small but is mainly due to the fact that the models have the same mass, the same age and are not selected on the basis of their seismic information. Sect. 5.4.4 shows a very different picture for its first target, a solar model including various physical processes fitted using individual small frequency separations without including these additional processes in the reference model.

5.4.4 Hare-and-hounds exercises

In this section, we present the results of hare-and-hounds exercises carried out to test the accuracy and the capabilities of the indicators based on the entropy proxy. We test these capabilities in similar exercises as in Buldgen, D. R. Reese, and M. A. Dupret (2015), using hares built with certain specificities that the hounds did not include. For example, some hares included strong overshooting or turbulent diffusion and were fitted with hounds without these processes. This approach attempts to simulate as best as possible the biases due to physical simplifications or approximations in our representation of stellar structure and evolution when carrying out seismic modelling of observed targets. It is also a good test of robustness and accuracy to see whether the linear approximation and the SOLA method are indeed capable of probing such aspects of stellar modelling.

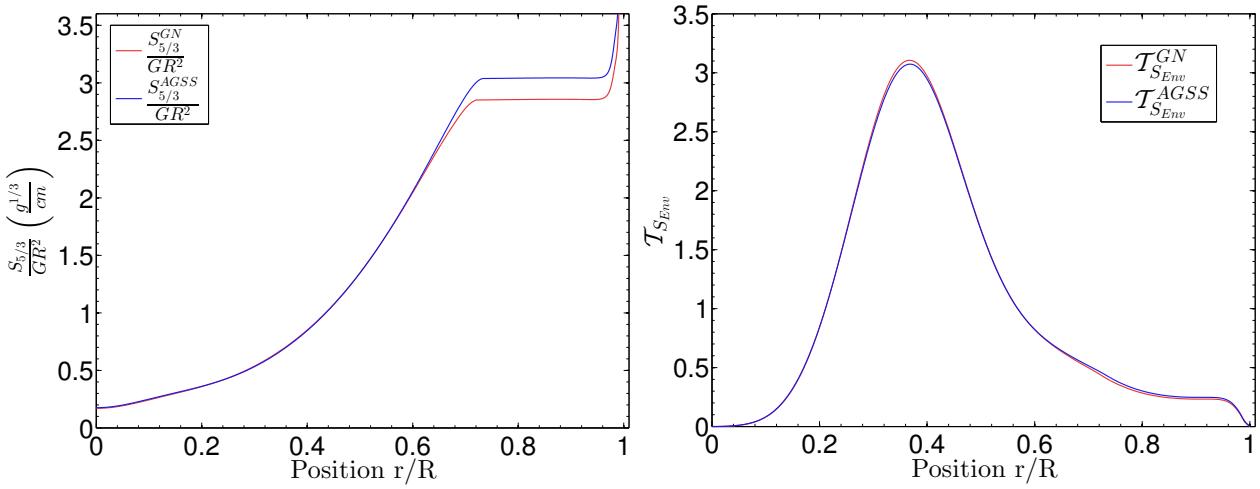

Figure 5.25: (Left panel) Scaled $S_{5/3}$ profile used in inversions for two standard solar models. The blue curve is associated with a model built using the AGSS09 abundances while the red one uses the GN93 abundances. (Right panel) Target function of the S_{env} indicator for both models.

Seismic diagnostic and accuracy

In total, we built 10 targets with various masses and ages, but only present 6 to avoid redundancy. The hounds were built by fitting the hare's individual small frequency separations and their effective temperatures. The fit was carried out using a Levenberg-Marquardt algorithm for the minimization. The observational spectrum of the hares is given in Table 5.24. An error bar of 80K was used on the effective temperature and the observational error bars on the frequencies were similar to those found of the best Kepler targets. The physical characteristics of the target models are given in Table 5.22. Some parameters have rather extreme values, in order to test the inversion and its limitations. Targets 1 to 5 were built using the OPAS opacities (Le Pennec et al. (2015) and Mondet et al. (2015)) and the Ceff equation of state (Christensen-Dalsgaard and Daeppen (1992)) with the AGSS09 abundances (Asplund, Grevesse, Sauval, and Scott (2009)) while target 6 was built using the OPAL opacities (Iglesias and Rogers (1996)) and the OPAL equation of state (Rogers, Swenson, and Iglesias (1996)) with its corrections (Rogers and Nayfonov (2002)). The reference models all used the Ceff equation of state and the OPAL opacities along with the GN93 abundances (Grevesse and Noels (1993)). None of the reference models included turbulent diffusion. The formalism used to implement turbulent diffusion in the target models is presented in Miglio, Montalbán, and Maceroni (2007). All models were computed using the Liège Stellar Evolution Code (CLES, Scuflaire, Théado, et al. (2008)) and the oscillations were computed using the Liège Oscillation Code (LOSC, Scuflaire, Montalbán, et al. (2008)). The reference models obtained from this first step of forward seismic modelling are presented in table 5.23. As can be seen, most of the hounds, denoted "*Ref*" still present significant structural differences with their respective target from table 5.22. The goal of the exercises is now to determine whether the inversions of the structural indicators can detect these mismatches, and thus provide additional information which could lead to refinements of the seismic modelling in the study of an observed target[13].

We also tested the impact of supplementary observed modes, for example $\ell = 4$ and 5

[13]Similar exercises can be found in Sect. 5 of Buldgen, D. R. Reese, and M. A. Dupret (2015)

Table 5.22: Characteristics of the target models used in this study.

	$Target_1$	$Target_2$	$Target_3$	$Target_4$	$Target_5$	$Target_6$
Mass ($M_\odot$)	1.0	1.1	0.86	1.14	1.05	1.07
Age (Gy)	4.5	6.0	2.0	3.5	1.5	5.0
Radius ($R_\odot$)	0.9896	1.3492	0.8178	1.0908	1.1033	1.56
T_{eff} (K)	5823	5907	5056	5748	5918	5.983
Z_0	0.02	0.02	0.015	0.03	0.02	0.013
X_0	0.69	0.69	0.67	0.7	0.65	0.68
Abundances	AGSS09	AGSS09	AGSS09	AGSS09	AGSS09	GN93
α_{MLT}	2.0	1.8	1.7	1.9	1.5	1.7
α_{Ov}	0.1	0.2	0.2	0.2	0.2	0.15
Microscopic Diffusion	Yes	Yes	Yes	Yes	Yes	Yes
Turbulent Diffusion	Yes	Yes	No	Yes	Yes	Yes

Table 5.23: Characteristics of the reference models obtained from the forward modelling process.

	Ref_1	Ref_2	Ref_3	Ref_4	Ref_5	Ref_6
Mass ($M_\odot$)	1.17	1.29	0.84	0.93	1.04	1.12
Age (Gy)	3.3	4.6	1.8	4.0	1.3	4.5
Radius ($R_\odot$)	1.05	1.42	0.80	1.02	1.10	1.55
T_{eff} (K)	5826	5991	5069	5751	5960	6035
Z_0	0.052	0.036	0.015	0.013	0.014	0.015
X_0	0.65	0.68	0.7	0.7	0.68	0.67
Abundances	GN93	GN93	GN93	GN93	GN93	GN93
α_{MLT}	2.5	2.2	1.4	1.4	1.4	1.8
α_{Ov}	0.0	0.1	0.0	0.1	0.2	0.1
Microscopic Diffusion	Yes	Yes	Yes	Yes	Yes	Yes
Turbulent Diffusion	No	No	No	No	No	No

modes but also modes with higher and lower n, on the accuracy of the inversion. Our goal was to assess which oscillations modes could help with extracting more information on stellar structure using inversions of integrated quantities. The error bars were usually taken to be similar to those of the best Kepler targets, i.e. around 3×10^{-1} μHz with slightly larger error bars for the lowest and highest frequencies, as expected in observed cases.

Results for S_{Core} inversions

In Table 5.25, we summarise the results of our test cases. Some kernels are illustrated in Fig. 5.26. In these hare and hounds exercices, we consider observed quantities, denoted with the subscript "*Tar*", to be those of the target models.

From the inversions for Targets 2 and 5, we can see that the S_{Core} indicator efficiently detects an inaccuracy in the stratification of the hounds, due to the absence of convective cores in these models. For Targets 3, we can see that the inversion provides an accurate result, but that the error bars on the inverted result are too large to conclude that the model has to be rejected. From a modelling point of view, we can see from tables 5.23 and 5.22 that Ref_3 is already a very good fit to $Target_3$. Adding more frequencies to this test case allowed to eliminate this problem but in practice, this would mean that for this

Table 5.24: Frequencies used to fit the simulated targets.

ℓ	0	1	2	3
n	$13-27$	$13-27$	$12-26$	$17-23$

Table 5.25: S_{Core} inversion results for the 6 targets using the $(S_{5/3},Y)$ kernels.

	$S^{\text{Ref}}_{Core}G$ $(cm/g^{1/3})$	$S^{\text{Inv}}_{Core}G$ $(cm/g^{1/3})$	$S^{\text{Tar}}_{Core}G$ $(cm/g^{1/3})$	$\varepsilon^{S_{5/3},Y}_{\text{Avg}}$	$\varepsilon^{S_{5/3},Y}_{\text{Cross}}$	$\varepsilon^{S_{5/3},Y}_{\text{Res}}$
Target_1	3.201	3.118 ± 0.0251	3.126	-3.085×10^{-3}	-1.744×10^{-4}	7.104×10^{-4}
Target_2	3.817	3.660 ± 0.067	3.668	-2.477×10^{-3}	-3.235×10^{-5}	1.110×10^{-4}
Target_3	2.789	2.786 ± 0.034	2.783	5.714×10^{-4}	1.868×10^{-4}	1.783×10^{-4}
Target_4	3.124	3.190 ± 0.048	3.184	1.706×10^{-3}	-1.383×10^{-4}	4.121×10^{-4}
Target_5	2.734	2.720 ± 0.007	2.726	-1.758×10^{-3}	2.424×10^{-4}	-5.751×10^{-4}
Target_6	3.408	3.434 ± 0.003	3.438	-1.357×10^{-3}	-5.035×10^{-5}	3.779×10^{-4}

particular case, the S_{Core} indicator would only be an additional check for the modelling. However, in most test cases, the observed differences between reference and inverted results are smaller than the error bars of the inverted result, meaning that we are still safe in terms of trade-off parameters.

Moreover, it should be noted that the values of the parameters in the definition of these indicators are not fixed. The number of frequencies available and the characteristics of the convective core (if present) imply that the parameters considered optimal in a case might be suboptimal in another case, depending on the mass, evolutionary stage or chemical composition of the model. For each of the targets in table 5.25, we fine tuned the parameters to analyse the diagnostic potential using the oscillation modes of table 5.24. Further tests on targets of the Kepler LEGACY sample (see Buldgen, D. Reese, and M.-A. Dupret (2017)) have also shown similar behaviours and proved that the method was indeed applicable to current seismic data.

From table 5.25, we can conclude that the inversion is efficient and can provide a diagnostic of inaccuracies in our modelling of deep regions of solar-like stars with convective cores. Very slight compensation is seen for Target 5 and 6, but further tests have shown these cases to be marginal. In addition, the averaging kernels illustrated in Fig 5.26 fit their target function to an acceptable level of accuracy.

Results for S_{Env} inversions

In Table 5.26, we present inversion results for the S_{Env} indicator. Some kernels are shown in Fig 5.27. We used the same targets, oscillation spectra and naming conventions as for the S_{Core} indicator.

From table 5.26, we can see that reproducing the value of S_{Env} can be done efficiently for most targets. However, for target 5, for example, the inversion is very difficult because of the proximity between the target and its hound. The variation of the indicator is too small to be seen with the typical accuracy of asteroseismic data. In comparison, some standard solar models show larger differences between each other than what is seen between target 5 and its hound. In addition, target 5 is more massive, meaning that its envelope does not go as deep as in a lower mass star. In fact, we found the base of the envelope to be around 0.75 fractional radii in its reference model. Therefore, the sensitivity of the indicator has to be increased by pushing the weight function towards upper regions. However, the structural kernels, illustrated in the right panel of Fig. 5.22 for a massive star with a convective core (noticeable by the peak in the deeper layers) show the exact opposite trend, the more massive the model, the steeper the decrease towards upper regions. Consequently, the amount of seismic information required to probe the convective

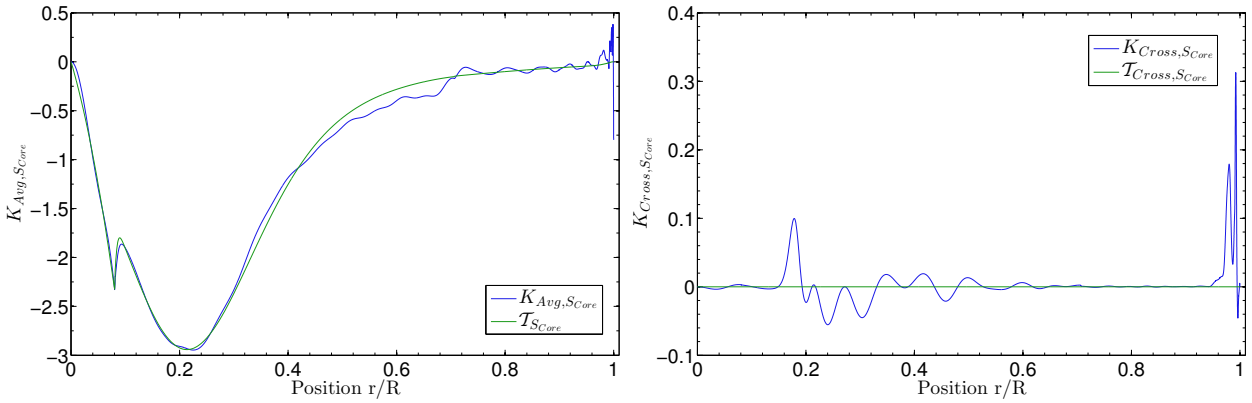

Figure 5.26: (Left panel) Averaging kernel for the S_{Core} indicator (blue) and the target function for the inversion (green). (Right panel) Cross term kernel for the S_{Core} inversion (blue), and target function which is 0 (green). These results are presented for Target 2 of table 5.22.

Table 5.26: S_{Env} inversion results for the 6 targets using the $(S_{5/3}, Y)$ kernels.

	$\frac{S^{Ref}_{Env}}{R^{4.5}_{Ref}G^{1/3}}$ $(g^{1/3}/cm)$	$\frac{S^{Inv}_{Env}}{GR^{4.5}_{Ref}}$ $(g^{1/3}/cm)$	$\frac{S^{Tar}_{Env}}{GR^{4.5}_{Tar}}$ $(g^{1/3}/cm)$	$\varepsilon^{S_{5/3},Y}_{\text{Avg}}$	$\varepsilon^{S_{5/3},Y}_{\text{Cross}}$	$\varepsilon^{S_{5/3},Y}_{\text{Res}}$
Target_1	1.682	1.805 ± 0.035	1.807	-2.079×10^{-3}	1.560×10^{-4}	4.110×10^{-2}
Target_2	1.611	1.759 ± 0.071	1.772	9.473×10^{-4}	9.717×10^{-6}	-8.521×10^{-3}
Target_3	1.127	1.050 ± 0.046	1.040	1.338×10^{-2}	2.127×10^{-5}	-3.964×10^{-3}
Target_4	0.924	0.914 ± 0.057	0.9083	5.787×10^{-3}	-8.729×10^{-5}	-8.189×10^{-4}
Target_5	1.626	1.627 ± 0.081	1.629	-5.462×10^{-4}	-2.837×10^{-5}	-6.224×10^{-4}
Target_6	1.777	1.849 ± 0.044	1.848	8.039×10^{-3}	-1.374×10^{-4}	-7.517×10^{-3}

envelope of massive stars is higher than for low mass stars, for which the entropy plateau goes deeper and the kernels are more suited to their purpose. We confirm this by carrying out supplementary test cases for additional low mass targets and show that these can be probed with the S_{Env} indicator. We illustrate one of these hare-and-hounds exercises in Fig. 5.28 and also test the effects of reducing the number of observed frequencies. For the S_{Core} indicator, going down to 44 frequencies still works. However, by changing the parameters in the target function of the indicator, valuable information can still be gained with as low as 35 observed frequencies. For the S_{Env} indicator, using fewer than 45 frequencies may already lead to imprecise results and we noticed that $\ell = 3$ modes were required to ensure an acceptable fit of the target function. Its range of application is therefore limited to the very best observed Kepler targets. In this particular case, we used a $0.9 M_{\odot}$ model including microscopic diffusion and fitted the individual large and small frequency separations of this artificial target with models that did not include microscopic diffusion and had a different helium mass fraction than the target.

Including higher ℓ modes can help improve the fit of the target function, but not all radial orders are equivalent in this matter. As already observed for the t_u inversion, low n modes are better at fitting custom-made global quantities, while high n modes are barely used and associated with lower inversion coefficients. Indeed, at very high values of n, one reaches the asymptotic regime and the oscillation spectrum becomes very regular, thus the information to be extracted from the modes is degenerate. Moreover, the large error bars on these high frequencies might make them very difficult to use for precise determinations of seismic indicators and these modes are more affected by the surface effects, biasing their seismic diagnostic.

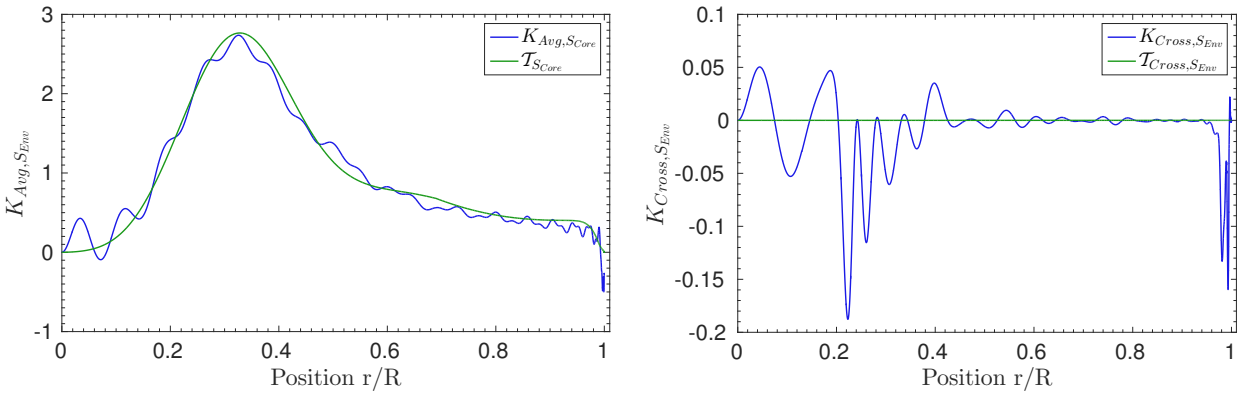

Figure 5.27: (Left panel) Averaging kernel for the S_{Env} indicator (blue) and the target function for the inversion (green). (Right panel) Cross term kernel for the S_{Env} inversion (blue), and target function which is 0 (green). These results are presented for Target 1 of table 5.22.

5.4.5 Conclusion

From Sect. 5.4.4, we can see that both indicators are well suited to probe convective cores and envelopes. We can see from table 5.25 that the residual error remains small compared to the variations of the S_{Core} indicator caused by the changes of the entropy plateau in the convective core. Consequently, we can conclude that the S_{Core} indicator is suitable in analysing mismatches in the deep layers of solar like stars, even if they present a convective core. The S_{Env} indicator, on the other hand, is quite efficient in its analysis of upper layers and can provide further constraints even if other indicators, such as the t_u indicator, are fitted within their error bars.

Another aspect of inversions that has to be re-analyzed is linked to the surface effects. While inversions related to core-sensitive structural aspects are naturally less prone to show problems, this might not be the case for all inversions. Actually, additional tests have shown that some inaccuracies, which appear as an increase of the residual error of the inversion, might be expected. Therefore, one needs to analyse how empirical corrections such as those of Sonoi et al. (2015) and Ball and Gizon (2014) might help solve the problem, since the classical surface-correcting method used in helioseismology cannot be used in asteroseismology due to the limited number of observed frequencies. This will be done in future studies.

In conclusion, we have proved that the amount of seismic information found in the typical spectra of solar-like Kepler targets is sufficient to carry out more robust inversions of a core condition indicator, applicable to more massive stars. We also showed that for the very best of these targets, for which octupole modes are observed, the inversion of a structural indicator probing the regions near the base of the convective envelope could be attempted, providing supplementary insights on the structural properties of the target. However, both S_{Core} and S_{Env} might require a slight adaptation of their target functions when applied to observations depending on the dataset and the reference model for the inversion. Nevertheless, they can be used alongside additional interferometric, spectroscopic or even seismic constraints such as, for example, glitch fitting techniques. In turn, the use of these indicators will help improve the physical accuracy of stellar models and provide stringent constraints on stellar fundamental parameters required by other fields such as exoplanetology and Galactic archeology.

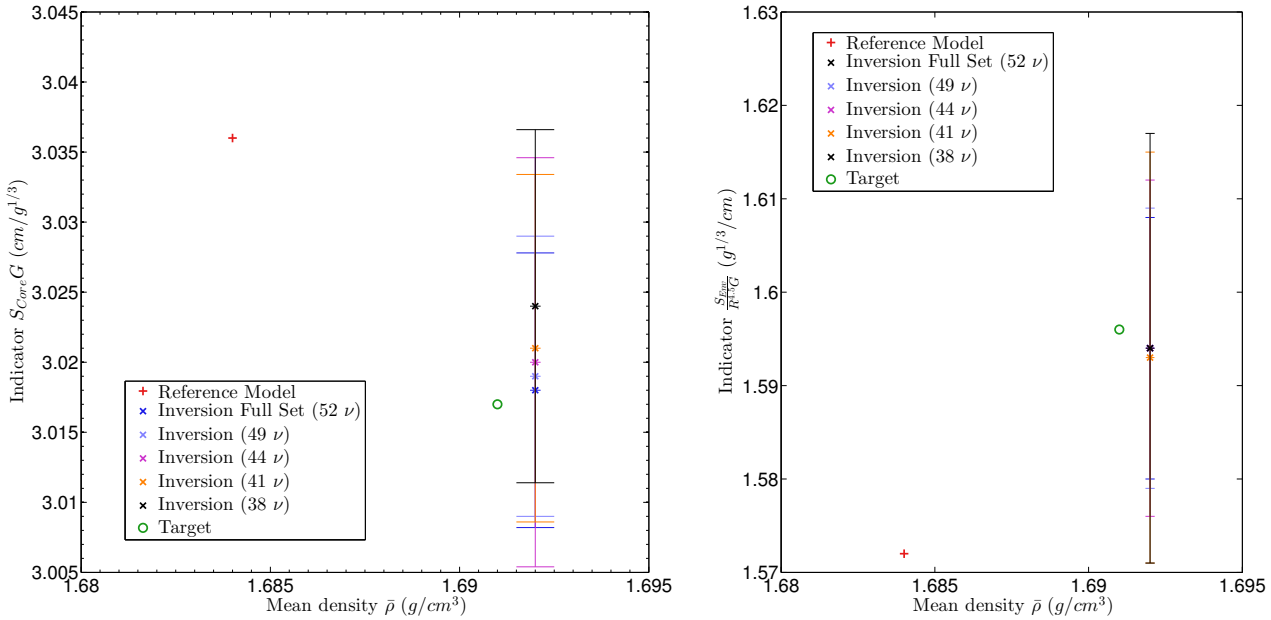

Figure 5.28: (Left panel) Illustration of the accuracy of the inversion of the S_{Core} indicator illustrated in a $\bar{\rho} - S_{Core}$ plane for various numbers of observed frequencies. The reference values are given in red, the target values are plotted in green and the inverted values are plotted in various colours according to the number of observed frequencies. (Right panel) Same for the S_{Env} indicator.

5.5 General Conclusion

In this chapter, we have presented how the SOLA method could be adapted to asteroseismology through the inversion of integrated quantities. We presented 5 new indicators with various goals and carried out additional investigations for the mean density, developed by D. R. Reese, Marques, et al. (2012). We showed that basing our reasoning on structural considerations, we could use variable changes in the variational expression to derive linear functionals sensitive to various aspects of stellar structure and evolution.

Various tests have been carried out to determine the stability and reliability of the inversion for conditions similar to those found for the best asteroseismic targets. The main conclusion is that this adaptation of the SOLA method can provide stringent constraints on stellar models beyond the capabilities of classical forward seismic modelling. It can provide diagnostics for potential mismatches in the physical ingredients of stellar models, thus greatly improving the determination of stellar fundamental parameters.

However, these successes are mitigated by three aspects that make the inversion tedious to carry out:

1. The optimal target function for an indicator can vary from one target to another. In other words, an essential quality of the technique can become its worst enemy, since the freedom to chose the target can mean having the freedom not to find it.
2. The trade-off problem has to be recalibrated for almost every reference model and every observed target, leaving the method not always well suited for large-scale automated studies but more specialised in specific, detailed studies.
3. Non-linearity has to be assessed individually for every target, using multiple reference models to ensure at least a first diagnostic of potential problems.

In addition to these difficulties, the method is very demanding in terms of the quality

of the seismic data. Typically, around 35 frequencies for modes with $\ell = 0, 1, 2$ and n as low as 13 are sufficient to carry out inversions of $\bar{\rho}$, τ and S_{Core}. Inversions of t_u and S_{Env} typically require more modes and are greatly improved by the presence of $\ell = 3$ modes and lower n modes. The errors bars should be small, similar to those found in Kepler observations. All these restrictions imply that the method will only be well-suited for the best asteroseismic targets. Furthermore, the method has only been tested with pressure modes of main sequence targets. Further extending the method to evolved targets exhibiting mixed modes, or massive stars exhibiting gravity modes will probably require additional developments and adaptations.

Last but not least, the treatment of surface effects and its impact on inversions needs to be assessed. As stated previously, using the individual frequency differences exposes the method to the impact of the upper layers and the importance of this effect has to be assessed and accounted for in future applications to observed targets. To this day, two solutions are possible:

1. to apply an empirical correction on the frequency differences before carrying out the inversion,
2. to use frequency ratio perturbations instead of frequency differences in the variational expression.

The first step is to quantify the impact of surface effects on the various indicators and to see whether some indicators are more sensitive to these effects than others. For example, the t_u indicator seems to be linked to frequency ratios. Therefore, it is possible that the impact of the surface effects for this indicator is naturally reduced. Such analyses will be performed in the near future, since they are of paramount importance to avoid biased determinations using the Kepler datasets.

Concerning large scale studies and targets exhibiting a smaller number of frequencies, the method could be adapted to build certain combination of frequencies related to those obtained by the inversion, but exhibiting smaller error bars, in a similar fashion to classical seismic indicators. Such constraints could then be used in addition to or as a replacement for classical seismic constraints like the r_{02} frequency ratios. Such studies would provide an interesting basis for seismic modelling using a smaller number of constraints that still encompass the information of the oscillation spectrum, and would help us understand what exact amount of independant physical information can be extracted from seismic observations.

III STUDIES OF OBSERVED TARGETS

6. THE 16CYGNI BINARY SYSTEM

6.1 General Introduction

The Kepler spacecraft has provided the best set of asteroseismic data for solar-like stars other than the Sun. Amongst the targets of this mission, the 16Cygni binary system holds a special place. Indeed, these stars, found at 21.4 *pc* are some of the brightest targets observed by the Kepler spacecraft, thus allowing a high number of frequencies to be precisely determined. Therefore, they consistute the best targets for which to attempt a structural inversion and to see whether additional information can indeed be gained beyond the classical forward modelling approach.

In this chapter, we will present some inversion results for both 16CygA and 16CygB using the full Kepler dataset from Davies et al. (2015). Sections 6.2 and 6.3 are composed of the publications presented in Astronomy and Astrophysics under the references Buldgen, D. R. Reese, and M. A. Dupret (2016) and Buldgen, S. J. A. J. Salmon, et al. (2016). We will show that for both components, structural inversions can be performed and that stringent constraints can be put on the age and chemical composition of this system. However, as we will see in our conclusion, the quality of the seismic data implies the need for a very high accuracy of the models and the seismic analysis techniques. While both sections of this chapter show the advantage of using inversion techniques, in particular the accuracy that can be gained from this approach, they certainly do not represent the most constraining study that can be carried out for this system. Indeed, the publication of new opacity tables by the Los Alamos National Laboratory (Colgan et al. (2016)), the implementation of a new equation of state in Cles (Irwin (2012)), as well as the requirement of an unbiased determination of helium using Cles models to calibrate the glitch in these stars seem to call for a complete remodelling of the system using an indisputable frequency set (see I. W Roxburgh (2016) for a discussion on the problems related to data treatment in the Kepler LEGACY) for which the importance of the surface effect corrections are tested.

6.2 Constraints on the structure of 16 Cyg *A* and 16 Cyg *B* using inversion techniques

6.2.1 Introduction

In a series of previous papers (Buldgen, D. R. Reese, M. A. Dupret, and Samadi (2015) and Buldgen, D. R. Reese, and M. A. Dupret (2015)), we analysed the theoretical aspects of the use of seismic inversion techniques to characterise extra mixing in stellar interiors. Instead of trying to determine entire structural profiles, as was successfully done in helioseismology (Basu, Christensen-Dalsgaard, Chaplin, et al. (1997), Basu, Christensen-Dalsgaard, Schou, et al. (1996), Basu and Christensen-Dalsgaard (1997b))[1], we make use of multiple indicators, defined as integrated quantities which are sensitive to various effects in the structure. These indicators are ultimately new seismic constraints using all the available information provided by the pulsation frequencies.

In this section, we apply our method to the binary system 16Cyg, which was observed by Kepler, for which data of unprecedented quality is available. Moreover, this system has already been extensively studied, particularly since the discovery of a red dwarf and a Jovian planet in it (see Cochran et al. (1997)). Using Kepler data, this system has been further constrained by asteroseismic studies (Metcalfe, Chaplin, et al. (2012), Gruberbauer et al. (2013), Mathur et al. (2012)), interferometric radii have also been determined (see White, Huber, et al. (2013)) and more recently, Verma, Faria, et al. (2014) have determined the surface helium abundance of both stars and Davies et al. (2015) analysed their rotation profiles and tested gyrochronologic relations for this system.

The excellent quality of the Kepler data for these stars enables us to use our inversion technique to constrain their structure. We use the previous studies as a starting point and determine the stellar parameters using spectroscopic constraints from Ramírez, Meléndez, and Asplund (2009) and Tucci Maia, Meléndez, and Ramírez (2014), the surface helium constraints from Verma, Faria, et al. (2014) and the frequencies from the full length of the Kepler mission used in Davies et al. (2015) and check for consistency with the interferometric radius from White, Huber, et al. (2013). The determination of the stellar model parameters is described in Sect. 6.2.2. We carry out a first modelling process then determine the acoustic radius and the mean density using the SOLA technique (Pijpers and Thompson (1994)) adapted to the determination of these integrated quantities (see Buldgen, D. R. Reese, M. A. Dupret, and Samadi (2015), D. R. Reese, Marques, et al. (2012)). In Sect. 6.2.3, we briefly recall the definition and purpose of the indicator t_u and carry out inversions of this indicator for both stars. We then discuss the accuracy of these results. Finally, in Sect. 6.2.4, we use the knowledge obtained from the inversion technique to provide additional and less model-dependent constraints on the chemical composition and microscopic diffusion in 16CygA. These constraints on the chemical and atomic diffusion properties allow us to provide accurate, yet of course model-dependent, ages for this system, using the most recent observational data. The philosophy behind our study matches the so-called "à la carte" asteroseismology of Lebreton and Goupil (2012) for HD52265, where one wishes to test the physics of the models and quantify the consequences of these changes. However, we add a substantial qualitative step by supplementing the classical seismic analysis with inversion techniques.

[1]Also see Christensen-Dalsgaard (2002) for an extensive review on helioseismology.

6.2.2 Determination of the reference models parameters

Initial fits and impact of diffusion processes

In this section, we describe the optimization process that led to the reference models for the inversions. We carried out an independent seismic modelling of both stars using the frequency spectrum from Davies et al. (2015), which was based on 928 days of Kepler data. A Levenberg-Marquardt algorithm was used to determine the optimal set of free parameters for our models. We used the CLES stellar evolution code and the LOSC oscillation code (Scuflaire, Théado, et al. (2008), Scuflaire, Montalbán, et al. (2008)) to build the models and calculate their oscillation frequencies. We used the CEFF equation of state (Christensen-Dalsgaard and Daeppen (1992)), the OPAL opacities from Iglesias and Rogers (1996), supplemented at low temperature by the opacities of Ferguson et al. (2005) and the effects of conductivity from Potekhin et al. (1999) and Cassisi et al. (2007). The nuclear reaction rates we used are those from the NACRE project (Angulo et al. (1999)), supplemented by the updated reaction rate from Formicola et al. (2004) and convection was implemented using the classical, local mixing-length theory (Böhm-Vitense (1958)). We also used the implementation of microscopic diffusion from Thoul, Bahcall, and Loeb (1994), for which three groups of elements are considered and treated separately: hydrogen, helium and the metals (all considered to have diffusion speeds of ^{56}Fe). No turbulent diffusion, penetrative convection and rotational effects have been included in the models. The empirical surface correction from Kjeldsen, Bedding, and Christensen-Dalsgaard (2008) was not used in this study. The following cost function was used when carrying out the minimization:

$$\mathscr{J} = \frac{1}{N-M} \sum_{i}^{N} \frac{\left(A^i_{obs} - A^i_{theo}\right)^2}{\sigma_i^2}, \tag{6.1}$$

where A^i_{obs} is an observational constraint (such as individual frequencies or frequency separation, average values thereof, etc.), A^i_{theo} the same quantity generated from the theoretical model, σ_i is the observational error bar associated with the quantity A^i_{obs}, N the number of observational constraints, and M the number of free parameters used to define the model. We can already comment on the use of the Levenberg-Marquardt algorithm, which is inherently a local minimization algorithm, strongly dependent on the initial values. In the following section, particular care was taken to mitigate the local character of the results since at least 35 models were computed independently for each star, using various observational constraints and initial parameter values. As far as the error bars are concerned, we looked at the scatter of the results with changes in the physical ingredients rather than the errors given by the Levenberg-Marquardt algorithm. The constraints vary according to the following two cases:

1. *The model does not include any microscopic diffusion:* We used the individual small frequency separations, the average large frequency separation and the effective temperature as A_i for the cost function. The chemical composition was fixed to the values given by Verma, Faria, et al. (2014) and Ramírez, Meléndez, and Asplund (2009). The fit used three free parameters since the chemical composition is fixed: the mixing-length parameter, denoted $\alpha_{\rm MLT}$, the mass and the age.
2. *The model includes microscopic diffusion:* We used the individual small frequency separations, the average large frequency separation, the effective temperature, the surface helium and surface metallicity constraints in the cost-function[2]. We used five

[2]The inclusion in the cost function of the surface composition constraints is of course due to the impact of microscopic diffusion and comes from the intrinsic difference between the initial chemical composition,

free parameters: the mixing-length parameter, $\alpha_{\rm MLT}$, the mass, the age, the initial hydrogen abundance, X_0 and the initial metallicity, Z_0.

In the case of the additional fits described in Section 6.2.2, we simply replaced the average large frequency separation by the mean density $\bar{\rho}$ and the acoustic radius τ, thus increasing by one the number of constraints used in the cost function $\mathscr{J}$.

We wish to emphasise that the use of other algorithms to select a reference model does not reduce the diagnostic potential of the inversions we describe in the next sections. Indeed, inversions take a qualitative step beyond forward-modelling techniques in the sense that they explore solutions outside of the initial model parameter space.

We used various seismic and non-seismic constraints in our selection process and focussed our study on the importance of the chemical constraints for these stars. Indeed, there is a small discrepancy in the literature. In Verma, Faria, et al. (2014), a less model-dependent glitch-fitting technique was used to determine the surface helium mass fraction, Y_f. It was found to be between 0.23 and 0.25 for 16CygA and between 0.218 and 0.26 for 16CygB (implying an initial helium abundance, Y_0, between 0.28 and 0.31, provided atomic diffusion is acting). In the seismic study of Metcalfe, Chaplin, et al. (2012), various evolutionary codes and optimization processes were used and the initial helium abundance was 0.25 ± 0.01 for a model that includes microscopic diffusion. In fact, the seismic study of Gruberbauer et al. (2013) already concluded that the initial helium mass fraction had to be higher than the values provided by Metcalfe, Chaplin, et al. (2012), which could result from the fact that they used three months of Kepler data for their study. Therefore, the starting point of our analysis was to obtain a seismic model consistent with the surface helium constraint from Verma, Faria, et al. (2014) and the metallicity constraint from Ramírez, Meléndez, and Asplund (2009). We started by searching for a model without including microscopic diffusion, and therefore the final surface abundances Y_f and Z_f are equal to the initial abundances Y_0 and Z_0. The metallicity can be determined using the following equation:

$$\left[\frac{\rm Fe}{\rm H}\right] = \log\left(\frac{Z}{X}\right) - \log\left(\frac{Z}{X}\right)_{\odot}, \tag{6.2}$$

where $\left(\frac{Z}{X}\right)_{\odot}$ is the solar value consistent with the abundances used in the spectroscopic differential analysis. We point out that in the spectroscopic study of Ramírez, Meléndez, and Asplund (2009), the "solar" references were the asteroids Cérès and Vesta. Their study is thus fully differential and does not depend on solar abundance results. In this study, we used the $\left(\frac{Z}{X}\right)_{\odot}$ value from AGSS09 (Asplund, Grevesse, Sauval, and Scott (2009)) to determine the value of the metallicity Z. From the error bars provided on these chemical constraints, we can determine a two-dimensional box for the final surface chemical composition of the model (which is the initial chemical composition if the model does not include any extra mixing). A summary of the observed properties for both components is presented in Table 6.1. The quality of the seismic data is such that we have 54 and 56 individual frequencies for 16CygA and 16CygB respectively, determined with very high precision (typical uncertainties of 0.15μHz). The uncertainties on the constraints in Table 6.1 were treated as allowed ranges for the model parameters and checked for consistency for each model we built. An initial reference model without microscopic diffusion was obtained using the effective temperature, $T_{\rm eff}$, the arithmetic average of the large frequency separation $<\Delta\nu>$, and the individual small frequency separations $\delta\nu_{n,\ell}$.

denoted with a 0 subscript and the surface chemical composition at the end of the evolution, denoted with a f subscript.

Table 6.1: Summary of observational properties of the system 16CygA and 16CygB considered for this study.

	16CygA	16CygB	References
R ($R_\odot$)	1.22 ± 0.02	1.12 ± 0.02	White, Huber, et al. (2013)
$T_{\rm eff,spec}$ (K)	5830 ± 7	5751 ± 6	Tucci Maia, Meléndez, and Ramírez (2014)
$T_{\rm eff,phot}$ (K)	5839 ± 42	5809 ± 39	White, Huber, et al. (2013)
L ($L_\odot$)	1.56 ± 0.05	1.27 ± 0.04	Metcalfe, Chaplin, et al. (2012)
[Fe/H] (dex)	0.096	0.051	Ramírez, Meléndez, and Asplund (2009)
Y_f	[0.23, 0.25]	[0.218, 0.260]	Verma, Faria, et al. (2014)
$<\Delta\nu>$ (μHz)	103.78	117.36	Davies et al. (2015)

We did not include individual large frequency separations because these quantities are sensitive to surface effects in the frequencies and they would have dominated our cost function. This would have been unfortunate since we want to focus our analysis on core regions. As we see from Table 6.2, the model $S_{A,1}$ was also able to fit constraints such as the interferometric radius from White, Huber, et al. (2013) and the luminosity from Metcalfe, Chaplin, et al. (2012) although these quantities were not included in the $\mathscr{J}$ of the original fit. The agreement between the observed and theoretical seismic constraints is illustrated in Fig. 6.1. These results might seem correct, but since we did not even include

Table 6.2: Optimal parameters obtained for 16CygA.

	$S_{A,1}$	$S_{A,2}$	$S_{A,3}$
Mass ($M_\odot$)	1.052	1.025	1.002
Radius ($R_\odot$)	1.240	1.229	1.218
Age (Gyr)	8.232	7.784	7.335
$T_{\rm eff}$ (K)	5825	5802	5801
L ($L_\odot$)	1.589	1.536	1.508
Z_0	0.0165	0.0190	0.0205
Y_0	0.24	0.271	0.2945
$\alpha_{\rm MLT}$	1.618	1.640	1.672
D	0.0	0.5	1.0
$<\Delta\nu>$ (μHz)	103.74	103.79	103.98
$\mathscr{J}$	1.18	1.19	1.30

microscopic diffusion, we should consider this model as rather unrealistic in terms of mixing processes[3]. Therefore, we computed a few supplementary models assuming a final surface chemical composition of $Y_f = 0.24$ and $\left(\frac{Z}{X}\right)_f = 0.0222$ which included microscopic diffusion following the prescriptions of Thoul, Bahcall, and Loeb (1994). In this case, the fit was carried out using five free parameters, the mass, the age, the mixing length parameter, $\alpha_{\rm MLT}$, the initial hydrogen abundance, X_0 and the initial metallicity, Z_0. We used the same constraints as for the first fit without diffusion, supplemented by the constraints on the surface chemical composition, Y_f and $(Z/X)_f$ providing direct and strong constraints on the initial chemical composition.

The effect of diffusion was mainly to reduce the mass, age and radius of the model,

[3]One should note that we do not imply here that microscopic diffusion is the only mixing process needed in a "realistic model".

Table 6.3: Optimal parameters obtained for 16CygB.

	$S_{B,1}$	$S_{B,2}$	$S_{B,3}$
Mass ($M_\odot$)	1.008	0.977	0.943
Radius ($R_\odot$)	1.123	1.107	1.098
Age (Gyr)	8.16178	7.71671	7.37336
$T_{\rm eff}$ (K)	5749	5742	5739
L ($L_\odot$)	1.236	1.196	1.174
Z_0	0.0151	0.0173	0.0185
Y_0	0.24	0.273	0.3015
$\alpha_{\rm MLT}$	1.567	1.603	1.615
D	0.0	0.5	1.0
$<\Delta\nu>$ (μHz)	117.36	118.00	117.37
$\mathscr{J}$	0.81	0.85	0.88

as illustrated in Fig. 6.2. This plot illustrates the effects of diffusion for various chemical compositions and diffusion velocities. The subscripts 0.0, 1.0, 0.5 are respectively related to a model without diffusion, with standard diffusion velocities and with half of these velocity values. We denote this factor D in the tables presenting the results. Each colour is associated with a particular surface chemical composition of these stars. All these models were fitted using the method described previously, and thus are compatible with all constraints that can be found in the literature for 16CygA. Therefore, the effect observed here is related to the impact of diffusion for a given model associated with a given set of frequencies. It is obvious that the reductions of the mass and radius are correlated since the mean density is kept nearly constant through the fit of the average large frequency separation. Therefore, the conclusion of this preliminary modelling process is that we obtain a degeneracy, meaning that we could build a whole family of acceptable models, inside the box of the chemical composition, with or without diffusion. This implies important uncertainties on the fundamental properties, as can be seen from the simple example in Fig. 6.2 for 16CygA. In the following section, we see how the use of inversion techniques and especially the inversion of t_u can help us reduce this scatter and restrict our uncertainties on fundamental properties.

Even when considering diffusion based on the work of Thoul, Bahcall, and Loeb (1994), one should note that the diffusion velocities are said to be around $15-20\%$ accurate for solar conditions. Therefore, in the particular case of 16CygA, for which we have strong constraints on the chemical composition, one can still only say that the mass has to be between 0.97 $M_\odot$ and 1.07 $M_\odot$, that the radius has to be between 1.185 $R_\odot$ and 1.230 $R_\odot$ and that the age has to be between 6.8 Gy and 8.3 Gy for this star. In other words, we have a $\pm5\%$ mass uncertainty, $\pm3\%$ radius uncertainty and $\pm8\%$ age uncertainty.

Inversion of acoustic radii and mean densities

In this section, we briefly present our results for the inversion of the mean density and the acoustic radius. The technical aspects of the inversions have been described in previous papers (see D. R. Reese, Marques, et al. (2012), Buldgen, D. R. Reese, M. A. Dupret, and Samadi (2015), Buldgen, D. R. Reese, and M. A. Dupret (2015) for example) but we recall them briefly at the beginning of Sect. 6.2.3. First, we note that the inverted results for the mean density and the acoustic radius are slightly different. There is a scatter of around 0.5% for both $\bar{\rho}$ and τ depending on the reference model used for the inversion. We therefore consider that the results are $\tau_A = 4593 \pm 15s$ and $\bar{\rho}_A = 0.830 \pm 0.005 g/cm^3$

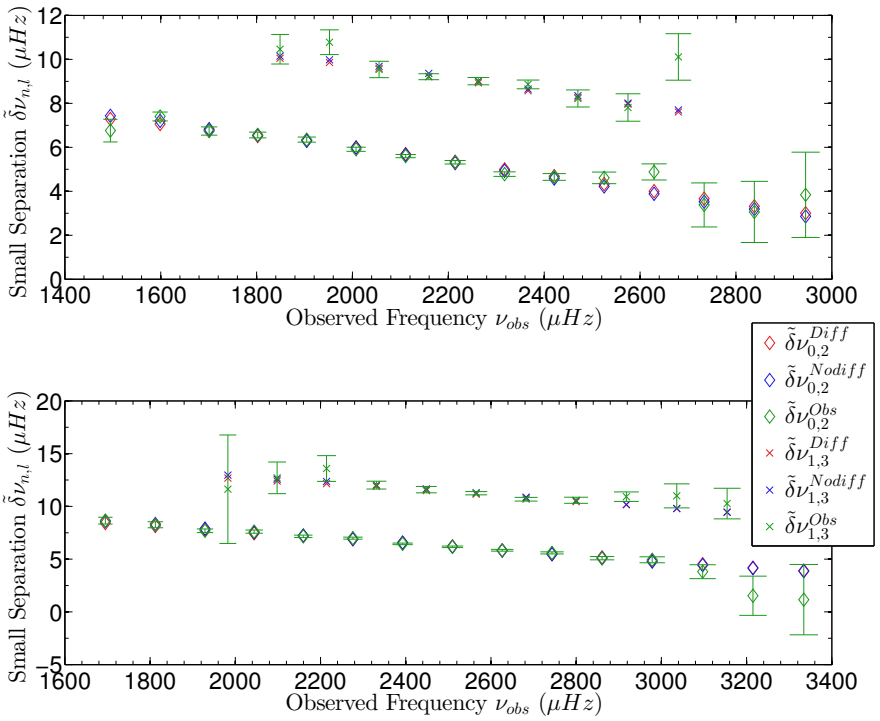

Figure 6.1: Upper panel: Fits of the small frequency separations $\tilde{\delta}_{02}$ and $\tilde{\delta}_{13}$ for 16CygA. Lower panel: Same as the upper panel for 16CygB. The observational values are the green symbols with error bars, the red symbols are associated with models including solar-calibrated diffusion and the blue symbols are associated with models without diffusion.

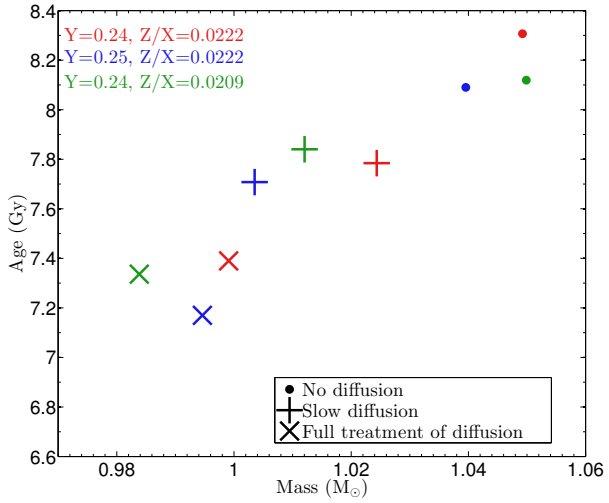

Figure 6.2: Effect of the progressive inclusion of diffusion in a model of 16CygA. Each model still fits the observational constraints.

to be consistent with the scatter we observe. For 16CygB, we obtain similar results, namely $\tau_B = 4066 \pm 15s$ and $\bar{\rho}_B = 1.066 \pm 0.005 g/cm^3$. The kernels are well fitted, as can be seen for a particular example in Fig. 6.3. One should note that the results for the

mean density are dependent on the ad-hoc surface corrections that is included in the SOLA cost function (D. R. Reese, Marques, et al. (2012)). If one does not include the surface correction, the mean density obtained for 16CygA is $\bar{\rho}_A = 0.817 \pm 0.005 g/cm^3$ and for 16CygB: $\bar{\rho}_B = 1.045 \pm 0.005 g/cm^3$. This implies a shift of around 1.5% in the inverted values. From our previous test cases, we have noted that inversion of the mean density including the surface regularization term can produce accurate results but in terms of kernel fits, the values without surface correction should be favoured. In what follows, the shift in the mean density value does not have a strong impact on the final conclusions of the results, but this issue should be further investigated in future studies since mean densities inversions could offer strong constraints on models obtained through forward-modelling approaches.

The scatter obtained because of the variations in the reference models justifies the fact that linear inversions are said to be "nearly model-independent". We emphasise that the physical ingredients for each model were different and that the scatter of the results is smaller than 0.50%. Before the inversion, the scatter of the mean density was of about 0.95% and significantly different from the inversion results. In that sense, the model dependency of these methods is rather small. However, the error bars determined by the simple amplification of the observational errors are much smaller than the model dependency, so that one has to consider that the result is accurate within the scatter owing to the reference models rather than using the error bars given by the inversion. Nevertheless, this scatter is small and therefore these determinations are extremely accurate.

We also observed that including additional individual large frequency separations in the seismic constraints could improve determination of both the acoustic radius and the mean density of the model. However, this can reduce the weight given to other seismic constraints and as we see in the next section, we can improve the determination of reference models using the acoustic radius and the mean density directly as constraints in the fit. We also note that neither the mean density nor the acoustic radius could help us disentangle the degeneracy observed in the previous section for the chemical composition and the effects of diffusion. Indeed, these quantities are more sensitive to changes in the mixing-length parameter, α_{MLT}, or strong changes in metallicity. However, as described in the following section, they can be used alongside other inverted structural quantities to analyse the convective boundaries and upper layers of these stars.

Determination of new reference models

After having carried out a first set of inversions using the acoustic radius and the mean density, we carried out a supplementary step of model parameter determination, replacing the average large frequency separation by the acoustic radius and the mean density themselves. We obtained a new family of reference models that were slightly different from those obtained using the average large frequency separation. We used the following naming convention for these models: the first letter, *A* or *B* is associated with the star, namely 16CygA or 16CygB; the second letter is associated with the chemical composition box in the right-hand panel of Fig. 6.7, where *C* is the central chemical composition, *L* the left-hand side, *R* the right-hand side, *U* the upper side, and *D* the lower side (*D* for down); the number 1 or 2 is associated with diffusion, 1 for models without microscopic diffusion, and 2 for models including the prescriptions of Thoul, Bahcall, and Loeb (1994) for microscopic diffusion. The numerical results of these supplementary fits are given in Table 6.7 for the A component and in Table 6.8 for the B component. A summary of the

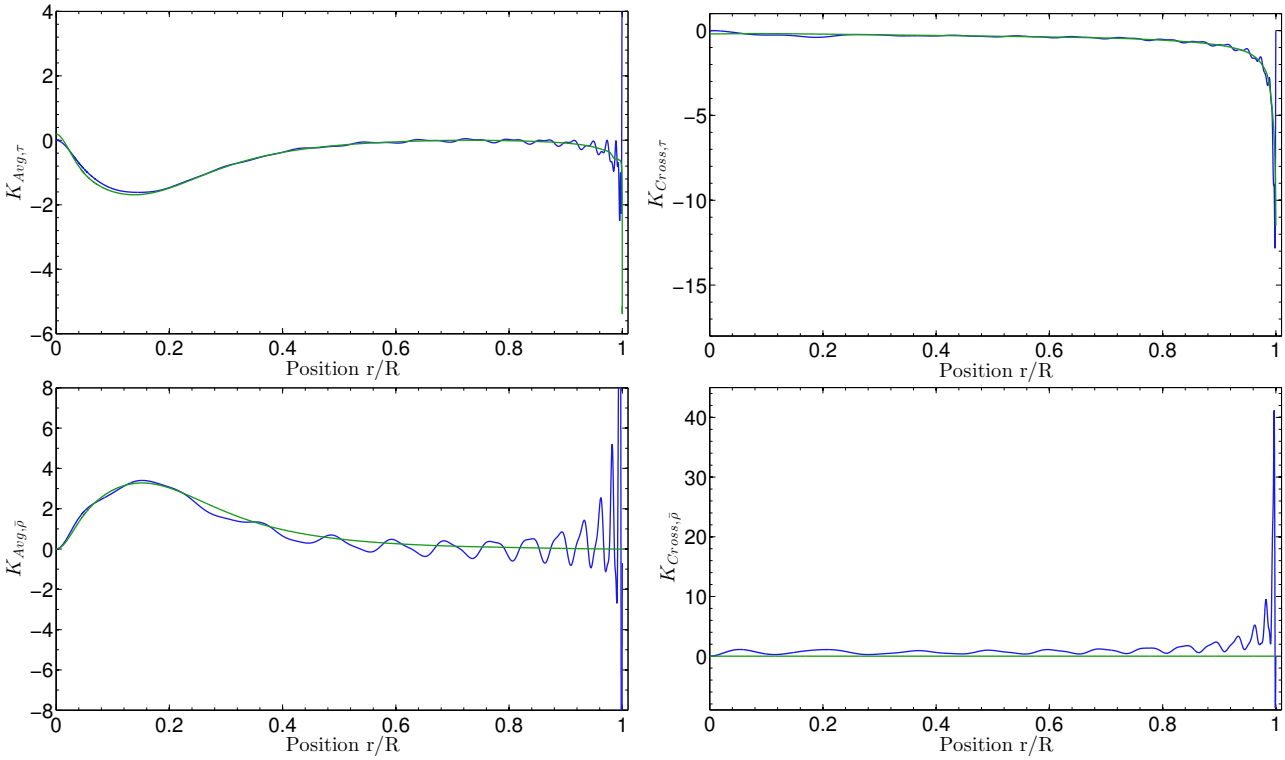

Figure 6.3: Upper panel: Example of Kernel fits for the inversion of the acoustic radius of 16CygA (Averaging kernel on the left and cross-term kernel on the right). Lower panel: Kernel fits for the inversion of the mean density for 16CygA (Averaging kernel on the left and cross-term kernel on the right). The target functions are in green and the SOLA kernels in blue.

two steps of forward modelling and the naming conventions associated with the models can be found in Table 6.4.

Table 6.4: Description of the naming conventions for both forward modelling steps.

First set of models (using $\langle\Delta\nu\rangle$) along with T_{eff}, individual $\tilde{\delta}\nu$, Y_f and $\left(\frac{Z}{X}\right)_f$	
Star	A = 16Cyg A or B = 16 cyg B
Diffusion	1= no diffusion; 2 = half of standard diffusion velocity; 3 = with diffusion
Second set of models (using $\bar{\rho}$ and τ) along with T_{eff}, individual $\tilde{\delta}\nu$, Y_f and $\left(\frac{Z}{X}\right)_f$	
Star	A = 16Cyg A; B = 16 cyg B
Chemical composition	C = central; L = left; R = right; U = up; D = down
Diffusion	1 = no diffusion; 2 = with diffusion

If we compare the model parameters obtained using τ and $\bar{\rho}$ for the model with $Y_f = 0.24$ and $(Z/X)_f = 0.0222$ (following our naming convention, model $S_{A,C,1}$) with those obtained with $<\Delta\nu>$, presented in Table 6.2 for model $S_{A,1}$, we note that there is a tendency to reduce the mass slightly and to increase the mixing length parameter. The same tendency is observed for the corresponding models including microscopic diffusion. What is more surprising is that when computing individual frequency differences between the observed stars and the reference models, we see that using the acoustic radius and the mean density allows us to obtain significantly better individual frequencies. This is a by-product of the use of inversion techniques that could be used to characterise stars in a

pipeline such as what will be developed for the upcoming PLATO mission (Rauer et al. (2014)).

Considering that these models are improved compared to what was obtained using the large frequency separation[4], we computed a family of models for different values of Y_f and $\left(\frac{Z}{X}\right)_f$. For each particular chemical composition, we computed models with and without microscopic diffusion. The properties of some models of this family are summarised in Table 6.7. As can be seen, some of the models do not reproduce the results for the effective temperature or the interferometric radius well. This means that we can use non-seismic constraint as indicators of inconsistent models in our study, although one should be careful about the conclusions derived from these quantities. For instance, the interferometric radii are different from the radii computed with the Clés models and some differences might result from the very definition of the radius. One should also note that these results are not totally incompatible since White, Huber, et al. (2013) conclude that the radius of 16CygA is 1.22 ± 0.02 $R_\odot$ and we find values around 1.185 and 1.230, outside the 1σ errors for the lower part of our scatter. The stellar luminosity also depends on these radii values and so should be considered with care. Ultimately, the effective temperature can be constraining although there might be a slight difference stemming from discrepancies between the physical ingredients in the stellar atmosphere models used for the spectroscopic study of Ramírez, Meléndez, and Asplund (2009) and Tucci Maia, Meléndez, and Ramírez (2014) and those used in the Clés models in this section. However, the inconsistencies observed for some of these models are too important and therefore these models should be rejected. The combination of all the information available are described in Sect. 6.2.4. In the next section, we use these models as references for our inversions of the t_u indicator. One should note that this first step was beneficial since obtaining reference models as accurate as possible for these stars is the best way to obtain accurate results for the more difficult inversion of the t_u indicator.

6.2.3 Inversion results for the t_u core condition indicator

Definition of the indicator and link to mixing processes

In Buldgen, D. R. Reese, and M. A. Dupret (2015), we defined and tested a new indicator for core conditions, which is applicable to a large number of stars[5] and very sensitive to microscopic diffusion or chemical composition mismatches in the core regions between the target and the reference model. The definition of this quantity was the following:

$$t_u = \int_0^R f(r) \left(\frac{du}{dr}\right)^2 dr, \tag{6.3}$$

where u is the squared isothermal sound speed, defined as $u = \frac{P}{\rho}$, $f(r)$ is a weighting function defined as follows:

$$f(r) = r\,(r-R)^2 \exp\left(-7\left(\frac{r}{R}\right)^2\right). \tag{6.4}$$

Owing to the effects of the radius differences between the observed target and reference model, we noted that the quantity measured was $\frac{t_u}{G^2 R_{tar}^6}$, where R_{tar} is the target radius. In Fig. 6.4, we illustrate the changes in the quantity from the effects of diffusion for two of

[4]Since they provide better fits of the individual frequencies and are more consistent with the acoustic radius and the mean density values provided by the inversion, which are less dependent on surface effects.

[5]Provided that there is sufficient seismic information for the studied stars.

our reference models, having the same surface chemical composition and fitting the same observational constraints. One can also see the effects of surface helium and metallicity changes on the profile of the integrant of Eq. 6.3. The whole parameter set of these models is given in Table 6.7 along with the explanation of the naming convention. The diagnostic potential of the t_u inversion is therefore clear, although the weighting function could be adapted to suit other needs if necessary. The inversion of this integrated quantity can be made using both the (u_0, Γ_1) or the (u_0, Y) kernels.

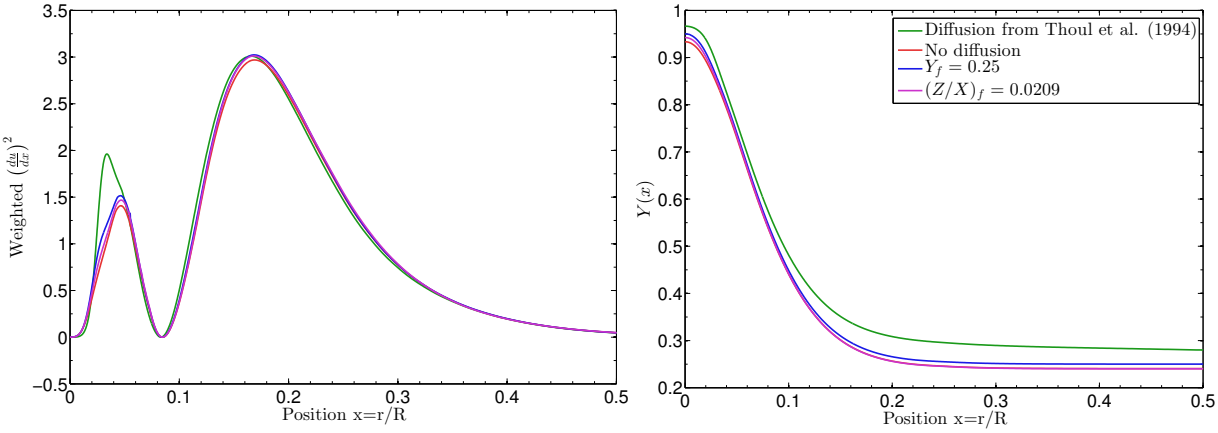

Figure 6.4: Left panel: Effect of diffusion, metallicity changes and helium abundance changes on the core regions for models $\mathbf{S}_{A,C1}$, $\mathbf{S}_{A,C2}$, $\mathbf{S}_{A,L1}$, $\mathbf{S}_{A,U1}$ on the target function of t_u. Since the quantity is integrated, the sensitivity is greatly improved. Right panel: the $Y(x)$ profile of these models is illustrated, thus showing the link between t_u and chemical composition and thus, its diagnostic potential.

The SOLA inversion technique

To carry out inversions of integrated quantities, we use the SOLA linear inversion technique developed by Pijpers and Thompson (1994). This technique uses the linear combinations of individual frequency differences to induce structural corrections. It is commonly used in helioseismology and has been recently adapted to the inversion of integrated quantities for asteroseismic targets. The philosophy of the SOLA inversion technique is to use a kernel-matching approach to derive the structural corrections. For the particular example of the t_u inversion, one would be using the following cost function:

$$\mathscr{J}_{t_u} = \int_0^1 \left[K_{\rm Avg} - \mathscr{T}_{t_u}\right]^2 dx + \beta \int_0^1 K_{\rm Cross}^2 dx + \tan(\theta) \sum_i^N (c_i \sigma_i)^2 + \eta \left[\sum_i^N c_i - k\right], \tag{6.5}$$

where $K_{\rm Avg}$ is the so-called averaging kernel and $K_{\rm Cross}$ the so-called cross-term kernel defined as follows for the (u, Y) structural pair:

$$K_{\rm Avg} = \sum_i^N c_i K^i_{u,Y}, \tag{6.6}$$

$$K_{\rm Cross} = \sum_i^N c_i K^i_{Y,u}. \tag{6.7}$$

The symbols θ and β are free parameters of the inversion and thus can change for a given indicator or observed frequency sets. Here, θ is related to the compromise between reducing the observational error bars (σ_i) and improving the averaging kernel, whereas β is allowed to vary to give more weight to elimination of the cross-term kernel. One should note that, ultimately, adjusting these free parameters is a problem of compromise and is made through hare-and-hounds exercises that have been presented in our previous papers. Various sanity checks can be used to analyse the robustness of the results. For example, one can use various reference models and analyse the variability of the inversion results or one can also use different structural pairs and see if this effect changes the results significantly.

In this expression of the kernels, N is the number of observed frequencies, c_i are the inversion coefficients, used to determine the correction that will be applied on the t_u value, η is a Lagrange multiplier and the last term appearing in the expression of the cost-function is a supplementary constraint applied to the inversion. Ultimately the correction on the t_u value obtained by the inversion is

$$\sum_{i=1}^{N} c_i \frac{\delta \nu_i}{\nu_i} \equiv \left(\frac{\delta t_u}{t_u} \right)_{inv} \tag{6.8}$$

One should note that the value obtained is an estimate whereas the previous equality is a definition. In fact, the inversion depends on some hypotheses that are used throughout the mathematical developments of the relation between frequency differences and structural differences and the definition of t_u. One should note that the particular definition of the cost function given above is very similar to the general expression for any integrated quantity and local correction, since one only has to change the target function, here denoted $\mathscr{T}_{t_u}$, to obtain other corrections.

Inversion results for 16CygA

The inversion results are summarised in Fig. 6.7 (represented as orange $\times$ in the $\bar{\rho} - \frac{t_u}{G}^2 R^6$ plot) and illustrated through an example of kernel fits in Fig. 6.5. We tried using both the (u_0, Γ_1) and the (u_0, Y) kernels. The high amplitude of the Γ_1 cross-term leads us to present the results from the (u_0, Y) kernels instead although they are quite similar in terms of the inverted values. However, one should note that the error bars are quite important, and we have to be careful when interpreting the inversion results.

This effect is due to both the very high amplitude of the inversion coefficients and the amplitude of the observational error bars. When compared to the somewhat underestimated error bars of the acoustic radius and mean density inversion, it illustrates perfectly well why it is always said that two inversion problems can be completely different. In this particular case, using various reference models allows us to already see a trend in the inversion results. We clearly see that the value of t_u for our reference models is too low and that the scatter of the inversion results is rather low, despite the large error bars. One should also note that the quality of the kernel fit is also a good indicator of the quality of the inverted result. For most cases, the kernels were very well fitted and the low scatter of the results means that there is indeed information to be extracted from the inversion. We will see how this behaviour is different for 16CygB.

Nevertheless, one could argue that a small change in t_u could be easily obtained through the use of diffusion or chemical composition changes. We see in Sect. 6.2.4 how combining

all the information with new constraints from the inversion technique can be extremely restrictive in terms of chemical composition and diffusion processes. Indeed, t_u should not be considered as a model-independent age determination or as an observed quantity that disentangles all physical processes occurring in stellar cores. In fact, it is simply a nearly model-independent determination of a structural quantity optimised to be more sensitive to any change in the physical conditions in stellar cores than classical seismic indicators. The amplitude of the error bars reminds us that this sensitivity comes at a cost and in this study we consider that having a reference model with a $\frac{t_u}{G^2 R_{ref}^6} \approx 3.2$ or $3.3\ \frac{g^2}{cm^6}$ will be acceptable if it still fits the other observational constraints.

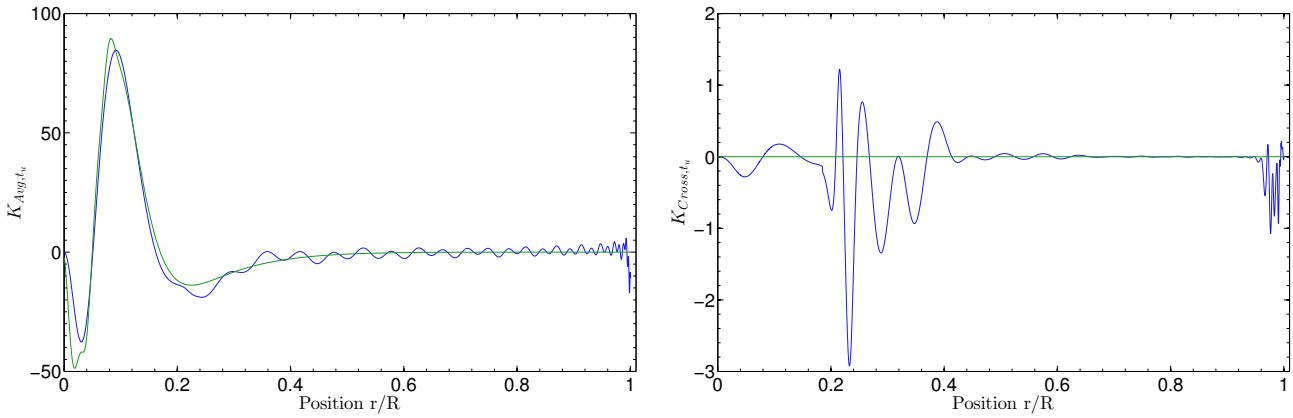

Figure 6.5: Example of kernel fits for the t_u inversion. The left panel is associated with the averaging kernel and the right panel is associated with the cross-term kernel. The target functions are in green and the SOLA kernels in blue.

Inversion results for 16CygB

The case of 16CygB is completely different. In fact, while the inversion for the acoustic radius and the mean density have been successful and we could build improved models for this star, the inversion of the t_u indicator was less successful. The results were good, in the sense that the kernels are well fitted. However, we can see from Fig. 6.6 that the amplification of the observational errors was too high to constrain the microscopic diffusion effects or the chemical composition. In fact, it is not surprising since the error bars on the observed frequencies are larger than for 16CygA.

As a matter of fact, the observational errors dominate the inversion result, as can be easily shown in Fig. 6.6. We see that the relative change in t_u is smaller when microscopic diffusion is included in the model but this is because the inversion result is closer to the reference value rather than the opposite. This therefore means that t_u can be used as a consistency check for future investigations to ensure that we stay within the error bars of the inverted value, but it seems that we cannot gain additional information for this star from this indicator.

6.2.4 Constraints on microscopic diffusion and chemical composition

Reducing the age, mass and radius scatter of 16CygA

In this section, we use the information given by t_u to further constrain chemical composition and microscopic diffusion. Previously, we always ensured that the reference models

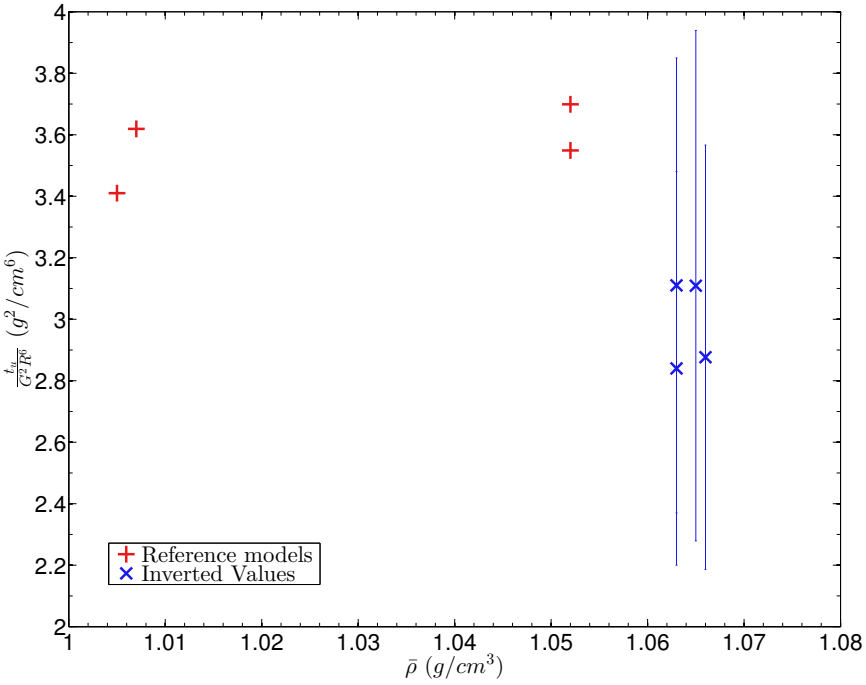

Figure 6.6: t_u inversion results for 16CygB. The red + are the reference models and the blue × the inverted results. The lower + are associated with the upper × and refer to models including solar-calibrated diffusion.

were inside the chemical composition box that was defined by the constraints on surface helium obtained by Verma, Faria, et al. (2014) and the spectroscopic constraints on surface metallicity obtained by Ramírez, Meléndez, and Asplund (2009). In Sect.6.2.3, we concluded that our model should have at least a $\frac{t_u}{G^2R^6_{ref}} \approx 3.2$ or 3.3 $\frac{g^2}{cm^6}$ or higher. The first question that arises is whether it is possible to obtain such values for $\frac{t_u}{G^2R^6}$ given the constraints on chemical composition. The second question is related to the impact of microscopic diffusion.

In fact, t_u is a measure of the intensity of the squared isothermal sound speed, u_0, gradients in the core regions. Thus, since $u_0 \approx \frac{T}{\mu}$, where T is the temperature and μ the mean molecular weight, including diffusion will increase the μ gradients, since it leads to the separation of heavy elements from lighter elements. It is then possible to increase the diffusion speed of the chemical elements significantly and to obtain a very high value of t_u for nearly any chemical composition. However, in Thoul, Bahcall, and Loeb (1994), the diffusion speed is said to be accurate to within $\sim 15-20\%$ and suited to solar conditions. Moreover, since increasing diffusion also accelerates the evolution, we could also end up with models that are too evolved to simultaneously fit t_u, the chemical composition constraints and the seismic constraints. Looking at the parameters of our reference models, we note that we are indeed very close to solar conditions, and we suppose that our diffusion speed should not be amplified or damped by more than 20%. The results of this analysis are summarised in Fig. 6.7, which is a $\bar{\rho} - \frac{t_u}{G^2R^6}$ plot where the reference models and the inverted results are represented. In what follows, we describe our reasoning more precisely and refer to Fig. 6.7 when necessary. We used a particular colour code and type of symbol to describe the changes we applied to our models. One

should keep in mind that these models are still built using the Levenberg-Marquardt algorithm and thus still fit the constraints used previously in the cost function. Firstly, colour is associated with the final surface helium mass fraction Y_f: blue for $Y_f = 0.24$, red if $Y_f < 0.24$, and green if $Y_f > 0.24$. Secondly, the symbol itself is related to the $\left(\frac{Z}{X}\right)_f$: a $\times$ for $\left(\frac{Z}{X}\right)_f < 0.0222$, a $\circ$ for $\left(\frac{Z}{X}\right)_f = 0.0222$, and a $\diamond$ for $\left(\frac{Z}{X}\right)_f > 0.0222$. The size of the symbol is related to the inclusion of microscopic diffusion, for example the large blue and red circles in Fig. 6.7 are related to models that include microscopic diffusion.

Since increasing diffusion should increase the t_u value, we computed a model with $Y_f = 0.24$ and $\left(\frac{Z}{X}\right)_f = 0.0222$, including diffusion from Thoul, Bahcall, and Loeb (1994) and fitting the seismic constraints and the effective temperature. This model is represented by the large blue dot and we note that including diffusion improves the agreement, but is not sufficient to reach what we defined to be our acceptable values for $\frac{t_u}{G^2R^6}$. This is illustrated by the fact that in Fig. 6.7, the large blue circle is above the small blue dot. Therefore we decided to analyse how t_u depends on the chemical composition. To do so, we computed a model for each corner and each side of the chemical composition box. These models are represented in Fig. 6.7 by the $\diamond$, $\circ$, and $\times$ of various colours. From these results, we see that increasing the helium content, namely considering that $Y_f \in [0.24, 0.25]$ increases t_u, as does considering $\left(\frac{Z}{X}\right)_f \in [0.0209, 0.0222]$. In simpler terms, we see that the green circle and the blue circle are above the blue dot in Fig. 6.7. The first tendency is quickly understood since increasing the helium abundance leads to higher central μ and therefore a local minimum in the u_0 profile. Because t_u is based on $\left(\frac{du}{dx}\right)^2$, this does not imply a reduction in the value of the indicator, but an increase due to a secondary lobe developing exactly in the same way as what happens when including diffusion (see Fig. 6.2). The second tendency can be understood by looking at the central hydrogen abundance. In this case, we see that the central hydrogen abundance is reduced and thus the mean molecular weight is increased and leads to a minimum in u_0 in the centre. One should note that this effect is not as intense as the change in helium but is still non-negligible.

Therefore, our seismic analysis favours models that lie within $Y_f \in [0.24, 0.25]$ and $\left(\frac{Z}{X}\right)_f \in [0.0209, 0.0222]$. Including diffusion in these models increases the $\frac{t_u}{G^2R^6}$ value even more and brings it in the range of the 3.2, 3.3 $\frac{g^2}{cm^6}$ values, which is much more consistent with the inversion results. These final models are represented in Fig. 6.7 by the large green $+$. One should also note that an upper boundary can be drawn from the effective temperature, interferometric radius and the seismic constraints. In other words, the fit of the other quantities can increase $\mathscr{J}$ slightly up to values of 1.6 and thus slightly reduce the quality of the fit. This is not alarming but still means that one should not put all the weight of the fit of the model on the inversion results but try to find a compromise between seismic, spectroscopic, and inverted constraints. Looking at Fig. 6.7, we can also see that the models do not fit the mean density values. This is due to improper fitting in the Levenberg-Marquardt algorithm. In fact, to build Fig. 6.7, we put more weight on the surface chemical composition, the acoustic radius and the seismic constraints at the expense of the mean density. This does not change the results on the t_u inversion since the vertical trend can also be seen for a model fitting the mean density value used in Fig. 6.7. It is also noteworthy to mention that the mean density values obtained for the models presented in Fig. 6.7 correspond to the value obtained without the polynomial surface correction. As we stated before, only further investigations with models including strong surface effects will be able to distinguish which of both

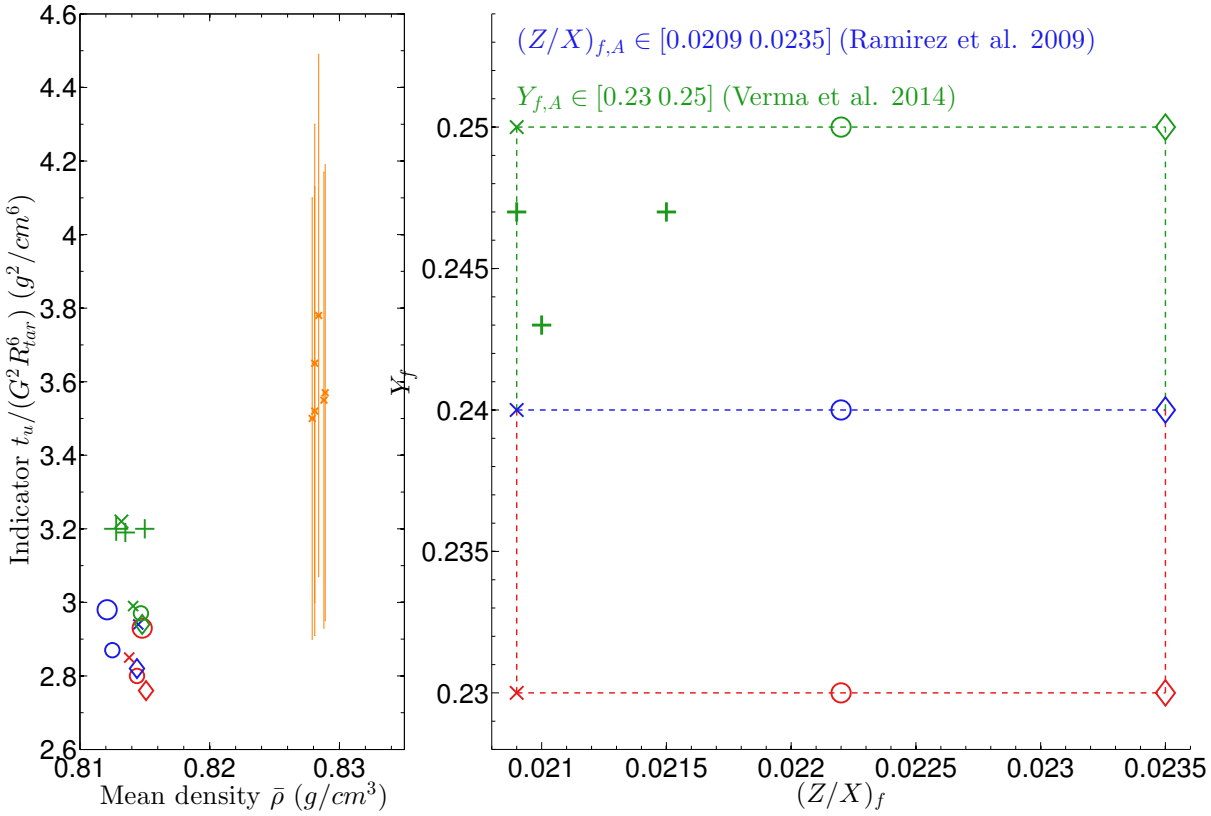

Figure 6.7: Results of the t_u inversions for 16CygA (left panel) and positions of the reference models in the chemical composition box derived from spectroscopic and seismic constraints (right panel). The orange $\times$ are the inversion results whereas the other symbols are associated with various reference models the positions of which are shown in the right-hand plot. The colour is associated with the Y_f value, the type of symbol with the $\left(\frac{Z}{X}\right)_f$ value, and the size of the symbol with the inclusion of diffusion.

values for the mean density inversions should be used. Ultimately, when considering models built with the Levenberg-Marquardt algorithm that are compatible with the t_u values, we are able to reduce the scatter previously observed. We thus conclude that the mass of 16CygA must be between 0.96 $M_\odot$ and 1.0 $M_\odot$, and its age must be between 7.0 Gy and 7.4 Gy. These values are subject to the hypotheses of this study and they depend on the physics used in the stellar models (opacities, nuclear reaction rates, abundances). We recall here that there is no way to provide a seismic fully model-independent age, but inversions allow us to at least check the consistency of our models with less model-dependent structural quantities. These consistency checks can lead to a refinement of the model parameters and, in this particular case, to constraints on microscopic diffusion.

For the sake of completion, we also analysed the importance of the abundances used to build the model. Because the [Fe/H] constraint are extremely dependent on the solar $\left(\frac{Z}{X}\right)_\odot$, we wanted to ask the question of whether the inversion would have also provided a diagnostic if we had used the GN93 abundances to determine the metallicity. Using these abundances and the associated $\left(\frac{Z}{X}\right)_\odot$ which is equal to 0.0244, one ends up with models having much higher metallicities, of the order of 0.0305 when no diffusion is included in the model. In fact we ended up with the same tendencies in the chemical composition box,

Table 6.5: Accepted parameters obtained for 16CygA when taking the constraints from the inversion of t_u into account.

	Accepted 16CygA models
M ($M_\odot$)	$0.96 - 1.00$
Age (Gy)	$7.0 - 7.4$
Y_0	$0.30 - 0.31$
Z_0	$0.0194 - 0.0199$
D	$1.00 - 1.15$
$\alpha_{\rm MLT}$	$1.75 - 1.90$
L ($L_\odot$)	$1.49 - 1.56$
R ($R_\odot$)	$1.19 - 1.20$

but with completely different values of $\left(\frac{Z}{X}\right)$, implying slightly higher masses of around 1.03 $M_\odot$ and slightly lower ages around 6.8Gy. However, when carrying out the t_u inversion, we noted that we still had to increase the helium content, include diffusion, and reduce the $\left(\frac{Z}{X}\right)$. The interesting point was that even the lowest $\left(\frac{Z}{X}\right)$, associated with the highest Y_f with increased diffusion could not produce a sufficiently high value of t_u. In that sense, it tends to prove what we already suspected, that the GN93 abundances should not be used in the spectroscopic determination of the $\left(\frac{Z}{X}\right)$ for this study. In this particular case, we see that the inversion of t_u is able to detect such inconsistencies, thanks to its sensitivity to metallicity mismatches. However, if the model is built with the $\left(\frac{Z}{X}\right)$ determined from the AGSS09 solar reference value, but using the GN93 solar heavy element mixture, we cannot detect inconsistencies. In fact, we obtain the same conclusion as before since these models are nearly identical in terms of internal structure.

Impact on the mass and radius scatter of 16CygB

In the previous section, we used the t_u inversion to reduce the age, mass and radius scatter of 16CygA. Moreover, we know from Sect. 6.2.3 that the inversion of t_u for 16CygB can only be used to check the consistency of the model but not to gain additional information. However, since these stars are binaries, we can say that the age values of the models 16CygB must be compatible with those obtained for 16CygA. From the inversion results of 16CygA, we have also deduced that we had to include atomic diffusion in the stellar models and since both stars are very much alike, there is no reason to discard microscopic diffusion from the models of the *B* component when we know that it has to be included in the models for the *A* component.

Therefore, we can ask the question of what would the mass and radius of 16CygB be if one includes diffusion as in 16CygA and ensures that the ages of the models remain compatible. The question of the chemical composition is also important since Ramírez, Meléndez, and Asplund (2009) find a somewhat lower value for the [Fe/H] of the *B* component and Verma, Faria, et al. (2014) found larger uncertainties for the surface helium abundance, although the centroid value was the same as that of 16CygA. To build these new models, we imposed that they include atomic diffusion with a coefficient D of 1.0 or 1.15. The age was to be between 7.0 *Gy* and 7.4 *Gy*. The metallicity was required to be within the error bars provided by Ramírez, Meléndez, and Asplund (2009) and the surface helium abundance was to be within $[0.24, 0.25]$. We used the same constraints as before to carry out the fits using the Levenberg-Marquardt algorithm and found that the mass was to be within 0.93 $M_\odot$ and 0.96 $M_\odot$, thus a 1.5% uncertainty and the radius was to

Table 6.6: Accepted parameters obtained for 16CygB when taking the constraints on 16CygA into account.

	Accepted 16CygB models
M ($M_\odot$)	$0.93 - 0.96$
Age (Gy)	$7.0 - 7.4$
Y_0	$0.30 - 0.31$
Z_0	$0.0151 - 0.0186$
D	$1.00 - 1.15$
$\alpha_{\rm MLT}$	$1.65 - 1.80$
L ($L_\odot$)	$1.17 - 1.24$
R ($R_\odot$)	$1.08 - 1.10$

be within 1.08 $R_\odot$ and 1.10 $R_\odot$, hence a 1% uncertainty. We would like to emphasise here that these values do of course depend on the results of the modelling of 16CygA and are thus more model-dependent since they do not result from constraints obtained through seismic inversions. They are a consequence of the binarity of the system. It is clear that a change in the values of the fundamental parameters for 16CygA will induce a change in the values of 16CygB.

Discussion

The starting point of this study was to determine fundamental parameters for both 16CygA and 16CygB using seismic, spectroscopic, and interferometric constraints. However, the differences between our results and those from Metcalfe, Chaplin, et al. (2012) raise questions. One could argue that the inversion leads to problematic results and that the diagnostic would have been different if the surface helium determination from Verma, Faria, et al. (2014) would have not been available.

Therefore, for the sake of comparison, we asked the question of what would have been the results of this study if we had not included the surface helium abundance from Verma, Faria, et al. (2014) in the model-selection process. We carried out a few supplementary fits, using the mass, age, α_{MLT}, X_0 and Z_0 as free parameters, using all the previous observational constraints as well as the prescription for microscopic diffusion from Thoul, Bahcall, and Loeb (1994), but excluding the Y_f value. The results speak for themselves since we end up with a model for the A component having a mass of $1.09 M_\odot$ and an age of 7.19Gy compatible with the results from Metcalfe, Chaplin, et al. (2012). This means that the determining property that leads to the changes in the fundamental parameters of the star was, as previously guessed, the surface helium value. Without this Y_f constraint, therefore, one would end up with two solutions with completely different masses and ages, but solutions that fit the same observational constraints. This does not mean that the results from Metcalfe, Chaplin, et al. (2012) are wrong, but that they were simply the best results one could obtain without the surface helium constraint and with three months of Kepler data. In fact, this is only an illustration of the importance of chemical composition constraints in stellar physics. The $Y_0 - M$ trend has already been described in Baudin et al. (2012) and that we find lower masses when increasing the helium abundance is, ultimately, no surprise.

At this point, we wanted to know what the inversion results would have been if we had used reference models with similar parameters as obtained in Metcalfe, Chaplin, et al. (2012). We ended up with similar results for both the acoustic radius and the mean density

inversion, but more interestingly, the t_u inversion also provided non-negligible corrections for this model. In fact, even with microscopic diffusion, the $\frac{t_{u,ref}}{R^6_{Ref}}$ value was: $2.72 g^2/cm^6$ whereas the inverted result was $\frac{t_{u,inv}}{R^6_{obs}} = 3.5 \pm 0.5 g^2/cm^6$. Therefore the diagnostic potential of the indicator is still clear, since it could have provided indications for a change in the core structure of the model. Assuming that diffusion velocities are accurate to around 20%, one could have invoked either an extra-mixing process or a change in the initial helium composition to explain this result. Disentangling both cases would then have probably required additional indicators.

6.2.5 Conclusion

In this section, we have applied the inversion techniques presented in a series of previous papers to the binary system 16CygA and 16CygB. The first part of this study consisted in determining suitable reference models for our inversion techniques. This was done using a Levenberg-Marquardt algorithm and all the seismic, spectroscopic and interferometric observational constraints available. We used the oscillation frequencies from Davies et al. (2015), the interferometric radii from White, Huber, et al. (2013), the spectroscopic constraints from Ramírez, Meléndez, and Asplund (2009) and Tucci Maia, Meléndez, and Ramírez (2014), and the surface helium constraints from Verma, Faria, et al. (2014).

These constraints on the surface chemical composition mean that our results are different from those of Metcalfe, Chaplin, et al. (2012). The test case we made without using the constraint on surface helium from Verma, Faria, et al. (2014) demonstrates the importance of constraints on the chemical composition for seismic studies. In fact, having to change the initial helium abundance from 0.25 to values around 0.30 is of course not negligible. This emphasises that we have to be careful when using free parameters for the stellar chemical composition in seismic modelling. The same can be said for the constraints on the stellar [Fe/H] from the study of Ramírez, Meléndez, and Asplund (2009). For this particular constraint, we have to add the importance of the solar mixture used in the spectroscopic study. Owing to the important changes in the $\left(\frac{Z}{X}\right)_\odot$ from the GN93 abundances to the AGSS09 abundances, we tested both abundances and found that the latter produces better results. We note that our reference models tend to be consistent with the spectroscopic, seismic and interferometric constraints and that independent modelling of both stars leads to consistent ages. We also note the presence of a certain modelling degeneracy in terms of chemical composition and microscopic diffusion. Accordingly, we could obtain rather different values for the mass, the radius and the age of both stars by assuming more intense diffusion and changing the chemical composition within the error bars from both Ramírez, Meléndez, and Asplund (2009) and Verma, Faria, et al. (2014).

Having obtained suitable reference models, we then carried out inversions for the mean density $\bar{\rho}$, the acoustic radius τ, and a core condition indicator t_u. The first two quantities were used to improve the quality of the reference models. As a by-product, we noted that models fitting both $\bar{\rho}$ and τ were in better agreement in terms of individual frequencies. We also found that both of these quantities could not differentiate the effect of the degeneracy in terms of diffusion and chemical composition. However, they could be well suited to analysing uppers layers along with other quantities.

After the second modelling process, we carried out inversion for the t_u indicator and noted that the degeneracy in terms of chemical composition and diffusion could be lifted for

16CygA. In fact, to agree with the inverted result, one has to consider the same diffusion speed as used in Thoul, Bahcall, and Loeb (1994) for the solar case or slightly higher (by 10% or 15%). Values higher than 20% were considered not to be physical by Thoul, Bahcall, and Loeb (1994) and were therefore not analysed in this study. Ultimately, we come up with a lower scatter in terms of mass and age for 16CygA, namely that this component should have a mass between $0.97M_\odot$ and $1.0M_\odot$, a radius between $1.188R_\odot$ and $1.200R_\odot$ and an age between 7.0Gy and 7.4Gy. Again the slight differences between the seismic radius provided here and the interferometric radius might stem from different definitions of the interferometric radius and the seismic one. We also conclude that the t_u inversion for 16CygB could only be used as a consistency check but could not help reduce the scatter in age. However, as these stars are binaries, a reduced age scatter for one component means that the second has to be consistent with this smaller age interval. Therefore, we were able to deduce a smaller mass and radius scatter for the second component, namely between 0.93 $M_\odot$ and 0.96 $M_\odot$ and between 1.08 $R_\odot$ and 1.10 $R_\odot$. We also note that when not considering the constraints on surface helium, we obtained results compatible with Metcalfe, Chaplin, et al. (2012) but the t_u values were too low even when diffusion was included in the models. This reinforces the importance of constraints on the chemical composition and illustrates to what extent inversions could be used given their intrinsic limitations.

Finally, we draw the attention of the reader to the following points. The age values we obtain are not model-independent, because we assumed physical properties for the models and assumed that the agreement in t_u was to be improved by varying the chemical composition within the observational constraints and by calibrating microscopic diffusion. This does not mean that no other mixing process has taken place during the evolutionary sequence that could somehow bias our age determination slightly. In that sense, further improved studies will be carried out, using additional structural quantities, more efficient global minimization tools for the selection of the reference models, and possibly improved physical ingredients for the models. In conclusion, we show in this study that inversions are indeed capable of improving our use of seismic information and therefore, through synergies with stellar modellers, of helping us build new generations of more physically accurate stellar models.

6.2.6 Appendix: Intermediate results of the forward modelling process

After the first step of forward modelling, we carried out supplementary fits to obtain new reference models for both 16CygA and 16CygB. In fact, we replaced the average large frequency separation by the acoustic radius and the mean density, as discussed in Sect. 6.2.2. We recall here the naming convention for these models: the first letter, *A* or *B* is associated with the star, namely 16CygA or 16CygB; the second letter is associated with the chemical composition box in the right panel of Fig. 6.7: *C* is the central chemical composition, *L* the left-hand side, *R* the right-hand side, *U* the upper side, and *D* the lower side (*D* for down); the number 1 or 2 is associated with diffusion, 1 is for models without microscopic diffusion, 2 is for models including the prescriptions of Thoul, Bahcall, and Loeb (1994) for microscopic diffusion. These results are illustrated in the following tables for both stars:

Table 6.7: Optimal parameters obtained for 16CygA using the acoustic radius and the mean density rather than $< \Delta\nu >$.

	$S_{A,C1}$	$S_{A,C2}$	$S_{A,U1}$	$S_{A,U2}$	$S_{A,D1}$	$S_{A,D2}$	$S_{A,R1}$	$S_{A,R2}$	$S_{A,L1}$	$S_{A,L2}$
M ($M_\odot$)	1.049	0.999	1.039	0.994	1.060	1.007	1.055	1.001	1.049	0.983
R ($R_\odot$)	1.221	1.201	1.216	1.198	1.227	1.203	1.222	1.201	1.220	1.195
Age (Gyr)	8.30	7.38	8.09	6.77	8.33	7.53	8.34	7.31	8.11	7.33
$T_{\rm eff}$ (K)	5852	5828	5903	5992	5842	5811	5827	5837	5912	5877
L ($L_\odot$)	1.570	1.494	1.613	1.662	1.574	1.482	1.546	1.504	1.633	1.529
Z_0	0.0165	0.0205	0.0162	0.0195	0.0167	0.0200	0.0174	0.0210	0.0155	0.0188
Y_0	0.240	0.295	0.250	0.308	0.230	0.286	0.240	0.297	0.240	0.299
$\alpha_{\rm MLT}$	1.68	1.74	1.75	1.97	1.69	1.72	1.67	1.76	1.75	1.78
D	0.0	1.0	0.0	1.0	0.0	1.0	0.0	1.0	0.0	1.0

Table 6.8: Optimal parameters obtained for 16CygB using the acoustic radius and the mean density rather than $< \Delta\nu >$.

	$S_{B,C1}$	$S_{B,C2}$
M ($M_\odot$)	1.008	0.961
R ($R_\odot$)	1.106	1.088
Age (Gyr)	8.162	7.236
$T_{\rm eff}$ (K)	5793	5829
$L_\odot$ ($L_\odot$)	1.235	1.228
Z_0	0.0151	0.0181
Y_0	0.240	0.292
$\alpha_{\rm MLT}$	1.667	1.780
D	0.0	1.0

6.3 In-depth study of 16CygB using inversion techniques

6.3.1 Introduction

In a previous paper (Buldgen, D. R. Reese, and M. A. Dupret (2016)), we studied the binaries 16CygA and 16CygB using the full Kepler dataset from Davies et al. (Davies et al. (2015)). The system is in fact more complex since a red dwarf orbits the *A* component and a Jovian planet orbits the *B* component (Cochran et al. (1997), Holman, Touma, and Tremaine (1997), Hauser and Marcy (1999)). We carried out a forward modelling process of both stars without taking into account binarity as a constraint and used our inversion techniques to further constrain their fundamental parameters, and demonstrated the importance of microscopic diffusion. The inversion technique provided strong constraints on the chemical composition and mixing of 16CygA, the brightest of the two components. However, when carrying out the same inversion for 16CygB, we faced the problem of the amplification of the observational error bars. The problem is well-known in the context of inversions, since the results are always a trade-off between amplifying the errors and fitting the target function of the inversion (Pijpers and Thompson (1994)). In the context of asteroseismology, since more weight has to be given to the fit of the target function due to the small number of observed frequencies compared to the solar case, we are always limited in terms of error amplification. Trying to reduce the error bars by amplifying the trade-off parameters can result in a significant reduction of the quality of the fit, thus implying that what is gained by reducing the propagation of observational error bars is lost due to the poor quality of the averaging kernel.

In the following sections, we re-analyse the trade-off problem of 16CygB and show

that the seismic information is sufficient to analyse this star independently with the t_u indicator. To explain the trend seen with the inversion, we try unsuccessfully to restore the agreement by modifying the surface chemical composition of this star. Since this leads to inconsistencies with the 16CygA results of our previous paper, we analyse the potential necessity of an additional mixing process, which has already been mentioned to explain the lithium depletion in this star (Deal, Richard, and Vauclair (2015)). We emphasise that the solution we propose for consistency with the inversion result is hypothetical and is subject to the same limitations and model-dependencies as our previous study on 16CygA. We compute models using a parametrised approach of the extra mixing which should not be considered as a physical solution but rather a hint that a certain amount of mixing is required in deep regions of the B component in order to reconcile the modelling of both components.

This section is structured as follows, we start by briefly presenting additional reference models in Sect 6.3.2. We then present our inversion results as well as the regularisation in Sect 6.3.3. These results are further analysed and discussed in Sect 6.3.5 in light of the possible necessity for extra mixing in 16CygB. We then conclude with the implications and perspectives of this study in Sect 6.3.6.

6.3.2 Reference models

In this section, we will describe the forward modelling process that has been carried out to obtain the reference models for the inversion. The process has been already described in Buldgen, D. R. Reese, and M. A. Dupret (2016), but we recall it here for the sake of clarity. Nevertheless, the number of models computed has been increased to improve the diagnostic process of the inversion and to ensure unbiased results.

In practice, we computed these models independently from the modelling of 16CygA presented in our previous paper. We used the frequency spectrum from Davies et al. (2015), which was based on 928 days of Kepler data[6]. A Levenberg-Marquardt algorithm was used to determine the optimal set of free parameters for our models. We used the CLES stellar evolution code and the LOSC oscillation code (Scuflaire, Théado, et al. (2008), Scuflaire, Montalbán, et al. (2008)). The stellar models used the CEFF equation of state (Christensen-Dalsgaard and Daeppen (1992)), the OPAL opacities from Iglesias and Rogers (1996) supplemented at low temperatures by the opacities of Ferguson et al. (2005). The nuclear reaction rates are those from the NACRE project (Angulo et al. (1999)), including the updated reaction rate for the $^{14}N(p,\gamma)^{15}O$ reaction from Formicola et al. (2004) and convection was implemented using the classical, local mixing-length theory (Böhm-Vitense (1958)). We also used the implementation of microscopic diffusion from Thoul, Bahcall, and Loeb (1994), for which three groups of elements are considered and treated separately: hydrogen, helium and the metals (all considered to have the diffusion speed of ^{56}Fe). No additional transport mechanism, beside microscopic diffusion, was included in the models. No surface correction of the individual frequencies was used in this study since we used quantities that are naturally less sensitive to these effects.

Moreover, since the inversion results for 16CygA implied that microscopic diffusion had to be included in the stellar models and since both stars are very similar, we considered that we had to include atomic diffusion in the models of 16CygB. We also emphasise that obtaining consistent results in age for both components is impossible if one considers that one component of the binary system is subject to microscopic diffusion effects while the other is not. Yet, we also want to stress that the implementation of microscopic diffusion

[6]The frequency tables are public and can be found at the url: `http://mnras.oxfordjournals.org/lookup/suppl/doi:10.1093/mnras/stu2331/-/DC1`.

has its own uncertainties. First, we consider here the implementation from Thoul, Bahcall, and Loeb (1994) which considers only three components to the mixing; secondly, in their own paper, Thoul, Bahcall, and Loeb (1994) consider the diffusion velocities obtained to be accurate within approximately 15%; thirdly, it may be possible that radiative accelerations play a role in competing with gravitational settling effects. Thus, the use of microscopic diffusion as a solution to be consistent with the inversion results for 16CygA is a first hypothesis of this study. It does not mean that another combination of mixing processes could not successfully reproduce the trends previously seen with the inversion technique for this star.

In this study, we substantially increased the number of reference models used to carry out the inversions for 16CygB but did not use any hypothesis on the chemical composition of this star. In fact, surface chemical composition differences between the *A* and *B* components have been claimed by Tucci Maia, Meléndez, and Ramírez (2014) when carrying out a differential spectroscopy analysis between both stars. Moreover, although the centroid of the present surface helium abundance, Y_f, interval found by Verma, Faria, et al. (2014) is the same, the scatter is larger for the *B* component, and if microscopic diffusion is included in the stellar models, it is also clear that surface chemical composition differences will be seen since this mixing will not have the same efficiency for stars of different masses[7].

Nevertheless, it should be noted that chemical composition differences between 16CygA and 16CygB are still under some debate since their existence has been claimed by Ramírez, Meléndez, and Asplund (2009) and Tucci Maia, Meléndez, and Ramírez (2014) as well as by previous studies (see Deliyannis et al. (2000)) but could not be confirmed by Schuler et al. (2011). In Tucci Maia, Meléndez, and Ramírez (2014), one finds $[\mathrm{Fe/H}]_A = 0.101 \pm 0.008$ and $[\mathrm{Fe/H}]_B = 0.054 \pm 0.008$ whereas Schuler et al. (2011) finds $[\mathrm{Fe/H}]_A = 0.07 \pm 0.05$ and $[\mathrm{Fe/H}]_B = 0.05 \pm 0.05$. These results are not totally incompatible, and what is more striking is the difference in error bars between various studies.

Moreover, these values depend on the reference solar metallicity assumed in the study since the observational constraint provided is the [Fe/H] value which must be translated in a $\frac{Z}{X}$ value using the Sun as a reference. In our previous paper, we used the most recent abundance tables given by AGSS09 (Asplund, Grevesse, Sauval, and Scott (2009)) and found that they led to a better agreement with the inversion results for 16CygA. In this study, we computed most models with the AGSS09 abundances but also used some models with the older GN93 abundances (Grevesse and Noels (1993)). We explain our motivations for using such models in Sect. 6.3.5. We summarise the observational constraints used for

Table 6.9: Summary of observational properties of the system 16CygA&B used in this study.

	16CygB	**References**
R ($R_\odot$)	1.12 ± 0.02	White, Huber, et al. (2013)
$T_{\mathrm{eff,spec}}$ (K)	5751 ± 6	Tucci Maia, Meléndez, and Ramírez (2014)
$T_{\mathrm{eff,phot}}$ (K)	5809 ± 39	White, Huber, et al. (2013)
L ($L_\odot$)	1.27 ± 0.04	Metcalfe, Chaplin, et al. (2012)
[Fe/H] (dex)	0.052 ± 0.021	Ramírez, Meléndez, and Asplund (2009)
Y_f	$[0.218, 0.260]$	Verma, Faria, et al. (2014)
$<\Delta\nu>$ (μHz)	117.36 ± 0.55	Davies et al. (2015)

16CygB in table 6.9 and the fundamental parameters obtained for some of the reference

[7]The differences due to diffusion should nonetheless remain small.

models in table 6.10. In this table, we also recall the intervals from the forward modelling process of 16CygA obtained previously. The forward modelling war carried out starting from various initial conditions with the Levenberg-Marquardt algorithm. The set-up of the minimization process was the following:

- Constraints: individual small frequency separations $d_{0,2}$ $d_{1,3}$, inverted mean density ($\bar{\rho}$) for which conservative error bars of 0.005 g/cm^3 were considered, acoustic radius (τ) for which conservative error bars of 30 s were considered, present surface metallicity (Z_f/X_f) from Ramírez, Meléndez, and Asplund (2009), present surface helium abundance (Y_f) from Verma, Faria, et al. (2014) and the effective temperature from Tucci Maia, Meléndez, and Ramírez (2014), for which we considered error bars of 30K.
- Free parameters: Mass, age, initial hydrogen abundance (X_0), initial abundance of heavy elements (Z_0), mixing-length parameter (α_{MLT}).

In total, we had 5 free parameters for 31 constraints. In addition to these constraints, we checked the values of the luminosity L, surface gravity $\log g$ and radius R after the forward modelling to see if they were consistent with the constraints from the literature. Models which were completely inconsistent with these additional constraints were disregarded. An additional comment should be made on some error bars used in the forward modelling. Firstly, we considered the errors from Tucci Maia, Meléndez, and Ramírez (2014) to be unrealistic and assumed a conservative 30K error bar which is already very accurate but more consistent with other studies. Secondly, both the inverted mean density and acoustic radius are known to have underestimated error bars with the SOLA method, from the multiple hare and hounds we performed to calibrate the inversion techniques, we noticed that a error bars of 0.5% were to be expected as a conservative error bar for the inverted values of the mean density. For the acoustic radius, the precision has to be assessed from the dispersion of the inverted values, in this particular case this led to a precision of around 0.7% was achieved. Consequently, we used these conservative error bars in the Levenberg-Marquardt algorithm rather than the error bars derived directly from the SOLA method.

Table 6.10: Parameters of the reference models of 16CygB

	Reference 16CygB Models	**Reference 16CygA Models**
Mass ($M_\odot$)	0.93-1.05	0.96-1.08
Radius ($R_\odot$)	1.07-1.13	1.19-1.24
Age (Gyr)	6.97-8.47	6.90-8.30
$L_\odot$ ($L_\odot$)	1.05-1.25	1.48-1.66
Z_0	0.0165-0.0194	0.0155-0.0210
Y_0	0.25-0.32	0.250-0.299
$\alpha_{\rm MLT}$	1.70-1.86	1.67-1.97
D	0.5-1.1	$0.0-1.1$

We can see that the scatter of fundamental parameters is very similar to that obtained for 16CygA. However, we only give the results for models including diffusion in table 6.10, as can be seen by looking at the values of the D parameter. This parameter is related to the implementation of diffusion we use, it is a multiplicative factor of the microscopic diffusion velocities such that if $D = 1.0$, one uses the diffusion velocities of standard solar models. We can see that some models have radii and luminosities that are below the observed values. Thus, these models can already be rejected or at least questioned in terms of quality. The age and chemical composition intervals are completely consistent with the

values obtained for the reference models of 16CygA recalled in the third column of table 6.10. We recall here that the models associated with ages above 7.4 Gy were rejected for 16CygA, based on the t_u inversion results and their implications on microscopic diffusion and chemical composition. A successful modelling of the binary system implies finding similar ages and initial chemical composition for both stars as well as being consistent with the seismic, spectroscopic and interferometric constraints at hand. Ultimately, the models shall also be compatible with the inversion results. This is not an easy task and requires a careful analysis and a good trade-off between all of the constraints.

6.3.3 Inversion results

In this section, we present updated inversion results for 16CygB. In our initial work, we faced the problem of large error bars for the t_u inversion. These error bars implied that we could not derive any additional constraints on the structure of 16CygB. In fact the inversion results showed that all models should be accepted, regardless of whether they included diffusion or not. However, we will show in the following sections that a more careful look at the frequency data can lead to an independent diagnostic with the inversion and provide additional interesting insights on the structure of this star.

The inversion technique we present is based on the linear integral equations presented in D. O. Gough and Thompson (1991) derived for the squared isothermal sound speed $u = \frac{P}{\rho}$ and the helium mass fraction, Y. The basic equation of the inversion is then written:

$$\frac{\delta\nu^{n,\ell}}{\nu^{n,\ell}} = \int_0^R K^{n,\ell}_{u,Y}\frac{\delta u}{u}dr + \int_0^R K^{n,\ell}_{Y,u}\delta Y dr, \tag{6.9}$$

where the notation $\frac{\delta x}{x}$ stands for the relative difference between observed quantities and quantities of the reference model, defined as follows:

$$\frac{\delta x}{x} = \frac{x^{obs} - x^{ref}}{x^{ref}}. \tag{6.10}$$

The most striking difference between inversions in asteroseismology and inversions in helioseismology is the number of observed frequencies, leading to the fact that the classical linear kernel based inversion methods cannot be used to derive full structural profiles of observed stars. In previous studies, we have adapted the SOLA inversion techniques from Pijpers and Thompson (1994) to carry out inversions of structural integrated quantities (see D. R. Reese, Marques, et al. (2012), Buldgen, D. R. Reese, and M. A. Dupret (2015), Buldgen, D. R. Reese, M. A. Dupret, and Samadi (2015) for various examples). Amongst the indicators derived, we defined a core condition indicator in Buldgen, D. R. Reese, and M. A. Dupret (2015) as follows:

$$t_u = \int_0^R f(r)\left(\frac{du}{dr}\right)^2 dr, \tag{6.11}$$

with $f(r) = r(r-R)^2\exp(-7\frac{r^2}{R^2})$, the weight function used for this inversion with R the stellar radius and r the radial coordinate associated with each layer inside the model, u is the squared isothermal sound-speed previously defined.

First, we recall a few basic equations of seismic inversion techniques. It is important to remember that seismic diagnostics using classical inversion techniques involve individual relative frequency differences (defined as in Eq. 6.10). In that sense, any inverted result is generated from a recombination of these frequency differences. When we use the linear

SOLA technique (Pijpers and Thompson (1994)), we build a linear combination of frequency differences. In the case of the t_u inversion, for example, we have:

$$\sum_i^N c_i \frac{\delta \nu_i}{\nu_i} \equiv \left(\frac{\delta t_u}{t_u}\right)_{inv}, \tag{6.12}$$

with the c_i being the inversion coefficients, which are determined by finding the optimal value of the SOLA cost function for given trade-off parameters values. The SOLA cost function is defined as follows for the t_u indicator and denoted $\mathscr{J}_{t_u}$:

$$\begin{aligned}\mathscr{J}_{t_u} = &\int_0^1 \left[K_{\text{Avg}} - \mathscr{T}_{t_u}\right]^2 dx + \beta \int_0^1 K_{\text{Cross}}^2 dx + \tan(\theta) \sum_i^N (c_i \sigma_i)^2 \\ &+ \eta \left[\sum_i^N c_i - k\right],\end{aligned} \tag{6.13}$$

where $\mathscr{T}_{t_u}$ is the target function associated with the indicator, K_{Avg} is the averaging kernel, and K_{Cross} the cross-term kernel, defined with respect to the fractional radius position $x = \frac{r}{R}$. η is a Lagrange multiplier, k is a regularization factor related to the non-linear generalisation of indicator inversions (see Buldgen, D. R. Reese, and M. A. Dupret (2015) for details), σ_i are the errors associated with each individual frequency and β and θ are the free parameters of the SOLA method, related to the trade-off with the cross-term and the amplification of observational errors and the accuracy of the fit of the target function. Nevertheless, for this particular inversion, no additional terms used to deal with surface effects have been added since they often bias the results and reduce the quality of the fit of the target function. This is also justified by the fact that the t_u indicator probes core regions and that its target function has low amplitude in the surface.

The averaging and cross-term kernels are defined as follows for the (u, Y) structural pair, with Y the helium mass fraction and $u = \frac{P}{\rho}$, the squared isothermal sound speed and the functions $K^i_{u,Y}$ and $K^i_{Y,u}$ the structural kernels associated with u and Y respectively:

$$K_{\text{Avg}} = \sum_i^N c_i K^i_{u,Y}, \tag{6.14}$$

$$K_{\text{Cross}} = \sum_i^N c_i K^i_{Y,u}. \tag{6.15}$$

The fact that we have two free parameters in the SOLA cost function is due to the ill-posed nature of the problem and leads to the well-known trade-off problem when using inversion techniques. In this particular case, the question of the trade-off is particularly important since we have three oscillation modes in particular that have larger error bars than the all the others and two of these could sometimes see their individual frequencies fitted within their error bars.

Another specificity of asteroseismic inversions is that they are performed with little or no knowledge of the radius of the observed target, noted R_{tar}. In section 2.1 of Buldgen, D. R. Reese, and M. A. Dupret (2015), we analysed the impact of this problem on equations of the type of Eq. 6.9. It was then shown that the inversion implicitely scaled the observed target to the same radius as the reference model used to perform the inversion while keeping its mean density constant. This meant that the target studied by the inversion was not defined by a mass M_{tar} and a radius R_{tar} but was a scaled target defined by a mass $\frac{M_{tar} R_{ref}^3}{R_{tar}^3}$ and a radius R_{ref}.

This does not restrict the diagnostic potential of the inversion technique but means that if we want to compare results from various reference models, we need to compare values of t_u/R^6_{tar} to get rid of the implicit scaling process introducing a dependency in R_{ref} in the inversion process.

Analysis of the error contributions

In Fig. 6.8, we illustrate in orange the initial inversion results of t_u/R^6_{Tar} with their quite large error bars, R_{Tar} being the target photospheric radius. They seemed disappointing since the kernel fits were excellent and implied that there were enough kernels to fit the target function of the t_u inversions.

This implied that the problem was simply stemming from the observational errors propagation term in the cost function of the SOLA method. The classical way to deal with this problem is to increase the θ parameter in the cost function thus reducing the propagation of observational errors. While this may be a solution, changing the θ parameter can lead to a much less accurate fit of the target function and thus reduces the quality of the inversion. This implies larger errors on the inverted result coming from the kernel fit as shown in Buldgen, D. R. Reese, and M. A. Dupret (2015). From our previous test cases, we also know that around 50 frequencies is sufficient to obtain an inverted value for t_u, especially if octupole modes are available. Consequently, we looked at the observed frequencies for which there were large uncertainties and found that the $\ell = 3$, $n = 14$ mode, the $\ell = 3$, $n = 15$ mode and the $\ell = 3$, $n = 16$ had much larger uncertainties than the other modes of similar radial order. The error bars on the individual frequencies were sometimes even larger than the frequency differences between 16CygB and the computed reference models with the Levenberg-Marquardt algorithm. This is of course somewhat inefficient since it implies that we are using frequency differences that cannot be exploited by the inversion techniques.

In fact, frequency differences with large error bars can dominate the error contribution in the inversion results, especially if the inversion coefficient associated with the particular mode is important. This is in fact simply due to the form of the term associated with the error propagation in the SOLA cost-function which is written:

$$\sum_i^N (c_i \sigma_i)^2. \tag{6.16}$$

It is thus clear that modes with high inversion coefficients and large uncertainties contribute the most to the error propagation. Although the SOLA method tends to mitigate the impact of the modes with large uncertainties, the result is always a compromise between precision and accuracy. This trade-off is realised through the change of the free parameters of the inversion.In the context of asteroseismic inversions, the fact that each oscillation spectra has its own error bars, that each star is fitted individually within a given accuracy that can be variable and that each star occupies a different position in the HR diagram for which the linear approximation might be irrelevant to a certain degree, makes each inversion process unique. Therefore, from the mathematical point of view, each inversion has to be analysed differently, although trends in terms of inversion parameters can be seen and are understandable since they are linked to the data and model quality which can be objectively assessed.

The trade-off problem of inversion techniques is illustrated by the so-called "trade-off" curves that can be seen in the original paper on the OLA method by Backus and Gilbert (1967) or Pijpers and Thompson (1994) for the SOLA method. Typically, each frequency set defines the number of coefficient available, thus the resolution of the inversion. However,

this resolution is mitigated by the error bars of these individual modes which limit the amplitude of the coefficient that can be built to fit the target function. The trade-off curve materialises this competition with respect to the parameter θ of the inversion. We describe a little bit more in depth the trade-off problem and the effect of eliminating modes in the frequency spectrum in Sect. 6.3.7.

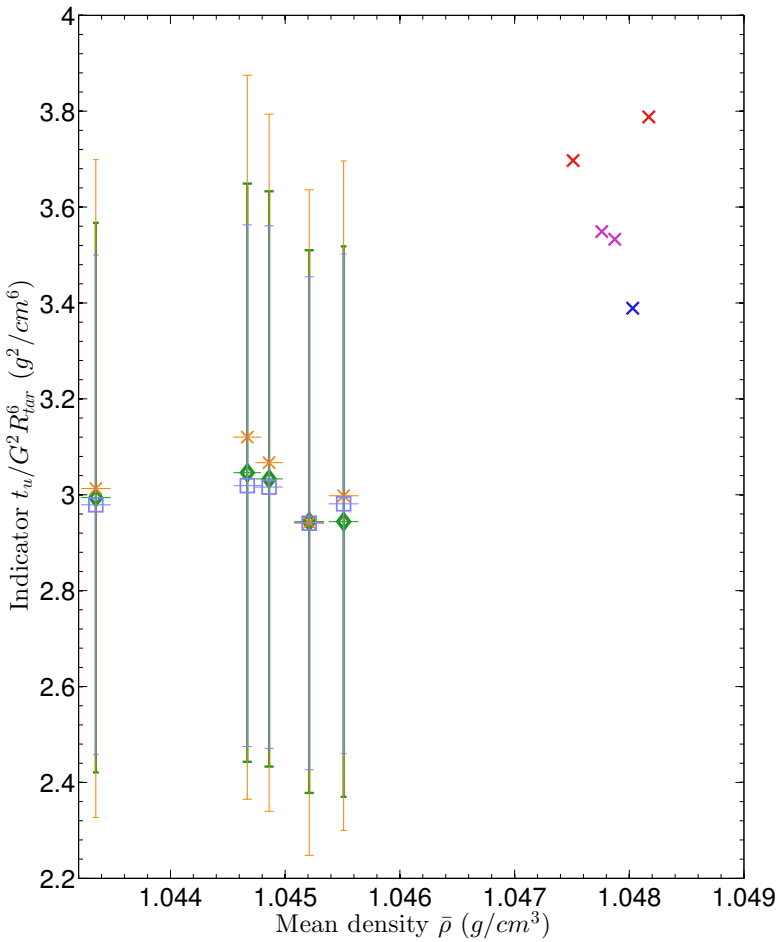

Figure 6.8: In orange, inversion results for the t_u indicator and $\bar{\rho}$ with the full set of modes for 16CygB. In green, inversion results for the same models excluding the modes with the largest error bars in the frequency set. The blue squares are associated with inversion results for which the trade-off parameter θ has been slightly enhanced. In red, blue and magenta, t_u and $\bar{\rho}$ values in the reference models (See text for the explanation of the colour code).

Important error bars can indeed be seen for the $\ell = 3$, $n = 14$ mode, which is the octupole mode of lowest radial order. We know indeed from our previous test cases (see Buldgen, D. R. Reese, and M. A. Dupret (2015)) that the t_u inversion uses preferentially the low order modes and tends to benefit from the presence of octupole modes and use them as much as possible. Since this particular mode has the highest error bar, we wanted to see how eliminating it from the frequency set used for the inversion could help us obtain a smaller error propagation. As previously explained, inversion techniques use individual frequencies to extract information. However, this is only possible if the frequencies used

by the inversions are not fitted within their observational error bars. Typically, if one eliminates a mode with large error bars, one reduces the amplification of the errors but also the resolution of the inversion. Ultimately, eliminating a mode from the frequency set is only justified if its detection is arguable or if it is already fitted within the error bars. Otherwise, reducing the error bars is more efficiently done by increasing slightly the value of the θ parameter.

In the particular case of 16CygB, some individual modes could be fitted within their error bars and thus could not bring any additional seismic constraints if used in an inversion process. Finally, eliminating the worst offenders in terms of error bars is a process that has also been described in helioseismic inversions (see Basu, Chaplin, et al. (2009)), since they can have strong impact on SOLA inversions when adjusting the trade-off parameters for the inversion.

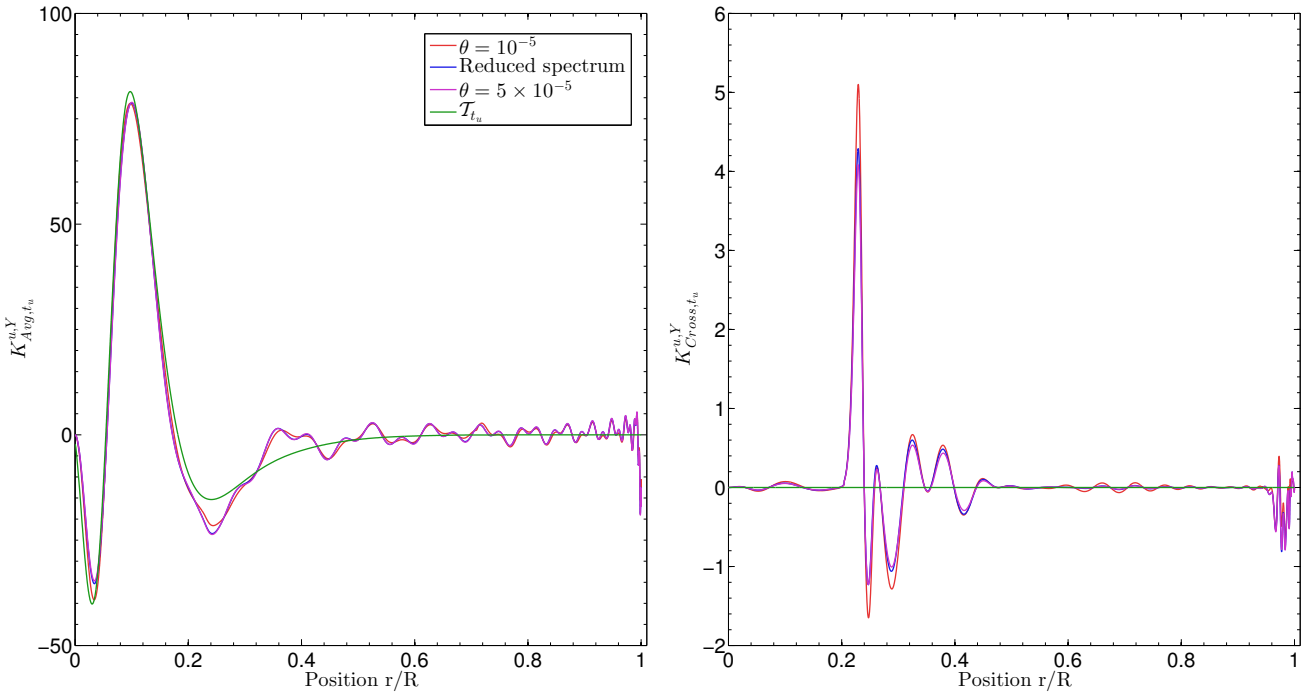

Figure 6.9: Left panel: averaging kernels for the core conditions indicator (t_u) for various θ values and reduced frequency spectrum. Right panel: same figure for the cross-term kernels of the t_u inversion. We used the (u,Y) structural pair in both plots.

In Fig. 6.8, we show the impact of the modes with the largest error bars on the final inversion error propagation and values of t_u and $\bar{\rho}$ for reference models. The new result with reduced error bars are illustrated in green and light-blue. The green results are obtained by eliminating problematic modes and the light-blue results are those obtained by slightly increasing the value of the θ parameter. We associated the following colour code for the values inferred from the reference models: a blue cross means that the t_u value agrees will all inversion results, a magenta cross that it agrees with some inversion results and a red cross that it does not agree with any result. We can see that eliminating the modes with large uncertainties reduces significantly the error bars on the inverted result, without changing much the actual inverted value. A change in the inverted value would have meant that the mode had a significant impact on the inversion result. In practice,

this could be seen by a change in the fit of the target function by the averaging kernel. This could be the case if one had fewer individual frequencies and that the problematic oscillation mode was used by the inversion despite its large error bars. In figure 6.9, we illustrate the change in the averaging and cross-term kernel fit that is induced by the elimination of the most problematic modes in terms of observational error bars and an increase of the trade-off parameter θ. As was the case for the inverted t_u values, the differences on the averaging kernels are minimal. Hence, an independent study of 16CygB in terms of t_u can be performed. In the next section, we present new inversions results using a greater number of models for different surface chemical compositions, yet within the observational constraints, and for different diffusion coefficients, in much the same way as what was done in our previous study, more focused on 16CygA.

t_u Inversion for 16CygB

In this section, we present the results for the t_u inversions for 16CygB. Using the reference models computed with our Levenberg-Marquardt algorithm and the more regularised inversions, we were able to obtain a value of t_u for 16CygB with lower error bars. However, the uncertainties are still non-negligible. Thus, we have to combine our analysis with other diagnostics and carefully discuss our final results, as was done in our previous study of 16CygA. In Fig 6.10, we present our results for various models with various surface chemical composition and changes of the factor D associated with atomic diffusion in Scuflaire, Théado, et al. (2008). The results we obtain are slightly model-dependent, which is very similar to what was obtained for 16CygA, but the trend is in this particular case opposite to what was seen before. Indeed, in Buldgen, D. R. Reese, and M. A. Dupret (2016), we saw that including microscopic diffusion provided much more consistent values of the t_u indicator when compared to the inverted values. For 16CygB, models with lower helium surface abundances, higher surface metallicities and less diffusion are favoured. In fact, reducing the t_u value is directly related to a reduction of the gradient of $u = \frac{P}{\rho} \approx \frac{T}{\mu}$, with T the temperature and μ the mean molecular weight. Consequently, reducing t_u implies reducing the mean molecular weight gradient within the star or changing the temperature gradient in the regions where the t_u indicator is sensitive. Reducing the mean molecular weight gradient can first be done by eliminating microscopic diffusion in the models. Indeed, this process tends to accumulate heavy elements in the deeper regions since for stars around $1.0M_{\odot}$, gravitational settling dominate the transport mechanism in the deep radiative regions. However, as stated before, not including this process leads to inconsistent ages and chemical compositions for both stars. Therefore, the reason for this discrepancy has to be explained using a more subtle effect.

We show in Fig. 6.11 the differences in chemical composition and in the weight function involved in the integral expression for the t_u indicator for two of our reference models in the chemical composition box. Model_1 is a model with a higher helium content ($Y_S = 0.26$), lower metallicity ($(Z/X)_S = 0.0208$) and microscopic diffusion ($D = 1.0$), thus following the prescription derived from our previous study. Consequently, it is also less massive ($M = 0.91M_{\odot}$) and within the "young" range of our reference models ($Age = 7.32Gy$). Due to the higher helium content and efficient microscopic diffusion, this model is rejected by the t_u inversion. Model_2 has a low helium content ($Y_S = 0.22$) and a higher metallicity ($(Z/X)_S = 0.0214$) and a less efficient microscopic diffusion ($D = 0.5$). This model is significantly more massive than Model_1 ($M = 1.01M_{\odot}$) but has a quite similar age of $7.54Gy$. The strong difference in mass is due to the well known degeneracy associated with the helium abundance. It should be noted that this model is validated by the t_u inversion.

This illustrates the fact that simply changing the surface chemical composition or microscopic diffusion has a strong impact on the fundamental parameters of the star and

implies strong changes in the internal structure even if the model fits all the observational constraints (although Model_1 should be rejected due to its lower radius). Both models were chosen because they were extreme cases and illustrated well the strong degeneracy due to helium abundance.

Comparison with 16CygA

If we consider again 16CygA, the models with masses around $1.01 M_{\odot}$, high helium content and ages 7.2Gy around were considered to be the best models of this star since they reproduced the t_u trend seen in our previous paper. This would mean that we would chose a model closer to Model_1 to be consistent in terms of the initial chemical composition of both components. However, since in this case we have to reduce the t_u values, and thus apply the opposite changes to the chemical composition and microscopic diffusion, the 16CygB have higher masses and ages (like Model_2 mentionned above), going up to $1.03 M_{\odot}$ and 8.0Gy.

The fact that the inversion is able to distinguish between Model_1 and Model_2 proves again the diagnostic potential of this approach. In this particular case, due to the fact that both stars are within a binary system, we are even able to see whether our selected result will be consistent with the previously determined parameters for 16CygA. Due to the very similar chemical composition derived spectroscopically and seismically, due to the results of independent forward modelling of both components leading to similar ages and initial chemical composition, we rather consider that the differences seen with the inversion technique is to be explained by inaccuracies in the models rather than considering the binary system to have merged from two isolated stars.

We also illustrate in Fig. 6.10 the results for one model using the GN93 abundances and models which were computed using the AGSS09 abundances and assuming a similar initial chemical composition to what was derived for 16CygA in our previous study. These models show values of t_u/R^6_{tar} around 3.7 g^2/cm^6 whereas the model with GN93 is more consistent with the inversion results of 3.0 ± 0.5 g^2/cm^6. It is clear that models computed assuming the same ingredients as 16CygA are incompatible from the point of view of the inversion. However, since these stars form a binary system and thus are thought to have formed together, we should be able to derive similar values of the initial chemical abundance and similar ages for both components of the system. This problem is also reflected in the effective temperature and radii determination. The well-known helium mass degeneracy leads to smaller radii for models with higher helium abundances, for example. We also tried using larger error bars on the effective temperature and looked at models with T_{eff} between 5600 K and 5900 K to see if this could affect the results. Ultimately, no trend was found since they are ultimately related to the chemical abundances and the way the elements are mixed within the star. These effects are well-known to affect the position of the models in the HR diagram at the end of its evolution. Thus, in what follows, we will focus on these aspects to try to reconcile our models of 16CygB with those of 16CygA and the inverted results.

In terms of precision and accuracy, it should be noted that neither the model-dependency, nor the regularisation can be held responsible for an inaccurate result. Hence, as shown in this section, in particular thanks to the large variety of reference models, we can see that surface chemical composition changes are not sufficient to explain the inverted values of t_u. In fact, taking $\theta = 10^{-4}$ still implies very similar inversion results with reduced error bars and a slightly worse fit to the target function. Moreover, we know from our previous numerous test cases that the t_u inversion provided accurate seismic diagnostic of core regions (see Buldgen, D. R. Reese, and M. A. Dupret (2015)).

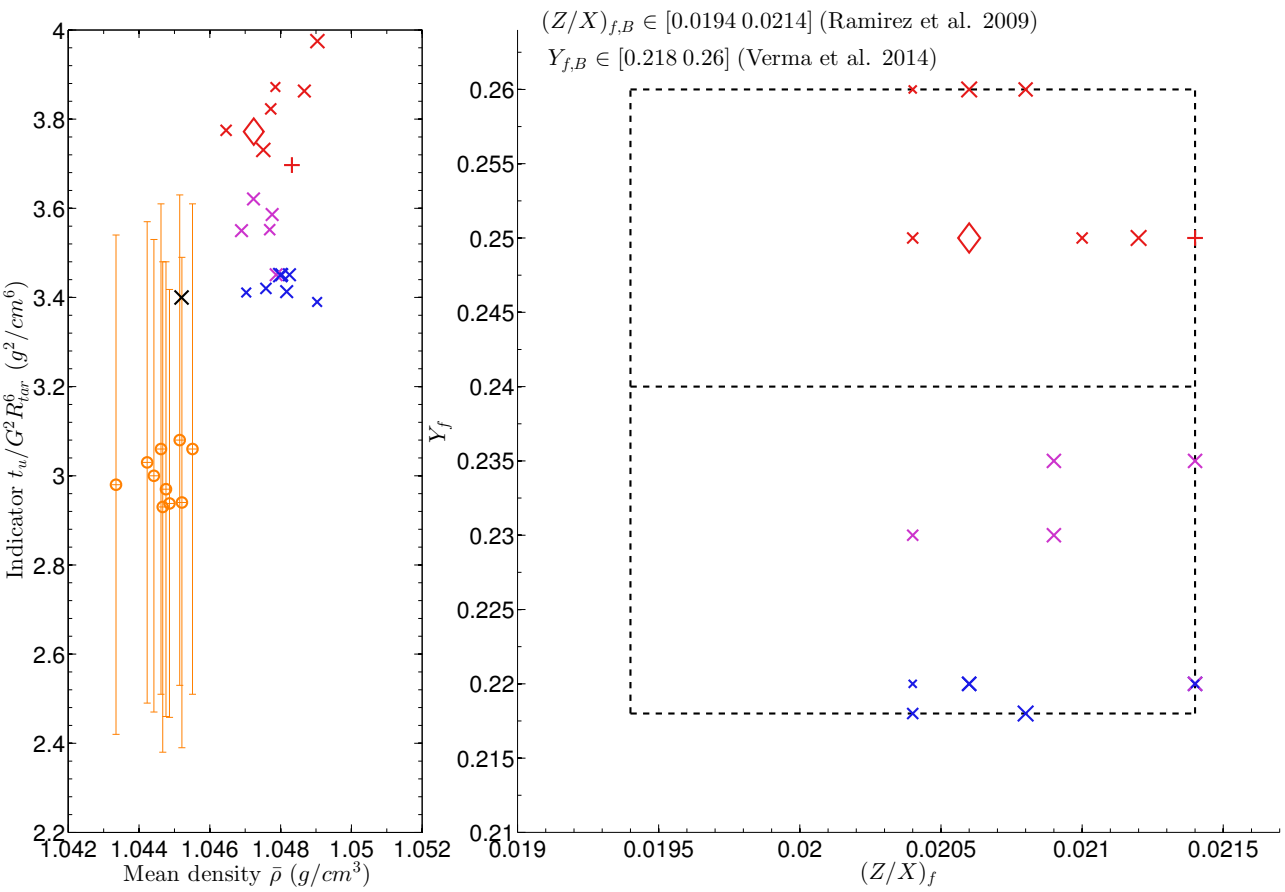

Figure 6.10: Left panel: mean density ($\bar{\rho}$) vs core conditions indicator (t_u) plot. The inversion results are plotted in orange with their respective error bars. The crosses are values for the reference models computed with the Levenberg-Marquardt algorithm with AGSS09, the black $\times$ shows one example of a model computed with GN93 and $Y_f = 0.25$. Right panel: surface chemical composition box for 16CygB. The colour code used allows direct trend comparisons between the surface chemical composition and the t_u values. The size of the symbols is related to the intensity of microscopic diffusion, the smaller the symbol, the smaller the D coefficient. The $+$ and the $\Diamond$ illustrate the impact of the metallicity on the t_u value.

6.3.4 Influence of physical parameters on t_u

When analysing the effects of microscopic diffusion, the problem is even worse, since if we trust the values of $Y_f \in [0.24\ 0.25]$ for the final surface helium abundance of 16CygA, we should obtain higher Y_f values for its less-massive counterpart due to the fact that its convective envelope goes slightly deeper and implies less-efficient microscopic diffusion. One should note that similar conclusions can be drawn for the surface heavy element abundance of this star. In fact, increasing the amount of heavy elements in the stars increases the opacity in the deep radiative regions where the t_u indicator is sensitive (see Fig. 6.9). Thus, it implies an increase of the temperature gradient, $\frac{dT}{dr}$. Now, since $t_u \propto \left(\frac{du}{dr}\right)^2$ (see Eq. 6.11), it is worth looking more in depth at the behaviour of this indicator with changes in the stellar structure. Using the ideal gaz approximation, we have a straightforward relation between u, T and μ.

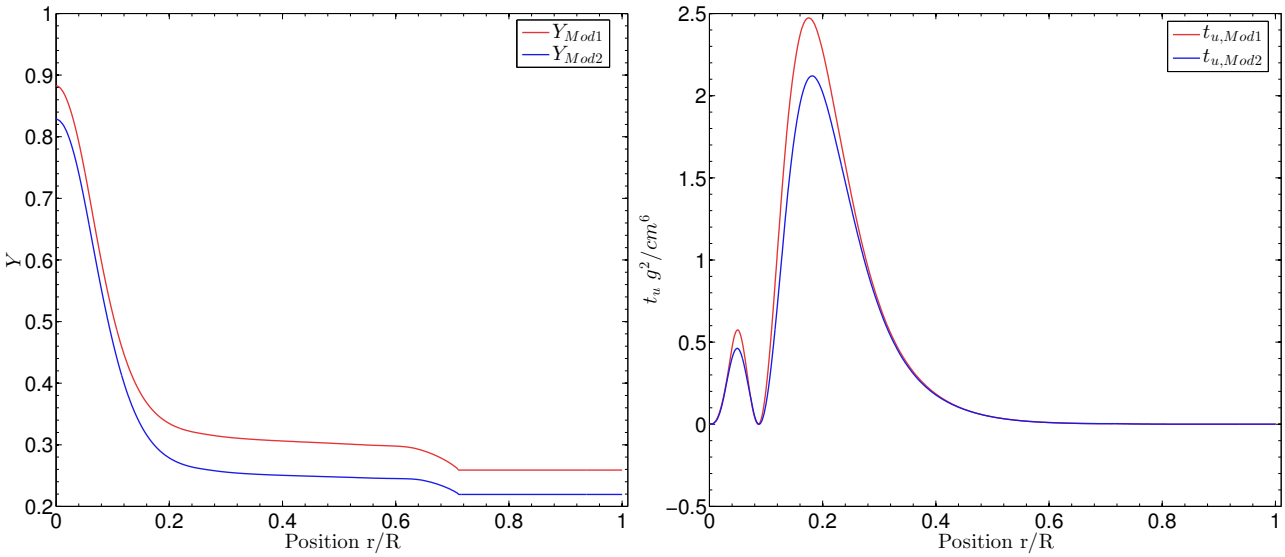

Figure 6.11: Left panel: In blue, helium abundance profile (Y) for one model with a lower surface helium abundance, around 0.22. In red, Y profile for a model with a higher surface abundance, around 0.26. Right panel: the profile of the target function of the core conditions indicator (t_u) is plotted in corresponding colours for both models.

$$\left(\frac{du}{dr}\right)^2 \approx \frac{T^2}{\mu^2}\left(\frac{d\ln T}{dr} - \frac{d\ln \mu}{dr}\right)^2. \tag{6.17}$$

This formula implies that the behaviour of the indicator depends on the values of the gradients themselves. As can be seen in the right panel of Fig. 6.12, it is not always straightforward to say whether an increase of the mean molecular weight gradient through diffusion will imply an increase of t_u. For example, below 0.1 R, with R the stellar radius, it will be the case because diffusion will increase the depth of the minimum just below 0.1 R. However, adding extra mixing around 0.2 R or 0.3 R will smooth the transition towards the chemically homogeneous convective envelope (around 0.7 for this model) thereby decreasing the value of t_u. Similarly, increasing the temperature gradient below 0.1 will reduce t_u, and reducing $\frac{dT}{dr}$ above 0.1 (thus sharpening the transition towards the convective envelope) will imply the same reduction for the indicator. One can see these effects in Fig. 6.12 where we illustrated the impact of different types of mixing on the temperature and μ gradients and thus on the t_u indicator. This gives us a clue as to what could be modified in the models to reconcile the inversion results with the other constraints. However, it does not mean that this is the only solution to the problem we presented previously. For the sake of illustration, we also illustrate the hydrogen gradient and the Brunt-Väisälä frequency of these models, showing the change of the slope of the hydrogen gradient at the bottom of the convective zone but also a significant deplacement of the base of the convective zone for these models due to the use of the new opacities from the OPAS project. The OPAS opacities are new opacity tables specifically designed for solar-like conditions, where great care has been given to the details of the absorption lines considered. These models also used the latest version of the OPAL equation of state (Rogers and Nayfonov (2002)). These changes of course affect the stratification below the

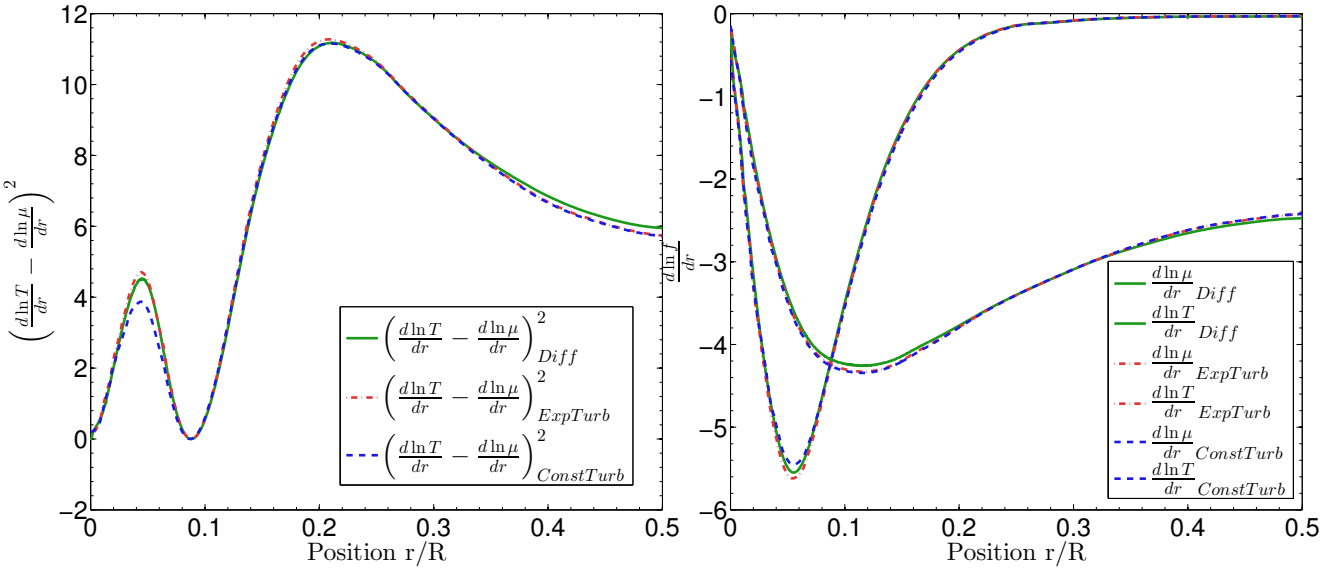

Figure 6.12: Left panel: plot showing the difference of the gradient of the natural logarithm of temperature (T) and that of the mean molecular weight (μ) for models including different mixing processes: the green curve is for a model with microscopic diffusion, the blue curve is for a model with a constant turbulent diffusion coefficient and the red curve is for an exponentially decaying turbulent diffusion coefficient. Right panel: the gradient of the natural logarithm of the mean molecular weight and of the temperature for the same models as in the left panel, the colour code has been respected.

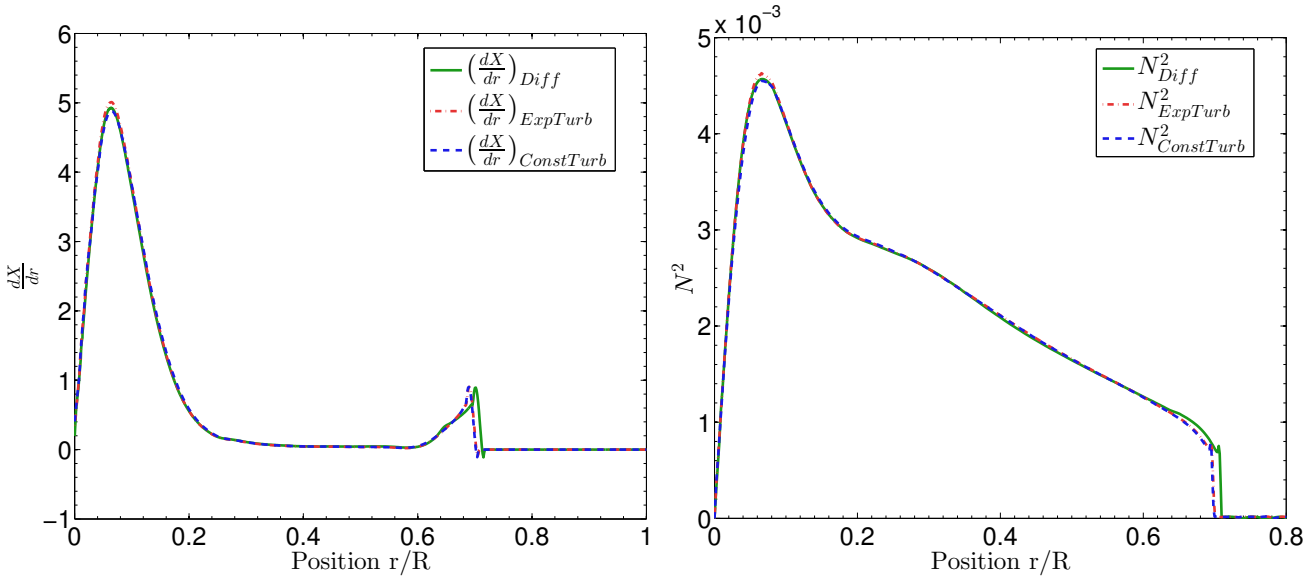

Figure 6.13: Left panel: plot showing the hydrogen gradient of the same models as in Fig. 6.12. Left panel: plot showing the Brunt-Väisälä frequency of these models.

convective zone and thus the behaviour of the t_u indicator. Turbulent diffusion also implied a change of the Brunt-Väisälä frequency in the very deep regions (below 0.1 R), this is

particulary seen for the model associated with constant turbulent diffusion.

In practice, all thermodynamic quantities are coupled through the equation of state. For example, adding a mixing process will affect the chemical composition, thus the mean molecular weight, but it will also affect the opacity and indirectly the temperature gradient. Consequently, the t_u inversion offers a new insight on some differences between the target and the reference model, but does not provide the physical cause of the observed differences in structure.

6.3.5 Impact of physical ingredients on the core conditions indicator

Adding extra mixing

Because of the t_u inversion results, we are faced with a very peculiar problem. We have two stars, in a binary system, with very similar surface chemical composition, similar masses and radii, that show significantly different seismic behaviours when carrying out inversions of their structure. The problem is that the models for both stars cannot be consistent with the inversion results and simultaneously present similar chemical composition and age. Small discrepancies in chemical composition between both stars have proven not to be sufficient to eliminate the discrepancy with the inverted t_u values. Therefore, we had to assume that something was neglected in the models for 16CygB, or 16CygA, or for both stars. In what follows, we study supplementary models including a parametrised approach for an additional mixing process. The physical nature of this mixing process is not discussed here, but we demonstrate that the t_u indicator is, as expected, able to discriminate between various processes inside the star. Figure 6.14 shows various t_u inversion results for different implementations of diffusion yielding different chemical compositions. At first, we still wish to see whether there is a way reconcile the chemical composition of 16CygB with that of 16CygA.

The parametrization of this additional mixing is based on an implementation of turbulent diffusion used in previous studies (see Miglio, Montalbán, and Maceroni (2007) for details). We tested different implementations of this mixing. First, we added a constant turbulent diffusion coefficient of around $20 cm^2 s^{-1}$ acting in the entire stellar structure and computed a few models fitting the observational constraints for 16CygB. The impact of the constant turbulent diffusion coefficient is quite strong. Indeed, gradients are quickly attenuated and the t_u value decreases, as can be seen in Fig. 6.14 with the positions of the blue $\diamond$ in the left panel. However, disagreement with other constraints is quickly found if this mixing is further increased. For example, it is impossible to fit the individual small frequency separations when the extra-mixing is too important although the acoustic radius, the mean density and other constraints of the cost function of the forward modelling can be accurately fitted.

We also computed models with a diffusion coefficient implemented as an exponential decay starting either from the bottom of the convective envelope or from the surface. Two parameters are used for this formalism, one multiplicative constant and the rate of exponential decay. From previous studies (Miglio, Montalbán, and Maceroni (2007)), we know that a multiplicative coefficient of around $100 cm^2 s^{-1}$ is consistent with the effects of rotation expected in solar-like stars. This value was used as a benchmark for the order of magnitude of the mixing, but we did not limit ourselves to this value since we wanted to investigate the effects of this parametric implementation on the t_u indicator. We thus allowed changes of up to $\pm 50 cm^2 s^{-1}$ in the value of this diffusion coefficient. From Fig. 6.14, where the models with the implementation of turbulent diffusion as an exponential decay starting from the surface are represented by blue +, we can see that it can indeed help to reconcile the models with the t_u values for 16CygB, even if a higher present surface

helium value is considered, as had to be done for 16CygA. The fundamental parameters of these models are presented in table 6.11, we note that they have slightly higher masses and ages than the models without turbulent diffusion for the same chemical composition.

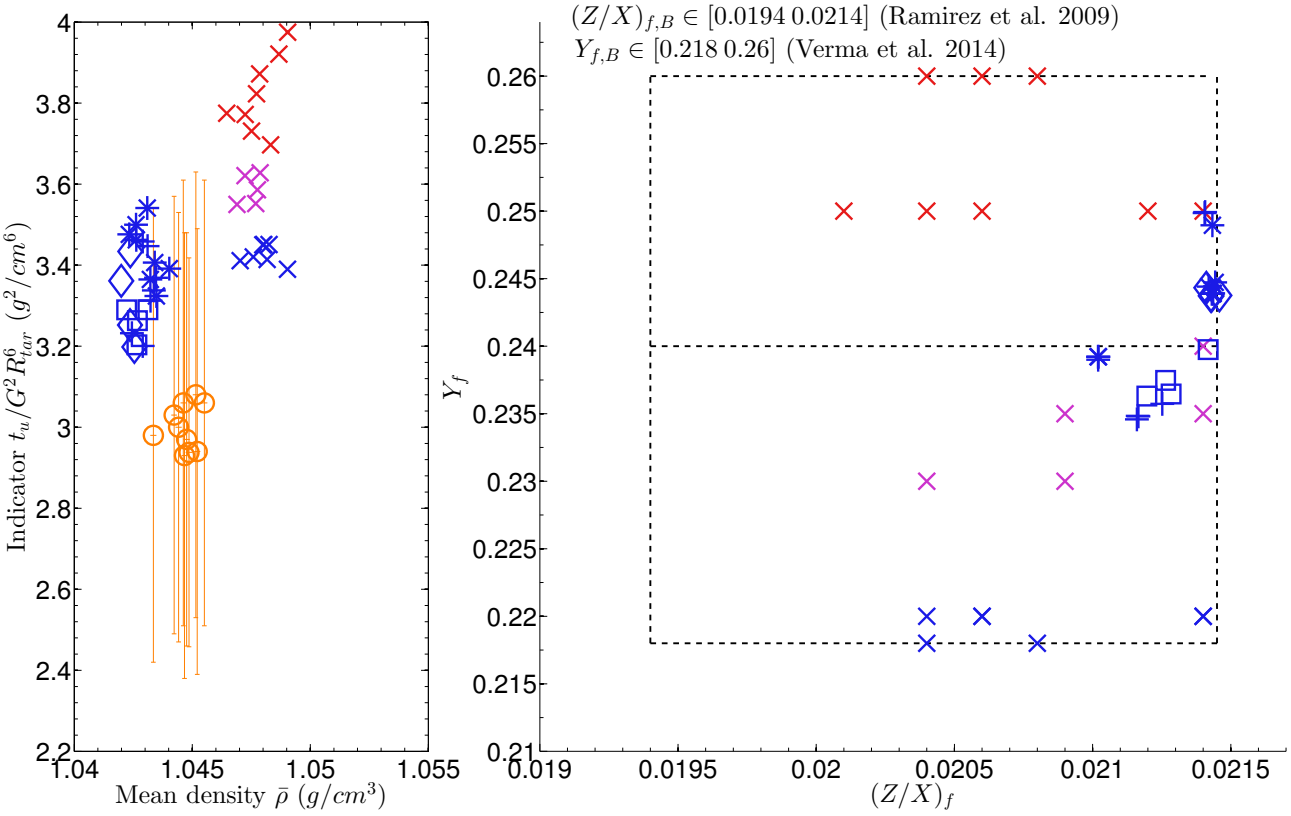

Figure 6.14: Left panel: mean density ($\bar{\rho}$) vs core conditions indicator (t_u) plot. The inversion results are plotted in orange with their respective error bars. The $\times$ are values for the reference models computed with the Levenberg-Marquardt algorithm without extra mixing. The $\square$ are related to models with a decaying exponential turbulent diffusion coefficient starting at the bottom of the convective envelope. The $+$ show models with a decaying exponential diffusion coefficient starting from the surface and the $\Diamond$ use a constant turbulent diffusion coefficient. The $*$ depict models using the new OPAS opacities and the decaying exponential coefficient starting from the surface. Right panel: surface chemical composition box for 16CygB. The colour code allows direct trend comparisons between the surface chemical composition and the t_u and $\bar{\rho}$ values as in Fig. 6.10.

As expected, additional mixing can indeed help to reconcile the chemical compositions of both stars, but does not reconcile them in age since some of the models computed with the extra mixing have ages up to 8Gy even if most are still around $7.4-7.7$Gy. It is also noticeable that the masses of the models in the present study tend to be slightly higher than those previously found in Buldgen, D. R. Reese, and M. A. Dupret (2016) using constraints from the 16CygA modelling. However, all of these models are still consistent with the radius, luminosity and $\log g$ constraints from the litterature. A clear trend is also seen in the fact that increasing the mixing improves the agreement between the reference models and the inversion. However, as the models come closer to the inverted values for t_u, they tend to be less consistent with the small frequency separation values, meaning that the extra mixing should not be too intense. Indeed, reducing the rate of exponential decay

(thereby extending the effects of extra mixing to lower regions) or increasing directly the turbulent diffusion coefficient leads to the same disagreement with the small frequency separations. To better understand the problems here, we plot the effects of the extra mixing on both the metallicity and helium profiles in Fig. 6.15. We see that the main effect is to reduce a metallicity peak right under the convective region. The more reduced the peak is, the closer the t_u values to the inverted ones. But in the meantime, we also degrade the agreement with the small frequency separations. Changes are also seen for the helium profile right under the convection zone. During the fitting process with the Levenberg-Marquardt algorithm, this affects the initial helium abundance required to be within the constraints from Verma, Faria, et al. (2014) and thus indirectly the hydrogen profile and thus the metallicity constraint.

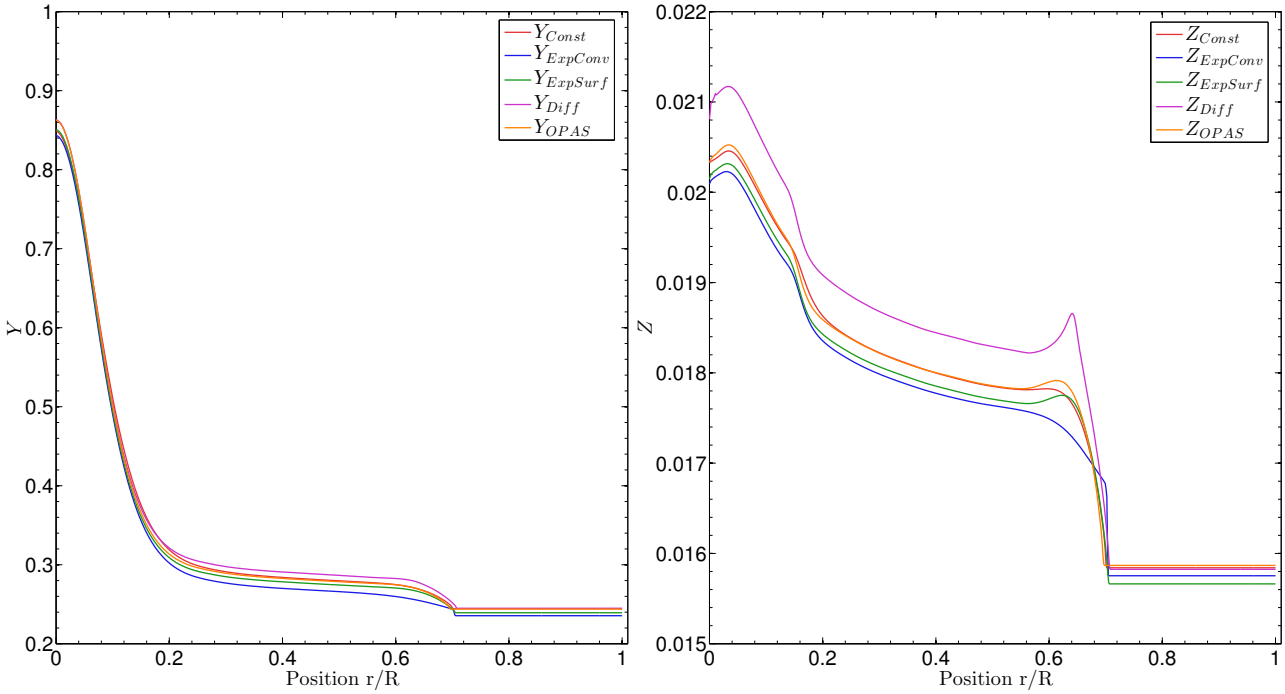

Figure 6.15: Left panel: helium abundance plot for three models with different implementations of turbulent diffusion. For the red curve, a constant mixing coefficient was applied throughout the structure and the evolution of the model. For the blue curve, we used an exponential decay starting from the base of the convective envelope of the model. For the green curve, we used an exponential decay starting from the surface of the model. For the magenta curve, we used a model including only microscopic diffusion. Right panel: The metallicity profiles of the three models described above.

Changing the opacities

To further investigate the problem, we computed additional models with the new OPAS opacities (Mondet et al. (2015), Le Pennec et al. (2015)) including atomic diffusion and the implementation of turbulent diffusion using a exponential decaying function starting from the surface. We used our forward modelling approach to compute these models and analysed whether they models could agree better with both the small frequency separations and the inverted values of t_u. As stated before, adding extra mixing could

reduce the agreement with the small frequency separations if its intensity was too high. However, when using the new opacities, we were able to further increase the intensity of the extra mixing, and thus the agreement with the t_u inversion, without degrading the agreement with the small frequency separations. As such, they provide a partial help to the problem of fitting the all constraints, as can be seen from the position of the blue $*$ in Fig. 6.14, but do not solve completely the problem. We can see the influence of these increased opacities, slightly moving deeper the base of the convective envelope and changing the efficiency of the mixing right below the base of the convective zone. We recall here that these models were still selected with the Levenberg-Marquardt algorithm using the observational constraints of 16CygB. The fundamental parameters of these models computed with were very similar to those obtained previously, but these models tended to show a slightly lower luminosity around $1.18 L_\odot$ and mass around $0.98 M_\odot$ and are thus responsible for the "lower" part of the intervals given in table 6.11.

Table 6.11: Parameters of the models of 16CygB with extra mixing and OPAS opacities

	16CygB models (Mixing)	**16CygB models (OPAS + mixing)**
Mass ($M_\odot$)	0.98-1.00	0.96-0.99
Radius ($R_\odot$)	1.07-1.10	1.07-1.09
Age (Gyr)	7.2-7.6	7.3-7.5
$L_\odot$ ($L_\odot$)	1.19-1.22	1.17-1.20
Z_0	0.0180-0.0190	0.185-0.019
Y_0	0.28-0.30	$0.28 - 0.30$
α_{MLT}	1.78-1.90	1.75-1.8

It can also be seen that when using a turbulent diffusion coefficient decaying from the lower boundary of the convective region, the effect on t_u is slightly more efficient, as illustrated by the position of the blue $\square$ in the $\bar{\rho} - t_u$ diagram of Fig. 6.14. Nevertheless, we did not seek here to fine-tune the parameters in this study since we are using a parametric approach to the problem without any physical background.

At this stage, we can already conclude that reconciling both models in terms of chemical composition and age will also probably need to remodel 16CygA to analyse whether effects other than diffusion could not be held responsible for the trend in t_u previously observed. In that sense, looking at constraints from the lithium abundance (King et al. (1997)) and combining these constraints in the modelling of both stars might change the derived fundamental parameters by a few percents.

6.3.6 Conclusion

In this section, we updated our study of the 16Cyg binary system by focusing our attention on 16CygB. From a re-analysis of the data, we were able to extract information from the t_u inversion and analyse the impact of extra mixing on the t_u values and other classical seismic indicators. First, we illustrated and solved the problem associated with the propagation of observational errors for inversions in 16CygB by analysing the impact of trade-off parameters and the presence of modes which in some cases were useless for the inversion technique. Ultimately, this approach could be used in similar situations for other observed targets.

From the t_u inversion, we were able to expose a problem in the surface chemical composition of 16CygB when compared to its companion. We computed a new set of models for this star, varying the surface chemical composition and restricting the effect of

diffusion. We then observed that when the models were consistent with the inversion results, they were systematically inconsistent with the surface chemical composition we obtained for 16CygA. Since changing the chemical composition was not the solution, we sought to implement an extra mixing process in the models of 16CygB and tried to analyse its potential impact on the t_u values. As intuitively guessed, an extra mixing in the form of turbulent diffusion was found to be able to reconcile the models both with the surface chemical composition of 16CygA and the inversion results. Furthermore, using the new OPAS opacity tables further improved the agreement with the inversion. One could argue that other implementations could be tested, such as extra mixing in the form of undershooting using the prescription of Zahn (1991) as was found in HD 52265 by Lebreton and Goupil (2012). However, as was described in Lebreton and Goupil (2012), this extra mixing would leave an oscillatory pattern in the rr_{01} and rr_{10} seismic indicators. Due to the quality of the seismic data of 16CygB, we were able compute these indicators and found no evidence for an oscillatory pattern but rather a decreasing trend with frequency that is well reproduced by models without undershooting.

To conclude, we can state that various physical processes could improve the agreement. For example, a change in opacity would further change the results of the forward modelling process and thus the stellar parameters obtained with the Levenberg-Marquardt algorithm, these new models could potentially be in agreement with the inversion of the t_u indicator. In this study, extra-mixing in the form of turbulent diffusion was invoked to reduce the disagreement between the inversion and the models. However, we did not seek to provide a physical explanation for this mixing and while it helps reducing the disagreement, further studies need to be performed to completely solve the problem. One first point would be to re-analyse 16CygA in the scope of the impact of extra-mixing. Indeed, we have shown here that turbulent diffusion can change the t_u values. It is also well-known that rotation induces such type of extra-mixing and it is believed to be responsible for the destruction of lithium in stars. Therefore, a first step would be to perform a thorough study of the impact of extra-mixing on lithium abundances and inversion results for 16CygA. The case of 16CygB should be re-analysed afterwards, since it is well-known that this star shows even lower lithium abundances and is believed to have triggered thermohaline diffusion by accreting planetary matter (see Deal, Richard, and Vauclair (2015)). As such, combining spectroscopic and seismic constraints in this binary system may provide new insights on stellar modelling of solar-like stars.

Moreover, additional indicators obtained through inversions seem to be a promising way to analyse the boundaries of convective envelopes. Consequently, from the sensitivity of seismic inversions and the quality of additional constraints, we are convinced that a re-analysis of the 16Cyg binary system with new stellar models should shed new lights on extra mixing processes in stellar interiors.

6.3.7 Appendix: The trade-off problem for t_u inversions

Origin of the trade-off problem

As described in section 6.3.3, the SOLA inversion technique we use to obtain values of the t_u indicator computes a linear combination of individual frequency differences. These coefficients are obtained through the minimization of the cost-function defined as Eq. 6.13.

We recall this definition here to better analyse the different contributions:

$$\mathscr{J}_{t_u} = \int_0^1 \left[K_{\text{Avg}} - \mathscr{T}_{t_u}\right]^2 dx + \beta \int_0^1 K_{\text{Cross}}^2 dx + \tan(\theta) \sum_i^N (c_i \sigma_i)^2 + \eta \left[\sum_i^N c_i - k\right], \tag{6.18}$$

The first integral is associated with the averaging kernel, denoted K_{Avg}, this term defines the accuracy of the inversion technique, the better the fit of the target function, here $\mathscr{T}_{\sqcup\sqcap}$, the more accurate the inversion is.

The second integral is associated with the cross-term kernel, denoted K_{Cross}. The cross-term stems from the presence of a second integral in Eq. 6.9, here for example associated with Y. Since the inversion only wants to extract information from the variable u, the contribution associated with Y as here to be damped. The trade-off between the reduction of the cross-term and the fit of the target function is calibrated by the free parameter β. In the case of the t_u inversion, the use of Y means that cross-term kernels have naturally smaller amplitudes due to the intrinsic small amplitude of helium kernels, as can be seen by comparing the right and left panels of Fig. 6.9. From previous hare and hounds, we know that the cross-term contribution is much smaller then the errors from the averaging kernels and have a negligible effect on the inversion results.

The third term of Eq. 6.18 is associated with the propagation of observational errors. This term regulates the precision of the inversion technique by damping the coefficients associated with large error bars. Since large coefficients are required for the t_u inversion, this term has an important impact on the final outcome of the inversion is at the centre of the trade-off problem we will discuss. The importance given to the observational error bars of individual oscillation mode is materialised by the free parameter θ. Ultimately, the SOLA method comes down to a trade-off between precision and accuracy. In practice, a large value of θ will imply small error bars, but also potentially a very bad fit of the target function and the reduction its accuracy. On the opposite, a very small value of θ means that the target function is well-fitted, but the result cannot be trusted due to its large error bars.

The fourth term is associated with an additional regularization based on homologous relations. The proper justification of the value of the coefficient k can be found in Sect. 3.2 of Buldgen, D. R. Reese, and M. A. Dupret (2015) and additional examples can be found in D. R. Reese, Marques, et al. (2012) and Buldgen, D. R. Reese, M. A. Dupret, and Samadi (2015) for other indicators. Eta is thus no free parameter but a Lagrange multiplier.

Effects of θ variations and mode suppression

As we stated in the previous section, the SOLA inversion is a compromise between precision and accuracy. This compromise is materialised by what is called a trade-off curve. It presents the accuracy of the result, in the form of the fit of the target function in abscissa plotted against the observational error amplification in ordinate for different values of the θ parameter. An example of a trade-off curve for the full-set of observation is plotted in Fig. 6.16.

As we can see, this trade-off curve is an L-shaped curve and it is also quickly understood that the optimal value of the free parameter θ is found nearby the edge of the trade-off curve. This position is associated with the best compromise achievable between precision and accuracy given a set of observational data. For the particular case of 16CygB, we started with values of $\theta = 10^{-5}$ and found out that values around 5×10^{-5} were better in terms of compromise between precision and accuracy. This is indeed seen in the

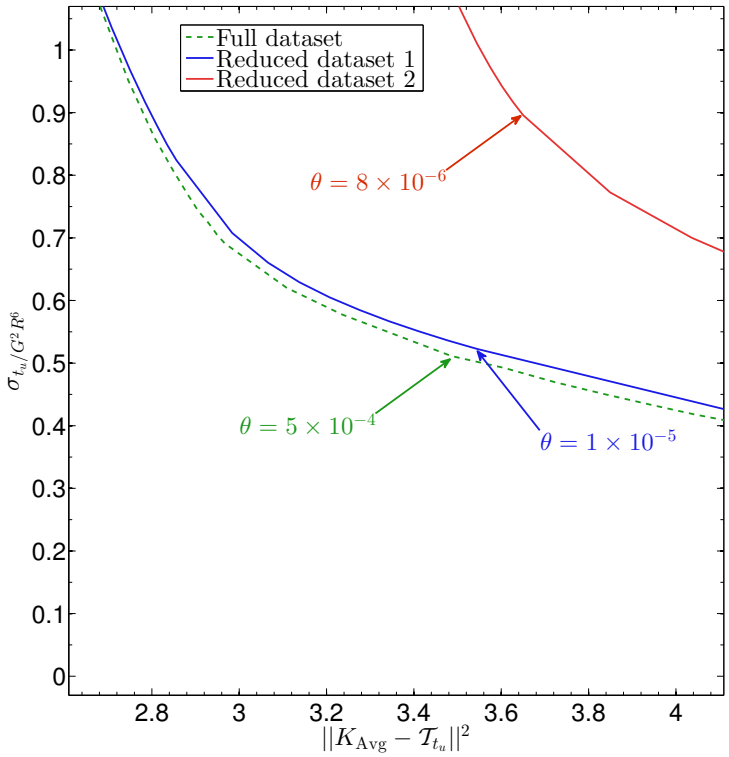

Figure 6.16: Trade-off curves for the t_u inversion using SOLA for the full dataset and for the dataset not using the three octupole modes with lowest radial order.

plot of the trade-off curve were we zoomed on regions associated with $\theta = 10^{-5}$. The green line is the trade-off curve obtained with the full set of data while the blue curve is associated with the trade-off curve when the $\ell = 3$ and $n = 14, 15$ and 16 modes have been suppressed from the data set. The green vertical line indicates the position on the green trade-off curve (full data set) associated with $\theta = 5 \times 10^{-5}$ while the blue vertical line indicates the position on the blue trade-off curve (restricted data set) for $\theta = 10^{-5}$. We can see that both positions are very close to each other in terms of error bars and fit of the target function values. However, the fact that the blue curve is always above and to the right of the green curve means that the compromise achieved with the restricted dataset will always be sub-optimal when compared to the compromise achieved with the full dataset. One can also see that the changes in error bars are quite quick when reducing θ to lower values. For example, if one considers the initial value of $\theta = 10^{-5}$, the error bars are 30% larger then at $\theta = 5 \times 10^{-5}$ (which is even more striking then the example given in Fig. 6.8).

To illustrate the reason why we tried to eliminate the modes associated with $\ell = 3$ and $n = 14, 15$ and 16, we plot in Fig. 6.17 the individual relative frequency differences with increasing frequencies. It can be seen that these three modes are well fitted and have larger error bars, this is why suppressing them helped us find a better compromise for the inversion technique. However, as stated above, this compromise is still sub-optimal in the strict mathematical sense due to the positions of the trade-off curves with respect to each other.

Further illustrations are provided in Fig. 6.18 and Table 6.12. In Fig. 6.18, we illustrate the variation of the fit of the averaging kernel for various sets of observed frequencies.

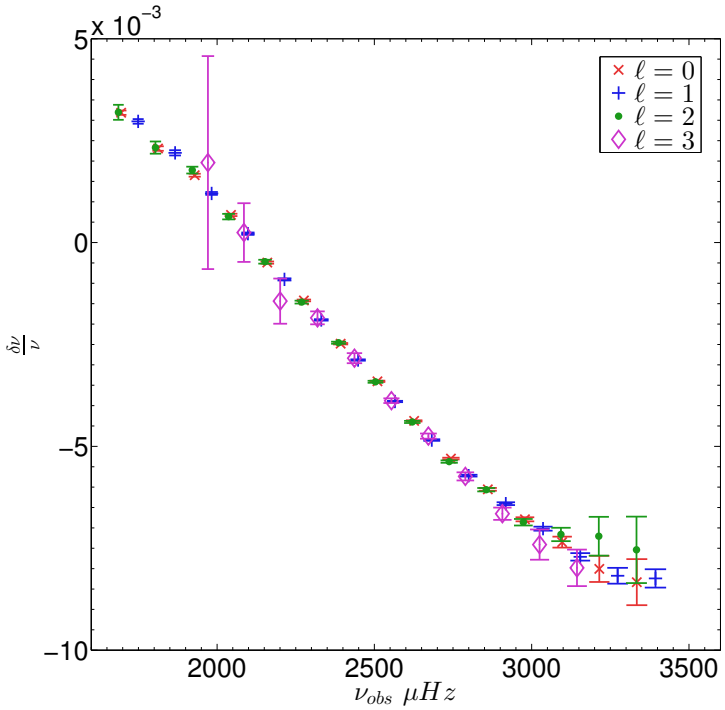

Figure 6.17: Relative frequency differences plotted with respect to the observed frequencies.

Each fit is also associated with a result in table 6.12. For the set of 47 frequencies and 39 frequencies, we suppressed modes with small error bars and low n, that are known to be used by the inversion. It can be seen that the degradation of the kernel is correlated with a reduction in accuracy and some instability of the inversion results. This is basically due to the fact that each time we change the dataset, we are on a different position on a different trade-off curve. Also, this does not mean that change θ will always be a solution, because at some point the seismic information will simply be insufficient to infer some diagnostic using the t_u inversion.

Table 6.12: Degradation of inversion results due to modes suppresion: t_u results.

Number of modes	t_u **values** ($\theta = 10^{-5}$)
56 (full set)	2.97 ± 0.69
54	2.94 ± 0.55
50	2.92 ± 0.42
47	3.47 ± 0.55
40	3.01 ± 0.32
39	3.28 ± 0.30

6.4 General Conclusion

As we have seen from this chapter, the 16Cyg binary system offers great opportunities for asteroseismology. To this day, it might the best laboratory for stellar models of solar-like stars (after the Sun, of course). The combination of high-quality seismic spectra with interferometric and spectroscopic observations are the key elements enabling such

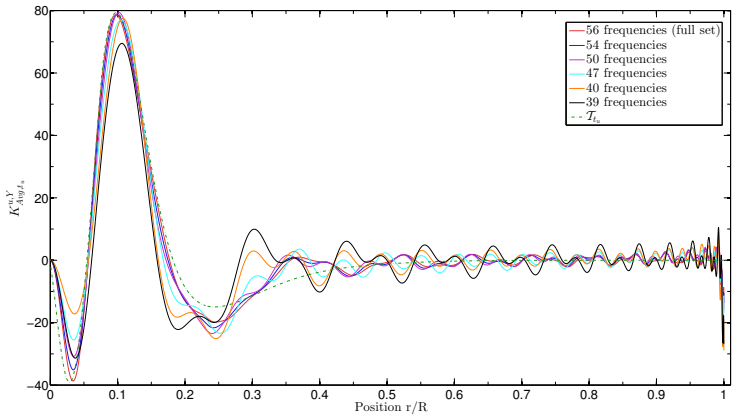

Figure 6.18: Effects of modes suppression on the averaging kernel of the t_u inversion, illustrating the decrease in quality of the target function (in green) fit for various frequency sets. The degradation of the kernel fit is associated with instabilities in the t_u values given in Table 6.12.

detailed studies. With the Gaia data releases and the advent of large scale spectroscopic surveys like the Apogee project, such studies could be carried out for additional targets. However, it should be stressed that generalizing such analyses does not mean automatising them. Indeed, detailed studies of specific high quality targets require adjusting multiple physical parameters and testing various hypotheses for the model. Currently, such tests are not achievable in large scale studies as found in Chaplin, Basu, et al. (2014) or Silva Aguirre et al. (2017a). While such approaches are crucial to providing the uncertainties of standard models and the internal error bars of the modelling process, going beyond this framework and increasing the accuracy of stellar modelling can only be achieved by minutious characterizations of benchmark stars such as those of the 16Cyg binary system.

In the future, a re-analysis of this system would be of primary importance to investigate whether the differences between the *A* and *B* components, hinted at by the structural inversions, are further confirmed by additional seismic studies. Aside from providing stringent constraints on the fundamental properties of both stars, such investigations would also provide insights on the physical ingredients of stellar models and potentially on the formation of the planetary system around 16CygB, informing us on how this could affect stellar properties.

7. A DIGRESSION INTO GLOBAL HELIOSEISMOLOGY

7.1 General Introduction

In the last 50 years, helioseismology has been one of the most successfull fields of astrophysics. The ability to seismically probe the internal structure of the Sun radically changed the picture for solar and stellar modelling. Historically, the first solar oscillations were detected in 1962 by Leighton, Noyes, and Simon (1962). During the next decade, additional observations by Mein (1966), Frazier (1968), Ulrich (1970), confirmed these results and Deubner (1975) unambiguously proved that the solar 5 min oscillations were due to trapped acoustic waves. In 1977, Rhodes, Ulrich and Simon published independent observations (Rhodes, Ulrich, and Simon (1977)), thereby confirming the acoustic nature of the oscillations and realising the first helioseismic inference by deriving constraints on the mass and depth of the solar convective zone. Meanwhile, additional observations were carried out by the Birmingham group, led by Georges Isaak (Brookes, Isaak, and van der Raay (1976)) and at the Crimean observatory under the direction of Andrei Severny (Severnyi, Kotov, and Tsap (1976)). In 1979, the Birmingham group observed for the first time very low degree acoustic modes and confirmed observationally the predictions of Vandakurov (Vandakurov (1967)) on the regularity of acoustic oscillation spectrum. The same year, Rhodes, Ulrich, and Deubner (1979) observed the first rotational splittings in the solar oscillation frequencies. First inferences on differential rotation in the solar interior were made by Kosovichev in 1988 (Kosovichev (1988)) from the data of Brown in 1987 (T. M. Brown and Morrow (1987)). The results, in contradiction with the classical theoretical predictions of stellar rotation, are still not fully explained, as is evident from the extensive litterature discussing angular momentum transport in stars as well as the modelling of the solar tachocline. Multiple solutions have been proposed to explain the solar rotation profile, including the interaction between various processes such as horizontal turbulence, the meridional circulation, the magnetic field and the transport of angular momentum by waves (Kumar, Talon, and Zahn (1999), Spruit (1999), Eggenberger, Maeder, and Meynet (2005), Charbonnel and Talon (2005)).

In the following decades, additional observational facilities were developed, such as

the GONG and BiSON networks and dedicated spacecrafts, such as the SOHO mission, increased significantly the quality of the data. In parallel to these developments of global helioseismology, one should also mention the Solar Dynamics Observatory and the future Solar Orbiter mission, which focusses on solar activity and local helioseismology, a field not described in this thesis, specialising in probing the three-dimensional structures of the upper convective region of the Sun.

Along with the improvement of the data quality, theoretical developments led to the first structural diagnostics in the late 1980*s*. Using the asymptotic formula of Duvall (1982), Christensen-Dalsgaard, Duvall, et al. (1985) carried out asymptotic sound-speed profile inversions. This methodology was quickly generalised thanks to the variational integral relations and non-asymptotic inversions were carried out (Antia and Basu (1994b), Antia (1996), S. V. Vorontsov (2001) , Marchenkov, I. Roxburgh, and S. Vorontsov (2000)) for the adiabatic and isothermal sound-speed, density, adiabatic exponent, and convective parameter profiles. Thanks to the development of a general formalism for the change of variables in the integral relations (Kosovichev (1999)), any function of acoustic variables could be probed by helioseismology. Perhaps the most famous inversion is that of the squared adiabatic sound speed, which has been carried out using various approaches.

These diagnostics led to some of the key achievements of helioseismology, but also exposed the weaknesses of standard solar models (Bahcall, Huebner, et al. (1982)). These achievements include the very precise positioning of the base of the solar convection zone and the necessity of microscopic diffusion in the computation of solar models (Kosovichev and Fedorova (1991), Basu and Antia (1997a), Basu, Christensen-Dalsgaard, Schou, et al. (1996)). However, sound speed inversions also revealed a hump at the base of the convective zone, showing that while microscopic diffusion significantly improved solar models, it failed to reproduce correctly the stratification just below the envelope. This disagreement with standard model was soon identified as the trace of additional mixing below the convection zone, due to the effects of shear turbulence, convective penetration, and potentially magnetism, which changed both the temperature and chemical composition gradients. Theoretical developments performed by Jean-Paul Zahn provided dynamical models of the tachocline and the phase shifts of solar oscillations (I. W. Roxburgh and S. V. Vorontsov (1994a)) led to analyses of the stratification in the layers that were penetrated by turbulent convective motions. However, as confirmed by the current extensive litterature on this topic we will shortly discuss in section 7.4, the modelling of the tachocline is far from clarified.

In addition to acoustic variable determinations, helioseismology provided an estimate of the helium mass fraction in the convective envelope (Antia and Basu (1994a), Richard, Dziembowski, et al. (1998), Basu and Antia (1995)). The current estimates vary from 0.24 to up to 0.255, and are strongly influenced by the microphysical ingredients used in solar models such as the equation of state or the opacities. Ultimately, all helium determinations are based on model calibrations and therefore, unlike the acoustic variables determinations, a certain degree of model dependence has to be assumed.

The successes of helioseismology were also highlighted by the outcome of the so-called solar neutrino problem. This crucial issue was first noticed in the 1960s when the first neutrino measurement experiments were carried out. The observed flux of neutrinos was much lower than predicted by the solar models and the discrepancy was thought to stem from an inaccurate modelling of the solar core. However, with the development of helioseismic techniques, the standard solar models were validated and it became clear that the solution was to be found in neutrino physics. Ultimately, the explanation was found to be the neutrino oscillations, confirmed by the Super-Kamiokande Observatory

in 1998 and the Sudbury Neutrino Observatory in 2001. The teams responsible for the observation of the deficit and the confirmation of the neutrino oscillations were both awarded the Nobel Prize in Physics in 2002 and 2015, respectively.

However, a new problem was soon encountered by the standard solar models when the heavy elements abundances were revised in 2004 (Asplund, Grevesse, Sauval, Allende Prieto, and Kiselman (2004), Asplund, Grevesse, Sauval, Allende Prieto, and Blomme (2005)). Before this revision, microphysical ingredients in standard models had already been updated several times, for example the radiative opacities in 1996 (Iglesias and Rogers (1996)) and the equation of state in 2002 (Rogers and Nayfonov (2002)). The Anders and Grevesse (1989) abundances were also slightly revised in 1993 (Grevesse and Noels (1993)) and 1998 (Grevesse and Sauval (1998)), but these small changes did not significantly alter the agreement with helioseismology. The scenery changed a few years later, when Asplund et al. revised the abundances using 3*D* models and a careful selection of the spectral lines to avoid blends. This revision led to a 20 to 30% decrease of the solar metallicity. It should be noted that such changes were deemed possible according to a metallicity inversion by Takata in 2001 (Takata and Shibahashi (2001)).

The metallicity change led to a reduction of the opacity at the base of the convective envelope, inducing a disagreement between the new standard solar models and every helioseismic diagnostic. Ever since, the solar abundance problem, or solar metallicity problem, awaits a solution. A further revision of the abundances in 2009 led to a slight reincrease of the metallicity (Asplund, Grevesse, Sauval, and Scott (2009)) and independent calculations were performed in 2011 (Caffau et al. (2011)). From these works, we now know that the 3*D* models, although not perfect, agree with each other and that the remaining differences are due to the selection of the spectral lines. Nevertheless, none of these calculations led to a metallicity as high as the determinations of the 90*s*. As said in A. Serenelli (2016), "What seems clear, however, is that the low metallicity solar abundances are here to stay" and the exact origin of the disagreement between the Sun and the solar models is still unknown.

From the helioseismic point of view, this disagreement led to attempts to determine the metallicity in the convective envelope from the oscillation frequencies. Initial attempts were performed by Takata and Shibahashi (2001), followed by attempts by Basu, Antia and Lin in 2006 and 2007 (Antia and Basu (2006), Basu and Antia (2006), Lin, Antia, and Basu (2007)), which concluded on multiple occasions that the solar metallicity agreed with the value derived from the 1*D* atmospheric models. More recently, S. V. Vorontsov et al. (2013) and S. V. Vorontsov et al. (2014) carried out a reanalysis of the problem by using solar envelope models and found a metallicity partially in agreement with the more recent spectroscopic determinations.

The main weakness of helioseismic determinations of metallicity is its dependency on additional microphysical ingredients, such as the opacity tables or the equation of state. This results from the intrinsic inability of seismology to directly probe other variables than those of the acoustic structure of the Sun. Therefore, all conclusions of these seismic studies are valid provided that the microphysical ingredients of solar models are correct. This is actually a very bold assumption given the ongoing debate on opacity calculations, illustrated by the extensive litterature following the recent experimental measurement of iron opacity by Bailey and collaborators (Bailey et al. (2015), Nahar and Pradhan (2016), Blancard, Colgan, et al. (2016)). Indeed, opacity calculations are not free of uncertainties (Krief, Feigel, and Gazit (2016), Iglesias and Hansen (2017), Mendoza (2017)) and we will see in the next section that the latest opacity tables calculated at the Las Alamos National Laboratory do not solve the problem of solar models, but rather lead to a more complex

picture. Besides the uncertainties on opacities, intrinsic differences in the equations of state used to compute solar models also exist (see Baturin et al. (2013) for a comparison), further complexifying the issue.

Unfortunately, to the uncertainties on the ingredients of the standard solar models, we have to add the possible impact of non-standard processes, like rotation, radiative accelerations, convective penetration, ... as discussed in section 2.3. This means that while further revisions of the opacities (expected from various studies Nahar and Pradhan (2016), Iglesias and Hansen (2017), Mendoza (2017)) will likely change the picture, the fact that the highest disagreement between standard models and the Sun is found in the vicinity of the tachocline, the exact region were the standard solar models are the most uncertain, is not to be neglected. In fact, theoretical studies favor a certain degree of convective penetration and some diffusive extra-mixing below the limit of the convective zone given by the temperature gradient transition. The main difficulty is the absence of a theoretical formulation to depict this transition region due to the uncertainties linked to the exact physical mechanisms acting within it.

In conclusion, the solar metallicity problem is the materialization of the central questions of stellar physics and while the debate seems linked to specific points of stellar structure, the consequences of the outcome of this problem are quite far-reaching since the standard solar model defines the basic recipe used to compute stellar models, which are then used as references in multiple fields of astrophysics.

In this chapter, we will present three new studies in the field of global helioseismology. Section 7.2 presents a study which has been accepted for publication in Astronomy and Astrophysics, section 7.3 presents a study which is accepted for publication in the Monthly Notices of the Royal Astronomical Society and section 7.4 presents a study which is currently submitted to the Monthly Notices of the Royal Astronomical Society.

7.2 Seismic inversion of the solar entropy: A case for improving the standard solar model

7.2.1 Introduction

Helioseismology, the science of interpreting the acoustic oscillations of the Sun to probe its internal structure, has led to striking success stories. The precise location of the base of the convective envelope at a fractional radius of 0.713 ± 0.001 (Kosovichev and Fedorova (1991), Christensen-Dalsgaard, D. O. Gough, and Thompson (1991), Basu and Antia (1997b)), the inversion of the solar sound speed, density and rotation profiles (Antia and Basu (1994b), Elsworth et al. (1990), Kosovichev, Schou, et al. (1997)), the determination of the helium mass fraction in the convective envelope at $Y = 0.2485 \pm 0.0035$ (Basu and Antia (1995)), and the outcome of the "solar neutrino problem" (Couvidat and Turck-Chieze (2004),Bahcall and Peña-Garay (2004)) are considered to be the greatest achievements in this field. In the 90*s*, the internal structure of the Sun was extremely well reproduced by standard solar models (hereafter SSMs). Consequently, the physical ingredients of these numerical models, particularly the solar chemical element abundances (Grevesse and Noels (1993), hereafter GN93), were applied to stars other than the Sun and used in the computation of grids of stellar models. Such grids are one of the basic components in various fields such as stellar population analysis, Galactic evolution, and exoplanetology for example.

The physical ingredients of the solar models, such as the equation of state (Rogers and Nayfonov (2002)) or the heavy element abundances were continuously refined (Grevesse and Sauval (1998), hereafter GS98), but the changes being quite small , the agreement of the models with helioseismology remained. However, two refinements with stronger

impacts were more recently brought forward.

The first one addressed the solar chemical mixture with a new set of heavy element abundances published by Asplund and collaborators (Asplund, Grevesse, Sauval, Allende Prieto, and Kiselman (2004), Asplund, Grevesse, Sauval, Allende Prieto, and Blomme (2005)). The most abundant heavy elements (C,N,O) saw a strong decrease of their abundances, when compared to GN93 and GS98, linked to the updated physics, the careful selection of atmospheric spectral lines and the use of 3D convection simulations in the spectral synthesis calculations. Consequently, the metallicity of the Sun was reduced by about 30%. Using these new abundances led to strong disagreements between standard solar models and every helioseismic diagnostic. The convective zone was too shallow, the helium abundance too low and the sound speed profile incompatible with that of the Sun (A. M. Serenelli et al. (2009)). Further revision of the spectroscopic determinations (Asplund, Grevesse, Sauval, and Scott (2009), hereafter AGSS09) led to slight reincreases of the metallicity, but these values were still too low to restore the agreement with helioseismology. The updated oxygen abundances were compared with the values found in the solar environment (Turck-Chièze, Couvidat, et al. (2004)), and the disagreement with helioseismology was suggested to originate in additional physical processes acting in the solar radiative zone. Solar models including some examples of processes were studied (Kumar, Talon, and Zahn (1999), Castro, Vauclair, and Richard (2007)), but could provide a clear and decisive answer on the issue. Simultaneously, other studies used seismology to estimate the solar metallicity. Some analyses confirmed the GS98 value (Basu and Antia (2006)) while others agreed with the AGSS09 value (S. V. Vorontsov et al. (2014)), illustrating the stalemate of this problem.

The second important change in solar modelling is the revision of the stellar material opacity. The solar abundance problem has indeed been linked to the opacity at the base of the convective envelope and a physical process inducing a local increase of the opacity has recurrently been proposed as the solution to the controversy (Basu and Antia (2008)). Until recently, the most commonly used opacity values were those computed from the OPAL opacity tables (Iglesias and Rogers (1996)) and an underestimate of the opacity in more massive stars was convincingly revealed by different studies (Zdravkov and Pamyatnykh (2008), S. Salmon et al. (2012), Cugier (2012),Turck-Chièze, Gilles, et al. (2013)). These findings initiated both innovative opacity measurements with high-energy laser facilities as well as numerical computational efforts to improve the determination of the solar opacity. Great care was devoted to the knowledge of the oxygen and iron spectral opacities, which are the atomic species that contribute the most to light absorption at the base of the solar convective envelope (Blancard, Cossé, and Faussurier (2012)). Reaching the physical conditions prevailing near the base of the solar convective envelope with laser experiments is an intricate problem, but the first results for iron revealed an important discrepancy with theoretical expectations (Bailey et al. (2015)). In parallel, two new sets of theoretical opacities were developed, one dedicated to the Sun from the OPAS consortium (Mondet et al. (2015)) and the other covering the wide range of stellar conditions, by the Los Alamos National Laboratory (Colgan et al. (2016), hereafter OPLIB opacities), which could become commonly used in stellar models, like the OPAL tables.

The solar issue impacts astrophysics as a whole since the "metallicity scale", used to relate spectroscopic observations to the metallicity of stellar models, is widely applied in other astrophysical fields. This scale uses the Sun as its reference and a 25% change in the reference obviously induces a 25% change for all stars. To this day, the so-called "solar metallicity problem" remains a tedious issue which is not only linked to the metallicity, but to the whole micro- and macrophysical representation of the solar structure. Asteroseismic

results have indeed already shown that our depiction of transport processes in stellar models is imperfect (Deheuvels, Doğan, et al. (2014), Mosser, Goupil, et al. (2012)). Due to the quality of the solar data, the Sun still constitutes our best laboratory to test the ingredients of stellar models. Consequently, providing new seismic diagnostics allowing a more in-depth probe of the solar structure is crucial. With this study, we provide such a new diagnostic by performing structural inversions of an entropy proxy. The sensitivity of this inversion to the stratification just below the convective zone paves the way for a re-analysis of the importance of additional physical processes required in the description of the solar structure. After having presented classical helioseismic tests and their limitations, we will show how our new diagnostic sheds new light on the solar structure problem.

7.2.2 Classical helioseismic tests of updated solar models

The models considered in this study are standard solar models (Christensen-Dalsgaard, Dappen, et al. (1996)), built using the Liège stellar evolution code (CLES, Scuflaire, Théado, et al. (2008)), for which the frequencies were computed with the Liège oscillation code (LOSC, Scuflaire, Montalbán, et al. (2008)). All models presented in this section are computed using the FreeEOS equation of state and either the OPAL, OPAS, or OPLIB opacity tables. In order to fully estimate the effects of a change in the heavy element abundances, we adopted the two extreme mixtures, namely GN93 and AGSS09.

The structural kernels and the inversions were computed with an adapted version of the InversionKit software (D. R. Reese, Marques, et al. (2012)) using both the SOLA (Pijpers and Thompson (1994)) and RLS techniques (Antia and Basu (1994b)). We used the same solar seismic dataset as in (Basu, Chaplin, et al. (2009)) and followed their definitions of the error bars for the SOLA technique.

The acoustic structure of a star is defined by a given set of thermodynamical quantities found in the pulsation equations, such as the pressure, P, the density, ρ, or the so-called Brunt-Väisälä frequency, N^2... The inversion technique allows us to seismically determine the relative differences between structural quantities of numerical solar models and the Sun itself, thus revealing whether these models accurately reproduce the solar acoustic structure. A classical test of the solar models is to compute the inversion of the relative differences of the squared adiabatic sound speed profile, denoted c^2, defined as $\frac{\Gamma_1 P}{\rho}$, with $\left(\frac{\partial \ln P}{\partial \ln \rho}\right)_S$, being the adiabatic exponent, with S the entropy of the plasma. We start in Fig. 7.1 by presenting inversion results for the squared adiabatic sound speed for various models using both the GN93 and AGSS09 abundances and different opacity tables. The blue and orange curves illustrate the results obtained with the past OPAL opacities (Iglesias and Rogers (1996)), namely an excellent agreement for GN93 and the worsening of this agreement when using AGSS09. Fig. 7.1 also presents the inversion results for models using GN93 (in red) and AGSS09 (in green) computed with OPLIB. First we note that although the convective zone is still too shallow in AGSS09 models, as can be seen in table 7.1, there is a significant improvement when compared to the performances of AGSS09 with the old OPAL opacities (Iglesias and Rogers (1996)). The level of agreement for the GN93 model is reduced when the new OPLIB opacities are used. However, this disagreement for the GN93 model is not that dramatic and it still seems that the GN93 mixture is performing better. It is only below 0.4 solar radii that the agreement of the AGSS09 standard models with the OPLIB becomes better or as good as the GN93 mixture. In conclusion, the sound speed inversion does not seem to imply that the use of the OPLIB opacities has significantly changed the picture of the solar metallicity problem, as was also found in (Guzik, Fontes, et al. (2015)).

In addition to the OPLIB opacities, we have also tested the OPAS opacity tables, which have been optimised for the base of the convective zone. Although they lead to a very slightly deeper convection zone (Guzik, Fontes, et al. (2015)), these tables do not cover the full solar conditions and thus were not optimal for full structural inversions of the Sun (Some results using OPAS are presented in the supplementary material.).

The improvements in AGSS09 models computed with the OPLIB opacities are however mitigated by an increased discrepancy with the helium abundance in the convective envelope. The helium abundance of these new models is found to be lower than with previous opacities, whether GN93 or AGSS09 abundances are used. This reduction in helium is linked to the fact that the OPLIB opacities are slightly lower in most parts of the solar structure. This opacity reduction induces a lower mean molecular weight in the solar models, thus a lower initial helium abundance, to ensure that the model reproduces the solar luminosity.

The issue becomes more intricate when one analyses the ratios of the small frequency separation to the large frequency separation (see supplementary material). These ratios, denoted r_{02} and r_{13}, are used to probe the solar core conditions (I. W. Roxburgh and S. V. Vorontsov (2003)) and show a clear preference for the latest AGSS09 mixture when the OPLIB opacities are used. This constitutes a clear change from the previous SSMs with the OPAL opacities, which showed better agreement with higher metallicity abundances, such as the GN93 or GS98 tables. Hence, the situation is quite confusing since the sound speed inversion seems to favor the old GN93 mixture when using the OPLIB opacities while the frequency ratios better agree with low metallicity models using the same opacity tables. It seems fair to admit that no clear solution emerges from classical helioseismic diagnostics.

	$r_{Conv}/R_\odot$	Y_{Conv}
Helioseismic measurements	0.713 ± 0.001	0.2485 ± 0.0035
SSM (AGSS09, FreeEOS, OPAL)	0.720	0.236
SSM (AGSS09, FreeEOS, OPLIB)	0.718	0.230
SSM (AGSS09, FreeEOS, OPAS)	0.717	0.232
SSM (GN93, FreeEOS, OPAL)	0.711	0.245
SSM (GN93, FreeEOS, OPLIB)	0.708	0.240

Table 7.1: Comparison of the depth of the convective zone and the helium mass fraction between helioseismic results and various standard solar models. The ingredients (abundance tables, equation of state, opacity tables) are listed in parentheses.

7.2.3 Inversion of the solar entropy: a new seismic diagnostic

To shed new light on the problem illustrated in Sect. 7.2.2, we propose a new seismic diagnostic. It consists in inverting a solar entropy proxy, defined as, which reproduces the behaviour of the entropy of the solar plasma. The constraining nature of the entropy proxy inversion originates in the plateau that is formed by this quantity in convective regions. This plateau is due to the high efficiency of convection in the deep layers of the solar envelope, where this phenomenon operates adiabatically. In turn, the height of the plateau is a direct marker of the way we model the radiative zones of the Sun. In the layers below the convective envelope, radiation dominates energy transport and the stratification is very sensitive to both opacity and chemical abundances. Consequently, a change in opacity, whatever its origin, or a variation of the abundances will impact both the temperature and mean molecular weight gradients and thus the height of the

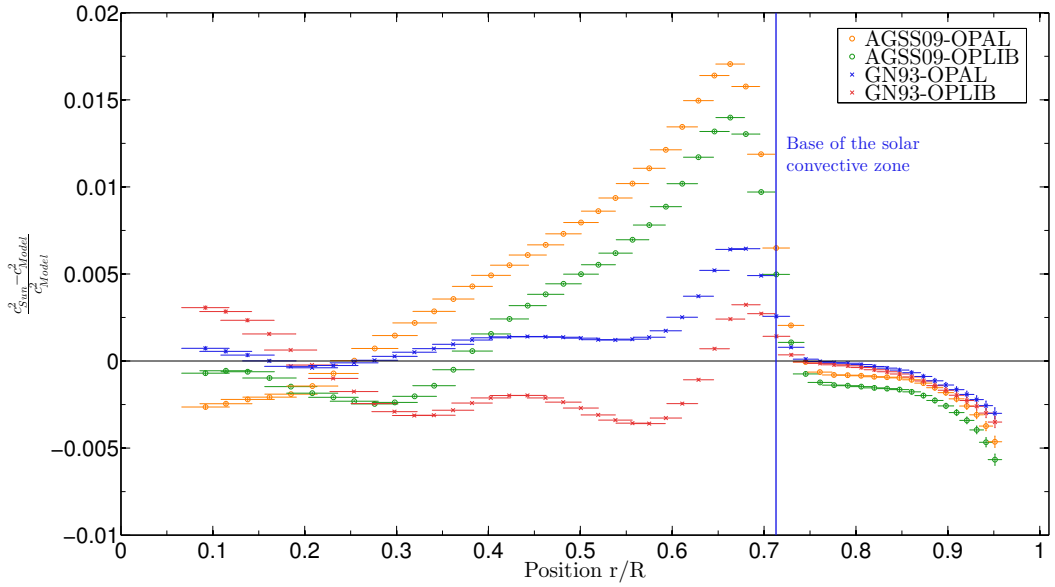

Figure 7.1: Sound speed inversions using the SOLA method for four SSMs. The crosses of various colours are related to GN93 standard models, blue crosses being associated with a model using the old OPAL opacities and the red crosses with a model using the latest OPLIB opacities. The circles are related to AGSS09 standard models, green denoting the use of the OPLIB opacities and orange the use of the former OPAL opacities. All models used the FreeEOS equation of state. Horizontal error bars show the interquartile width of the averaging kernels while the vertical error bars are the 1σ errors from the propagation of the observational 1σ errors.

plateau in a given solar model. Testing this height through seismic inversions offers a straightforward diagnostic. Indeed, as shown in the supplementary materials, there is a clear relation implying that an increased opacity at the base of the convective zone induces a lower entropy plateau in the convective zone. Moreover, non-standard processes may also change the height of the plateau, making this diagnostic a very sensitive probe of the layers just below the convective envelope, which are precisely the ones for which the disagreement with the solar model is the largest and where the physical hypotheses of the standard models are the most uncertain.

The inversion of the entropy proxy profile was made possible by the derivation of new structural kernels using a method mentioned in a previous paper (Buldgen, D. R. Reese, and M. A. Dupret (2017)). Inversions were conducted using both the SOLA and RLS methods to guarantee the reliability of the results. We followed previous studies (Rabello-Soares, Basu, and Christensen-Dalsgaard (1999), Basu and Thompson (1996)) to calibrate the free parameters of both methods and hare-and-hounds exercises were also performed to further assess the robustness of this new seismic inference (see supplementary).

Inversion results of the entropy proxy profile are given in Fig. 7.2 for two solar models using the GN93 abundances and either the former OPAL or the new OPLIB opacities. The plateau of the entropy proxy is shifted by about 2% due to the opacity changes between the OPAL and OPLIB opacity tables (blue and red results). While the agreement between the Sun and the GN93 SSMs is still of the order of 0.7%, which is quite good, the sign of the differences in the plateau has critical implications. A positive difference between the Sun and the GN93 model means that the entropy plateau in the model is too low. If one were

to reconcile the GN93 abundances with the entropy profile of the Sun, it would necessarily require some change inducing a reduction of the opacity at the base of the convective zone in order to raise the entropy plateau up to the solar value. This appears to be in contradiction with the experimental results of Bailey et al. (Bailey et al. (2015)) for iron in the physical conditions present at the base of the envelope. Furthermore, theoretical calculations of iron spectral opacity in these conditions are still a matter of debate and could as well change in the future (Iglesias and Hansen (2017), Nahar and Pradhan (2016), Blancard, Colgan, et al. (2016)). It is worth noting that the height of the plateau is nearly independent of the equation of state. We show in the supplementary material that it is hardly shifted if one uses the OPAL equation of state (Rogers and Nayfonov (2002)) instead of the FreeEOS equation of state adopted in our models.

The inversion of the entropy proxy for the AGSS09 standard models is presented in Fig. 7.3. The orange circles illustrate the disagreement found in solar models built using the old OPAL opacities. Switching to the OPLIB tables (green circles) induces an improved agreement at all fractional radii. As can be seen, these models are in better agreement in the radiative region of the solar structure and still show negative differences in the convective envelope. It is worth noting that the linear trend seen in the plateau seems to come from both the wrong position of the base of the convective envelope and the formalism used for convection (here the mixing-length theory). This means that for the low-metallicity AGSS09 solar models, a further opacity increase as seen in experimental measurements could improve the agreement with the Sun. In additional test cases, we showed that a global uniform 5% increase of the opacity induced a 0.4% change of the position of the entropy plateau. This of course only serves as an indication. Using ad-hoc localised increases of the opacity just below the convective zone, we observed a lowering of around 1% of the height of the entropy plateau in SSMs. This indicates that the entropy inversion is very sensitive to the layers right below the convective zone. This sensitivity can efficiently constrain non-standard processes. Indeed, additional mechanisms would alter both temperature and mean molecular weight gradients and the changes would be clearly seen in the variations of the height of the plateau.

7.2.4 Conclusion

The change of scenery caused by the use of the OPLIB tables in SSMs points out weaknesses for both high- and low-metallicity abundances tables. An intermediate metallicity value or an increased opacity at the base of the convective envelope could marginally restore the agreement for standard models, but the discrepancies in helium seem to point out additional mechanisms, some physical ingredients that have to be included in the solar models whatever abundance tables are used. The uncertainties illustrated in this study and the sensitivity of the seismic diagnostic we developed lead us to advocate for a re-opening of the case of potential additional ingredients in helioseismic analyses using constraints such as the lithium abundance and the solar rotational profile in combined studies using simultaneously all seismic information available. Changes in the physical ingredients of solar and stellar models will impact our determinations of stellar fundamental parameters. It is a necessary step if we want to bring these models to a new level of physical accuracy. For that purpose, seismic inversions of the entropy profile offer unprecedented opportunities to further test the structure of the Sun.

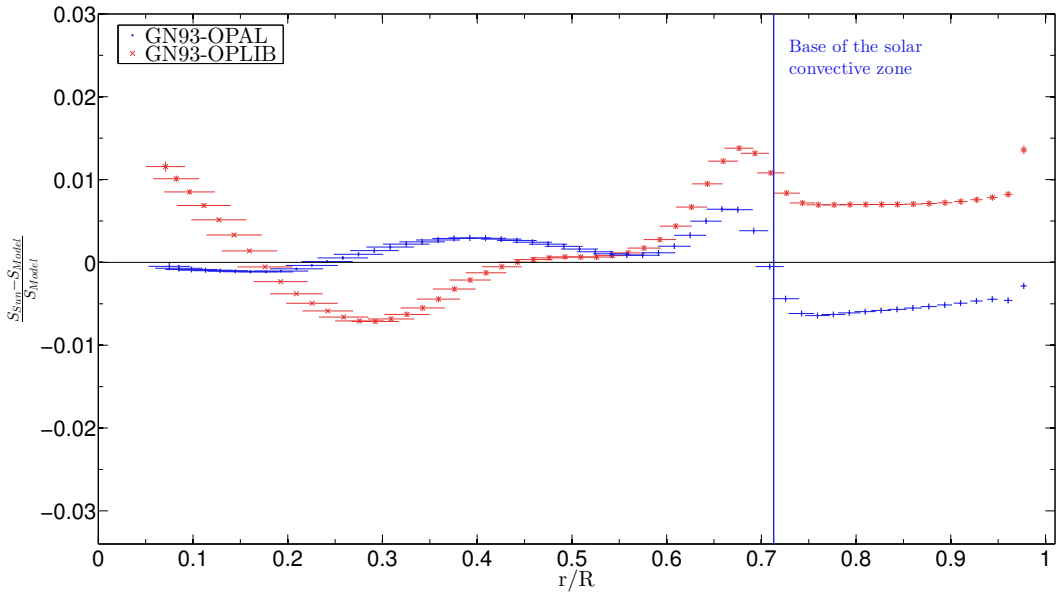

Figure 7.2: Effects of the opacities on the entropy profile of GN93 SSMs. The symbols of various colours illustrate inversion results for the entropy proxy solar profile, $S_{5/3}$. The difference between the purple and red crosses emphasises the effects of changing the opacity table when building solar models. The horizontal and vertical error bars are defined as in 7.1

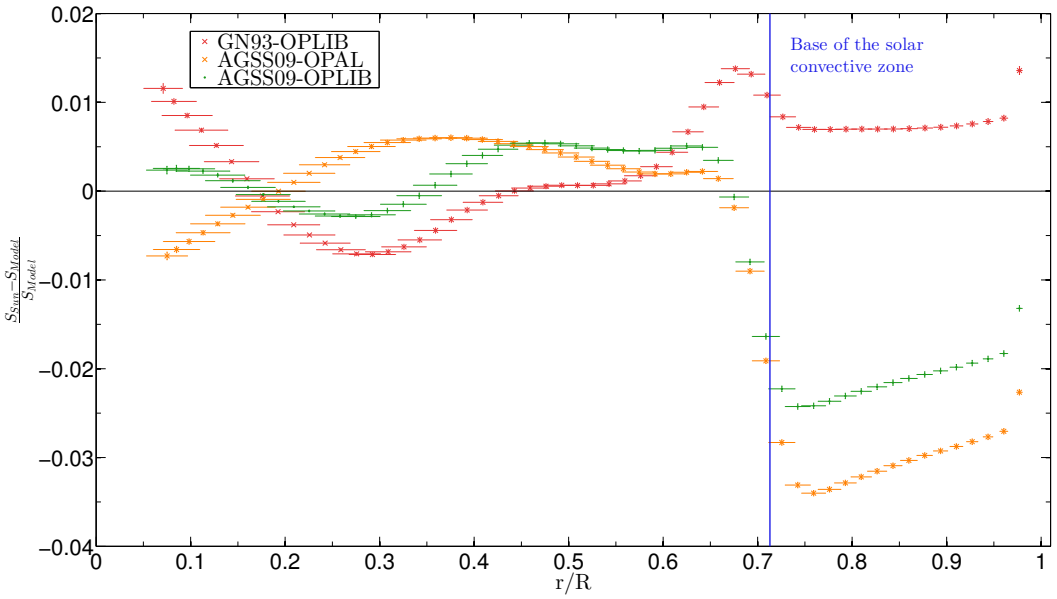

Figure 7.3: Comparison of the entropy profile between AGSS09 and GN93 SSMs. The red crosses illustrate inversion results for the profile of the entropy proxy in the Sun for the GN93 SSM built with the OPLIB opacities. The green circles and orange crosses illustrate the effects of changing from the old OPAL opacities to the recent OPLIB opacities in AGSS09 SSMs.

7.2.5 Supplementary Materials

Checking the frequency ratios of low degree modes

Another classical helioseismic test consists in comparing the frequency ratios denoted r_{02} and r_{13} of stellar models with those of the Sun. These frequency combinations are thought to be very sensitive to the core conditions of the Sun and were thought to be able to constrain the mean molecular weight of the solar core (Chaplin, A. M. Serenelli, et al. (2007)). In Fig. 7.4, we illustrate the agreement between the ratios obtained from solar data and that from standard solar models using both the GN93 and the AGSS09 abundances along with the OPAL and OPLIB opacities and the FreeEOS equation of state. The dashed lines illustrate the results obtained for OPAL tables, with the GN93 abundances (orange) agreeing almost perfectly to the solar values while the AGSS09 abundances (green) clearly disagreed. This result was interpreted as a requirement for a high metallicity to reproduce the mean molecular weight gradients in the deep layers of solar structure (Chaplin, A. M. Serenelli, et al. (2007)). However, from the results obtained with the OPLIB opacities, illustrated as plain lines, we can see that the AGSS09 abundances are now clearly favored. This is also seen in the sound speed and entropy inversions where the AGSS09 abundances perform much better below 0.4 solar radii than the GN93 mixture. This increases the complexity of the problem since we no longer have one heavy element mixture that agrees better with the solar structure at all radii. In addition, this confirms that these ratios actually depend on multiple ingredients which come into play in solar core conditions rather than only the mean molecular weight.

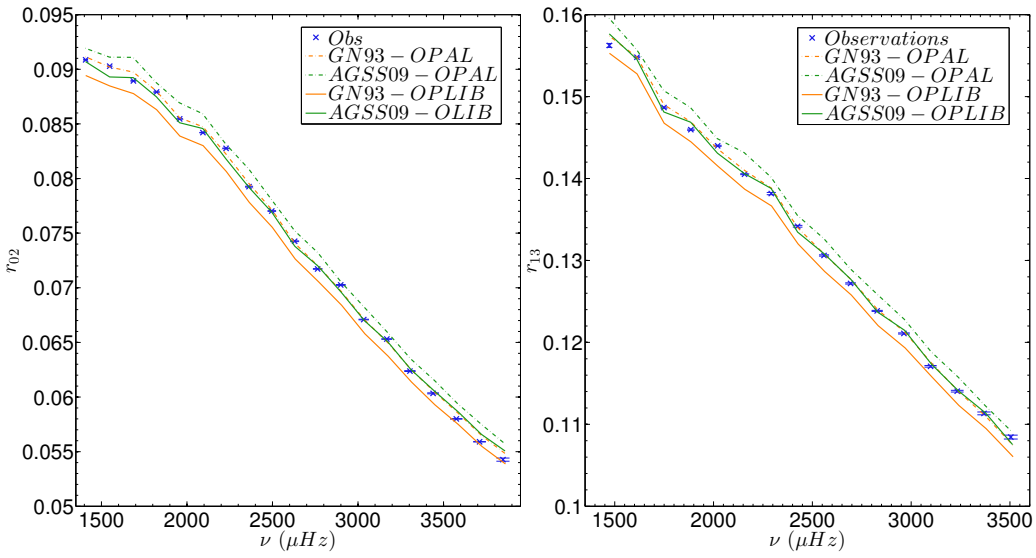

Figure 7.4: Frequency ratios r_{02} and r_{13} for the Sun and two SSMs. The observations are given with their error bars in blue, while the dashed green line show the results for an SSM built using the OPAL opacities, the FreeEOS equation of state and the AGSS09 abundance tables. The dashed orange line show the values of these ratios for an SSM built with GN93 abundances, the OPAL opacities and the FreeEOS equation of state. The plain green and orange lines show the changes in the ratios values when using the OPLIB opacities instead of the OPAL opacities for the AGSS09 and GN93 abundances respectively.

Additional verifications of the seismic diagnostic of the entropy proxy

Our entropy proxy, denoted $S_{5/3} = \frac{P}{\rho^{5/3}}$ comes from the Sackur-Tetrode equation for the entropy of a mono-atomic non-degenerate ideal gas, which reads

$$S = \frac{3k_B}{2}\left(\mu m_u \ln\left(\frac{P}{\rho^{5/3}}\right) + f(\mu)\right), \tag{7.1}$$

with k_B the Boltzmann constant, μ the mean molecular weight, m_u the atomic mass unit, P the local pressure, ρ the density and $f(\mu)$ a function that only depends on the mean molecular weight and physical constants. The most striking advantage of this proxy is its unambiguous behaviour towards opacity changes just below the convection zone. Indeed, if one takes the derivative of the natural logarithm of $S_{5/3}$ with respect to the natural logarithm of P for an ideal gas, one obtains

$$\frac{d\ln S_{5/3}}{d\ln P} = \frac{-2}{3} + \frac{5}{3}\left(\frac{d\ln T}{d\ln P} - \frac{d\ln \mu}{d\ln P}\right) \tag{7.2}$$

Now, for a given energy flux (as determined by the solar luminosity), an increased opacity below the convection zone induces a steeper temperature gradient against pressure, i.e. more energy is absorbed by stellar matter. This, in turn, will increase the logarithmic derivative of $S_{5/3}$ and brings it closer to 0 since $\frac{d\ln S_{5/3}}{d\ln P}$ is negative as can be seen in Fig. 7.5. Therefore, the increase in entropy versus the radius is thus smaller as the pressure decreases and the height of the plateau is accordingly reduced with the steepening of the temperature gradient just below the convective envelope. This effect is illustrated in Fig. 7.6, where the near 2% shift results from changing the opacity tables used in the SSMs. The steeper temperature gradient is a consequence of steeper dependence of the OPLIB opacities with temperature (see Colgan et al. (2016)). Therefore, although they are lower then the OPAL opacities in most of the solar structure, they can still induce a lower base of the convective zone and a lower entropy gradient in SSMs. The effect of a localised ad hoc opacity increase on this indicator has been observed in all test cases involving the past OPAL and the latest OPLIB and OPAS opacities. These tests on structural models have confirmed the trends we can see using the equations of thermodynamics. We illustrate these trends in Fig. 7.6 where we plot the temperature, mean molecular weight and entropy gradients with respect to pressure. One can see the correlation between changes in the gradient and the height of the entropy plateau, but changes are also seen in the deep radiative regions, thereby explaining the disagreement of the GN93 abundances with OPLIB with the solar structure for these layers.

Of course, the behaviour of this entropy proxy is slightly dependent on the equation of state and small changes can be seen in the height of the plateau if different equations of state are used. In Fig. 7.7, we illustrate this effect by using the OPAL equation of state instead of the FreeEOS equation of state in our SSM. The orange results are for OPAL and the red results are for the FreeEOS equation of state. The changes are quite small, more than ten times smaller than the difference between the Sun and SSMs or between models which use OPLIB and OPAL opacities. As the equations of state are generally calibrated on the Sun, it is not a surprise that changing this ingredient leads to limited variations. Consequently, it seems very improbable that changes in the equation of state would have a strong impact. The effects illustrated in Fig. 7.7 are seen with either abundance tables. In conclusion, most of the changes in the entropy plateau are to be expected from non-standard processes or updates in the opacity tables. Indeed, such effects would imply significant variations of both temperature and mean molecular weight gradients that would be clearly witnessed by the entropy profile.

As mentioned in the core of this section, we also computed SSMs with the AGSS09 abundances and the OPAS opacity tables that we combined with the OPLIB opacities. The combination is required since the OPAS tables do not cover the whole range of density and temperature necessary to build a solar model from the center to the photosphere. The results for these models are illustrated in Fig. 7.7 in blue. The use of the OPAS tables leads to a slightly lower opacity in the convective envelope, inducing a less steep temperature gradient right below the envelope. Consequently, it is no surprise that the agreement is slightly worse for these models than for models built only with the OPLIB opacities. The main issue with the OPAS opacity tables is their limited range in temperature and density. This induces uncertainties and makes them not very well suited for full inversions of the solar structure. However, the behaviour of the plateau against the opacity changes proves again the sensitivity of this seismic diagnostic and the trends that we expect in the case of any localised opacity increase in the solar models, as could be induced by a change in iron opacity. Unfortunately, these opacity tables have only been built for the AGSS09 mixture and could be not be tested with SSMs built using the GN93 abundance tables.

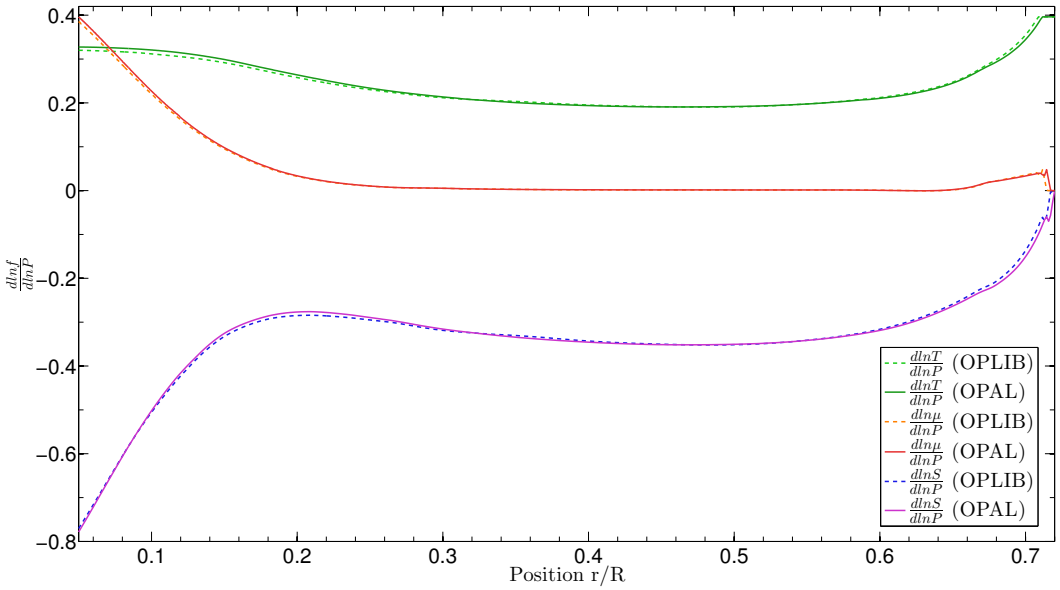

Figure 7.5: Logarithm derivatives of temperature, mean molecular weight and entropy with respect to pressure. The magenta, red and green curves are associated with a standard solar model built with the GN93 and OPAL opacities, while the blue, orange and light green dashed curves are associated with an SSM built with GN93 and the OPLIB opacities.

Additional tests of the inversion techniques

To further test the robustness of the inversions, we carried out some hare-and-hounds exercises to see whether both the SOLA and the RLS techniques could recover the entropy plateau of a given solar-like target model. We considered the same dataset as for our solar inversions, using for each mode the actual observed uncertainties on the individual frequencies of the Sun. We used one of the standard solar models from our sample built with the AGSS09 abundance tables, the OPLIB opacities and the FreeEOS equation of state as a hound and tried to reproduce the entropy profile of a target model, the hare, which was chosen as another standard solar model built with the OPLIB opacities, the OPAL equation of state and the GN93 abundances. From Fig. 7.8, we can see that both methods reproduce the trends of the entropy profile, although very deep regions are not

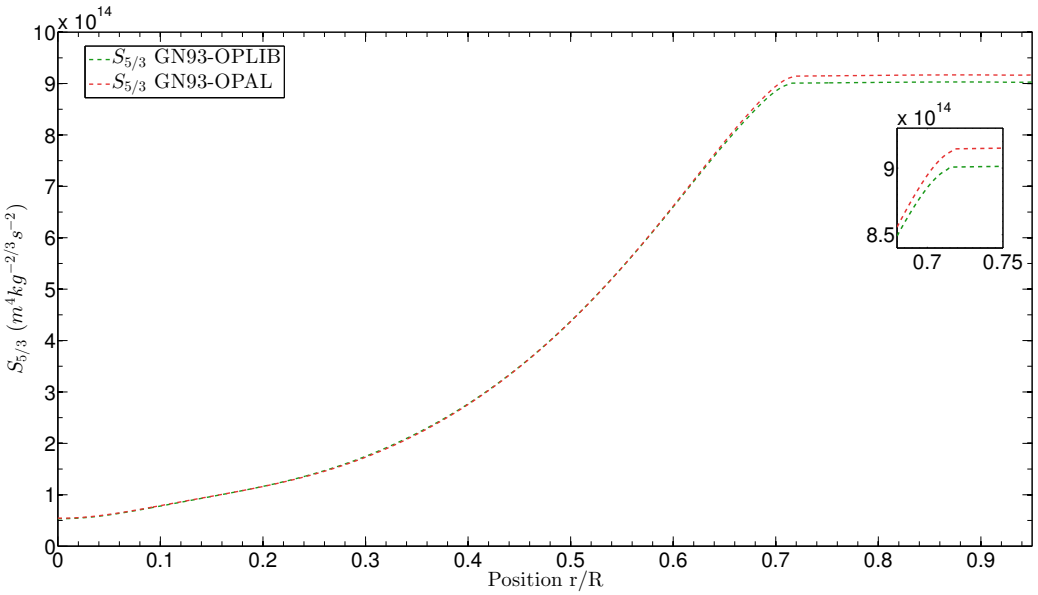

Figure 7.6: Effect of an opacity increase on the plateau of the entropy proxy. The red and green curves illustrate the entropy proxy profile for two standard solar models, both built with the GN93 abundance tables, the FreeEOS equation of state and either the OPAL or the OPLIB opacities.

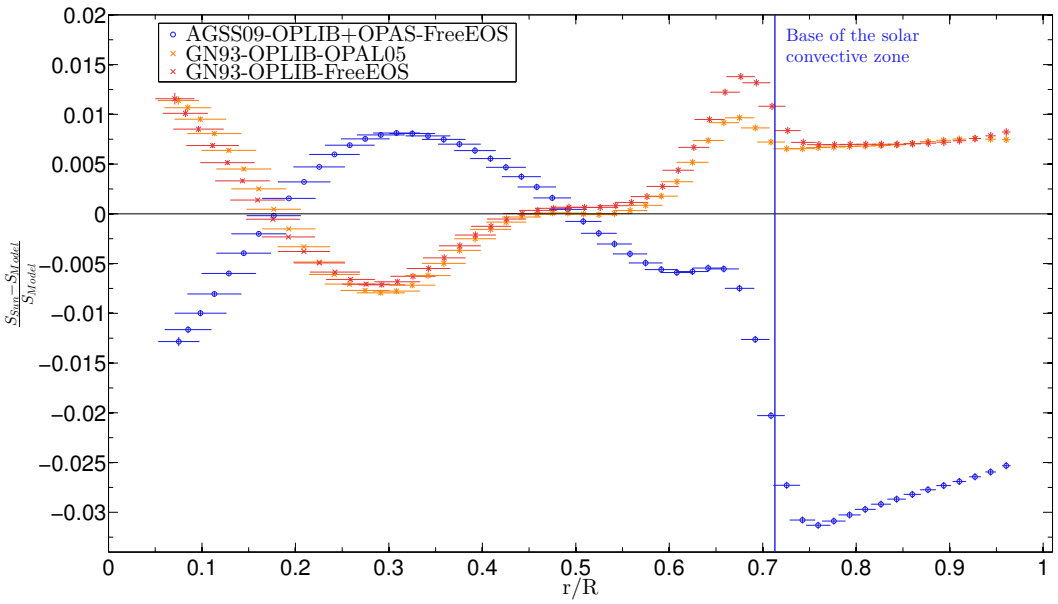

Figure 7.7: Inversion results for the OPAL equation of state and the OPAS opacity tables using the SOLA technique. The red and orange crosses show the comparison between the Sun and GN93 SSMs built respectively with the FreeEOS and the OPAL equation of state. The blue circles show the comparison between the Sun and an SSM built using the FreeEOS equation of state, the OPAS opacities and the AGSS09 abundance tables. Each results is plotted with its uncertainties as defined in the core of this section.

always well reproduced. This uncertainty is linked to the fact we do not have oscillation modes whose nature allows us to have a good resolution below 0.1 solar radii. It is also

present for other structural inversions, such as sound speed inversions for example. We can however see that the SOLA method reproduces very well the entropy plateau. This constitutes a proof of concept of the method in terms of reliability and accuracy.

Further checks of the quality of the averaging kernels for the SOLA method were performed, to ensure the accuracy of the results. We also compared the results of SOLA inversions with RLS inversions. These results are compared in Fig. 7.9, where we present in the left panel inversion results for the RLS and SOLA techniques for an SSM with the AGSS09 abundances, OPLIB opacities and the FreeEOS equation of state. We can see that the entropy plateau is nearly at the same position for both methods and that very similar trends are observed. In the right panel, we illustrate the averaging kernels of the SOLA method for various positions inside the Sun. One can clearly see that the target function in green is well reproduced at every depth, although some inaccuracies are present below 0.1 solar radii. This is expected since we lack very low degree and radial order modes able to probe efficiently the deepest layer of the solar structure.

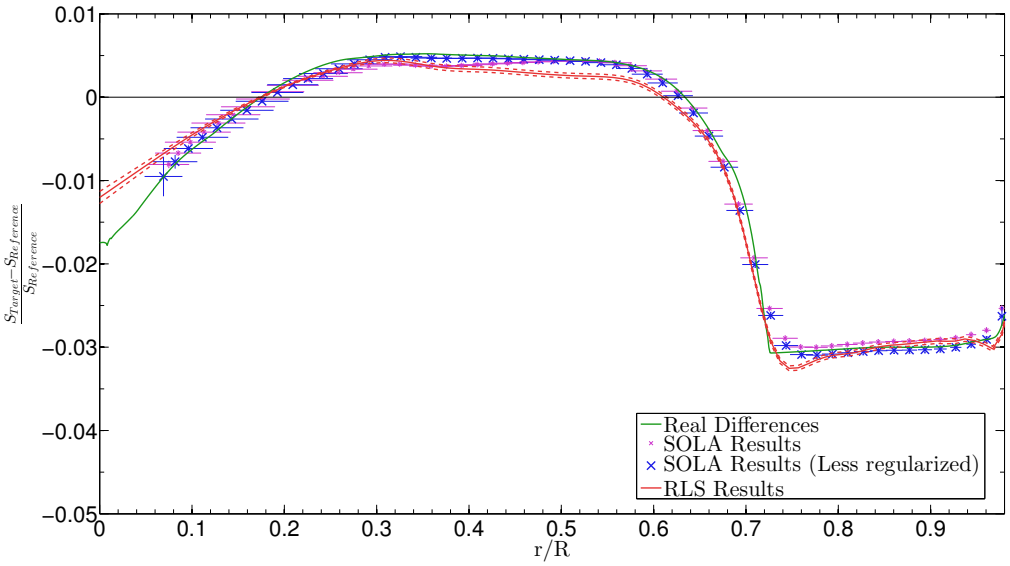

Figure 7.8: Results from the hare-and-hounds exercise between SSMs for the entropy proxy inversion. The green curve illustrates the real differences between two SSMs for the entropy proxy while the blue and magenta crosses show various SOLA results with changes in the free parameters used for regularization. The red curve shows the same profile as obtained from the RLS inversion technique. The red dashed lines show the 1σ error bars on this inversion.

7.3 Determining the metallicity of the solar envelope using seismic inversion techniques

7.3.1 Introduction

Helioseismology, the study of solar pulsations, has led to a number of successes. Amongst these achievements, one finds the determination of the position of the base of the solar convective envelope (Basu and Antia (1997a) and Kosovichev and Fedorova (1991)), the determination of the helium abundance in this region (Basu and Antia (1995)) as well as the demonstration of the necessity of microscopic diffusion to accurately reproduce the

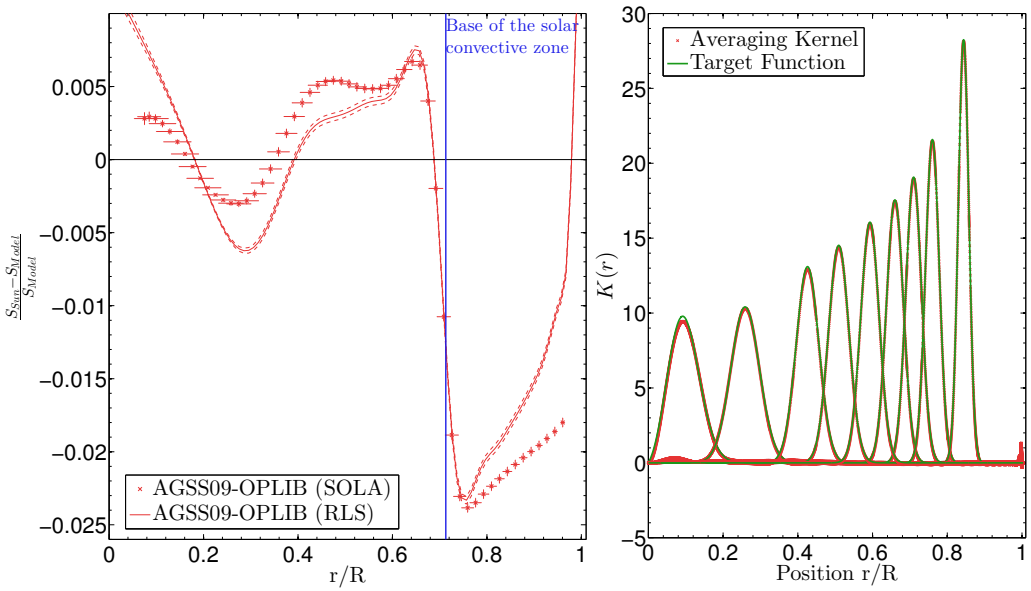

Figure 7.9: (Left panel) Comparison between SOLA and RLS inversions for the entropy proxy profile inversion of the Sun. The red crosses illustrate the SOLA results with their uncertainties while the red line shows the RLS inversion results with the 1σ envelope given by the dashed red lines. (Right panel) Illustration of SOLA averaging kernels and comparison with their target functions at various depth. The green curves show the Gaussian target functions of the SOLA inversion for various depths inside the Sun while the red dashed curves show the averaging kernels.

acoustic structure of the Sun (Basu, Christensen-Dalsgaard, Schou, et al. (1996)). Another important result of helioseismology was the determination of the solar rotation profile (T. M. Brown, Christensen-Dalsgaard, Dziembowski, et al. (1989), Kosovichev, Schou, et al. (1997), and Schou, Antia, et al. (1998)). However, the agreement that existed between solar models and structural inversions has been reduced since the publication of updated abundance tables by Asplund, Grevesse, and Sauval (2005) which showed a significant decrease of the metallicity with respect to the value commonly used in the standard solar models in the 90s (Grevesse and Noels (1993) and Grevesse and Sauval (1998) hereafter GN93 and GS98, respectively) These tables were further improved in Asplund, Grevesse, Sauval, and Scott (2009) and have been at the center of what is now called the "solar metallicity problem". Recently, Caffau et al. (2011) published new abundance tables for which the metallicity was again re-increased. Attempts were also made to carry out seismic determinations of the solar metallicity, the first of which being that of Takata and Shibahashi (2001) that hinted at a possible metallicity decrease 3 years before the release of the new spectroscopic abundances, but could not conclude to the uncertainties in their inversion results. Antia and Basu (2006) determined its value as 0.0172 ± 0.002 using an analysis of the dimensionless sound-speed gradient, denoted $W(r)$. In contrast, S. V. Vorontsov et al. (2014) determined that it should lie within 0.008 and 0.013 using a detailed analysis of the adiabatic exponent of solar envelope models for various equations of state.

In this study, we present a new method to derive an estimate of the metallicity in the solar envelope using the SOLA inversion technique (Pijpers and Thompson (1994)) and the classical linear integral relations between frequency differences and structural corrections

developped for metallicity kernels. In Sect. 7.3.2, we present the structural kernels used and the target function of our metallicity estimate. We also present the possible causes of uncertainties in this method. In Sect. 7.3.3, we test our methodology in hare-and-hounds exercises and quantify the various contributions to the inversion errors. In Sect. 7.3.4, we compute inversions of the solar metallicity for various trade-off parameters and reference models using different equations of state, we then discuss the reliability of our results and how further tests could complement and improve our study.

7.3.2 Methodology

To carry out our structural inversions, we use the linear integral relations obtained from the variational developments of the pulsation equations. The classical formulation of these relations is

$$\frac{\delta\nu^{n,\ell}}{\nu^{n,\ell}} = \int_0^1 K^{n,\ell}_{\rho,c^2}\frac{\delta\rho}{\rho}dx + \int_0^1 K^{n,\ell}_{c^2,\rho}\frac{\delta c^2}{c^2}dx, \tag{7.3}$$

which is used to carry out inversions of the solar sound speed profile. In this expression the notation δ denotes difference according to the following convention

$$\frac{\delta x}{x} = \frac{x_{obs} - x_{ref}}{x_{ref}}, \tag{7.4}$$

where x can be an individual frequency of harmonic degree ℓ and radial order n or a structural variable such as the density, ρ, or the squared adiabatic sound speed, $c^2 = \frac{P}{\Gamma_1\rho}$, with P the pressure and $\Gamma_1 = \left(\frac{d\ln P}{d\ln\rho}\right)_S$, the adiabatic exponent, where S is the entropy. The differences between structural variables are taken at fixed fractional radius r/R with R the total radius and r the radial position. The $K^{n,\ell}$ functions are the structural kernels associated with the thermodynamical variables found in the variational expression. These functions only depend on equilibrium quantities and the eigenfunctions of the so-called reference model of the inversion.

Using appropriate techniques (see Buldgen, D. R. Reese, and M. A. Dupret (2017)), one can derive structural kernels for a large number of variables. Amongst them, one finds the kernels related to the convective parameter, A, defined as

$$A = \frac{d\ln\rho}{d\ln r} - \frac{1}{\Gamma_1}\frac{d\ln P}{d\ln r}, \tag{7.5}$$

presented in Elliott (1996) as part of the (A,Γ_1) structural pair. It was initially used to test the equation of state. In this section, we use the kernels of the (A,Y,Z) triplet presented in Buldgen, D. R. Reese, and M. A. Dupret (2017), where Y is the helium mass fraction and Z the metallicity. We illustrate these kernels in figure 7.10. The first interesting point to notice is that the kernels associated with A have a very small amplitude compared to those of Y and Z. In addition, A has the convenient property of being 0 in the adiabatic region of the convective envelope. Similarly to Elliott (1996) who considered the (A,Γ_1) kernels for carrying inversions of the Γ_1 profile in the Sun, the kernels we suggest in the present study can be used to efficiently carry out seismic inversions of both Y and Z in convective regions. The variational relation we use to carry out our inversion hence reads as

$$\frac{\delta\nu^{n,\ell}}{\nu^{n,\ell}} = \int_0^1 K^{n,\ell}_{A,Y,Z}\delta A dx + \int_0^1 K^{n,\ell}_{Y,A,Z}\delta Y dx + \int_0^1 K^{n,\ell}_{Z,Y,A}\delta Z dx, \tag{7.6}$$

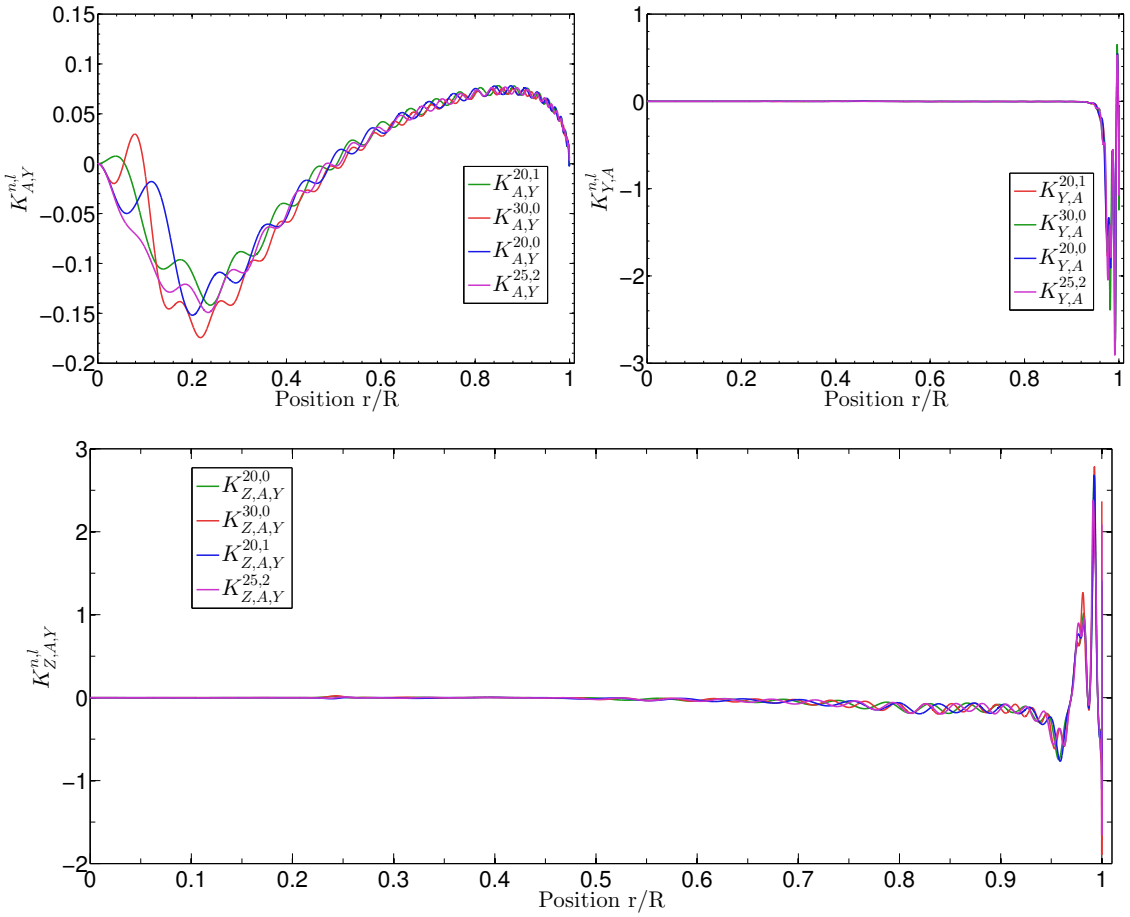

Figure 7.10: Kernels of the (A,Y,Z) triplet for various oscillation modes (Upper left panel, A Kernels) (Upper right panel, Y kernels) (Lower panel, Z kernels)

with x the fractional radius.

Although this study focusses on determinations of Z, we also carried out inversions of the helium abundance and found them to be in agreement with the classical helioseismic result of 0.2485 ± 0.0035, yet, less precise. As a comparison, S. V. Vorontsov et al. (2014) found that the helium mass fraction in the solar envelope was betweeen 0.24 and 0.255, which is also in agreement with the interval of [0.242 0.255] we find. The main uncertainty in our determination is related to the physical ingredients in the models, leading to differences in Γ_1. Indeed, one uses the relation

$$\frac{\delta\Gamma_1}{\Gamma_1} = \left(\frac{\partial \ln\Gamma_1}{\partial \ln P}\right)_{\rho,Y,Z} \frac{\delta P}{P} + \left(\frac{\partial \ln\Gamma_1}{\partial \ln \rho}\right)_{P,Y,Z} \frac{\delta \rho}{\rho} + \left(\frac{\partial \ln\Gamma_1}{\partial Y}\right)_{P,\rho,Z} \delta Y + \left(\frac{\partial \ln\Gamma_1}{\partial Z}\right)_{P,\rho,Y} \delta Z, \tag{7.7}$$

to obtain perturbations of Y and Z in the variational expression. The main weakness in this approach is that the state derivatives of Γ_1 can vary not only with the equation of state but also with the calibration. Indeed, the calibration process will lead to slight differences in the acoustic structure when various physical ingredients (such as the opacity tables or the heavy elements abundance) are used. To assess this dependency, we use various physical ingredients in our hare-and-hounds exercises and our solar reference models used to determine the solar metallicity. A first illustration can be made, by comparing these derivatives for both the CEFF (Christensen-Dalsgaard and Daeppen (1992)) and FreeEOS[1](Irwin (2012)) equations of state in a standard solar model. Both derivatives with respect to Y and Z are plotted in figure 7.11 and illustrate that the general behaviour of both curves is extremely similar. However, differences of nearly 0.001 can be seen in some regions and this of course means that, at the level of precision demanded, the choice of the equation of state will have an impact on the result. This is illustrated by the subplot of Fig. 7.11, where we take a closer look at the differences between the state derivatives with respect to Z.

We define the target function of our indicator as follows,

$$\delta\mathscr{Z} = \frac{\int_0^1 (1-x)^2 \exp^{-800(x-0.79)^2} \delta Z dx}{\int_0^1 (1-x)^2 \exp^{-800(x-0.79)^2} dx} = \int_0^1 \mathscr{T}_{\mathscr{Z}} \delta Z dx, \tag{7.8}$$

which of course implies $\delta\mathscr{Z} = \delta Z$ in the envelope up to an excellent accuracy, firstly because the chemical abundances are constant in the fully mixed convective zone of the Sun and secondly, the weight function of the indicator is virtually 0 outside of a small interval (in normalised radius) within the envelope. The location of the Gaussian has been chosen such that it is not close to the helium ionization zone, which would imply a very strong correlation with the helium cross-term. The Gaussian width is also small enough so that there is no intensity in the radiative zone, which is not fully mixed.

Looking at Figs. 7.10 and 7.11, one can also see that this region is characterised by a rather large intensity in the Γ_1 derivatives with respect to Z, hence its associated kernels still having a non-negligible intensity around 0.8 while the helium kernels are nearly 0 at those depths.

[1]http://freeeos.sourceforge.net/

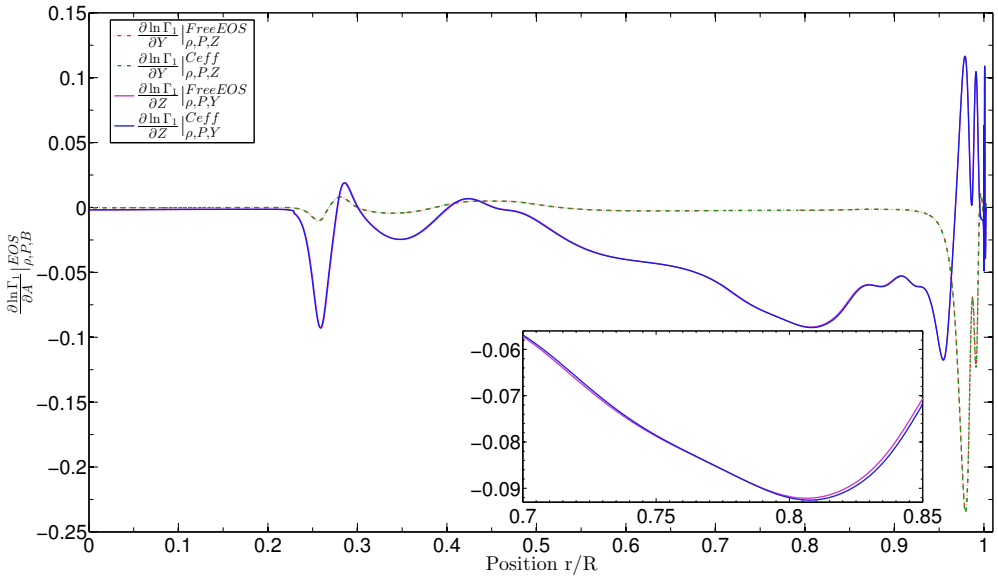

Figure 7.11: (Green and red curves) State derivatives of the natural logarithm of Γ_1 with respect to Y for the FreeEOS and CEFF equations of state. (Magenta and blue curves) State derivatives of the natural logarithm of Γ_1 with respect to Z for the FreeEOS and CEFF equations of state.

For this indicator, the cost function of the SOLA inversion is written as,

$$\mathscr{J}_{\mathscr{Z}} = \int_0^1 \left[K_{\mathrm{Avg}} - \mathscr{T}_{\mathscr{Z}}\right]^2 dx + \beta \int_0^1 K^2_{\mathrm{Cross},Y} dx + \beta_2 \int_0^1 K^2_{\mathrm{Cross},A} dx + \tan(\theta) \sum_i^N (c_i \sigma_i)^2 + \lambda \left[1 - \int_0^1 K_{\mathrm{Avg}} dx\right], \tag{7.9}$$

where K_{Avg}, $K_{\mathrm{Cross},A}$ and $K_{\mathrm{Cross},Y}$ are the so-called averaging and cross-term kernels (Pijpers and Thompson (1994)). The averaging kernel is responsible for the matching of the target function of the inversion (thus the accuracy of the method). Meanwhile, the cross-term kernels are contributions for the additional variables found in Eq. 7.6 and which cannot be completely annihilated. For this particular inversion, two cross-terms have to be taken into account since we work with a triplet of variables instead of a pair. This means that the trade-off problem (Backus and Gilbert (1967)) has to be analysed in depth and particular care has to be taken to check for possible compensation of the various error contributions in certain regions of the parameter space. The trade-off problem is assessed in the classical way, using the parameter θ to avoid a large contribution from the observational errors and the parameters β and β_2 to reduce each cross-term contribution. The variable λ is no free parameter, but a Lagrange multiplier associated with the unimodularity constraint.

The trade-off problem, and thus the quality of the inversion, is analysed by looking separately at the amplitudes of the terms associated with the averaging and cross-term

kernels in Eq. 7.9. These terms are denoted

$$||K_{avg}||^2 = \int_0^1 \left[K_{\mathrm{Avg}} - \mathscr{T}_{\mathscr{Z}}\right]^2 dx, \tag{7.10}$$

$$||K_{Cross,Y}||^2 = \int_0^1 K^2_{\mathrm{Cross,Y}} dx, \tag{7.11}$$

$$||K_{Cross,A}||^2 = \int_0^1 K^2_{\mathrm{Cross,A}} dx. \tag{7.12}$$

However, these contributions do not contain all the information about the inversion technique. It is also useful to analyse separately each term of the inverted correction in hare-and-hounds exercises, to detect potential compensation effects. Therefore, we also analyse each error source of the inversion separately, using the definitions of Buldgen, D. R. Reese, and M. A. Dupret (2015), which for this specific case are

$$\varepsilon_{\mathrm{AVG}} = \int_0^1 \left[K_{\mathrm{Avg}} - \mathscr{T}_{\mathscr{Z}}\right] \delta Z dx, \tag{7.13}$$

$$\varepsilon_{\mathrm{Cross},Y} = \int_0^1 K_{\mathrm{Cross,Y}} \delta Y dx, \tag{7.14}$$

$$\varepsilon_{\mathrm{Cross},A} = \int_0^1 K_{\mathrm{Cross,A}} \delta A dx, \tag{7.15}$$

$$\varepsilon_{\mathrm{Res}} = Z_{Tar} - Z_{Ref} - \delta Z_{Inv} - \varepsilon_{\mathrm{AVG}} - \varepsilon_{\mathrm{Cross},Y} - \varepsilon_{\mathrm{Cross},A}, \tag{7.16}$$

with Z_{Tar} the metallicity of the target, which is known in a hare-and-hounds exercises, Z_{Ref} the metallicity of the hound, δZ_{Inv} the inverted correction found using the inversion. The residual error, $\varepsilon_{\mathrm{Res}}$, which is obtained once all the other errors have been subtracted from the inversion results, encompasses all aspects that are not properly treated by the inversion. These include, in the hare-and-hounds exercises, the potential inadequacy of the surface effect corrections or the non-linear aspects stemming from the non-verification of the linear equations 7.6 or the assumptions on the equation of state made through Eq. 7.7.

7.3.3 Hare-and-hounds exercises

Before carrying out the inversion on the actual solar seismic data, we carried out hare-and-hounds exercises to test the reliability of the metallicity determination. The stellar models used in the exercises were computed using the Liège stellar evolution code (CLES, Scuflaire, Théado, et al. (2008)). Their frequencies and eigenfunctions were computed using the Liège adiabatic oscillation code (LOSC, Scuflaire, Montalbán, et al. (2008)). The inversions were computed using a customised version of the InversionKit software (D. R. Reese, Marques, et al. (2012)).

Methodology and results

We used a calibrated standard solar model built with the past solar GN93 (Grevesse and Noels (1993)) abundances (high metallicity, Z) and the latest version of the OPAL equation of state (Rogers and Nayfonov (2002)) as our hare. Furthermore, we used the latest OPLIB opacities (Colgan et al. (2016)) supplemented at low temperature by the opacities of Ferguson et al. (2005) and the effects of conductivity from Potekhin et al. (1999) and Cassisi et al. (2007). The nuclear reaction rates implemented were those from the NACRE project (Angulo et al. (1999)), supplemented by the updated reaction rate from Formicola et al. (2004) and we used the classical, local mixing-length theory (Böhm-Vitense (1958)) to describe convective motions. The hounds were fitted to the hare to ensure that they had

exactly the same radii and similar luminosities. They were computed with the AGSS09 abundances and either the CEFF or the FreeEOS equation of state. There are two reasons justifying the fact that we did not use the OPAL equation of state in our reference models. Firstly, this allows us to test for the biases stemming from the equation of state in our inversions. Secondly, the OPAL equation of state, being defined on a grid with finite resolution, is not well suited to compute the Γ_1 derivatives numerically with high accuracy. The CEFF and FreeEOS equations of state, being defined with analytical relations, do not suffer from this problem and were thus favoured.

We summarise the properties of the hare and the hounds in table 7.2. As can be seen, some of these reference models differ significantly from the target. These differences result from the way the hounds were generated, which was not a classical solar calibration as is usually done for the Sun. All hounds reproduce accurately the radius of target 1, a given value of helium abundance in the convective envelope and the position of its base within a less constraining accuracy. We did not limit the values of helium abundance and position of the base of the convective envelope to those of target 1 to assess the effects of those constraints on the cross-term contributions. To further assess the uncertainties, additional changes were induced in Ref 1, 2 and 3 by not including microscopic diffusion of the heavy elements. The changes in the position of the base of the convective envelope for the various hounds were induced by changing the value of an undershoot parameter within values up to 0.2 of the local pressure scale height before recalibrating the hounds. As can be seen from the luminosity and age values in table 7.2, this calibration method can lead to quite large differences between the models, hence sometimes implying larger differences in acoustic structure between the hare and the hounds than in a classical solar calibration approach.

We used the radius, the helium abundance in the convective envelope and the position of its base as constraints for the fit of the hounds to the hare. Once a satisfying fit was obtained, we changed an undershoot parameter and the diffusion velocities, while still fitting the radius, to be able to analyze the behaviour of the inversion when facing changes in A and Y. Consequently, some non-linearities could be observed for a few of these perturbed models and could help us understand the cases were the inversion was not so stable. To be as close to reality as possible, we used the exact same set of low ℓ oscillation modes observed for the Sun as presented in Basu, Chaplin, et al. (2009), namely 2189 oscillation modes with ℓ from 0 up to 250, and used the same uncertainties on the frequencies as those of the actual solar modes. We tested a total of 17 hounds and analysed whether the inversion was efficient in determining the metallicity of the hare. Due to the large differences between the hitherto seismically determined values of the solar metallicity, we wanted to assess whether our method would be able to distinguish between several solutions.

The results of these inversions are given in table 7.3 and illustrated in Fig. 7.12. For all the cases illustrated here, the inversion could determine an estimate of the metallicity in the convective envelope. However, one can see that for reference models (hounds) 2, 10, 11 and 13, these estimates are not so accurate. Globally, a spread of around 4×10^{-3} is found for the inversion results. This spread is due to multiple sources: e.g., for models 10, 11 and 13, the equation of state was the CEFF equation of state, which leads to much larger differences in Γ_1 with the OPAL equation of state than does the FreeEOS equation of state. Besides the differences from the equation of state, intrinsic differences in Γ_1 due to differences in stratification of the model, can have a strong impact on the accuracy of the method. It is important to bear in mind that the variables Y and Z are not directly seismically constrained but are obtained via an equation of state which is furthermore

Table 7.2: Characteristics of the models used in the hare-and-hounds exercises

	Mass ($M_\odot$)	Age (Gy)	Radius ($R_\odot$)	L ($L_\odot$)	Y_{CZ}	Z_{CZ}	$\left(\frac{r}{R}\right)_{CZ}$	EOS
Target 1	1.0	4.5794	1.0	0.9997	0.2397	0.01818	0.07087	OPAL
Ref 1	1.0	4.8073	1.0	0.9564	0.2307	0.01513	0.07087	FreeEOS
Ref 2	1.0	4.8038	1.0	0.9558	0.2294	0.01513	0.7125	FreeEOS
Ref 3	1.0	4.5097	1.0	0.9740	0.2342	0.01513	0.716	FreeEOS
Ref 4	1.0	4.2502	1.0	0.9933	0.2421	0.01513	0.7068	FreeEOS
Ref 5	1.0	4.4130	1.0	1.0107	0.2455	0.01373	0.7161	FreeEOS
Ref 6	1.0	5.0004	1.0	0.9749	0.2301	0.01375	0.7087	FreeEOS
Ref 7	1.0	4.8743	1.0	0.9817	0.2300	0.01373	0.7171	FreeEOS
Ref 8	1.0	4.4081	1.0	1.0100	0.2419	0.01381	0.7066	FreeEOS
Ref 9	1.0	4.5285	1.0	1.0035	0.2381	0.01369	0.7160	FreeEOS
Ref 10	1.0	5.3522	1.0	0.9695	0.2285	0.01358	0.7090	CEFF
Ref 11	1.0	5.2909	1.0	0.9731	0.2282	0.01349	0.7150	CEFF
Ref 12	1.0	5.2253	1.0	0.9761	0.2283	0.01345	0.7170	CEFF
Ref 13	1.0	4.7455	1.0	1.0046	0.2402	0.01373	0.7055	CEFF
Ref 14	1.0	4.8635	1.0	0.9982	0.2364	0.01361	0.7160	FreeEOS
Ref 15	1.0	4.7433	1.0	1.0054	0.2283	0.01355	0.7236	FreeEOS
Ref 16	1.0	4.5651	1.0	1.0155	0.2435	0.01376	0.7075	FreeEOS
Ref 17	1.0	4.5790	1.0	0.9993	0.2435	0.01344	0.7120	FreeEOS
Target 2	1.0	4.5787	1.0	1.0002	0.2386	0.01820	0.7080	FreeEOS

linearised using to Eq. 7.7. Consequently, errors in the derivatives of Γ_1 can quickly arise and reduce the accuracy of the results. Moreover, hounds having a poor representation of the stratification of the hare model will also have rather large A differences and thus intrinsically larger cross-term contributions. In Sect. 7.3.3, we further investigates this point and discuss the determination of the trade-off parameters and what they can teach us about the characteristics of our approach.

Analysis of the stability of the inversion technique

Quality of the kernel fits

We have seen in Sect. 7.3.3 that an indication of the metallicity of the Sun can be provided by seismology. However, inversion techniques can sometimes provide accurate results because of compensation of their errors. Therefore, their reliability and stability should be properly assessed.

We propose to first assess the quality of the kernel fits by looking at the amplitude of the first three terms of Eq. 7.9, in the last columns of table 7.3. To give a better idea of what these represent, we illustrate in Fig. 7.13 the fit of the averaging kernel and the cross-term kernels for the inversion of Ref 3. From a first visual inspection, the fit of the averaging kernel seems good and the contribution from the cross-term associated with A seems close to 0. By inspecting the helium cross-term kernel, we can see a strong correlation with the averaging kernel. However, the height of this peak is around 45 times smaller than the height of the averaging kernel. This means that the helium contribution should be kept small, as can be seen in Fig. 7.14. This difference in amplitude is a consequence of the choice of the position for the peak in the target function. Had we chosen a target much closer to the helium ionization zones, then the correlation with the helium kernels would have been much more problematic.

To analyse whether compensation is present in the inversion, we plot in figure 7.14 the real error contributions for all hounds. The kernel fits are informative of the quality of the inversion. However plotting the real error contributions can indicate whether what

Table 7.3: Inversion results for the hare-and-hounds exercises.

	Z_{Ref}	Z_{Inv}	$\|\|K_{Avg} - \mathcal{T}_{\mathscr{Z}}\|\|^2$	$\|\|K_{Cross,Y}\|\|^2$	$\|\|K_{Cross,A}\|\|^2$
Ref 1	0.01513	$0.01914 \pm 4.35 \times 10^{-4}$	0.0211	0.07683	5.000×10^{-3}
Ref 2	0.01513	$0.01996 \pm 4.26 \times 10^{-4}$	0.02198	0.07680	4.53×10^{-3}
Ref 3	0.01513	$0.01841 \pm 4.25 \times 10^{-4}$	0.02169	0.07602	4.549×10^{-3}
Ref 4	0.01513	$0.01936 \pm 2.15 \times 10^{-5}$	0.02230	0.07538	1.816
Ref 5	0.01373	$0.01803 \pm 5.09 \times 10^{-5}$	0.1245	0.07144	1.409
Ref 6	0.01366	$0.01894 \pm 4.15 \times 10^{-4}$	0.0254	0.07376	0.02959
Ref 7	0.01355	$0.01825 \times 4.15 \times 10^{-4}$	0.02036	0.07321	1.967×10^{-2}
Ref 8	0.01382	$0.01864 \pm 2.14 \times 10^{-5}$	0.02026	0.07253	1.820
Ref 9	0.01370	$0.01789 \pm 5.09 \times 10^{-5}$	0.1245	0.07145	1.410
Ref 10	0.01358	$0.02154 \pm 3.87 \times 10^{-4}$	0.1230	0.07182	0.03715
Ref 11	0.01350	$0.02161 \pm 3.71 \times 10^{-4}$	0.05124	0.07404	0.04631
Ref 12	0.01373	$0.01918 \pm 4.57 \times 10^{-4}$	0.01603	0.07280	3.552×10^{-4}
Ref 13	0.01346	$0.02151 \pm 4.49 \times 10^{-4}$	0.01666	0.07348	1.516×10^{-3}
Ref 14	0.01361	$0.01859 \pm 3.76 \times 10^{-4}$	0.05211	0.07313	0.02439
Ref 15	0.01356	$0.01818 \pm 4.23 \times 10^{-4}$	0.02022	0.07238	4.572×10^{-3}
Ref 16	0.01344	$0.01744 \pm 4.48 \times 10^{-4}$	0.01642	0.07257	1.509×10^{-3}
Ref 17	0.01377	$0.01768 \pm 4.24 \times 10^{-4}$	0.0228	0.07246	4.578×10^{-3}

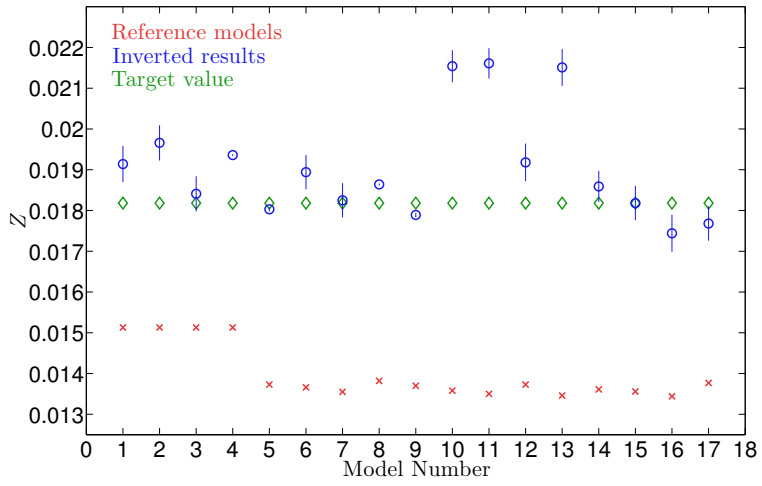

Figure 7.12: Inversion results for the hare-and-hounds exercises between the 17 reference models and the target model of table 7.2.

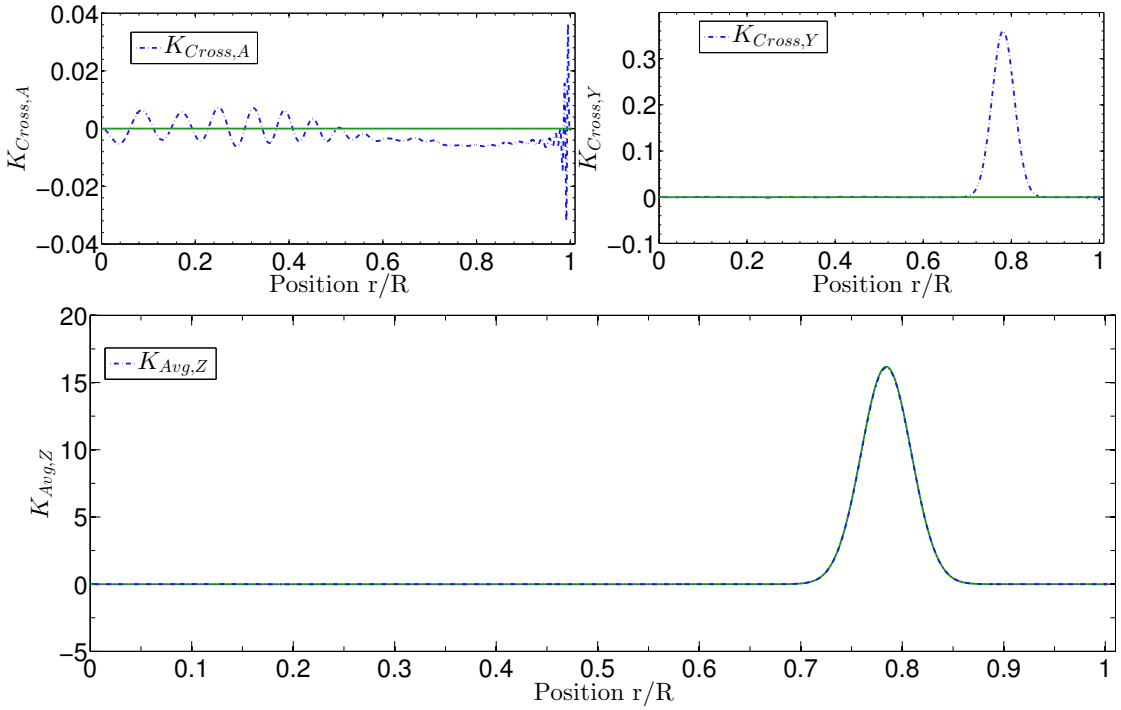

Figure 7.13: (Upper-left panel) Cross-term associated with A in blue and the target function (being 0 here) in green. (Upper-right panel) Cross-term associated with Y in blue and the target function (being 0) in green. (Lower panel) Averaging kernel of the inversion in blue and the respective target function in green.

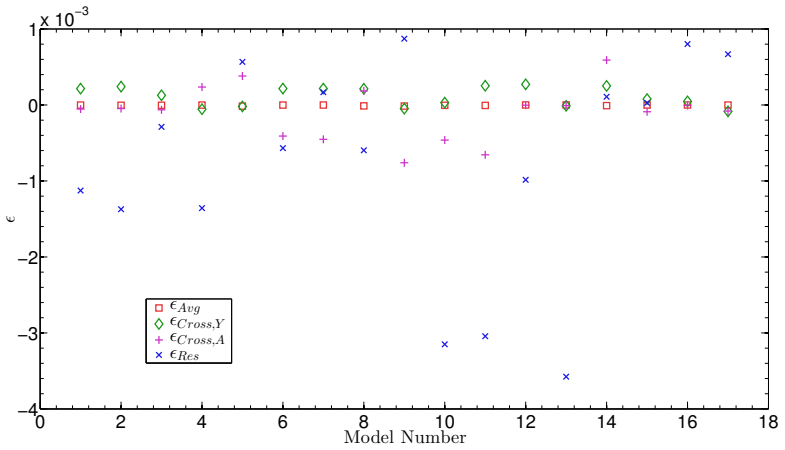

Figure 7.14: Error contributions, denoted ε_{Avg},ε_{CrossY},$\varepsilon_{Cross,A}$,ε_{Res} for the hare-and-hounds exercises.

appears visually as a satisfactory fit is actually the reason for the accuracy of the result.

Analysis of the parameter space

The main difficulty of carrying out the inversion is to find a given set of parameters for which the real errors of the inversion, here defined as the ε_i in Eqs. 7.13 to 7.16, are small and do not present compensation effects, and where the squared norm of the differences between the averaging and cross-term kernels, defined in Eqs. 7.10 to 7.11, and their respective targets have reduced amplitudes. Depending on the quality of the reference model or the dataset, the trade-off problem will be different and multiple sets of parameters can be found. Therefore, to further understand the reliability of the inversion and its parameter dependency, we did for Ref 3 a brief scan of the parameter space, which is illustrated in Fig. 7.15. Firstly, we note from the lowest left panel in Fig. 7.15, illustrating the differences between the inverted Z value and the target value of Z, that the changes in the parameter do not induce a large deviation of the inversion results from the value found with the optimal set of parameters. However, other inversions in our hare-and-hounds exercises were not as stable, mainly due to an increase of the residual error or to the cross-term contribution associated with the convective parameter. For this scan, we fixed a value of β_2 to 1.0 and varied θ from 10^{-4} to 10^{-9} and β from 10^{-2} to $10^{1.5}$ (see eq. 7.9). A first observation that can be made is that the variations of all quantities are regular with the parameters. Sudden and steep variations in the accuracy of the solution and the real error contributions would indicate that the inversion is not sufficiently regularised. In such cases, one has no real control on the trade-off problem and thus no means of ensuring a correct result.

In Fig. 7.15, we can see that for a fixed value of β_2 the optimum is found for a low θ and a low β. However, the low β value has to be considered carefully when the helium abundance differences are larger. For this particular test between Ref 3 and Target 1, the differences is of the order of 0.005, thus intrinsically quite small, which naturally reduces the value of $\varepsilon_{Cross,Y}$. In addition to the helium cross-term contribution, the amplitude of the error bars could be strongly increased by the reduction of the θ parameter. In this particular case, the lower plot of Fig. 7.15 shows that the error bars remained quite small for the whole scan but this will not necessarily be the case for other inversions.

Overall, we can see from the lower plot of Fig. 7.15 that the inversion is very stable, since the errors remain of the order of 10^{-4}, with the exception of the residual error that can reach is this case the order of 10^{-3} for a particular region of the parameter set. This region is related to high values of β and β_2 (which is fixed) and a range of low θ values of around 10^{-8} and 10^{-9}. This is a consequence of the regularising nature of the θ parameter, which is used to adjust the trade-off between precision and accuracy of the method. In this particular case, the instability of the inversion is a consequence of the very low weight given to the damping of the error bars, and thus the precision of the method. A similar behaviour can also be observed in solar inversions of full structural profiles, were the observational error bars remain small, but the profile already shows an unphysical oscillatory behaviour.

β and β_2 Parameter

Our hare-and-hound exercises allowed us to define various parameter values for which the inversion was stable, depending on the reference model quality. In most cases, the value of β, the free parameter associated with the helium contribution, was set between approximately 0.1 and 10, as can be seen in table 7.4, depending on the intrinsic difference in helium content between the target and the reference model. Indeed, if the helium abundance value is naturally close to that of the target, it is unnecessary to strongly damp the helium cross-term and penalise the elimination of the convective parameter cross-term. Actually, it should be noted that β and β_2 are correlated. As damping the helium cross-term is done by reducing the amplitude of the inversion coefficients, it can sometimes have a similar effect on the convective parameter cross-term.

The value of β_2, associated with the cross-term contribution of A, was set to 0.1 most of the time, although some inversions required a value as high as 1 to efficiently damp the cross term contributions and others only required a value as low as 0.01. The values of β_2 for each individual inversion illustrated in Fig. 7.12 are also illustrated in table 7.4. An important remark has to be made about the cross-term associated with A. Due to the fact that A is exactly 0 in the convective envelope, damping the cross-term in A using β_2 can have unwanted consequences, as damping the total integral does not necessarily mean that the real contribution to the error, stemming from the radiative zone, will be always damped. For example, the inversions associated with a low β_2 parameter show a high peak in the convective envelope that contributes to the norm $||K_{Cross,A}||^2$, but does not contribute to the real error, $\varepsilon_{Cross,A}$. Increasing β_2 reduces the peak in the convective zones but increases the amplitude of the cross-term kernel in the radiative zone which leads to an increase of the total error This effect is illustrated in Fig. 7.16. However, systematically keeping very low values of β_2 can also imply large contributions from the cross-term associated with A, and thus an inaccurate inversion. It is clear that some compensation in the integral definition of $\varepsilon_{Cross,A}$ is responsible for the very low error contribution for the models having larger $||K_{Cross,A}||^2$, namely Refs 4, 5, 8 and 9.

θ Parameter

From table 7.4, we can see that optimal value of the θ parameter was found to vary around 10^{-6} for most inversions. Four cases showed higher optimal values of θ, going up to 10^{-3}, marking a clear separation with most of the parameter sets which are very similar. All these models showed slightly unstable behaviours and a higher θ value seems logical since it is a regularization parameter. One can also point out that Refs 4 and

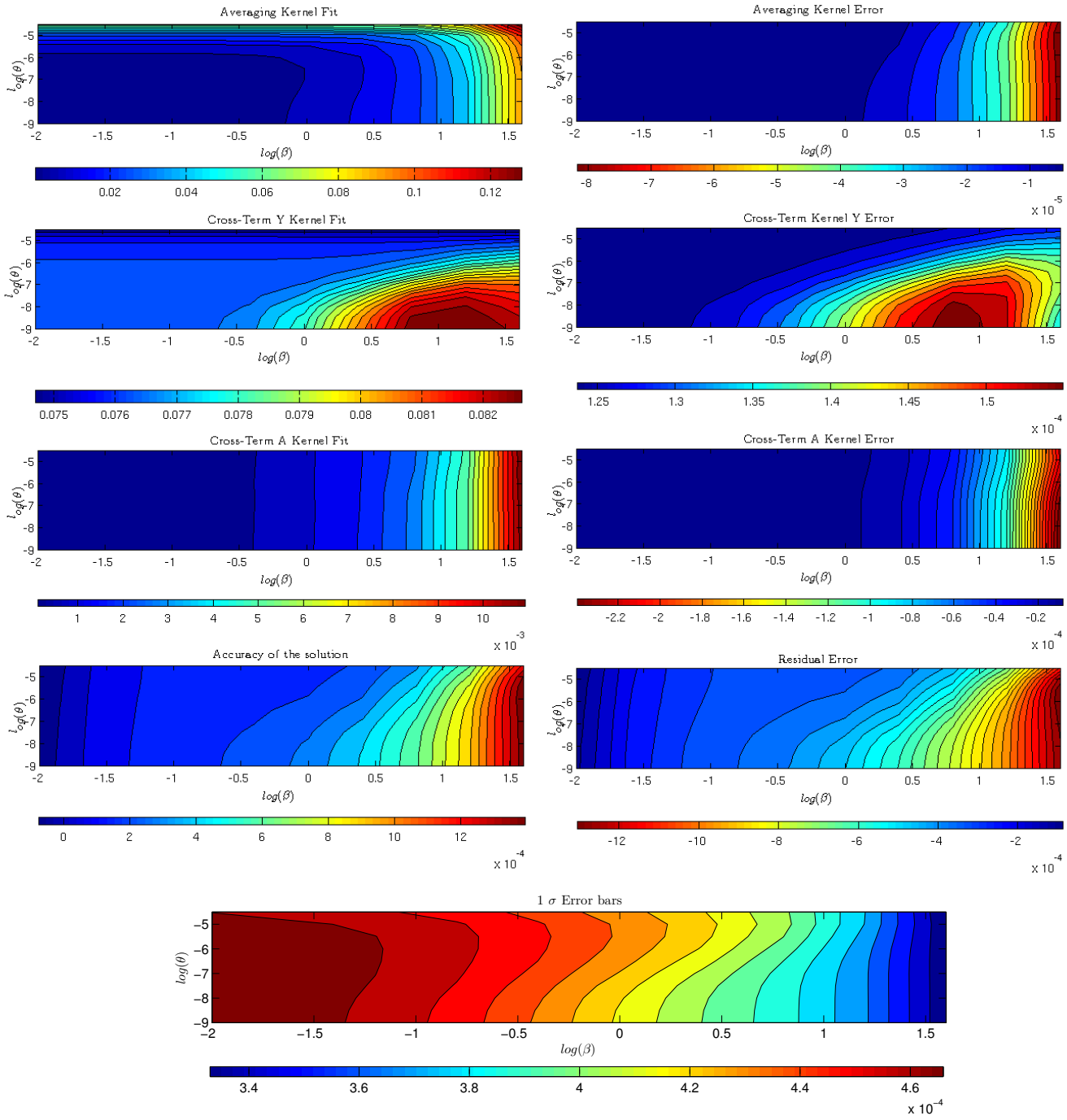

Figure 7.15: Variations of various quality checks during scan of the $\beta - \theta$ plane for a fixed β_2 value of 1. (Upper line left) $||K_{Avg} - \mathscr{T}_{\mathscr{Z}}||^2$, defined in Eq. 7.10, (Upper line right) ε_{Avg}, defined in Eq. 7.13, (Second line left) $||K_{Cross,Y}||^2$, defined in Eq. 7.11, (Second line right) ε_Y, defined in Eq. 7.14, (Third line left) $||K_{Cross,A}||^2$, defined in Eq. 7.12, (Third line right) ε_A, defined in Eq. 7.15, (Fourth line left) Accuracy of the result, defined as $Z_{Tar} - Z_{Inv}$, (Fourth line right) ε_{Res}, defined in Eq. 7.16, (Lower plot) 1 σ error bars of the inversion results, illustrated here for Ref 3 (The blue regions are associated with smaller errors.).

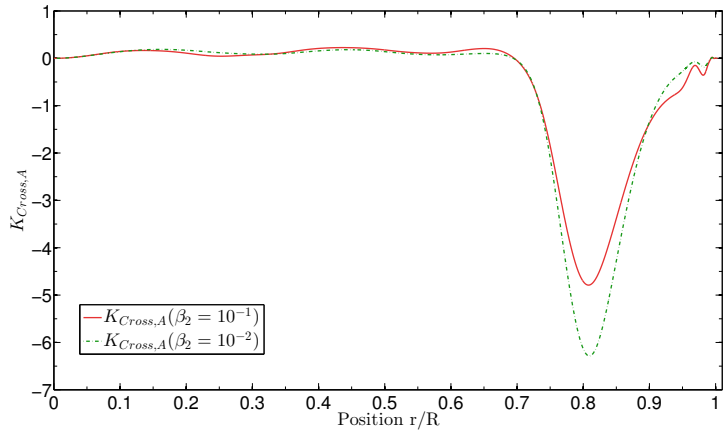

Figure 7.16: Cross-terms from inversions with a differente β_2 parameter. The red curve, associated with a high β_2 shows a lower amplitude than the green curve in the convective zone, but a higher amplitude in the radiative zone, where A is non zero.

Table 7.4: Trade-off parameters values for the hare-and-hounds exercises.

	θ	β	β_2
Ref 1,2,3,6,7,12,15,17	10^{-6}	10	1.0
Ref 4,8	10^{-3}	10	10^{-3}
Ref 5	10^{-3}	10^{-1}	10^{-1}
Ref 9	10^{-3}	1	0.1
Ref 10	10^{-5}	10	0.1
Ref 11	10^{-5}	70	0.1
Ref 13	10^{-8}	10	1.0
Ref 14,16	10^{-6}	1.0	0.1

8 had much larger individual frequency differences[2] with the hare. This implies that the differences in acoustic structure between these models and the hare are larger than between other references models and the hare. This is confirmed by the observation that these models showed larger discrepancies in $\left(\frac{\partial \ln \Gamma_1}{\partial Z}\right)_{P,\rho,Y}$ at the point where the target function is located. These discrepancies are the main reason for the inaccuracies of the method, since this factor directly multiplies the estimated metallicity. They can arise from differences in Γ_1 present either in the equation of state or stemming from the calibration. These differences can also be seen in sound speed and density profile comparisons. Physically, the reason why Ref 4 or Ref 8 shows larger discrepancies than Ref 1 or Ref 6 is linked to the temperature gradient in the radiative region of the models. Indeed, Ref 1 (respectively Ref 6) has the same metallicity than Ref 4 (respectively Ref 8) but has a lower helium abundance, and thus a higher hydrogen abundance meaning that overall, the opacity in the radiative region will be increased and thus lead to an acoustic structure in better agreement with that of Target 1 which has a high metallicity.

Using the same equation of state in the hare and the hounds

To quantify more reliably the effects of the equation of state, we compare metallicity

[2]Ranging from a factor 2 up to a factor 10 when compared to individual differences of models such as model 1 or 7.

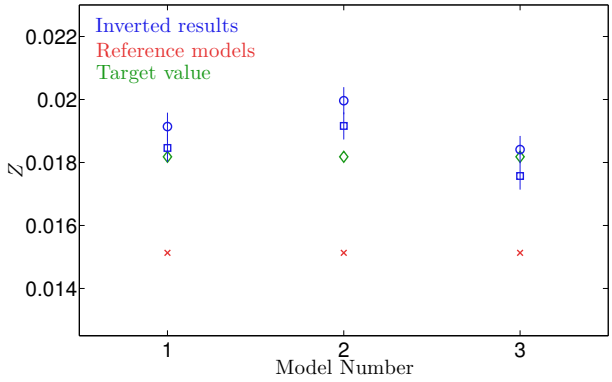

Figure 7.17: Inversion results for Ref 1, 2 and 3 of the hare and hounds exercises. The blue squares depict inversion results for the target using the FreeEOS equation of state and the blue circles depict the results for the target using the OPAL equation of state.

Table 7.5: Inversion results for the hare-and-hounds exercises for the target built with the FreeEOS equation of state.

	Z_{Ref}	Z_{Inv}	$\|\|K_{Avg} - \mathscr{T}_{\mathscr{Z}}\|\|^2$	$\|\|K_{Cross,Y}\|\|^2$	$\|\|K_{Cross,A}\|\|^2$
Ref 1	0.01513	$0.01846 \pm 4.35 \times 10^{-4}$	0.02109	0.07683	5.000×10^{-3}
Ref 2	0.01513	$0.01916 \pm 4.26 \times 10^{-4}$	0.02198	0.07680	4.543×10^{-3}
Ref 3	0.01513	$0.01757 \pm 4.25 \times 10^{-4}$	0.02169	0.07602	4.549×10^{-3}

inversions obtained from Ref 1, 2 and 3 for a calibrated standard solar model, denoted target 2, built using the same physical ingredients as the target 1 of table 7.2, with the exception of the equation of state which is the FreeEOS equation of state used in the hounds. The chemical composition of this new target is only very slightly different than the one given in table 7.2, since the changes induced by using the FreeEOS equation of state instead of the OPAL equation of state are very small. Indeed, the metallicity in the envelope of this new target is $Z_{CZ} = 0.01820$ and its helium abundance is $Y_{CZ} = 0.2386$. The inversions are carried out using the optimal set of trade-off parameters given in table 7.4. The inversion results are illustrated in Fig. 7.17, where we used circles as the notation for the inversions on the target using the OPAL equation of state and squares for the inversions on the target using the FreeEOS equation of state. Due to the closeness of the value Z_{CZ}, for both targets, we plotted only one metallicity value to ease the readibility of figure 7.17. Similarly, the error contributions are illustrated in Fig. 7.18, where we again differentiated the two targets by using different symbols. The kernels fits are also given in table 7.5.

From figure 7.17, we can see that using the same equation of state improves the inversion results for 2 of the 3 models. Analysing the results of table 7.5, we can see that the kernel fits have not changed when compared to the values found for the same models in table 7.3. However, from figure 7.18, it clearly appears that the variation of the results is due to a variation of the residual error for all models. This is expected since it is this error contribution that should be affected by the change in the equation of state. For Refs 1 and 2, ε_{Res} is clearly reduced by using the same equation of state in the target and reference model. Yet, the degradation of the results for Ref 3 illustrate that the good quality of the results obtained for the target built with the OPAL equation of state might sometimes be fortuitous.

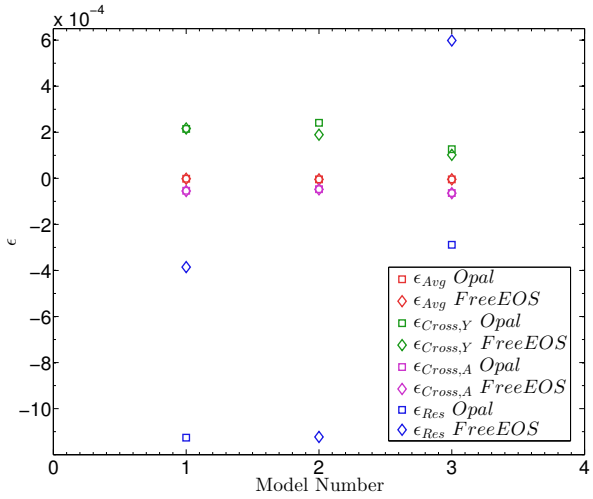

Figure 7.18: Error contributions, denoted ε_{Avg},ε_{CrossY},$\varepsilon_{Cross,A}$,ε_{Res} for the hare-and-hounds exercises for both targets using OPAL and FreeEOS equations of state.

Table 7.6: Inversion results for the supplementary hare-and-hounds exercises between reference models.

	Z_{Ref}	Z_{Inv}	Z_{Tar}	$\|\|K_{Avg} - \mathscr{T}_{\mathscr{Z}}\|\|^2$	$\|\|K_{Cross,Y}\|\|^2$	$\|\|K_{Cross,A}\|\|^2$
Ref 1 to Ref 8	0.01513	$0.01163 \pm 2.154 \times 10^{-5}$	0.01381	0.02214	0.07680	1.832
Ref 4 to Ref 13	0.01513	$0.01264 \pm 2.229 \times 10^{-5}$	0.01373	0.03248	0.07518	1.765

Changing the difference in Z between the hares and the hound

The next step in analysing the behaviour of the inversion is to see how it would behave if smaller metallicity differences were present. Indeed, in the previous test cases, we specifically built our target and reference models such that they showed clear differences in metallicity. Assessing the behaviour of the inversion if the metallicity is already close is crucial since the real solar case is slightly more complicated. Indeed, metallicity determinations have ranged from 0.0201 in Anders and Grevesse (1989) to 0.0122 in Asplund, Grevesse, and Sauval (2005), with intermediate values found in Grevesse and Noels (1993), Grevesse and Sauval (1998) or Caffau et al. (2011), and one has to be able to assess the stability of the inversion for various differences in metallicity between reference and target. This has already been done to some extent with the four first reference models, which had a higher metallicity of 0.01513 in the convective zone.

We now supplement these test cases by carrying out metallicity inversions using Ref 8 and 13 as our new targets. We chose Ref 1 and Ref 4 for respective hounds of Ref 8 and Ref 13. The results are given in table 7.6. They show that smaller changes in metallicity can be seen but the inversion starts to be less reliable. This is expected since the value of the residual error, illustrated in table 7.7, which can go as high as 3×10^{-3}. Moreover,

Table 7.7: Error contributions for the supplementary hare-and-hounds exercises between reference models.

	ε_{Avg}	$\varepsilon_{Cross,Y}$	$\varepsilon_{Cross,A}$	ε_{Res}
Ref 1 to Ref 8	-3.785×10^{-7}	2.594×10^{-4}	-6.667×10^{-4}	2.598×10^{-3}
Ref 4 to Ref 13	-4.4674×10^{-6}	-4.301×10^{-5}	-5.289×10^{-5}	1.197×10^{-3}

Table 7.8: Properties of the solar models used for the inversion.

	Model 1	Model 2	Model 3	Model 4	Model 5	Model 6	Model 7
Mass ($M_\odot$)	1.0	1.0	1.0	1.0	1.0	1.0	1.0
Age (Gy)	4.58	4.58	4.58	4.58	4.58	4.58	4.58
Radius ($R_\odot$)	1.0	1.0	1.0	1.0	1.0	1.0	1.0
L ($L_\odot$)	1.0	1.0	1.0	1.0	1.0	1.0	1.0
Y_{CZ}	0.2385	0.2475	0.2445	0.2416	0.2432	0.2292	0.2435
Z_{CZ}	0.01820	0.01803	0.01809	0.01813	0.01805	0.01370	0.01344
$\left(\frac{r}{R}\right)_{CZ}$	0.708	0.708	0.711	0.712	0.711	0.718	0.712
Opacity	OPLIB	OPLIB×1.05	OPLIB	OPAL	OPLIB	OPLIB	OPLIB
EOS	FreeEOS	FreeEOS	FreeEOS	CEFF	FreeEOS	FreeEOS	FreeEOS
Abundances	GN93	GN93	GN93	GN93	GN93	AGSS09	AGSS09

as δZ decreases, the importance of the contributions of the other integrals, associated with δY and δA is increased, and the information on the metallicity is consequently more difficult to extract. However, these exercises also show that in such cases, the parameters leading to an accurate inversion result are slightly different than what is found before. Indeed, the parameters were then $\beta = 10$, $\beta_2 = 10^{-2}$ and $\theta = 10^{-3}$, with the inversion being rather stable around those values, but sometimes showing erratic behaviour since the contribution from helium or the convective parameter are much higher compared to the contribution of the metallicity in the frequency differences. Thanks to these results, we are now able to assess the quality of the inversion of the real solar metallicity.

7.3.4 Solar inversions

Inverted results and trade-off analysis

Using the parameter sets of table 7.4 and the analysis performed in our hare-and-hounds exercises, we can now carry out inversions on the actual solar data. We used various models calibrated on the Sun as references for the inversion. We used the solar radius, luminosity and current value of $\left(\frac{Z}{X}\right)_\odot$ according to the abundance tables used for the model as constraints for the solar calibration. We started with models built using the GN93 and AGSS09 abundance tables with multiple combinations of physical ingredients, such as the CEFF or FreeEOS equations of state and the OPAL (Iglesias and Rogers (1996)) or OPLIB (Colgan et al. (2016)) opacity tables, summarised in table 7.8. It should also be noted that Model 5 was built using a uniform reduction of 25% of the efficiency of diffusion, resulting in a higher helium abundance and shallower base of the convective zone than Model 1. Similarly, Model 7 was built with an ad-hoc temperature-dependent modification of the diffusion coefficients of the heavy elements that led to significant changes in helium abundance in the convection zone. In addition to this modification, an undershoot of 0.15 of the local pressure scale height was added to improve the agreement with the helioseismic determination of the base of the convection zone.

The inversions were carried out for the various combinations of parameters found in the hare-and-hounds exercises and illustrated in table 7.4. We illustrate in Fig 7.19 the fits of the averaging and cross-term kernels of the inversion, showing that the quality of the inversion in the solar case is comparable to that of the hare-and-hounds exercises. The inversion results are illustrated in Fig 7.20 for various reference models identified by their number in abscissa, and where each symbol corresponds to one set of trade-off parameters. Namely, the triangles correspond to the sets associated with higher values of θ and lower values of β_2, whereas the other symbols are associated with values of θ between 10^{-5} and 10^{-8}.

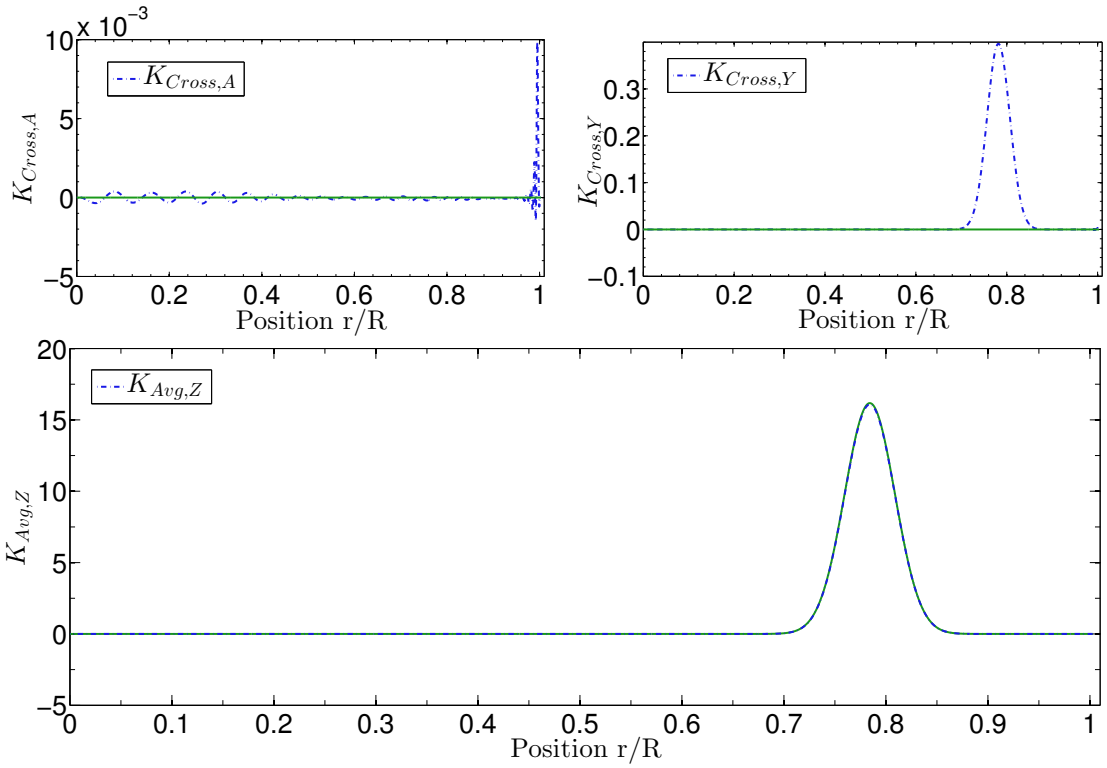

Figure 7.19: Same as Fig. 7.13 for a solar inversion.

The first result is that a very large majority of inversions favour a low metallicity, as presented in S. V. Vorontsov et al. (2014). Only one small region of the parameter space, for the inversion of Model 4, built with the CEFF equation of state, gives a high metallicity as a solution. However, this solution is not very trustworthy since it is associated with a high cross-term kernel of A. This high cross-term value is a consequence of the parameter set used, which is that of the less stable inversions presented in Sect. 7.3.3. Inversions of the convective parameter have shown that Model 4 presented large discrepancies with the Sun in its A profile, thus showing the need to damp the the cross-term contribution for this model. When such a damping is realised, the solution directly changes to a low-metallicity one. This leads us to consider that these particular results, obtained with a particular parameter set are not to be trusted. Moreover, even for the other models, this set gave higher metallicities, indicating that a systematic error, stemming from the A differences with the Sun, was potentially re-introduced. Based on these considerations, we consider that the inverted results obtained with this parameter set are not to be trusted. Ultimately, one finds out that the given interval is between $[0.008, 0.0014]$. While the lowest values of this inversion seem unrealistically low, one should keep in mind that errors of the order of 3.0×10^{-3} have been observed in the hare-and-hounds exercises, explaining the interval obtained here. This spread is a consequence of the variations in the ingredients of the microphysics in the models, which lead to better or worse agreement with the acoustic structure of the Sun.

Similar tests have been performed with low metallicity AGSS09 models, to assess whether they would favour a high metallicity solar envelope, as in our hare-and-hounds exercises. The results are quite different. For all parameters sets used in the first sets of hare-and-hounds exercises, the inversion gives unrealistic results, ranging from negative

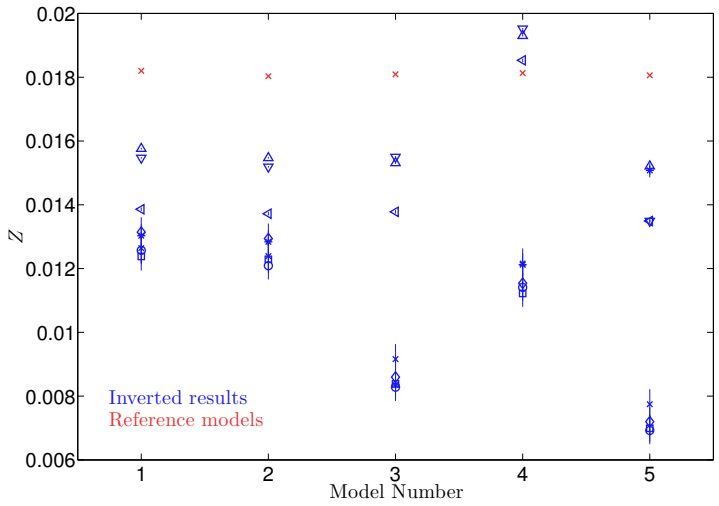

Figure 7.20: Inversion results for various solar models. The reference metallicity values are ploted in red, while the inverted values are given in blue with each symbol corresponding to a trade-off parameters set. Model 6 and 7 are excluded from the plot (see manuscript for justification).

metallicities to values of the order of 0.1 or more, depending on the models and parameter sets. This is not surprising since one infers directly the metallicity difference, δZ, from Eq. 7.6. This means that if this contribution is very small, it will be dominated by the other differences, δA and δY. However, in Sect. 7.3.3, we attempted a few inversions for smaller metallicity differences between targets and reference models. We showed that in some cases, it was possible to infer the result but that the accuracy was reduced and the cross-term could dominate the results. Using the same parameters as in our supplementary hare-and-hounds exercises, we find that the AGSS09 models place the solar metallicity value around 1.1×10^{-2}, which is in agreement with the previous results.

The differences in acoustic structure are expected to be larger between the Sun and the low metallicity standard models than between two numerical models of various metallicities considered in our H&H exercises. Hence, it is not surprising that the inversions performed in our H&H exercises are more successful than real solar inversions of low metallicity standard models. The large differences imply larger cross-term contributions, especially in the uppermost convective region where A is of very high amplitude. Another weakness of low metallicity standard solar models is that they do not reproduce the helium abundance in the convective zone. For example, the value found in Model 6 could be different from the solar value by up to 0.025, implying that even if the helium cross-term kernel is strongly damped, it could still strongly pollute the results of the solar inversion. In contrast, the models used in the hare-and-hounds exercises were calibrated to fit the helium value within an accuracy of 0.01. This problem was less present for Model 7, for which the ad-hoc changes in the ingredients lead to a better agreement with helioseismic constraints and consequently, the inversion was slightly more stable. However, the sound speed, density and convective parameter profile inversions still showed larger differences than for GN93 models despite the changes. Therefore, we deem the reliability of the solar inversions from the AGSS09 models, especially that of Model 6, which is particularly unstable, to be less robust and constraining as the inversions from the GN93 models. Therefore we excluded these models from Fig 7.20.

Despite these uncertainties, the indications obtained from these models for a restricted region of the parameter space, combined with the fact that the inversions from GN93 solar models favour a low solar metallicity, still lead us to advocate for a low value of the solar metallicity. However, the precision of this value is quite poor and limited by the intrinsic errors in Γ_1 and the uncertainties on the equation of state. Still, we can conclude that our results do not favour the GN93 abundance tables and any other table leading to similar solar metallicities, like the GS98 or AG89 tables. Had the solar metallicity been that of these abundance tables, a clear trend should have been seen when carrying out solar inversions from low-metallicity AGSS09 models.

Consequences for solar models

The results presented in section 7.3.4 have significant consequences for solar modelling since they confirm the low metallicity values found by S. V. Vorontsov et al. (2014). This result implies that the observed discrepancies found in sound speed inversions (e.g. A. M. Serenelli et al. (2009)) are not to be corrected by increasing the metallicity back to former values, but could rather originate from inaccuracies in the physical ingredients of the models. Amongst other, the opacities constitute the physical input of standard solar models that is currently the most uncertain. Recently, experimental determinations of the iron opacity in physical conditions close to those of the base of the solar convective zone have shown discrepancies with theoretical calculations of between 30% and 400% (Bailey et al. (2015)). The outcome of the current debate (see for example Blancard, Colgan, et al. (2016), Iglesias and Hansen (2017), and Nahar and Pradhan (2016) amongst others) in the opacity community that these measurements have caused will certainly influence standard solar models and the so-called "solar modelling problem".

Besides the uncertainties in the opacities, the inadequacy of the low-metallicity solar models could also result from an inaccurate reproduction of the sharp transition region below the convection zone. In current standard models, this region is not at all modelled, although it is supposed to be the seat of multiple physical processes (see Hughes, Rosner, and N. O. Weiss (2007) for a thorough review) that would affect the temperature and chemical composition gradients, and thus the sound speed profile of solar models.

In addition to these main contributors, further refinements of physical ingredients such as the equation of state (see for example Baturin et al. (2013) and S. V. Vorontsov et al. (2013) for recent studies) or the diffusion velocities could also slightly alter the agreement of low-metallicity solar models and the Sun (see for example Turcotte et al. (1998) for a study of the effects of diffusion).

7.3.5 Conclusion

In this section, we presented a new approach to determine the solar metallicity value, using direct linear kernel-based inversions. We developed in Sect. 7.3.2 an indicator that could allow us to restimate the value of the solar metallicity, provided that the seismic information was sufficient. We showed that the accuracy of the method was limited by intrinsic errors in Γ_1 and differences in the equation of state.

In Sect. 7.3.3, we carried out extensive tests of the inversion technique, using various physical ingredients and reference models. These tests showed that while the inversion could distinguish between various abundance tables such as those of AGSS09 and higher metallicity abundances, like those of GN93 or GS98, it could not be used to determine very accurately the value of the solar metallicity, due to intrinsic uncertainties of the method and models.

In Sect. 7.3.4, we applied our method on solar data, using the inversion parameters calibrated in the hare-and-hounds exercises carried out previously. We concluded that our

method favours a low metallicity value, as shown in S. V. Vorontsov et al. (2014). However, further refinements to the technique are necessary to improve the precision beyond that achieved in this study.

Firstly, developing a better treatment of the cross-term contribution from the convective parameter, A, taking into account its 0 value in the convective zone, could help with the analysis of the trade-off problem. Secondly, using other equations of state could help with understanding the uncertainties this ingredient induces on the inversion results. Thirdly, the use of a seismic solar model based on inversions of the A and Γ_1 profiles as a reference, rather than calibrated solar models, could reduce the impact of the intrinsic Γ_1 errors, thus reducing the main contributor to the uncertainties of the inversion and provide more accurate and precise results for this inversion.

7.4 Inversions of the convective parameter: a closer look at the tachocline

7.4.1 Introduction

The base of the solar convective envelope has always been under the spotlight and solar scientists are still debating today on the implications of the tachocline modelling on the magnetic and rotational properties of the Sun. Historically, the tachocline was defined by Jean-Paul Zahn and Edward Spiegel in 1992 as the transition region between the differentially rotating convective envelope and the uniformly rotating radiative zone. It came in the spotlight after the successful inversions of the rotation profile of the Sun (Kosovichev (1988)), revealing the importance of this very thin region, extending over less than 4% of the solar radius (Corbard et al. (1999) and Elliott and D. O. Gough (1999)) between 0.708 and 0.713 $r/R_\odot$. Historically, solar rotation was, and still is, an issue. The transition in the rotation rate is thought to result from the combined effects of multiple complex physical processes (see Kumar, Talon, and Zahn (1999), Spiegel and Zahn (1992), and Spruit (1999) for example). The tachocline encompasses all uncertain phenomena of stellar interiors (see Hughes, Rosner, and N. O. Weiss (2007) and references therein): it is influenced by turbulent convection, rotational transport and is thought to be the seat of the solar dynamo. It is strongly impacted by convective penetration (see Christensen-Dalsgaard, Monteiro, et al. (2011) for a recent study) and therefore is influenced by the various studies aiming at refining the current mixing-length formalism used for stellar convection (Zahn (1999), C.-G. Zhang et al. (2013), and Q. S. Zhang and Li (2012a,b)). Thus, this very thin region of the solar structure materializes all weaknesses of standard models.

Besides convective penetration and horizontal turbulence, the magnetic properties of the solar wind also play a strong role, since the extraction of angular momentum will depend on the surface conditions to properly reproduce the current solar rotation profile (see Hughes, Rosner, and N. O. Weiss (2007) for a complete review). In recent years, the advent of 3D hydrodynamical simulations has enabled more in-depth studies of the solar tachocline (Acevedo-Arreguin, P. Garaud, and Wood (2013), P. Garaud (2002), and P. Garaud and J.-D. Garaud (2008)). However, while such studies are crucial to gaining more knowledge on the potential interactions between the various processes acting in this region, they often operate at a turbulence regime far lower than what is expected at the base of the solar convection zone and do not include all physical processes potentially acting in these regions. Moreover, there would still be a long way to go from a perfect depiction of the current state of the tachocline in a numerical simulation, to the inclusion of its effects in a stellar evolutionary code (Brun, Miesch, and Toomre (2011)).

While its effects have first been seen in the rotation profile of the Sun, the tachocline also leaves a mark in the sound speed profile of the Sun (Antia and Chitre (1998) and

Monteiro, Christensen-Dalsgaard, and Thompson (1994)). The effects of extra mixing acting below the convective zone during the evolution of the Sun are also witnessed in the lithium and beryllium abundances, whose depletion is closely related to the amount of mixing required. Some studies in global helioseismology have attempted to include its effects in their modelling and determine the changes in the sound speed profile and helium abundance resulting from its presence (Brun, Antia, et al. (2002), Richard, Théado, and Vauclair (2004), Richard and Vauclair (1997), and Richard, Vauclair, et al. (1996)). With this study, we show that a more efficient thermodynamical quantity can be determined to constrain the stratification near the tachocline. This inversion involves the convective parameter[3], defined as $A = \frac{d\ln\rho}{dr} - \frac{1}{\Gamma_1}\frac{d\ln P}{dr}$, with r the radial position, P the pressure, ρ the density and $\Gamma_1 = \frac{\partial \ln P}{\partial \ln \rho}|_S$, the first adiabatic exponent, with S the entropy. This quantity is related to the Brunt-Väisälä frequency and is consequently an excellent probe of local variations near the base of the convective zone.

Inversions of the convective parameter have been performed by D. O. Gough and Kosovichev (1993b), who attempted to generalize its use to stars other than the Sun (D. O. Gough and Kosovichev (1993a) and Takata and Montgomery (2002)). Unfortunately, the diagnostic potential of this inversion was never used to calibrate the stratification just below the convective zone. Moreover, no comparison between standard solar models (SSMs) with various abundances has been performed, although this inversion probes the region were the low metallicity models seem to be at odds with solar structure (A. M. Serenelli et al. (2009)). In the following sections, we carry out inversions for SSMs built with various abundances and opacity tables. We illustrate the importance of additional mixing below the limit of the adiabatic convection zone at $0.713 r/R_\odot$ (Kosovichev and Fedorova (1991)) to reduce inaccuracies between SSMs and the Sun. We discuss how this inversion, coupled with classical helioseismic studies and the entropy inversion presented in section 7.2, can be used to carry out an in-depth study of the solar tachocline.

7.4.2 Inversion results for standard solar models

As we have seen in section 7.4.1, the base of the solar convective envelope is a physically uncertain region. In this section, we will show how inversions of the convective parameter can be used to better understand the successes and failures of the standard models and how they can be used in combination with classical tools of helioseismology to refine the structural models of the Sun.

The standard models used in this study are built using the Liège stellar evolution code (CLES, Scuflaire, Théado, et al. (2008)), for which the frequencies were computed with the Liège oscillation code (LOSC, Scuflaire, Montalbán, et al. (2008)). All models used the FreeEOS equation of state (Irwin (2012)) and either the OPAL (Iglesias and Rogers (1996)), or OPLIB opacity tables (Colgan et al. (2016)). We considered the AGSS09 (Asplund, Grevesse, Sauval, and Scott (2009)), GS98 (Grevesse and Sauval (1998)) and GN93 (Grevesse and Noels (1993)) heavy elements abundances. The structural kernels of (A, Γ_1) structural pair (D. O. Gough and Kosovichev (1993b)) and the inversions were computed using a customised version of the InversionKit software using the SOLA inversion technique (Pijpers and Thompson (1994)). We used the solar seismic dataset of Basu, Chaplin, et al. (2009) and followed their definitions of the error bars for the SOLA method.

In figure 7.21, we illustrate inversions of the convective parameter for standard solar models using both the AGSS09 and GN93 abundances along the OPAL and OPLIB opacities. As one can see, the GN93 OPLIB models, in red, show the smallest disagreements in terms

[3] In some references, this quantity can be denoted as the Ledoux discriminant.

of convective parameter inversions while the AGSS09 OPAL models, in orange, show strong differences right below the convective zone. This result is not surprising since models built with the AGSS09 abundances do not set the base of the convective zone at the location it is found in helioseismology and the sound speed inversion also show a strong disagreement in this region.

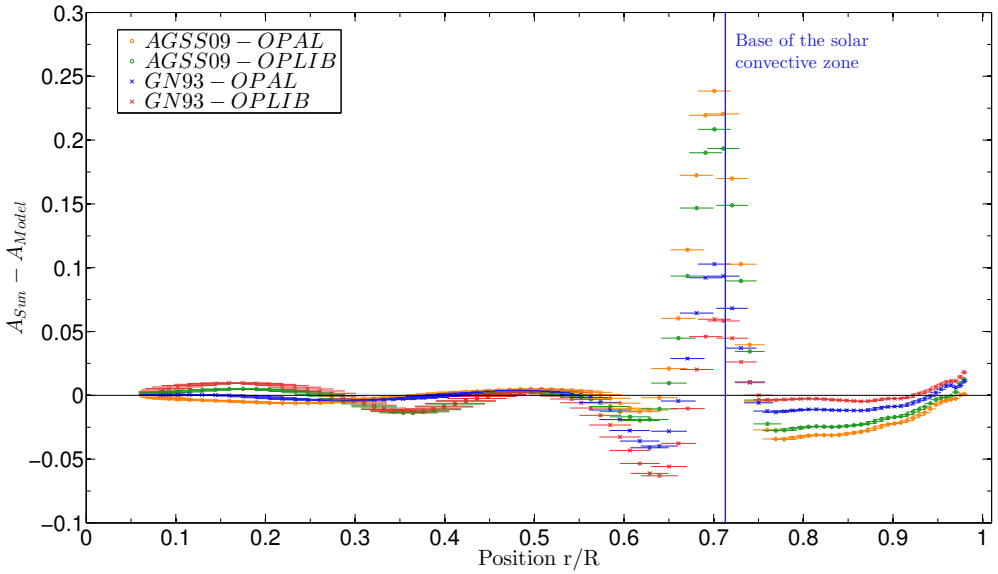

Figure 7.21: Effects of the opacities on the convective parameter profile of SSMs. The orange and green symbols are related to SSMs built with the AGSS09 abundances and the OPAL and OPLIB opacity tables, respectively, while the blue and red symbols are related to SSMs built with the GN93 abundances and the OPAL and OPLIB opacity tables, respectively. Horizontal error bars show the interquartile width of the averaging kernels while the vertical error bars are the 1σ errors from the propagation of the observational 1σ errors.

However, it is more surprising to see that in the region right below the tachocline, around 0.65 normalised radii, the GN93 models seem to perform less well than the AGSS09 models. This trend is seen for both the OPAL and the OPLIB opacity tables. We attempted to see what is causing this disagreement and computed models using the AGSS09 abundance tables but the GN93 Z/X value, to see if the overall heavy elements mass fraction could be causing this disagreement. These results are illustrated in green in figure 7.22. Similarly, we analysed GS98 models, illustrated in orange in figure 7.22 and observed the same trend in their A profile. In addition to these tests, we also computed models with an increased opacity in the region where the disagreement appeared and could reproduce the trend observed in standard models built with the GN93 abundances in models including the AGSS09 abundances. This inversion is also presented in figure 7.22 in purple. From this analysis it seemed that the error in the convective parameter stems from a too steep temperature gradient in this region, which is either a consequence of a higher heavy elements mass fraction or a higher opacity.

This is further confirmed in figure 7.23, where we have separated A into contributions from the temperature and mean molecular weight gradient using the equation of state as

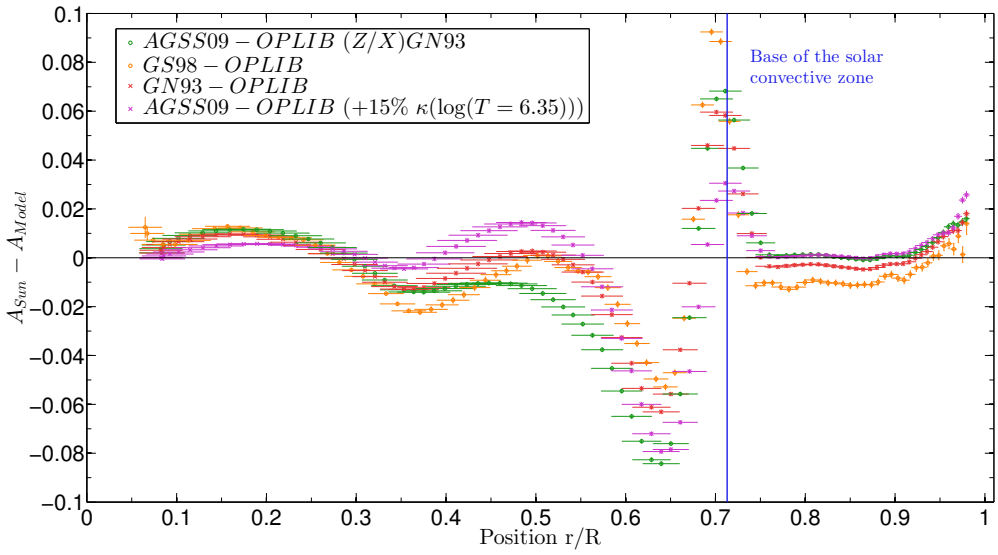

Figure 7.22: Analysis of the disagreement in high metallicity models. The green symbols are related to an SSMs built with the AGSS09 abundances but the (Z/X) value used is that of the GN93 tables. The orange and red symbols are related to an SSM built using the GS98 and the GN93 abundances, respectively. The magenta symbols are related to a standard model using the AGSS09 abundances but where the opacity profile has includes a Gaussian increase around $\log(T) = 6.35$. All models were built using the OPLIB opacity tables and the FreeEOS equation of state. Horizontal and vertical error bars are defined as in figure 7.21.

follows

$$A = -\frac{r\delta}{H_P}\left(\nabla_{ad} - \nabla + \frac{\phi}{\delta}\nabla_{mu}\right), \tag{7.17}$$

we have adopted the following notation for figure 7.23

$$A^T = -\frac{r\delta}{H_P}\left(\nabla_{ad} - \nabla\right), \tag{7.18}$$

$$A^\mu = -\frac{r}{H_P\phi}\nabla_{mu}. \tag{7.19}$$

In figure 7.23, we can indeed see that the steepness of the temperature gradient is significantly changed when using different abundance tables. It should also be noted that the mean molecular weight gradient cannot be considered responsible for this variation, since its amplitude is rather low in these regions and is nearly the same for both models. Consequently, the amplitude of the deviation is only slightly modified by the inclusion of an additional mixing right below the convection zone, as we will see in the next section. The most straightforward way to correct these discrepancies is to lower the metallicity of the SSMs. However this would imply acknowledging a significant increase in the inaccuracies of the layers just below the convection zone, as can be seen from inversions of AGSS09 models in figure 7.21.

The problem becomes more complicated when combining this information to the entropy proxy and squared adiabatic sound speed profile inversions. Indeed, increasing

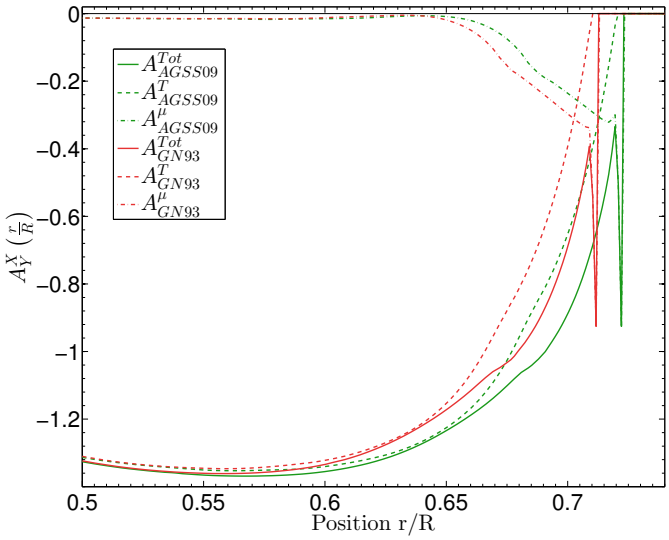

Figure 7.23: Decomposition of the Ledoux convective parameters in its contribution from temperature and mean molecular weight gradients.

the metallicity or the opacity around $\log(T) = 6.3$, in region of the so-called deep iron opacity peak reduces the discrepancies between solar models and the Sun, as is expected from previous helioseismic studies. This is illustrated in figure 7.24, where one can see that some models including a steeper temperature gradient can indeed reduce and even reverse the trends seen in the sound speed inversion. In figure 7.25, we can see that increasing either metallicity or opacity significantly helps for the position of the plateau, but also degrades the agreement in the radiative region. This implies that the entropy proxy inversion indicates that a steepening of the temperature gradient is required, but the convective parameter inversion shows that this steepening cannot stem from a high metallicity increase or from an opacity increase at $\log(T) = 6.35$ as we have performed. Combining both diagnostics thus offers a powerful tool to constrain the possible changes that can be made in the standard models to solve their current disagreements with the Sun.

From the convective parameter inversion, it could seem that the changes in opacity induces a sort of compensation of the errors of the solar models. In other words, that the too steep temperature gradient around 0.65 in normalised radius could help correcting the errors that will naturally emerge from the non-inclusion of an accurate representation of the tachocline in the standard solar models. The overestimation of the temperature gradient around 0.65 $r/R_\odot$ in solar models built using the GN93 abundances would also imply that their agreement with the Sun results, at least partially, from a certain degree of compensation. The steeper temperature gradient, resulting from the higher metallicity of these models, reduces the discrepancies observed in the tachocline. This compensation would also explain why the GN93 models reproduce well the steep variations in sound speed observed at 0.713 $r/R_\odot$, resulting from the transition from the adiabatic to the radiative temperature gradient in the Sun without the need for any convective penetration.

From a theoretical perspective, the Schwarzschild limit derived by using the mixing-length theory, as done in standard solar models, should not be located at the same depth as the observed solar transition. In the Sun, the variation in the sound speed is located at the kinetic limit of the convective elements which is influenced by convective penetration

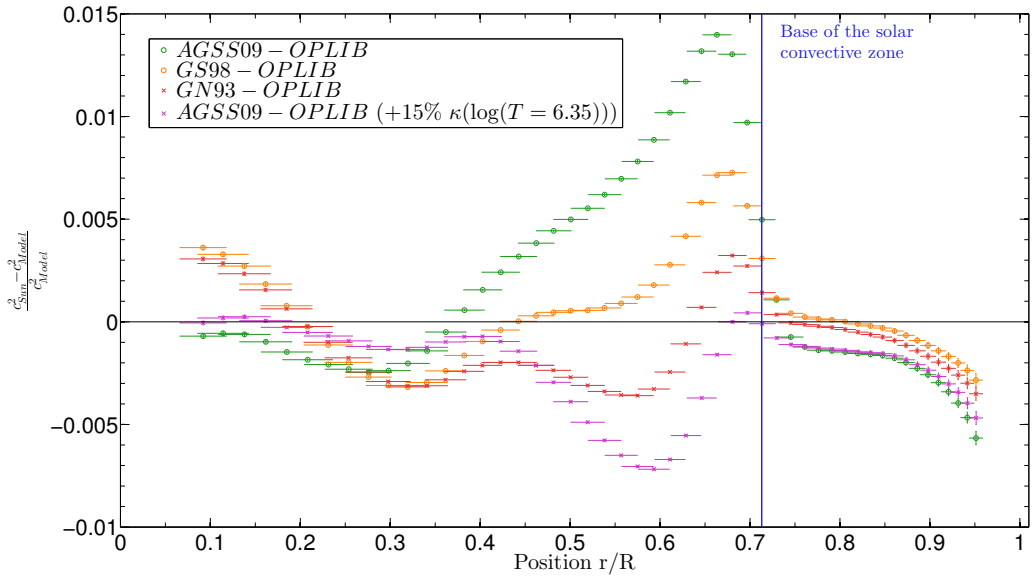

Figure 7.24: Inversions of the squared adiabatic sound speed profile for the models illustrated in 7.22, the colour code and the errors are those of figure 7.22.

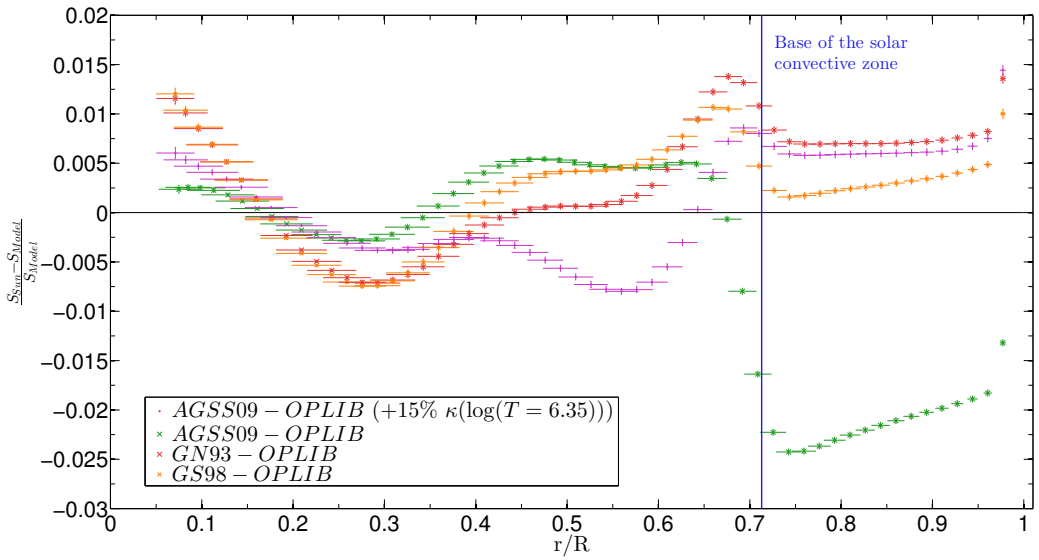

Figure 7.25: Inversions of the entropy proxy profile for the models illustrated in 7.22, the colour code and the errors are those of figure 7.22.

and differs from the limit derived solely by the mixing-length theory in standard solar models. Moreover, the effects of shear could induce an additional mixing of the chemical elements below the transition in temperature gradients, meaning that the fully mixed zone will extend slightly deeper than 0.713 $r/R_\odot$. This justifies investigations of the impact of an additional chemical mixing in the regions just below the transition of the temperature gradients.

7.4.3 Impact of additional mixing on the convective parameter profile

From the test cases presented in the previous section, it seems that most of the discrepancies in the standard solar models are stemming from a very narrow region right below the convective zone. As stated above, the tachocline is a very complex problem and while from the chemical point of view, a certain degree of mixing is expected due to shear, horizontal turbulence and convective plumes, there is currently no agreement on the behaviour of the temperature gradient in this region. From the seismic point of view, various attempts have been made to use the phase shifts to constrain the transition in the temperature gradients (see for example I. W. Roxburgh and S. V. Vorontsov (1994a)), finding that while the transition is not discontinuous, it should still be quite steep.

Using the convective parameter inversions, we have analysed the impact of turbulent diffusion right below the convective zone. We used solar models including the AGSS09 abundances, the OPLIB opacities and the FreeEOS equation of state. We added a $0.1H_P$ undershooting at the base of the envelope, so that the temperature gradients transition would fit that found in the Sun. To approximate the effects of a tachocline, we used a simple exponential formulation of the diffusion coefficient with a scale height related to density, as done in Miglio, Montalbán, and Maceroni (2007). The extent of the mixing was reduced to a slight zone of around 0.05 solar radii, of the order of the radial extent of the tachocline (Corbard et al. (1999)). The inversion results of the convective parameter are illustrated in figure 7.26. As can be seen, the discrepancies with the Sun are reduced by around 0.08 due to the extra-mixing below the convective zone. However, it should be noted that neither the sound speed nor the entropy profile inversions are significantly improved by these changes, as can be seen in figure 7.27 and 7.28.

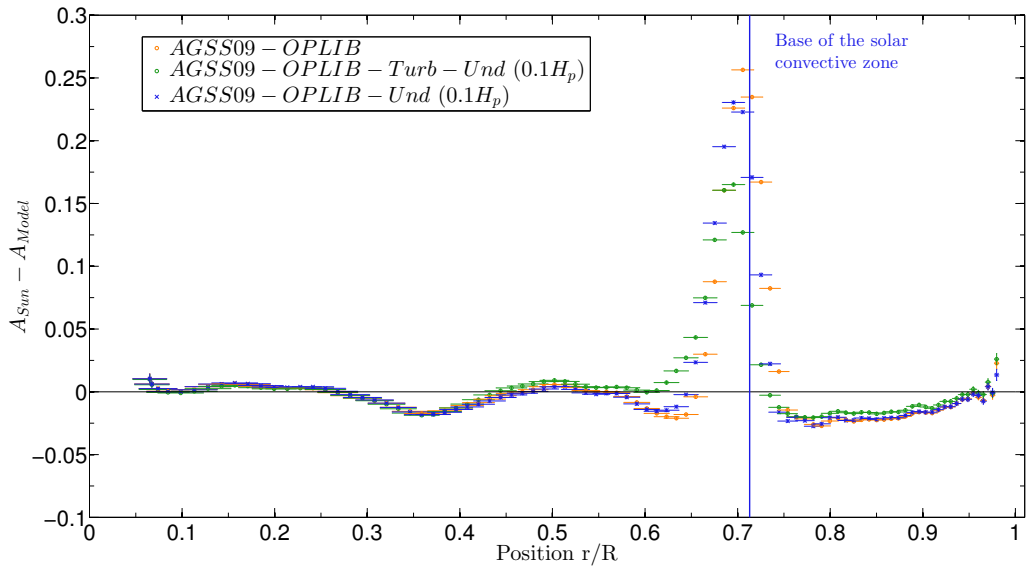

Figure 7.26: Inversions of the convective parameter for models built with the FreeEOS equation of state, the OPLIB opacities and the AGSS09 abundances including extra mixing. The orange symbols are associated with the SSM presented in previous plots, the blue symbols are associated with a model including a small undershooting coefficient to reproduce the transition in temperature gradients. The green symbols are associated with a model including a small convective penetration and an additional diffusive mixing localised below the transition of the temperature gradients. The horizontal and vertical error bars follow the definition adopted in previous figures.

From these tests, we conclude that mixing alone cannot correct the observed discrepancies and that the remaining errors may stem from inaccuracies in the temperature profile. This is confirmed by the fact that further increasing the intensity or extent of the mixing results in similar discrepancies than with a SSM rather than further improving the agreement with the Sun. The observed inaccuracies could stem from various effects, such as for example the surrounding opacity profile or the modelling of the transition of temperature gradients in the tachocline. Indeed, there is currently no agreement on the description of the transition from the adiabatic to radiative gradient around $0.713 r/R_{\odot}$. Ad-hoc parametrizations could be used to analyze the effects of attempting to properly reproduce the transition region in the sound-speed, entropy and convective parameter profiles. However, this analysis would be strongly limited, since it assumes that the opacities are perfectly accurate. From figure 7.22, we can see that opacity changes can indeed significantly affect the convective parameter profile. Therefore, due to the current debate in the opacity community, the analysis provided by parametric approaches should not be overinterpreted and supplemented by theoretical inputs from hydrodynamical simulations.

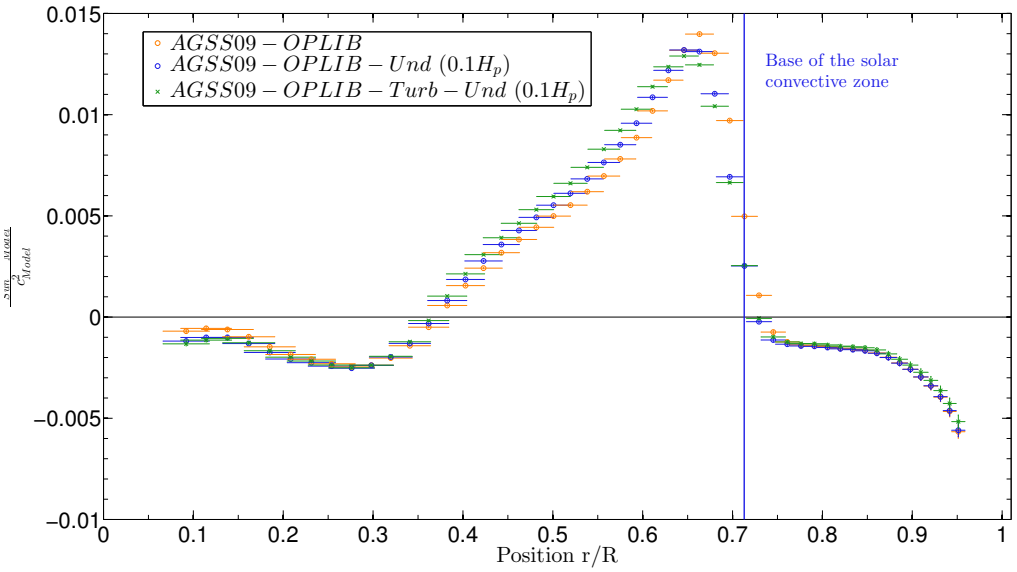

Figure 7.27: Inversions of the squared adiabatic sound speed profile for the models illustrated in 7.26, the colour code and the errors are those of figure 7.26.

In addition to these processes, additional refinements of the SSMs might be required to reproduce the solar structure. For example, using individual elements instead of an average metallic element might induce changes in the opacity calculations. Moreover, using individual elements would allow a better inclusion of partial ionisation effects in the computation of the diffusion velocities. Such refinements would impact both temperature and chemical composition gradients. Additional updates of the equation of state will also slightly alter the results and while it would not eliminate the errors just below the convection zone, it might influence the deeper radiative regions (see 7.4.5 for an illustration of the effect of the equation of state). The link between such effects and the lithium abundances should also be carefully studied with models including the effects of rotation and properly reproducing the lithium and berylium abundances.

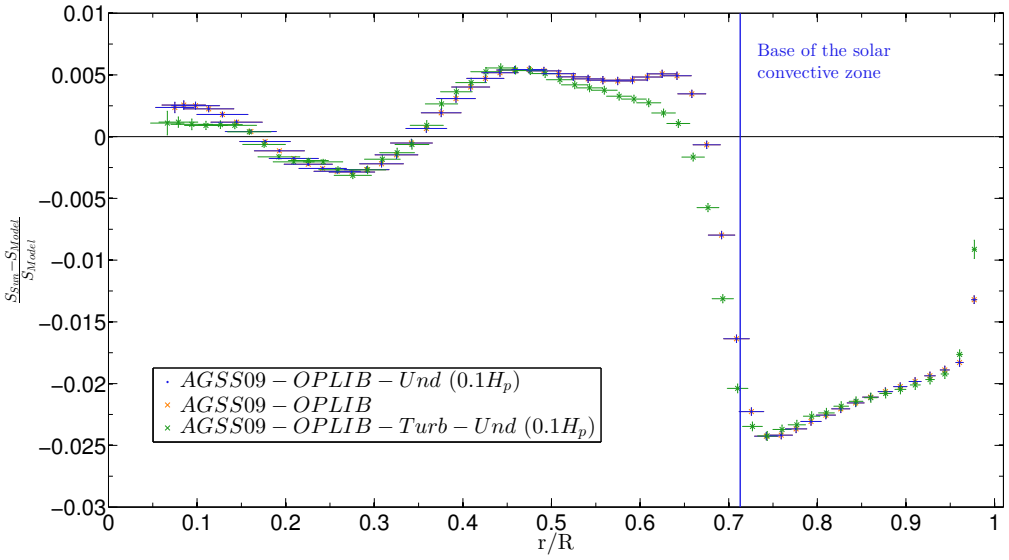

Figure 7.28: Inversions of the entropy proxy profile for the models illustrated in 7.26, the colour code and the errors are those of figure 7.26.

7.4.4 Conclusion

The inversion of the convective parameter offers very strong diagnostics on the stratification right below the solar convective zone. Thanks to its very localised sensitivity, it can be used efficiently alongside the entropy inversions presented in section 7.2 to constrain both temperature and mean molecular weight gradients in the solar tachocline. In standard models, the convective parameter inversion can potentially lead to interpret the reason of the success of the high metallicity models as the result of a form of possible compensatory behaviour in the temperature gradient near the base of the convective envelope. Combining the knowledge of these diagnostics, we are already able to demonstrate that a certain amount of diffusive mixing below the temperature gradient transition at $0.713 r/R_\odot$ helps in reducing the disagreement with the Sun. However, additional mixing is insufficient and the remaining inaccuracies are the proof of an inadequate reproduction of the temperature gradient in the lower part of the tachocline. Parametrizations of the transition region could provide further insights into the problem, keeping in mind that non-radial variations can also be expected in the tachocline and would thus limit the predictive power of 1*D* structural inversions. Moreover, as a consequence of the current debate in the opacity community, these studies should not aim at providing a full agreement, but rather be used to reinforce the strong links between stellar models, hydrodynamical simulations and theoretical developments, for progress in these fields is necessary to improve our current depiction of solar and therefore stellar interiors.

7.4.5 Supplementary material

Inversions for various equations of state, abundances and opacity tables

To further analyse the diagnostic provided by the inversion of the convective parameter, we carried out inversions using standard solar models built with the OPAL and Ceff equations of state. Both results are illustrated in figure 7.29 alongside the results obtained with the FreeEOS equation of state for a solar model using the GN93 abundances and the OPLIB opacity tables. As can be seen, changing the equation of state alters the

agreement with the deeper radiative regions and it seems that the FreeEOS and the Opal equations of state should be favoured to the Ceff equation of state. However, changing this physical ingredient does not correct the deviations found at the base of the convective zone and does not reduce the discrepancy found with the GN93 abundances. Using the

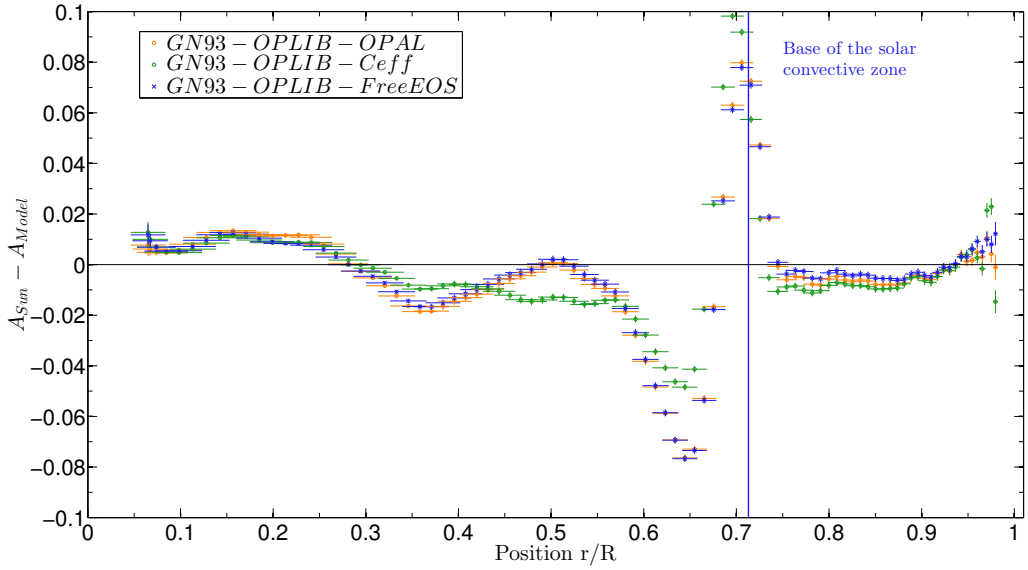

Figure 7.29: Inversions of the convective parameter profile models using the GN93 abundances, the OPLIB opacity tables and the Ceff, OPAL and FreeEOS equations of state, illustrated in green, orange and blue, respectively.

OPAS opacities instead of the OPLIB tables alongside the AGSS09 abundances also slightly changes the results, as illustrated in figure 7.30. However, the fact that these opacities do not cover the whole range of density and temperature of the solar structure reduces their diagnostic potential. Indeed, this implies that they have to be reconnected near the base of the convective envelope to other tables (either OPAL or OPLIB). This of course leads to inconsistencies if one wishes to analyse fine variations of the temperature gradient in these regions. As we have seen from section 7.2, changing the opacity just above the convective zone also changes the temperature gradient since this quantity is also influenced by the derivatives of opacity.

Quality checks of the inverted results

To confirm the results obtained for the Sun, we carried out a hare-and-hounds exercise using standard solar models. We used the same set of modes as for our solar inversions, using the actual observed uncertainties on the individual frequencies of the Sun for each mode. Our hound was the standard solar model of our sample built with the AGSS09 abundances, the OPLIB opacities, and the FreeEOS equation of state, while the hare was another standard solar model built with the OPLIB opacities, the OPAL equation of state, and the GN93 abundances. From Fig. 7.31, we illustrate the differences in A between the targert and the reference model as $\delta A = A_{\rm Tar} - A_{\rm Ref}$. We can see that the SOLA method reproduces the trends of the convective parameter profile differences, with the exception of the very deep regions, which remain poorly constrained by the acoustic oscillations observed for the Sun. We can however see that the SOLA method reproduces quite well the upper radiative zone, especially the variations around 0.65. However, we can also see that the very steep variations, above 0.7 are not well reproduced. This is a consequence of

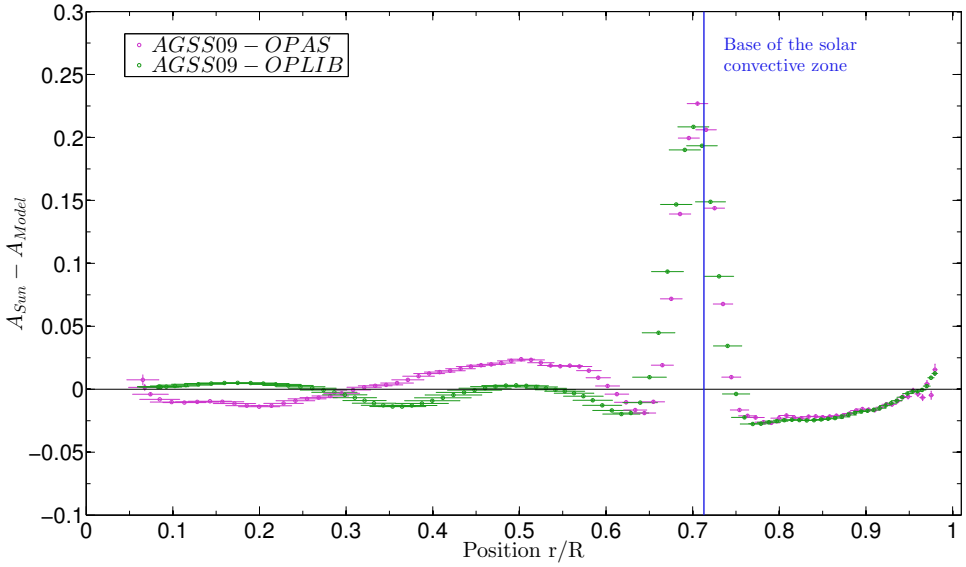

Figure 7.30: Inversions of the convective parameter profile for models built using the AGSS09 abundances, the FreeEOS equation of state and the OPLIB and OPAS opacities plotted in green and purple, respectively.

the finite width of the inversion kernels, which are unable to capture properly the strong discontinuity in A at the base of the envelope. Similar problems are seen in Kosovichev (2011) for model S and are intrinsic to this specific inversion. From a mathematical point of view, this discontinuity will never be properly sampled since trying to further localise the kernels only introduces Gibbs oscillations in the inverted profile. A certain degree of pollution is also present in the result in the convective envelope. This inaccuracy is reduced by further increasing the localisation of the kernels. However, as stated before, this introduces an oscillatory behaviour in the inverted profile. In figure 7.32, we illustrate the averaging kernels of this inversion, showing a good fit of their target in most of the radiative region. Below $0.1 r/R_{\odot}$, however, the kernels are not properly localised and thus the inversion cannot be trusted. In the convective zone, however, the kernels are well localised and the large non-zero value in the A profile does not seem to stem from an inaccurate fit to the target. The inversion sometimes attributes a too large value of δA in such regions, which is clearly an artefact. It does not seem that this value stems from an inaccurate fit of the target. Instead, it seems to be linked to the amplitude of the lobe just below the convective zone in the inversion, since models built with the GN93 abundances show a better agreement with the expected small value than the AGSS09 models. Similar problems have also been seen in Kosovichev (2011) for solar inversions, but they do not affect the diagnostic in the radiative region.

7.5 General Conclusion

In this chapter, we have attempted to demonstrate the necessity of a re-investigation of the solar modelling problem, in light of the recent update of the opacity tables by the Los Alamos National Laboratory group. However, we have shown in section 7.2 that classical helioseismic tests were not sufficient to probe all the weaknesses of solar models, since they did not seem to favour either of the abundance tables. Consequently, we have attempted to provide additional helioseismic tests, allowing for a more in-depth study of

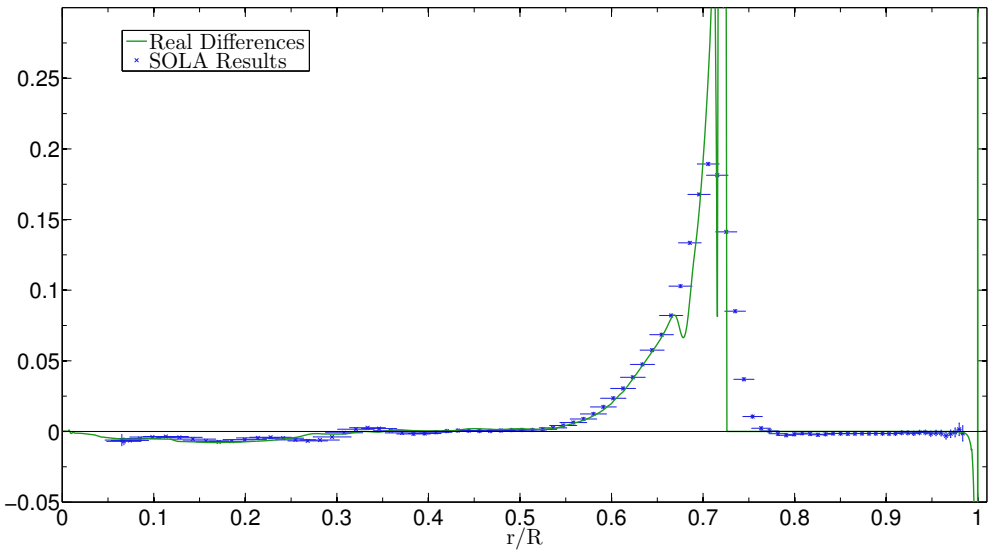

Figure 7.31: Results of the hare-and-hounds exercises. The real differences in A are illustrated in green while the blue symbols are the SOLA inversion results.

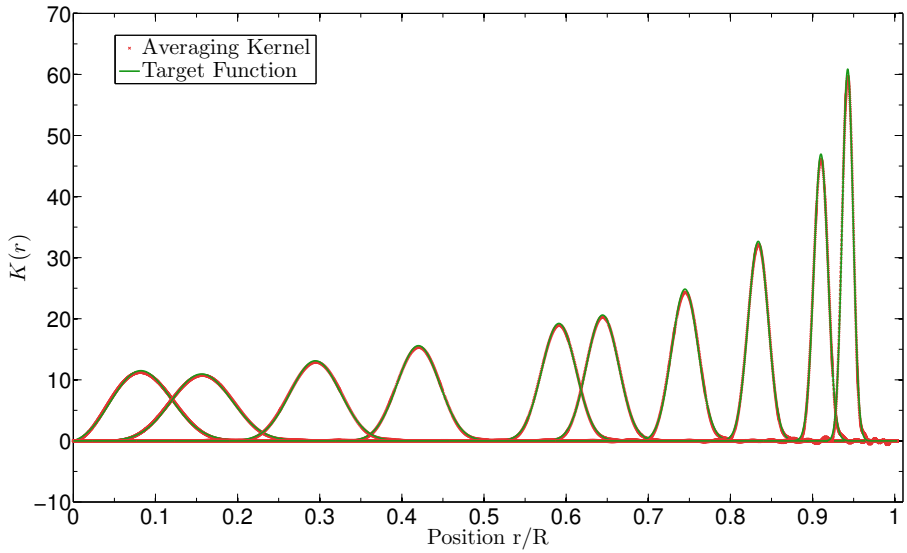

Figure 7.32: Illustration of SOLA averaging kernels and comparison with their target functions at various depth. The green curves show the Gaussian target functions of the SOLA inversion for various depths inside the Sun while the red dashed curves show the averaging kernels.

the current solar issue.

From section 7.2, we have seen that the entropy proxy inversions could provide strong constraints on the overall steepness of the temperature gradient in the solar radiative zone. Such constraints are extremely valuable since they echo the current debate in the opacity community concerning iron spectral opacity calculations. However, these inversions are, of course, sensitive to some extent to the mean molecular weight gradient right below the

convective zone, and slight changes could be expected from additional mixing processes which would alter both the chemical composition but also indirectly the temperature gradient right below the convective zone.

In combination with the inversion of the entropy proxy, we have demonstrated that the seismic determination of the Ledoux convective parameter, developed by Kosovichev (1999), could be of great use for probing the solar stratification right below the convective zone. From this inversion, we were able to demonstrate that the success of the high metallicity solar abundances might be explained by a compensatory effect in the stratification just below the convective zone and that most of the discrepancies between standard solar models and the Sun are located in the last 6% of the solar radiative zone, thus mostly in the so-called tachocline. These results add weight to the argument that the solution of the solar issue is partially to be found in the proper modelling of the (magneto-)hydrodynamical processes acting at the base of the convective zone. Initial tests using both convective penetration and turbulent diffusive mixing have shown that it could improve the agreement with the Sun but are insufficient to place the entropy proxy plateau at the correct height and reduce the discrepancies found in the sound speed inversions. This result demonstrates the complementary nature of the entropy proxy and convective parameter inversions, which can be complemented by the frequency ratios and the sound speed inversions, to ensure consistency with classical helioseismic tests.

In section 7.3, we have carried out an inversion of the solar heavy element abundance in the convective envelope. We used extensive hare-and-hounds exercises to calibrate the method and analyse the trade-off problem and the possible compensations. We have thus shown that helioseismic investigations favour a low metallicity in the convective zone. However, as discussed in the conclusion of this section, further refinements to the method are required to allow a sufficiently precise determination of the metallicity, for it to be considered constraining when building calibrated solar models.

Ultimately, this chapter has only scratched the surface of the solar modelling problem, since most of the theoretical analysis still needs to be done to reconciliate the low-metallicity solar models with helioseismic determinations of solar structure. The main conclusion of this chapter is that high-metallicity models, using either the GN93 or GS98 abundances, are ruled out since they might rely on a compensation of their inaccuracies in the radiative region for their accurate reproduction of solar structure and are not supported by the metallicity inversions. Consequently, this implies that low-metallicity models have to be used in asteroseismic modelling, keeping in mind that the current uncertainties on potential hydrodynamical processes and opacity calculations reduce the accuracy of these modelling results.

8. KEPLER LEGACY

8.1 Introduction

In the last decade, the space photometry missions CoRoT and Kepler have provided us with a wealth of precise seismic data for a large number of stars. This revolution is now allowing us to carry out precise seismic modelling for these stars and to test the physical inputs of our stellar models. As a by-product of this modelling, asteroseismology also delivers precise and accurate fundamental parameters, which are essential to other fields such as Galactic archeology or exoplanetology.

Amongst the observed targets, the Kepler LEGACY sample contains the dwarfs that have the best frequency sets within the Kepler data (see Lund et al. (2017) for a description of the dataset and Silva Aguirre et al. (2017b) for forward modelling results of the Kepler LEGACY sample). As such, they can be seen as benchmark stars to test our inputs of stellar models and the efficiency of seismic modelling. Due to their high number of frequencies and the precision of these determinations, they are also the ideal targets with which to carry out structural seismic inversions. In this chapter[1], we will present forward modelling and inversion results for two targets of the LEGACY sample: namely Doris (KIC8006161) and Saxo (KIC6603624). In Sect. 8.2, we present the targets and the forward modelling results for each one of them. In Sect. 8.3, we present the inversion procedure we used to further constrain the models of both stars and present the results of this process in Sect. 8.4. The implications of these results are then presented in Sect. 8.5.

8.2 Targets selection and forward modelling

The targets were selected by the number and precision of their observed frequencies as well as their estimated mass from a crude grid-based modelling approach. We specifically selected stars with masses close to $1M_{\odot}$. Firstly, stars closer to the Sun are easier to model, and we know from helioseismology and from our theoretical test cases where it

[1]The results presented here are a reproduction of the article Buldgen, D. Reese, and M.-A. Dupret 2017, to appear in the proceedings of the *TASC*2/*KASC*9 Workshop.

was possible to obtain a sufficiently good modelling that linear inversion techniques can be applied to constrain their structure (see Basu, Chaplin, et al. (2009) for an application to the solar case). This is potentially not the case for more massive stars for which the boundary of the convective core may not be reproduced accurately enough and thus the evolutionary stage of the target not very well constrained. In such cases, using a linear approximation may be questionable. The second reason is that we wanted to avoid convective cores in the reference models because we used specific indicators using radial derivatives to constrain the internal structure of the targets (Buldgen, D. R. Reese, and M. A. Dupret (2015)). The thermodynamical quantities used in these indicators can have discontinuous derivatives which will appear in the target function of the SOLA method. Such targets are then impossible to fit with the continuous structural kernels built using the eigenfunctions of solar-like oscillation modes.

Before trying to carry out structural inversions, we obtained reference models for each target using a classical seismic forward modelling approach. This modelling was carried out using a Levenberg-Marquardt algorithm. The models were built using the Liège stellar evolution code (CLES, Scuflaire, Théado, et al. (2008)) and the oscillations were computed using the Liège oscillation code (LOSC, Scuflaire, Montalbán, et al. (2008)). We used the Ceff equation of state (Christensen-Dalsgaard and Daeppen (1992)), the OPAL opacities (Iglesias and Rogers (1996)) supplemented at low temperatures by the opacities from Ferguson et al. (2005) and the nuclear reaction rates from the NACRE project (Angulo et al. (1999)) including the updated reaction rate for the $^{14}\mathrm{N}(p,\gamma)^{15}\mathrm{O}$ reaction from Formicola et al. (2004). Convection was implemented using the classical, local mixing-length theory (Böhm-Vitense (1958)). We used the individual small frequency separations, d_{02} and d_{13}, the effective temperature, T_{eff}, and the metallicity, [Fe/H], as constraints for our structural models. Some fits were also carried out using the frequency ratios r_{01} and r_{02} (I. W. Roxburgh and S. V. Vorontsov (2003)) and this led to very similar results. No surface correction was applied to the frequencies. The free parameters of the Levenberg-Marquardt algorithm were the mass of the star, M, its age, its hydrogen mass fraction, X, its metallicity, Z, and the mixing-length parameter, α_{MLT}. Both stars were modelled using the AGSS09 abundance tables (Asplund, Grevesse, Sauval, and Scott (2009)), but tests were carried out using the old GN93 abundances (Grevesse and Noels (1993)) to see whether some comments could be made on the metallicity scale used to relate stellar metallicity to solar metallicity.

8.2.1 Doris a.k.a KIC8006161

In Fig. 8.1, we illustrate the echelle diagram for Doris. This star has 54 observed individual frequencies with a mean 1σ uncertainty of 0.49 μHz, an effective temperature of $5488 \pm 77K$ and a $[Fe/H] = 0.34 \pm 0.10$. The initial mass estimate was $0.96M_{\odot}$. We illustrate in table 8.1 the results from the forward modelling process. These results are in agreement with the first estimate to within a reasonable accuracy. We note that most of the uncertainty stems from the well-known helium-mass degeneracy in seismic fitting and the intensity of diffusion. It also seems clear that extra-mixing processes acting inside the star would have an impact on these determinations. We only considered models with microscopic diffusion but without including turbulent diffusion. We note that it was possible to fit this target with both the GN93 abundances and the AGSS09 abundances within the same accuracy. Had we included extra-mixing, the scatter of the fundamental parameters would have been slightly larger.

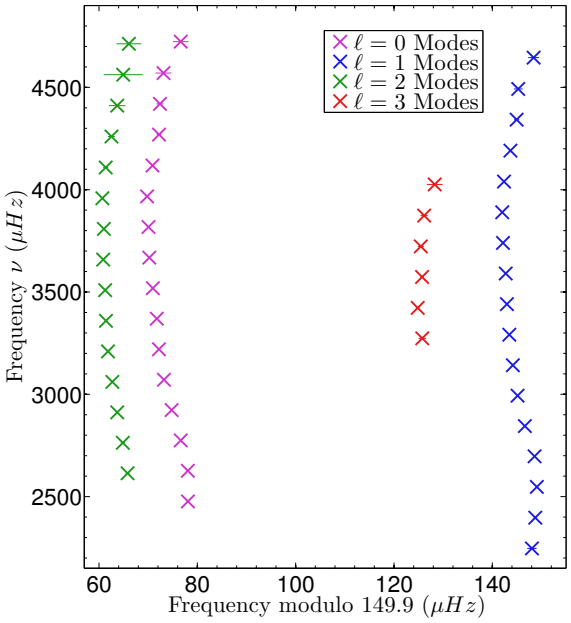

Figure 8.1: Echelle diagram for Doris (KIC8006161) illustrating the ridges of the $\ell = 0, 1, 2, 3$ modes.

Table 8.1: Forward modelling results for Doris and Saxo

	Doris	Saxo
Mass ($M_\odot$)	$0.91 - 1.02$	$0.93 - 1.05$
Age (Gy)	$4.6 - 5.3$	$7.6 - 8.7$

8.2.2 Saxo a.k.a KIC6603624

In Fig. 8.2, we illustrate the echelle diagram for Saxo. This target has 44 individual frequencies with an average uncertainty of 0.336 μHz. Although the frequencies are accurately determined, we wish to point out a small deviation in the echelle diagram, the octupole mode of lowest frequency seems to be deviating from the ridge formed by the other octupole modes. This irregularity made this mode very difficult to fit and it seemed that it could be due to a miscalculation of the frequency value (differences between different fitters have indeed been reported in I. W. Roxburgh (2017)). It seemed improbable that this difference could be physical so we eliminated this mode and used only 43 frequencies to calculate the small frequency separations used in our fits. In addition to the seismic data, we used the same constraints as for Doris, namely the effective temperature, at a value of 5674 ± 77 and the $[Fe/H] = 0.28 \pm 0.10$. Our results, given in table 8.1 are in agreement with the initial mass estimate of $1.01 M_\odot$. Again, this target could be fitted using both the old GN93 and the new AGSS09 solar abundances.

8.3 Inversion Procedure

In this section we briefly present the inversion procedure used for both targets. We followed the same methodology as in our study of the 16Cyg binary system (Buldgen, D. R. Reese, and M. A. Dupret (2016)) and carried out inversions for both the mean density and a core condition indicator based on the derivative of the squared isothermal sound

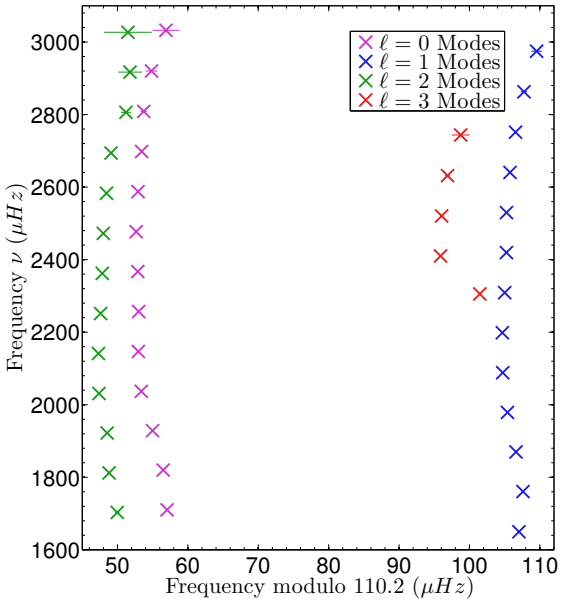

Figure 8.2: Echelle diagram for Saxo (KIC6603624) illustrating the ridges of the $\ell = 0, 1, 2, 3$ modes.

speed, denoted t_u. The mean density inversions have been described in D. R. Reese, Marques, et al. (2012) and the t_u inversions have been presented in Buldgen, D. R. Reese, and M. A. Dupret (2015). The SOLA inversion technique (Pijpers and Thompson (1994)) was used to related the relative frequency differences to corrections of these integrated quantities, assuming the following relation

$$\sum_i^N c_i \frac{\delta \nu_i}{\nu_i} \equiv \left(\frac{\delta A}{A}\right)_{inv}, \tag{8.1}$$

where the c_i are the inversion coefficients, found by minimizing the cost function of the SOLA method, and A is the integrated quantity whose correction is sought. Structural inversions in asteroseismology are carried out using a sample of reference models to analyze whether model dependency dominates the results or not. This is a consequence of the linearity hypothesis used to compute the structural corrections from seismic observations. To obtain the corrections of integrated quantities, we use the linear relations between frequency and structure from D. O. Gough and Thompson (1991)

$$\frac{\delta \nu^{n,\ell}}{\nu^{n,\ell}} = \int_0^R K^{n,\ell}_{s_A,s_B} \frac{\delta s_A}{s_A} dr + \int_0^R K^{n,\ell}_{s_B,s_A} \frac{\delta s_B}{s_B} dr, \tag{8.2}$$

with s_A and s_B being structural quantities like the squared adiabatic sound speed, c^2, and the density, ρ, as in classical helioseismic inversions. The $K^{n,\ell}$ functions are the structural kernels, which depend only on the reference model and its eigenfunctions. The δ notation is related to the differences between observed and reference quantities following the convention

$$\frac{\delta x}{x} = \frac{x_{obs} - x_{ref}}{x_{ref}}, \tag{8.3}$$

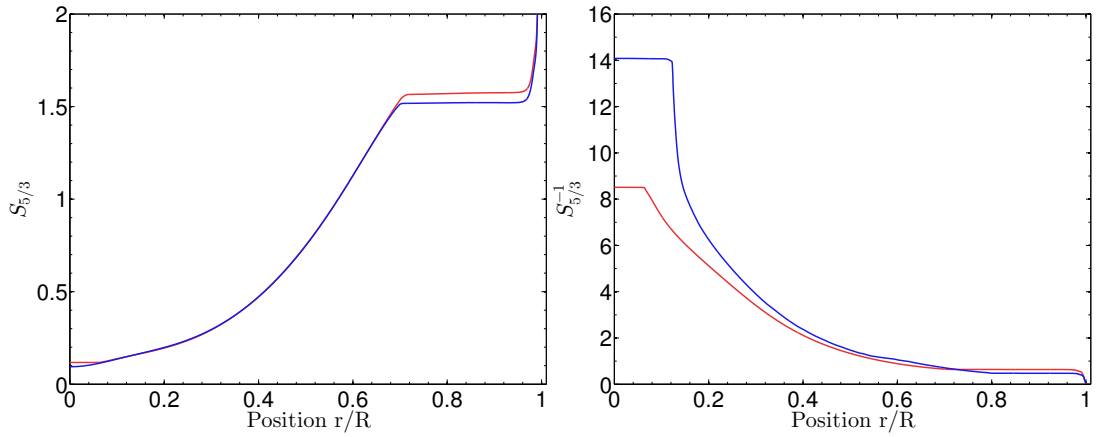

Figure 8.3: Left panel: radial profile of $S_{5/3}$ for two stellar models of various mass and age, illustrating the plateau in the convective region. Right panel: radial profile of $S_{5/3}^{-1}$ for two stellar models, illustrating the plateau of the proxy in convective cores.

where x can be a frequency or a structural quantity. The main problem in the context of asteroseismology is that the linearization hypothesis may not be valid. Thus, one can use multiple reference models to check for the robustness of the inference made with the inversion technique.

The definition of the t_u indicator is

$$t_u = \int_0^R f(r) \left(\frac{du}{dr}\right)^2 dr, \tag{8.4}$$

with $f(r) = r(r-R)^2 \exp(-7\frac{r^2}{R^2})$, the weight function used for this inversion, R the stellar radius, r the radial coordinate associated with each layer inside the model, and u the squared isothermal sound-speed defined as $u = \frac{P}{\rho}$. This quantity is very sensitive to changes in the deep layers of stars and can be used to assess the reliability of the representation of the stratification of the deep layers by the models. In fact, one can show that $u \approx \frac{T}{\mu}$ in the core regions and thus, this quantity will be very sensitive to the effects of mixing processes that will change the temperature, T, and mean molecular weight, μ, gradients.

Besides this indicator, we also carried out inversions using a new core condition indicator based on an entropy proxy, denoted $S_{5/3} = \frac{P}{\rho^{5/3}}$. We consider the inversion results of this indicator to be preliminary and a follow up with the definition and limitations of this inversion will be presented in a future paper. This proxy is particularly well suited for stars with a convective core since it will show a plateau in regions where convection dominate. The width of the plateau is linked to the extent of the convective regions and the height is sensitive to the transition with radiative regions, thus to the temperature and chemical composition gradient. In Fig 8.3, we show the behaviour of $S_{5/3}$ for the convective envelope in the left panel and of $S_{5/3}^{-1}$ in the right panel for a convective core.

8.4 Inversion Results

In Fig. 8.4, we illustrate the inversion results for Doris for the t_u indicator and an indicator based on $S_{5/3}^{-1}$, denoted S_{Core}. The green crosses are the inverted results while the red

circles illustrate the reference models computed using the Levenberg-Marquardt algorithm. As can be seen, some models are in agreement with the inversion results while others are not. There is also a clear trend showing that models not fitting the inverted mean density, given here in abscissa, are incompatible with the other indicators. As already seen in Buldgen, D. R. Reese, and M. A. Dupret (2016), the error bars on the t_u inversion are quite large, but there is a clear trend that can be deduced and used to select a subsample of models from our initial forward modelling. The numerical value obtained for the inverted $t_u/G^2R_{Tar}^6$ value is around $5.8 \pm 0.7 g^2/cm^6$, with R_{Tar} the target photospheric radius and G the graviational constant. The S_{Core} indicator shows an inverted $S_{Core}GR_{Tar}^{1/3}$ value around $2.110 \pm 0.005 cm/gm^{1/3}$. Again only a subset of models are in agreement with these inversion results.

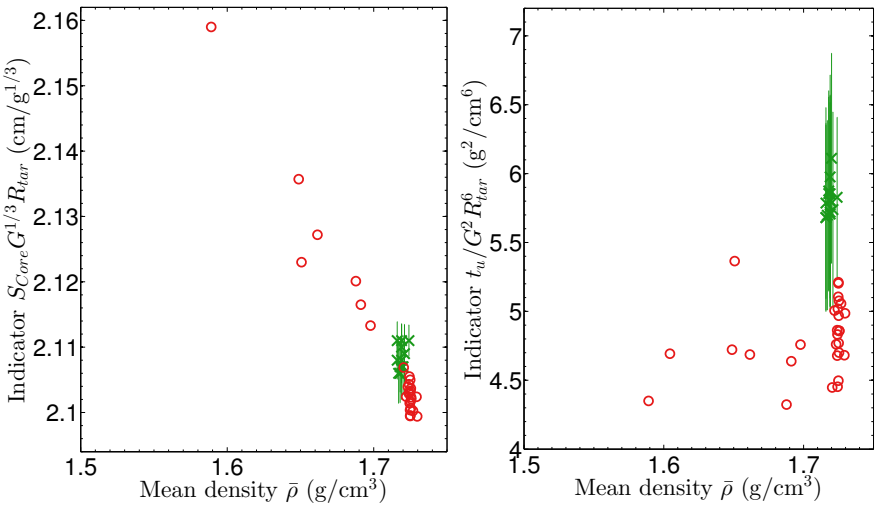

Figure 8.4: Inversion results for Doris. Left panel: $\bar{\rho} - S_{Core}G^{1/3}R_{tar}$ plane where the red circles illustrate the position of the reference models and the green crosses show the inversion results with their error bars. Right panel: $\bar{\rho} - t_u/(G^2R_{tar}^6)$ plane following the same notations as the left panel.

In fig. 8.5, we illustrate the inversion results for Saxo for the t_u and the S_{Core} indicator. In this case, the results are stunningly different, since no model seems to agree with the inverted results, although the models were fitted to the observations with the same accuracy as for Doris. The difference is particularly significant for the S_{Core} indicators and seems to indicate that something has been wrongly reproduced in the reference models. A small trend is seen with the mean density, as for the results for Doris, but the disagreement is still much larger. For the t_u indicator, the value found is around $1.5 \pm 1 g^2/cm^6$ while the S_{Core} inversion leads to a result around $1.7 \pm 0.06 cm/g^{1/3}$.

8.5 Implications for the modelling of Doris and Saxo

Using the inversion results for Doris, we could define a subsample of reference models, selected in agreement with the determinations of the mean density, the t_u and the S_{Core} indicators. These models are represented in Fig. 8.6, where the blue crosses represent the models of our sample which are in agreement with the inversion procedure, the purple crosses are models found in agreement with some but not all inversion results and the red dots are the models which disagree with the inversion results. We point out that all of these models included microscopic diffusion, so that the selection process is somewhat

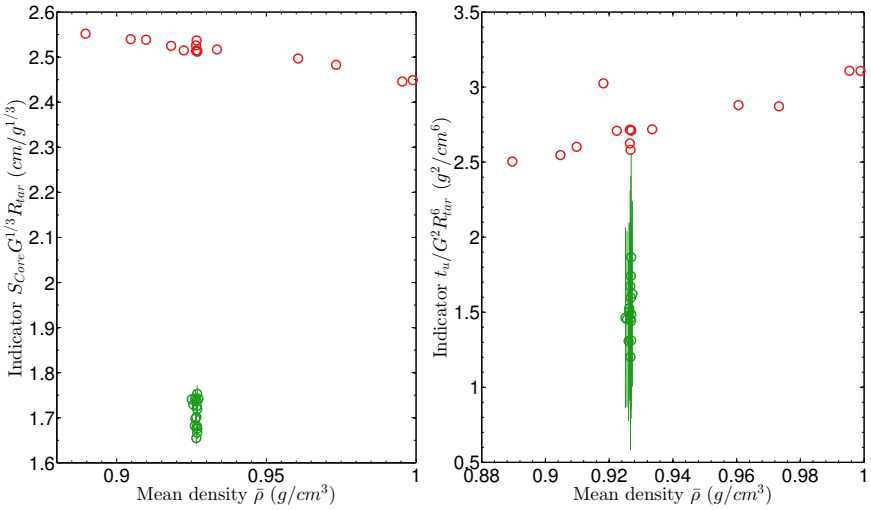

Figure 8.5: Inversion results for Saxo. Left panel: $\bar{\rho} - S_{Core}G^{1/3}R_{tar}$ plane where the red circles illustrate the position of the reference models and the green crosses show the inversion results with their error bars. Right panel: $\bar{\rho} - t_u/(G^2R_{tar}^6)$ plane following the same notations as the left panel.

less spectacular than what is found in our study of 16Cyg. It should be noted however, that models without microscopic diffusion for Doris are systematically rejected by both inversions and have thus not been included in this study. Another point worth mentioning is that unlike 16Cyg, Doris has no determination of its surface helium abundance and thus further constraints could be brought on this model by determining the helium abundance of the convective envelope of this target. This could lead to further studies of this star and constrain mixing processes inside this star, as is currently being done for 16Cyg.

Nonetheless, the use of constraints from the inversions leads us to select a subsample of models with a 2.5% uncertainty in mass and 4.5% uncertainty in age, thus illustrating the diagnostic potential of the inversion technique and its efficiency in constraining fundamental parameters. The selection effect in age is very small since we did not plot models without microscopic diffusion, which were systematically rejected by the inversion technique. These uncertainties are of course internal error bars and do not take into account possible inaccuracies in the physical ingredients of the model.

In the case of Saxo, no model seemed to fit the inverted constraints and thus a solution still has to be found. Moreover, the reliability of the frequencies has to be assessed before further inversions can be carried out. It is well known that the SOLA method is sensitive to outliers and it is also clear that any misfits to the frequencies would significantly affect the inversion results, and thus the diagnostic provided by the method. If these results are confirmed, then it would seem that something is clearly missing in the description of this target and further investigations would be needed.

8.6 Conclusions

In this chapter, we applied the inversions of integrated quantities as defined in D. R. Reese, Marques, et al. (2012) and Buldgen, D. R. Reese, and M. A. Dupret (2015) to two targets of the Kepler LEGACY sample. This sample of 66 dwarfs is considered to be the best sample of solar-like and F-type stars observed by Kepler. This means that these targets can be used as benchmark stars to constrain stellar physics and seismic modelling. Due

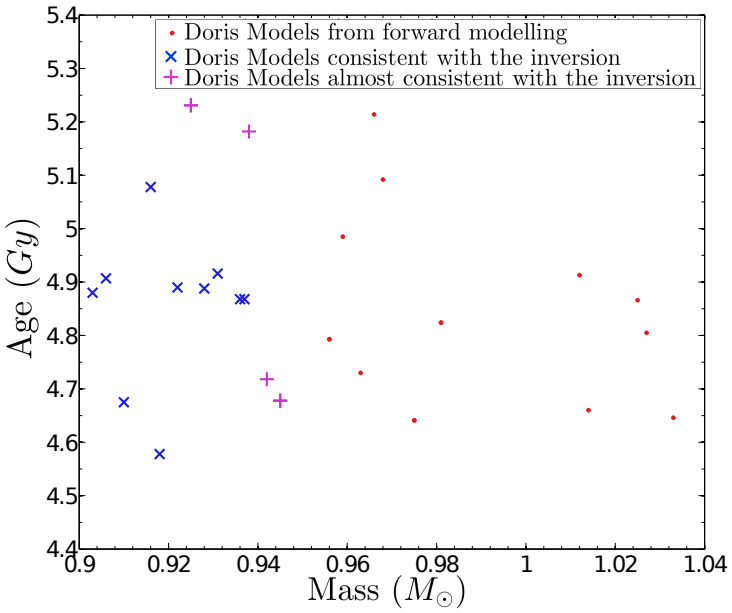

Figure 8.6: Illustration in terms of mass and age of the models validated by the inversions for Doris. The blue crosses are the models in agreement with the inversions, the purple crosses are at the borders of the intervals validated by the inversions and the red dots are rejected by the inversions.

to the high quality of the seismic data, they are very well suited for structural inversion techniques. We demonstrated this by applying our methods to Doris and Saxo, and showed that there was indeed a diagnostic from the inversion technique.

For Doris, this diagnostic allowed us to further constrain the fundamental parameters of this star and led to a final uncertainty of 2.5% in mass and 4.5% in age. These results are, of course, model-dependent and should be considered as internal error bars, not taking into account potential errors in the physical ingredients of the stellar models.

In the case of Saxo, a clear disagreement with the models was brought to light. The main problem with this result, but also with the seismic diagnostic for Doris, is linked to the uncertainties in the frequency determinations of the Kepler LEGACY (see I. W. Roxburgh (2017)). These results should then be checked again once this problem is clarified.

IV CONCLUSIONS AND PERSPECTIVES

9. Discussion, summary and future prospects

9.1 Asteroseismic inversions

In this thesis, we have attempted to provide additional constraints on stellar structure using seismic inversion techniques. The philosophy of our approach was to extract relevant structural constraints one at a time by deriving linear combinations of frequencies using the classical SOLA linear inversion technique used successfully in helioseismology. The main advantage of this method is that it allows us to test specific aspects of stellar structure far beyond what is achievable by classic seismic forward modelling. Consequently, the inversions we developed can put stringent constraints on fundamental parameters of stars and help us refine our stellar structural models.

However, we have shown that our technique could only be applied to some of the best asteroseismic targets available, because despite the very high quality of the data, it is still far worse than solar seismic observations. Another major problem of our technique is its sensitivity to surface effects, which has to be further tested and taken into account in its implementation. So far, empirical corrections such as those of Ball and Gizon (2014) and Sonoi et al. (2015) seem to be the most promising approaches to suppress surface contributions, but complementary techniques could be developed, like those found in D. O. Gough and Kosovichev (1993b) where small frequency separations were used as the primary components of the inversion technique. However, the major drawback with this method is that it partially eliminates the main advantage of the inversion, which is the freedom of choice for the information to be extracted by the technique. By using small frequency separations, or frequency ratios, as the basis of the linear combination derived by the inversion, the process might be biased and the versatility of the inversion, thus its main advantage, will be reduced.

In summary, the optimal strategy to extract information from structural seismic inversion techniques still needs a few refinements in the near future. However, its constraining potential and its applicability to current seismic data are clear. In the foreseable future, the application of such techniques on the Kepler LEGACY sample could shed new light on the quality of the models of solar-like stars, but also on the limitations of

our modelling of solar-like oscillators. Such analyses would not only help further improve the accuracy of stellar models, but also assess in a more realistic way the uncertainties on the stellar fundamental parameters we provide to other fields of astrophysics.

Despite our in-depth investigation of the 16Cyg binary system, the conclusion of section 6.3 is very clear and foretells some of our future projects. Indeed, a full reanalysis of this system, with a various combination of seismic analysis techniques, is in preparation, in collaboration with Patrick Eggenberger from Geneva Observatory and Morgan Deal from Paris Observatory. The extension of such in-depth analyses is also foreseen for the whole Kepler LEGACY sample, using the AIMS software (D. R. Reese (2016)).

On a longer timescale, adapting structural inversion techniques to mixed modes would also be a breakthrough for stellar seismology. It would allow us to probe in a very efficient way the impact of the supposed angular momentum transport mechanisms on other thermodynamic variables and assess how wrong our structural models of evolved stars actually are. From a technical point of view, such adaptations would require the development of well-suited non-linear inversion techniques. Such investigations would also be of primary importance for the young field of Galactic archeology, which strongly relies on accurate fundamental parameters of evolved stars.

These developments are also part of future prospects, but first will require substantial analytical developments. While first explorations have been undertaken, we believe that investigations towards pre-existing formalisms in the field of quantum mechanics, where the variational analysis is much more common, could help provide an elegant approach for mixed modes.

In addition to evolved stars, applying structural inversions to γ Dor stars would also provide important constraints on the internal mixing occuring near the border of convective cores and would probably help refining our modelling of these regions in stellar evolution codes. However, these developments will first require a clear assessment of the validity of the linear approximation for models of γ Dor stars. Exploratory work with gravity modes has been undertaken but will certainly require further substantial developments.

From a purely methodological point of view, it should also be kept in mind that other inversion techniques do exist in asteroseismology and that comparisons between methods should also be attempted to assess the reliability and applicability domains of the various approaches. Combining methodologies would further reinforce potentially important results and confirm the position of asteroseismology as a central field of astrophysics to constrain stellar structure and evolution.

9.2 What's wrong with the Sun?

Besides attempting to constrain the internal structure of solar-like stars, we have also revisited the modelling problem of perhaps the most solar-like of all stars, the Sun itself. We have analysed the agreement of standard solar models for the new opacity tables published by the National Los Alamos Laboratory group. These investigations have shown that using the latest opacity tables slightly improved some aspects of the solar-modelling problem but increased significantly the disagreements of other helioseismic tests. Facing this stalemate, we used the various structural kernels we had developed for asteroseismic applications to determine inverted profiles of various thermodynamic quantities, such as the entropy proxy or the Ledoux convective parameter. These inversions revealed that most of the weaknesses of the standard solar models were located right below the convective region, in the tachocline. The fact that the standard models fail in a region where they are supposed to fail can be considered reassuring, to some extent, but means

that significant efforts have to be made on the theoretical side to improve the quality of our models.

Such developments will require the combination of all the available information, e.g. constraints from neutrinos, spectroscopy (especially lithium and beryllium abundances), and helioseismic inversions. From this global analysis, we can expect to be able to test in depth the effects of the non-standard processes acting in the Sun. As stated in the manuscript, the combination of all seismic diagnostics could be used to provide ad-hoc profiles of temperature and mean molecular weight just below the convective zone, which could be compared to the results of hydrodynamical simulations and help refine the formalism of mixing processes in stellar evolution codes. Moreover, an in-depth comparison of solar models is required, to quantify the level of trust we can have in the numerical quality of our structural models. All these efforts are not to be undertaken alone, but are part of a global project, of which the publications presented in this manuscript are only the very first step. A collaboration between Geneva Observatory, the stellar physics group of Montpellier University and the stellar physics group of the University of Liège currently prepares such a study. The inclusion of additional participants to this collaborative effort is also foreseen, since the expertise of multiple actors is required to assess the solar problem in its full complexity.

In addition to p mode seismology, the recent detection of solar gravity modes (Fossat et al. (2017)) is a game changer since these pulsations are able to put very strong constraints on the central temperature of the Sun and complement the neutrino measurements.

From early analyses not presented in this manuscript, we confirm that standard solar models show an asymptotic period spacing between 35 and 36 min, as shown in previous publications in the litterature (e.g. Provost et al. (1991)). These values are in strong contradiction with the value of 34 min observed by Fossat et al. (2017) and are found for the CEFF, OPAL and FreeEOS equations of state, when using either the OPAL, OPLIB or OPAS opacity tables alongside either high or low metallicity abundances. This clear disagreement between models and observations adds up to the current uncertainties on the physical ingredients of solar models. The shift in period spacing could result from the effects of mixing, since the rotation rate of the solar core predicted from the splitting of the g modes is found to be nearly 4 times larger than that of the upper radiative layers. However, other structural ingredients, such as the screening factors or perhaps the cross-sections of the nuclear reaction rates could perhaps suffer from inaccuracies of a few percents, which would alter the period spacing of the models. The alteration of the Brunt-Väisälä frequency required to agree with the observed asymptotic period spacing would of course result in variations in the neutrino fluxes and could radically change the scenery of the solar modelling problem.

However, it should also be kept in mind that the issue will of course also be influenced by the outcome of the current debate in the opacity community and that, perhaps now more than ever, the stellar modelling community relies on the results of atomic physics. Nervertheless, investigations can still be carried out from a stellar modelling perspective, by combining the information from rotation inversions with the expected impact on the solar structure of the transport processes required to be consistent with the solar rotation profile. Again, solar gravity modes exert here an enormous influence, since they strongly constrain the type and efficiency of the expected physical mechanism. Ultimately, the solar modelling problem is perhaps as much a problem of combining all the pieces of a puzzle together as one of adding new pieces to the game. However, what seems to be very clear, is that the standard solar model is now showing its limitations and we have to step away from its recipe if we want to bring stellar physics to a new level of accuracy.

BIBLIOGRAPHY

Acevedo-Arreguin, L. A., P. Garaud, and T. S. Wood (2013). "Dynamics of the solar tachocline - III. Numerical solutions of the Gough and McIntyre model". In: *MNRAS* 434, pages 720–741 (cited on page 256).

Aerts, C., J. Christensen-Dalsgaard, and D. W. Kurtz (2010). *Asteroseismology* (cited on page 50).

Anders, E. and N. Grevesse (1989). "Abundances of the elements - Meteoritic and solar". In: *Geochimica et Cosmochimica Acta* 53, pages 197–214 (cited on pages 223, 251).

Angulo, C. et al. (1999). "A compilation of charged-particle induced thermonuclear reaction rates". In: *Nuclear Physics A* 656, pages 3–183 (cited on pages 92, 179, 198, 241, 270).

Antia, H. M. (1996). "Nonasymptotic helioseismic inversion: iterated seismic solar model." In: *A&Ap* 307, pages 609–623 (cited on pages 17, 222).

Antia, H. M. and S. Basu (1994a). "Measuring the helium abundance in the solar envelope: The role of the equation of state". In: *ApJ* 426, pages 801–811 (cited on pages 154, 222).

— (1994b). "Nonasymptotic helioseismic inversion for solar structure." In: *A&Aps* 107, pages 421–444 (cited on pages 13, 109, 154, 222, 224, 226).

— (2006). "Determining Solar Abundances Using Helioseismology". In: *ApJ* 644, pages 1292–1298 (cited on pages 223, 236).

Antia, H. M. and S. M. Chitre (1998). "Determination of temperature and chemical composition profiles in the solar interior from seismic models". In: *A&Ap* 339, pages 239–251 (cited on page 256).

Appourchaux, T. et al. (2014). "Oscillation mode linewidths and heights of 23 main-sequence stars observed by Kepler". In: *A&Ap* 566, A20 (cited on page 76).

Asplund, M., N. Grevesse, and A. J. Sauval (2005). "The Solar Chemical Composition". In: *Cosmic Abundances as Records of Stellar Evolution and Nucleosynthesis*. Edited by T. G. Barnes III and F. N. Bash. Volume 336. Astronomical Society of the Pacific Conference Series, page 25 (cited on pages 118, 236, 251).

Asplund, M., N. Grevesse, A. J. Sauval, C. Allende Prieto, and R. Blomme (2005). "Line formation in solar granulation. VI. [C I], C I, CH and C_2 lines and the photospheric C abundance". In: *A&Ap* 431, pages 693–705 (cited on pages 223, 225).

Asplund, M., N. Grevesse, A. J. Sauval, C. Allende Prieto, and D. Kiselman (2004). "Line formation in solar granulation. IV. [O I], O I and OH lines and the photospheric O abundance". In: *A&Ap* 417, pages 751–768 (cited on pages 223, 225).

Asplund, M., N. Grevesse, A. J. Sauval, and P. Scott (2009). "The Chemical Composition of the Sun". In: *ARA&A* 47, pages 481–522 (cited on pages 98, 145, 168, 180, 199, 223, 225, 236, 257, 270).

Backus, G. E. and J. F. Gilbert (1967). "Numerical Applications of a Formalism for Geophysical Inverse Problems". In: *Geophysical Journal* 13, pages 247–276 (cited on pages 68, 71, 110, 160, 203, 240).

Baglin, A. et al. (2009). "CoRoT: Description of the Mission and Early Results". In: *IAU Symposium*. Edited by F. Pont, D. Sasselov, and M. J. Holman. Volume 253. IAU Symposium, pages 71–81 (cited on pages 14, 82, 155).

Bahcall, J. N., W. F. Huebner, et al. (1982). "Standard solar models and the uncertainties in predicted capture rates of solar neutrinos". In: *Reviews of Modern Physics* 54, pages 767–799 (cited on pages 14, 222).

Bahcall, J. N. and C. Peña-Garay (2004). "Solar models and solar neutrino oscillations". In: *New Journal of Physics* 6, page 63 (cited on pages 14, 224).

Bailey, J. E. et al. (2015). "A higher-than-predicted measurement of iron opacity at solar interior temperatures". In: *Nature* 517, page 3 (cited on pages 223, 225, 229, 255).

Ball, W. H., B. Beeck, et al. (2016). "MESA meets MURaM. Surface effects in main-sequence solar-like oscillators computed using three-dimensional radiation hydrodynamics simulations". In: *A&Ap* 592, A159 (cited on page 76).

Ball, W. H. and L. Gizon (2014). "A new correction of stellar oscillation frequencies for near-surface effects". In: *A&Ap* 568, A123 (cited on pages 76, 172, 279).

Basu, S. (2003). "Stellar Inversions". In: *ApSS* 284, pages 153–164 (cited on pages 17, 84, 100, 135, 154, 155, 160).

— (2016). "Global seismology of the Sun". In: *Living Reviews in Solar Physics* 13, page 2 (cited on page 17).

Basu, S. and H. M. Antia (1995). "Helium abundance in the solar envelope". In: *MNRAS* 276, pages 1402–1408 (cited on pages 222, 224, 235).

— (1997a). "Seismic measurement of the depth of the solar convection zone". In: *MNRAS* 287, pages 189–198 (cited on pages 222, 235).

— (1997b). "Seismic measurement of the depth of the solar convection zone". In: *MNRAS* 287, pages 189–198 (cited on page 224).

— (2006). "Seismic Determination of Solar Heavy Element Abundances". In: *SOHO-17. 10 Years of SOHO and Beyond*. Volume 617. ESA Special Publication, page 36.1 (cited on pages 223, 225).

— (2008). "Helioseismology and solar abundances". In: *Physics Reports* 457, pages 217–283 (cited on pages 82, 225).

Basu, S., W. J. Chaplin, et al. (2009). "Fresh Insights on the Structure of the Solar Core". In: *ApJ* 699, pages 1403–1417 (cited on pages 76, 205, 226, 242, 257, 270).

Basu, S. and J. Christensen-Dalsgaard (1997a). "Equation of state and helioseismic inversions." In: *A&Ap* 322, pages L5–L8 (cited on pages 66, 67).

— (1997b). "Equation of state and helioseismic inversions." In: *A&Ap* 322, pages L5–L8 (cited on page 178).

Basu, S., J. Christensen-Dalsgaard, W. J. Chaplin, et al. (1997). "Solar internal sound speed as inferred from combined BiSON and LOWL oscillation frequencies". In: *MNRAS* 292, page 243 (cited on page 178).

Basu, S., J. Christensen-Dalsgaard, J. Schou, et al. (1996). "Solar structure as revealed by 1 year LOWL data". In: *Bulletin of the Astronomical Society of India* 24, page 147 (cited on pages 13, 133, 141, 178, 222, 236).

Basu, S. and M. J. Thompson (1996). "On constructing seismic models of the Sun." In: *A&Ap* 305, page 631 (cited on page 228).

Basu, S. et al. (1996a). "Filtering out near-surface uncertainties from helioseismic inversions". In: *MNRAS* 280, page 651 (cited on page 75).

— (1996b). "Filtering out near-surface uncertainties from helioseismic inversions". In: *MNRAS* 280, page 651 (cited on page 134).

Baturin, V. A. et al. (2013). "The Current Version of the SAHA-S Equation of State: Improvement and Perspective". In: *Progress in Physics of the Sun and Stars: A New Era in Helio- and Asteroseismology*. Edited by H. Shibahashi and A. E. Lynas-Gray. Volume 479. Astronomical Society of the Pacific Conference Series, page 11 (cited on pages 27, 32, 224, 255).

Baudin, F. et al. (2012). "Modelling a high-mass red giant observed by CoRoT". In: *A&Ap* 538, A73 (cited on page 194).

Bazot, M., S. Bourguignon, and J. Christensen-Dalsgaard (2012). "A Bayesian approach to the modelling of α Cen A". In: *MNRAS* 427, pages 1847–1866 (cited on page 107).

Beck, P. G., T. R. Bedding, et al. (2011). "Kepler Detected Gravity-Mode Period Spacings in a Red Giant Star". In: *Science* 332, page 205 (cited on page 43).

Beck, P. G., J. Montalban, et al. (2012). "Fast core rotation in red-giant stars as revealed by gravity-dominated mixed modes". In: *Nature* 481, pages 55–57 (cited on page 51).

Bedding, T. R., R. P. Butler, et al. (2001). "Evidence for Solar-like Oscillations in β Hydri". In: *ApJl* 549, pages L105–L108 (cited on page 14).

Bedding, T. R., B. Mosser, et al. (2011). "Gravity modes as a way to distinguish between hydrogen- and helium-burning red giant stars". In: *Nature* 471, pages 608–611 (cited on pages 43, 51).

Belkacem, K., M. J. Goupil, et al. (2011). "The underlying physical meaning of the ν_{max} - ν_c relation". In: *A&Ap* 530, A142 (cited on pages 49, 51).

Belkacem, K., J. P. Marques, M. J. Goupil, B. Mosser, et al. (2015). "Angular momentum redistribution by mixed modes in evolved low-mass stars. II. Spin-down of the core of red giants induced by mixed modes". In: *A&Ap* 579, A31 (cited on page 43).

Belkacem, K., J. P. Marques, M. J. Goupil, T. Sonoi, et al. (2015). "Angular momentum redistribution by mixed modes in evolved low-mass stars. I. Theoretical formalism". In: *A&Ap* 579, A30 (cited on page 43).

Belkacem, K., R. Samadi, et al. (2009). "Solar-Like Oscillations in a Massive Star". In: *Science* 324, page 1540 (cited on page 51).

Blancard, C., J. Colgan, et al. (2016). "Comment on "Large Enhancement in High-Energy Photoionization of Fe XVII and Missing Continuum Plasma Opacity"". In: *Physical Review Letters* 117.24, page 249501 (cited on pages 223, 229, 255).

Blancard, C., P. Cossé, and G. Faussurier (2012). "Solar Mixture Opacity Calculations Using Detailed Configuration and Level Accounting Treatments". In: *ApJ* 745, page 10 (cited on page 225).

Böhm-Vitense, E. (1958). "Über die Wasserstoffkonvektionszone in Sternen verschiedener Effektivtemperaturen und Leuchtkräfte. Mit 5 Textabbildungen". In: *Zeitschrift für Astrophysik* 46, page 108 (cited on pages 29, 92, 179, 198, 241, 270).

Borucki, W. J. et al. (2010). "Kepler Planet-Detection Mission: Introduction and First Results". In: *Science* 327, pages 977– (cited on pages 14, 82, 155).

Bouabid, M. P. (2011). "Effets des paramètres physiques et de la rotation modérées sur les propriétés simisiques des étoiles γ Doradus". PhD thesis. Université de Liège (cited on pages 42, 46).

Bouchy, F. and F. Carrier (2001). "P-mode observations on α Cen A". In: *A&Ap* 374, pages L5–L8 (cited on page 14).

Brodsky, M. and S. V. Vorontsov (1993). "Asymptotic theory of intermediate- and high-degree solar acoustic oscillations". In: *ApJ* 409, pages 455–464 (cited on page 45).

Brookes, J. R., G. R. Isaak, and H. B. van der Raay (1976). "Observation of free oscillations of the sun". In: *Nature* 259, pages 92–95 (cited on page 221).

Brown, J. M., P. Garaud, and S. Stellmach (2013). "Chemical Transport and Spontaneous Layer Formation in Fingering Convection in Astrophysics". In: *ApJ* 768, page 34 (cited on page 34).

Brown, T. M., J. Christensen-Dalsgaard, W. A. Dziembowski, et al. (1989). "Inferring the sun's internal angular velocity from observed p-mode frequency splittings". In: *ApJ* 343, pages 526–546 (cited on page 236).

Brown, T. M., J. Christensen-Dalsgaard, B. Weibel-Mihalas, et al. (1994). "The effectiveness of oscillation frequencies in constraining stellar model parameters". In: *ApJ* 427, pages 1013–1034 (cited on page 132).

Brown, T. M., R. L. Gilliland, et al. (1991). "Detection of possible p-mode oscillations on Procyon". In: *ApJ* 368, pages 599–609 (cited on page 14).

Brown, T. M. and C. A. Morrow (1987). "Depth and latitude dependence of solar rotation". In: *ApJl* 314, pages L21–L26 (cited on page 221).

Brun, A. S., H. M. Antia, et al. (2002). "Seismic tests for solar models with tachocline mixing". In: *A&Ap* 391, pages 725–739 (cited on page 257).

Brun, A. S., M. S. Miesch, and J. Toomre (2011). "Modeling the Dynamical Coupling of Solar Convection with the Radiative Interior". In: *ApJ* 742, page 79 (cited on page 256).

Buldgen, G., D. R. Reese, and M. A. Dupret (2015). "Using seismic inversions to obtain an indicator of internal mixing processes in main-sequence solar-like stars". In: *A&Ap* 583, A62 (cited on pages 84, 85, 100, 106, 155, 156, 162, 165–168, 178, 182, 186, 201–204, 207, 216, 241, 270, 272, 275).

— (2016). "Constraints on the structure of 16 Cygni A and 16 Cygni B using inversion techniques". In: *A&Ap* 585, A109 (cited on pages 177, 197, 198, 206, 212, 271, 274).

— (2017). "Analysis of the linear approximation of seismic inversions for various structural pairs". In: *A&Ap* 598, A21 (cited on pages 81, 155–158, 228, 237).

Buldgen, G., D. R. Reese, M. A. Dupret, and R. Samadi (2015). "Stellar acoustic radii, mean densities, and ages from seismic inversion techniques". In: *A&Ap* 574, A42 (cited on pages 106, 133, 140–145, 153, 155, 162, 178, 182, 201, 216).

Buldgen, G., D. Reese, and M.-A. Dupret (2017). "Asteroseismic inversions in the Kepler era: application to the Kepler Legacy sample". In: *ArXiv e-prints* (cited on pages 170, 269).

Buldgen, G., S. J. A. J. Salmon, et al. (2016). "In-depth study of 16CygB using inversion techniques". In: *A&Ap* 596, A73 (cited on page 177).

Busse, F. H. (1981). "Do Eddington-Sweet circulations exist". In: *Geophysical and Astrophysical Fluid Dynamics* 17, pages 215–235 (cited on page 30).

Caffau, E. et al. (2011). "Solar Chemical Abundances Determined with a CO5BOLD 3D Model Atmosphere". In: *Sol. Phys.* 268, pages 255–269 (cited on pages 223, 236, 251).

Canuto, V. M., I. Goldman, and I. Mazzitelli (1996). "Stellar Turbulent Convection: A Self-consistent Model". In: *ApJ* 473, page 550 (cited on pages 26, 29).

Cassisi, S. et al. (2007). "Updated Electron-Conduction Opacities: The Impact on Low-Mass Stellar Models". In: *ApJ* 661, pages 1094–1104 (cited on pages 92, 179, 241).

Castro, M., S. Vauclair, and O. Richard (2007). "Low abundances of heavy elements in the solar outer layers: comparisons of solar models with helioseismic inversions". In: *A&Ap* 463, pages 755–758 (cited on page 225).

Chandrasekhar, S. (1964). "A General Variational Principle Governing the Radial and the Non-Radial Oscillations of Gaseous Masses." In: *ApJ* 139, page 664 (cited on pages 53, 60, 82).

Chaplin, W. J., S. Basu, et al. (2014). "Asteroseismic Fundamental Properties of Solar-type Stars Observed by the NASA Kepler Mission". In: *ApJs* 210, page 1 (cited on page 219).

Chaplin, W. J., M. N. Lund, et al. (2015). "Asteroseismology of Solar-Type Stars with K2: Detection of Oscillations in C1 Data". In: *Publications of the Astronomical Society of Pacific* 127, pages 1038–1044 (cited on page 82).

Chaplin, W. J. and A. Miglio (2013). "Asteroseismology of Solar-Type and Red-Giant Stars". In: *ARA&A* 51, pages 353–392 (cited on pages 14, 49, 51, 107).

Chaplin, W. J., A. M. Serenelli, et al. (2007). "Solar Heavy-Element Abundance: Constraints from Frequency Separation Ratios of Low-Degree p-Modes". In: *ApJ* 670, pages 872–884 (cited on page 231).

Charbonnel, C. and S. Talon (2005). "Influence of Gravity Waves on the Internal Rotation and Li Abundance of Solar-Type Stars". In: *Science* 309, pages 2189–2191 (cited on pages 31, 221).

Charpinet, S. et al. (2008). "Testing the forward modeling approach in asteroseismology. II. Structure and internal dynamics of the hot B subdwarf component in the close eclipsing binary system PG 1336-018". In: *A&Ap* 489, pages 377–394 (cited on pages 107, 118).

Chené, A.-N. et al. (2011). "A 10-h period revealed in optical spectra of the highly variable WN8 Wolf-Rayet star WR 123". In: *A&Ap* 530, A151 (cited on page 49).

Christensen-Dalsgaard, J. (1986). "Theoretical aspects of helio- and asteroseismology". In: *NATO ASIC Proc. 169: Seismology of the Sun and the Distant Stars*. Edited by D. O. Gough, pages 23–53 (cited on page 109).

— (1991). "Some aspects of the theory of solar oscillations". In: *Geophysical and Astrophysical Fluid Dynamics* 62, pages 123–152 (cited on page 112).

— (1993a). "On the Asteroseismic HR Diagram". In: *GONG 1992. Seismic Investigation of the Sun and Stars*. Edited by T. M. Brown. Volume 42. Astronomical Society of the Pacific Conference Series, page 347 (cited on pages 45, 112).

— (1993b). "On the Asteroseismic HR Diagram". In: *GONG 1992. Seismic Investigation of the Sun and Stars*. Edited by T. M. Brown. Volume 42. Astronomical Society of the Pacific Conference Series, page 347 (cited on page 46).

— (2002). "Helioseismology". In: *Reviews of Modern Physics* 74, pages 1073–1129 (cited on pages 17, 178).

— (2003). "Lecture Notes on Stellar Oscillations" (cited on pages 50, 74, 75).

— (2012). "Stellar model fits and inversions". In: *Astronomische Nachrichten* 333, page 914 (cited on page 51).

Christensen-Dalsgaard, J. and W. Daeppen (1992). "Solar oscillations and the equation of state". In: *Astronomy and Astrophysics Review* 4, pages 267–361 (cited on pages 27, 32, 92, 168, 179, 198, 239, 270).

Christensen-Dalsgaard, J., W. Dappen, et al. (1996). "The Current State of Solar Modeling". In: *Science* 272, pages 1286–1292 (cited on page 226).

Christensen-Dalsgaard, J., T. L. Duvall Jr., et al. (1985). "Speed of sound in the solar interior". In: *Nature* 315, pages 378–382 (cited on pages 17, 222).

Christensen-Dalsgaard, J., D. O. Gough, and F. Perez Hernandez (1988). "Stellar disharmony". In: *MNRAS* 235, pages 875–880 (cited on page 75).

Christensen-Dalsgaard, J., D. O. Gough, and M. J. Thompson (1991). "The depth of the solar convection zone". In: *ApJ* 378, pages 413–437 (cited on page 224).

Christensen-Dalsgaard, J., D. Gough, and J. Toomre (1985). "Seismology of the sun". In: *Science* 229, pages 923–931 (cited on page 13).

Christensen-Dalsgaard, J., M. J. P. F. G. Monteiro, et al. (2011). "A more realistic representation of overshoot at the base of the solar convective envelope as seen by helioseismology". In: *MNRAS* 414, pages 1158–1174 (cited on page 256).

Christensen-Dalsgaard, J. and M. J. Thompson (1997). "On solar p-mode frequency shifts caused by near-surface model changes". In: *MNRAS* 284, pages 527–540 (cited on page 61).

Claret, A. and G. Torres (2016). "The dependence of convective core overshooting on stellar mass". In: *A&Ap* 592, A15 (cited on page 161).

Claverie, A. et al. (1979). "Solar structure from global studies of the 5-minute oscillation". In: *Nature* 282, pages 591–594 (cited on page 13).

Clement, M. J. (1964). "A General Variational Principle Governing the Oscillations of a Rotating Gaseous Mass." In: *ApJ* 140, page 1045 (cited on pages 53, 82).

Cochran, W. D. et al. (1997). "The Discovery of a Planetary Companion to 16 Cygni B". In: *ApJ* 483, pages 457–463 (cited on pages 178, 197).

Cody, A. M. (2012). "A Search for Pulsation in Young Brown Dwarfs and Very Low Mass Stars". PhD thesis. California Institute of Technology (cited on page 49).

Colgan, J. et al. (2016). "A New Generation of Los Alamos Opacity Tables". In: *ApJ* 817, page 116 (cited on pages 33, 177, 225, 232, 241, 252, 257).

Corbard, T. et al. (1999). "Non linear regularization for helioseismic inversions. Application for the study of the solar tachocline". In: *A&Ap* 344, pages 696–708 (cited on pages 17, 256, 262).

Couvidat, S. and S. Turck-Chieze (2004). "The solar neutrino puzzle". In: *Frontiers of the Universe*. Edited by L. Celnikier and J. T. Thanh van, page 191 (cited on page 224).

Cox, A. N. et al. (1992). "An opacity mechanism for the pulsations of OB stars". In: *ApJ* 393, pages 272–277 (cited on page 34).

Cox, J. P. (1980). *Theory of stellar pulsation* (cited on page 50).

Cugier, H. (2012). "Testing the opacity and equation of state of LTE and non-LTE model atmospheres with OPAL and OP data for early-type stars". In: *A&Ap* 547, A42 (cited on page 225).

Daeppen, W. et al. (1988). "The equation of state for stellar envelopes. III - Thermodynamic quantities". In: *ApJ* 332, pages 261–270 (cited on pages 27, 32).

Däppen, W. et al. (1991). "A New Inversion for the Hydrostatic Stratification of the Sun". In: *Challenges to Theories of the Structure of Moderate-Mass Stars*. Edited by D. Gough and J. Toomre. Volume 388. Lecture Notes in Physics, Berlin Springer Verlag, page 111 (cited on page 134).

Davies, G. R. et al. (2015). "Asteroseismic inference on rotation, gyrochronology and planetary system dynamics of 16 Cygni". In: *MNRAS* 446, pages 2959–2966 (cited on pages 45, 71, 177–179, 181, 195, 197–199).

De Ridder, J. et al. (2009). "Non-radial oscillation modes with long lifetimes in giant stars". In: *Nature* 459, pages 398–400 (cited on page 14).

Deal, M., O. Richard, and S. Vauclair (2015). "Accretion of planetary matter and the lithium problem in the 16 Cygni stellar system". In: *A&Ap* 584, A105 (cited on pages 198, 215).
— (2016). "Hydrodynamical instabilities induced by atomic diffusion in A stars and their consequences". In: *A&Ap* 589, A140 (cited on page 34).
Degroote, P. et al. (2010). "Detection of frequency spacings in the young O-type binary HD 46149 from CoRoT photometry". In: *A&Ap* 519, A38 (cited on page 51).
Deheuvels, S., I. Brandão, et al. (2016). "Measuring the extent of convective cores in low-mass stars using Kepler data: toward a calibration of core overshooting". In: *A&Ap* 589, A93 (cited on page 161).
Deheuvels, S., G. Doğan, et al. (2014). "Seismic constraints on the radial dependence of the internal rotation profiles of six Kepler subgiants and young red giants". In: *A&Ap* 564, A27 (cited on pages 24, 31, 43, 51, 133, 226).
Deheuvels, S., R. A. García, et al. (2012). "Seismic Evidence for a Rapidly Rotating Core in a Lower-giant-branch Star Observed with Kepler". In: *ApJ* 756, page 19 (cited on page 31).
Deliyannis, C. P. et al. (2000). "Beryllium and Iron Abundances of the Solar Twins 16 Cygni A and B". In: *Astr. J.* 119, pages 2437–2444 (cited on page 199).
Denissenkov, P. A. (2010). "Numerical Simulations of Thermohaline Convection: Implications for Extra-mixing in Low-mass RGB Stars". In: *ApJ* 723, pages 563–579 (cited on page 34).
Deubner, F.-L. (1975). "Observations of low wavenumber nonradial eigenmodes of the sun". In: *A&Ap* 44, pages 371–375 (cited on pages 13, 221).
Deubner, F.-L., R. K. Ulrich, and E. J. Rhodes Jr. (1979). "Solar p-mode oscillations as a tracer of radial differential rotation". In: *A&Ap* 72, pages 177–185 (cited on page 13).
Dupret, M. A. (2001). "Nonradial nonadiabatic stellar pulsations: A numerical method and its application to a beta Cephei model". In: *A&Ap* 366, pages 166–173 (cited on pages 122, 126).
Dupret, M.-A. (2008). "Problems and prospects in stellar physics". In: *Communications in Asteroseismology* 157, pages 16–21 (cited on page 133).
Dupret, M.-A., K. Belkacem, et al. (2009). "Theoretical amplitudes and lifetimes of non-radial solar-like oscillations in red giants". In: *A&Ap* 506, pages 57–67 (cited on page 14).
Dupret, M.-A., A. Grigahcène, et al. (2005). "Convection-pulsation coupling. II. Excitation and stabilization mechanisms in δ Sct and γ Dor stars". In: *A&Ap* 435, pages 927–939 (cited on page 49).
Dupret, M.-A., R. Samadi, et al. (2006). "Non-local time-dependent treatments of convection in A-G type stars". In: *Communications in Asteroseismology* 147, pages 85–88 (cited on pages 122, 126).
Duvall Jr., T. L. (1982). "A dispersion law for solar oscillations". In: *Nature* 300, page 242 (cited on pages 44, 222).
Dziembowski, W. A. and A. A. Pamiatnykh (1993). "The opacity mechanism in B-type stars. I - Unstable modes in Beta Cephei star models". In: *MNRAS* 262, pages 204–212 (cited on page 34).
Dziembowski, W. A., A. A. Pamyatnykh, and R. Sienkiewicz (1990). "Solar model from helioseismology and the neutrino flux problem". In: *MNRAS* 244, pages 542–550 (cited on pages 17, 60, 134, 155, 156).
Eggenberger, P., A. Maeder, and G. Meynet (2005). "Stellar evolution with rotation and magnetic fields. IV. The solar rotation profile". In: *A&Ap* 440, pages L9–L12 (cited on pages 31, 221).
Eggenberger, P., G. Meynet, et al. (2010). "Effects of rotational mixing on the asteroseismic properties of solar-type stars". In: *A&Ap* 519, A116 (cited on page 132).

Elliott, J. R. (1996). "Equation of state in the solar convection zone and the implications of helioseismology". In: *MNRAS* 280, pages 1244–1256 (cited on pages 88, 134, 237).

Elliott, J. R. and D. O. Gough (1999). "Calibration of the Thickness of the Solar Tachocline". In: *ApJ* 516, pages 475–481 (cited on page 256).

Elsworth, Y. et al. (1990). "Evidence from solar seismology against non-standard solar-core models". In: *Nature* 347, pages 536–539 (cited on pages 133, 224).

Ferguson, J. W. et al. (2005). "Low-Temperature Opacities". In: *ApJ* 623, pages 585–596 (cited on pages 92, 179, 198, 241, 270).

Formicola, A. et al. (2004). "Astrophysical S-factor of ^{14}N(p,γ)^{15}O". In: *Physics Letters B* 591, pages 61–68 (cited on pages 92, 179, 198, 241, 270).

Fossat, E. et al. (2017). "Asymptotic g modes: Evidence for a rapid rotation of the solar core". In: *ArXiv e-prints* (cited on page 281).

Frazier, E. N. (1968). "An Observational Study of the Hydrodynamics of the Lower Solar Photosphere". In: *ApJ* 152, page 557 (cited on page 221).

Gabriel, M., A. Noels, et al. (2014). "Proper use of Schwarzschild Ledoux criteria in stellar evolution computations". In: *A&Ap* 569, A63 (cited on pages 26, 156).

Gabriel, M. and R. Scuflaire (1979). "Properties of non-radial stellar oscillations". In: *Acta Astronomica* 29, pages 135–149 (cited on page 41).

Garaud, P. (2002). "Dynamics of the solar tachocline - I. An incompressible study". In: *MNRAS* 329, pages 1–17 (cited on page 256).

Garaud, P. and J.-D. Garaud (2008). "Dynamics of the solar tachocline - II. The stratified case". In: *MNRAS* 391, pages 1239–1258 (cited on page 256).

Gizon, L. and A. C. Birch (2005). "Local Helioseismology". In: *Living Reviews in Solar Physics* 2, page 6 (cited on page 17).

Gough, D. (1985). "Inverting helioseismic data". In: *Sol. Phys.* 100, pages 65–99 (cited on pages 16, 118).

Gough, D. O. (1986). "EBK Quantization of Stellar Waves". In: *Hydrodynamic and Magnetodynamic Problems in the Sun and Stars*. Edited by Y. Osaki, page 117 (cited on page 45).

Gough, D. O. and A. G. Kosovichev (1988). "An attempt to understand the Stanford p-mode data". In: *Seismology of the Sun and Sun-Like Stars*. Edited by E. J. Rolfe. Volume 286. ESA Special Publication (cited on page 81).

— (1993a). "Initial asteroseismic inversions". In: *IAU Colloq. 137: Inside the Stars*. Edited by W. W. Weiss and A. Baglin. Volume 40. Astronomical Society of the Pacific Conference Series, page 541 (cited on pages 17, 81, 155, 257).

— (1993b). "Seismic Analysis of Stellar P-Mode Spectra". In: *GONG 1992. Seismic Investigation of the Sun and Stars*. Edited by T. M. Brown. Volume 42. Astronomical Society of the Pacific Conference Series, page 351 (cited on pages 17, 81, 155, 257, 279).

Gough, D. O. and M. J. Thompson (1991). "The inversion problem". In: *Solar Interior and Atmosphere*. Edited by A. N. Cox, W. C. Livingston, and M. S. Matthews, pages 519–561 (cited on pages 83, 85, 109, 111, 134, 201, 272).

Grevesse, N. and A. Noels (1993). "Cosmic abundances of the elements." In: *Origin and Evolution of the Elements*. Edited by N. Prantzos, E. Vangioni-Flam, and M. Casse, pages 15–25 (cited on pages 98, 118, 144, 168, 199, 223, 224, 236, 241, 251, 257, 270).

Grevesse, N. and A. J. Sauval (1998). "Standard Solar Composition". In: *Space Science Reviews* 85, pages 161–174 (cited on pages 223, 224, 236, 251, 257).

Grigahcène, A. et al. (2005). "Convection-pulsation coupling. I. A mixing-length perturbative theory". In: *A&Ap* 434, pages 1055–1062 (cited on page 126).

Gruberbauer, M. et al. (2013). "Bayesian asteroseismology of 23 solar-like Kepler targets". In: *MNRAS* 435, pages 242–254 (cited on pages 178, 180).

Grundahl, F. et al. (2007). "Stellar Oscillations Network Group". In: *Communications in Asteroseismology* 150, page 300 (cited on page 154).

Guzik, J. A., C. Fontes, et al. (2015). "Sound speed and oscillation frequencies for a solar model evolved with Los Alamos ATOMIC opacities". In: *IAU General Assembly* 22, page 2253707 (cited on pages 226, 227).

Guzik, J. A., A. B. Kaye, et al. (2000). "Driving the Gravity-Mode Pulsations in γ Doradus Variables". In: *ApJL* 542, pages L57–L60 (cited on page 49).

Hauser, H. M. and G. W. Marcy (1999). "The Orbit of 16 Cygni AB". In: *Publications of the Astronomical Society of Pacific* 111, pages 321–334 (cited on page 197).

Hirschi, R., G. Meynet, and A. Maeder (2004). "Stellar evolution with rotation. XII. Pre-supernova models". In: *A&Ap* 425, pages 649–670 (cited on page 30).

— (2005). "Stellar evolution with rotation. XIII. Predicted GRB rates at various Z". In: *A&Ap* 443, pages 581–591 (cited on page 30).

Holman, M., J. Touma, and S. Tremaine (1997). "Chaotic variations in the eccentricity of the planet orbiting 16 Cygni B". In: *Nature* 386, pages 254–256 (cited on page 197).

Houdek, G. and D. O. Gough (2007). "An asteroseismic signature of helium ionization". In: *MNRAS* 375, pages 861–880 (cited on page 16).

Houdek, G., R. Trampedach, et al. (2017). "On the surface physics affecting solar oscillation frequencies". In: *MNRAS* 464 (cited on page 76).

Hughes, D. W., R. Rosner, and N. O. Weiss (2007). *The Solar Tachocline* (cited on pages 255, 256).

Hummer, D. G. and D. Mihalas (1988). "The equation of state for stellar envelopes. I - an occupation probability formalism for the truncation of internal partition functions". In: *ApJ* 331, pages 794–814 (cited on pages 27, 32).

Iglesias, C. A. and S. B. Hansen (2017). "Fe XVII Opacity at Solar Interior Conditions". In: *ApJ* 835, page 284 (cited on pages 223, 224, 229, 255).

Iglesias, C. A. and F. J. Rogers (1996). "Updated Opal Opacities". In: *ApJ* 464, page 943 (cited on pages 33, 92, 168, 179, 198, 223, 225, 226, 252, 257, 270).

Irwin, A. W. (2012). *FreeEOS: Equation of State for stellar interiors calculations*. Astrophysics Source Code Library (cited on pages 27, 32, 177, 239, 257).

Kallinger, T. et al. (2010). "Oscillating red giants in the CoRoT exofield: asteroseismic mass and radius determination". In: *A&Ap* 509, A77 (cited on page 15).

King, J. R. et al. (1997). "Lithium Abundances in the Solar Twins 16 CYG A and B and the Solar Analog alpha CEN A, Calibration of the 6707 Angstrom Li Region Linelist, and Implications". In: *Astr. J.* 113, page 1871 (cited on page 214).

Kippenhahn, R., A. Weigert, and A. Weiss (2012). *Stellar Structure and Evolution* (cited on pages 21, 49).

Kjeldsen, H. and T. R. Bedding (1995). "Amplitudes of stellar oscillations: the implications for asteroseismology." In: *A&Ap* 293, pages 87–106 (cited on page 51).

Kjeldsen, H., T. R. Bedding, I. K. Baldry, et al. (2003). "Confirmation of Solar-like Oscillations in η Bootis". In: *Astr. J.* 126, pages 1483–1488 (cited on page 14).

Kjeldsen, H., T. R. Bedding, and J. Christensen-Dalsgaard (2008). "Correcting Stellar Oscillation Frequencies for Near-Surface Effects". In: *ApJl* 683, pages L175–L178 (cited on pages 76, 117, 127, 179).

Kosovichev, A. G. (1988). "The Internal Rotation of the Sun from Helioseismological Data". In: *Soviet Astronomy Letters* 14, page 145 (cited on pages 13, 47, 221, 256).

Kosovichev, A. G. (1993). "Seismic measurements of the helium abundance and the depth of stellar convection zones". In: *MNRAS* 265, page 1053 (cited on pages 154, 155).
— (1999). "Inversion methods in helioseismology and solar tomography." In: *Journal of Computational and Applied Mathematics* 109, pages 1–39 (cited on pages 88, 134, 222, 268).
— (2011). "Advances in Global and Local Helioseismology: An Introductory Review". In: *Lecture Notes in Physics, Berlin Springer Verlag*. Edited by J.-P. Rozelot and C. Neiner. Volume 832. Lecture Notes in Physics, Berlin Springer Verlag, page 3 (cited on pages 17, 266).
Kosovichev, A. G. and A. V. Fedorova (1991). "Construction of a Seismic Model of the Sun". In: *Soviet Astronomy* 35, page 507 (cited on pages 13, 17, 154, 222, 224, 235, 257).
Kosovichev, A. G., J. Schou, et al. (1997). "Structure and Rotation of the Solar Interior: Initial Results from the MDI Medium-L Program". In: *Sol. Phys.* 170, pages 43–61 (cited on pages 47, 224, 236).
Krief, M., A. Feigel, and D. Gazit (2016). "Line Broadening and the Solar Opacity Problem". In: *ApJ* 824, page 98 (cited on page 223).
Kumar, P., S. Talon, and J.-P. Zahn (1999). "Angular Momentum Redistribution by Waves in the Sun". In: *ApJ* 520, pages 859–870 (cited on pages 31, 221, 225, 256).
Le Pennec, M. et al. (2015). "First New Solar Models with OPAS Opacity Tables". In: *ApJl* 813, page L42 (cited on pages 168, 213).
LeBlanc, F. and G. Alecian (2004). "New method for fast and easy computation of radiative accelerations in stars". In: *MNRAS* 352, pages 1329–1334 (cited on page 34).
Lebreton, Y. and M. J. Goupil (2012). "Seismic signature of envelope penetrative convection: the CoRoT star HD 52265". In: *A&Ap* 544, page L13 (cited on pages 156, 178, 215).
Lebreton, Y., M. J. Goupil, and J. Montalbán (2014a). "How accurate are stellar ages based on stellar models?. I. The impact of stellar models uncertainties". In: *EAS Publications Series*. Volume 65. EAS Publications Series, pages 99–176 (cited on pages 15, 132).
— (2014b). "How accurate are stellar ages based on stellar models?. II. The impact of asteroseismology". In: *EAS Publications Series*. Volume 65. EAS Publications Series, pages 177–223 (cited on pages 15, 132).
Ledoux, P. (1949). *Contribution a l'etude de la structure interne des etoiles et de leur stabilite.* (Cited on page 17).
Ledoux, P. and P. Smeyers (1966). "Sur le Spectre des Oscillations Non Radiales d'un Modèle Stellaire". In: *Academie des Sciences Paris Comptes Rendus Serie B Sciences Physiques* 262, pages 841–844 (cited on page 13).
Ledoux, P. and T. Walraven (1958). "Variable Stars." In: *Handbuch der Physik* 51, pages 353–604 (cited on page 13).
Leighton, R. B. (1960). In: *Aerodynamic Phenomena in Stellar Atmospheres*. Edited by R. N. Thomas. Volume 12. IAU Symposium, pages 321–325 (cited on page 13).
Leighton, R. B., R. W. Noyes, and G. W. Simon (1962). "Velocity Fields in the Solar Atmosphere. I. Preliminary Report." In: *ApJ* 135, page 474 (cited on pages 13, 221).
Lin, C.-H., H. M. Antia, and S. Basu (2007). "Seismic Study of the Chemical Composition of the Solar Convection Zone". In: *ApJ* 668, pages 603–610 (cited on page 223).
Lund, M. N. et al. (2017). "Standing on the Shoulders of Dwarfs: the Kepler Asteroseismic LEGACY Sample. I. Oscillation Mode Parameters". In: *ApJ* 835, page 172 (cited on pages 71, 76, 269).
Lynden-Bell, D. and J. P. Ostriker (1967). "On the stability of differentially rotating bodies". In: *MNRAS* 136, page 293 (cited on pages 17, 53, 54, 82, 111).

Maeder, A. (1997). "Stellar evolution with rotation. II. A new approach for shear mixing." In: *A&Ap* 321, pages 134–144 (cited on page 30).
— (1999). "Stellar evolution with rotation IV: von Zeipel's theorem and anisotropic losses of mass and angular momentum". In: *A&Ap* 347, pages 185–193 (cited on page 30).
— (2002). "Stellar evolution with rotation. IX. The effects of the production of asymmetric nebulae on the internal evolution". In: 392, pages 575–584 (cited on page 30).
— (2009). *Physics, Formation and Evolution of Rotating Stars* (cited on pages 21, 30).
Maeder, A. and G. Meynet (2000). "Stellar evolution with rotation. VI. The Eddington and Omega -limits, the rotational mass loss for OB and LBV stars". In: *A&Ap* 361, pages 159–166 (cited on page 30).
— (2001). "Stellar evolution with rotation. VII. . Low metallicity models and the blue to red supergiant ratio in the SMC". In: *A&Ap* 373, pages 555–571 (cited on page 30).
Maeder, A. and J.-P. Zahn (1998). "Stellar evolution with rotation. III. Meridional circulation with MU -gradients and non-stationarity". In: *A&Ap* 334, pages 1000–1006 (cited on page 30).
Marchenkov, K., I. Roxburgh, and S. Vorontsov (2000). "Non-linear inversion for the hydrostatic structure of the solar interior". In: *MNRAS* 312, pages 39–50 (cited on pages 17, 222).
Marques, J. P., M. J. Goupil, et al. (2013). "Seismic diagnostics for transport of angular momentum in stars. I. Rotational splittings from the pre-main sequence to the red-giant branch". In: *A&Ap* 549, A74 (cited on pages 26, 121).
Marques, J. P., M. J. P. F. G. Monteiro, and J. M. Fernandes (2008). "Grids of stellar evolution models for asteroseismology (cesam + posc)". In: *ApSS* 316, pages 173–178 (cited on page 118).
Masters, G. (1979). "Observational constraints on the chemical and thermal structure of the Earth's deep interior". In: *Geophysical Journal International* 57, pages 507–534 (cited on pages 85, 86, 134, 135, 154).
Mathis, S. and J.-P. Zahn (2005). "Transport and mixing in the radiation zones of rotating stars. II. Axisymmetric magnetic field". In: *A&Ap* 440, pages 653–666 (cited on page 31).
Mathur, S. et al. (2012). "A Uniform Asteroseismic Analysis of 22 Solar-type Stars Observed by Kepler". In: *ApJ* 749, page 152 (cited on page 178).
Mein, P. (1966). "Champ macroscopique des vitesses dans l'atmosphère solaire d'après les mesures de déplacements des raies de Fraunhofer". In: *Annales d'Astrophysique* 29, page 153 (cited on page 221).
Mendoza, C. (2017). "Computation of astrophysical opacities". In: *ArXiv e-prints* (cited on pages 223, 224).
Metcalfe, T. S., W. J. Chaplin, et al. (2012). "Asteroseismology of the Solar Analogs 16 Cyg A and B from Kepler Observations". In: *ApJl* 748, page L10 (cited on pages 148, 178, 180, 181, 194–196, 199).
Metcalfe, T. S., M. J. P. F. G. Monteiro, et al. (2010). "Asteroseismology of solar-type stars with Kepler: II. Stellar modeling". In: *Astronomische Nachrichten* 331, page 977 (cited on pages 16, 107).
Meynet, G. and A. Maeder (1997). "Stellar evolution with rotation. I. The computational method and the inhibiting effect of the μ-gradient." In: *A&Ap* 321, pages 465–476 (cited on page 30).
— (2000). "Stellar evolution with rotation. V. Changes in all the outputs of massive star models". In: *A&Ap* 361, pages 101–120 (cited on page 30).
— (2002). "Stellar evolution with rotation. VIII. Models at Z = 10^{-5} and CNO yields for early galactic evolution". In: *A&Ap* 390, pages 561–583 (cited on page 30).

Meynet, G. and A. Maeder (2003). "Stellar evolution with rotation. X. Wolf-Rayet star populations at solar metallicity". In: *A&Ap* 404, pages 975–990 (cited on page 30).
— (2005). "Stellar evolution with rotation. XI. Wolf-Rayet star populations at different metallicities". In: *A&Ap* 429, pages 581–598 (cited on page 30).
Miglio, A., L. Girardi, et al. (2015). "Solar-Like Oscillating Stars as Standard Clocks and Rulers for Galactic Studies". In: *Astrophysics and Space Science Proceedings* 39, page 11 (cited on page 132).
Miglio, A. and J. Montalbán (2005). "Constraining fundamental stellar parameters using seismology. Application to α Centauri AB". In: *A&Ap* 441, pages 615–629 (cited on pages 14, 16, 161).
Miglio, A., J. Montalbán, and C. Maceroni (2007). "12 Boötis: a test-bed for extra-mixing processes in stars". In: *MNRAS* 377, pages 373–382 (cited on pages 16, 168, 211, 262).
Miglio, A., J. Montalbán, A. Noels, et al. (2008). "Probing the properties of convective cores through g modes: high-order g modes in SPB and γ Doradus stars". In: *MNRAS* 386, pages 1487–1502 (cited on page 46).
Mihalas, D., W. Dappen, and D. G. Hummer (1988). "The equation of state for stellar envelopes. II - Algorithm and selected results". In: *ApJ* 331, pages 815–825 (cited on pages 27, 32).
Mihalas, D., D. G. Hummer, et al. (1990). "The equation of state for stellar envelopes. IV - Thermodynamic quantities and selected ionization fractions for six elemental mixes". In: *ApJ* 350, pages 300–308 (cited on pages 27, 32).
Mondet, G. et al. (2015). "Opacity Calculations for Solar Mixtures". In: *ApJs* 220, page 2 (cited on pages 33, 168, 213, 225).
Montalbán, J. et al. (2013). "Testing Convective-core Overshooting Using Period Spacings of Dipole Modes in Red Giants". In: *ApJ* 766, page 118 (cited on pages 43, 51).
Monteiro, M. J. P. F. G., J. Christensen-Dalsgaard, and M. J. Thompson (1994). "Seismic study of overshoot at the base of the solar convective envelope". In: *A&Ap* 283, pages 247–262 (cited on pages 16, 156, 256).
— (2000). "Seismic study of stellar convective regions: the base of the convective envelope in low-mass stars". In: *MNRAS* 316, pages 165–172 (cited on pages 16, 156).
Mosser, B., K. Belkacem, et al. (2010). "Red-giant seismic properties analyzed with CoRoT". In: *A&Ap* 517, A22 (cited on page 15).
Mosser, B., M. J. Goupil, et al. (2012). "Spin down of the core rotation in red giants". In: *A&Ap* 548, A10 (cited on pages 24, 31, 43, 51, 226).
Nahar, S. N. and A. K. Pradhan (2016). "Large Enhancement in High-Energy Photoionization of Fe XVII and Missing Continuum Plasma Opacity". In: *Physical Review Letters* 116.23, page 235003 (cited on pages 223, 224, 229, 255).
Neiner, C. et al. (2009). "The pulsations of the B5IVe star HD 181231 observed with CoRoT and ground-based spectroscopy". In: *A&Ap* 506, pages 143–151 (cited on page 51).
Ouazzani, R.-M., M.-A. Dupret, and D. R. Reese (2012). "Pulsations of rapidly rotating stars. I. The ACOR numerical code". In: *A&Ap* 547, A75 (cited on page 47).
Pamyatnykh, A. A. (1999). "Pulsational Instability Domains in the Upper Main Sequence". In: *ACA* 49, pages 119–148 (cited on page 48).
Pietrinferni, A., S. Cassisi, and M. Salaris (2010). "The impact of an updated ^{14}N(p, γ)^{15}O reaction rate on advanced evolutionary stages of low-mass stellar models". In: *A&Ap* 522, A76 (cited on page 32).
Pijpers, F. P. (2006). *Methods in helio- and asteroseismology*. Imperial College Press (cited on page 15).

Pijpers, F. P. and M. J. Thompson (1994). "The SOLA method for helioseismic inversion". In: *A&Ap* 281, pages 231–240 (cited on pages 68, 70, 109, 112, 133, 141, 155, 159, 160, 178, 187, 197, 201–203, 226, 236, 240, 257, 272).

Pinçon, C., K. Belkacem, and M. J. Goupil (2016). "Generation of internal gravity waves by penetrative convection". In: *A&Ap* 588, A122 (cited on page 43).

Pinsonneault, M. H. et al. (1989). "Evolutionary models of the rotating sun". In: *ApJ* 338, pages 424–452 (cited on page 31).

Potekhin, A. Y. et al. (1999). "Transport properties of degenerate electrons in neutron star envelopes and white dwarf cores". In: *A&Ap* 346, pages 345–353 (cited on pages 92, 179, 241).

Pourbaix, D. and H. M. J. Boffin (2016). "Parallax and masses of α Centauri revisited". In: *A&Ap* 586, A90 (cited on page 23).

Prandtl, L. (1925). "Bericht über Untersuchungen zur ausgebildeten Turbulenz". In: *Z. Angew. Math. Mech.* 5, pages 136–139 (cited on page 25).

Provost, J. et al. (1991). "The Spectrum of Gravity Modes as a Function of the Solar Structure - Model with a Mixed Core". In: *Solar Physics* 133, pages 139–140 (cited on page 281).

Rabello-Soares, M. C., S. Basu, and J. Christensen-Dalsgaard (1999). "On the choice of parameters in solar-structure inversion". In: *MNRAS* 309, pages 35–47 (cited on pages 72, 160, 228).

Ramírez, I., J. Meléndez, and M. Asplund (2009). "Accurate abundance patterns of solar twins and analogs. Does the anomalous solar chemical composition come from planet formation?" In: *A&Ap* 508, pages L17–L20 (cited on pages 178–181, 186, 190, 193, 195, 199, 200).

Rauer, H. et al. (2014). "The PLATO 2.0 mission". In: *Experimental Astronomy* 38, pages 249–330 (cited on pages 82, 133, 155, 186).

Reese, D. R. (2013). "Stable higher order finite-difference schemes for stellar pulsation calculations". In: *A&Ap* 555, A148 (cited on pages 87, 137).

— (2016). *AIMS: Asteroseismic Inference on a Massive Scale*. Astrophysics Source Code Library (cited on page 280).

Reese, D. R., J. P. Marques, et al. (2012). "Estimating stellar mean density through seismic inversions". In: *A&Ap* 539, A63 (cited on pages 72, 105, 108, 110, 111, 113, 117, 118, 133, 142, 143, 145, 155, 160, 165, 173, 178, 182, 184, 201, 216, 226, 241, 272, 275).

Reese, D. R., V. Prat, C. Barban, C. van 't Veer-Menneret, et al. (2013). "Mode visibilities in rapidly rotating stars". In: *A&Ap* 550, A77 (cited on page 47).

Reese, D. R., V. Prat, C. Barban, C. van't Veer-Menneret, et al. (2012). "Signatures of rotation in oscillation spectra". In: *SF2A-2012: Proceedings of the Annual meeting of the French Society of Astronomy and Astrophysics*. Edited by S. Boissier et al., pages 211–214 (cited on page 47).

Rhodes Jr., E. J., R. K. Ulrich, and F.-L. Deubner (1979). "A new technique for measuring solar rotation". In: *ApJ* 227, pages 629–637 (cited on pages 13, 221).

Rhodes Jr., E. J., R. K. Ulrich, and G. W. Simon (1977). "Observations of nonradial p-mode oscillations on the sun". In: *ApJ* 218, pages 901–919 (cited on page 221).

Richard, O., W. A. Dziembowski, et al. (1998). "On the accuracy of helioseismic determination of solar helium abundance". In: *A&Ap* 338, pages 756–760 (cited on page 222).

Richard, O., G. Michaud, and J. Richer (2001). "Iron Convection Zones in B, A, and F Stars". In: *ApJ* 558, pages 377–391 (cited on page 34).

— (2005). "Implications of WMAP Observations on Li Abundance and Stellar Evolution Models". In: *ApJ* 619, pages 538–548 (cited on page 31).

Richard, O., G. Michaud, J. Richer, et al. (2002). "Models of Metal-poor Stars with Gravitational Settling and Radiative Accelerations. I. Evolution and Abundance Anomalies". In: *ApJ* 568, pages 979–997 (cited on page 31).

Richard, O., S. Théado, and S. Vauclair (2004). "Updated Toulouse solar models including the diffusion-circulation coupling and the effect of μ-gradients". In: *Sol. Phys.* 220, pages 243–259 (cited on page 257).

Richard, O. and S. Vauclair (1997). "Local mixing near the solar core, neutrino fluxes and helioseismology." In: *A&Ap* 322, pages 671–673 (cited on page 257).

Richard, O., S. Vauclair, et al. (1996). "New solar models including helioseismological constraints and light-element depletion." In: *A&Ap* 312, pages 1000–1011 (cited on page 257).

Rogers, F. J. and A. Nayfonov (2002). "Updated and Expanded OPAL Equation-of-State Tables: Implications for Helioseismology". In: *ApJ* 576, pages 1064–1074 (cited on pages 27, 32, 97, 168, 209, 223, 224, 229, 241).

Rogers, F. J., F. J. Swenson, and C. A. Iglesias (1996). "OPAL Equation-of-State Tables for Astrophysical Applications". In: *ApJ* 456, page 902 (cited on pages 27, 168).

Roxburgh, I. W. (1964a). "On stellar rotation, I. The rotation of upper main-sequence stars". In: *MNRAS* 128, page 157 (cited on page 30).

— (1964b). "On stellar rotation, II. The rotation of lower main-sequence stars". In: *MNRAS* 128, page 237 (cited on page 30).

— (1989). "Integral constraints on convective overshooting". In: *A&Ap* 211, pages 361–364 (cited on page 29).

— (2010). "Asteroseismology of solar and stellar models". In: *ApSS* 328, pages 3–11 (cited on pages 17, 104, 133).

— (2015a). "Surface layer independent model fitting by phase matching: theory and application to HD 49933 and HD 177153 (aka Perky)". In: *A&Ap* 574, A45 (cited on page 16).

— (2015b). "Surface layer independent model fitting by phase matching: theory and application to HD 49933 and HD 177153 (aka Perky)". In: *A&Ap* 574, A45 (cited on pages 17, 104, 133).

Roxburgh, I. W (2016). "16CygA&B and Kepler Legacy values : Differences between the values of frequencies by different fitters". In: *ArXiv e-prints* (cited on page 177).

Roxburgh, I. W. (2016a). "Asteroseismic model fitting by comparing ε_{nl} values". In: *A&Ap* 585, A63 (cited on page 16).

— (2016b). "Asteroseismic model fitting by comparing ε_{nl} values (Corrigendum)". In: *A&Ap* 586, page C2 (cited on page 16).

— (2017). "Anomalies in the Kepler Asteroseismic Legacy Project Data A re-analysis of 16 Cyg A & B, KIC 8379927 and 6 solar-like stars". In: *A&Ap* 604, A42 (cited on pages 71, 271, 276).

Roxburgh, I. W. and S. V. Vorontsov (1994a). "Seismology of the Solar Envelope - the Base of the Convective Zone as Seen in the Phase Shift of Acoustic Waves". In: *MNRAS* 268, page 880 (cited on pages 222, 262).

— (1994b). "The Asymptotic Theory of Stellar Acoustic Oscillations - a Fourth-Order Approximation for Low-Degree Modes". In: *MNRAS* 268, page 143 (cited on page 45).

— (1996). "An asymptotic description of solar acoustic oscillation of low and intermediate degree". In: *MNRAS* 278, pages 940–946 (cited on page 45).

— (2003). "The ratio of small to large separations of acoustic oscillations as a diagnostic of the interior of solar-like stars". In: *A&Ap* 411, pages 215–220 (cited on pages 45, 106, 227, 270).

Roxburgh, I. and S. Vorontsov (2003). "Diagnostics of the Internal Structure of Stars using the Differential Response Technique". In: *ApSS* 284, pages 187–191 (cited on page 17).

Salmon, S. et al. (2012). "Testing the effects of opacity and the chemical mixture on the excitation of pulsations in B stars of the Magellanic Clouds". In: *MNRAS* 422, pages 3460–3474 (cited on pages 34, 225).

Schou, J., H. M. Antia, et al. (1998). "Helioseismic Studies of Differential Rotation in the Solar Envelope by the Solar Oscillations Investigation Using the Michelson Doppler Imager". In: *ApJ* 505, pages 390–417 (cited on pages 32, 82, 236).

Schou, J., J. Christensen-Dalsgaard, and M. J. Thompson (1994). "On comparing helioseismic two-dimensional inversion methods". In: *ApJ* 433, pages 389–416 (cited on pages 47, 141).

Schuler, S. C. et al. (2011). "Detailed Abundances of the Solar Twins 16 Cygni A and B: Constraining Planet Formation Models". In: *ApJl* 737, page L32 (cited on page 199).

Schwarzschild, K. (1906). "On the equilibrium of the Sun's atmosphere". In: *Nachrichten von der Königlichen Gesellschaft der Wissenschaften zu Göttingen. Math.-phys. Klasse, 195, p. 41–53* 195, pages 41–53 (cited on page 26).

Scuflaire, R. (1974a). "Space oscillations of stellar non radial eigen-functions". In: *A&Ap* 34, pages 449–451 (cited on page 42).

— (1974b). "The Non Radial Oscillations of Condensed Polytropes". In: *A&Ap* 36, page 107 (cited on page 13).

Scuflaire, R., J. Montalbán, et al. (2008). "The Liège Oscillation code". In: *ApSS* 316, pages 149–154 (cited on pages 93, 121, 145, 168, 179, 198, 226, 241, 257, 270).

Scuflaire, R., S. Théado, et al. (2008). "CLÉS, Code Liégeois d'Évolution Stellaire". In: *ApSS* 316, pages 83–91 (cited on pages 26, 92, 145, 168, 179, 198, 206, 226, 241, 257, 270).

Seaton, M. J. (2005). "Opacity Project data on CD for mean opacities and radiative accelerations". In: *MNRAS* 362, pages L1–L3 (cited on page 33).

Serenelli, A. (2016). "Alive and well: A short review about standard solar models". In: *European Physical Journal A* 52, page 78 (cited on page 223).

Serenelli, A. M. et al. (2009). "New Solar Composition: The Problem with Solar Models Revisited". In: *ApJl* 705, pages L123–L127 (cited on pages 225, 255, 257).

Severnyi, A. B., V. A. Kotov, and T. T. Tsap (1976). "Observations of solar pulsations". In: *Nature* 259, pages 87–89 (cited on page 221).

Sharp, C. M., R. C. Smith, and D. L. Moss (1977). "On stellar models with circulation-free rotation laws". In: *MNRAS* 179, pages 699–704 (cited on page 30).

Silva Aguirre, V., S. Basu, et al. (2013). "Stellar Ages and Convective Cores in Field Main-sequence Stars: First Asteroseismic Application to Two Kepler Targets". In: *ApJ* 769, page 141 (cited on page 16).

Silva Aguirre, V. et al. (2017a). "Standing on the Shoulders of Dwarfs: the Kepler Asteroseismic LEGACY Sample. II.Radii, Masses, and Ages". In: *ApJ* 835, page 173 (cited on page 219).

— (2017b). "Standing on the Shoulders of Dwarfs: the Kepler Asteroseismic LEGACY Sample. II.Radii, Masses, and Ages". In: *ApJ* 835, page 173 (cited on page 269).

Soderblom, D. R. (2010). "The Ages of Stars". In: *ARA&A* 48, pages 581–629 (cited on page 107).

Sonoi, T. et al. (2015). "Surface-effect corrections for solar-like oscillations using 3D hydrodynamical simulations. I. Adiabatic oscillations". In: *A&Ap* 583, A112 (cited on pages 76, 172, 279).

Spiegel, E. A. and J.-P. Zahn (1992). "The solar tachocline". In: *A&Ap* 265, pages 106–114 (cited on pages 13, 256).

Spruit, H. C. (1999). "Differential rotation and magnetic fields in stellar interiors". In: *A&Ap* 349, pages 189–202 (cited on pages 221, 256).

Stancliffe, R. J. et al. (2016). "Confronting uncertainties in stellar physics. II. Exploring differences in main-sequence stellar evolution tracks". In: *A&Ap* 586, A119 (cited on page 32).

Stein, R. F. and J. Leibacher (1974). "Waves in the solar atmosphere". In: *ARA&A* 12, pages 407–435 (cited on page 13).

Takata, M. (2016). "Asymptotic analysis of dipolar mixed modes of oscillations in red giant stars". In: *Publications of the Astronomical Society of Japan* 68, page 109 (cited on page 43).

Takata, M. and M. H. Montgomery (2002). "Seismic Inversions for White Dwarf Stars". In: *IAU Colloq. 185: Radial and Nonradial Pulsationsn as Probes of Stellar Physics*. Edited by C. Aerts, T. R. Bedding, and J. Christensen-Dalsgaard. Volume 259. Astronomical Society of the Pacific Conference Series, page 606 (cited on pages 17, 52, 104, 155, 257).

Takata, M. and H. Shibahashi (2001). "Solar Metal Abundance Inferred from Helioseismology". In: *Recent Insights into the Physics of the Sun and Heliosphere: Highlights from SOHO and Other Space Missions*. Edited by P. Brekke, B. Fleck, and J. B. Gurman. Volume 203. IAU Symposium, page 43 (cited on pages 223, 236).

Tarantola, Albert (2005). *Inverse Problem Theory and Methods for Model Parameter Estimation*. Society for Industrial and Applied Mathematics (cited on pages 16, 68, 118).

Tassoul, M. (1980). "Asymptotic approximations for stellar nonradial pulsations". In: *ApJs* 43, pages 469–490 (cited on pages 43, 44, 46, 108, 112, 117, 140).

Thompson, M. J. (1993). "Seismic Investigation of the Sun's Internal Structure and Rotation". In: *GONG 1992. Seismic Investigation of the Sun and Stars*. Edited by T. M. Brown. Volume 42. Astronomical Society of the Pacific Conference Series, page 141 (cited on page 70).

Thompson, M. J. et al. (1996). "Differential Rotation and Dynamics of the Solar Interior". In: *Science* 272, pages 1300–1305 (cited on page 17).

Thoul, A. A., J. N. Bahcall, and A. Loeb (1994). "Element diffusion in the solar interior". In: *ApJ* 421, pages 828–842 (cited on pages 35, 92, 144, 179, 181, 182, 184, 190, 191, 194, 196, 198, 199).

Tucci Maia, M., J. Meléndez, and I. Ramírez (2014). "High Precision Abundances in the 16 Cyg Binary System: A Signature of the Rocky Core in the Giant Planet". In: *ApJl* 790, page L25 (cited on pages 178, 181, 186, 195, 199, 200).

Turck-Chièze, S., S. Couvidat, et al. (2004). "Surprising Sun: A New Step Towards a Complete Picture?" In: *Physical Review Letters* 93.21, page 211102 (cited on page 225).

Turck-Chièze, S., D. Gilles, et al. (2013). "Radiative properties of stellar envelopes: Comparison of asteroseismic results to opacity calculations and measurements for iron and nickel". In: *High Energy Density Physics* 9, pages 473–479 (cited on page 225).

Turcotte, S. et al. (1998). "Consistent Solar Evolution Model Including Diffusion and Radiative Acceleration Effects". In: *ApJ* 504, pages 539–558 (cited on pages 34, 35, 255).

Ulrich, R. K. (1970). "The Five-Minute Oscillations on the Solar Surface". In: *ApJ* 162, page 993 (cited on page 221).

Ulrich, R. K., E. J. Rhodes Jr., and F.-L. Deubner (1979). "The effect of a radial rotational velocity gradient on p-mode eigenfrequencies". In: *ApJ* 227, pages 638–644 (cited on page 13).

Unno, W. et al. (1989). *Nonradial oscillations of stars* (cited on pages 40, 44, 50, 89).

Vandakurov, Y. V. (1967). "The Frequency Distribution of Stellar Oscillations." In: *Astronomicheskii Zhurnal* 44, page 786 (cited on pages 13, 108, 112, 116, 221).

Verma, K., H. M. Antia, et al. (2014). "A Theoretical Study of Acoustic Glitches in Low-mass Main-sequence Stars". In: *ApJ* 794, page 114 (cited on page 16).
Verma, K., J. P. Faria, et al. (2014). "Asteroseismic Estimate of Helium Abundance of a Solar Analog Binary System". In: *ApJ* 790, page 138 (cited on pages 134, 145, 148, 178–181, 190, 193–195, 199, 200, 213).
Verma, K., S. Hanasoge, et al. (2016). "Asteroseismic determination of fundamental parameters of Sun-like stars using multilayered neural networks". In: *MNRAS* 461, pages 4206–4214 (cited on page 16).
Verma, K., K. Raodeo, et al. (2017). "Seismic Measurement of the Locations of the Base of Convection Zone and Helium Ionization Zone for Stars in the Kepler Seismic LEGACY Sample". In: *ApJ* 837, page 47 (cited on page 156).
Vick, M. et al. (2010). "AmFm and lithium gap stars. Stellar evolution models with mass loss". In: *A&Ap* 521, A62 (cited on page 31).
— (2011). "Abundance anomalies in pre-main-sequence stars. Stellar evolution models with mass loss". In: *A&Ap* 526, A37 (cited on page 31).
— (2013). "Population II stars and the Spite plateau. Stellar evolution models with mass loss". In: *A&Ap* 552, A131 (cited on page 31).
Vogel, Curtis R. (2002). *Computational Methods for Inverse Problems*. Philadelphia, PA, USA: Society for Industrial and Applied Mathematics (cited on pages 16, 68).
Vorontsov, S. V. (2001). "Inversion for the solar hydrostatic structure". In: *SOHO 10/GONG 2000 Workshop: Helio- and Asteroseismology at the Dawn of the Millennium*. Edited by A. Wilson and P. L. Pallé. Volume 464. ESA Special Publication, pages 563–566 (cited on page 222).
Vorontsov, S. V. et al. (2013). "Helioseismic calibration of the equation of state and chemical composition in the solar convective envelope". In: *MNRAS* 430, pages 1636–1652 (cited on pages 223, 255).
— (2014). "Helioseismic measurements in the solar envelope using group velocities of surface waves". In: *MNRAS* 441, pages 3296–3305 (cited on pages 223, 225, 236, 239, 253, 255, 256).
White, T. R., T. R. Bedding, et al. (2011). "Calculating Asteroseismic Diagrams for Solar-like Oscillations". In: *ApJ* 743, page 161 (cited on page 112).
White, T. R., D. Huber, et al. (2013). "Interferometric radii of bright Kepler stars with the CHARA Array: θ Cygni and 16 Cygni A and B". In: *MNRAS* 433, pages 1262–1270 (cited on pages 148, 178, 181, 186, 195, 199).
Yang, J. Y. and Y. Li (2007). "Testing turbulent convection theory in solar models - II. Solar p-mode oscillations". In: *MNRAS* 375, pages 403–414 (cited on page 29).
Zahn, J.-P. (1991). "Convective penetration in stellar interiors". In: *A&Ap* 252, pages 179–188 (cited on page 215).
— (1992). "Circulation and turbulence in rotating stars". In: *A&Ap* 265, pages 115–132 (cited on pages 30, 31).
— (1999). "Beyond the Mixing-Length Treatment: Why and How?" In: *Stellar Structure: Theory and Test of Connective Energy Transport*. Edited by A. Gimenez, E. F. Guinan, and B. Montesinos. Volume 173. Astronomical Society of the Pacific Conference Series, page 121 (cited on page 256).
— (2005). "The Spite plateau: a puzzle and a challenge for the stellar physicist". In: *From Lithium to Uranium: Elemental Tracers of Early Cosmic Evolution*. Edited by V. Hill, P. Francois, and F. Primas. Volume 228. IAU Symposium, pages 41–46 (cited on page 31).
— (2007). "Hydrodynamic models of the tachocline". In: *The Solar Tachocline*. Edited by D. W. Hughes, R. Rosner, and N. O. Weiss, page 89 (cited on page 155).

Zdravkov, T. and A. A. Pamyatnykh (2008). "Can opacity changes help to reproduce the hybrid star pulsations?" In: *Communications in Asteroseismology* 157, pages 385–386 (cited on page 225).

Zhang, C.-G. et al. (2013). "Seismic study of solar convection and overshooting: results of nonlocal convection". In: *Research in Astronomy and Astrophysics* 13, pages 1127–1140 (cited on page 256).

Zhang, Q. S. and Y. Li (2012a). "Turbulent Convection Model in the Overshooting Region. I. Effects of the Convective Mixing in the Solar Overshooting Region". In: *ApJ* 746, page 50 (cited on page 256).

— (2012b). "Turbulent Convection Model in the Overshooting Region. II. Theoretical Analysis". In: *ApJ* 750, page 11 (cited on page 256).

Appendices

10. List of publications

10.1 Publications in peer-reviewed journals

- Buldgen, G.; Reese, D.R.; Dupret, M.-A. and Samadi, R. *Stellar acoustic radii, mean densities, and ages from seismic inversion techniques*, (2015) Astronomy and Astrophysics, 574, A42.
- Buldgen, G.; Reese, D.R. and Dupret, M.-A. *Using seismic inversions to obtain an indicator of internal mixing processes in main-sequence solar-like stars*, (2015) Astronomy and Astrophysics, 583, A62.
- Buldgen, G.; Reese, D.R. and Dupret, M.-A. *Constraints on the structure of 16 Cygni A and 16 Cygni B using inversion techniques*, (2016) Astronomy and Astrophysics, 585, A109.
- Reese, D.R.; Chaplin, W.J.; Davies, G.R.; Miglio, A.; Antia, H.M.; Ball, W.H.; Basu, S.; Buldgen, G.; Christensen-Dalsgaard, J.; Coelho, H.R.; Hekker, S.; Houdek, G.; Lebreton, Y.; Mazumdar, A.; Metcalfe, T.S.; Silva Aguirre, V.; Stello, D. and Verma, K. *SpaceInn hare-and-hounds exercise: Estimation of stellar properties using space-based asteroseismic data*, (2016) Astronomy and Astrophysics, 592, A14.
- Buldgen, G.; Salmon, S.J.A.J.; Reese, D.R. and Dupret, M.-A. *In-depth study of 16CygB using inversion techniques*, (2016) Astronomy and Astrophysics, 596, A73.
- Buldgen, G.; Reese, D.R. and Dupret, M.-A. *Analysis of the linear approximation of seismic inversions for various structural pairs*, (2017) Astronomy and Astrophysics, 598, A21.
- Buldgen, G.; Salmon, S.J.A.J; Noels, A.; Scuflaire, R.; Reese, D.R.; Dupret, M.-A.; Colgan, J.; Fontes, C.J.; Eggenberger, P.; Hakel, P.; Kilcrease, D.P. and Turck-Chièze, S. *Seismic inversion of the solar entropy: A case for improving the Standard Solar Model*, (2017) Astronomy and Astrophysics, In Press.
- Buldgen, G.; D. R. Reese, D.R.; and Dupret, M.-A. *Constraining convective regions with asteroseismic linear structural inversions*, submitted for publication in Astronomy and Astrophysics.
- Buldgen G.; Salmon, S. J. A. J.; Noels, A.; Scuflaire, R.; Dupret, M.-A.; and D. R. Reese

Determining the metallicity of the solar envelope using seismic inversion techniques, accepted for publication in The Monthly Notices of the Royal Astronomical Society.

- Buldgen, G.; Salmon, S.J.A.J; Godart, M.; Noels, A.; Scuflaire, R.; Reese, D.R.; Dupret, M.-A.; Colgan, J.; Fontes, C.J.; Eggenberger, P.; Hakel, P.; Kilcrease, D.P. and Richard, O. *Inversions of the Ledoux discriminant: a closer look at the tachocline*, submitted for publication in The Monthly Notices of the Royal Astronomical Society.

10.2 Publications in conference proceedings

- Buldgen, G.; Reese, D.R.; Dupret, M.-A. and Samadi, R. *Stellar acoustic radii and ages from seismic inversion techniques*, (2015) European Physical Journal Web of Conferences, 101, 06015.
- Buldgen, G.; Reese, D.R. and Dupret, M.-A. *Asteroseismic inversions in the Kepler era: application to the Kepler LEGACY sample*, (2017) to appear in the proceedings of the *TASC*2/*KASC*9 Workshop.
- Buldgen, G.; Reese, D.R. and Dupret, M.-A. *Linear approximation of seismic inversions: new kernels and structural effects*, (2017) to appear in the proceedings of the AstroFluid 2016 conference.

11. List of oral presentations

11.1 Presentation in international conferences

- *Asteroseismic Inversions in the Context of PLATO*, (2014) contributed talk at the Plato2.0 Science Conference in Taormina.
- *Constraining mixing processes in 16CygA using Kepler data and seismic inversion techniques*, (2015) contributed talk at the *TASC*1/*KASC*8 workshop.
- *Constraining mixing processes in 16CygA&B using Kepler data and seismic inversion techniques*, (2015) contributed talk at the SOLARNET *III* / HELAS *VII* / SpaceInn Conference.
- *Asteroseismic inversions in the Kepler era: application to the Kepler LEGACY sample*, (2016) contributed talk at the *TASC*2/*KASC*9 workshop.

11.2 Seminars

- *Development of inverse methods in asteroseismology*, (2014) seminar held at the School of Physics and Astronomy, University of Birmingham.
- *Development and application of inversion techniques in asteroseismology*, (2015) seminar held at the Stellar Astrophysics Centre, Aarhus.
- *Development and application of inversion techniques in asteroseismology*, (2015) seminar held at the Institute of Astronomy, Leuven.
- *Inversion techniques in asteroseismology: theoretical developments and applications to Solar-Like Stars*, (2016) seminar held at the Laboratoire Univers et Particules, Université de Montpellier.
- *Inversion Techniques in asteroseismology: structural kernels and regularization problems*, (2016) seminar held at the Stellar Astrophysics Centre, Aarhus.
- *Structural inversion Techniques in helio- and asteroseismology*, (2017) seminar held at Paris Observatory.
- *New Methods in Helio- and Asteroseismology: Consequences for the Solar Abundance Problem and Stellar Modelling*, (2017) seminar held at Geneva Observatory.